

Aero

TJ778
.M41
.G24
no. 208

**ACTIVE CONTROL OF ROTATING STALL
IN AXIAL COMPRESSORS**

by

James D. Paduano

GTL Report #208

March 1992



GAS TURBINE LABORATORY
MASSACHUSETTS INSTITUTE OF TECHNOLOGY
CAMBRIDGE, MASSACHUSETTS

**ACTIVE CONTROL OF ROTATING STALL
IN AXIAL COMPRESSORS**

by

James D. Paduano

GTL Report #208

March 1992

This project was supported by the U.S. Air Force Office of Scientific Research, Dr. J. McMichael, Technical Monitor, and by the Office of Naval Research, Dr. R.J. Hansen, Technical Monitor.

Active Control of Rotating Stall in Axial Compressors

by

James Donald Paduano

Abstract

An active control system has been implemented on a low-speed single-stage axial compressor. This control system stabilizes the perturbations which normally lead to rotating stall, thus extending the range of operation of the compressor to a flow coefficient 23% below the natural stall flow coefficient. Sensing of the perturbations which precede stall is accomplished using a circumferential set of hot wires mounted at an axial station ahead of the rotors. Actuation is accomplished by a set of 12 high-response inlet guide vanes, whose individual deflections can be controlled independently by a digital computer.

The feedback scheme used in this work is motivated by a recently developed model for rotating stall. In this model, the perturbation axial velocity as a function of circumferential position at any axial station completely determines the state of the system. Furthermore, circumferential sinusoidal waves of the perturbation are the fundamental eigenmodes, and these eigenmodes develop as rotating waves around the annulus. When the eigenvalues associated with these eigenmodes become unstable, the system diverges into rotating stall. Therefore, feedback stabilization of these rotating waves is used as the technique to eliminate rotating stall.

The model for rotating stall is extended to include the effects of high-response inlet-guide-vane actuation. This model is then converted from a system of partial differential equations (PDEs) to a set of ordinary differential equations (ODEs). This conversion will be shown to yield a model to which standard control and identification techniques can be applied.

The experimental investigation consisted of two main parts. The first part is systematic identification of the relevant compressor dynamics. The procedures described yield an accurate model of the compressor input-output behavior over the frequency range of interest (DC to twice rotor rotation frequency), for flow coefficients which span the entire range of stable and unstable (stabilized) operation of the system. This identification verifies the basic behavior predicted by the model and provides quantitative information for control system design.

The second part of the experimental investigation is active stabilization. The goal of active control is to extend the range of the compressor to the lowest flow coefficient possible. It is shown that, in the compressor studied, the circumferential sinusoidal modes go unstable in succession - first mode, followed by second, followed by third, as flow coefficient is reduced. Thus, additional range of the compressor is gained for each additional mode stabilized.

Acknowledgements

The project described in this thesis is both interdisciplinary and experimental. Either of these aspects alone would impose the following requirement: the joint effort of a lot of different people with different areas of expertise. So it is the sincere truth when I say that the success of this project (whatever that may be) belongs to the people I will mention here.

First I would like to thank my thesis supervisor, Professor Lena Valavani, for her unerring support. Her enthusiasm and success-oriented attitude have kept me going through all aspects of the doctoral program, and our many brain-storming discussions have born fruits that are visible throughout the thesis.

Professor Alan Epstein deserves most of the credit for conceptualizing, designing, and pushing forward active control of rotating stall. His support, both moral and substantial, have been prime movers in the success of this project.

I would also like to thank Professors Wallace Vander Velde and Andrew Von Flowtow for their support as members of my thesis committee. Their suggestions and comments always turned out to be useful and instructive.

Now its time to get down to brass tacks. Who built the rig? Professors Epstein and Greitzer designed the configuration of the experiment, with the help of Dr. Gerry Guenette, Mr. Peter Silkowski, and Professor Valavani. Professor Epstein and Dr. Guenette designed the IGV ring, and Dr. Guenette, Victor Dubrowski, and Andreas Schulmeyer made sure it fit. Roy Andrews and Jim Nash built the cart which supports the IGV ring, and Jim Nash put together the cooling ducts and air filters. The IGV blades themselves were designed by Professor Epstein and Dr. Guenette. Dr. Guenette provided the know-how to make the epoxy blades, and worked with Victor Dubrowski and Peter Silkowski in setting up the casting. Peter Silkowski did most of the work in casting the IGVs. Assembly of the IGV ring was assisted by Dr. Guenette, Victor Dubrowski, Jim Nash, and Roy Andrews. The amplifier rack was wired up and assembled by Jim Nash. Victor Dubrowski machined many small parts (a.k.a. doodads) for the rig, machined fittings into the upstream ductwork, and spent long hours getting everything measured out, lined up, and tied down. Professor Epstein lent his considerable expertise in scoping out and procuring the hot wires, A/D, motor controllers, amplifiers, filters, cables, nuts, bolts, and - what not? - and he also knew the right way to put them all together. Dr. Guenette was also indispensable as a consultant during various phases of the instrumentation set-up. Programs originally written by Phil Lavrich and Vincent Garnier were modified and used for data acquisition and reduction. Bob Haines kept the computers running and advised me on 386 Assembly, and Dave Dvore got the compters to talk to each other. Jon Simon provided consultation (and some code) for getting the servos working, and Victor Filipenco helped me trouble-shoot and understand the experimental setup. Holly Rathbun was the administrative backbone of the project, solving all monetary and procurement problems efficiently and exuberantly. Jim Nash kept a constant eye on the project, and used his sensibilities to get things together and working. I'm sure I left some people out, but that gives you an idea of the team effort involved, and kind of makes you wonder - what did Jim P. do?

On the theoretical side, as many people aided the project's progress. Professor Greitzer is the first name that comes to mind. He has consistently motivated me and others on the project to strive for higher levels of intellectual acumen. Much of the compressor modeling presented in this thesis bears his stamp. Dr. John P. Longley also deserves considerable credit for his efforts in modeling all the relevant fluid mechanical effects. As a consultant on all things fluid mechanical, he was always available, accurate, and outspoken. Dr. Ivor J. Day also contributed substantially through his comments, and through his parallel efforts at the Whittle Laboratory. Several fellow students deserve special note for their contribution to my education. Jon Simon, as the other 'controls guy' in a fluids lab, never failed to listen attentively and critically to any problem, and inevitably had elucidating suggestions. He also provided many provocative (and often humbling) questions about relevant control issues. He proof-read the hardest part of this thesis, too - three times. Dr. Victor Filipenco educated me on too many topics to mention, and always did so in an entertaining and enlightened way. Brent Appleby and Greg Chamitoff were classmates and study mates of extraordinary caliber, and I owe much of my understanding of estimation, stochastic processes, and optimal control to them. Vincent Garnier taught me, belatedly, how to interpret the PSD of a complex time function; other Fourier transform concepts trickled down to me from his thesis. Andreas Schulmeyer helped me through some of the fluids concepts, as did Jon Simon, Dr. Longley, and Dr. Filipenco.

Preparation of this thesis was assisted by: Dr. Qing Sun-Padavano, who spent many patient hours making detailed figures for this thesis; Diana Park, who also provided many beautiful figures, and passed on a small portion of her Mac wizardry; and Victor Filipenco, who provided T3 consultation. Dr. Longley, Professor Greitzer, and Joel Haynes proof-read and provided many useful comments, as did Jon Simon. Professors Epstein, Valavani, Vander Velde, and Von Flowtow also diligently proof-read my typo-ridden first draft, and helped whip things into shape.

Finally, I would like to thank a few people for being close friends: Dan Wang, Feng Chen, Petra Turowski, Brian Tan, Eva Ng, Theresa Vangeli, Lee Weinstein, Kim Lu, Sharlene Liu, Wendy Liu, Brian Bennett, and Dr. Downing. Providing necessary diversions were: Victor and his flock of flying phantasmagoria, Jon and his consternating control-theory cornucopia, the Lee-Petra-Eva-Tepeza coalition, the boisterous bodacious BDC (and all its members), and the impish invigorating infant Claire. This thesis is dedicated to my wife Qing, who has quietly earned my deep respect and adoration, and to my parents, who supported me throughout.

This project was supported by the U.S. Air Force Office of Scientific Research (contract #AFOSR-90-0059), Dr. J. McMichael, Technical Monitor, and by the Office of Naval Research (contract #N00014-87-K-0352), Dr. R. J. Hansen, Technical Monitor. Their support is gratefully acknowledged.

Table of Contents

Abstract	2
Acknowledgements	3
List of Figures	9
List of Tables	13
Nomenclature	14
1 Introduction and Review of Previous Work	20
1.1 <u>Background - Rotating Stall in Axial Compressors</u>	22
1.2 <u>Description of Rotating Stall</u>	27
1.3 <u>Motivation and Previous Efforts</u>	32
1.4 <u>Purpose and Procedure</u>	33
2 Experimental Apparatus	34
2.1 <u>Design of Experimental Apparatus</u>	34
2.2 <u>Mechanical Layout</u>	36
2.3 <u>Sensors, Signal Processors, and Computers</u>	46
2.3.1 Hot Wire Probes and Anemometers	46
2.3.2 Low-Pass Filters	49
2.3.3 A/D Board	49
2.3.4 HP Vectra 486 Computer	50
2.3.5 Servo Motion Control Boards	50
2.3.6 Amplifiers	51
2.3.7 DC Servo Motors	54
2.3.8 IGV Blades	54
2.3.9 Pressure Probes	54
2.3.10 Scanivalve	56
2.3.11 A/D	56
2.3.12 VAX	56
2.4 <u>Signal Flow Paths</u>	56
2.4.1 Calibration	57
2.4.2 Speed Line and Operating Condition Monitoring	57
2.4.3 High-Response Data Acquisition and Control	58
2.4.4 Data Reduction	58
2.5 <u>Programming Considerations</u>	58
2.5.1 A/D Interface Routines	58
2.5.2 Motion Control Board Interface Routines	59
2.5.3 Feedback Control Program	60
2.6 <u>A Typical Run</u>	61
2.6.1 Parameters Which Define The Configuration of a Run	63

3	Modeling Compressor Higher-Mode Dynamics	66
3.1	<u>Modeling Preliminaries</u>	67
3.1.1	Assumptions	67
3.1.2	Notation and Non-dimensionalization	69
3.1.2.1	Non-dimensionalizing Parameters	69
3.1.2.2	Independent Variables	70
3.1.2.3	Dependent Variables	70
3.1.2.4	Compressor Characterization	70
3.1.2.5	Perturbation Variables	71
3.1.2.6	Spatial Fourier Coefficients (SFCs)	71
3.2	<u>Modeling</u>	72
3.2.1	Overview	72
3.2.2	Overall Total to Static Pressure Balance	73
3.2.3	Upstream Flow Field Total Pressure Change	74
3.2.4	Total Pressure Change Across the IGVs	74
3.2.5	Compressor Total-to-Static Pressure Rise	76
3.2.6	Downstream Flow Field Static Pressure Change	77
3.2.7	Combining Equations and Solving	78
3.2.8	Discussion	80
3.3	<u>Alternate Forms of the Model</u>	82
3.3.1	SISO Complex Form	82
3.3.2	MIMO Real-Value Form	84
3.3.3	Rotating Reference Frame Form	87
3.3.4	Lumped Parameter Model of Rotating Stall Dynamics	89
4	Additional Modeling for Active Control	94
4.1	<u>Conversion to Spatial Fourier Coefficients (SFCs)</u>	94
4.1.1	Inlet Guide Vanes	98
4.1.2	Hot Wires	100
4.1.3	Input and Output Channels	101
4.2	<u>System Dynamics</u>	103
4.2.1	Servos	103
4.2.2	Sensors, Signal Processors, and Delays	104
4.3	<u>Time Discretization</u>	105
4.3.1	Tustin Transformation	106
4.3.2	Zero-Order Hold (ZOH) Transformation	107

5	Development and Application of Techniques for Identification of Compressor Higher-Mode Dynamics	108
5.1	<u>Non-Parametric Estimation</u>	109
5.1.1	Sinusoidal Excitation Method	109
5.1.2	Spectral Estimation Method	111
5.2	<u>Parametric Estimation</u>	116
5.2.1	Transfer Function Fitting	116
5.2.2	The Instrumental-Variable Method	118
5.2.2.1	Basic IV Procedure	119
5.2.2.2	Young's Refined Instrumental Variable - Approximate Maximum Likelihood (RIV-AML) Technique	122
5.2.2.3	Choice of Closed-Loop Instruments	124
5.2.2.4	Modification of the RIV-AML Prefilters for Unstable Plant Dynamics	128
5.2.2.5	Application to the MIMO Rotating Stall System	133
5.2.2.5	A Typical Run	134
5.3	<u>Results and Discussion</u>	135
5.3.1	Comparison of Various Methods	137
5.3.2	Results for the Single-Stage Active Control Research Compress	141
5.3.3	Configuration Studies	158
6	Active Stabilization of a Single-Stage Low-Speed Research Compressor	179
6.1	<u>Experimental Results</u>	183
6.1.1	Feedback Phase Sensitivity of First Mode Stability	184
6.1.2	Speed Lines	186
6.1.3	Stall Events	188
6.1.4	Power Spectra	201
6.1.5	Discussion	208
6.2	<u>Gain Determination Using Linear Control Theory</u>	209
6.2.1	Prediction of Closed-Loop Performance	210
6.2.2	Gain Determination Using Root Loci	220
7	Summary, Conclusions, and Recommendations	227
7.1	<u>Summary</u>	227
7.2	<u>Conclusions</u>	228
7.3	<u>Recommendations for Future Work</u>	229
	References	231

Appendix A Modifications to the Compression System Model	235
A.1 <u>Upstream and Downstream Flowfields</u>	235
A.2 <u>Unsteady Losses and Deviations</u>	235
A.3 <u>Modifications to the Inertia Parameter, λ</u>	236
A.4 <u>Swirl Sensitivity</u>	237
A.5 <u>Other Work</u>	237
Appendix B Theoretical Representation of Waves in Axial Compressors	239
Appendix C Stall Inception Data for Various Compressor Builds	247
C.1 <u>Fully-Developed Stall and Stall Inception Behavior</u>	248
C.2 <u>Description of the Experiments</u>	249
C.3 <u>Measurements of Part-Span and Full-Span Stall Inception</u>	250
C.4 <u>Discussion</u>	252
Appendix D Frequency Response Data	295

List of Figures

1.1	Compression system components	21
1.2	Schematic compressor characteristic, showing rotating stall condition . .	21
1.3	Two-dimensional compressor duct	24
1.4	Fully developed rotating stall cell shape (from [3])	25
1.5	Three-dimensional image of rotating stall inception	25
1.6	Flow coefficient time evolution at a single circumferential position - . .	26
	transient leading to rotatin stall	
1.7	The unstable extension to the axisymmetric compressor map	31
2.1	Axial compressor test rig	37
2.2	Compressor geometry definitions	40
2.3	Twelve motors mounted on IGV ring	41
2.4	IGV ring, servo motors, and IGVs	43
2.5	Close-up of servo motors and epoxy inlet guide vanes	44
2.6	Instrumentation layout	45
2.7	Elements of the feedback path	47
2.8	Pressure data acquisition equipment	48
2.9	Operation of one axis of DMC-430 DC motor controller	52
2.10	Amplifer rack	53
2.11	Inlet guide vane detail (full scale)	55
2.12	Input velocity data and output blade deflections for one second of a . . .	64
	typical closed-loop run	
3.1	Stations in a 2-D axial compression system	68
3.2	Effect of non-axisymmetric IGV turning	75
3.3	Different representations of a sinusoid	85
4.1	Conceptual diagram of spatially discrete and spatially continuous	95
	portions of the system	
4.2	Parallel modal dynamics representation of the system	96
4.3	Comparison of theoretical and actual turning behind the IGVs	99

5.1	Transfer function estimate using sinusoidal excitation (open circles).	112
	Dotted line shows a transfer function fit to open circles.	
5.2a	Example of pseudo-random binary excitation and resulting response.	114
	This is a portion of the data used to generate the spectral estimate in Figure 5.2b	
5.2b	Spectral estimate resulting from the data in Figure 5.2a. Dotted line	115
	shows a transfer function fit to the spectral estimate.	
5.3	Closed-loop system notation	125
5.4	Example of different impulse responses associated with different regions	132
	of convergence.	
5.5	Example of data for IV estimation techniques. Dotted lines are results	136
	of a noise-free simulation, based on a NF/RIV-AML estimate.	
5.6	Comparison between sinusoidal excitation (open circles) and spectral	138
	estimation method (solid line).	
5.7	Comparison of spectral (solid line) and RIV-AML (dashed line)	139
	estimates.	
5.8	Comparison of spectral estimate (solid line), NF/RIV-AML estimate	140
	(dashed line) and TR/RIV-AML estimate (dotted line, barely visible because of coincidence with NF estimate).	
5.9	Parameter estimates plotted as functions of flow coefficient - first mode	142
5.10	Parameter estimates plotted as functions of flow coefficient - second	143
	mode	
5.11	Parameter estimates plotted as functions of flow coefficient - third mode	144
5.12	First mode pole and zero migration with flow coefficient.	145
5.13	Second mode pole and zero migration with flow coefficient.	146
5.14	Third mode pole and zero migration with flow coefficient.	147
5.15	Comparison of stability variation with flow coefficient for the first three	149
	modes. Hot wires are upstream of the IGVs.	
5.16	Estimated slope of the compressor characteristic, based on a 4th-order	150
	curve fit to the speed line.	
5.17	Comparison of rotation frequency variation with flow coefficient for the	153
	first three modes - ω_{rs} plot.	
5.18	Comparison of rotation frequency variation with flow coefficient for the	153
	first three modes - ω_{rs}/n plot.	

5.19	Magnitude of the steady-state gain, M_{ss} , for the first three modes.	155
5.20	Phase of the steady-state gain, M_{ss} , for the first three modes.	155
5.21	Variation of the real part of the zero with flow coefficient, for the first . . .	157
	three modes.	
5.22	Parameter estimates plotted as functions of flow coefficient - second . . .	159
	mode, spacer ring in (compare to no spacer ring data, Figure 5.9)	
5.23	Parameter estimates plotted as functions of flow coefficient - first mode, .	160
	spacer ring in (compare to no spacer ring data, Figure 5.10)	
5.24	Effect of intermediate IGVs on $\delta\psi/\delta\theta$	162
5.25	Effect of intermediate stationary IGVs on the first mode transfer function .	163
	at $\phi=0.475$. Dotted line shows transfer function without intermediate	
	IGVs, solid line shows transfer function with intermediate IGVs. Hot	
	wires are upstream of the IGVs.	
5.26	Effect of intermediate stationary IGVs on the second mode transfer . . .	164
	function at $\phi=0.475$. Dotted line shows transfer function without	
	intermediate IGVs, solid line shows transfer function with intermediate	
	IGVs. Hot wires are upstream of the IGVs.	
5.27	Effect of intermediate stationary IGVs on the first mode transfer function .	165
	at $\phi=0.500$. Dotted line shows transfer function without intermediate	
	IGVs, solid line shows transfer function with intermediate IGVs. Hot	
	wires are upstream of the IGVs.	
5.28	Effect of intermediate stationary IGVs on the second mode transfer . . .	166
	function at $\phi=0.500$. Dotted line shows transfer function without	
	intermediate IGVs, solid line shows transfer function with intermediate	
	IGVs. Hot wires are upstream of the IGVs.	
5.29	Effect of moving the hot wires downstream of the IGVs on the first . . .	169
	mode transfer function at $\phi=0.475$. Dotted line shows transfer function	
	upstream of the IGVs, solid lines shows transfer function downstream of	
	the IGVs. In both cases, the intermediate spacer ring is in.	
5.30	Effect of moving the hot wires downstream of the IGVs on the second . .	170
	mode transfer function at $\phi=0.475$. Dotted line shows transfer function	
	upstream of the IGVs, solid lines shows transfer function downstream of	
	the IGVs. In both cases, the intermediate spacer ring is in.	
5.31	Transfer function fit to spectral estimate of $G_1(s)$ downstream of the . . .	171
	IGVs. Two poles and two zeros are used to achieve the fit shown.	

6.1	Effect of feedback phase on magnitude of spectral peak	185
6.2	Effect of feedback phase on the stall flow coefficient	185
6.3	Speed lines for various levels of active control	187
6.4	Examples of wrapped and unwrapped phase plots	189
6.5	Examples of (a) exponential growth into stall and (b) resonance leading to stall	190
6.6	Hot wire traces for a stall event with no control.	193
6.7	Magnitude and phase of first three Fourier coefficients during the stall event with no control, computed from the hot wire data in Figure 6.4.	194
6.8	Hot wire traces for a stall event with Z1 control.	195
6.9	Magnitude and phase of first three Fourier coefficients during the stall event with Z1 control, computed from the hot wire data in Figure 6.6.	196
6.10	Hot wire traces for a stall event with Z1+Z2 control.	197
6.11	Magnitude and phase of first three Fourier coefficients during the stall event with Z1+Z2 control, computed from the hot wire data in Figure 6.8.	198
6.12	Hot wire traces for a stall event with Z1+Z2+Z3 control.	199
6.13	Magnitude and phase of first three Fourier coefficients during the stall event with Z1+Z2+Z3 control, computed from the hot wire data in Figure 6.10.	200
6.14	PSDs of the first three SFCs, using data immediately prior to stall, with no control (i.e. open loop).	203
6.15	PSDs of the first three SFCs, using data immediately prior to stall, during Z1 control.	204
6.16	PSDs of the first four SFCs, using data immediately prior to stall, during Z1+Z2 control.	205
6.17	PSDs of the first four SFCs, using data immediately prior to stall, during Z1+Z2+Z3 control.	206
6.18	Closed loop system notation	211
6.19	Comparison of predicted (dashed lines) and actual (solid lines) closed-loop transfer functions for the first mode. Feedback gain is shown at the top of the figure. Data taken with 13 hot wires downstream of the IGVs, at $\phi=0.475$	213
6.20	Root locus of dominant roots for the first mode, $\bar{\phi}=0.375$	221
6.21	Root locus of dominant roots for the second mode, $\bar{\phi}=0.375$	222
6.22	Root locus of dominant roots for the third mode, $\bar{\phi}=0.375$	223

List of Tables

2.1	Compressor Geometry	39
5.1	Parameter Identification Results (no spacer ring, upstream hot wires) . .	173
5.2	Parameter Identification Results (spacer ring IN, upstream hot wires) . .	176

Nomenclature

Symbols

$B(z)$	} numerator, denominator polynomials in discrete model (5.23)
$A(z)$	
$A_u(z)$	polynomial whose roots coincide with the unstable roots of $A(z)$ (5.42)
$A_s(z)$	polynomial whose roots coincide with the stable roots of $A(z)$ (5.42)
a_i	denominator coefficients of z^{-1} in discrete models (5.23, 5.52)
b_i	numerator coefficients of z^{-1} in discrete models (5.23, 5.52)
b_{rn}	} control power parameters for the n^{th} mode, (3.39)
b_{in}	
g_{in}	
b_{IGV}	} IGV, rotor, and stator chords, non-dimensionalized by r (Table 2.1)
b_r	
b_s	
C_n	discrete Fourier transform of $\delta\phi$
$C(z)$	} numerator, denominator polynomials in discrete noise model (5.24)
$D(z)$	
e	prediction error (5.26)
g_{in}	coefficient of $\dot{\tilde{\gamma}}_n$ in (3.39)
$G_n(s)$	transfer function between $\tilde{\gamma}_n(s)$ and $\tilde{\phi}_n(s)$ (3.47)
$G_{rn}(s)$	transfer function between $u_{rn}(s)$ and $x_{rn}(s)$ (3.55)
$G_{in}(s)$	transfer function between $u_{in}(s)$ and $x_{in}(s)$ (3.55)
$G_c(z)$	dynamics in the feedback path of closed loop system (Figure 5.3)
$G_s(z)$	dynamics in forward path of closed loop system (Figure 5.3)
$h(k)$	impulse response (Section 5.2.2.4)
i, j	$\sqrt{-1}$
k	time counter for discrete systems
M	magnitude of a complex number
M_{ssn}	steady-state magnitude of $G_n(s)$ (5.57)
n	spatial mode number
\mathcal{P}_t	total pressure, normalized by ρU^2
\mathcal{P}_s	static pressure, normalized by ρU^2

$Q(s)$	transfer function which accounts for all of the filters and delays in the feedback system (Figure 4.2, Section 4.2.2)
r	rotor mean radius
$r(k)$	external input for discrete-time closed-loop system (5.40, Figure 5.3)
r_r, r_i	real and imaginary parts of $r(k)$
s	Laplace transform variable
$S(s)$	servo transfer function (Figure 4.2, Section 4.2.2)
t	time, seconds
U	rotor velocity at the mean radius
$u(k)$	input of discrete-time model in the instrumental variable method (5.23)
\tilde{u}_{cn}	commanded IGV deflection n^{th} spatial Fourier coefficient (Section 4.1)
u_{cr}, u_{ci}	real and imaginary parts of \tilde{u}_c
u_{rn}, u_{in}	real and imaginary parts of $\tilde{\gamma}_n$ (Section 4.1)
$v(\eta, \theta, \tau)$	circumferential fluid velocity, normalized by U (Section 3.1.2.3)
w^{-1}	delay operator for 2 kHz discrete-time system (2.2)
x_r, x_i	real and imaginary parts of $\tilde{\phi}_n$ (Section 4.1)
$y(k)$	output of discrete-time model in instrumental variable method (5.23)
\tilde{y}_n	measured perturbation flow coefficient (Figure 4.2, Section 4.1)
y_r, y_i	real and imaginary parts of \tilde{y}
z	z -transform variable (z^{-1} can be interpreted as the unit delay operator)
Z_n	complex feedback gain

Greek symbols

α	angle of attack (4.4)
β	phase angle (argument) of a complex number
$\beta(k)$	vector of instruments in the AML method (5.39)
γ	IGV, rotor, and stator staggers (Table 2.1, Figure 2.2)
γ_r	
γ_s	
$\tilde{\gamma}_n(\tau)$	n^{th} spatial Fourier coefficient of $\delta\gamma$ (3.33)
$\delta\gamma(\theta, t)$	circumferential distribution of perturbation IGV deflection (3.13)

η	axial position, normalized by rotor radius (3.1.2.2)
η_{HW}	axial position of axial velocity measurements
η	parameter vector in AML method (5.37)
λ	rotor fluid inertia parameter (3.1)
μ	overall compressor fluid inertia parameter (3.4)
μ_{C}	compressor fluid inertia parameter (excluding IGVs) (3.2)
μ_{IGV}	inlet guide vane fluid inertia parameter (3.3)
$v(k)$	additive (colored) noise random process (5.24)
$\phi(\eta, \theta, \tau)$	compressor axial flow coefficient, normalized by U
$\bar{\phi}$	annulus averaged axial flow coefficient
$\delta\phi(\theta, t)$	circumferentially non-uniform ϕ perturbation
$\tilde{\phi}_n$	n^{th} spatial Fourier coefficient of $\delta\phi$
ϕ_{L}	lumped parameter representation of $\delta\phi$
$\Phi(k)$	regressors vector (system inputs and outputs) in IV prediction (5.25)
$\Phi_n(k)$	regressors matrix for rotating stall n^{th} mode (5.52)
$\Phi_{\text{xx}}(\omega)$	power spectral density (autospectrum) for the argument x (5.10)
$\Phi_{\text{xy}}(\omega)$	cross-spectral density between arguments x and y (5.10)
$\psi(\bar{\phi})$	compressor total-to-static pressure rise characteristic normalized by ρU^2
$\psi_{\text{c}}(\bar{\phi})$	compressor total-to-static pressure rise characteristic (excluding IGVs)
θ	circumferential position, radians
$\hat{\Theta}$	parameter vector in instrumental variable prediction equation (5.42)
$\Theta(n, \bar{\phi})$	parameter set which characterizes the compressor dynamics n^{th} mode (3.49)
ρ	fluid density
σ_{rs_n}	stability parameter for the n^{th} mode (3.40)
σ_{P}	real part of the zero of $G_n(s)$ (5.58)
ω_{rs_n}	rotation frequency for the n^{th} mode (3.42)
τ	time, non-dimensionalized by rotor rotation period (Section 3.1.2.3)
ξ	white noise random process (5.24)
ζ	vector of instruments in instrumental variable method (5.27)
ζ_n	matrix of instruments for compressor dynamics n^{th} mode (5.53)
φ	regressors vector in AML method (5.37)

Operators, superscripts, and subscripts

$\delta(\cdot)$	small perturbation of the argument
$(\tilde{\cdot})$	spatial Fourier coefficient (argument is a function of θ Section 3.1.2.6)
$(\hat{\cdot})$	prediction or estimation
$(\dot{\cdot})$	derivative with respect to non-dimensionalized time, τ
$(\cdot)^f$	filtered version of argument
$(\cdot)^T$	transpose
$(\cdot)_n$	n^{th} mode version of the argument
$(\cdot)^c$	alternate signal which is highly correlated with the argument
$(\cdot)^*$	complex conjugate
$(\cdot)_r$	real part
$(\cdot)_i$	imaginary part
$(\cdot)_i$	i^{th} column of matrix argument, i^{th} element of vector argument
$(\cdot)_{ij}$	(i,j) element of matrix argument
$ \cdot $	absolute value
$\angle(\cdot)$	phase angle (argument) of complex number
$\text{Re}\{\cdot\}$	real part
$\text{Im}\{\cdot\}$	imaginary part
$E\{\cdot\}$	expected value
$Z\{\cdot\}$	Z-transform
$Z^{-1}\{\cdot\}$	inverse Z-transform
Σ	Summation
Π	Product

Acronyms

A/D	analog to digital
AML	approximate maximum likelihood
DFT	discrete Fourier transform
IGV	inlet guide vane
IV	instrumental variable
NF	noise-free
NMP	non-minimum phase
ODE	ordinary differential equation
PDE	partial differential equation
PID	proportional-integral-derivative
ML	maximum likelihood
MIMO	multi-input multi-output
RIV	refined instrumental variable
ROC	region of convergence
RPM	revolutions per minute
SISO	single-input single-output
TR	test-repeat
c	causal
ac	anticausal
snc	stable, noncausal
uc	unstable, causal
uac	unstable, anticausal

CHAPTER 1

Introduction and Review of Previous Work

1.1 Background - Rotating Stall in Axial Compressors

The compressor is one of the three primary components of a gas turbine engine (the other two being the combustion chamber and the turbine). *Axial* compressors are distinguished from other types by their flow path - air flows axially, or parallel to the shaft of the machine, through an annular passage. Rows of vanes or *blades* span this annular passage radially; spinning blade rows (*rotors*) alternate with stationary blade rows (*stators*) to impart a pressure rise to the fluid. Figure 1.1 shows the layout schematically. The compressor shown has only one rotor and one stator; thus, it is said to be a *single-stage* axial compressor (aircraft engines typically have 8 to 20 stages). A few other terms must be defined for the discussion of rotating stall: the inner radius of the compressor annulus is called the *hub*; the outer radius is called the *casing*. The *tip* is the outer radius of the rotor; the *tip clearance* is the distance from the tip to the casing.

The operating condition of a compressor is determined by the *flow coefficient* which is the ratio of the mean axial flow velocity to the velocity of the rotor at the mean radius. Compressor performance is generally characterized by a 'speed line' or 'characteristic': that is, a plot of pressure rise delivered as a function of flow coefficient. Figure 1.2 shows a schematic compressor characteristic: as the flow velocity through the compressor is decreased (i.e. as the downstream throttle closes in an experiment), the pressure rise increases. This trend continues until the system goes into either *rotating stall* or *surge*. Both of these conditions are disruptions in the

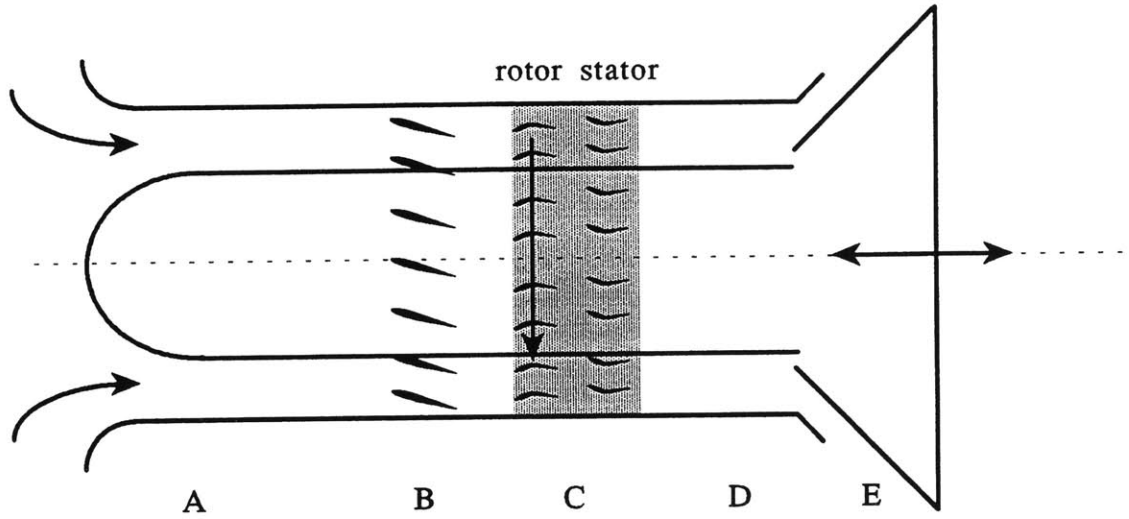


Figure 1.1 - Compression system components: A - Inlet duct; B - Inlet guide vanes (IGVs); C - Compressor; D - Downstream duct; E - Throttle

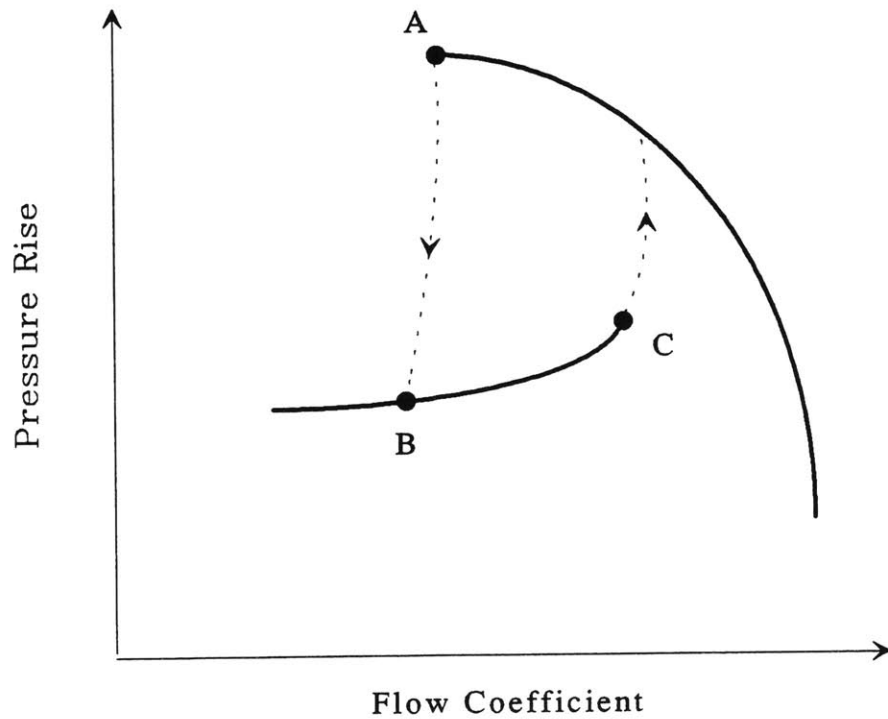


Figure 1.2 - Schematic compressor characteristic, showing rotating stall condition (segment BC)

steady, symmetric flow of air through the compressor. Rotating stall is a severely non-axisymmetric distribution of axial velocity around the annulus of the compressor, taking the form of a wave or 'stall cell', that propagates in the circumferential direction at a fraction of the rotor speed. Surge, on the other hand, is an axisymmetric, unsteady operating state involving limit-cycle type oscillation in mass flow through the entire compression system. Rotating stall and surge are both considered unacceptable operating conditions in gas turbine engine compressors.

The interactions between rotating stall and surge have been studied both theoretically [1] and experimentally [2]. All indications to date are that these phenomena are coupled, but in a way that is well enough defined that each can be studied alone. Furthermore, one can readily set up an experimental compressor that goes into rotating stall but does not surge. Therefore, we will discuss rotating stall alone, mentioning surge only briefly to help motivate stabilization.

1.2 Description of Rotating Stall

The transition from normal compressor operation into rotating stall is depicted in Figure 1.2. The lowest flow coefficient at which the compressor can operate with axisymmetric flow is point A, the peak of the characteristic. At lower flows, an abrupt transition occurs into rotating stall (point B). This condition will persist until the flow is increased to point C. Thus, there exists a severe 'hysteresis', or range of flow coefficients at which two stable operating conditions exist - steady symmetric flow and rotating stall. The fact that a transition occurs suggests that the equilibrium point at stall inception (point A in Figure 1.2) and, perhaps, points at lower flow coefficients represent unstable equilibria. Stabilizing these unstable equilibrium points is the subject of this thesis.

During rotating stall, the flow through the compressor is a function of both time and position in the compressor. Thus even the most introductory explanation

requires some notation and simplifying assumptions. First, we will assume that the compressor annulus is narrow - i.e. the ratio of the hub radius to the tip radius is nearly one. This assumption allows variations in flow velocity with radial position to be ignored, and for the compressor annulus to be 'unwrapped' into a 2-D duct. Figure 1.3 illustrates the result: the annulus is hereafter considered as a 2-dimensional duct, in which 2-D cascades replace the rotor and stator vanes. Circumferential (θ) and axial (x) position are the space variables. Flow coefficient is written as a function of space and time, $\phi(x,\theta,t)$. Functionality with x , while strong, is relatively uninteresting in low-speed machines, so we will look at the flow coefficient at a specific axial location (usually upstream of the rotor), $\phi_{x1}(\theta,t)$.

Functionality with t can also be eliminated when looking at *fully-developed* rotating stall, because in this condition the shape of the stall cell does not change much as it rotates around the compressor annulus. Thus, if we fix ourselves in the reference frame of the moving stall cell, we see a wave shape $\phi_{x1}(\theta-\omega_{rs}t)$. Lavrich [3] has taken great care in resolving this wave shape using ensemble averaging techniques; his results provide a view of a typical stall cell in a low-speed compressor, Figure 1.4. This figure illustrates the severe magnitude and abrupt nature of the unsteadiness experienced by the blades during rotating stall - remember, this cell is traveling at a fraction of rotor speed (38% in this case), so both the rotors and the stators are passing through the velocity field shown.

To show rotating stall *inception*, the time evolution of the wave shape must be plotted. This can be done using a 3-dimensional plot of $\phi_{x1}(\theta,t)$, as in Figure 1.5. One can also plot flow coefficient at a specific circumferential location, $\phi_{x1,\theta1}(t)$, to study stall inception. Such a plot is given in Figure 1.6. Here each dip in the local flow coefficient represents one passage of the stall cell. Figures 1.5 and 1.6 are difficult to interpret in detail; we will adopt a modal approach later in the thesis. These figures do show, however, that a transient exists between steady symmetric

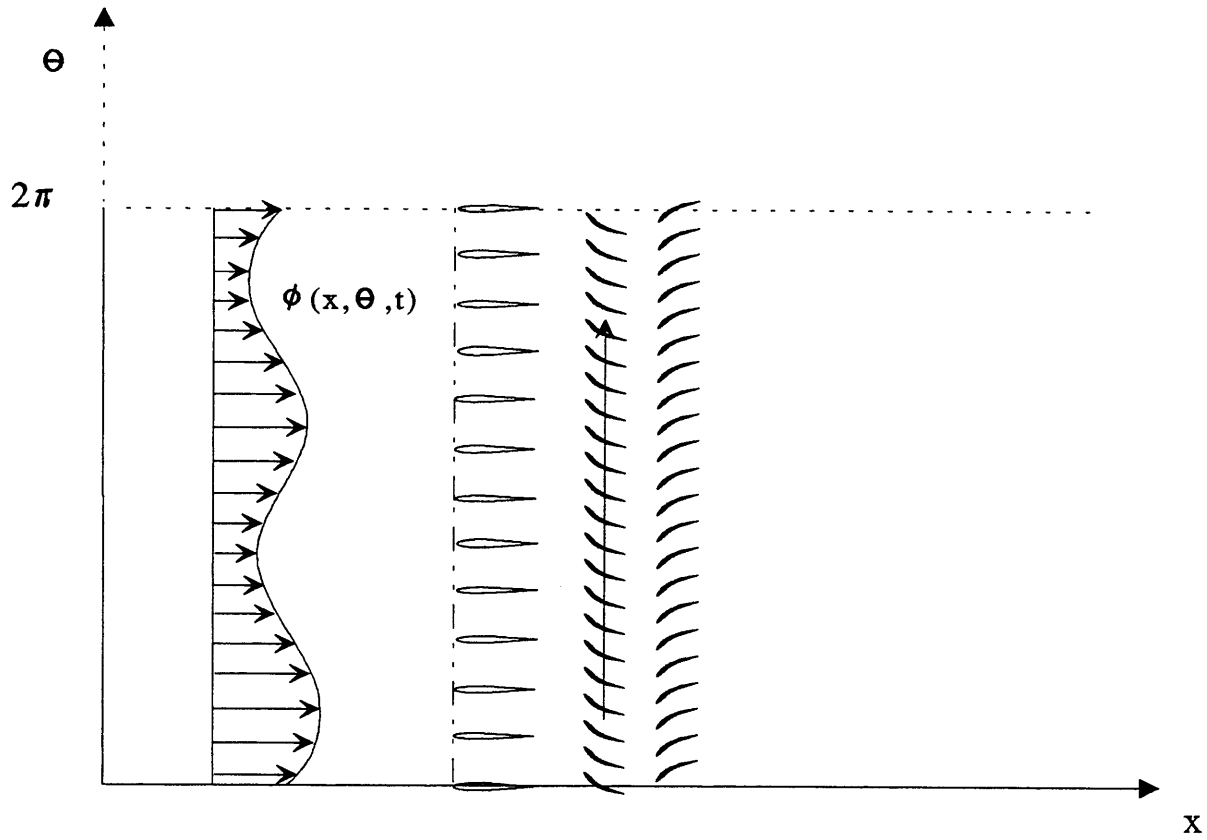


Figure 1.3 - Two-dimensional compressor duct

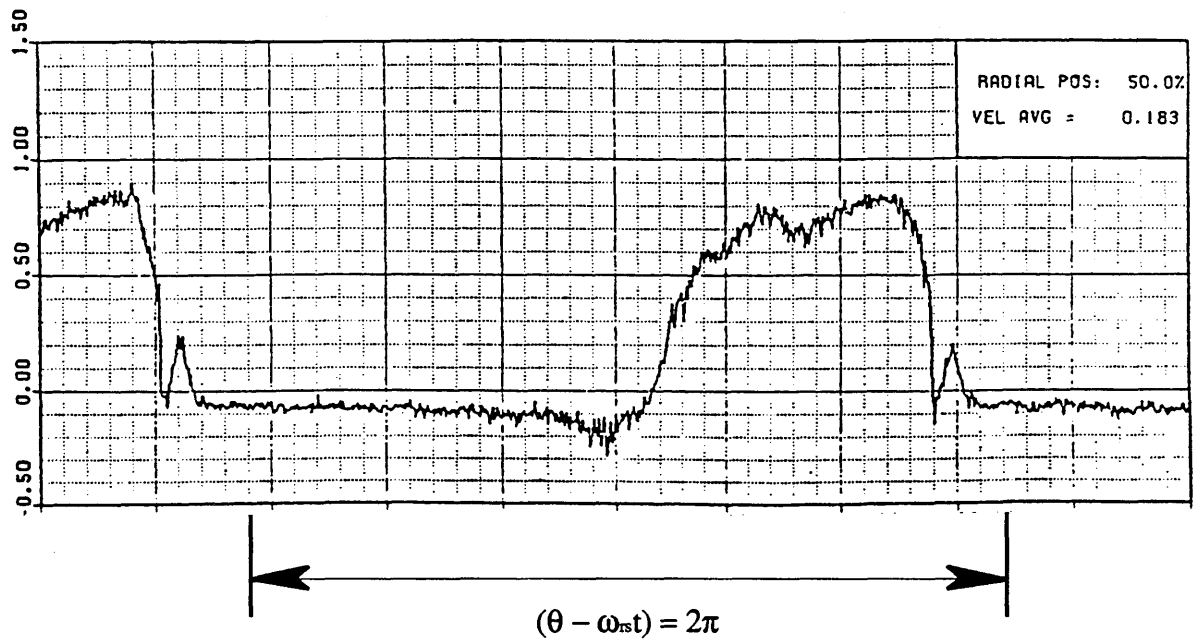


Figure 1.4 - Fully developed rotating stall cell shape (from [3])

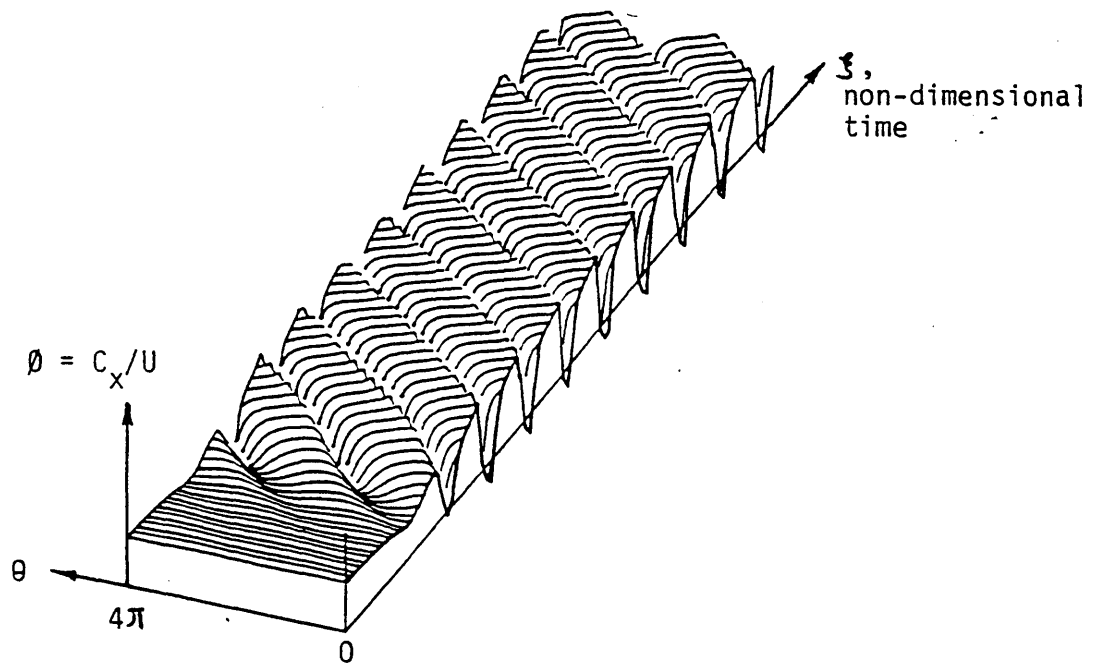


Figure 1.5 - Three-dimensional image of rotating stall inception (from simulation, [18])

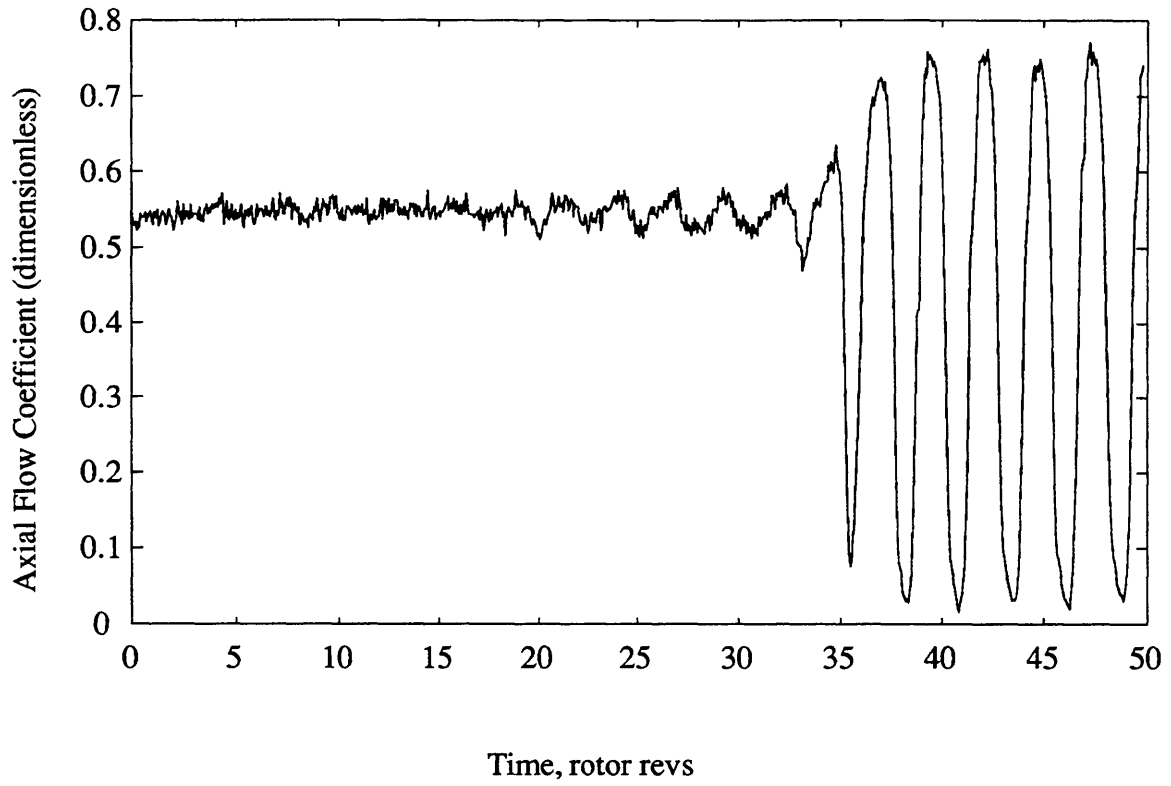


Figure 1.6 - Flow coefficient time evolution at a single circumferential position - transient leading to rotating stall

flow and fully-developed rotating stall, thus suggesting that the former is an unstable operating condition, and the latter is a stable limit cycle to which the unstable flow converges. 'Unstable' here means that waves of non-axisymmetric velocity tend to grow.

The growth of velocity waves in compressors *at stall inception* has been the subject of several previous studies. The growth (or decay) of velocity waves at operating conditions *away* from stall inception has not been studied. The experimental setup used in this thesis provides the unique opportunity for study of the entire continuum of growth rates - from negative (decaying) through zero (inception) to significantly positive (highly unstable). That such a continuum exists, and that it can be characterized using linear theory, are new results that are central to this thesis. Without such results, stabilization at flow coefficients well below the 'natural stall' flow coefficient would be much more speculative.

1.3 Motivation and Previous Efforts

To motivate the idea of stabilization, consider operation at point B in Figure 1.2. The pressure rise delivered by the compressor drops sharply when the compressor transitions into rotating stall. This alone compromises engine performance. But rotating stall often induces surge as well, which can in turn cause engine flame-out, shut-down, and damage. If the engine does not surge, then engine re-start may be required to clear the stall. Because the rotating stall cell travels with respect to both the rotor and the stators, all the blades in the engine see severely unsteady loading. Thus operation in rotating stall for any length of time is deemed unacceptable.

Traditionally, rotating stall has been avoided by avoiding operation too close to point A. This solution necessitates leaving an ample 'stall margin', so that transients in flow rate and ingestion of non-axisymmetric or otherwise disturbing flow

will not drive the system to the rotating stall operating condition. Concomitantly, a performance penalty is often paid, because the highest pressure rise and, sometimes, the highest efficiency, lie at flow coefficients below the minimum imposed by the stall margin. Therefore, it is desirable to reduce the minimum allowable flow coefficient without putting the system in danger of stall and/or surge.

Theoretical and experimental investigations over the past two decades have been aimed at two different methods to reduce the minimum allowable flow coefficient. First, the flow coefficient at which stall occurs can be reduced, so that, with the same stall margin, the compressor can operate at a lower flow. Second, operation closer to the stall flow rate can be made safer, so that the stall margin itself can be reduced.

Much research, both experimental and theoretical, has been aimed at simply understanding the mechanisms involved in rotating stall. This understanding would then presumably be used to help designers reduce the minimum allowable flow coefficient by changing the initial design. Work by Takata and Nagano [4] and by Pandolfi and Colasurdo [5] are examples of attempts to numerically simulate the behavior found in rotating stall. These methods generally require the input of blade row parameters such as loss and turning near or beyond stall or in unsteady situations. Reliable correlations for cascade characteristics in the regimes of interest are needed to insure the accuracy of this type of approach, but useful design rules have been developed [6].

Another method of reducing the stalling flow coefficient, thus reducing the minimum allowable flow, is motivated by the realization that stall is sometimes strongly affected by the conditions in the tip clearance region. Significant improvements in stall flow can be achieved using casing treatments, which are slots or grooves in the casing of the compressor, usually at the tips of the rotors [7]. This method involves a trade-off between efficiency and stalling flow coefficient, and is

effective only for the case of 'endwall related stall', as opposed to 'airfoil stall' [8]. In the latter case, the entire passage stalls, while in the former, the rotor tip section stalls first.

Finally, a form of active control has been experimentally employed in an attempt to reduce the required stall margin [9]. In this method, the stall flow coefficient was not significantly reduced, but the operation near stall was made somewhat safer. This was done by detecting the onset of stall and subsequently opening bleed doors or valves to 'back away' from the flow condition until the small initial cell cleared. This 'stall avoidance' scheme met with only limited success, due to difficulty in detecting the stall onset and the subsequent large control action required for avoidance.

Recently, a new approach to the problem has been suggested, based on the work of Moore [10], Greitzer [11], Ffowcs-Williams [12], and others. In their view, fluid mechanical instabilities should be viewed at their inception as small amplitude disturbances which are, consequently, amenable to linearized fluid mechanical description. Stabilizing these small disturbances has proven effective in delaying the onset of such phenomena as combustion 'reheat buzz' and compressor surge. If a small amplitude disturbance model for rotating stall could be developed and verified, this would pave the way for stabilization. Such stabilization would reduce the flow coefficient at which stall occurs, potentially to a greater extent than any of the techniques mentioned above.

Such a model exists, and its validity was the subject of research by McDougall [13], Longley [14], and Garnier [15]. In this model, the disturbances that lead to stall are not localized, as in many previous models of rotating stall, but take the form of circumferential waves that propagate according to linearized fluid mechanics. These waves either grow or shrink, depending on the flow rate. When they grow, the system is unstable and a fully developed nonlinear stall cell results.

The success of the studies using this model indicated that it was sufficiently accurate to warrant the study of active control. Epstein, Ffowcs-Williams, and Greitzer [16] presented an analysis of the feasibility of feeding back measurements of these waves in order to stabilize them and prevent the onset of rotating stall. One way to view this approach is shown in Figure 1.7. Since the onset of rotating stall is seen as the growth of unstable, though initially small, perturbations, there must exist an unstable extension of the compressor map. If this set of unstable equilibria can be stabilized using active control, then the actual compressor map can be extended. Epstein et al predicted significant improvement using this approach.

While this work presented strong evidence to motivate further research, several issues were left unresolved. The control effectiveness, and the fluid mechanical interaction of the actuation scheme with the flow field was not studied. The dynamics of the controller were also ignored, for clarity of presentation - in fact, the partial differential equation model used is not particularly useful for control system design. Finally, no experimental evidence was presented - only the suggestion that such experiments would be successful.

The details of the complex fluid mechanical interactions leading to rotating stall are still not well understood. For this reason, considerable controversy still exists about the validity of any one model of stall onset, especially if that model is 2-dimensional in nature, as is the Moore-Greitzer model. Recently, Day [17] showed that certain features of the stall inception process in some compressors are not easily predicted by this model, and proposed an alternative explanation. Based on this explanation, Day has devised an active control scheme very different from the one proposed here. Results of this work are presented in [2].

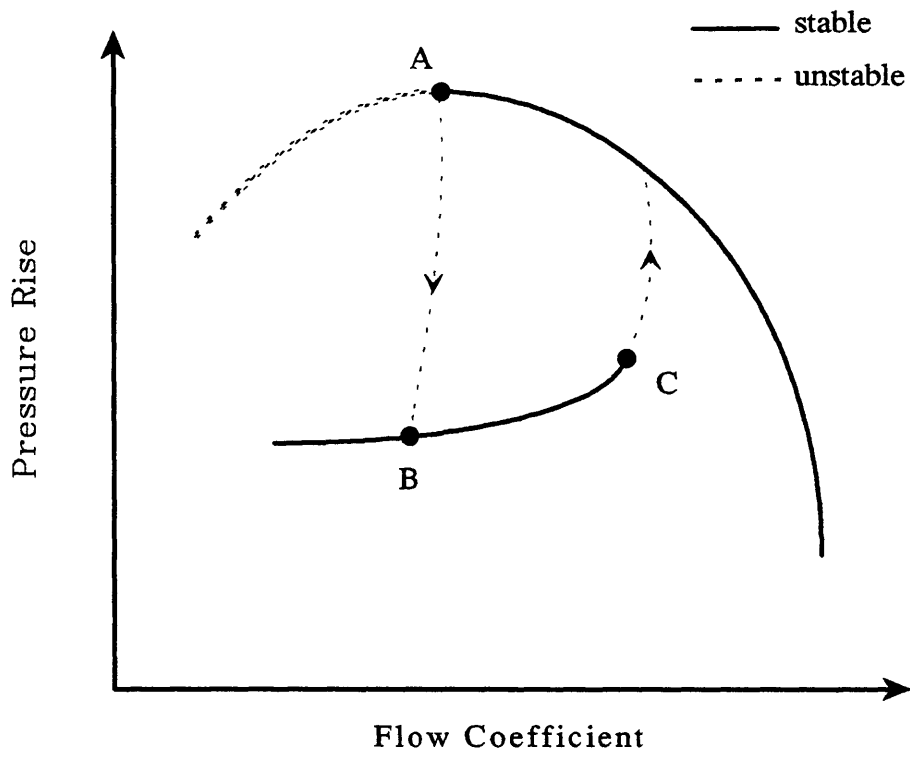


Figure 1.7 - The unstable extension to the axisymmetric compressor map

1.4 Purpose and Procedure

The primary purpose of this research is to demonstrate a reduction in the flow coefficient at which rotating stall occurs. This demonstration will be carried out on a low-speed single-stage compressor, described in Chapter 2. The technique used to reduce the flow coefficient is active control; the design of the sensing, actuation, and control laws is guided by the linearized model developed by Moore and Greitzer.

The first step in applying the Moore-Greitzer model to the problem of active control is to extend it to include the effects of the actuators. This development is given in Chapter 3. Once this is done, the model is converted to the ordinary differential equation (ODE) format that is needed for the application of control theory. This is also presented in Chapter 3. Chapter 4 further augments this model with the sensing, computation, and actuation dynamics that exist in the experiment.

The model developed in Chapter 3 is validated and shown to be adequate for designing stabilizing controllers in several ways. In Chapter 5, methods are developed and applied that allow the systematic quantitative identification of the system dynamics. If these dynamics show behavior that agrees qualitatively with the model, then confidence in its applicability, if not its predictive capability, is increased. In Chapter 6, the now quantitative system model is used to investigate the stabilization of the system when it becomes unstable. The success of the model in helping to design effective control systems is, of course, a direct measure of the model's adequacy in the context of control. The ultimate test of the model is to see if it can predict, based on geometry alone, the dynamic behavior of the system. The quantitative prediction of the system dynamics is an area still under development, and the current 'state of the art' is discussed in Appendix A. The quantitative experimental data provided in this thesis can be used to validate predictive procedures, when they are sufficiently mature. For this reason, Chapter 5 includes an

extensive set of experimental results.

Finally, the purpose of this research is to investigate and elucidate the concepts necessary for successful application of active control methods. A compressor is a distributed fluid mechanical system, whose dynamics are poorly known a priori. Control requires multiple measurements and actuators which must operate at high bandwidth in a noisy environment. The system linearity is a strong function of its state, but the relationship between linearity and operating condition remains unknown. This thesis will present an approach to these problems that has proven to be successful. It further provides a framework for thinking about and improving the understanding of rotating stall stabilization.

CHAPTER 2

Experimental Apparatus

A low-speed single-stage axial research compressor has been retrofitted with inlet guide vanes (IGVs) whose incidences can be individually controlled at high bandwidth. This compressor has also been fitted with hot wire anemometers, for measuring instantaneous flow velocity, at various circumferential and axial locations. Instrumentation and computer equipment for logging this data, together with total and static pressure data, and for feeding back signals to the IGV actuators in real time, has been installed. A complete description of the experimental apparatus is contained in this chapter. Section 2.1 first describes the rationale for the design of the experimental apparatus. Section 2.2 then describes the mechanical layout of the compressor, IGVs and instrumentation. Section 2.3 describes the computers and electronics, and shows the functional interconnections that exist; Section 2.4 describes the signal flow paths for various data acquisition and control tasks. Section 2.5 gives some programming considerations. Finally, Section 2.6 describes a typical experiment, and gives the parameters which define the configuration of a particular run.

2.1 Design of the Experimental Apparatus

The apparatus described in this chapter constitutes the first attempt to sense and actuate the circumferentially distributed dynamics of a compressor in a distributed, proportional (i.e. not simply on-off) manner. For this reason, the design of the experimental apparatus was made as straightforward as possible. Every attempt

was made to maximize the possibility of success of the experiments, in keeping with our purpose of demonstrating rotating stall stabilization. Nevertheless, we will assert that the resulting apparatus is an adequate first step toward stabilization of real compressors.

The compressor chosen for this study is the single-stage, low-speed axial research compressor at the MIT Gas Turbine Laboratory. This compressor is described in Section 2.2. The size and configuration of the compressor facilitate retrofitting sensors and actuators. Furthermore, the low speed (2700 RPM, tip Mach number ~ 0.25) allows the modeling techniques of Moore and Greitzer [10,11] to be applied directly. Extension to high-speed machines is a current area of research [41,44], but measurements presented by Garnier [15] indicate that the relevant 'pre-stall wave' behavior does exist in some high-speed compressors. If such pre-stall wave behavior exists in the experimental compressor, then we judge the low-speed, single-stage nature of the compressor to be secondary to the purpose of demonstrating stabilization. Haynes [40] has demonstrated results very similar to those presented in this thesis on a 3-stage low-speed compressor, verifying that the single-stage nature of this compressor does not restrict the results.

Hot wires were chosen to sense axial velocity in the compressor for several reasons. Mass flow is the relevant variable in compressor dynamics and, in a low speed compressor, mass flow and axial velocity are proportional. Furthermore, hot wires are the most direct, high-sensitivity, high-bandwidth technique for measuring axial velocity. Higher speed machines would probably use high-response pressure measurements, because pressure transducers are more rugged than hot wires, and because pressure measurements are sensitive enough in a high-speed environment. The hot wires are positioned relatively far upstream of the compressor, so that the higher harmonic components of the disturbances generated by the compressor are filtered (see discussion in Section 4.1.2). This reduces the likelihood of spatial

aliasing of the signals. Eight hot wires are used for most of the experiments, so that waves with 1, 2 or 3 lobes can be measured without aliasing.

There are many ways to actuate travelling waves in an axial compressor. Techniques involving oscillating the inlet guide vanes (IGVs), vanes with oscillating flaps, jet flaps, peripheral arrays of jets or suction ports, tip bleed above the rotor, whirling the entire rotor, and acoustic arrays were all considered on the basis of effectiveness, complexity, cost, and technical risk [46]. Oscillating the IGVs was chosen on the basis of minimum technical risk - it was deemed feasible to both implement and accurately model moving IGVs. Results of modeling the IGVs [20] do in fact match experimental results quite well - see, for instance, Figure 4.3. The design of the IGVs, their size and number, and the actuation hardware were all driven by the desire to maximize control effectiveness and minimize complexity and cost. See [46] for a discussion of the design process. The resulting configuration is discussed in Section 2.2 and 2.3.

The bandwidth of the instrumentation in the feedback path was designed to be adequate to stabilize the maximum projected instability rate based on measurements and theoretical studies. Control algorithms were benchmarked, and a 80386-based PC-type computer was judged fast enough for the application. This computer was later upgraded to an 80486-based machine. Use of an IBM PC compatible computer made finding off-the-shelf hardware for data acquisition and servo control relatively easy and inexpensive.

2.2 Mechanical Layout

Figure 2.1 shows a blow-up of the single-stage axial research compressor, and the IGV ring which has been constructed for this project. The upstream annulus and bell mouth are mounted on a rolling cart, as is the IGV ring. These two assemblies roll on a pair of I-beams, one of which engages the wheels on an alignment track.

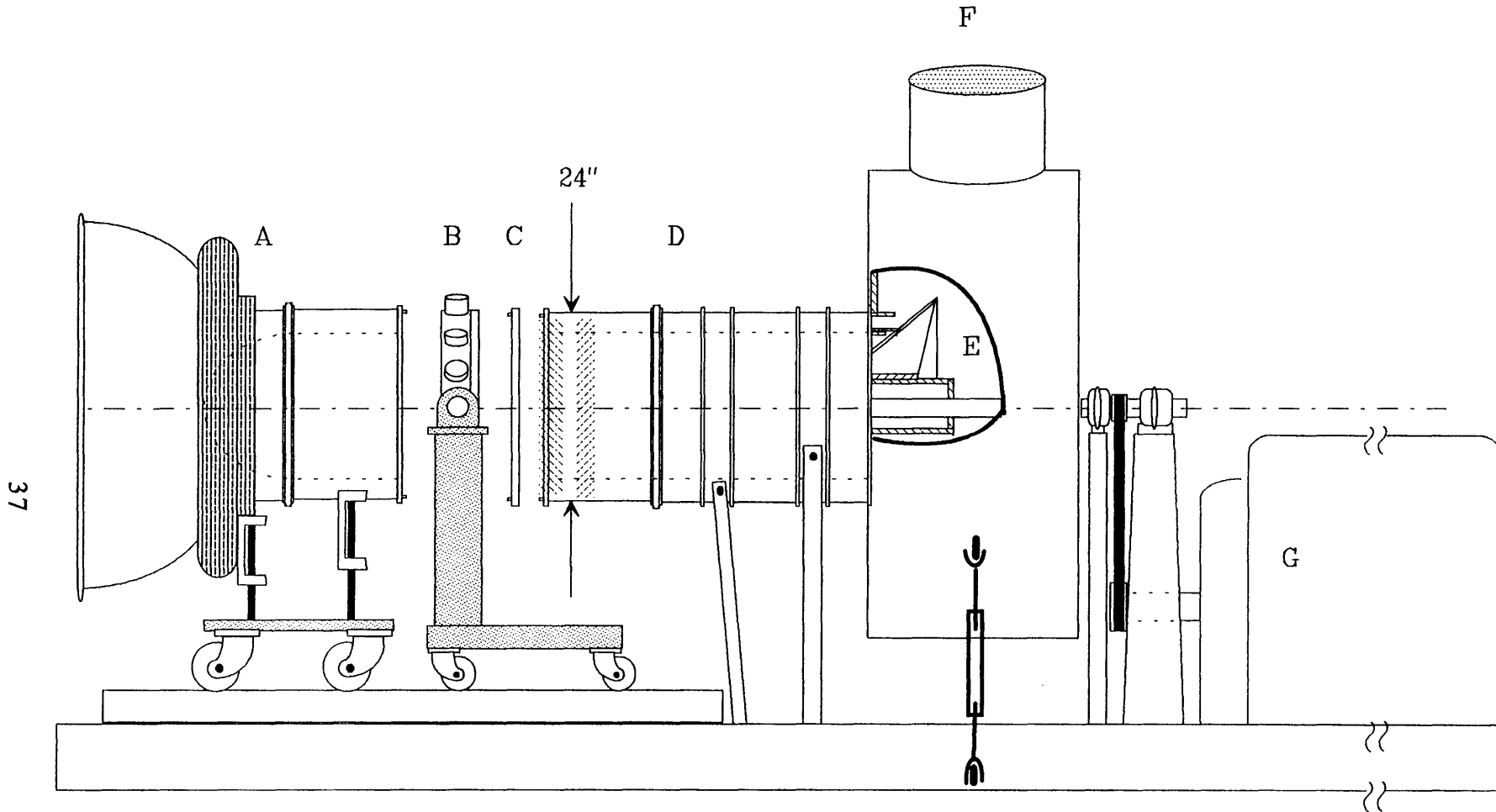


Figure 2.1 - Axial compressor test rig - shown separated are: A - upstream ducting;
 B - IGV ring with servos; C - spacer ring; D - compressor & downstream ducting;
 E - throttle arrangement; F - exhaust duct; G - drive motor.

The compressor and downstream ducting are fixed to the same pair of I-beams, and the rotor shaft is supported by struts emanating from these beams. The rotor is spun by a 250 horsepower DC electric motor. The throttle arrangement is shown in cutaway in Figure 2.1: it consists of a conic section mounted on a pair of screw jacks. A variable-speed electric motor turns the screw jacks and positions the throttle, under the control of the experimenter. Downstream of the throttle, ductwork leads to a roof fan, which provides extra suction to overcome the losses in the ducts. The compressor alone can only barely overcome these losses, so the extra suction provided by the roof fan is necessary to reach certain parts of the compressor map.

The compressor which was modified for this project (also described in [19]) consists of a constant-area duct with a hub/tip ratio of .75, in which a rotor and stator stage are mounted, each of which has a solidity of about 1.0. The geometry of the compressor is given in Table 2.1; nomenclature of compressor geometry is defined in Figure 2.2. For all of the experiments described in this thesis, the rotor was spun at 2700 RPM, which corresponds to a tip Mach number of .245.

The original section of casing on which the IGVs were mounted has been removed, and replaced with a new casing ring. This ring is shown in Figure 2.3: it has been designed so that up to 24 IGV blades can be mounted. These blades can be either mounted with bolts, so that they are fixed, or mounted on the shafts of dc servomotors, so that their angle relative to the incoming flow can be controlled in real time. Figure 2.3 shows the configuration which was used in this thesis: 12 motors evenly spaced around the annulus with an IGV blade mounted on the shaft of each motor. The casing ring is split, to allow the motors to be mounted easily. It also provides stops for the motors, so they cannot spin continuously, and mounting holes for instrumentation downstream of the IGVs. There are 25 such holes, evenly spaced. The combination of 24 blade stations with 25 instrumentation holes means that each hole is behind a different location with respect to the IGV blade passages. Thus, the

Table 2.1 Compressor geometry

Number of stages	1
Tip diameter	0.591 m (23.75 in)
Hub diameter	0.445 m (17.5 in)
Hub/tip radius ratio	0.75
Mean radius	0.259 m (10.187 in)
IGV/rotor gap	18 mm (+ 14.5 mm when spacer ring is in)
Rotor/stator gap	48 mm

<u>Stage</u>	<u>Number of blades</u>	<u>Chord¹ (mm)</u>	<u>Camber¹ (deg)</u>	<u>Stagger (@ mean radius)</u>	<u>Twist²</u>	<u>Solidity</u>	<u>b³</u>
<u>Inlet Guide Vanes-</u> NACA 0009 pivoted at 42% chord hub clearance: 1mm ± 0.5	12	81	0	$\gamma=0$	0	0.6	0.314
<u>Rotor-</u> NACA 64-009 pivoted at 50% chord tip clearance: 1mm ± 0.6	44	38	25 (at midspan*)	$\gamma_r=35$	30	1.03	0.147
<u>Stator-</u> Unknown 9% thickness airfoil pivoted at 50% chord hub clearance: 1.5 mm	45	38	30	$\gamma_s=22.5$	-5	1.08	0.151

Notes:

- 1) chord and camber are constant across span, *EXCEPT for rotor, which has variable camber
- 2) twist is a linear function of span - twist column indicates (tip stagger) - (hub stagger)
- 3) b = (chord)/(mean radius)

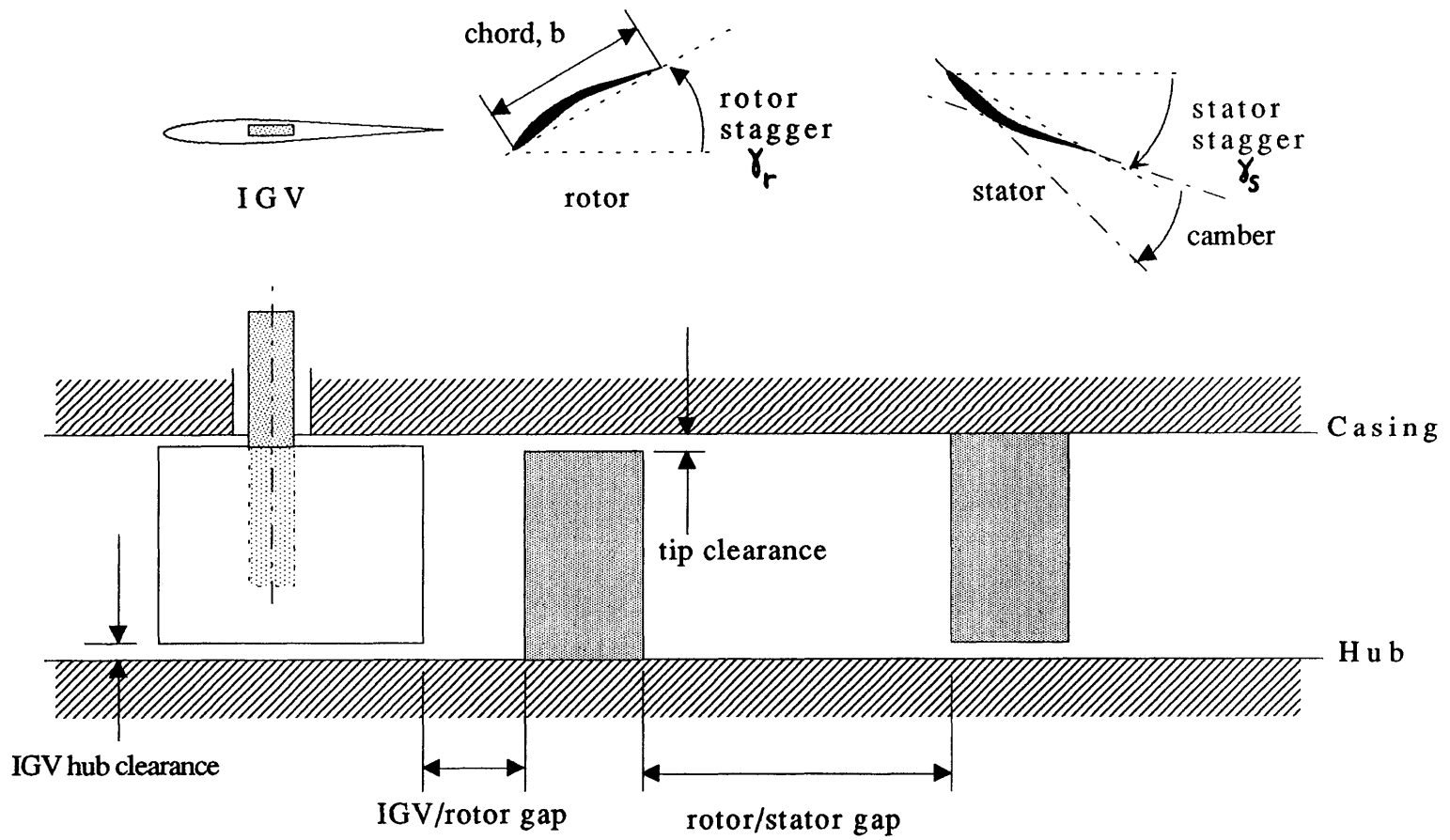


Figure 2.2 - Compressor geometry definitions

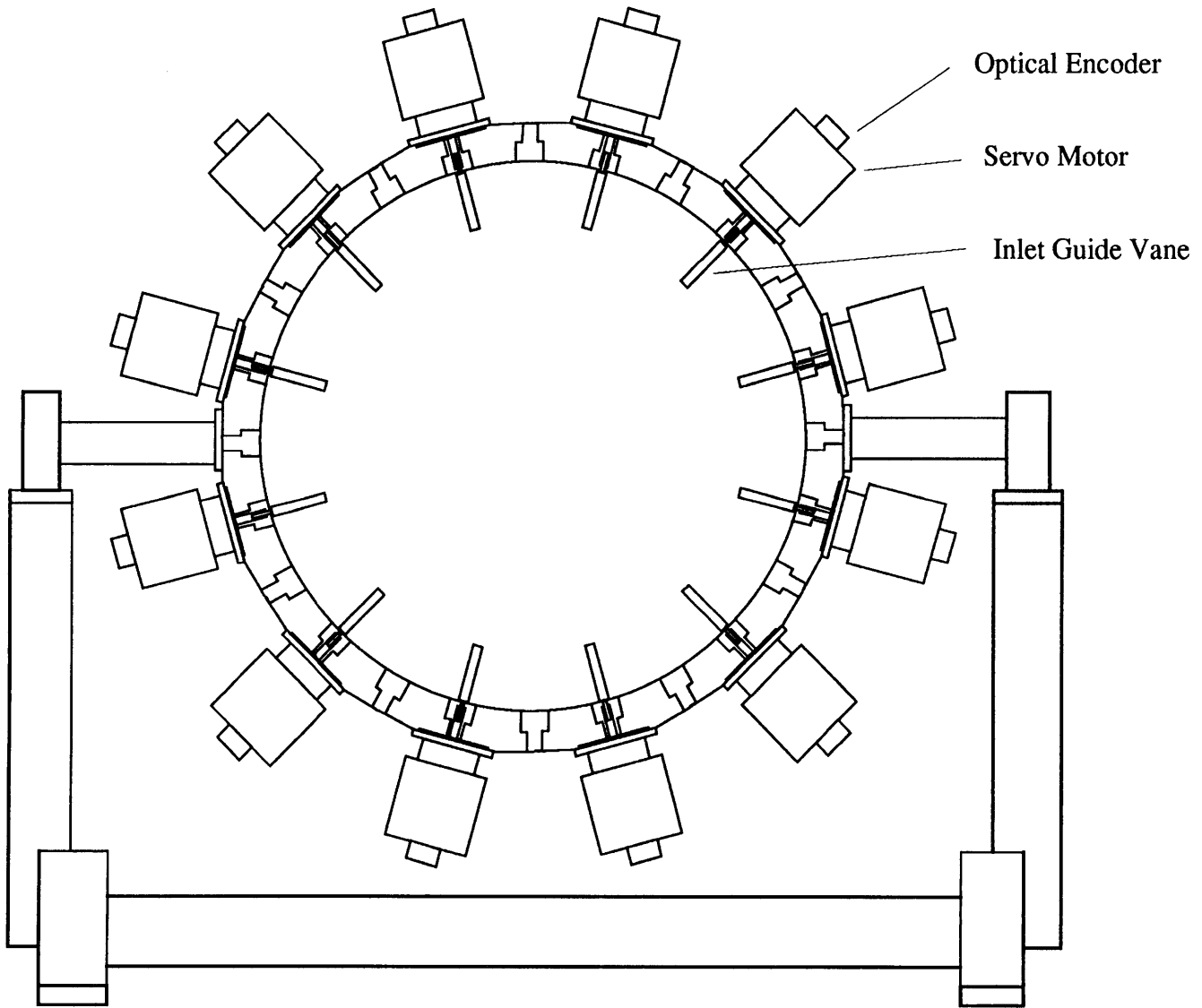


Figure 2.3 - Twelve motors mounted on IGV ring

flow field across the entire blade passage can be studied by mounting instrumentation in different holes.

Silkowski [20] studied the control effectiveness expected from a set of moving IGVs, and this information was used to determine the size and number of IGV blades required. By choosing a blade with a relatively long chord, and eliminating stationary IGV blades between the moving IGV blades, it was determined that 12 moving blades would provide sufficient control power [20,46]. IGVs with zero incidence and symmetrical airfoil shape were chosen to allow both positive and negative deflections. NACA 0009 was chosen as the IGV airfoil shape because of its ability to operate at high angles of attack (± 15 degrees).

The final consideration for design of the IGV blades was bandwidth. In order to provide the highest possible actuation bandwidth, the inertia of both the servomotors and the blades was minimized. Low-inertia, high-current capacity DC servo motors, type 4VM62-220-1, from Pacific Scientific, were chosen as the highest bandwidth servomotors available. The inertia of the IGV blades was kept to a minimum by casting them out of epoxy. Metal blades of exactly the same shape as the cast blades were numerically machined; these are used when stationary blades are desired.

Photographs of the IGV ring, servo motors, and IGV blades are given in Figures 2.4 and 2.5.

To complete the mechanical description of the rig, the instrumentation layout is shown in Figure 2.6. The static pressure ports are wall taps flush with the casing. The dynamic pressure taps are kiel-head probes. Upstream total and static pressure measurements are combined to give an annulus-averaged axial velocity. A pitot-static tube provides another check of the axial flow velocity. Downstream static pressure ports are used when measuring the total-to-static pressure rise of the compressor for speed lines. Mountings for hot wires exist upstream of the IGVs, between the IGVs

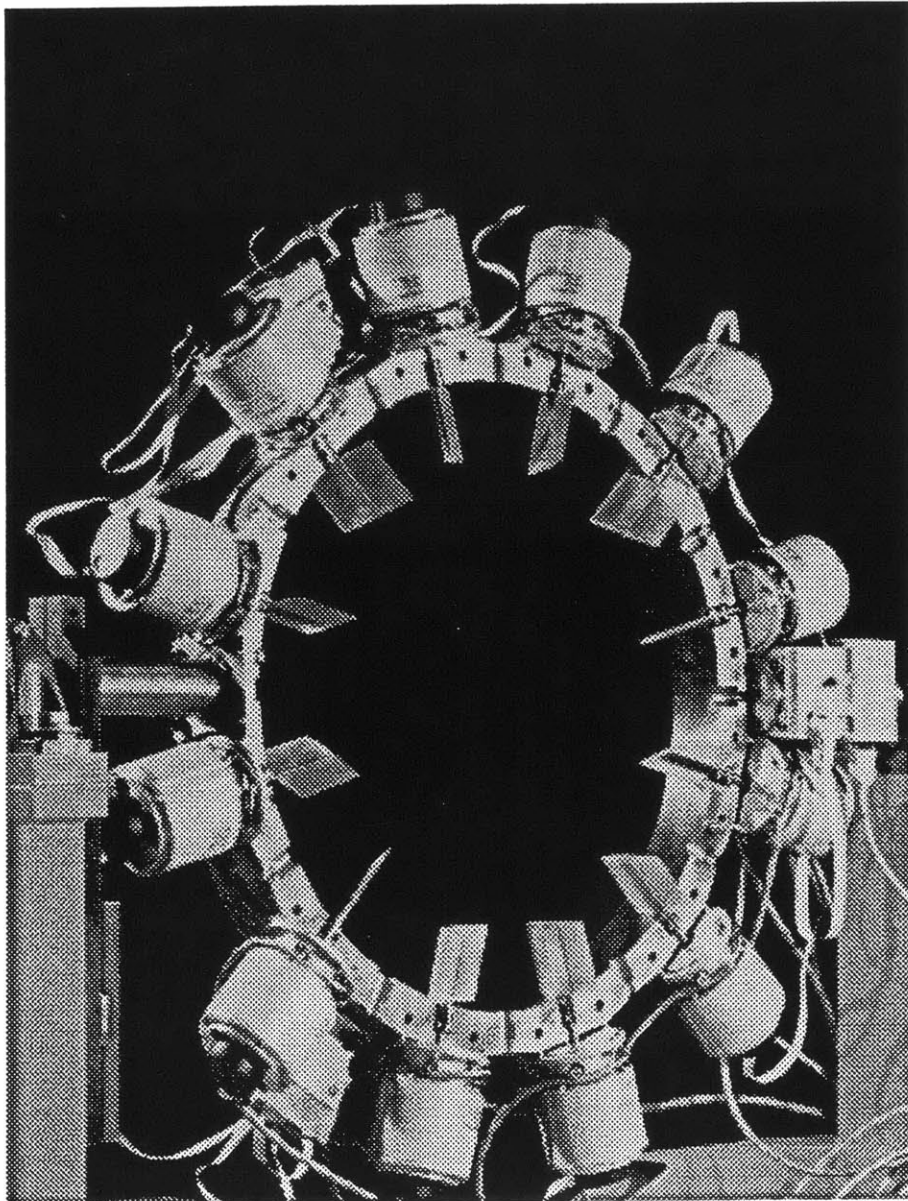


Figure 2.4 - IGV ring, servo motors, and IGVs

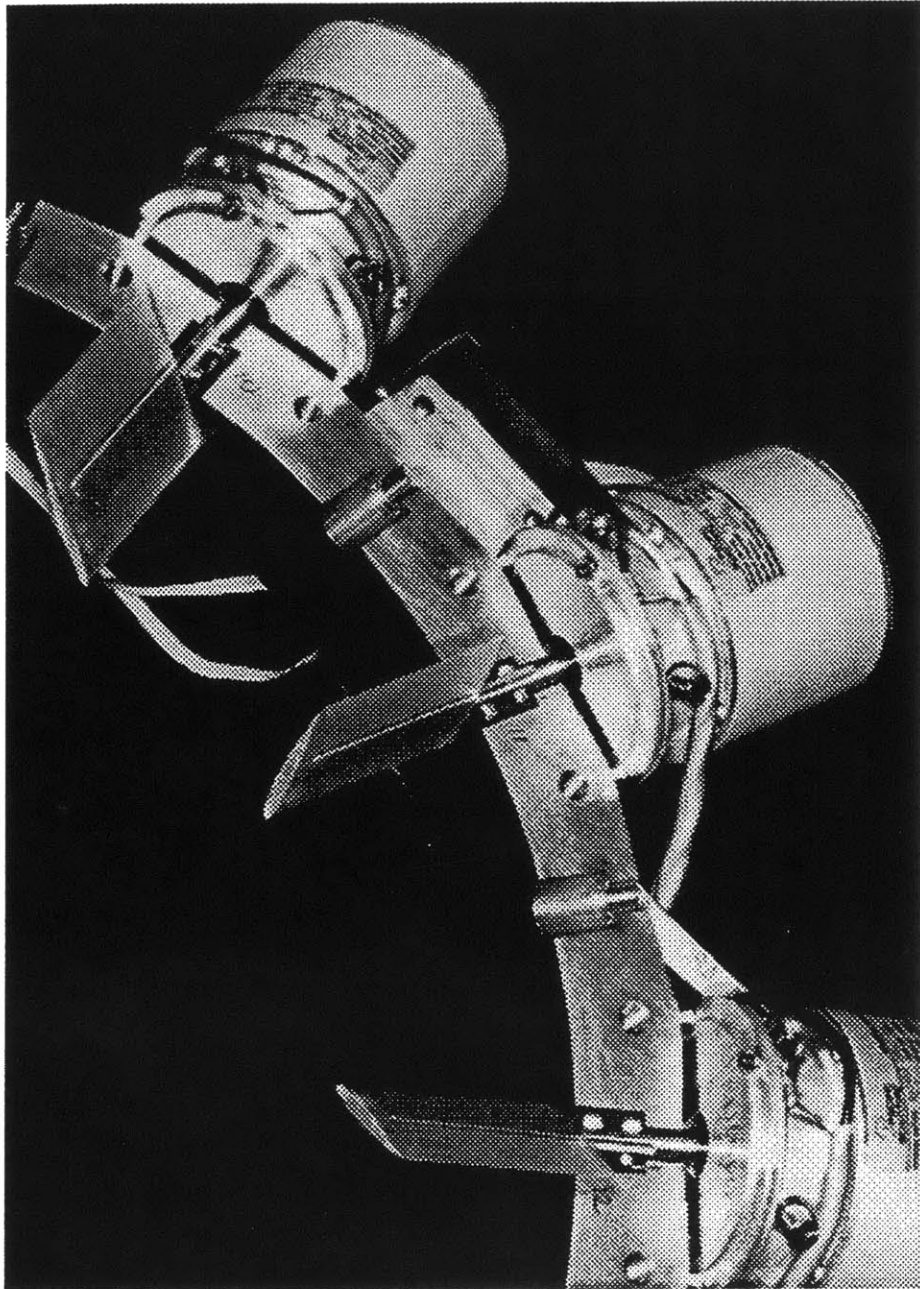


Figure 2.5 - Close-up of servo motors and epoxy inlet guide vanes

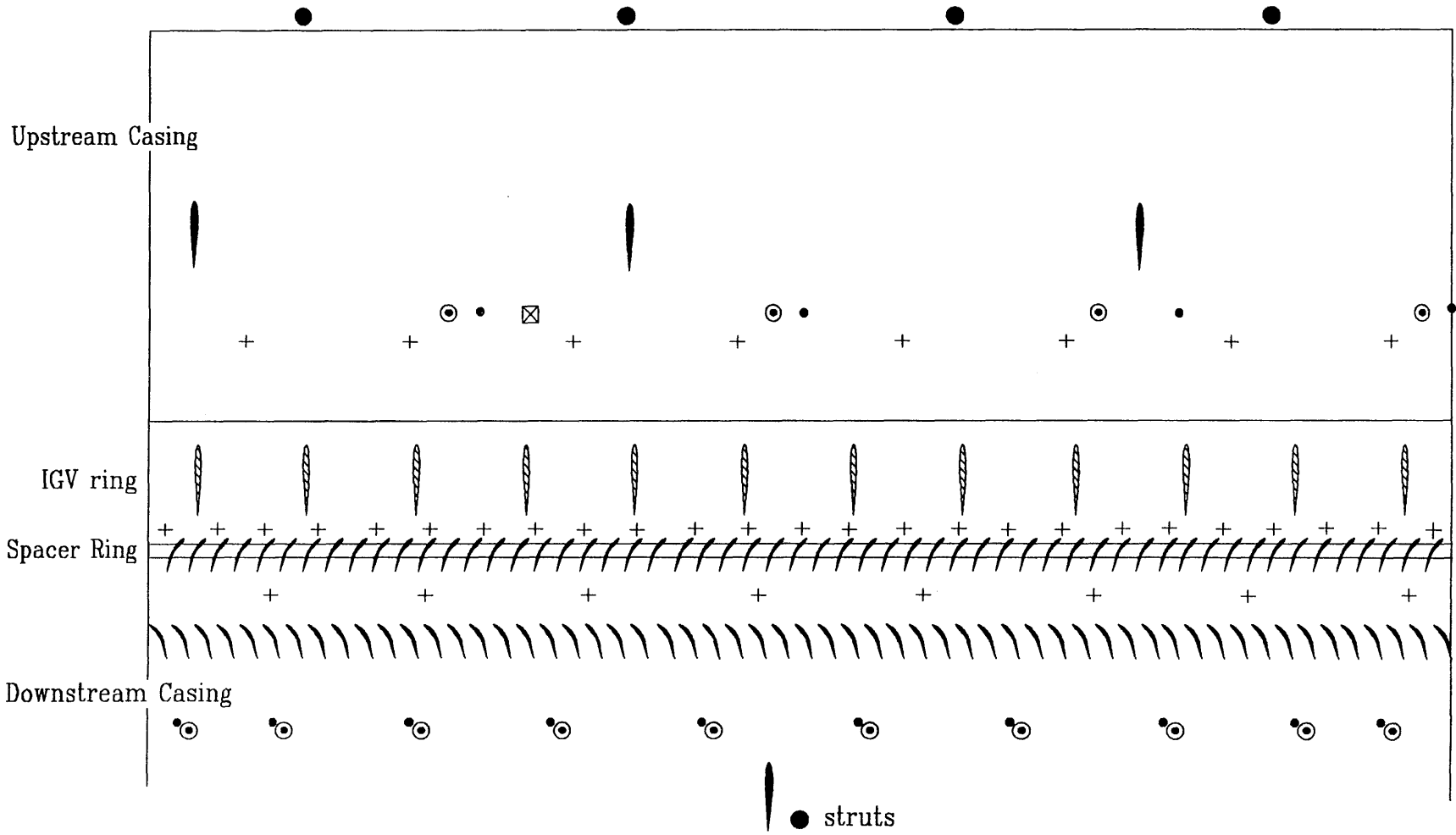
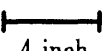


Figure 2.6 - Instrumentation layout.

- struts
- ⊙ total pressure taps (kiel head)
- + fittings for hot wire probes
- static pressure taps (wall)
- ⊠ pitot-static tube

scale 1:8

 4 inch

and the rotor, and behind the rotor. To mount hot wires behind the IGVs, an extra 0.57" spacer ring must be added to the casing ring, so that the rotor does not hit the hot wires (see Figure 2.1). Figure 2.6 shows where all the probes are located; a more complete description of the way that the measurements are taken, calibrated and used is given in Section 2.3.

2.3 Sensors, Signal Processors, and Computers

The high-response measurement and actuation equipment is depicted in Figure 2.7. This is the feedback loop used for active control of rotating stall. In parallel, low-response (time-averaged) pressure data can be acquired. Figure 2.8 shows the equipment used for pressure data acquisition. The individual elements in these two diagrams are described in this section.

2.3.1 Hot Wire Probes and Anemometers

Dantec type 55-P11 hot-wire probes are used for time-resolved axial velocity measurements. Each probe consists of a 20 μm tungsten wire, about 1.2 mm long, extending between two posts. A Dantec 56C17 CTA Bridge anemometer unit provides the current necessary to keep the tungsten wire at a constant resistance level, which, due to the properties of the wire, implies constant temperature. The current required to keep the wire at constant temperature is a function of the cooling provided by air passing over the wire, which is in turn a function of the airflow velocity perpendicular to the wire. Thus, the current provided to the hot wire probe is an indirect measure of the flow velocity over the probe. The anemometer unit has a voltage output which is proportional to the current provided to the probe. The relationship between anemometer output voltage and velocity is given by King's law [21]:

$$E^2 = A_0 + A_1 V^n, \quad (2.1)$$

where E is the voltage output of the anemometer (expressed in A/D counts), A_0 and

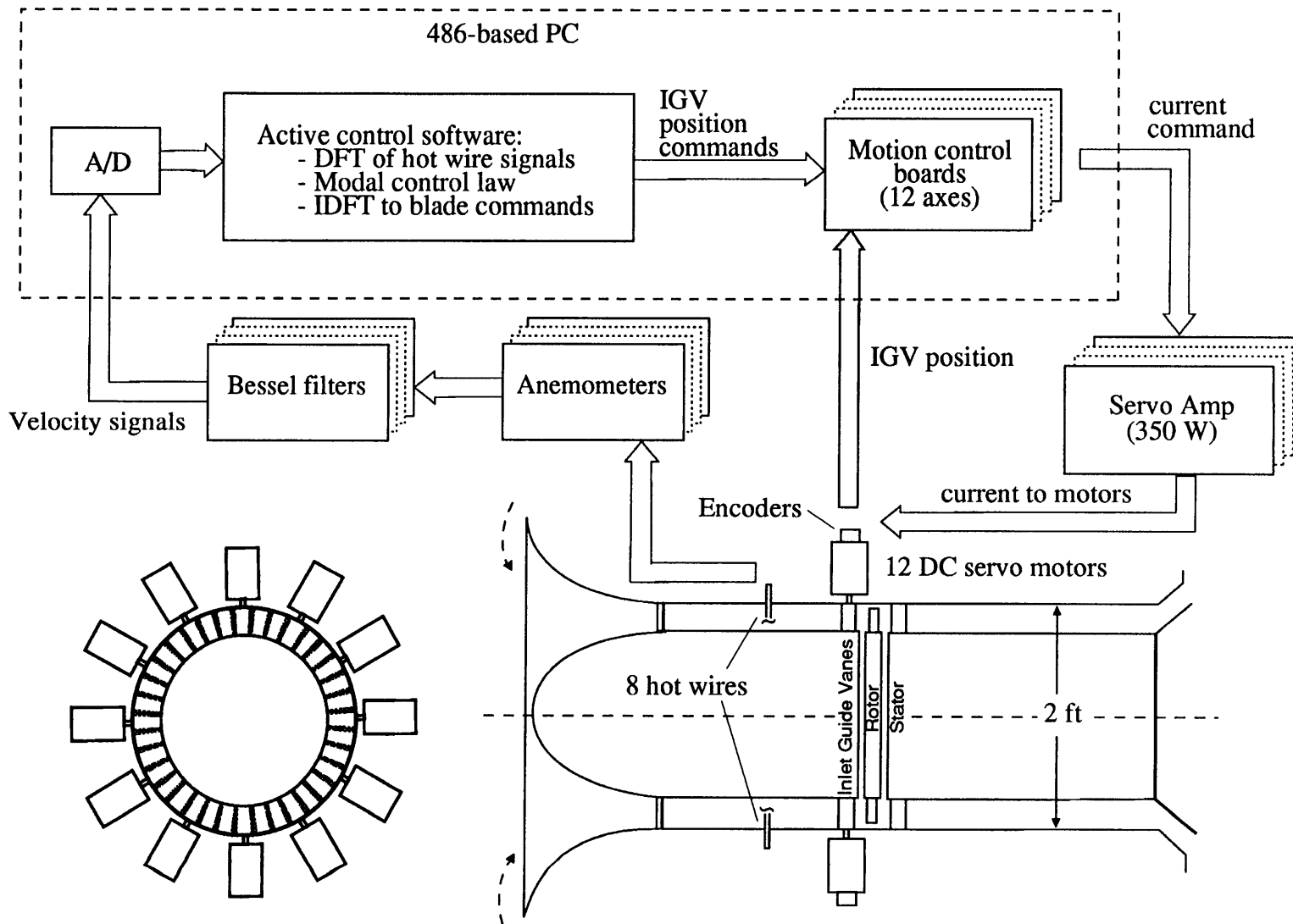


Figure 2.7 - Elements of the feedback path

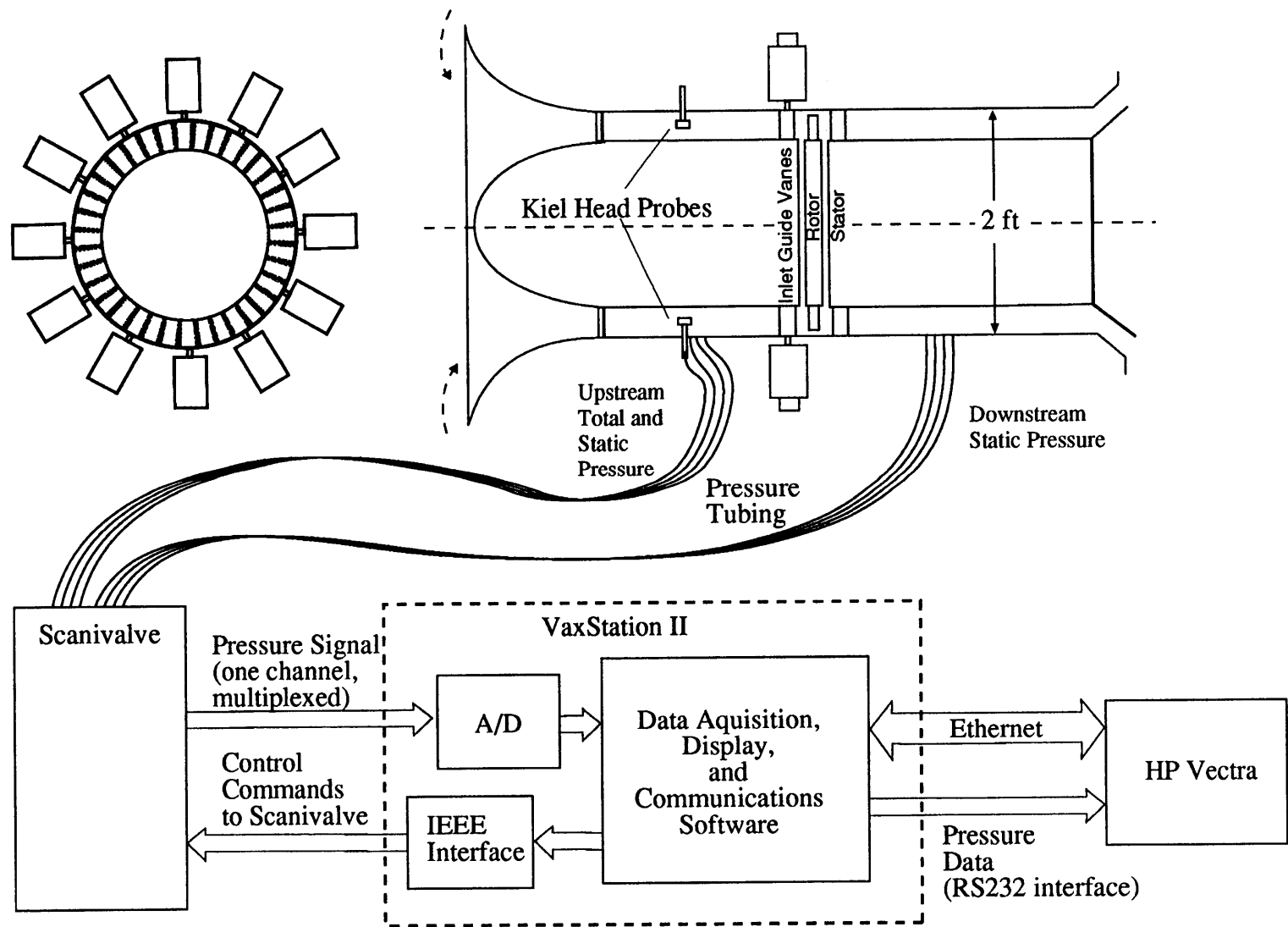


Figure 2.8 - Pressure data acquisition equipment

A_1 are calibration constants, V is the velocity at the hot wire in m/s, and n is a calibration constant (usually about .5). The calibration constants in this equation must be determined experimentally, each time the experiment is run, because the calibration tends to drift dramatically over time.

The sensitivity of velocity measurements was found to be about .10 to .15 m/s per A/D count, or .08 to .12 m/s per mV. The bandwidth of the measurements (as claimed by the manufacturer) is 50 kHz, well above the sampling frequency used in these experiments.

2.3.2 Low-Pass Filters

Each hot wire signal is filtered by a 4-pole analog Bessel filter, whose cutoff frequency has been set at 1000 Hz. This frequency is well below the blade passing frequency (1980 Hz for a 44 blade rotor spinning at 2700 RPM). At the same time, the cutoff frequency is well above the Nyquist frequency of the control system (250 Hz), so that the lag seen by the control system due to the filters is negligible. Anti-aliasing filters are usually chosen to roll off at frequencies *below* the Nyquist frequency, to prevent aliasing. It has been verified that, in this compressor, a signal measured at 5000 Hz provides no significant spectral information beyond that found in a signal measured at 500 Hz. Thus, aliasing is not a problem when the filter cutoff frequency is set to 1000 Hz.

2.3.3 A/D Board

The outputs of the Bessel filters are fed into a Metrabyte DASH-16F analog to digital converter, mounted in a HP Vectra 486 computer (see next section). The A/D unit mounts directly in an expansion slot and provides direct memory access (DMA), sampling at 100kHz. The range is set to 0 to 5 volts, and the sensitivity is 12 bits, or 4096 divisions, about 1.22 mV per A/D count. Since the hot wire signal consists of small fluctuations (typically 10-25 mV) modulating a DC signal of about 2.5 Volts,

the sensitivity of the A/D is barely adequate. Fortunately, the noise introduced by the A/D is extraordinarily low, on the order of 1 to 3 A/D counts, so that meaningful feedback can still be accomplished. Combining the incoming channels into Fourier coefficients (described in later chapters) also increases the effective signal-to-noise ratio of the overall sensing system.

2.3.4 HP Vectra 486 Computer

The primary computer for real-time data acquisition and control is a Hewlett-Packard Vectra 80486-based microcomputer, running at 25 MHz and hosting the A/D and Motion Control Boards. This computer has a 80487 Math Coprocessor, 8 Mb of RAM, a 300 Mb hard disk, and a tape drive to back up data. Programs to interface with the A/D, take hot wire data, compute control commands, and communicate with the motion control boards (which ultimately control the servo motor positions) were written in Fortran and Assembly. Utilities to quickly plot out data, and to do data reduction, were also written. Some of the more interesting programming considerations are discussed in Section 2.5.

2.3.5 Servo Motion Control Boards

Also mounted in the HP computer expansion slots are 4 Galil DMC-430 servo motion control boards. Each of these boards controls 3 servomotors, for a total of 12. Each motion control 'axis' is a completely independent set of special-purpose electronics which perform the following functions:

1. Decoding optical encoder information from the servo-motor;
2. Operating a digital proportional-integral-derivative (PID) control loop, which feeds back encoder information to a current command;
3. Computing and sending out an analog (-10V to 10V) current command;
4. Communicating with the PC's main (80486) processor, to get information about the desired position of the servomotor.

It is important to note that these operations are performed 'off line' as far as the main computer processor is concerned; the 80486 needs only to provide the commanded position of each blade. Thus an enormous computational burden is lifted from the main processor; accuracy and repeatability of servo operation is also insured by using industry-developed off-the-shelf hardware.

Figure 2.9 illustrates the operation of one axis of a DMC-430 board. Each servomotor feedback loop is operating at 2 kHz, feeding back optical encoder counts from the motor and comparing this information with the command from the computer. The algorithm is the discrete-time equivalent of a PID controller:

$$(\text{current command}) = D(w) \cdot (\text{commanded} - \text{actual position}), \quad (2.2)$$

where

$$D(w) = K \frac{w - A}{w - B} + \frac{C}{w - 1},$$

and w^{-1} is the .5 msec delay operator. The computer updates the commanded blade angles every 2 msec, and the command is assumed constant between updates. The output of the motion control boards is updated every .5 msec through a zero-order hold. The constants K, A, B, and C are set by the experimenter. These constants have been tuned so the bandwidth of the servos is about 80 Hz.

2.3.6 Amplifiers

Each DC motor must be driven by an amplifier. The amplifiers chosen for this system are Copley Controls Model 240H pulse-width modulated DC amplifiers. The switching frequency is 22kHz, the maximum current capability is 30A, and the RMS current capability is 15A. The 12 amplifiers are mounted in 3 instrumentation rack drawers, each of which houses 4 amplifiers and a transformer/rectifier combination rated at 60A @ 60VDC. These mounting drawers also display an LED bar-graph of the current command to the motors. Figure 2.10 is a photograph of the amplifier rack. A low voltage current command for each servo comes into the unit,

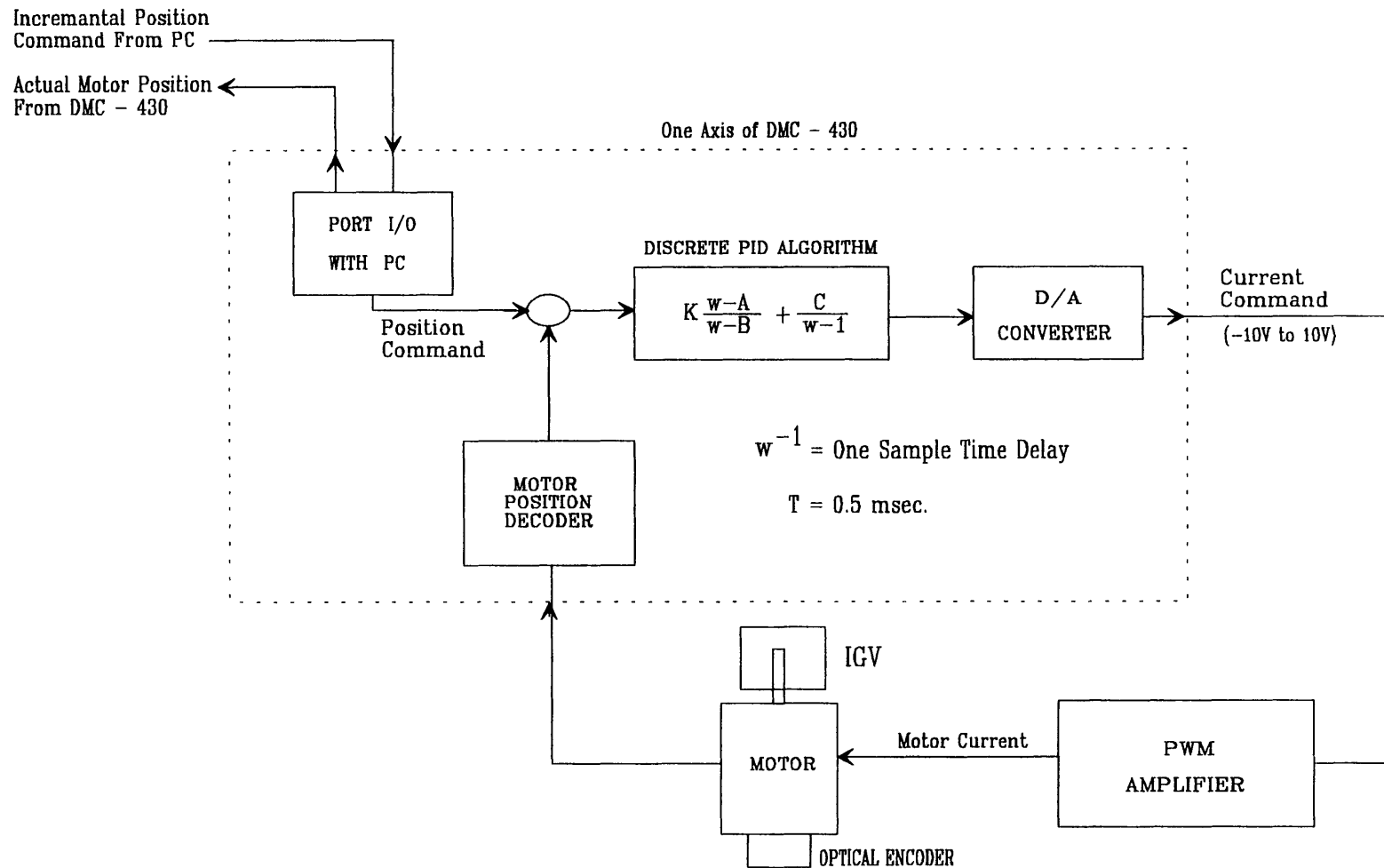


Figure 2.9 - Operation of one axis of DMC-430 DC motor controller

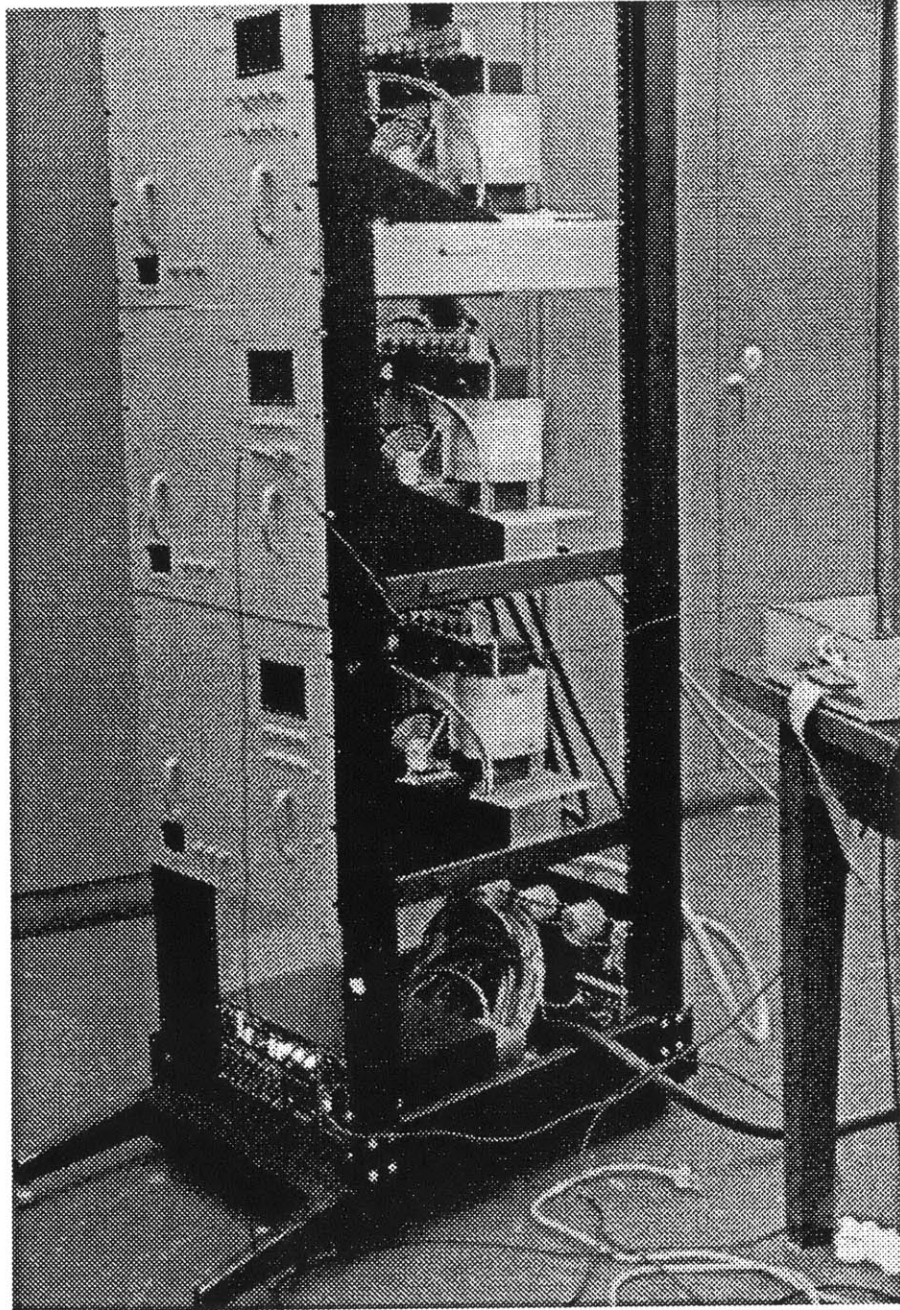


Figure 2.10 - Amplifier Rack

and the commanded current comes out.

2.3.7 DC Servo Motors

Pacific Scientific 4VM62-220-1 permanent magnet servo motors position the inlet guide vanes (see Figures 2.4 and 2.5). These motors are of hollow-core construction - that is, the windings are impregnated in an epoxy cylinder, and the metal core does not rotate. This construction provides a very low-inertia, high-torque servo motor, a combination that allows for extremely high response. The motors are air-cooled by a blower which draws air through the motors at approximately 1 standard cubic foot per minute. At this cooling rate, the motors can dissipate 100 Watts of heat (I^2R) power. The inertia of the motors is 3.8×10^{-6} kg-m², the maximum current capability is 40 amps (short duration), and the rms current capability is 7.2A.

2.3.8 IGV Blades

Figure 2.11 shows an IGV blade, giving the dimensions and airfoil shape, which is NACA 0009. These blades were cast from low specific gravity (about .7) epoxy; the estimated inertia which resulted is 3.32×10^{-6} kg-m².

This completes the description of all the elements in the feedback path, from the hot wire probes to the moving blades. There is another signal path whose elements must be described: the pressure-probe to logged-data path. The elements are the probes, the Scanivalve, the VAX A/D, and the VAX computer (see Figure 2.8).

2.3.9 Pressure Probes

Three types of pressure probe are used in the compressor. For static pressure, simple wall static taps are used. For stagnation pressure, kiel-head probes are used, mounted at midspan. This type of probe provides insensitivity to errors in the angle

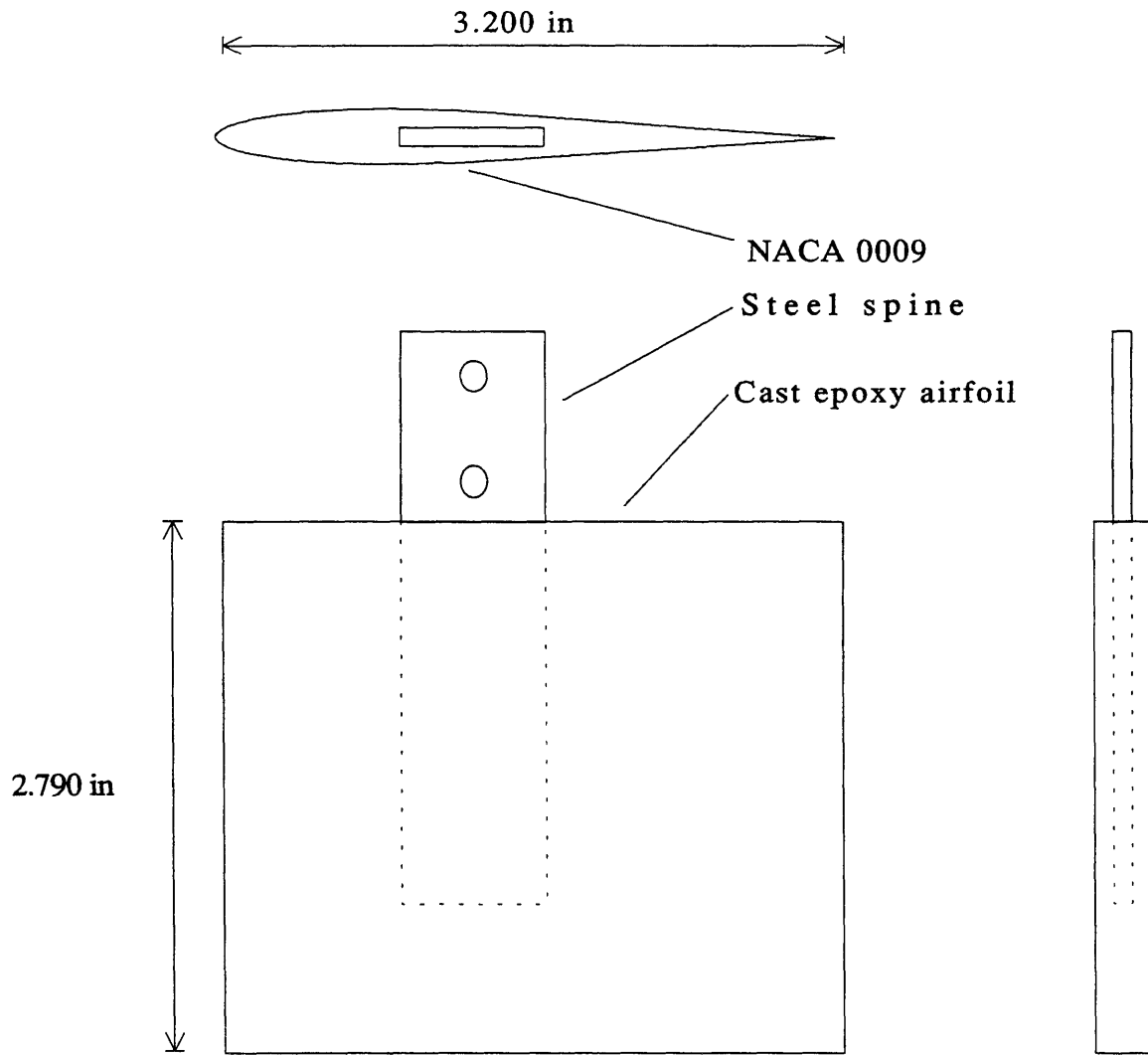


Figure 2.11 - Inlet guide vane detail (full scale)

of the probe with respect to the flow direction (up to at least 30° [3]) Finally, a pitot-static tube provides a second way to check the axial flow velocity.

2.3.10 Scanivalve

A Scanivalve is used to acquire steady-state pressure measurements. The pressure transducer in the Scanivalve was a Spectra strain-gauge type transducer with a pressure range of ± 2.5 psid. Periodic calibration of the pressure transducer in the Scanivalve was performed using an MKS Baratron unit.

2.3.11 A/D

The Scanivalve pressure transducer voltage output is fed into a Data Translations DT3382 A/D mounted in a VAXStation II computer. This A/D operates at 1 kHz; signals are averaged over a .1 second interval (100 samples).

2.3.12 VAX

A VAXStation II workstation is a part of the data acquisition and reduction equipment. The Scanivalve is controlled via an IEEE bus hosted by the VAX, so pressure data is taken using the VAX. This setup allows annulus-averaged, low bandwidth (about once per 10 seconds) monitoring of the compressor pressure rise during an experiment. The VAXStation is also used for much of the data reduction and plotting.

The VAX and the HP computer are connected via a serial communication line. This allows information from the pressure measurements to be transferred to the HP, when necessary. An Ethernet network interconnection between the two computers also exists, to allow fast transfer of large quantities of data.

2.4 Signal Flow Paths

The primary operations performed by the experimental setup will now be described. Refer to Figures 2.7 and 2.8.

2.4.1 Calibration

Calibration requires use of all of the instrumentation, computers, and their interconnections. The purpose of the calibration procedure is to provide a relationship between velocity (in m/s) at a hot wire probe, and voltage (in A/D counts) measured by the corresponding channel of the Metrabyte A/D in the HP computer. An estimate of the velocity at the hot wire probe is obtained by measuring the upstream total and static pressure, and computing the velocity as

$$V = \frac{2 \cdot \sqrt{P_t - P_s}}{\rho} \quad (2.3)$$

P_t and P_s are taken as average measurements from the upstream total and static pressure ports, respectively. The Scanivalve steps through these pressure ports, the VAX determines the average pressures, and these pressures are transferred to the HP computer via the serial interconnect. At the same condition, the HP samples the on-board A/D for the voltage (in counts) at each hot wire channel. It computes the velocity using the transmitted pressure measurements, and puts a point on the calibration relationship. This procedure can be repeated at different flow velocities until enough points for a calibration curve have been obtained.

2.4.2 Speed Line and Operating Condition Monitoring

Measuring the speed line and monitoring the compressor's position on the speed line are tasks performed by the VAX computer and the Scanivalve. Once the ambient conditions are recorded, pressure data is all that is required to determine the flow coefficient and pressure rise, so these can be determined by the VAX alone, scanning through the pressure taps. Print-out on the terminal, as well as a continuously updated plot of the speed line data provide a real-time (although extremely low bandwidth) monitor of the operating condition.

2.4.3 High-Response Data Acquisition and Control

High bandwidth data acquisition and control requires the use of the hot wires and the HP computer and A/D. The VAX and Scanivalve are not used for high-speed operation.

Signal flow is from the hot wire anemometers, through the analog filters, into the A/D, where digital velocity samples are placed in the HP computer memory via direct memory access. Velocity data can then be stored in arrays, and eventually on disk. In addition, the computer can compute (as feedback) or generate (open loop) IGV angle commands, which it communicates to the motion control boards via ports. These boards compute the necessary current commands to send to the servo motors, based on a PID algorithm, which compares motor encoder positions to commanded IGV angles. These current commands are then converted to analog signals, which are sent to the amplifiers, which in turn send current to the motors.

2.4.4 Data Reduction

Data stored in memory during a run is transferred to the HP hard disk at the end of the run. This data can then be transferred to the VAX via the Ethernet connection, in order to perform data reduction. MATLAB is the primary software tool used for data reduction, analysis, and plotting.

2.5 Programming Considerations

A few interesting features of the routines used for data acquisition and control will be detailed here.

2.5.1 A/D interface routines

Assembly language software, provided by Metrabyte, was modified for the specific mode of A/D operation used in this project. Since it was desired to sample between 10 and 16 channels of data as fast as possible, and do so at the beginning of

every control sample period, a two-clock structure was set up. Both clocks are programmable clocks on the Metrabyte A/D board. One clock is set to the sample rate of the control loop, 500 Hz. This is called the 'slow clock'. The other clock, the 'fast clock', is set to run at 100 kHz. This is the maximum sample rate available on the A/D. At every tick of the slow clock, a direct memory access (DMA) data transfer from the A/D to the memory of the HP computer is set up. This DMA then proceeds, for one scan of the A/D channels, at the fast clock rate. This method minimizes skew between channels, and leaves the maximum amount of time between slow clock ticks for computation of feedback commands, communication with the motion control boards, and other operations which must be performed during each sample time of the control loop.

Metrabyte Assembly language routines for DMA transfer were modified to wait for the slow clock tick before proceeding. In addition, the code was translated from 16-bit (80286) assembly language to 32-bit (80386) protected-mode assembly. Finally, translation of the input from the A/D, which is a 12-bit integer, into a 2-byte real number specifying the velocity, takes place in Assembly language via a look-up table. This look-up table is based on the calibration, and allows near-instantaneous translation of A/D samples into velocity information.

2.5.2 Motion Control Board Interface Routines

The Galil motion control boards are basically designed for profile control - that is, through simple ASCII commands sent to the boards via I/O ports, profiles of angular position can easily be commanded and repeated. This however, is not the mode of operation which is desired for this project. Instead, it is desired to send position commands to each servo once per sample period (i.e. at 500 Hz), and to do so in a fraction of the sample period. Since there are 12 motors, it is necessary to communicate with each in less than 100 μ sec, so that no more than about 1 msec of

the 2 msec sample time will be spent in communication with the servos.

To provide this type of communication, an option of the motion control boards is initialized at the beginning of a run. This option, sent as an ASCII command, tells the board that subsequent commands are *not* ASCII commands, but integers representing the increment in IGV position command. From that point on, the board takes each byte received on its I/O port as an increment to the IGV position command. This command is then compared to the actual IGV position (from the motor optical encoder) and the error drives the PID algorithm to generate current commands. Thus, the system is in a command-following mode.

Each board is internally clocked at 2 kHz, and can thus receive an increment to the position command once every 500 μ sec. Since the boards have independent clocks, they run asynchronously. Thus, communication with *all* of the boards is actually possible within 500 μ sec. Assembly language software was written to initialize and execute this communication; experience has shown that, in fact, all of the boards can have their commands updated within 500 μ sec, well within the desired time.

2.5.3 Feedback Control Program

The feedback control program is written in NDP Fortran, which compiles into protected mode assembly language, so that the full capabilities of the 80486 processor can be realized. The program operates as follows:

I. Initialization

- A. Initialize A/D clocks
- B. Prompt user for desired gains, initialize control gains
- C. Initialization sequence for servomotors
 - 1) Initialize slow gains for PID loop
 - 2) Drive IGVs to clockwise stop
 - 3) Drive IGVs counter-clockwise until they reach the encoder index (the index is a once per revolution pulse which provides a reference position)
 - 4) Initialize fast gains in PID loops
 - 5) Position all IGVs at axial (the index is not necessarily at axial)

- D. Place servomotors in 'incremental command' mode
- E. Prompt user for type of run
- F. Sample hot wires for 5 seconds, obtain a mean velocity estimate for each channel

II. Control Loop

- A) Wait for slow (500 Hz) clock tick
- B) Take hot wire data at fast clock rate (100 kHz)
- C) Compute spatial Fourier coefficients of hot wire signals (discrete Fourier transform)
- D) Compute feedback commands to IGVs in spatial Fourier coefficients
- E) Compute individual IGV commands (inverse discrete Fourier transform)
- F) Check commands, send increment to motion control boards
- G) Save data for this time step
- H) Increment counter, return to A)

III. Control Loop Proceeds for N cycles, N determined by user. At the end of N cycles, check keyboard for a quit or reconfigure command from keyboard.

- A) If quit, prompt to store data on disk and exit program
- B) If reconfigure, increment gains or change input as commanded
- C) If no command from keyboard, go to II and repeat N cycles of control loop.

It is clear from the description above that data is taken in blocks of N samples. If the user does not halt operation after these N samples have been taken, they are discarded and a new set of N samples is taken.

2.6 A Typical Run

A typical experimental run will be described, in order to tie together all the concepts of this chapter. First, ambient pressure and temperature are measured and recorded, for use in various routines. Then all of the equipment is turned on, and the servomotors are initialized so that they hold position as the compressor is spun up. The electric motor which spins the rotor is then turned on and brought up to ~1600 RPM. This speed is much lower than the speed at which actual data is taken, which means that the compressor will stall at a lower axial through-flow velocity than it will at full speed. Thus, a more complete calibration is possible (since we will be stabilizing the system, we will be operating below the natural stall point, so the

calibration curve should go down to these low flow values). The exhaust fan is next turned on to help the compressor force air through the ductwork.

Once the compressor is running, the hot wires can be calibrated. Typically, calibration is performed at 2 m/s increments between 20 m/s and 40 m/s (the manually controlled throttle position determines the mean axial velocity through the compressor). The measured calibration points are then fit to calibration curves using a procedure developed by Garnier [22]. These calibration curves are stored on disk for use by the control program.

The compressor is now brought up to full speed, 2700 RPM, and the VAX program to monitor the speed line is started. The VAX Workstation from this point on is continually adding to a plot of pressure rise versus flow coefficient, providing a monitor of the compressor operating point. The throttle is closed to a point near stall, but still stable.

Now the control program is begun. After running through the initialization procedures and setting up the feedback gains, the system begins to operate in closed loop. The system is still open loop stable, but the feedback system is nevertheless correcting for small perturbations which it measures. The throttle is next closed at an extremely slow rate (less than .1% in flow coefficient per second). The compressor flow coefficient slowly drops below the natural stall line, and the extension of the speed line is monitored graphically on the VAX. When the compressor finally stalls, the control loop is stopped. This allows the stall event to be stored on disk for later use. The minimum flow coefficient to which the system operated is then recorded, and the procedure is repeated. Typically 3 to 5 such stalls are performed to insure consistency and repeatability of the closed-loop stall flow coefficient.

During closed loop operation, the gains of the system can be changed, to try to allow the system to operate at lower flow coefficients. Also, an external command can be added to the feedback signal to allow for system identification. Many other

options are possible; these are just a few to illustrate the kind of tests done. Once the data desired has been gathered, the system is shut down, the data is checked on the HP (and perhaps partially reduced). Some data and/or reduced data is then sent to the VAX for further processing.

A complete set of raw data from a one second run is displayed in Figure 2.12. It is apparent that since there are many channels coming in and going out, a lot of data is logged during a run - about 10,000 points/sec of velocity and IGV position data, and about 20,000 points/sec of diagnostic data which is derivable from the velocity and IGV position data.

2.6.1 Parameters Which Define The Configuration of a Run

Because of the complex nature of the experimental setup, there are numerous variables in the configuration which, if changed, might affect the results. The attempt in this thesis is to minimize the number of configurations and parametric variations, where these variations are not of interest to the studies at hand. For instance, the RPM at which the tests are run is consistent throughout the entire thesis - this parameter is considered of secondary interest in the study of stabilization of rotating stall. Parameters which are consistent throughout this thesis are:

- Basic geometry of the rig:
 - rig dimensions (Table 2.1)
 - pressure tap locations
 - IGV, rotor and stator geometry and incidences (Table 2.1)
(Appendix C discusses variations in some of these parameters)
- Rotor rotation rate - 2700 RPM
- Exhaust fan is ON
- Hot wire overheat ratio - ~1.5
- Analog filter cutoff frequency - 1000 Hz
- Sample rate (slow clock) - 500 Hz
- DMA rate (fast clock) - 100 kHz
- Servomotor PID gains, amplifier current limits, etc.
- Mean velocity estimation procedure

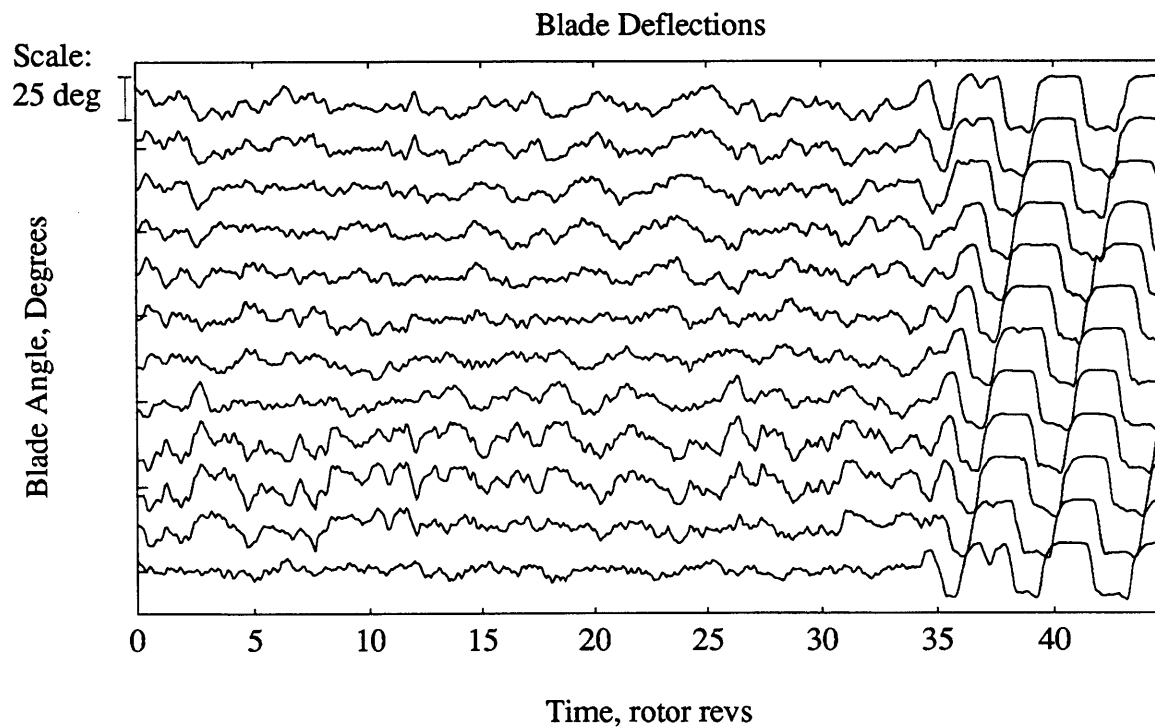
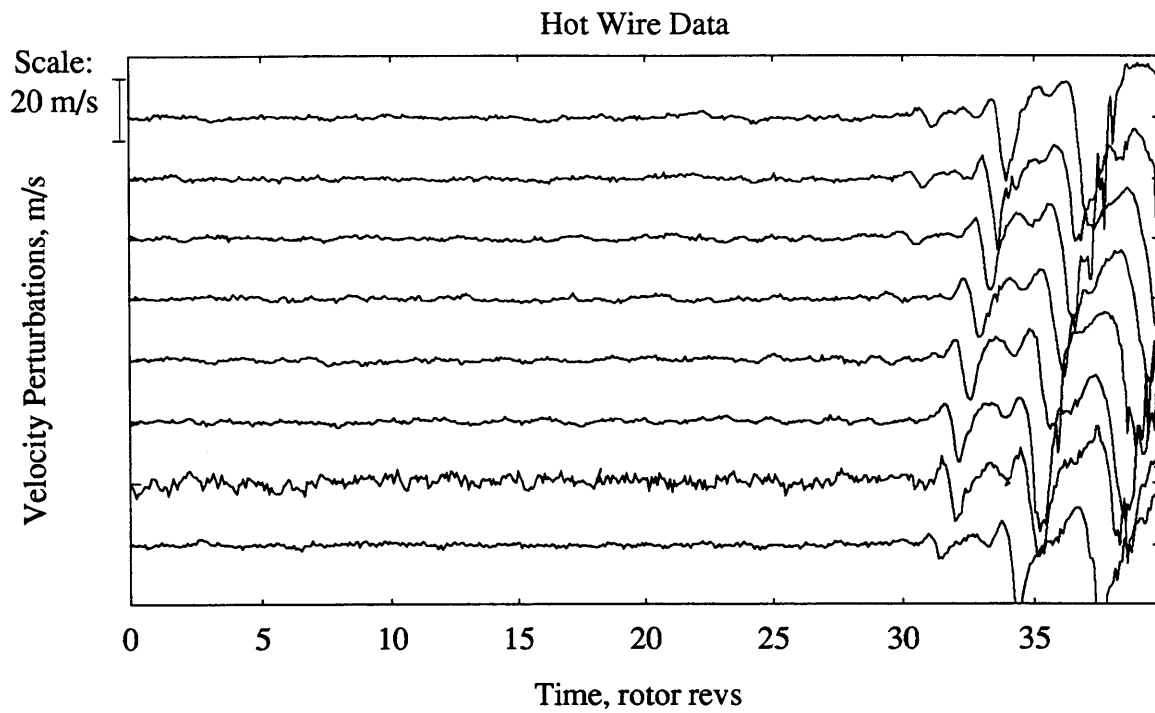


Figure 2.12 - Input velocity data and output blade deflections for one second of a typical closed-loop run

Parameters which may change from one run to the next are:

- Flow coefficient
- Number of hot wires and their locations
 - this includes axial location, circumferential locations, and radial locations
- Feedback law for closed-loop runs
- Stationary IGVs in or out
- .57" axial extension ring in or out

The last two entries constitute changes to the compressor geometry, which can either be put in or taken out. The first change is a set of 12 stationary metal IGVs, placed one between each pair of moving IGVs, to study the effects of solidity and non-moving IGVs. The second change is a .57" axial extension to the casing, which increases the gap between the IGVs and the rotor, allowing hot wires to be placed behind the IGVs.

CHAPTER 3

Modeling Compressor Higher-Mode Dynamics

This chapter presents the current model of axial compressor 'higher-mode dynamics'. Higher-mode dynamics refers to the compressor's response to disturbances which have a circumferential mode number of 1 or greater, as distinguished from those which are axisymmetric (i.e. mode number 0).

We postulate that higher-mode axial velocity disturbances will grow into rotating stall when they are unstable. Thus we are interested in modeling and, subsequently, in stabilizing these disturbances. The terminology 'higher-mode dynamics' is used to distinguish this model from models of 'rotating stall dynamics', which often attempt to model the mechanisms which govern *fully-developed* rotating stall. As we have seen in Chapter 1, fully-developed rotating stall involves large velocity perturbations, so any model of its behavior must be inherently nonlinear. The higher-mode dynamics presented here, on the other hand, describe the *small perturbation* behavior of the compressor. We will be stabilizing these small perturbations, so they will remain small and never grow into rotating stall. Thus we can develop a linearized model without making unrealistic assumptions. We can then study compressor response to small disturbances over a large range of operating conditions, some which are stable, and others which are unstable.

The approach taken is to derive the simplest form of the model which still retains its full structure. More detailed modeling has been conducted [18,24,25,38,42], and some of these results are reviewed in Appendix A. These additions only change the coefficients of the differential equations, without changing their basic form.

As such, they are of interest for prediction, rather than for understanding the system behavior. We will first explain the assumptions and notation used throughout the chapter, then proceed with the derivation. Alternate forms of the model are then presented.

3.1 Modeling Preliminaries

3.1.1 Assumptions

Figure 3.1 shows the compression system to be modeled. It consists of an upstream duct, a set of movable inlet guide vanes, a compressor, and a downstream duct. The following assumptions are made:

Compressibility effects are negligible - This assumption is usually considered valid when the Mach number is $\ll 1$. There are two relevant Mach numbers. Blade Mach number is computed as U/a , where U is the speed of the blades at the mean radius, and a is the speed of sound. In all the experiments described here blade Mach number is 0.24. This implies that the pressure rise across the compressor is small compared to atmospheric pressure ($\Delta P/P_{\text{atm}} \ll 1$), so that compressibility effects within the compressor are negligible. For rotating stall disturbances, Mach number is computed as $\omega L/a$, where ω is the reduced frequency associated with the traveling waves and L is their characteristic length. In the current set of experiments, this Mach number is ~ 0.1 independent of the modal content of the perturbation waves.

The effects of viscosity are negligible outside the blade rows - The Reynolds number in our experiments is about $5 \times 10^5/n$, where n is the highest mode number in the disturbance. Thus even for high modal content in the disturbance waves, viscous effects outside the blade rows are much smaller than inertial effects, and can be ignored.

Uniform inlet flow - The upstream flow is assumed to come into the compression system from a reservoir at uniform conditions. Far upstream it will thus be

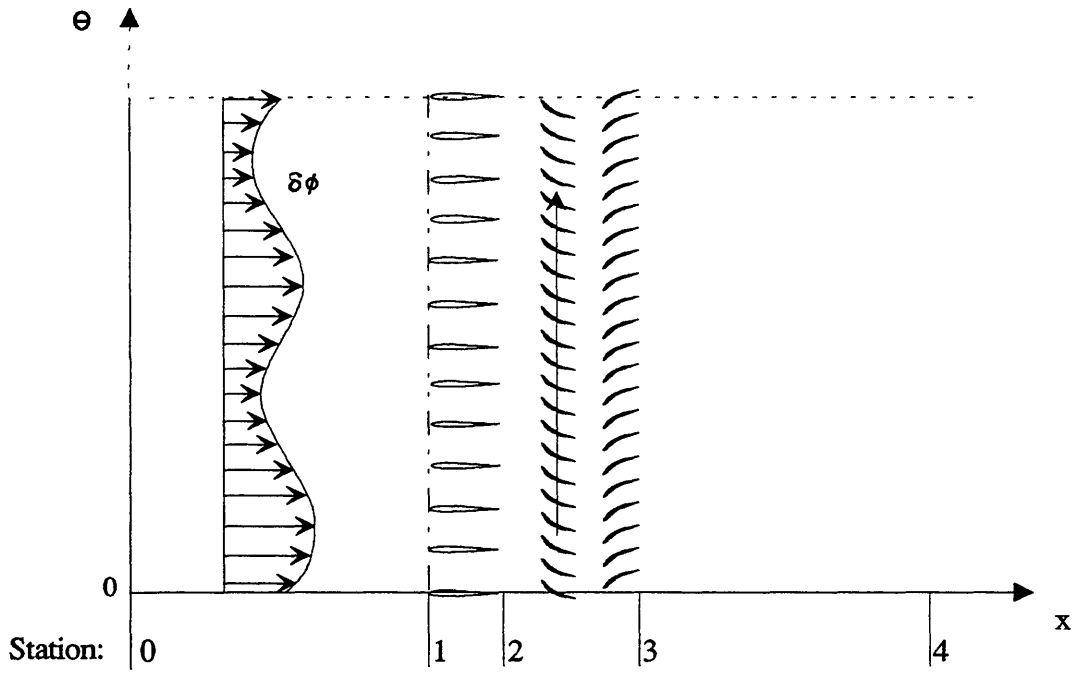


Figure 3.1 - Stations in a 2-D axial compression system

axisymmetric (no distortions), and will contain no vorticity. This permits the upstream flow to be considered as a potential flow.

No radial variation of the flow parameters (2-D flow) - For high hub-to-tip ratio machines, one often considers only the axial and circumferential variations in the flow. Blade row parameters (which will be imbedded in the compressor characteristic) are used to account for 3-dimensional effects within the compressor to some extent, but 3-dimensional stall behavior per se is not modeled, because the flowfield outside the compressor is considered to be 2-D.

The compressor is a semi-actuator disk - this is an extension of the classical actuator disk approximation, which will be described first.

The actuator disk model assumes two things: infinitesimal axial length, and an infinite number of blades. The first assumption allows the effects *across* the compressor to be modeled without modeling the details of the internal flow. The second assumption allows blade-to-blade variations in the flow field to be ignored. Thus, only circumferential disturbances which are long compared to the blade pitch are considered [14]. The actuator disk, then, is simply a surface across which the quasi-steady pressure rise and flow turning are specified to match those of the actual compressor.

The semi-actuator disk model, which must be employed when unsteady flow is important (e.g. the situation of rotating stall), accounts in a simple way for unsteady effects within the compressor by modeling the inertia of the fluid in the blade passages. In every other way it resembles the actuator disk model. Details of this modeling appear in Section 3.2.5.

Surge dynamics can be neglected - For small perturbations in the compressor flow coefficient, surge and rotating stall are decoupled. Furthermore, because the Greitzer 'B Parameter' is < 0.1 in this experiment, surge-type (zeroth mode) oscillations are never encountered. Therefore, we will neglect surge entirely in this discussion.

3.1.2 Notation and Non-dimensionalization

3.1.2.1 Non-dimensionalizing Parameters

Non-dimensionalization of the equations is accomplished using parameters which define the geometry and 'size' of a specific compressor. The non-dimensionalizing parameters are:

- r - rotor mean radius
- U - wheel speed = (rotor rotation rate) $\times r$
- ρU^2 - 'dynamic head' based on rotor speed (ρ is fluid density)

3.1.2.2 Independent Variables

The independent variables of the problem are 2-D space and time. Axial position is non-dimensionalized by the rotor radius. Circumferential position is in radians, so it need not be non-dimensionalized. Time is non-dimensionalized by the rotor rotation rate. The notation is as follows:

- η - (axial position)/ r
The origin for η will be placed at the compressor face
- θ - circumferential position in radians, positive in the direction of rotor rotation
- τ - (time) $\cdot U/r$

3.1.2.3 Dependent Variables

The variables which determine the state of the system are the total and static pressure, and the axial and circumferential flow velocity. Additionally, we can define a velocity potential upstream of the compressor. We also let the IGV deflections be variable; eventually, these will be commanded by the control system. The notation is:

- $\mathcal{P}t(\eta, \theta, \tau)$ - (total pressure)/ ρU^2
- $\mathcal{P}s(\eta, \theta, \tau)$ - (static pressure)/ ρU^2
- $\phi(\eta, \theta, \tau)$ - 'flow coefficient' - (axial velocity)/ U
- $v(\eta, \theta, \tau)$ - (circumferential velocity)/ U
- $\Phi(\eta, \theta, \tau)$ - velocity potential, defined such that:

$$\frac{\partial \Phi}{\partial \eta} = \phi, \quad \frac{\partial \Phi}{\partial \theta} = v$$

- $\gamma(\theta, \tau)$ - IGV deflection angle (here we are assuming a circumferential continuum of blades)

3.1.2.4 Compressor Characterization

The compressor geometry and performance determine the specific behavior of the higher-mode dynamics. The specifications of the compressor required by this model are as follows (Section 3.2 explains the use of these parameters):

$\psi(\phi, \gamma)$ - overall compressor steady-state total-to-static pressure rise characteristic, $(\mathcal{P}_{s3} - \mathcal{P}_{t1})_{ss}$ - for instance, Figure 1.2

$\psi_c(\phi_2, \gamma)$ - compressor steady-state total-to-static pressure rise characteristic not including IGVs, $(\mathcal{P}_{s3} - \mathcal{P}_{t2})_{ss}$

η_{HW} - axial location of axial velocity measurements

λ - rotor fluid inertia parameter,

$$\lambda = \sum_{\text{rotors}} \left[\frac{b_R}{\cos(\gamma_R)} \right] \quad (3.1)$$

μ_C - compressor fluid inertia parameter (excluding IGVs),

$$\mu_C = \lambda + \sum_{\text{stators}} \left[\frac{b_s}{\cos(\gamma_s)} \right] \quad (3.2)$$

μ_{IGV} - inlet guide vane fluid inertia parameter,

$$\mu_{IGV} = \frac{b_{IGV}}{\cos(\gamma)} \quad (3.3)$$

μ - overall compressor fluid inertia parameter

$$\mu = \mu_{IGV} + \mu_C \quad (3.4)$$

In these definitions, b is the chord length of the blade specified by the subscript, non-dimensionalized by r . γ , γ_R and γ_s are the stagger angles of the IGV, rotor, and stator, respectively. Figure 2.2 and Table 2.1 further describe γ and b .

The use of the inertia parameters λ , μ_C , μ_{IGV} , and μ for characterizing the compressor unsteady performance is described in Sections 3.2.4 and 3.2.5.

3.1.2.5 Perturbation Variables

We will be developing a linearized description of the flow field, and we will use the following notation for mean flow and perturbation quantities (where q is any

of the dependent variables defined above):

$$q = \bar{q} + \delta q,$$

where \bar{q} is constant in τ and θ (i.e. the background flow is axisymmetric). We will also make use of the approximation

$$\begin{aligned} q(v) &= \bar{q}(v) + \delta q(\delta v) \\ &= \bar{q}(v) + \frac{\partial q}{\partial v} \delta v, \end{aligned}$$

where v is any independent variable of interest.

3.1.2.6 Spatial Fourier Coefficients (SFCs)

Variables which are functions of θ , denoted here as $p(\theta)$, will be decomposed into spatial Fourier coefficients (SFCs), denoted by a tilde: \tilde{p}_n , $n=1,2,\dots$. A slightly non-standard transform pair will be adopted, which is equivalent to the standard formulae, as long as the functions $p(\theta)$ are real:

$$\begin{aligned} p(\theta) &= \sum_{n>0} \text{Re} \{ \tilde{p}_n^* \cdot e^{in\theta} \} \\ \tilde{p}_n &= \frac{2}{\pi} \int_0^{2\pi} p(\theta) \cdot e^{in\theta} d\theta, \end{aligned}$$

where $*$ denotes complex conjugate. Using these definitions, the SFCs have a very intuitive interpretation: If there is a sinusoid in $p(\theta)$ with mode number n , $|\tilde{p}_n|$ is its amplitude, and $\angle \tilde{p}_n$ is the angular position of its peak. In the above transform pair, $n=0$ is omitted because surge-type disturbances are neglected in this analysis.

3.2 Modeling

3.2.1 Overview

The approach used is to write a pressure balance across the entire compression system. This allows the flowfield assumptions upstream and downstream to be made an integral part of the set of differential equations derived. The pressure balance is written as follows (refer to Figure 3.1):

$$\delta(\mathcal{P}_{s_4}-\mathcal{P}_{t_0}) = \delta(\mathcal{P}_{t_1}-\mathcal{P}_{t_0}) + \delta(\mathcal{P}_{t_2}-\mathcal{P}_{t_1}) + \delta(\mathcal{P}_{s_3}-\mathcal{P}_{t_2}) + \delta(\mathcal{P}_{s_4}-\mathcal{P}_{s_3}), \quad (3.5)$$

where

$\delta(\mathcal{P}_{s_4}-\mathcal{P}_{t_0})$ is overall total to static pressure balance,

$\delta(\mathcal{P}_{t_1}-\mathcal{P}_{t_0})$ is the upstream flow field total pressure change,

$\delta(\mathcal{P}_{t_2}-\mathcal{P}_{t_1})$ is the total pressure change across the IGVs,

$\delta(\mathcal{P}_{s_3}-\mathcal{P}_{t_2})$ is the compressor total-to-static pressure rise,

$\delta(\mathcal{P}_{s_4}-\mathcal{P}_{s_3})$ is the downstream flow field static pressure change.

We will derive differential equations (or, in some cases, *systems* of differential equations) for these expressions in Sections 3.2.2 through 3.2.6. In Section 3.2.7, the individual terms are combined into Equation (3.5), and the resulting system of differential equations is solved in a unique way which allows control theory to be applied to the result.

The basic form of the derivation presented here was first given by Moore [10]. Several refinements and additions to the model followed, most notably by Moore and Greitzer [23] and by Hynes and Greitzer [24]. All of these studies assumed stationary IGVs. Epstein, Ffowcs-Williams, and Greitzer [16] first considered the case of 'wave launchers' upstream of the compressor for the purpose of control. Longley [14], Silkowski [20], and Strang [38] further developed these ideas, and the results of their efforts are presented here and in Appendix A.

3.2.2 Overall Total to Static Pressure Balance { $\delta(\mathcal{P}_{s_4}-\mathcal{P}_{t_0})$ }

The upstream boundary condition has been specified as uniform flow. Thus, $\delta\mathcal{P}_{t_0} \equiv \delta\mathcal{P}_{t(-\infty)} = 0$. Downstream, linearization of the Euler equations yields $\nabla^2(\delta\mathcal{P}_s)=0$ [10, 23]. Analysis of the solutions to this equation [14, 20] reveals that higher-mode pressure perturbations at the compressor will decay exponentially downstream, so that $\delta\mathcal{P}_{s_4} \equiv \delta\mathcal{P}_{s(+\infty)} = 0$. Therefore the left hand side of (3.5) is

$$\delta(\mathcal{P}_{s_4}-\mathcal{P}_{t_0}) = 0 \quad (3.6)$$

(If zeroth mode dynamics were modeled, to couple surge into the problem, then Equation (3.6) would change accordingly).

3.2.3 Upstream Flow Field Total Pressure Change { $\delta(\mathcal{P}_1 - \mathcal{P}_0)$ }

Integration of the momentum equation upstream yields the next part of the overall pressure balance. The result is derived using the unsteady Bernoulli equation:

$$\frac{\partial(\delta\Phi)}{\partial\tau} + \delta\mathcal{P} = \text{constant}, \quad (3.7)$$

where we have introduced $\delta\Phi(\eta, \theta, \tau)$, the velocity potential, as the most convenient representation of the flow field upstream of the compressor. Comparing the points 0 and 1 in Figure 3.1 and realizing, as before, that $\frac{\partial(\delta\Phi_0)}{\partial\tau} = 0$ (i.e. all perturbations die away far upstream), Equation (3.7) implies that

$$\delta(\mathcal{P}_1 - \mathcal{P}_0) = -\frac{\partial(\delta\Phi_1)}{\partial\tau}. \quad (3.8)$$

The introduction of $\delta\Phi$ requires that we also solve Laplace's equation upstream of the compressor, i.e.:

$$\nabla^2(\delta\Phi)_{\text{upstream}} = 0. \quad (3.9)$$

Finally, to connect the upstream flowfield to the flow in the compressor, which will be written in terms of $\delta\phi$, we use the relationship

$$\delta\phi_1 = \frac{\partial(\delta\Phi_1)}{\partial\eta}. \quad (3.10)$$

3.2.4 Total Pressure Change Across the IGVs { $\delta(\mathcal{P}_2 - \mathcal{P}_1)$ }

The total pressure change across the IGVs, $\delta(\mathcal{P}_2 - \mathcal{P}_1)$, is generally close to zero, if all of the IGVs are at the same incidence $\bar{\gamma}$. However, if there is an incidence variation around the annulus $\delta\gamma(\theta, \tau)$, such as occurs in the case of active control, then certain blade passages look like diffusers, while others look like nozzles, as in Figure 3.2. The approximate effect can be derived by applying the unsteady Bernoulli equation (Equation (3.7)) along the IGV passage and assuming a linear velocity change through the blade passages [25]. The result is

$$\delta(\mathcal{P}_2 - \mathcal{P}_1) = -\mu_{\text{IGV}} \cdot \frac{\partial}{\partial\tau} \left\{ \delta\phi_2 + \frac{\bar{\phi}}{2} \mu_{\text{IGV}} \frac{\partial(\delta\gamma)}{\partial\theta} \right\}. \quad (3.11)$$

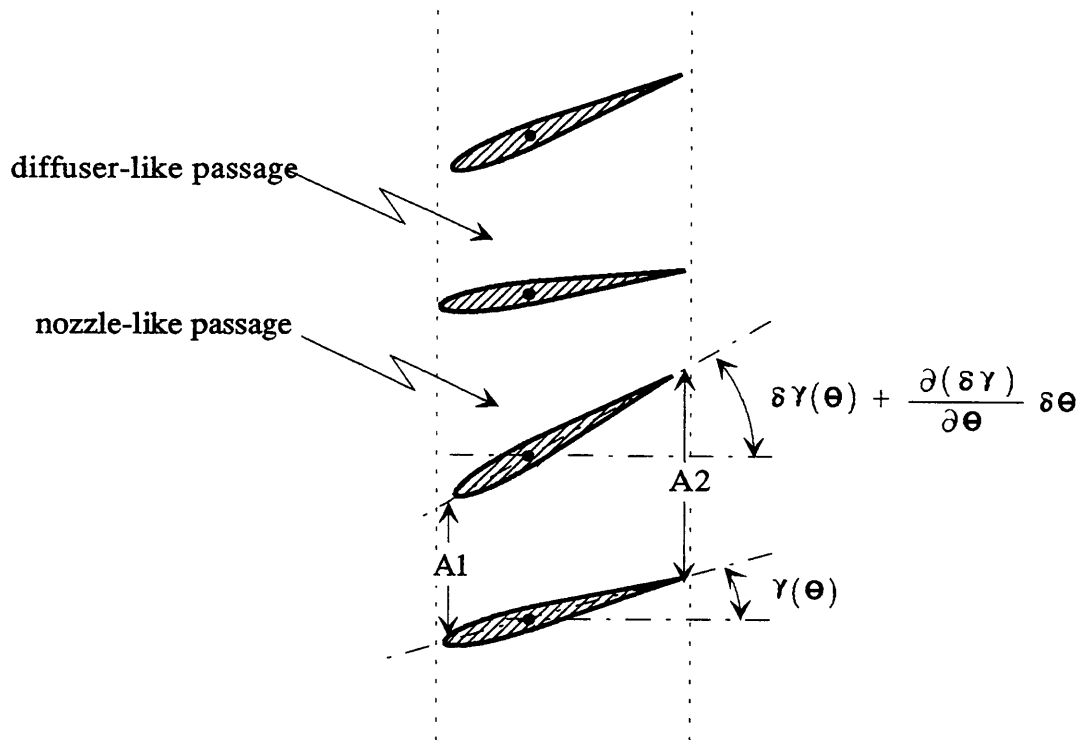


Figure 3.2 - Effect of non-axisymmetric IGV turning

$\delta\phi_2$ can be related to the upstream flow variables by using mass conservation across the individual IGV passages:

$$\delta\phi_2 = \delta\phi_1 - \bar{\phi} \cdot \mu_{IGV} \cdot \frac{\partial(\delta\gamma)}{\partial\theta}. \quad (3.12)$$

Figure 3.2 illustrates the effects of asymmetrical IGV turning on passage geometry.

3.2.5 Compressor Total-to-Static Pressure Rise { $\delta(\mathcal{P}_{S3}-\mathcal{P}_{t2})$ }

The total-to-static pressure rise across the compressor comprises the heart of the rotating stall model. It is based on the pressure rise associated with the quasi-steady compressor performance, plus a correction to account for the unsteady pressure rise due to acceleration of the fluid in the blade passages.

The quasi-steady effects account for the flow coefficient and IGV stagger sensitivity of the compressor:

$$\delta(\mathcal{P}_{S3}-\mathcal{P}_{t2}) \Big|_{\text{quasi-steady}} = \frac{\partial\psi_c}{\partial\phi_2} \delta\phi_2 + \frac{\partial\psi_c}{\partial\gamma} \delta\gamma, \quad (3.13)$$

where $\frac{\partial\psi_c}{\partial\phi_2}$ and $\frac{\partial\psi_c}{\partial\gamma}$ are the quasi-steady, uniform flow sensitivities. The subscripts in the derivatives will subsequently be dropped, because in quasi-steady flow there is assumed to be no total pressure loss across the IGVs, and $\phi_2 = \phi_1$, so the derivatives above are the same for ψ as for ψ_c .

To model the unsteady effects on pressure rise, $\psi_c(\phi, \gamma)$ is first broken up into static-to-static pressure rise and dynamic pressure:

$$\psi_c(\phi) = (\mathcal{P}_{S3}-\mathcal{P}_{S2}) - \frac{1}{2}\phi^2. \quad (3.14)$$

There is an unsteady component of $(\mathcal{P}_{S3}-\mathcal{P}_{S2})$ due to acceleration of the fluid in the compressor. If we view the blade passage as a channel, we can write a one-dimensional expression for the static pressure rise *across a single blade row*:

$$\Delta\mathcal{P}_{S \text{ unsteady}} = -b \cdot \frac{\partial c}{\partial \tau}, \quad (3.15)$$

where b is the non-dimensional chord-length of the passage, and c is the non-dimensional velocity in the passage. The quantity c is different for the rotor

passages than for the stator passages, because the rotor is moving through a non-uniform velocity field. This must be taken into account when computing $\partial c/\partial \tau$ based on $\delta\phi$ for the rotor. The stagger angle of the passages must also be taken into account; this is done by assuming that $c = (\text{axial velocity})/\cos(\text{blade stagger})$. The resulting equations for the fluid acceleration in the stator and the rotor passages are:

$$\left. \frac{\partial c}{\partial \tau} \right|_{\text{stator}} = \frac{1}{\cos(\gamma_s)} \frac{\partial(\delta\phi_2)}{\partial \tau}, \quad (3.16)$$

$$\left. \frac{\partial c}{\partial \tau} \right|_{\text{rotor}} = \frac{1}{\cos(\gamma_r)} \left[\frac{\partial(\delta\phi_2)}{\partial \tau} + \frac{\partial(\delta\phi_2)}{\partial \theta} \right], \quad (3.17)$$

where the term $\frac{\partial(\delta\phi_2)}{\partial \theta}$ in the expression for $\left. \frac{\partial c}{\partial \tau} \right|_{\text{rotor}}$ accounts for the movement of the rotor through the velocity field; its simplicity derives from the fact that time has been non-dimensionalized by the rotor velocity. If the unsteady static pressure rise effects ($\Delta\mathcal{P}_{s_{\text{unsteady}}}$ in (3.15)) are summed across all of the rotor and stator passages, the coefficients of $\frac{\partial(\delta\phi_2)}{\partial \tau}$ and $\frac{\partial(\delta\phi_2)}{\partial \theta}$ in Equations (3.16) and (3.17) can be combined, yielding the terms μ_c and λ given in Section 3.1.2.4:

$$\begin{aligned} \delta\mathcal{P}_{s_{\text{unsteady}}} &= \sum_{\substack{\text{rotors +} \\ \text{stators}}} \Delta\mathcal{P}_{s_{\text{unsteady}}} \\ &= -\mu_c \frac{\partial(\delta\phi_2)}{\partial \tau} - \lambda \frac{\partial(\delta\phi_2)}{\partial \theta}. \end{aligned} \quad (3.18)$$

The *steady* contributions to perturbation pressure rise (Equation (3.13)) can now be added to form an overall total-to-static pressure rise equation:

$$\delta(\mathcal{P}_{s_3} - \mathcal{P}_{t_2}) = \frac{\partial\psi}{\partial\phi} \delta\phi_2 + \frac{\partial\psi}{\partial\gamma} \delta\gamma - \mu_c \frac{\partial(\delta\phi_2)}{\partial \tau} - \lambda \frac{\partial(\delta\phi_2)}{\partial \theta}. \quad (3.19)$$

3.2.6 Downstream Flow Field Static Pressure Change { $\delta(\mathcal{P}_{s_4} - \mathcal{P}_{s_3})$ }

Since $\delta\mathcal{P}_{s_4} \equiv 0$ as described in Section 3.2.2, we need only determine $\delta\mathcal{P}_{s_3}$. Writing the axial Euler equation at station 3, and using continuity across the compressor, we can write:

$$\frac{\partial(\delta\mathcal{P}_{s_3})}{\partial\eta} = -\frac{\partial(\delta\phi_3)}{\partial\tau} = -\frac{\partial(\delta\phi_2)}{\partial\tau}. \quad (3.20)$$

Here we have assumed that the exit flow angle is constant at station 3. To solve this differential equation, we must solve for δp_s downstream of the compressor. The linearized equation governing downstream static pressure perturbations is Laplace's equation, as discussed in Section 3.2.2:

$$\nabla^2(\delta p_s)_{\text{downstream}} = 0. \quad (3.21)$$

3.2.7 Combining Equations and Solving

We can summarize the results of the preceding sections with the following set of differential equations, in which $\delta\Phi$, $\delta\phi$, and δp_s are variables and $\delta\gamma$ is a forcing function:

UPSTREAM: (Equations (3.9) and (3.10))

$$\nabla^2(\delta\Phi) = 0 \quad (3.22)$$

$$\delta\phi_1 = \frac{\partial(\delta\Phi_1)}{\partial\eta} \quad (3.23)$$

ACROSS COMPRESSOR: (Substituting Equations (3.6), (3.8), (3.11) and (3.19) into Equation (3.5)):

$$0 = - \frac{\partial(\delta\Phi_1)}{\partial\tau} \quad (3.24)$$

$$\begin{aligned} & - \mu_{IGV} \frac{\partial(\delta\phi_2)}{\partial\tau} - \frac{\bar{\phi}}{2} \cdot \mu_{IGV}^2 \frac{\partial^2(\delta\gamma)}{\partial\theta\partial\tau} \\ & + \frac{\partial\psi}{\partial\phi} \delta\phi_2 + \frac{\partial\psi}{\partial\gamma} \delta\gamma - \mu_C \frac{\partial(\delta\phi_2)}{\partial\tau} - \lambda \frac{\partial(\delta\phi_2)}{\partial\theta} \\ & - \delta p_{s3} \end{aligned}$$

$$\delta\phi_2 = \delta\phi_1 - \bar{\phi} \cdot \mu_{IGV} \frac{\partial(\delta\gamma)}{\partial\theta} \quad (3.25)$$

DOWNSTREAM: (Equations (3.20) and (3.21))

$$\frac{\partial(\delta p_{s3})}{\partial\eta} = - \frac{\partial(\delta\phi_2)}{\partial\tau} \quad (3.26)$$

$$\nabla^2(\delta p_s) = 0 \quad (3.27)$$

We have 6 equations for the 4 unknowns $\delta\Phi$, $\delta\phi_1$, $\delta\phi_2$, and δp_{s3} . However, Equations (3.23) and (3.26) are actually boundary conditions which link Equations (3.22)

to (3.24) and (3.24) to (3.27) respectively. Thus, there is no excess of equations.

We will first present the solutions for the upstream and downstream flow fields. We will then rewrite all of the above equations in terms of spatial Fourier coefficients (SFCs, defined in Section 3.1.2.6), and eliminate intermediate variables.

The solution for the velocity potential upstream depends on the boundary conditions. These boundary conditions are:

- 1) Periodicity in θ ,
- 2) Upstream uniform flow: $\delta\Phi(-\infty, \theta, \tau) = 0$.

The solution to Laplace's equation with these boundary conditions can be written

$$\delta\Phi = \sum_{n>0} \text{Re}\{ A_n^*(\tau) \cdot e^{n\eta} \cdot e^{in\theta} \}. \quad (3.28)$$

This representation of the solution leaves partials with respect to τ unsolved. We will discuss the utility of this approach in Section 3.2.8.

The downstream solution for δp_s is similar to the upstream solution for $\delta\Phi$.

The boundary conditions are:

- 1) Periodicity in θ ,
- 2) Downstream uniform static pressure: $\delta p_s(+\infty, \theta, \tau) = 0$.

The solution is then:

$$\delta p_s(\text{downstream}) = \sum_{n>0} \text{Re}\{ \delta\tilde{p}_{3n}^*(\tau) \cdot e^{-n\eta} \cdot e^{in\theta} \}, \quad (3.29)$$

where we have again left the solution with respect to τ undetermined.

The form of the upstream and downstream solutions can be adopted for all of the variables in our system of equations (all summations are for $n>0$):

$$\delta\phi_{\text{upstream}} = \sum \text{Re}\{ \tilde{\phi}_n^*(\tau) \cdot e^{n(\eta-\eta_{\text{HW}})} \cdot e^{in\theta} \} \quad (3.30)$$

$$\delta\phi_1 = \sum \text{Re}\{ \tilde{\phi}_n^*(\tau) \cdot e^{(-n\eta_{\text{HW}})} \cdot e^{in\theta} \} \quad (3.31)$$

$$\delta\phi_2 = \sum \text{Re}\{ \tilde{\phi}_{2n}^*(\tau) \cdot e^{in\theta} \} \quad (3.32)$$

$$\delta\gamma = \sum \text{Re}\{ \tilde{\gamma}_n^*(\tau) \cdot e^{in\theta} \} \quad (3.33)$$

Note in (3.30, 3.31) that $\tilde{\phi}_n$ is defined as the SFC at the measurement station η_{HW} .

Using (3.28)-(3.33), the system of Equations (3.22)-(3.27) can be written in terms of SFCs as follows (the Laplace equations have already been solved, so they are not included):

UPSTREAM:

$$A_n = \frac{\exp(-n\eta_{HW})}{n} \cdot \tilde{\phi}_n \quad (3.34)$$

ACROSS COMPRESSOR:

$$0 = \sum_{n>0} \text{Re} \left\{ \left[-\dot{A}_n - \mu_{IGV} \dot{\tilde{\phi}}_{2n} + \frac{\bar{\phi}}{2} \mu_{IGV}^2 \cdot \text{in} \cdot \dot{\tilde{\gamma}}_n + \frac{\partial \psi}{\partial \phi} \tilde{\phi}_{2n} \right. \right. \quad (3.35)$$

$$\left. \left. + \frac{\partial \psi}{\partial \gamma} \tilde{\gamma}_n - \mu_C \dot{\tilde{\phi}}_{2n} + \lambda \cdot \text{in} \cdot \tilde{\phi}_{2n} - \delta \tilde{p}_{3n} \right]^* \cdot e^{in\theta} \right\}$$

$$\tilde{\phi}_{2n} = e^{(-n\eta_{HW})} \cdot \tilde{\phi}_n + \bar{\phi} \cdot \mu_{IGV} \cdot \text{in} \cdot \tilde{\gamma}_n \quad (3.36)$$

DOWNSTREAM:

$$\delta \tilde{p}_{3n} = \frac{1}{n} \dot{\tilde{\phi}}_{2n}(\tau) \quad (3.37)$$

Here we have used the fact that $\eta = 0$ at stations 1 and 2. Now it is straightforward to eliminate A_n , $\tilde{\phi}_{2n}$, and $\delta \tilde{p}_{3n}$ from these equations. Using orthogonality of $e^{in\theta}$, we can also eliminate the summation in Equation (3.35), and instead equate each of the coefficients of $e^{in\theta}$ to zero. Thus we have the following ODE for each mode n of the velocity perturbation:

$$e^{(-n\eta_{HW})} \cdot \left[\frac{2}{n} + \mu \right] \dot{\tilde{\phi}}_n = e^{(-n\eta_{HW})} \cdot \left[\frac{\partial \psi}{\partial \phi} + \text{in} \cdot \lambda \right] \tilde{\phi}_n \quad (3.38)$$

$$+ \left[\left(\frac{\partial \psi}{\partial \gamma} - n^2 \bar{\phi} \lambda \mu_{IGV} \right) + \text{in} \bar{\phi} \mu_{IGV} \frac{\partial \psi}{\partial \phi} \right] \tilde{\gamma}_n$$

$$- \text{in} \bar{\phi} \mu_{IGV} \left[\frac{1}{n} + \mu - \frac{\mu_{IGV}}{2} \right] \dot{\tilde{\gamma}}_n,$$

where we have used the fact that $\mu = \mu_C + \mu_{IGV}$.

3.2.8 Discussion

Equation (3.38) is a *partial* solution of the set of differential equations. The partial derivatives with respect to η and θ have been eliminated ("solved"), leaving only the derivatives with respect to time, $\dot{\tilde{\phi}}_n$ and $\dot{\tilde{\gamma}}_n$. It is important to recognize that we now have a *set* of decoupled ordinary differential equations, rather than a system of coupled partial differential equations. Each equation in the set relates the n^{th} SFC of perturbation velocity, $\tilde{\phi}_n$, to the n^{th} SFC of IGV deflection, $\tilde{\gamma}_n$. These equations are decoupled; that is $\tilde{\phi}_n$ is unaffected by $\tilde{\phi}_{n+1}$, $\tilde{\phi}_{n-1}$, $\tilde{\gamma}_{n+1}$, $\tilde{\gamma}_{n-1}$, etc. This decoupling of the spatial modes simplifies the system dynamics considerably - it allows each mode to be modeled, identified, and stabilized separately. Such decoupling relies on the linearity of the system and the axisymmetry of the background flow. One purpose of this thesis is to determine whether the assumptions inherent in this representation are reasonable in the context of control. If we can stabilize the system using a decoupled approach, then we gain confidence in at least the usefulness of the model, if not its complete accuracy.

The considerations in designing actuation for rotating stall are also clarified by this approach. If we can determine the relative stability of each of the modes in Equation (3.38), we can determine the number of modes which we would like to stabilize, which in turn determines the complexity of the actuation. In the experimental setup described in Chapter 2, there are 12 moving IGVs. This number can theoretically affect the first through the fifth modes of $\delta\phi$ but, realistically, three or perhaps four modes can be accessed with these actuators. Chapters 4 and 5 will discuss whether this is enough, and what is perhaps happening to mode numbers greater than 3 or 4.

Previous derivations of the compressor dynamics differed from the above in two ways. First of all, the differential equations were previously *unforced* (except

perhaps the model in [16], in which a forcing term was arbitrarily added with no derivation). Second, the homogeneous dynamics were solved deterministically in time as well as space. In other words, an explicit solution $\delta\phi(\eta,\theta,\tau)$ was derived. This solution was then checked for stability by looking at the time evolution of the spatial modes - if they grew, the system was deemed unstable.

We have instead cast the equations into time-ODEs with general forcing functions $\tilde{\gamma}_n(\tau)$. This is the standard form in control theory. We can manipulate Equation (3.38) in various ways to determine stability, input-output characteristics, system parameterizations, feedback laws, etc. Since such manipulation is the subject of the remainder of the thesis, Equation (3.38) is in the most useful form for our purposes. Modifications are discussed in Section 3.3, but they are all time-ODE input-output equations like Equation (3.38).

Finally, it should be mentioned that the perturbation IGV movement is not the only forcing function in a real system. The system is also forced by various random processes - such as non-uniformities in the inlet flow, vibration of the rotor and stator vanes, turbulence, separation, imperfections in the blading, etc. These forcing functions, aside from being of a random nature, are extremely hard to model or measure. Therefore, they are lumped together into a nebulous quantity called 'noise which drives the system'. Characterization of noise has yet to be carried out for axial compressor higher-mode dynamics.

3.3 Alternate Forms of the Model

Several alternate forms for the model in Equation (3.38) have been derived through the course of this research. The philosophy and usefulness of each form will be discussed section by section.

3.3.1 SISO Complex Form

Parametric representation of Equation (3.38) gives the following set of single-input, single-output (SISO) complex-coefficient, complex state ODEs:

$$\dot{\tilde{\phi}}_n = (\sigma_{rs} + i \cdot \omega_{rs})\tilde{\phi}_n + (b_r + i \cdot b_i)\tilde{\gamma}_n + i \cdot g_i \cdot \dot{\tilde{\gamma}}_n, \quad (3.39)$$

where, if we let $\zeta = \left[\frac{2}{n} + \mu \right]$:

$$\sigma_{rs}(n, \bar{\phi}) = \frac{\partial \psi}{\partial \bar{\phi}} / \zeta \quad (3.40)$$

$$\omega_{rs}(n, \bar{\phi}) = n \cdot \lambda / \zeta \quad (3.41)$$

$$b_r(n, \bar{\phi}) = e^{(n\eta_{HW})} \cdot \left(\frac{\partial \psi}{\partial \gamma} - n^2 \bar{\phi} \lambda \mu_{IGV} \right) / \zeta \quad (3.42)$$

$$b_i(n, \bar{\phi}) = e^{(n\eta_{HW})} \cdot n \bar{\phi} \mu_{IGV} \frac{\partial \psi}{\partial \bar{\phi}} / \zeta \quad (3.43)$$

$$g_i(n, \bar{\phi}) = -e^{(n\eta_{HW})} \cdot n \bar{\phi} \mu_{IGV} \left[\frac{1}{n} + \mu - \frac{\mu_{IGV}}{2} \right] / \zeta \quad (3.44)$$

This representation of the system dynamics employs the fewest possible parameters. This is important in the context of identification, because redundant parameters make it more difficult for methods to converge to a solution. It also is a convenient way to present the system, because the dynamics of each SFC is SISO. If we use the complex sinusoidal excitation

$$\tilde{\gamma}_n = e^{j\omega\tau},$$

then the system will respond (after a transient period) with a sinusoid which has a magnitude M and phase β which depend on the system dynamics in Equation (3.39):

$$\begin{aligned} \tilde{\phi}_n &= M_n e^{j(\omega\tau + \beta_n)} \\ &= M_n e^{j\beta_n} \cdot e^{j\omega\tau} \\ &= G_n(j\omega) \cdot e^{j\omega\tau}, \end{aligned} \quad (3.45)$$

where the last equality serves to define the transfer function $G_n(j\omega)$. Substituting this steady-state solution into (3.39) gives the transfer functions for the system:

$$\begin{aligned} j\omega \cdot M_n e^{j(\omega\tau + \beta_n)} &= (\sigma_{rs} + i \cdot \omega_{rs}) \cdot M_n e^{j(\omega\tau + \beta_n)} + (b_r + i \cdot b_i) e^{j\omega\tau} + j\omega \cdot i \cdot g_i \cdot e^{j\omega\tau} \\ M_n e^{j\beta_n} &= \frac{j\omega \cdot i \cdot g_i + (b_r + i \cdot b_i)}{j\omega - (\sigma_{rs} + i \cdot \omega_{rs})} \end{aligned} \quad (3.46)$$

or, if we let $s=j\omega$,

$$\tilde{\phi}_n(s) = G_n(s) \cdot \tilde{\gamma}_n \quad (3.47)$$

where:

$$G_n(s) = \frac{i \cdot g_i \cdot s + (b_r + i \cdot b_i)}{s - (\sigma_{rs} + i \cdot \omega_{rs})} . \quad (3.48)$$

The transfer function description of the system is now in standard form, except that the coefficients in $G_n(s)$ are complex. This is not a trivial difference. It means that the system does not obey typical root-locus, Nyquist, and Bode construction and stability criteria, because the poles and zeros do not appear in complex-conjugate pairs. However, if care is taken, many of the techniques for control system design and analysis can still be applied. The advantages of this form are its SISO appearance, and the fact that the parameterization is minimal. The five parameters in Equations (3.40)-(3.44) completely characterize the n th mode of the system, so they constitute the parameter set for that mode, at any particular flow coefficient:

$$\Theta(n, \bar{\phi}) = \begin{bmatrix} \sigma_{rs} \\ \omega_{rs} \\ b_r \\ b_i \\ g_i \end{bmatrix}_n . \quad (3.49)$$

3.3.2 MIMO Real-Valued Form

In this section, we will derive a real-valued multi-input multi-output (MIMO) form for the set of equations (3.39). The equations we will derive are sometimes useful for design and analysis because all of the terms in them are real-valued. Thus the eigenvalues appear in complex-conjugate pairs and all of the procedures available in control theory can be used.

To motivate the MIMO form, consider the different representations of an n^{th} mode wave (which exists at some instant of time τ_0 in the annulus):

$$\begin{aligned} \delta\phi_n(\tau_0) &= M \cdot \cos(n\theta + \beta) \\ &\equiv x_{rn} \cos(n\theta) + x_{in} \sin(n\theta) \\ &\equiv \text{Re}\{ \tilde{\phi}_n^* e^{in\theta} \} . \end{aligned} \quad (3.50)$$

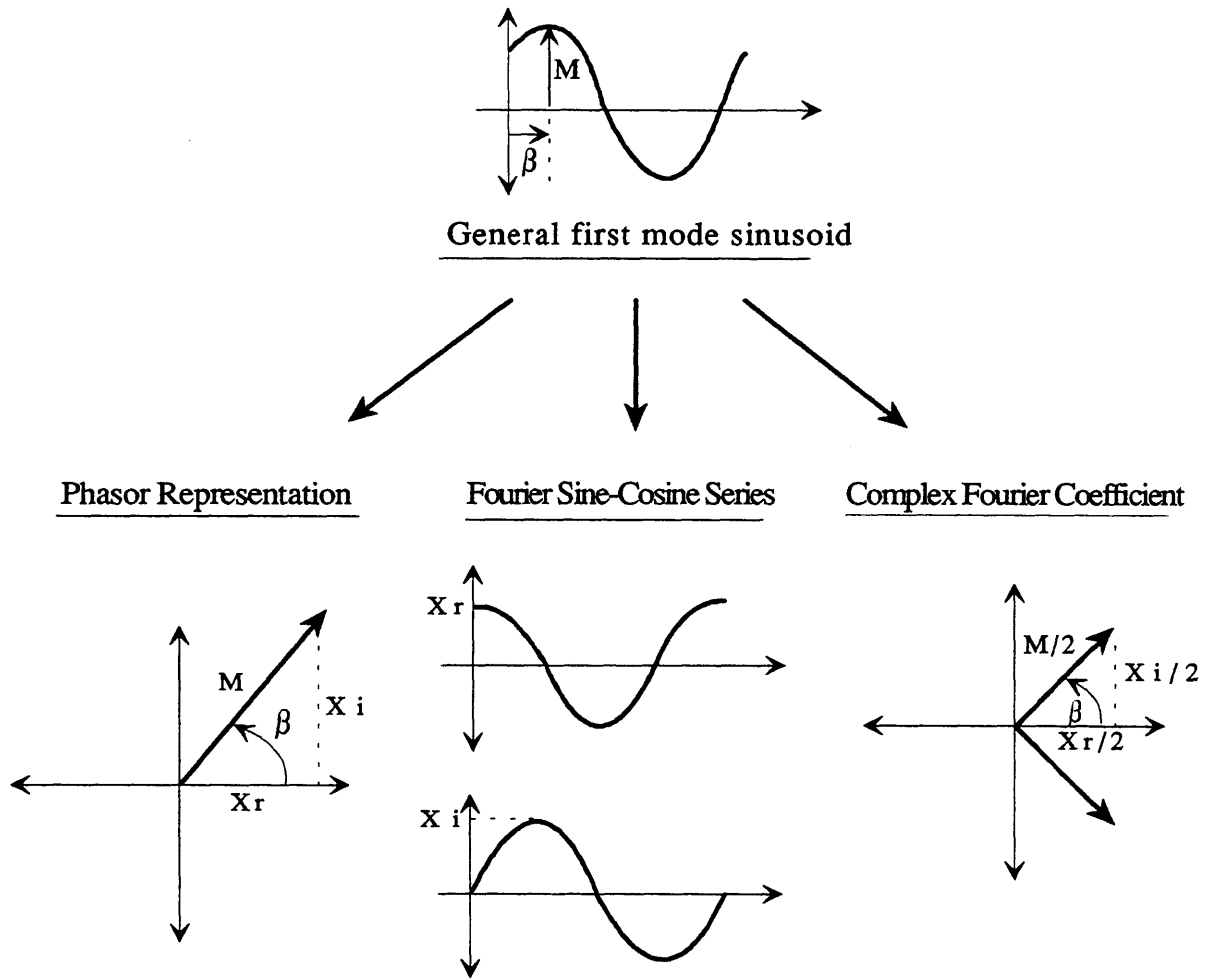


Figure 3.3 - Different representations of a sinusoid

Each of these representations of the wave contains two parameters which together give the phase and magnitude of the wave. In the first case, the pair is (M, β) . In the second case, it is (x_{r_n}, x_{i_n}) . The third pair is $(\text{Re}\{\tilde{\phi}_n\}, \text{Im}\{\tilde{\phi}_n\})$. All of these pairings can be related by simple trigonometric and exponential identities. The most important such identity for this presentation is

$$\begin{bmatrix} x_r \\ x_i \end{bmatrix}_n \equiv \begin{bmatrix} \text{Re}\{\tilde{\phi}_n\} \\ \text{Im}\{\tilde{\phi}_n\} \end{bmatrix}. \quad (3.51)$$

We can use this identity to derive the MIMO dynamic system from (3.39), if we use the fact that matrix multiplication of 2×2 matrices resembles complex multiplication. For example, the following equation evaluates the product $(\sigma_{rs} + i \cdot \omega_{rs}) \cdot \tilde{\phi}_n$ using matrices and vectors:

$$\begin{bmatrix} \text{Re}\{(\sigma_{rs} + i \cdot \omega_{rs}) \cdot \tilde{\phi}_n\} \\ \text{Im}\{(\sigma_{rs} + i \cdot \omega_{rs}) \cdot \tilde{\phi}_n\} \end{bmatrix} \equiv \begin{bmatrix} \sigma_{rs} & -\omega_{rs} \\ \omega_{rs} & \sigma_{rs} \end{bmatrix} \cdot \begin{bmatrix} \text{Re}\{\tilde{\phi}_n\} \\ \text{Im}\{\tilde{\phi}_n\} \end{bmatrix}. \quad (3.52)$$

Using identities such as this, we find that the real-valued, vector-matrix representation of Equation (3.39) is:

$$\begin{bmatrix} \dot{x}_r \\ \dot{x}_i \end{bmatrix}_n = \begin{bmatrix} \sigma_{rs} & -\omega_{rs} \\ \omega_{rs} & \sigma_{rs} \end{bmatrix}_n \begin{bmatrix} x_r \\ x_i \end{bmatrix}_n + \begin{bmatrix} b_r & -b_i \\ b_i & b_r \end{bmatrix}_n \begin{bmatrix} u_r \\ u_i \end{bmatrix}_n + \begin{bmatrix} 0 & -g_i \\ g_i & 0 \end{bmatrix}_n \begin{bmatrix} \dot{u}_r \\ \dot{u}_i \end{bmatrix}_n, \quad (3.53)$$

where we have replaced $\tilde{\gamma}_n$ by the real vector $[u_r \ u_i]_n^T$ using the definition

$$\begin{bmatrix} u_r \\ u_i \end{bmatrix}_n \equiv \begin{bmatrix} \text{Re}(\tilde{\gamma}_n) \\ \text{Im}(\tilde{\gamma}_n) \end{bmatrix}. \quad (3.54)$$

We can also write a transfer function description of the system:

$$\begin{bmatrix} x_r(s) \\ x_i(s) \end{bmatrix}_n = \begin{bmatrix} G_r(s) & -G_i(s) \\ G_i(s) & G_r(s) \end{bmatrix}_n \begin{bmatrix} u_r(s) \\ u_i(s) \end{bmatrix}_n, \quad (3.55)$$

where G_{r_n} and G_{i_n} are derivable from (3.53), and it can be verified that

$$G_n(s) = G_{r_n}(s) + i \cdot G_{i_n}(s). \quad (3.56)$$

The states x_{r_n} and x_{i_n} are the real and imaginary parts of $\tilde{\phi}_n$, which can be viewed as a phasor representation of the n^{th} mode wave in the compressor (see

Figure 3.3). x_{r_n} and x_{i_n} are also the coefficients of the Fourier series for the wave:

$$\delta\phi = \sum_{n>0} \left[x_{r_n} \cdot \cos(n\theta) + x_{i_n} \cdot \sin(n\theta) \right]. \quad (3.57)$$

Thus $[x_r \ x_i]_n^T$ represents the *state* (phase and magnitude) of the n^{th} mode wave that exists in the compressor at any time τ . Similarly, $[u_r \ u_i]_n^T$ represents the n^{th} mode wave of perturbation IGV deflection. Equations (3.53) and (3.55) relate these quantities dynamically.

3.3.3 Rotating Reference Frame Form

Both the theoretical derivation above and experimental measurements indicate that rotating stall inception is a traveling wave phenomenon. The wave travels at a constant speed (which depends on the rotor speed, the inertial parameters of the compressor, and the flow coefficient). It has a first order response to IGV deflections, which is not necessarily in spatial phase with the deflections themselves. Transients in IGV deflection ($\frac{\partial(\delta\gamma)}{\partial\tau}$) also have a direct effect on the evolution of the wave.

The ODE representations we have presented model all of these effects. Propagation of the wave is modeled by coupling the real and imaginary parts of $\tilde{\phi}_n$ (or, equivalently, x_{r_n} and x_{i_n}) dynamically. Phase shift of the input is represented by the relative magnitudes of b_r and b_i . Finally, transient effects are modeled by the parameter g_i . These various effects complicate the model and make control system design more difficult. With a proper change of variables, however, we can transform this system into a *pair* of decoupled, first order, real-valued, SISO systems *in a rotating reference frame*. Once control laws are designed, they can be transformed back into physical variables. Thus, we can temporarily incorporate the coupling between x_{r_n} and x_{i_n} into a change of reference frames, to simplify the problem of control design.

First, let us eliminate the $\dot{\tilde{\gamma}}_n$ term by introducing a new state variable ξ :

$$\text{Let } \xi = \tilde{\phi}_n - i \cdot g_i \cdot \tilde{\gamma}_n;$$

then:

$$\begin{aligned}
\dot{\xi} &= \dot{\tilde{\phi}}_n - i \cdot g_i \cdot \dot{\tilde{\gamma}}_n \\
&= (\sigma_{rs} + i \cdot \omega_{rs}) \tilde{\phi}_n + (b_r + i \cdot b_i) \tilde{\gamma}_n \\
&= (\sigma_{rs} + i \cdot \omega_{rs}) \cdot (\xi + i \cdot g_i \cdot \tilde{\gamma}_n) + (b_r + i \cdot b_i) \tilde{\gamma}_n \\
&= (\sigma_{rs} + i \cdot \omega_{rs}) \xi + [(\sigma_{rs} + i \cdot \omega_{rs}) i \cdot g_i + (b_r + i \cdot b_i)] \tilde{\gamma}_n .
\end{aligned} \tag{3.58}$$

This form can be rewritten as

$$\dot{\xi} = (\sigma_{rs} + i \cdot \omega_{rs}) \cdot \xi + b \cdot \tilde{\gamma}_n . \tag{3.59}$$

The next step is to put the model into the reference frame of the rotating wave. This is possible because, according to the model, the wave rotates at constant speed. The state, x , and control, p , in the rotating frame are:

$$x = \xi e^{-j\omega_{rs}\tau} \quad \text{and} \quad p = \tilde{\gamma}_n e^{-j\omega_{rs}\tau} . \tag{3.60}$$

The dynamics can be transformed into the rotating reference frame using the chain rule and subsequently substituting in (3.59):

$$\begin{aligned}
\dot{x} &= (\dot{\xi} - j\omega_{rs}\xi) \cdot e^{-j\omega_{rs}\tau} \\
&= [(\sigma_{rs} + i \cdot \omega_{rs}) \xi + b \cdot \tilde{\gamma}_n - j\omega_{rs}\xi] \cdot e^{-j\omega_{rs}\tau} \\
&= \sigma_{rs} \cdot x + b \cdot p .
\end{aligned} \tag{3.61}$$

Now, x and p are complex, but σ_{rs} is real, so that the real and imaginary parts of the state are no longer coupled - the wave does not rotate in this reference frame. This system requires one more step of simplification, because b is still complex, and couples the input-output system. Thus we introduce the control

$$u = \frac{b}{|b|} \cdot p, \tag{3.62}$$

which preserves the magnitude of the control power, but shifts its phase, resulting in the following equation for the system:

$$\dot{x} = \sigma_{rs} \cdot x + |b| \cdot u. \tag{3.63}$$

This is the simplest possible representation of the system, owing its form to the unique set of variables defined. It is a completely decoupled representation and can thus be treated as a *pair* of real-valued SISO systems.

Once a control law is developed for this system, it must be put back into the form of the physical variables. This requires only algebraic manipulations of the above equations. If the rotating frame control law is

$$u(s) = K(s)x(s), \quad (3.64)$$

the equivalent stationary frame control law is:

$$\tilde{\gamma}_n(s) = \frac{K(s-j\omega_{rs})}{\frac{b}{|b|} + i \cdot g_i \cdot K(s-j\omega_{rs})}. \quad (3.65)$$

The system representation (3.63) allows for a very straightforward design methodology. It is a plant inversion of sorts and, as such, it carries the restriction that the original system be minimum phase - if there are zeros in the left-half plane of $G_n(s)$, then the above defined controller may have unstable poles.

3.3.4 Lumped Parameter Model of Rotating Stall Dynamics

The lumped parameter form for the model is quite different from the models presented previously, because it does not rely on the eigenfunction form of the system, i.e. it is not expressed in terms of the Fourier coefficients. As such it allows the system to be modeled under conditions which yield different eigenfunctions, such as non-axisymmetric inlet conditions. This form is also useful when the pressure rise characteristic $\psi(\phi)$ contains significant nonlinearity that we wish to model.

Our derivation begins with a partial differential representation of the system dynamics. We will demonstrate with the simplest PDE which captures the character of the problem; extension to more complicated cases is straightforward. Consider the PDE for the unforced (stationary IGVs) 2-D compressor:

$$0 = -2 \frac{\partial(\delta\Phi_1)}{\partial\tau} + \delta\psi(\delta\phi_1) - \mu \frac{\partial(\delta\phi_1)}{\partial\tau} - \lambda \frac{\partial(\delta\phi_1)}{\partial\theta}. \quad (3.66)$$

This equation can be derived from the equations in Section 3.2.7. The perturbation flow coefficient $\delta\phi_1$ is a function of both θ and τ . We would like to get rid of the functionality with θ , but not by using the Fourier decomposition. Instead, we will

create a lumped representation of $\delta\phi_1$, which we will call ϕ_L :

$$\phi_L(\tau) = [\delta\phi_1(\theta_1, \tau) \quad \delta\phi_1(\theta_2, \tau) \quad \cdots \quad \delta\phi_1(\theta_K, \tau)]^T. \quad (3.67)$$

We will also use the notation $\phi_L(\tau) = [- \delta\phi_1(\theta_k, \tau) -]^T$. We next proceed to derive each of the terms in the differential equation (3.66) in lumped form.

To derive the first term in (3.66), $\frac{\partial(\delta\Phi_1)}{\partial\tau}$, we write the upstream flowfield solution (3.28) at a specific position θ_j with a finite number of discrete Fourier coefficients C_n :

$$\delta\Phi(\theta_j) = \sum_{n=-K/2}^{K/2-1} \frac{1}{|n|} \cdot C_n \cdot e^{|n|\eta + in\theta_j}, \quad (3.68)$$

but we want to express this as a function of ϕ_L , so we substitute in the DFT formula for C_n :

$$\delta\Phi(\theta_j) = \sum_{n=-K/2}^{K/2-1} \frac{1}{|n|} \cdot \left\{ \frac{1}{K} \sum_{k=1}^K \delta\phi_1(\theta_k) \cdot e^{-in\theta_k} \right\} \cdot e^{|n|\eta + in\theta_j}. \quad (3.69)$$

Using this, we can write $\frac{\partial(\delta\Phi_1)}{\partial\tau}$ (where the subscript '1' indicates that $\eta=0$):

$$\frac{\partial(\delta\Phi_1)}{\partial\tau}(\theta_j) = \sum_{n=-K/2}^{K/2-1} \frac{1}{|n|} \cdot \left\{ \frac{1}{K} \sum_{k=1}^K \frac{\partial(\delta\phi_1(\theta_k))}{\partial\tau} \cdot e^{-in\theta_k} \right\} \cdot e^{in\theta_j}. \quad (3.70)$$

If the innermost summation is replaced by an inner product, we have:

$$\frac{\partial(\delta\Phi_1)}{\partial\tau}(\theta_j) = \frac{1}{K} \cdot \sum_{n=-K/2}^{K/2-1} \frac{1}{|n|} \cdot \left\{ [- e^{-in\theta_k} -] \frac{\partial}{\partial\tau} \phi_L \right\} \cdot e^{in\theta_j}. \quad (3.71)$$

This formula gives $\frac{\partial(\delta\Phi_1)}{\partial\tau}$ for one value of θ_j , but we would like a vector representation for all $j=1, \dots, K$:

$$[- \frac{\partial(\delta\Phi_1)}{\partial\tau}(\theta_j) -]^T = \frac{1}{K} \cdot \sum_{n=-K/2}^{K/2-1} \frac{1}{|n|} \cdot \left\{ [- e^{-in\theta_k} -] \frac{\partial}{\partial\tau} \phi_L \right\} \cdot [- e^{in\theta_j} -]^T. \quad (3.72)$$

This can be rearranged, using the fact that $(A^T B)C = C(A^T B)$ when $(A^T B)$ is scalar:

$$\left[-\frac{\partial(\delta\Phi_1)}{\partial\tau}(\theta_j) \right]^T = \frac{1}{K} \cdot \sum_{n=-K/2}^{K/2-1} \frac{1}{|n|} \left[-e^{in\theta_j} \right]^T \left[-e^{-in\theta_k} \right] \cdot \frac{\partial}{\partial\tau} \phi_L. \quad (3.73)$$

The resulting product of exponentials yields a matrix $\{e^{in(\theta_j-\theta_k)}\}_{jk}$ in the summation. Further simplification is possible if the summations for $n < 0$ are combined with those for $n > 0$, to give cosines instead of exponentials. The result is

$$\left[-\frac{\partial(\delta\Phi_1)}{\partial\tau}(\theta_j) \right]^T = P \dot{\phi}_L, \quad (3.74)$$

where:

$$P = \frac{1}{K} \cdot \left\{ \frac{2}{K} \cos[K/2(\theta_j-\theta_k)] + \sum_{n=1}^{K/2-1} \frac{2}{n} \cos[n(\theta_j-\theta_k)] \right\}_{jk}. \quad (3.75)$$

Equation (3.74) expresses the first term in Equation (3.66) as a matrix multiplying the time derivative of the system state, $\dot{\phi}_L$. This is the form we need to write a lumped parameter model.

To determine the lumped form of the second term in (3.66), $\delta\psi(\delta\phi_1)$, we simply evaluate $\delta\psi$ at each value $\delta\phi(\theta_k)$. We write the resulting vector $\left[-\delta\psi(\phi_L) \right]^T$.

The third term in (3.66), $\frac{\partial(\delta\phi_1)}{\partial\tau}$, requires no modification; we can use the vector form $\dot{\phi}_L$ directly.

The last term in (3.66), $\frac{\partial(\delta\phi_1)}{\partial\theta}$, requires that we derive a matrix multiplication of ϕ_L which will give in an approximation to $\frac{\partial(\delta\phi_1)}{\partial\theta}$. This can be done in any number of ways; two examples will be given here. The first approach is similar to that used for $\frac{\partial(\delta\Phi_1)}{\partial\tau}$. First we write out the discrete Fourier series for $\delta\phi_1$:

$$\delta\phi_1(\theta_j) = \sum_{n=-K/2}^{K/2-1} C_n \cdot e^{in\theta_j}. \quad (3.76)$$

We then substitute the DFT formula for C_n :

$$\delta\phi_1(\theta_j) = \sum_{n=-K/2}^{K/2-1} \left\{ \frac{1}{K} \sum_{k=1}^K \delta\phi_1(\theta_k) \cdot e^{-in\theta_k} \right\} \cdot e^{in\theta_j}. \quad (3.77)$$

We can then write an approximation for $\frac{\partial(\delta\phi_1)}{\partial\theta}$:

$$\frac{\partial(\delta\phi_1)}{\partial\theta}(\theta_j) = \sum_{n=-K/2}^{K/2-1} \left\{ \frac{1}{K} \sum_{k=1}^K -\delta\phi_1(\theta_k) \cdot in \cdot e^{-in\theta_k} \right\} \cdot e^{in\theta_j} \quad (3.78)$$

simplifying this as before, and dropping the Nyquist component $K/2$, we get:

$$\left[-\frac{\partial(\delta\phi_1)}{\partial\theta}(\theta_j) \right]^T = R \cdot \phi_L, \quad (3.79)$$

where:

$$R = \frac{1}{K} \cdot \left\{ - \sum_{n=1}^{K/2-1} 2n \cdot \cos[n(\theta_j - \theta_k)] \right\}_{jk}. \quad (3.80)$$

Equation (3.79) expresses the last term in (3.66) as a matrix multiplying the time-derivative of the system state, ϕ_L .

A second way to approximate $\frac{\partial(\delta\phi_1)}{\partial\theta}$ is to use a finite difference approximation, for instance:

$$\frac{\partial(\delta\phi_1)}{\partial\theta}(\theta_j) \cong \frac{\delta\phi_1(\theta_{j+1}) - \delta\phi_1(\theta_{j-1})}{\Delta\theta}, \quad \Delta\theta = \frac{4\pi}{N}. \quad (3.81)$$

This approximation can be written as a matrix multiplication:

$$\left[-\frac{\partial(\delta\phi_1)}{\partial\theta}(\theta_j) \right]^T = R \cdot \phi_L, \quad (3.82)$$

where:

$$R = \frac{N}{4\pi} \begin{bmatrix} 0 & 1 & 0 & 0 & \dots & 0 & 1 \\ -1 & 0 & 1 & 0 & 0 & \dots & 0 \\ 0 & -1 & 0 & 1 & 0 & 0 & \dots \\ \vdots & & & & & & \\ 0 & 0 & \dots & & -1 & 0 & 1 \\ 1 & 0 & 0 & 0 & \dots & 0 & -1 & 0 \end{bmatrix}. \quad (3.83)$$

Thus we have two matrix estimates R for the last term in (3.66).

We now have all of the terms necessary to write the differential equation (3.66) in lumped-parameter form. The final result is

$$0 = -2P\dot{\phi}_L + [- \delta\psi(\phi_L) -]^T - \mu\dot{\phi}_L - \lambda R\phi_L \quad (3.84)$$

$$(\mu + 2P)\dot{\phi}_L = [- \delta\psi(\phi_L) -]^T - \lambda R\phi_L, \quad (3.85)$$

where P and R are defined above. Note that non-linearities in $\delta\psi$, or circumferential variations in $\delta\psi$ due to inlet distortion, can now be modeled. Since the equation is now in ODE form, these effects are much easier to assess than they would be in the context of a PDE. Furthermore, the system of equations is in a form amenable to the application of nonlinear system and control theory.

This subsection has focused on the methods used to convert to a lumped-parameter representation, without going into the details of converting the entire model. Any of the modeling discussed in this thesis can be lumped using these techniques. The main drawback of this method is that there are numerical difficulties in using R, unless care is taken in choosing it. The examples given here for calculating R work well only if the modal content of the initial conditions is low compared to the number of lumps in the model. To model higher modal content, better choices for R must be made.

CHAPTER 4

Additional Modeling for Active Control

This chapter models the feedback system presented in Chapter 2 (Figure 2.7), incorporating the compressor dynamics derived in Chapter 3. The discrete arrays of sensors and actuators are represented in spatial Fourier coefficient (SFC) notation in Section 4.1. This allows a decoupled model for each mode to be developed in Section 4.2. Discretization of the dynamics will be discussed in Section 4.3.

4.1 Conversion to Spatial Fourier Coefficients (SFCs)

Since the plant described in Chapter 3 relates the SFCs of the inputs and outputs, we would like to model the rest of the system on the same basis. But, except for the plant itself, the system is not truly distributed - it is a discrete approximation of a distributed system (see Figure 4.1). On the input side, the IGVs are discrete elements being used to force the (spatially) continuous dynamics of the compressor. On the output side, the continuous function $\delta\phi(\theta, \tau)$ is measured at spatially discrete points around the annulus. Additionally, there are filters and other dynamics which act on *each channel* of the spatial array. We would like to represent all of these signals and dynamic elements in terms of SFCs.

Because the considerations are slightly different for the IGVs, the hot wires, and the signal processors, each will be considered separately in the following subsections. The final result is the representation in Figure 4.2: all of the signals in the system have been converted to *spatially continuous* Fourier coefficients. Each spatial mode n is decoupled from the other modes in this representation - this simplifies the

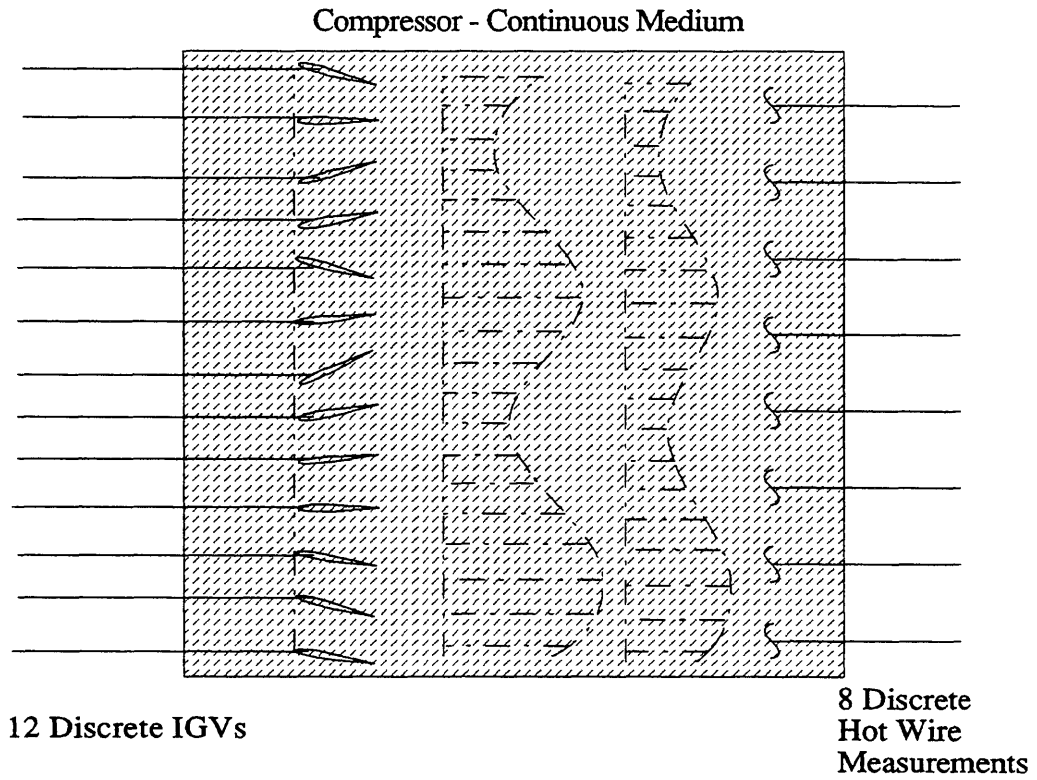


Figure 4.1 - Conceptual diagram of spatially discrete and spatially continuous portions of the system

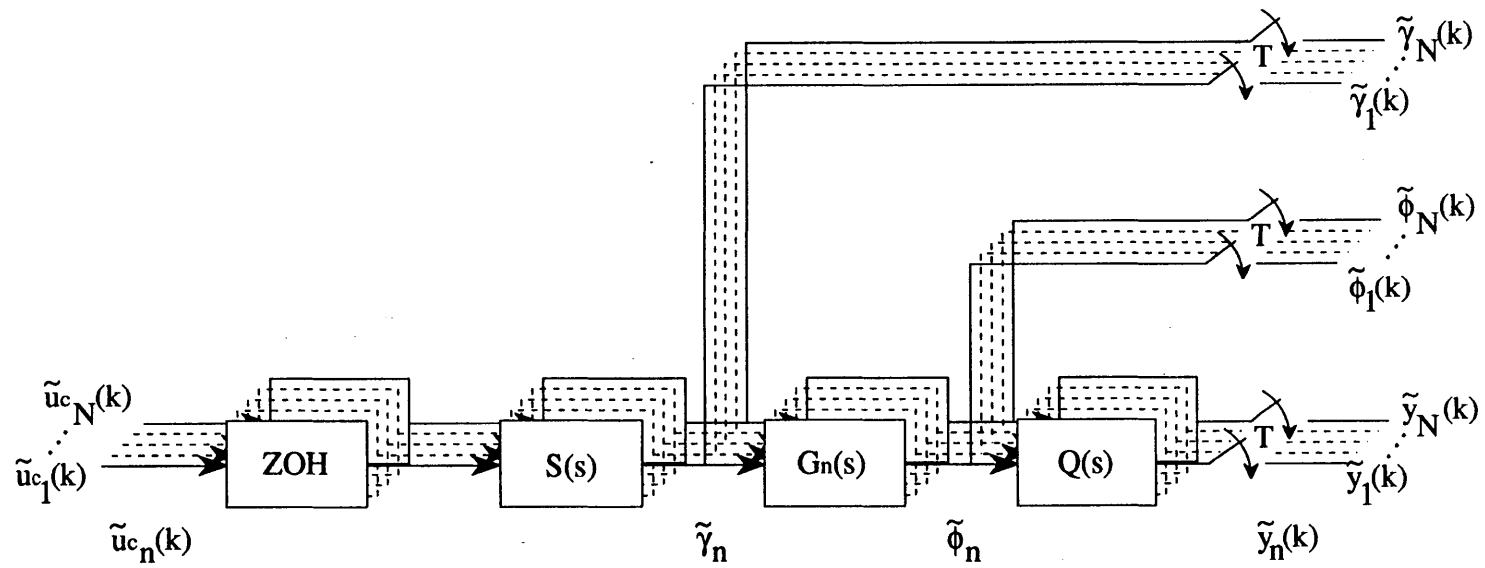


Figure 4.2 - Parallel modal dynamics representation of the system

problem of identification (Chapter 5) and control (Chapter 6) considerably. Also, we will show that the dynamics of individual channels in the spatial array become the dynamics of the SFCs, because of the linearity of the Fourier transformation.

The notation for the signals and transfer functions in Figure 4.2 follows from the discussions in Sections 3.2.7 and 3.3.2. SFCs can be written as complex numbers, or as cosine and sine coefficients:

$$\begin{aligned}
 \tilde{u}_{cn} & \text{ or } \begin{bmatrix} u_{cr} \\ u_{ci} \end{bmatrix}_n & - \text{commanded IGV angle} \\
 \tilde{\gamma}_n & \text{ or } \begin{bmatrix} u_r \\ u_i \end{bmatrix}_n & - \text{actual IGV angle (includes servo response)} \\
 \tilde{\phi}_n & \text{ or } \begin{bmatrix} x_r \\ x_i \end{bmatrix}_n & - \text{perturbation flow coefficient at } \eta_{HW} \\
 \tilde{y}_n & \text{ or } \begin{bmatrix} y_r \\ y_i \end{bmatrix}_n & - \text{measured perturbation flow coefficient (includes} \\
 & & \text{response of filters and delays)}
 \end{aligned}$$

The transfer functions between these signals are:

$$\begin{aligned}
 \tilde{u}_n &= S(s) \cdot \tilde{u}_{cn}; & \begin{bmatrix} u_r \\ u_i \end{bmatrix}_n &= \begin{bmatrix} S(s) & 0 \\ 0 & S(s) \end{bmatrix} \begin{bmatrix} u_{cr} \\ u_{ci} \end{bmatrix}_n \\
 \tilde{\phi}_n &= G_n(s) \cdot \tilde{\gamma}_n; & \begin{bmatrix} x_r \\ x_i \end{bmatrix}_n &= \begin{bmatrix} G_r(s) & -G_i(s) \\ G_i(s) & G_r(s) \end{bmatrix}_n \begin{bmatrix} u_r \\ u_i \end{bmatrix}_n \\
 \tilde{y}_n &= Q(s) \cdot \tilde{\phi}_n; & \begin{bmatrix} y_r \\ y_i \end{bmatrix}_n &= \begin{bmatrix} Q(s) & 0 \\ 0 & Q(s) \end{bmatrix} \begin{bmatrix} x_r \\ x_i \end{bmatrix}_n
 \end{aligned} \tag{4.1}$$

Note that the $S(s)$ and $Q(s)$ are transfer functions with real coefficients (hence the diagonal form for the matrix representation). Also note that $S(s)$ and $Q(s)$ are the same for every mode n . The form of $S(s)$ and $Q(s)$ will be justified in Section 4.1.3.

We will now discuss the conversion of the inlet guide vanes, the hot wires, and the signal channels into continuous Fourier coefficient form. Section 4.2 then discusses the dynamic models $S(s)$ and $Q(s)$.

4.1.1 Inlet Guide Vanes

The IGV turning is represented as $\delta\gamma(\theta, \tau)$ in Chapter 3. The true system consists of 12 discrete IGVs, so the actual form is

$$\delta\gamma(\theta_m, \tau) \text{ where } \theta_m = \frac{2\pi m}{12}, m = 0, 1, 2 \dots 11. \quad (4.2)$$

Thus the IGV turning $\tilde{\gamma}_n$ will be approximated by the discrete IGVs as follows:

$$\delta\gamma(\theta_m, \tau) = \sum_{n=-5}^6 \text{Re} \{ \tilde{\gamma}_n^*(\tau) \cdot e^{(in\theta_m)} \}. \quad (4.3)$$

The discrete nature of the IGVs has two consequences. First, we are limited to actuation waves with modal content no higher than mode number 6 (hence the limits of the summation in Equation (4.3)). Second, the flow turning introduced by the IGVs is no longer a continuous function of θ . This is because the solidity in the true system is not infinite (in fact, because of the limited number of IGVs, the solidity is only 0.6). Silkowski [20] computed the effects of discrete IGVs by introducing an extra term into the computation of IGV effectiveness:

$$\frac{\partial\psi}{\partial\gamma} = \frac{\partial\psi}{\partial\alpha} \cdot \frac{\partial\alpha}{\partial\gamma}, \quad (4.4)$$

where $\delta\alpha(\theta, \tau)$ is the perturbation change in flow angle relative to axial, measured at the rotor face (station 2 in Figure 3.1). One of his results is shown in Figure 4.3: here we see that a first mode turning of discrete IGVs actually causes the flow angle $\delta\alpha$ to be excited in all modes, most notably the 1st and 12th mode. Unwanted modes are small compared to the commanded mode and mix out downstream of the IGVs [20]. Figure 4.3 shows that, at the rotor face, the 'effective IGV turning' $\frac{\partial\alpha}{\partial\gamma} \cdot \delta\gamma$ contains mostly the first mode, but some attenuation of this mode is encountered ($\frac{\partial\alpha}{\partial\gamma} \cong 0.6$) and a small amount of cross-coupling to higher modes

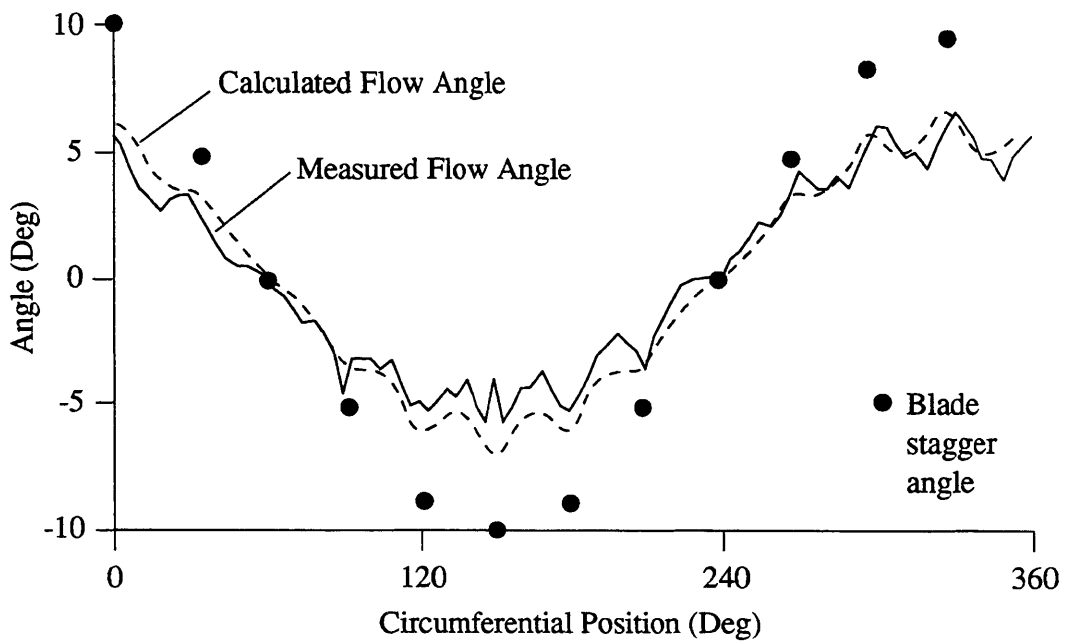


Figure 4.3 - A comparison of the measured and calculated flow angle generated 0.3 chords downstream by a 10 degree cosine stagger pattern on the inlet guide vanes. Calculated flow angles are from Silkowski, [20].

occurs. Attenuation is handled by incorporating $\frac{\partial \alpha}{\partial \gamma}$ into the transfer function $G_n(s)$. Cross-coupling between the modes of interest in this thesis (1, 2, and 3) is small, so we will, for the present, ignore this effect. Cross-coupling to the 12th mode is larger, but this mode will probably be well damped, based on the results of Chapter 5.

Based on this discussion, it is reasonable to use the spatially continuous Fourier transform $\tilde{\gamma}_n$, provided we do three things:

- 1) Account for the attenuation of IGV commands in some way.
- 2) Command modes no higher than the 5th (phase for the Nyquist mode cannot be specified, so use of mode 6 is impractical).
- 3) Check the level of cross-coupling between modes experimentally.

4.1.2 Hot Wires

The hot wires present a somewhat different problem than the IGVs. In this case, we are measuring a continuous function of circumference, $\delta\phi(\eta_{HW}, \theta, \tau)$, which may contain any modal content. We use the discrete Fourier transform approximation for K hot wires

$$\tilde{\phi}_n(\eta, \tau) \equiv \frac{2}{K} \sum_{k=0}^{K-1} \delta\phi(\eta_{HW}, \theta_k, \tau) \cdot e^{jn\theta_k}, \quad (4.5)$$

where

$$\theta_k = \frac{2\pi k}{K}, \quad k = 1, 2, \dots, K.$$

It is possible for modal content greater than $K/2$ (the spatial Nyquist frequency) to exist in $\delta\phi$. This information would alias into the computation of the lower modes. According to Equation (3.30), however, these modes die away very quickly upstream of the compressor (i.e. as η becomes more negative in the following expression):

$$\tilde{\phi}_n(\tau) = e^{(n\eta_{HW})} \cdot \frac{2}{\pi} \int_0^{2\pi} \delta\phi_1(\theta, \tau) \cdot e^{in\theta} d\theta. \quad (4.6)$$

In most of the experiments discussed in this thesis, the hot wires are located

at $\eta \cong 0.5$, and there are 8 hot wires. Thus mode number $K/2 + 1 = 5$ is the first mode that might alias. This and higher modes are probably very well damped, based on the results of Chapters 5 and 6. Furthermore, $\tilde{\phi}_5(\tau)$ is attenuated by $e^{-5 \cdot (0.5)} = .082$ at the measurement point; higher modes are attenuated even more. Thus it will be assumed that aliasing is negligible upstream of the compressor. Measurements taken behind the IGVs rely solely on the damping of the higher modes to prevent aliasing; this may not be sufficient at low flow coefficients, where even relatively high modes can become underdamped.

Cross-coupling between modes due to discrete hot wire measurements would require that some mode n affect the computation of the Fourier coefficient for some other mode m . As long as $n \neq (m + lK/2)$ for some integer l (i.e. as long as n does not *alias* into m), and as long as the hot wires are evenly spaced, no such cross-coupling will occur. This is because the signal being transformed by the DFT is truly periodic in θ , due to the annular configuration. Thus there are no 'end effects' on the DFT and, in the absence of aliasing, the discrete Fourier coefficients match identically the coefficients of the Fourier series for the periodic signal $\delta\phi(\eta_{\text{HW}}, \theta)$. Uneven spacing of the hot wires *will* cause cross-coupling between modes, because orthogonality cannot be preserved in this case. The extent of cross-coupling between modes due to uneven hot wire spacing depends strongly on the spacing itself, and must be examined on a case-by-case basis [22].

4.1.3 Input and Output Channels

The rest of the feedback system consists of multiple channels, each representing a discrete circumferential location. These channels can be transformed into SFCs in the same way as the hot wire signals. Furthermore, we will show that *the SFCs of the channels are related by the same transfer functions as the individual channels*.

For example, the bank of Bessel filters in Figure 2.7 is a K-input K-output

system, and can be represented as a transfer matrix, transforming a vector of hot wire measurements ϕ to a vector of filtered measurements ϕ_f :

$$\phi_f = G_B(s) \cdot \phi, \quad (4.7)$$

where

$$\phi = [\delta\phi(\theta_1,s) \quad \delta\phi(\theta_2,s) \quad \cdots \quad \delta\phi(\theta_K,s)]^T, \text{ and}$$

$$\phi_f = [G_b(s) \cdot \delta\phi(\theta_1,s) \quad G_b(s) \cdot \delta\phi(\theta_2,s) \quad \cdots \quad G_b(s) \cdot \delta\phi(\theta_K,s)].$$

The diagonality of G_B is apparent from the definition of ϕ_f . The discrete Fourier transform of the input, $\delta\phi$, appears in Equation (4.5). It can be put into matrix notation, resulting in a matrix transformation from the individual measurements to the SFCs:

$$\tilde{\phi} = C \cdot \phi, \text{ where} \quad (4.8)$$

$$\tilde{\phi} = [\tilde{\phi}_1 \quad \tilde{\phi}_2 \quad \cdots \quad \tilde{\phi}_{K-1}]$$

and the \sim denotes the spatial Fourier coefficient (SFC). The matrix C can transform ϕ_f similarly:

$$\tilde{\phi}_f = C \cdot \phi_f, \text{ where} \quad (4.9)$$

$$\tilde{\phi}_f = [\tilde{\phi}_{f1} \quad \tilde{\phi}_{f2} \quad \cdots \quad \tilde{\phi}_{fK-1}].$$

The equation for the individual elements of $\tilde{\phi}_f$ can now be derived as follows: Multiplying both sides of Equation (4.7) by C we get

$$C \cdot \phi_f = C \cdot G_B \cdot \phi. \quad (4.10)$$

But, since $G_B = G_b \cdot I$, C and G_B can commute, which gives:

$$\tilde{\phi}_f = G_B \cdot C \cdot \phi = G_B \cdot \tilde{\phi}. \quad (4.11)$$

This implies, using the definitions in (4.7), that

$$\tilde{\phi}_{fn} = G_b(s) \tilde{\phi}_n. \quad (4.12)$$

This shows that *the dynamics which relate the individual channels and the dynamics which relate the SFCs are identical*. Note also that every mode is related by the same transfer function (e.g. there is no subscript 'n' on $G_b(s)$).

4.2 System Dynamics

Having shown that we can in fact use the representation in Figure 4.2, we proceed to set up the transfer functions in this diagram. $G_n(s)$ is discussed in Section 3.3.1 and 3.3.2; $S(s)$ and $Q(s)$ are discussed in the following subsections.

4.2.1 Servos

The servo transfer function $S(s)$ is used to represent the dynamics of the entire servo system: motors, amplifiers, and servo motion control boards. These elements are described in Sections 2.2.5 through 2.2.7. We take a simplified view of the system which takes advantage of the fact that the motion controllers and amplifiers have much higher bandwidth than the motor dynamics. The entire system is modeled as a second order system whose frequency and damping characteristics are determined experimentally. Thus we have:

$$S(s) = \frac{\omega_s^2}{s^2 + 2\zeta_s\omega_s \cdot s + \omega_s^2}, \quad (4.13)$$

where the servo natural frequency is ~ 80 Hz ($\omega_s=1.75$) and the servo damping ratio (ζ_s) is ~ 0.75 . The digital commands to the servos go through a zero order hold at a rate of 500 Hz (see Figure 4.2).

We will also model a fluid-mechanical delay between IGV turning and adjustment of the flow in the compressor. The minimum possible value for this delay would be the time necessary for sound to travel through the compressor. This is about 0.64 msec (0.18 units non-dimensional time). The maximum possible value is harder to compute - one could use the transport delay through the entire compressor, but this would be unrealistically large, because all of the blade rows are adjusting to changes in IGV angle simultaneously, rather than serially. Instead, we estimate the maximum delay by assuming that the flow through the rotor and stator adjust in parallel to the adjustment of flow over the IGVs. Since the IGVs are about twice as

long as the rotor and stator, it is reasonable to assume that the entire compressor lag is associated with the time for flow to adjust over the IGVs, with a slight additional lag due to the speed of sound. A rough approximation for the maximum value of fluid-dynamic lag, based on this approach and the lags measured in [26], is about 3.5 msec (about 1 unit non-dimensional time).

The fluid mechanical delay will be lumped into the delays in $Q(s)$, so the transfer function $S(s)$ remains as shown in Equation (4.13).

4.2.2 Sensors, Signal Processors, and Delays

The transfer function $Q(s)$ accounts for the dynamics of the hot wires, the Bessel filters, the fluid mechanical delay, and the computational delay in the computer. All of the delays can be lumped into a single delay term T_d , so the transfer function $Q(s)$ can be written

$$Q(s) = G_b(s) \cdot e^{-sT_d}, \quad (4.14)$$

where $G_b(s)$ is the Bessel filter transfer function.

The hot wires are extremely high bandwidth devices (about 50 kHz) and so their dynamics are negligible within the bandwidth of interest. They are assumed to provide an instantaneous measure of the velocity at the hot wire locations. There is a delay, however, between the velocity which occurs at the compressor face and the velocity measured upstream, where the hot wires are often located. In a potential flow this delay is assumed to be zero; in a real flow there will be a delay which depends on the speed of sound. Therefore, the sensors are modeled as a pure delay, whose value is estimated as the time it would take sound to travel from the compressor face to the hot wire axial location. This delay is between 0.4 and 0.6 msec (0.113 to 0.170 units non-dimensional time), depending on whether the distance to the hot wires is measured from the face of the IGVs or the face of the rotor.

The Bessel filters are 4th-order analog devices, and their specific linear model is given as [27]:

$$G_b(s) = \frac{52.5 \omega_0^4}{s^4 + 5 \cdot \omega_0 s^3 + 22.5 \cdot \omega_0^2 s^2 + 52.5 \cdot \omega_0^3 s + 52.5 \cdot \omega_0^4}, \quad (4.15)$$

where ω_0 is the 3 dB cutoff frequency of the filter. For our experiments, the cutoff frequency was 1000 Hz ($\omega_0=22.2$). Where possible, Equation (4.15) is used. It is sometimes more convenient to model the filters as pure delays, however. This is a very good approximation up to the sample frequency of the system (500 Hz), because Bessel filters are specifically designed to have linear phase (that is, behave like a pure delay) up to their cutoff frequency. For 1000 Hz cutoff, the equivalent delay of the Bessel filters is 0.32 msec (0.090 units non-dimensional time).

Within the computer, there is a delay between the sampling of the hot wires and the output of an analog command to the servos. This delay is 0.57 msec (0.161 units non-dimensional time).

The total value for T_d is between 1.6 and 4.7 msec (0.45 to 1.33 units non-dimensional time), depending on which estimates are used for the individual delays. If we replace $G_b(s)$ with a pure delay, then we can write $Q(s)$ as

$$Q(s) = e^{sT_q}, \quad (4.16)$$

where $T_q = T_d + 0.090$. Although $Q(s)$ is a severe simplification of the high frequency dynamics, more careful modeling would place an array of high-frequency poles and zeros in the model, which would not affect the transfer function in the frequency range of interest.

4.3 Time Discretization

Two types of time discretization are discussed in this section. Tustin's bilinear transformation is used to set up a discrete-time model of the system dynamics for identification. Zero-order hold discretization is used to discretize the system for simulation and control.

4.3.1 Tustin Transformation

Chapter 5 discusses identification of the system dynamics. This must be done in the context of a discretized system, because the data is taken by a computer. The measured inputs and outputs which will be used for identification are shown in Figure 4.2: The input is $\tilde{\gamma}_n(k)$, which does not include the effect of $S(s)$. The output is $\tilde{y}_n(k)$, which includes the effect of $Q(s)$. The effect of $Q(s)$ can be taken out when doing off-line identification, however, by time-shifting the output sequence $\tilde{y}_n(k)$; that is, applying a lead to compensate for the lag in $Q(s)$ by one or two samples (two or four msec). Thus the problem is reduced to identifying $G_n(s)$ directly.

A discretization is required for $G_n(s)$. Note in Figure 4.2 that both the input and the output of $G_n(s)$ are sampled, but there is no zero-order hold in the system. Thus a ZOH discretization of the continuous dynamics would be inappropriate. The discretization which gives the best fidelity in the frequency response of the system is Tustin's bilinear transformation [28],

$$s = \frac{2}{T} \frac{z-1}{z+1} . \quad (4.17)$$

With this transformation, the frequency response shape is approximately preserved for the frequency range of interest in this thesis, which is 0 to 100 Hz, if the sample rate is 500 Hz:

$$G_n(z) \Big|_{z=e^{j\omega T}} \cong G_n(s) \Big|_{s=j\omega} \quad \text{for } \omega = 0 \text{ to } 2.2 \text{ (T=0.5655)}. \quad (4.18)$$

This similarity has been verified computationally. Thus the discretization of the dynamics between the measured input and output is

$$\frac{\tilde{\phi}_n(z)}{\tilde{\gamma}_n(z)} \cong z \cdot \frac{\tilde{y}_n(z)}{\tilde{\gamma}_n(z)} \cong G_n(z) = \frac{ig_r s + (b_r + i b_r)}{s - (\sigma_{rs} + i\omega_{rs})} \Big|_{s=\frac{2}{T} \frac{z-1}{z+1}} , \quad (4.19)$$

where the z is used to approximately take out the time delay discussed Section 4.2. Similar transformation, and use of the methods for converting complex to real systems

described in Section 3.3.2, gives $G_{r_n}(z)$ and $G_{i_n}(z)$:

$$G_{r_n}(z) = \frac{(b_1 z + b_2)(z+1)}{a_1 z^2 + a_2 z + a_3} \quad (4.20)$$

$$G_{i_n}(z) = \frac{b_3 z^2 + b_4 z + b_5}{a_1 z^2 + a_2 z + a_3} . \quad (4.21)$$

The coefficients of the transfer function $G_n(z)$ can be algebraically related to the coefficients above by using the fact that

$$G_n(z) = G_{r_n}(z) + i \cdot G_{i_n}(z) \quad (4.22)$$

4.3.2 Zero-Order Hold (ZOH) Transformation

For simulation and discrete-time control design, the complete continuous dynamics must be discretized. In this case, the input is $\tilde{u}_{c_n}(k)$, and the output is $\tilde{y}_n(k)$. To do the ZOH transformation, all of the continuous dynamics (excluding delays) are put into a state space system:

$$\dot{x} = Ax + Bu_c \quad (4.23)$$

$$y = Cx + Du_c \quad (4.24)$$

The system is then discretized using the formulae [29]

$$Ad = e^{AT} \quad (4.25)$$

$$Bd = \int_0^T e^{At} dt \cdot B \quad (4.26)$$

Delays and digital dynamics (such as the control law) are then appended to the system.

CHAPTER 5
Development and Application
of Techniques for
Identification of Compressor Higher-Mode Dynamics

Identification of the system dynamics serves several purposes: first, it helps verify the model structure hypothesized in Chapter 3. Second, it provides a data base of quantitative information to which predictive methods can compare. Third, quantitative models aid control system design. Finally, system identification results should lead to a better understanding of how compressor dynamics vary with flow coefficient, mode number, and compressor configuration.

System identification techniques fall into two categories: non-parametric and parametric. Non-parametric or spectral techniques concentrate on determining transfer function shapes, without determining the specifics of the model which generates these shapes. Parametric techniques assign a model structure to the system, and then determine the parameters of the model. Both methods will be used here; several cross-checks will then be available between the methods.

Two non-parametric methods are described in Section 5.1. Both are methods for determining approximate transfer-function magnitude and phase plots.

In Section 5.2, two parametric methods are described. The first estimates model parameters by doing fits to the transfer function shapes found in Section 5.1. The second uses a time-domain correlation technique called instrumental-variables, which has been extended to allow identification of closed-loop, possibly unstable systems.

Section 5.3 applies the various methods to data from the single-stage research

compressor. The various methods are compared, and then the experimental results are discussed in detail.

5.1 Non-Parametric Estimation

The transfer function shape that is of most direct interest for this study is $G_n(s)$ (Section 3.3.1). But because we are using sampled data, we determine $G_n(z)$ instead, and use the approximation from Section 4.3.1:

$$G_n(s) \Big|_{s=j\omega} \cong G_n(z) \Big|_{z=e^{j\omega T}} \quad (5.1)$$

Two separate methods are used to get $G_n(z)$ as a function of frequency. The first is to excite the system sinusoidally at various discrete frequencies. We will call this the sinusoidal excitation method. The second is to excite the system with random inputs. We will call this the spectral estimation method.

5.1.1 Sinusoidal Excitation Method

Sinusoidal excitation to estimate a transfer function shape is done using sinusoidal input, and measuring sinusoidal output:

$$\begin{aligned} \text{input} &= \sin(\omega_e \tau) \\ \text{output} &= M \sin(\omega_e \tau + \beta) \\ \text{where } M e^{i\beta} &= G_n(j\omega_e) \end{aligned} \quad (5.2)$$

and ω_e is the excitation frequency. For multi-input multi-output systems, each input must be excited separately, and the resulting sinusoid at each output determines the corresponding element of the matrix of transfer functions between inputs and outputs.

As described in Section 3.3.2, each mode of the compressor model has two inputs (u_{r_n} and u_{i_n}) and two outputs (x_{r_n} and x_{i_n}) if looked at in the context of real signals. Hence, one way to identify the dynamics is to do two experiments: one exciting u_r , and one exciting u_i . Estimates $\hat{G}_{r_n}(j\omega_e)$ and $\hat{G}_{i_n}(j\omega_e)$ can then be determined using Equations (5.2) (actually, if the model structure in Equation (3.55) is

correct, two estimates of $G_{r_n}(j\omega)$ and $G_{i_n}(j\omega)$ will be made by this method, since each appears twice in the transfer matrix (3.55)). $\hat{G}_{r_n}(j\omega_e)$ and $\hat{G}_{i_n}(j\omega_e)$ can then be combined to give $\hat{G}_n(j\omega_e)$, using the fact that $G_n(j\omega) = G_{r_n}(j\omega) + i \cdot G_{i_n}(j\omega)$.

The complex form of the original model (Equation 3.48) suggests an alternative excitation to the system - one which excites $G_n(j\omega)$ directly. Mathematically, the proper excitation is complex:

$$\tilde{\gamma}_n(\tau) = e^{(j\omega_e \tau)}, \quad (5.3)$$

and the resulting output is also complex:

$$\tilde{\phi}_n(\tau) = |G_n(j\omega_e)| \cdot e^{j \cdot [\omega_e \tau + \angle G_n(j\omega_e)]}. \quad (5.4)$$

These signals correspond (using Section 3.1.2.6 definitions) to a rotating wave input:

$$\delta\gamma(\theta, \tau) = \cos(n\theta - \omega_e \tau), \quad (5.5)$$

and a rotating wave output

$$\delta\phi(0, \theta, \tau) = |G_n(j\omega_e)| \cos(n\theta - \omega_e \tau - \angle G_n(j\omega_e)). \quad (5.6)$$

We need only measure the magnitude and phase of the output relative to the input to determine G_n at the frequency of the excitation, ω_e .

The types of excitation employed can be summarized using the MIMO real-valued notation:

1) cosine-part excitation:

$$u_r = \alpha \cdot \cos(\omega_e \tau)$$

$$u_i = 0$$

2) sine-part excitation:

$$u_r = 0$$

$$u_i = \alpha \cdot \cos(\omega_e \tau)$$

3) rotating wave excitation:

$$u_r = \alpha \cdot \sin(\omega_e \tau)$$

$$u_i = \alpha \cdot \cos(\omega_e \tau)$$

The last pair of inputs produces the rotating wave (5.5), as can be verified using Equation (3.54).

Once the input and output sinusoids are obtained, the transfer function estimate at ω_e is computed using the correlation method described by Ljung [30].

For example, if u_r excitation is used (case 1 above), the transfer function estimate $\hat{G}_r(z)$ is computed as follows:

$$I_c(N) = \frac{1}{N} \sum_{m=1}^N x_{r_n}(m) \cos(\omega_e mT)$$

$$I_s(N) = \frac{1}{N} \sum_{m=1}^N x_{r_n}(m) \sin(\omega_e mT)$$
(5.7)

$$|\hat{G}_{r_n}(e^{j\omega_e})| = \frac{\sqrt{I_c^2 + I_s^2}}{\alpha/2}$$

$$\angle |\hat{G}_{r_n}(e^{j\omega_e})| = -\arctan \frac{I_s}{I_c}$$
(5.8)

Computation of \hat{G}_{i_n} and \hat{G}_n proceeds in a similar fashion.

In practice, $[u_r \ u_i]_n^T$ cannot be specified directly - the IGV commands $[u_{cr} \ u_{ci}]_n^T$ are the only signals driven directly by the computer. But if the computer commands are sinusoidal, so will be the IGV motions. Furthermore, we can accurately measure $[u_r \ u_i]_n^T$ using the optical encoders. Thus in an experiment we let u_{cr_n} and u_{ci_n} be sinusoidal and measure both the input and output. The method then proceeds exactly as described above, where $\cos(\omega_e mT)$ and $\sin(\omega_e mT)$ are *measurements* of u_r and u_i .

An example of $\hat{G}_n(j\omega_k)$ computed using the sinusoidal excitation approach, with a rotating wave input, is shown in Figure 5.1.

5.1.2 Spectral Estimation Method

The sinusoidal excitation method is time consuming experimentally, because each frequency point in the transfer function must be obtained separately. A more efficient method is to excite the system with a broadband signal and form an estimate of the transfer function using a spectral technique.

The broadband input signal chosen for these experiments is a pseudo-random binary signal (PRBS). This is a signal which alternates between two levels, at random

$$\frac{\tilde{\Phi}_1(s)}{\tilde{\Upsilon}_1(s)}, \text{ First mode, } \bar{\phi} = 0.475, \text{ Upstream Hot Wires}$$

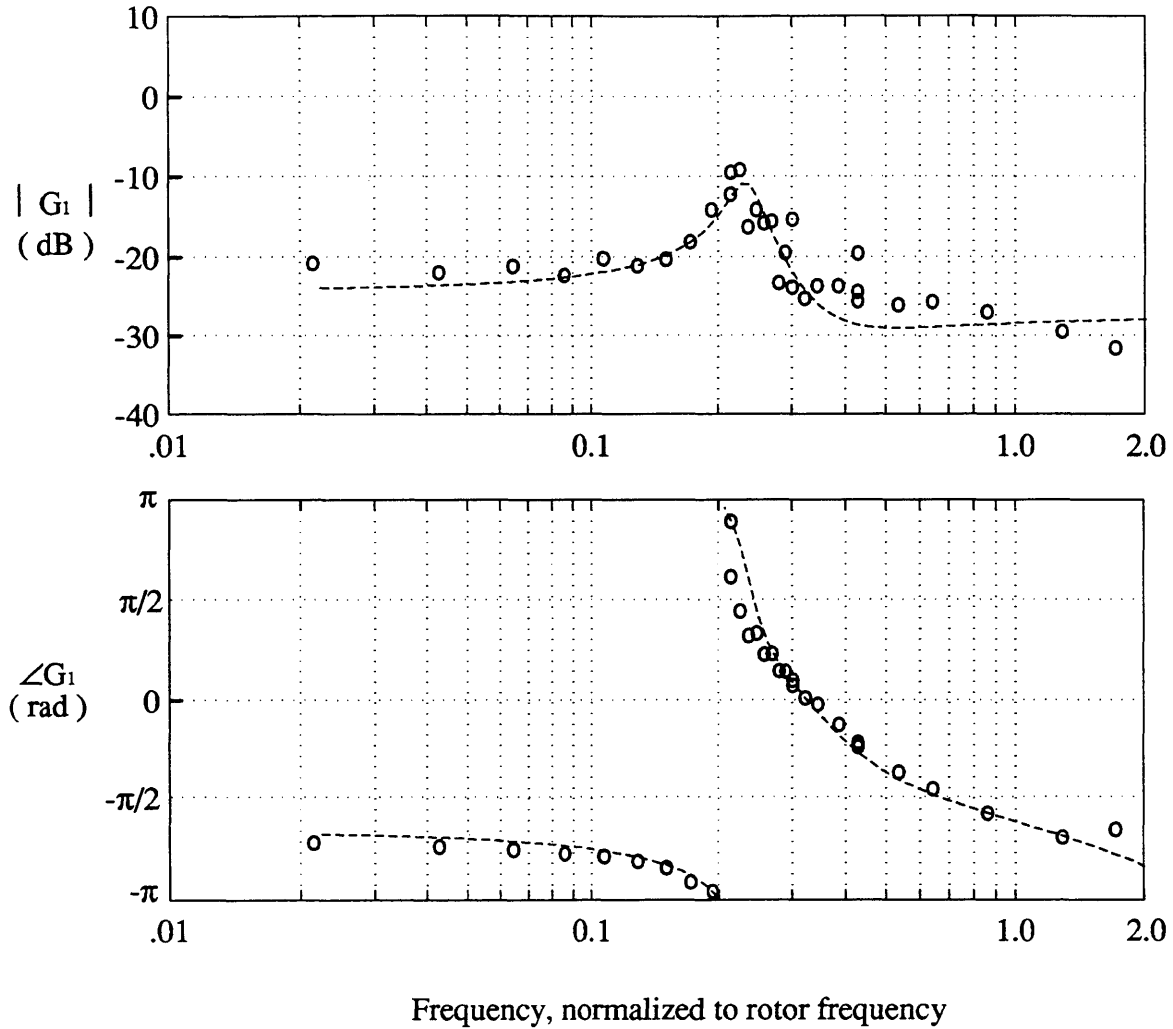


Figure 5.1 - Transfer function estimate using sinusoidal excitation (open circles).
 Dotted line shows a transfer function fit to the open circles,
 $\Theta = [-0.0226 \ 0.234 \ -0.0132 \ 0.055 \ -0.0417]$
 Transfer function for first SFC, at $\bar{\phi} = 0.475$, hot wires upstream of IGVs.

intervals. The randomness of the interval between signal changes causes the input spectrum to be broadband. In a typical experiment, u_r or u_i or both are commanded to alternate between $+10^\circ$ and -10° :

$$\text{PRBS} = 0.1745 \cdot \text{sign}(w(k)), \quad (5.9)$$

where $w(k)$ is a zero-mean random variable with Gaussian distribution. The bandwidth of the input signal can be limited by specifying a minimum value for the switch interval.

As in the previous section, the experiment is conducted by commanding u_{crn} and u_{cin} and measuring u_{rn} , u_{in} , y_{rn} and y_{in} (see Figure 4.2). Here the actual IGV positions will not be binary as commanded, but broadband excitation will occur nevertheless - this technique does not rely on the exact form of the input signal. Three types of excitation are used in the spectral estimation experiments:

1) cosine-part excitation:

$$\begin{aligned} u_{cr} &= \text{PRBS} \\ u_{ci} &= 0 \end{aligned}$$

2) sine-part excitation:

$$\begin{aligned} u_{cr} &= 0 \\ u_{ci} &= \text{PRBS} \end{aligned}$$

3) general wave excitation:

$$\begin{aligned} u_{cr} &= \text{PRBS}_1 \\ u_{ci} &= \text{PRBS}_2 \end{aligned}$$

The spectral estimate is computed as (using case 1 as an example):

$$\hat{G}_{rn}(e^{j\omega}) = \frac{\hat{\Phi}_{y_r u_r}(\omega)}{\hat{\Phi}_{u_r u_r}(\omega)}, \quad (5.10)$$

where $\hat{\Phi}_{y_r u_r}(\omega)$ is the estimated cross-spectrum between y_{rn} and u_{rn} , and $\hat{\Phi}_{u_r u_r}(\omega)$ is the estimated spectrum of u_{rn} [30]. Similar relationships hold for all three excitation types; in the third, multi-input case, matrix spectra must be used. In all cases, the MATLAB routine SPAM [31] generates the estimates \hat{G}_{rn} and \hat{G}_{in} . These are then combined using the relationship $\hat{G}_n = \hat{G}_{rn} + i \cdot \hat{G}_{in}$.

Figure 5.2 shows a segment of data from a typical spectral estimation experiment, as well as the resulting estimate of $\hat{G}_2(j\omega)$. Note that the variance of the

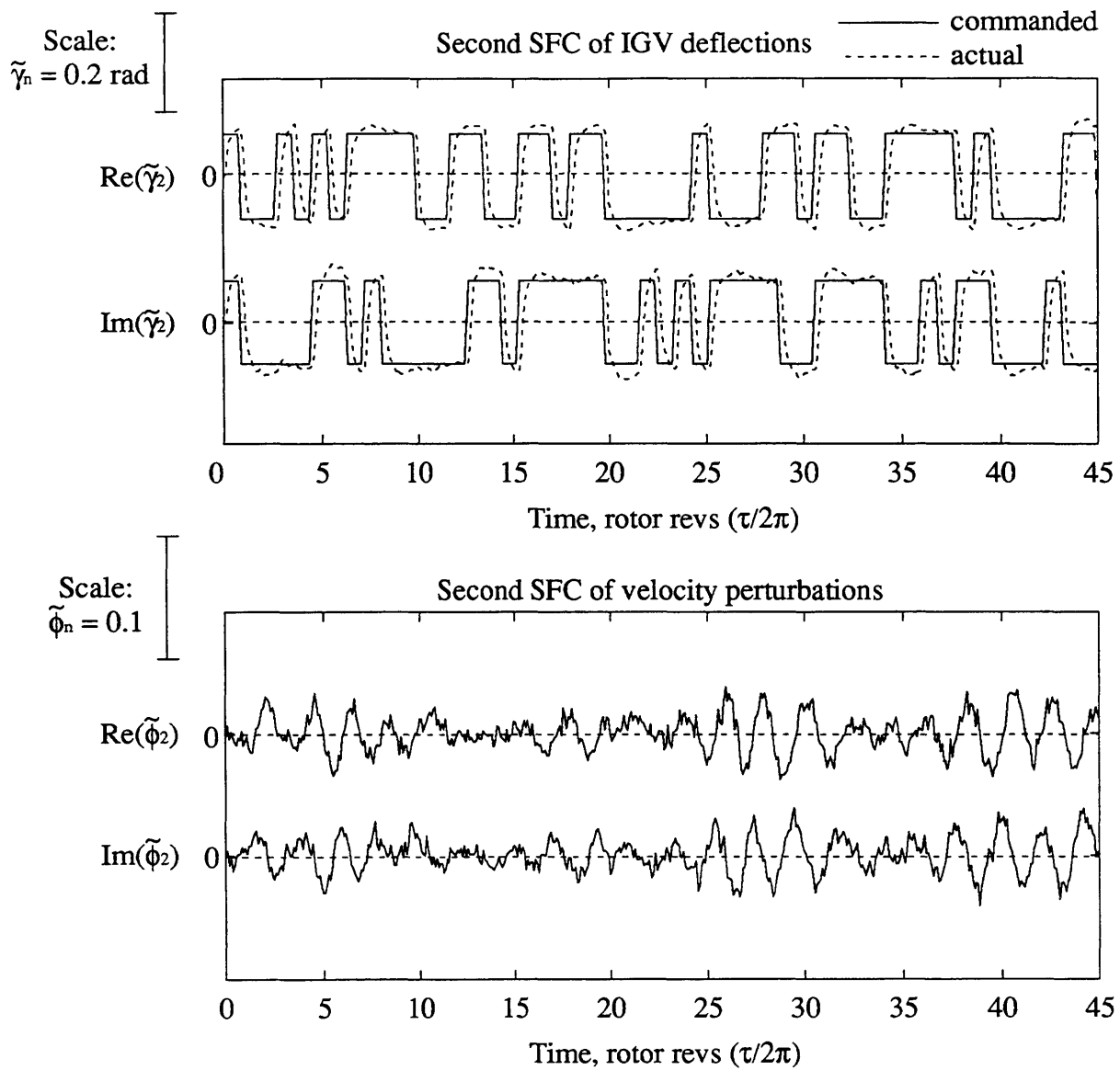


Figure 5.2a - Example of pseudo-random binary excitation and resulting response. This is a portion of the data used to generate the spectral estimate in Figure 5.2b.

$$\frac{\tilde{\Phi}_2(s)}{\tilde{\Upsilon}_2(s)}, \text{ Second Mode, } \bar{\phi} = 0.420, \text{ Downstream Hot Wires}$$

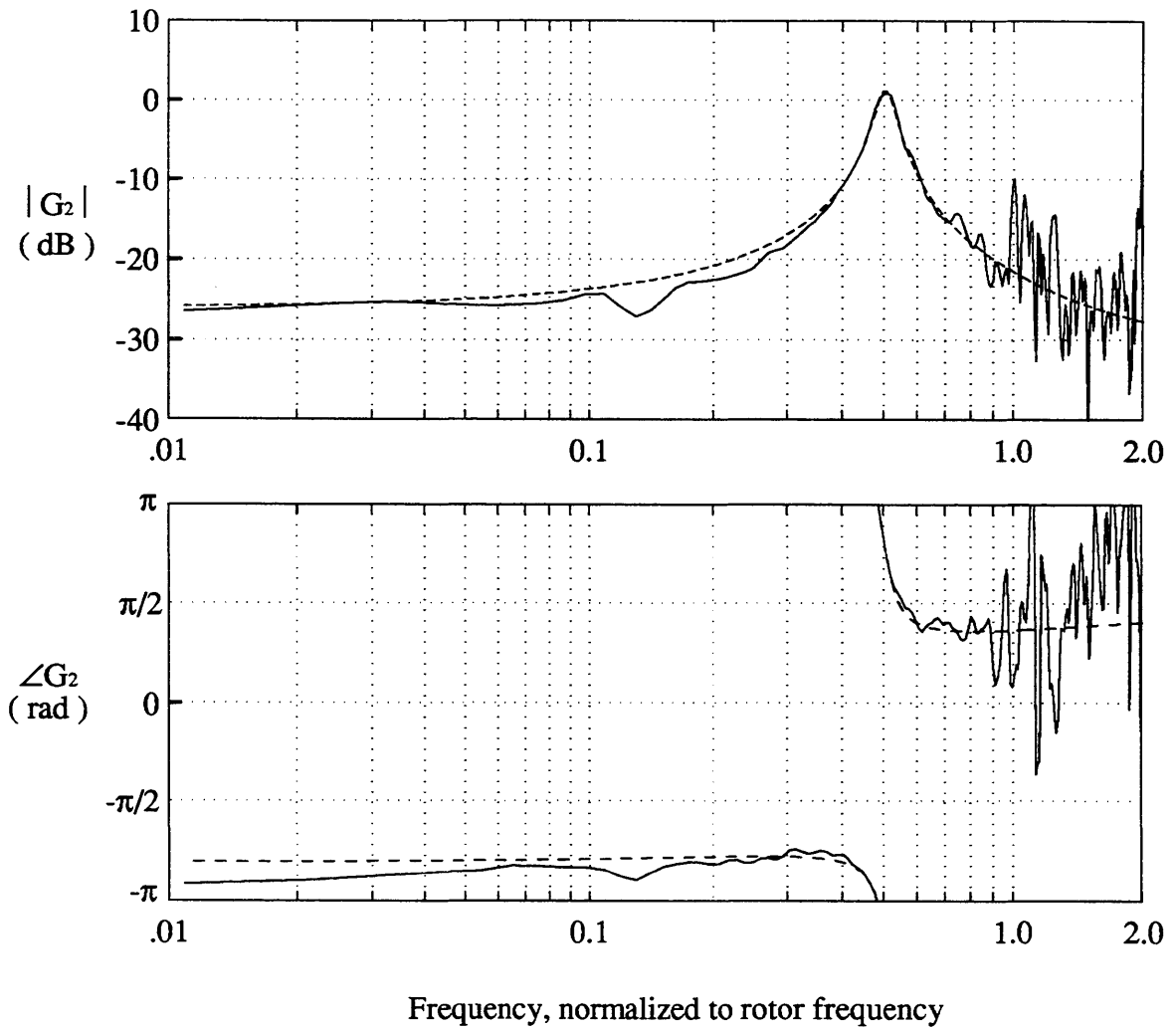


Figure 5.2b - Spectral estimate resulting from the data in Figure 5.2a.
 Dotted line shows a transfer function fit to the spectral estimate,
 $\Theta = [-0.0285 \ 0.505 \ -0.0157 \ 0.0194 \ 0.0214]$
 Transfer function for second SFC, at $\bar{\phi}=0.420$, hot wires
 downstream of the IGVs.

estimate becomes very large at frequencies above $\omega = 1$ (45 Hz); this is because the excitation bandwidth chosen for this experiment was 1.1 (50 Hz). Above this frequency, very little information about the input-output properties is available in the signals, and high variance results.

5.2 Parametric Estimation

Two parametric estimation techniques will be described in this section. The first method involves fitting transfer functions to the non-parametric estimates from Section 5.1. This method, called transfer function fitting, is discussed in Section 5.2.1. Direct parametric estimation using the instrumental-variable method is described in Section 5.2.2.

5.2.1 Transfer Function Fitting

Once $\hat{G}_n(j\omega)$ is obtained using the methods described in Section 5.1, a fit to the data using the model structure obtained in Chapter 3 can be attempted. The relevant equations are repeated here for convenience:

$$\tilde{\phi}_n(s) = G_n(s) \cdot \tilde{\gamma}_n \quad (5.11)$$

where:

$$G_n(s) = \frac{i \cdot g_i \cdot s + (b_r + i \cdot b_i)}{s - (\sigma_{rs} + i \cdot \omega_{rs})} .$$

The parameter vector for this system is:

$$\Theta(n, \tilde{\phi}) = \begin{bmatrix} \sigma_{rs} \\ \omega_{rs} \\ b_r \\ b_i \\ g_i \end{bmatrix} . \quad (5.12)$$

Lamaire [32] has developed a technique to convert the transfer-function fitting problem into a least-squares type problem. First, cross-multiply Equation (5.11), and rearrange:

$$sG_n(s) = (\sigma_{rs} + i \cdot \omega_{rs})G_n(s) + (b_r + i \cdot b_i) + i \cdot g_i \cdot s . \quad (5.13)$$

Next write this in inner-product form:

$$sG_n(s) = [G_n(s) \quad i \cdot G_n(s) \quad 1 \quad i \quad i \cdot s] \cdot \Theta. \quad (5.14)$$

Now we replace $G_n(s)$ with its estimate, and s with $j\omega_l$:

$$j\omega_l \hat{G}_n(j\omega_l) = [\hat{G}_n(j\omega_l) \quad i \cdot \hat{G}_n(j\omega_l) \quad 1 \quad i \quad i \cdot j\omega_l] \cdot \Theta, \quad (5.15)$$

where $l = 1, 2, \dots, L$.

This equation can be cast as a linear regression problem by setting up matrices for the right- and left-hand side, where each row is a different value of ω_l . We must also split up the real and imaginary parts of the complex numbers, to get real matrices.

The resulting matrices are:

$$A\{\hat{G}_n\} = \begin{bmatrix} \text{Re}\{\hat{G}_n(j\omega_1)\} & \text{Re}\{i \cdot \hat{G}_n(j\omega_1)\} & 1 & 0 & -\omega_1 \\ \vdots & \vdots & \vdots & \vdots & \vdots \\ \text{Re}\{\hat{G}_n(j\omega_L)\} & \text{Re}\{i \cdot \hat{G}_n(j\omega_L)\} & 1 & 0 & -\omega_L \\ \text{Im}\{\hat{G}_n(j\omega_1)\} & \text{Im}\{i \cdot \hat{G}_n(j\omega_1)\} & 0 & 1 & 0 \\ \vdots & \vdots & \vdots & \vdots & \vdots \\ \text{Im}\{\hat{G}_n(j\omega_L)\} & \text{Im}\{i \cdot \hat{G}_n(j\omega_L)\} & 0 & 1 & 0 \end{bmatrix} \quad (5.16)$$

$$B\{\hat{G}_n\} = \begin{bmatrix} \text{Re}\{j\omega_1 \cdot \hat{G}_n(j\omega_1)\} \\ \vdots \\ \text{Re}\{j\omega_L \cdot \hat{G}_n(j\omega_L)\} \\ \text{Im}\{j\omega_1 \cdot \hat{G}_n(j\omega_1)\} \\ \vdots \\ \text{Im}\{j\omega_L \cdot \hat{G}_n(j\omega_L)\} \end{bmatrix} \quad (5.17)$$

With this notation, we have

$$A\{\hat{G}_n\} \Theta = B\{\hat{G}_n\}. \quad (5.18)$$

This is a linear regression problem stated in matrix form. The parameter estimate $\hat{\Theta}$

is chosen to minimize the frequency weighted norm of the error vector

$$W \cdot [A\{\hat{G}_n\}\hat{\Theta} - B\{\hat{G}_n\}], \quad (5.19)$$

where the weighting matrix is a diagonal matrix:

$$W = \text{diag}\{ f(\omega_1) \ f(\omega_2) \cdots f(\omega_L), f(\omega_1) \ f(\omega_2) \cdots f(\omega_L) \}, \quad (5.20)$$

and $f(\omega_l)$ is a weighting function, chosen in this case to concentrate on the region around the pole and the zero frequencies [32]. The solution to this weighted least squares problem is computed as

$$\hat{\Theta} = (A^T W^T W A)^{-1} A^T W^T W B. \quad (5.21)$$

Thus for every transfer-function estimate generated using the non-parametric methods in Section 5.1, we can generate an estimate of the model parameters $\hat{\Theta}$. Figures 5.1 and 5.2 show typical parametric fits, and list the resulting parameters, as examples of the closeness of fit which can be obtained with this method.

5.2.2 The Instrumental-Variable Method

We have shown that spectral estimation methods combined with transfer function fits can provide good estimates of the system parameters, provided the system is operating open-loop. Some of the good properties of spectral estimates are lost, however, during closed-loop operation. This motivates the use of the instrumental-variable method.

Spectral estimates are able to minimize the effect of noise because the excitation is uncorrelated with the noise. For example, if u_r excitation is used, y_r will be corrupted by noise as follows:

$$y_r = G_{rn} \cdot u_r + v_r. \quad (5.22)$$

But, since u_r and v_r are uncorrelated, the cross-spectrum will be unaffected by v_r :

$$\Phi_{u_r y_r} = G_r \Phi_{u_r u_r} G_r^* + \Phi_{v_r u_r},$$

but

$$\Phi_{v_r u_r} = 0.$$

The second equality holds (even if v_r is colored noise) because the noise v_r is independent from the signal u_r . In practice, we can only obtain *estimates* of the desired cross-spectra, and these estimates will be affected by noise. But the variance of the estimate $\hat{\Phi}_{u_r y_r}(\omega)$ approaches zero as the number of samples becomes very large [30], and is tractably small for realizable sample lengths, as witnessed by the results shown in Figure 5.2.

The close-loop case is quite different, however. Here, the outputs, which are corrupted by the noise, are being fed back, so that they actually drive the inputs. Thus u_r and v_r are no longer independent in our example - in fact they are highly correlated, rather than uncorrelated, because stabilization of unstable dynamics is a high-gain feedback situation. Thus, for closed loop identification, we cannot use spectral estimation.

The instrumental variable (IV) procedure can be adapted to solve the problem of correlation between the noise and the inputs. Section 5.2.2.1 reviews the basic IV method for SISO systems. Section 5.2.2.2 outlines Young's Refined IV - Approximate Maximum Likelihood (RIV-AML) method. Modifications to this approach necessary to handle the closed loop case are discussed in Section 5.2.2.3, and modifications for unstable plants are discussed in Section 5.2.2.4. Finally, a brief discussion of how the MIMO estimation for the rotating stall system is efficiently computed appears in Section 5.2.2.5.

5.2.2.1 Basic IV Procedure

Consider the system

$$y(k) = \frac{B(z)}{A(z)} \cdot u(k) + v(k) \quad (5.23)$$

where:

$$A(z) = (1 + a_1 z^{-1} + a_2 z^{-2} + \dots),$$

$$B(z) = (b_1 + b_2 z^{-1} + b_3 z^{-2} + \dots),$$

and $v(k)$ is additive noise conforming to the following model:

$$v(k) = \frac{C(z)}{D(z)} \cdot \xi(k). \quad (5.24)$$

In this formulation, $C(z)$ and $D(z)$ are monic, and $\xi(k)$ is an uncorrelated sequence with Gaussian amplitude distribution over the sample interval:

$$\underline{\xi} \sim N(0, \sigma^2 \cdot I) \quad \underline{\xi} = [\xi(1), \xi(2), \dots, \xi(T)].$$

The variable z in (5.23) and (5.24) is the Z-transform variable, but can be interpreted as the delay operation when manipulating causal difference equations.

We can build a one-step-ahead predictor for this system:

$$\hat{y}(k) = \Phi^T(k) \cdot \hat{\Theta}, \quad (5.25)$$

where:

$$\begin{aligned} \Phi^T(k) &= [-y(k-1) \ -y(k-2) \ \dots \ u(k) \ u(k-2) \ u(k-2) \ \dots], \\ \hat{\Theta} &= [\hat{a}_1 \ \hat{a}_2 \ \dots \ \hat{b}_1 \ \hat{b}_2 \ \hat{b}_3 \ \dots]^T, \end{aligned}$$

and the $\hat{(\)}$ indicates prediction or estimation. The prediction error can then be written as

$$e(k) = y(k) - \Phi^T(k) \cdot \hat{\Theta}. \quad (5.26)$$

The instrumental variable (IV) method [33] finds the value of $\hat{\Theta}$ which will cause the error to be uncorrelated with some chosen set of instruments

$$\zeta(k) = [\zeta_1(k) \ \zeta_2(k) \ \dots]^T. \quad (5.27)$$

This condition can be written as follows:

$$\hat{\Theta} = \text{sol} \left\{ \frac{1}{N} \sum_{k=1}^N \zeta(k) \cdot e(k) = 0 \right\}, \quad (5.28)$$

where $\text{sol}\{ \cdot \}$ indicates that $\hat{\Theta}$ is the value of Θ for which the equation in brackets is satisfied. Substituting in Equation (5.26):

$$\hat{\Theta} = \text{sol} \left\{ \frac{1}{N} \sum_{k=1}^N \zeta(k) \left(y(k) - \Phi^T(k) \cdot \hat{\Theta} \right) = 0 \right\}. \quad (5.29)$$

The philosophy of the IV approach is this: if the instruments are chosen to be related to the system inputs and outputs, and $\hat{\Theta}$ does *not* satisfy (5.28), then there is additional information about the input-output dynamics left in the prediction error. Therefore, a good estimate of Θ should extract this information, making the correlation in (5.28) disappear.

The solution to (5.29) is

$$\hat{\Theta} = \left[\frac{1}{N} \sum_{k=1}^N \zeta(k) \Phi^T(k) \right]^{-1} \cdot \left[\frac{1}{N} \sum_{k=1}^N \zeta(k) y(k) \right]. \quad (5.30)$$

The IV method will have good convergence and consistency properties if the following two conditions are met:

$$\sum_{k=1}^N \zeta(k) \Phi^T(k) \quad \text{nonsingular}, \quad (5.31a)$$

$$E \left\{ \sum_{k=1}^N \zeta(k) v(k) \right\} = 0, \quad (5.31b)$$

where $E\{\cdot\}$ is the expectation operator. Condition (5.31a) guarantees invertibility in (5.30), and also indicates that ζ is correlated with the system dynamics, which is necessary for Equation (5.28) to yield good estimates. In fact, if $\zeta(k) = \Phi(k)$, then (5.31a) is satisfied trivially and the estimate becomes the least-squares estimate of Θ .

Condition (5.31b) specifies that the instruments be uncorrelated with the noise, so that colored noise will not corrupt the estimates. This condition is often not met in the least-squares case ($\zeta(k) = \Phi(k)$), hence the need for a different set of instruments [30]. Pre-filtered versions of the elements of $\Phi(k)$ are usually used in this case. Ljung [30] gives a complete description of the IV method, its convergence and consistency properties, and methods for constructing instruments which are uncorrelated with the noise.

5.2.2.2 Young's Refined Instrumental Variable - Approximate Maximum Likelihood (RIV-AML) Technique [33]

Many filtering schemes have been proposed for constructing the instruments $\zeta(k)$ in the IV procedure. Young [33] has developed a particularly attractive set of pre-filters and instruments in the context of maximum likelihood estimation, for the noise model given in (5.24). In this approach, the input-output data is first pre-filtered, which introduces a new set of variables:

$$y^f(k) = \frac{D}{A \cdot C} \cdot y(k) ; \quad u^f(k) = \frac{D}{A \cdot C} \cdot u(k) ; \quad \hat{y}^f(k) = \frac{B}{A} \cdot u^f(k) \quad (5.32)$$

Young shows that, with these definitions, the maximum-likelihood estimation estimate can be stated as the solution to the IV problem:

$$\hat{\Theta} = \left[\frac{1}{N} \sum_{k=1}^N \zeta(k) \Phi_f^T(k) \right]^{-1} \cdot \left[\frac{1}{N} \sum_{k=1}^N \zeta(k) y^f(k) \right] \quad (5.33)$$

where

$$\Phi_f(k) = [-y^f(k-1) \ -y^f(k-2) \ \dots \ u^f(k) \ u^f(k-1) \ u^f(k-2) \ \dots]^T,$$

and

$$\zeta(k) = [-\hat{y}^f(k-1) \ -\hat{y}^f(k-2) \ \dots \ u^f(k) \ u^f(k-1) \ u^f(k-2) \ \dots]^T.$$

In other words, if the above defined variables and instruments are used, then $\hat{\Theta}$ is the maximum likelihood estimate. This is called the refined IV, or RIV, estimate.

Of course, the polynomials $A(z)$, $B(z)$, $C(z)$, and $D(z)$ in Equation (5.32) are not known a priori. Initial estimates of these must be made, and the RIV method applied iteratively to improve the estimates. The parameters in $\hat{\Theta}$ constitute the updates for \hat{A} and \hat{B} in such a scheme, so iteration on Θ is sufficient as a search on the maximum likelihood estimates of A and B . C and D , on the other hand, are not estimated by the procedure. Thus an estimation algorithm for C and D must be added to the iteration.

Young provides an approximate maximum likelihood approach to do exactly that. It provides a way to estimate C and D , based on the current estimates of A , B , C , and D . The basic philosophy is to form an error term based on the current

estimates \hat{A} and \hat{B} . This error term is then considered to be the output of a dynamic system driven by white noise, and the dynamics are estimated using a procedure similar to the RIV procedure described above. The specifics of this procedure, called approximate likelihood (AML), are as follows:

We first take the prediction error $e(k)$ in (5.26) as a measurement of $v(k)$:

$$\begin{aligned} v(z) &= y(z) - \frac{B(z)}{A(z)} \cdot u(z) \\ \Rightarrow \hat{v}(z) &= y(z) - \hat{y}(z) \\ &= e(z). \end{aligned} \quad (5.34)$$

The dynamics in (5.24) are then written

$$D(z) \cdot e(z) = C(z) \cdot \xi(z). \quad (5.35)$$

A 'one-step-ahead predictor' for this system is

$$\hat{v}(k) = \hat{e}(k) = \varphi^T \hat{\eta}, \quad (5.36)$$

where:

$$\begin{aligned} \varphi &= [-\hat{v}(k-1) \quad -\hat{v}(k-2) \quad \cdots \quad \xi(k-1) \quad \xi(k-2) \quad \cdots]^T \\ \eta &= [d_1 \quad d_2 \quad \cdots \quad c_1 \quad c_2 \quad \cdots]^T. \end{aligned} \quad (5.37)$$

To compute an approximate maximum likelihood estimate of the noise system, prefilter as follows:

$$\begin{aligned} \hat{v}^f(k) &= \frac{1}{\hat{C}(z)} \cdot \hat{v}(k), \\ \hat{\xi}^f(k) &= \frac{1}{\hat{C}(z)} \cdot \hat{\xi}(k) = \frac{\hat{D}(z)}{\hat{C}(z)} \cdot \hat{v}^f(k). \end{aligned} \quad (5.38)$$

The estimate for the noise model is then:

$$\hat{\eta} = \left[\frac{1}{N} \sum_{k=1}^N \beta(k) \varphi^T(k) \right]^{-1} \cdot \left[\frac{1}{N} \sum_{k=1}^N \beta(k) \hat{v}(k) \right], \quad (5.39)$$

where:

$$\beta(k) = [-\hat{v}^f(k-1) \quad -\hat{v}^f(k-2) \quad \cdots \quad \hat{\xi}^f(k-1) \quad \hat{\xi}^f(k-2) \quad \cdots]^T$$

The notation here has been made as similar to the IV notation as possible, to show the parallel between this procedure and the RIV procedure described above. Note that we use some set of past estimates \hat{A} , \hat{B} , \hat{C} , and \hat{D} to allow us to best estimate $\hat{\eta}$, which is the updated estimate for C and D. Young gives more detail about the properties of the estimates, and also gives a recursive algorithm for its application.

We now have an estimation procedure for C and D, which can be integrated into the iteration for the maximum likelihood estimates of A and B. The complete RIV-AML recursion algorithm, then, is [33]

1. Begin with initial estimates for $\hat{A}(z)$, $\hat{B}(z)$, $\hat{C}(z)$, and $\hat{D}(z)$.
2. Use the AML procedure (Equations (5.34)-(5.39)) to update \hat{C} and \hat{D} .
3. Use the RIV procedure (Equations (5.32)-(5.33)), using the updated estimates of \hat{C} and \hat{D} , to update \hat{A} and \hat{B} .
4. Go to 2, repeat with the new values of \hat{A} and \hat{B} .

One purpose of the filters in Equations (5.32) is to eliminate as much as possible the effect of the colored noise on the outputs. Such 'pre-whitening' filters attempt to insure that $y^f(k)$ is uncorrelated with the disturbances $v(k)$. $y^f(k)$ must be uncorrelated with $v(k)$ in order to satisfy Equation (5.31b), because $y^f(k)$ is a part of the instruments. The filtered inputs $u^f(k)$, which make up the remainder of the instruments, must also be uncorrelated with $v(k)$ in order to satisfy Equation (5.31b). During open-loop operation, this condition is automatically satisfied, because $\xi(k)$ in Equation (5.24) is uncorrelated with $u(k)$. During closed-loop operation, however, $v(k)$ and $u(k)$ are correlated (this will be shown in the next section). The above method must, therefore, be modified for closed-loop identification. This is the subject of the following section.

5.2.2.3 Choice of Closed-Loop Instruments

Figure 5.3 shows the layout and notation for closed-loop operation. The system dynamics remain as in Equation (5.23). In addition, we introduce the external

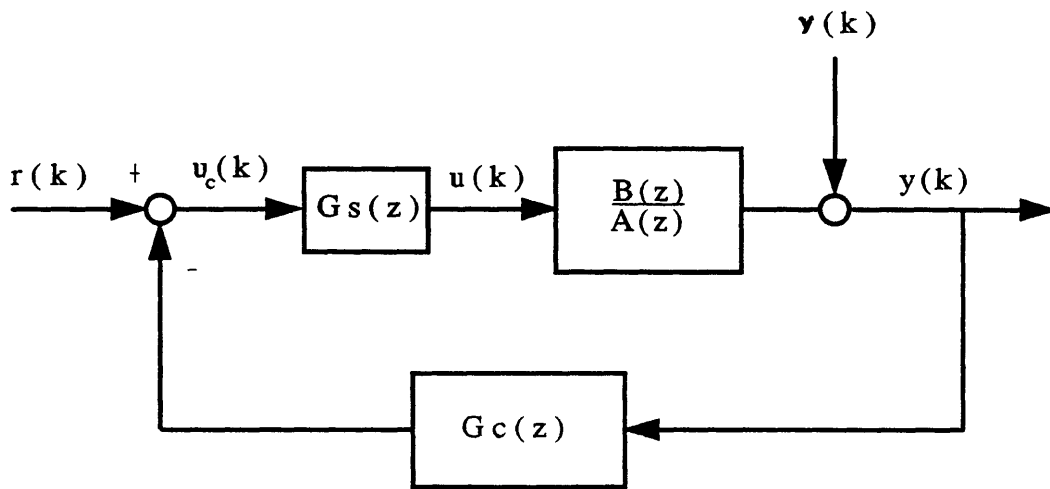


Figure 5.3 - Closed-loop system notation

input signal, $r(k)$, and the following feedback law:

$$u(z) = G_s \cdot (r(z) - G_c \cdot y(z)), \quad (5.40)$$

where $G_c(z)$ and $G_s(z)$ are rational transfer functions representing dynamics in the feedback and forward paths. For the rotating stall controller, these dynamics are well defined (see Chapter 4), so here we will assume that they are known. Since $y(k)$ is corrupted by $v(k)$, $u(k)$ will now be correlated with the noise, and Equation (5.31b) will be violated:

$$u(k) = G_c(z) \cdot (r(k) - G_s \cdot (G \cdot u(k) + v(k))),$$

$$\Rightarrow E \left\{ \sum_{k=1}^N \zeta(k)v(k) \right\} \neq 0,$$

because $\zeta(k)$ contains $u(k)$. This is a very real problem which does not constitute a mere theoretical technicality. In a high-gain feedback situation such as occurs during stabilization of unstable dynamics, it renders the IV methods described so far useless. Fortunately, these methods regain their applicability if the proper substitutions are made to insure that the resulting instruments fulfill Equations (5.31).

References [34] and [35] discuss in detail the problem of closed-loop estimation, and the methods they describe will be used here. The idea is to replace $\{ y(k), u(k) \}$ in the computation of the instruments with some $\{ y^c(k), u^c(k) \}$ which are highly correlated with their respective counterparts (condition (5.31a), but which are uncorrelated with the disturbances (condition (5.31b)). The two methods used to accomplish this are described below. In both cases, we assume $r(k)$ is a known external excitation.

Method I: Test-Repeat (TR) Instrumental Variables

This method, introduced in [34], achieves uncorrelated instruments by repeating the experiment twice, with identical $r(k)$ in both cases. The measured inputs and outputs for the two tests are denoted $\{ u(k), y(k) \}$ and $\{ u^c(k), y^c(k) \}$.

The procedure is to use one of these input-output pairs to compute the instruments, and the other to compute the estimates. The RIV-AML estimation proceeds exactly as described in Section 5.2.2.2, using $\{ u^c(k), y^c(k) \}$ to compute the instruments and $\{ u(k), y(k) \}$ to compute the parameter estimates (The roles of the two input-output pairs can be switched).

Using identical $r(k)$ in the two tests insures high correlation between the instruments and the measurements (condition 5.31a), and poses no particular difficulty in a digital control environment. Also, because $v(k)$ and $v^c(k)$ are incurred at different times, they are uncorrelated, which means that the instruments (from the first test) will be uncorrelated with the disturbances (from the second test) even if the system is operating closed loop (condition 5.31b). Reference [34] proves these claims, and discusses the consistency properties of the Test Repeat (TR) method.

Method II: Noise-Free (NF) Instruments

Both [34] and [35] discuss this method, which uses noise-free (NF) simulation of the test to generate the instruments. In this case $\{ u^c(k), y^c(k) \}$ comes from a simulation, using an a priori estimate of the system dynamics (i.e. $\hat{\Theta}$). $v^c(k)$ will thus be identically zero. The same input $r(k)$ is then applied to the real system to get $\{ u(k), y(k) \}$. The RIV-AML algorithm can now be applied, using $\{ u^c(k), y^c(k) \}$ to compute the instruments and $\{ u(k), y(k) \}$ as the measurements (in this case the roles of the two input-output pairs cannot be switched).

The same reasoning applies here as in the TR case. The noise-free instruments will naturally be uncorrelated with the noise (condition (5.31a)). The degree of correlation between the instruments and the measurements (condition (5.31b)) will depend on the accuracy of the a priori estimate of the system dynamics, but (except in trivial cases) some correlation will exist. Closed-loop operation changes none of these observations. References [34] and [35] discuss NF estimation more rigorously.

5.2.2.4 Modification of the RIV-AML Prefilters for Unstable Plant Dynamics

The test-repeat instrumental variable (TR/IV) and the noise-free instrumental-variable (NF/IV) methods allow identification of system dynamics during closed-loop operation, even when the plant is unstable. Experience with these methods has suggested, however, that the covariance of the estimates can be large for standard choices of instruments. Thus we have combined the TR and NF methods with the RIV-AML method to obtain more accurate estimates. If the open-loop plant is stable, this presents no problem: the hybrid techniques, termed TR/RIV-AML and NF/RIV-AML, can be synthesized without additional modifications. However, if the open-loop plant is unstable, many of the prefilters required by the RIV-AML procedure (Equations (5.32) and (5.34)) are also unstable - they contain $\frac{1}{A(z)}$, which is unstable if implemented as a causal filter.

To use the TR/RIV-AML and NF/RIV-AML procedure when the open-loop plant is unstable, we must modify the prefiltering scheme to avoid filters which blow up. This problem is primarily one of understanding the prefilters in the context of the maximum-likelihood (ML) problem, and applying them properly. To develop the RIV-AML method, Young [33] first writes the log-likelihood function for the observations $y(k)$, and then reduces the ML problem to the minimization of the following term:

$$L = \left[-\frac{D}{C} \left(y - \frac{B}{A} \cdot u \right) \right]^T \left[-\frac{D}{C} \left(y - \frac{B}{A} \cdot u \right) \right]. \quad (5.41)$$

The RIV and AML prefilters are then formulated by writing $\partial L / \partial a_i = 0$, $\partial L / \partial b_i = 0$, etc. Thus the prefilters contain $\frac{1}{\hat{A}}$ because the log-likelihood function contains the prediction error $\left(y - \frac{\hat{B}}{\hat{A}} \cdot u \right)$.

When the closed-loop system is stabilizing an open-loop unstable plant, we are faced with the following problem: $y(k)$ and $u(k)$ are 'stable' signals; that is, their

Z-transforms $y(z)$ and $u(z)$ converge on the unit circle ($|z| = 1$). But $\frac{B(z)}{A(z)}$ is unstable; that is, it is the Z-transform of a causal impulse response, and it contains poles outside the unit circle. Given these conditions, can we compute an estimate of $y(k)$ based on $u(k)$, $\hat{A}(z)$, and $\hat{B}(z)$ alone? If we can, then the prediction error can be formulated, and the prefilters necessary for the RIV-AML procedure can be found.

To answer this question, consider our system representation (5.23,5.24):

$$y(z) = \frac{B(z)}{A(z)} \cdot u(z) + \frac{C(z)}{D(z)} \cdot \xi(z). \quad (5.42)$$

We can break $A(z)$ into a polynomial whose roots are stable, times a polynomial whose roots are unstable:

$$A(z) \equiv A_s(z) \cdot A_u(z), \quad (5.43)$$

where:

$$A_s(z) = \prod_j (1 - q_j \cdot z^{-1}); \quad |q_j| < 1,$$

$$A_u(z) = \prod_i (1 - p_i \cdot z^{-1}); \quad |p_i| \geq 1.$$

This factorization of $A(z)$ allows us to rewrite (5.42) to reflect the possibility that the noise dynamics are affected by the unstable poles:

$$y(z) = \frac{B(z)}{A_u(z)A_s(z)} \cdot u(z) + \frac{E(z)}{A_u(z)F(z)} \cdot \xi(z). \quad (5.44)$$

where $\frac{E}{F}$ is defined such that $\frac{C}{D} = \frac{E}{A_u F}$. Generality is retained in this formulation because $E(z)$ cancels any poles of $A_u(z)$ that are not part of $D(z)$. The transfer function $\frac{E}{F}$ is stable if the system is stabilizable, so we can write:

$$\begin{aligned} y(z) &= \frac{1}{A_u(z)} \cdot \left[\frac{B(z)}{A_s(z)} \cdot u(z) + \frac{E(z)}{F(z)} \cdot \xi(z) \right] \\ &\equiv \frac{1}{A_u(z)} \cdot [q(z)] \end{aligned} \quad (5.45)$$

where $q(z)$ is bounded for $|z| = 1$, because of our conditions on A_s (stated in 5.43), $\frac{E}{F}$ (stated above), $u(k)$ (its Z-transform converges on the unit circle), and $\xi(k)$ (stated after (5.24) - the important point being that $\xi(k)$ is a finite-duration

(windowed) sequence). We have also specified that a feedback system is stabilizing the plant, so that $y(z)$ converges for $|z|=1$. Thus, by studying (5.45), one concludes that $q(z)$ must contain zeros which cancel the unstable poles of $\frac{1}{A_u}$. We write this condition as follows:

$$\begin{aligned} q(z) &= A_u(z) \cdot w(z) & (5.46) \\ \Rightarrow y(z) &= \frac{1}{A_u(z)} \cdot [A_u(z) \cdot w(z)]. \end{aligned}$$

where $w(z)$ also converges for $|z|=1$. The pole-zero cancellation implied by (5.46) can be derived constructively (although somewhat tediously) by writing the closed-loop transfer function from any external signal (such as $r(z)$ or $\xi(z)$) to $y(z)$.

The representation (5.46) can be used to motivate a filtering scheme as follows: $\frac{1}{A_u(z)}$ is the (two-sided) Z-transform of at least *two distinct impulse responses* [36]: 1) a causal, unstable impulse response, which we will call h_c , and 2) an anticausal, stable impulse response, which we will call h_{ac} . The Z-transform of h_c converges in the region of convergence (ROC) $|z| > \max(p_i)$, while the Z-transform of h_{ac} converges in the ROC $|z| < \min(p_i)$. The ambiguity of the Z-transform is usually cleared up by invoking causality: because (5.42) represents a causal dynamic system, we know that the physically meaningful inverse of $\frac{1}{A_u(z)}$ is $h_c(k)$, and that the convolution corresponding to (5.46) is:

$$y(k) = h_c(k) * [h_A(k) * w(k)], \quad (5.47)$$

where $*$ indicates convolution and

$$\begin{aligned} h_c(k) &\equiv Z^{-1} \left\{ \frac{1}{A_u(z)} \right\} & \text{ROC: } |z| > \max(p_i), \\ h_A(k) &\equiv Z^{-1} \{ A_u \} & \text{ROC: all } z. \end{aligned}$$

As we have noted, $h_c(k)$ is causal, but because the poles of $\frac{1}{A_u(z)}$ lie outside the unit circle, $h_c(k)$ grows without bound as $k \rightarrow \infty$. However, it can be shown that the causal, unstable impulse response $h_c(k)$ can be replaced by its

anticausal, stable counterpart $h_{ac}(k)$, if a pole-zero cancellation such as (5.46) occurs.

We can write this statement as follows:

$$h_{ac}(k) * [h_A(k) * w(k)] = h_c(k) * [h_A(k) * w(k)] \quad (5.48)$$

where

$$h_{ac}(k) = Z^{-1} \left\{ \frac{1}{A_u(z)} \right\} \quad \text{ROC: } |z| < \min(p_i).$$

Note here that the ROC overlaps the unit circle. Computing the inverse Z-transform over this ROC gives an impulse response which is bounded for all k [36]. Thus we expect that replacing h_c with h_{ac} will yield a stable (although noncausal) way to predict $y(k)$.

Substituting (5.48) into (5.47), we have the following equation for $y(k)$:

$$y(k) = h_{ac}(k) * [h_A(k) * w(k)]. \quad (5.49)$$

Since all of the sequences in this equation are stable, their Z-transforms exist on the unit circle, and we can convert back to the Z-domain:

$$\begin{aligned} y(z) &= \frac{1}{A_u(z)} \Big|_{ac} \cdot [A_u(z) \cdot w(z)] \\ &= \frac{B(z)}{A(z)} \Big|_{snc} \cdot u(z) + \frac{C(z)}{D(z)} \Big|_{snc} \xi(z). \\ \Rightarrow \hat{y}(z) &= \frac{\hat{B}(z)}{\hat{A}(z)} \Big|_{snc} \cdot u(z), \end{aligned} \quad (5.50)$$

where we denote the Z-transform of h_{ac} as $\frac{1}{A_u(z)} \Big|_{ac}$, to distinguish it from the Z-transform of h_c . The operations between transfer functions implied by (5.50) are valid for the transfer functions and signals we have defined, because they all converge on the unit circle. The subscript 'snc' is used to indicate that we will use a stable, noncausal time-domain implementation of the filter - the anticausal part coming from the unstable poles, and the causal part coming from the stable poles. Figure 5.4 gives an example of the regions of convergence associated with $\frac{1}{A(z)}$, and the corresponding impulse responses.

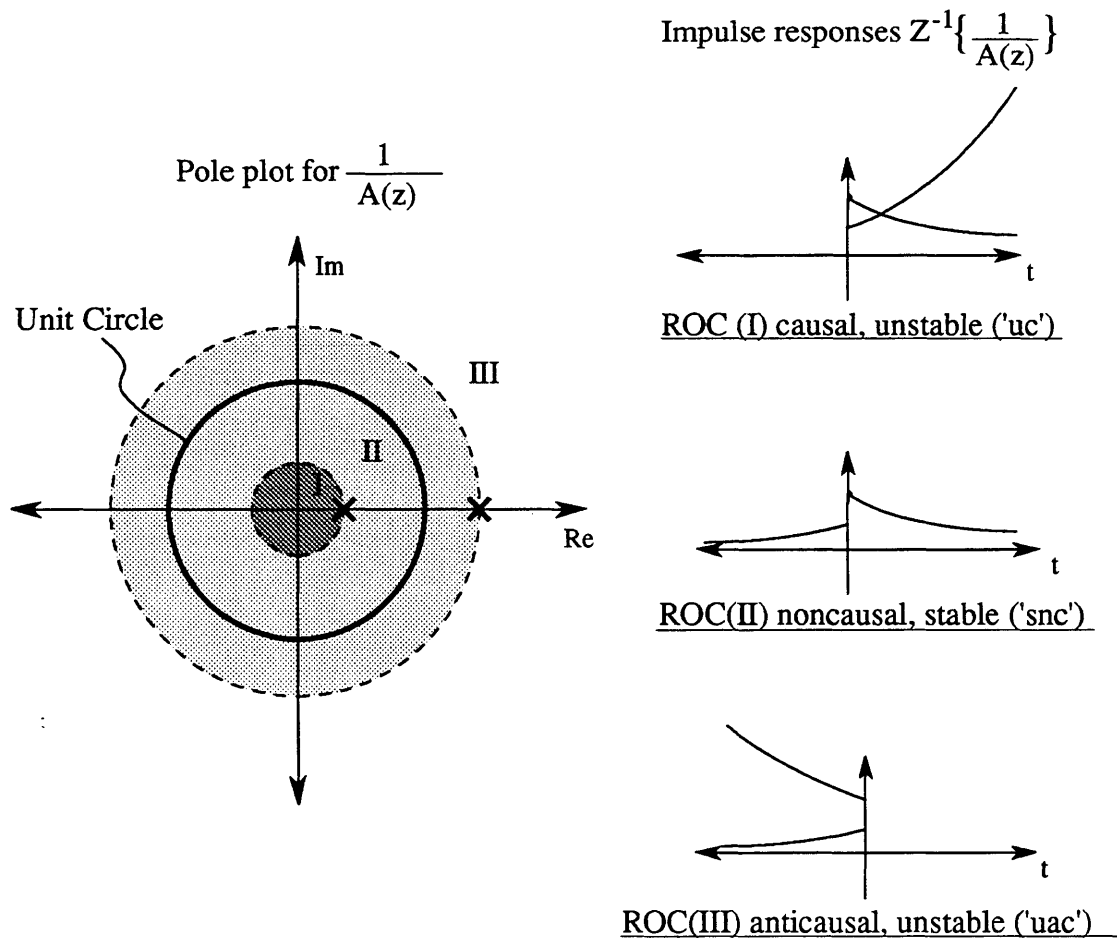


Figure 5.4 - Example of different impulse responses associated with the same transfer function. The inverse Z-transform of $A(z)$ can be computed over any of the three regions of convergence (ROCs) shown (I, II, or III). The impulse response in each case is the sum of the truncated exponentials shown at right.

We have shown how the transfer function between $u(z)$ and $\hat{y}(z)$ must be altered when the open-loop plant is unstable. It can be shown that all of the filtering and prediction described in Sections 5.2.2.2 can be similarly altered, without changing the maximum-likelihood results of Young [33]. Thus, our scheme is noncausal when the plant is unstable, and must be implemented off-line, but otherwise it proceeds as described in Sections 5.2.2.1-5.2.2.3, with $\frac{1}{A(z)}$ replaced by $\frac{1}{A(z)} \Big|_{\text{snc}}$.

5.2.2.5 Application to the MIMO Rotating Stall System

The rotating stall system which we would like to identify can be derived by using Equations (4.1) and (4.19-4.21):

$$\begin{aligned} \begin{bmatrix} y_r \\ y_i \end{bmatrix}_n &= z^{-1} \cdot \begin{bmatrix} x_r \\ x_i \end{bmatrix}_n + \begin{bmatrix} v_r \\ v_i \end{bmatrix}_n & (5.51) \\ &= \frac{1}{a_1 z^2 + a_2 z + a_3} \begin{bmatrix} (b_1 z + b_2)(z+1) & -(b_3 z + b_4 z + b_5) \\ (b_3 z + b_4 z + b_5) & (b_1 z + b_2)(z+1) \end{bmatrix} \begin{bmatrix} u_r \\ u_i \end{bmatrix}_n \cdot z^{-1} + \begin{bmatrix} v_r \\ v_i \end{bmatrix}_n \end{aligned}$$

where the a's and b's are all functions of n and $\bar{\phi}$. Note the extra delay (indicated by z^{-1}), which accounts for various time delays in the system (Sections 4.2.2 and 4.3.1). \tilde{y}_n is, according to (5.51), a delayed and noise-corrupted version of $\tilde{\phi}_n$. Its real and imaginary parts, y_r and y_i , evolve according to (5.51), which is a MIMO version of (5.23). All of the states and coefficients in (5.51) are real-valued.

The system in (5.51) is both multi-modal and MIMO. The multi-modal nature of the system requires that dynamics be identified for each mode number n . This identification can be done mode-by-mode, since the dynamics are decoupled. But each mode constitutes a two-input two-output system. This adds complexity, but otherwise requires no modification to the procedure. Some specifics of the MIMO analysis will be given as an illustration and to demonstrate an algorithmic simplification.

The one-step-ahead predictor for the system described in Equation (5.51) is:

$$\begin{bmatrix} \hat{y}_{r_n} \\ \hat{y}_{i_n} \end{bmatrix}_k = \Phi_n^T(k) \cdot \hat{\Theta}_n$$

where:

(5.52)

$$\Phi_n^T(k) = \begin{bmatrix} \Phi_{r_n}^T \\ \Phi_{i_n}^T \end{bmatrix}_k$$

$$= \begin{bmatrix} y_r(k-1) & y_r(k-2) & u_r(k-1)+u_r(k-2) & u_r(k-2)+u_r(k-3) & -u_i(k-1) & -u_i(k-2) & -u_i(k-3) \\ y_i(k-1) & y_i(k-2) & u_i(k-1)+u_i(k-2) & u_i(k-2)+u_i(k-3) & u_r(k-1) & u_r(k-2) & u_r(k-3) \end{bmatrix}_n$$

$$\hat{\Theta}_n = [a_1 \ a_2 \ b_1 \ b_2 \ b_3 \ b_4 \ b_5]_n^T$$

Here we have taken advantage of the structure of (5.51) to minimize the number of parameters which need to be identified. The instruments must match the dimension of Φ_n , so we have:

$$\zeta_n^T(k) = \begin{bmatrix} \zeta_{1_n}^T \\ \zeta_{2_n}^T \end{bmatrix} = \begin{bmatrix} \zeta_{11}(k) & \zeta_{21}(k) & \cdots & \zeta_{71}(k) \\ \zeta_{12}(k) & \zeta_{22}(k) & \cdots & \zeta_{72}(k) \end{bmatrix}_n. \quad (5.53)$$

Equations (5.28) through (5.39) proceed as before, with the understanding that the summations now contain matrix multiplications rather than scalar and inner products. Equation (5.30) can be made more efficient computationally by breaking up the matrices $\zeta_n(k)$ and $\Phi_n(k)$ into their constituent vectors. The resulting solution to the IV problem is as follows:

$$\hat{\Theta}_n = [\sum \zeta_{1_n} \cdot \Phi_{1_n}^T + \sum \zeta_{2_n} \cdot \Phi_{2_n}^T]^{-1} \cdot [\sum \zeta_{1_n} \cdot y_{1_n} + \sum \zeta_{2_n} \cdot y_{2_n}], \quad (5.54)$$

where subscripts k have been suppressed.

5.2.2.5 A Typical Run

A typical closed-loop IV parameter identification experiment is conducted as follows: First the control system is initialized and closed loop operation begins. Next

the downstream throttle is used to manually set the flow coefficient to the value at which the test will be run. This may or may not be an open-loop unstable operating point. The signal $[r_r(k) \ r_i(k)]_n^T$ is then applied, and measurements are made of $[u_r(k) \ u_i(k)]_n^T$ and $[y_r(k) \ y_i(k)]_n^T$ (see Figure 5.3). The test can then be repeated for the TR method. The complete data set is then put through the TR/RIV-AML procedure or the NF/RIV-AML procedure described above.

A portion of a typical data set appears in Figure 5.5, taken at $\bar{\phi} = 0.40$ for a mode number of one ($n=1$). The command is a band-limited pseudo-random binary signal of magnitude 10° (0.1745 rads) on each channel of the input vector $[r_r \ r_i]_n^T$. The bandwidth is limited to $\omega = 1.1$ (50 Hz), which is about five times the natural frequency (ω_{rs}) of the system. The actual IGV deflections, $[u_r \ u_i]_n^T$, are responding to both this command and the feedback signal, as shown in Figure 5.3 and in Equation (5.40). It is apparent from the differences between $[r_r \ r_i]_n^T$ and $[u_r \ u_i]_n^T$ that the feedback signal is a major part of the excitation to the system. The outputs $[y_r \ y_i]_n^T$ are also shown in Figure 5.5. Also shown in Figure 5.5 are the results of the noise-free simulation. The good agreement between the noise-free simulation (which relies only on $[r_r \ r_i]_n^T$) and the actual system inputs and outputs indicates that the method is yielding good estimates.

5.3 Results and Discussion

All of the methods described in this chapter were applied to data from the single-stage active control research compressor. Section 5.3.1 compares the estimation procedures we have described. Section 5.3.2 presents the parameter estimates $\hat{\Theta}(n, \bar{\phi})$ for $n=1, 2$, and 3, and for the range of flow coefficients $\bar{\phi} = 0.350$ to 0.550. Section 5.3.3 presents some configuration studies. Refer to Figure 6.1 for a steady-state characteristic ($\psi(\bar{\phi})$) of the compressor.

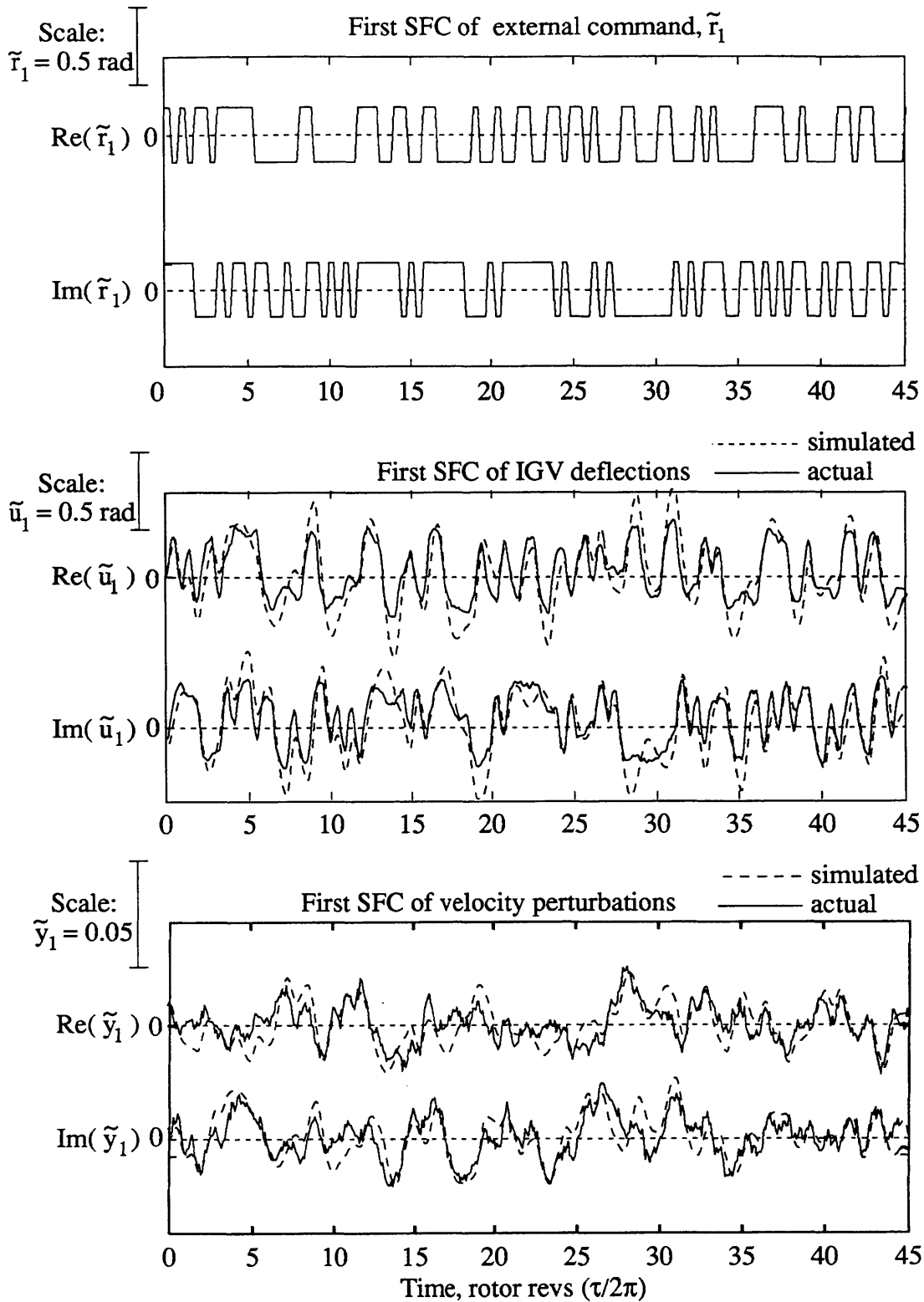


Figure 5.5 - Example of data for IV estimation techniques. Dotted lines are results of a noise-free simulation, based on a NF/RIV-AML estimate. First mode T.F., $\bar{\phi} = 0.400$, hot wires downstream of IGVs. $\Theta_{\text{NF/RIV-AML}} = [.0174 \ 0.183 \ -0.0109 \ 0.0001 \ -0.0357]$

5.3.1 Comparison of Various Methods

The purpose of developing several methods to determine $\hat{G}_n(s)$ and $\hat{\Theta}$ is to provide cross-checks between methods, so that the results can be validated. Instrumental-variable methods are applicable over the entire range of flow coefficients, but they converge less reliably than the transfer function fit method. The sinusoidal excitation and spectral estimation methods are reliable, but provide no parametric estimates (unless combined with the transfer function fit method), and they do not work at all during closed-loop operation. Thus the less speculative methods, although they have limited applicability, provide verification that more sophisticated methods are actually working.

Figure 5.6 is the first such comparison of methods. It shows a first-mode sinusoidal excitation estimate co-plotted with a spectral estimate. Agreement is quite good, indicating that the methods are formulated and applied correctly. It is interesting to note that the sinusoidal excitation estimate is made using rotating wave excitation which directly excites $G_n(s)$, while the spectral estimate uses the formula $G_n(s) = G_r(s) + i \cdot G_i(s)$. Agreement between the estimates suggests that linearity arguments are valid.

Figure 5.7 compares the spectral estimate and the RIV-AML estimate of $G_n(s)$. Both methods use the same data set, and yield approximately the same results. Since the IV method is a time-domain procedure, it does not optimize the frequency response fit explicitly; this sometimes causes discrepancies in the frequency domain between spectral and instrument-variable estimates. Nevertheless, the *parameter estimates* that result from the two methods tend to be close. Results later in this section will verify this statement.

The closed-loop IV methods (TR/RIV-AML and NF/RIV-AML) are designed to operate in a regime where spectral estimates are not available - that is, during

$\frac{\tilde{\Phi}_1(s)}{\tilde{\Upsilon}_1(s)}$, First Mode, $\bar{\phi} = 0.475$, Downstream Hot Wires

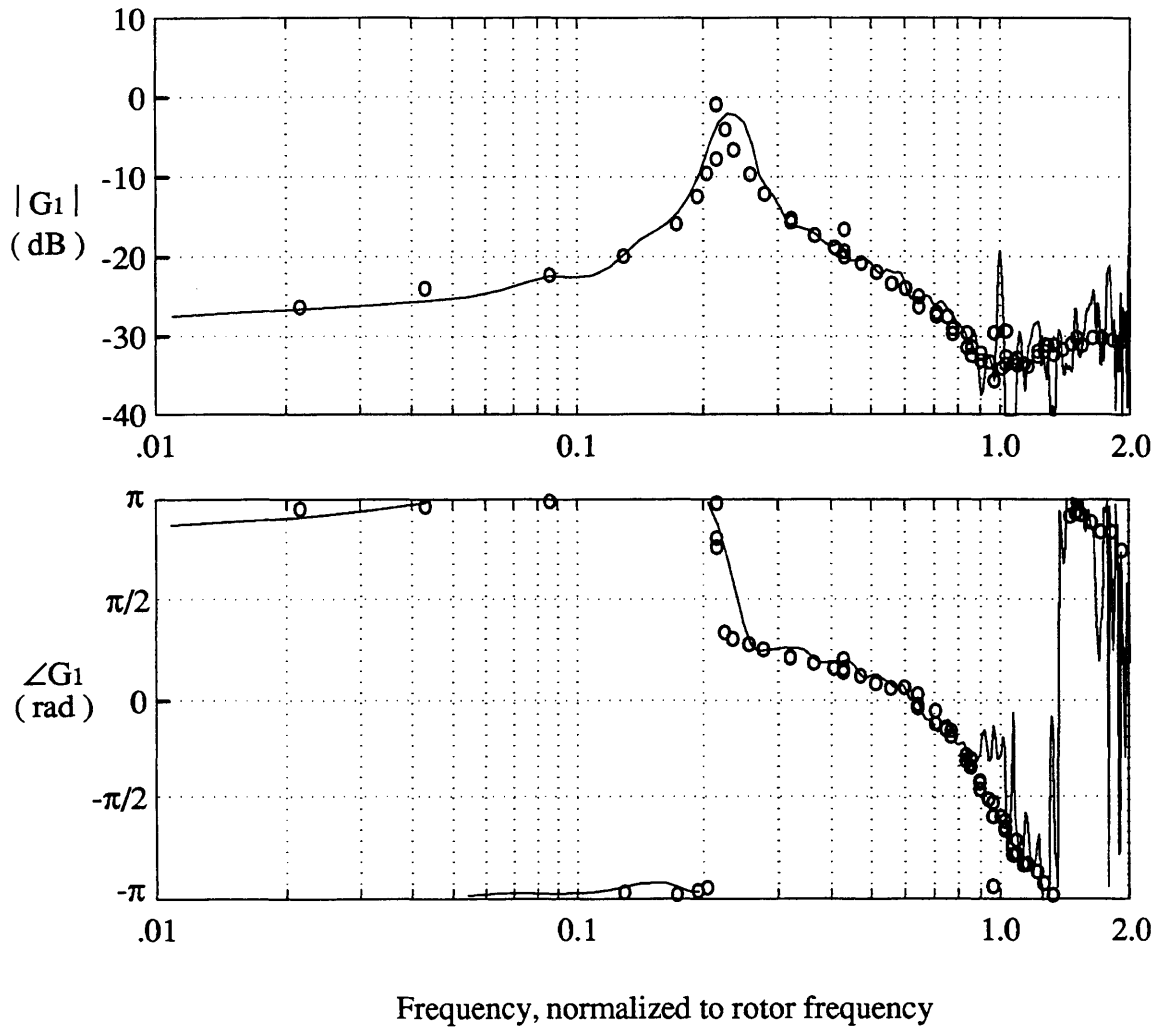


Figure 5.6- Comparison between sinusoidal excitation (open circles) and spectral estimation method (solid line). Transfer function for the first SFC, at $\bar{\phi}=0.475$, hot wires downstream of the IGVs.

$\frac{\tilde{\Phi}_2(s)}{\tilde{\Upsilon}_2(s)}$, 2nd Mode, $\bar{\phi} = 0.420$, Upstream Hot Wires, Intermediate IGVs IN

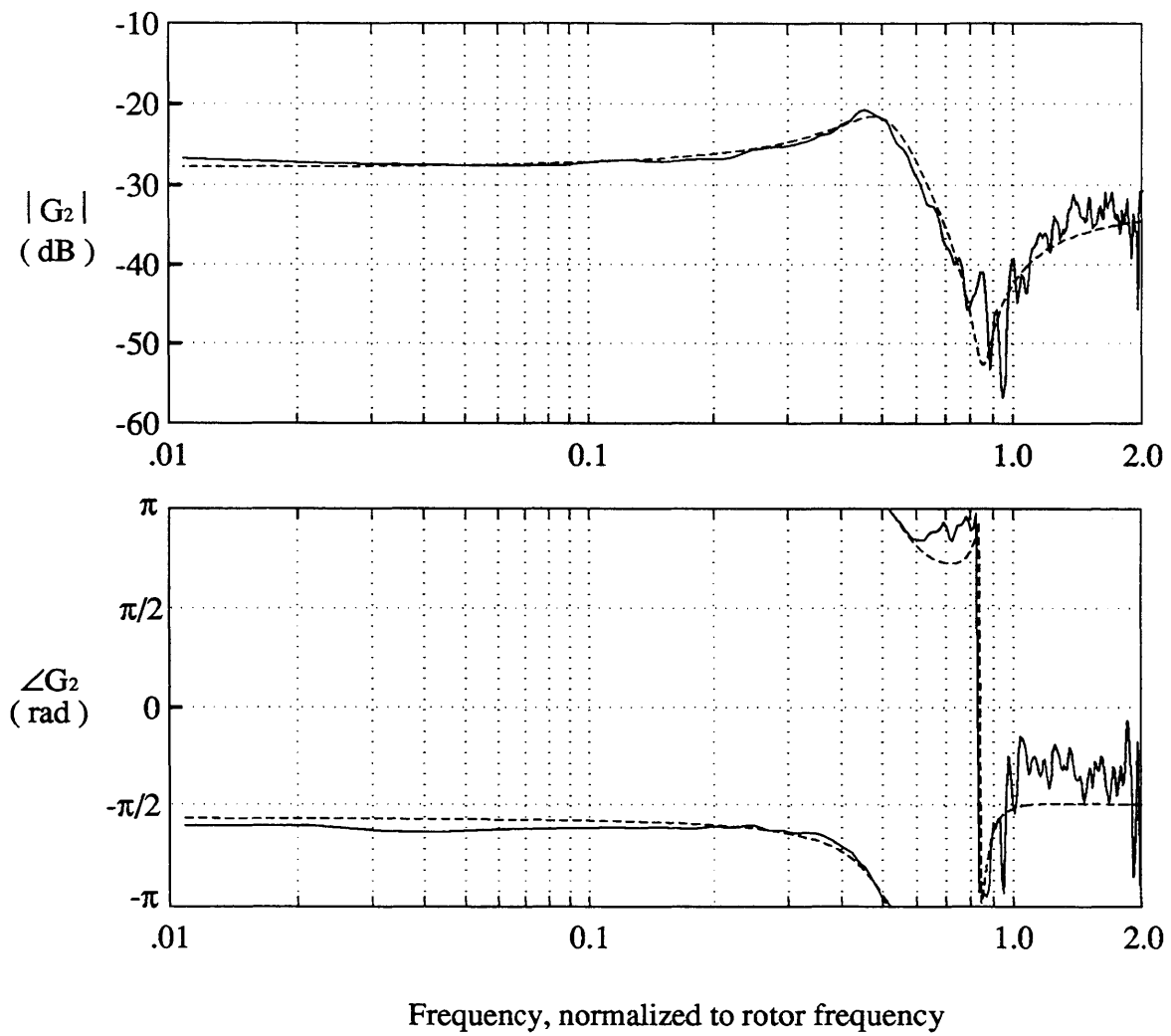


Figure 5.7 - Comparison of spectral (solid line) and RIV-AML (dashed line) estimates. T.F. of second SFC, at $\bar{\phi}=0.475$, upstream hot wires, intermediate IGVs IN (see Section 5.3.3):

$$\Theta_{\text{RIV-AML}} = [-0.107 \quad 0.511 \quad -0.0140 \quad -0.0006 \quad -0.0164]$$

$\frac{\tilde{\Phi}_1(s)}{\tilde{\Upsilon}_1(s)}$, First Mode, $\bar{\phi} = 0.475$, Upstream Hot Wires

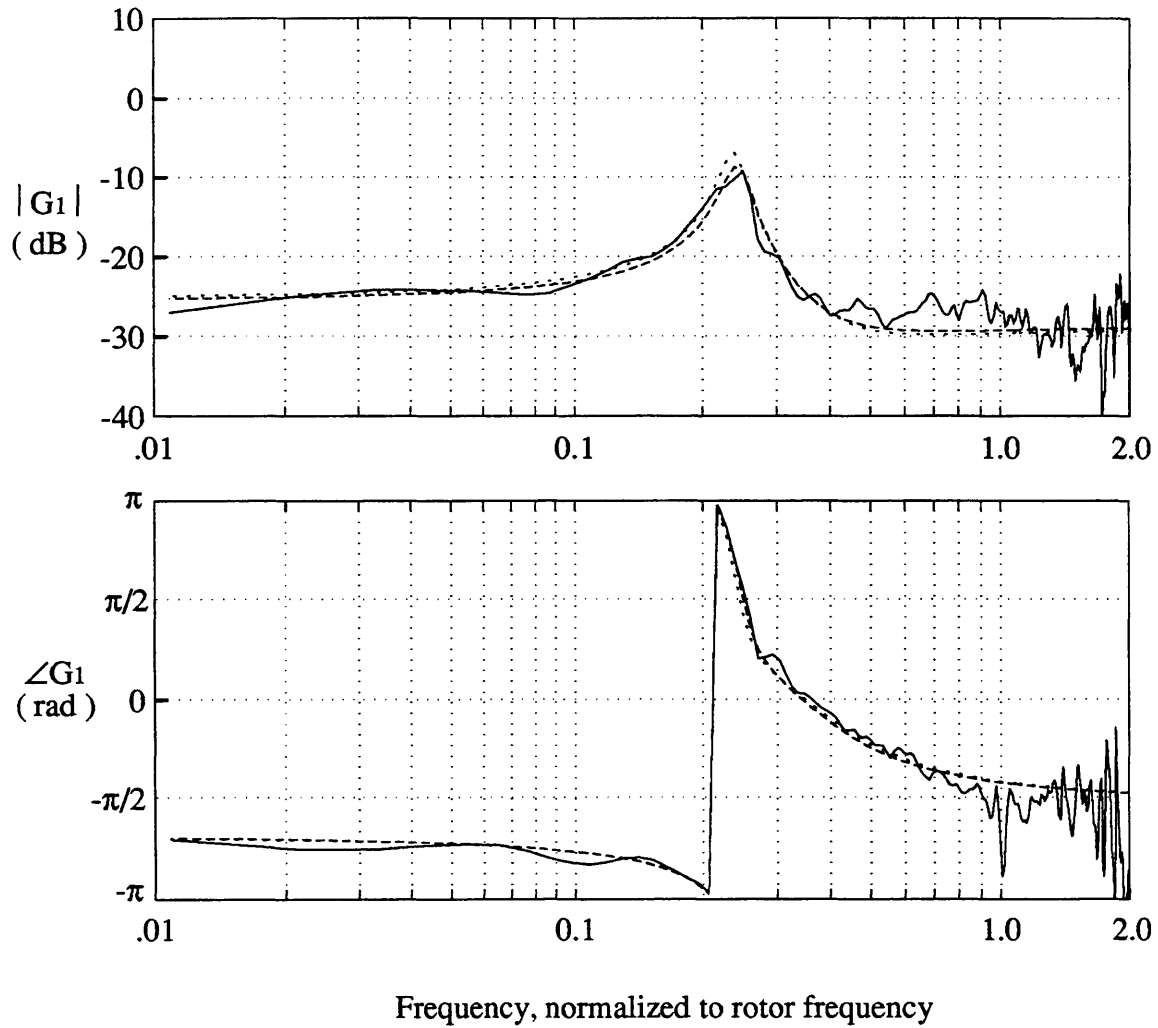


Figure 5.8- Comparison of spectral estimate (solid line), NF/RIV-AML estimate (dashed line) and TR/RIV-AML estimate (dotted line, barely visible because of coincidence with NF estimate). Transfer function for first SFC, at $\bar{\phi} = 0.475$, hot wires upstream of the IGVs.

$$\Theta_{NF} = [-0.0184 \quad 0.242 \quad -0.0114 \quad 0.0063 \quad -0.0367]$$

$$\Theta_{TR} = [-0.0162 \quad 0.237 \quad -0.0114 \quad 0.0066 \quad -0.0356]$$

stabilization of unstable operating points. However, closed-loop data sets can be taken at flow coefficients which are open-loop stable. Such tests can be used to verify that closed-loop IV methods properly account for the loop closure and still provide good estimates. Figure 5.8 shows the results of such a test. A spectral estimate (based on open-loop data) is compared to both a TR/RIV-AML and a NF/RIV-AML estimate (based on closed-loop data). Good agreement between the frequency responses is obtained, and parameter values are comparable.

5.3.2 Results for the Single-Stage Active Control Research Compressor

The parameter set Θ (Equation (5.12)) is a function of mode number n , mean flow coefficient $\bar{\phi}$, and compressor configuration. Estimation of Θ has been conducted for $n=1,2$, and 3 , at flow coefficients from $\bar{\phi}=0.350$ to $\bar{\phi}=0.550$ (to see $\psi(\bar{\phi})$ for this range, refer to Figures 5.16 and 6.1). There were 8 hot wires mounted upstream of the compressor ($\eta_{\text{HW}} = -0.5$) for these tests, and the 0.57" spacer ring was not in.

At each test point $(n, \bar{\phi})$, multiple data sets were taken. The parameters were then estimated from each data set using all of the applicable techniques. Open-loop data was analyzed using the transfer function fit method and the RIV-AML method. Closed-loop data was analyzed using both the NF/RIV-AML method and the TR/RIV-AML method. At some flow coefficients (those near stall but still stable, $\bar{\phi} = 0.475$ and $\bar{\phi} = 0.50$) both open-loop and closed-loop tests were run, to allow the results of all of the methods to be compared.

Three different methods of presentation are used to show the results. First, the parameter estimates are tabulated in Tables 5.1 and 5.2, which appear at the end of this chapter. Second, the parameters are plotted as functions of $\bar{\phi}$ in Figures 5.9 through 5.11. Polynomial curve fits to the data in these plots are also shown. Third, pole-zero loci are given for each mode number n in Figures 5.12 through 5.14. These loci were constructed using the polynomial curve fits from Figures 5.9 through 5.11.

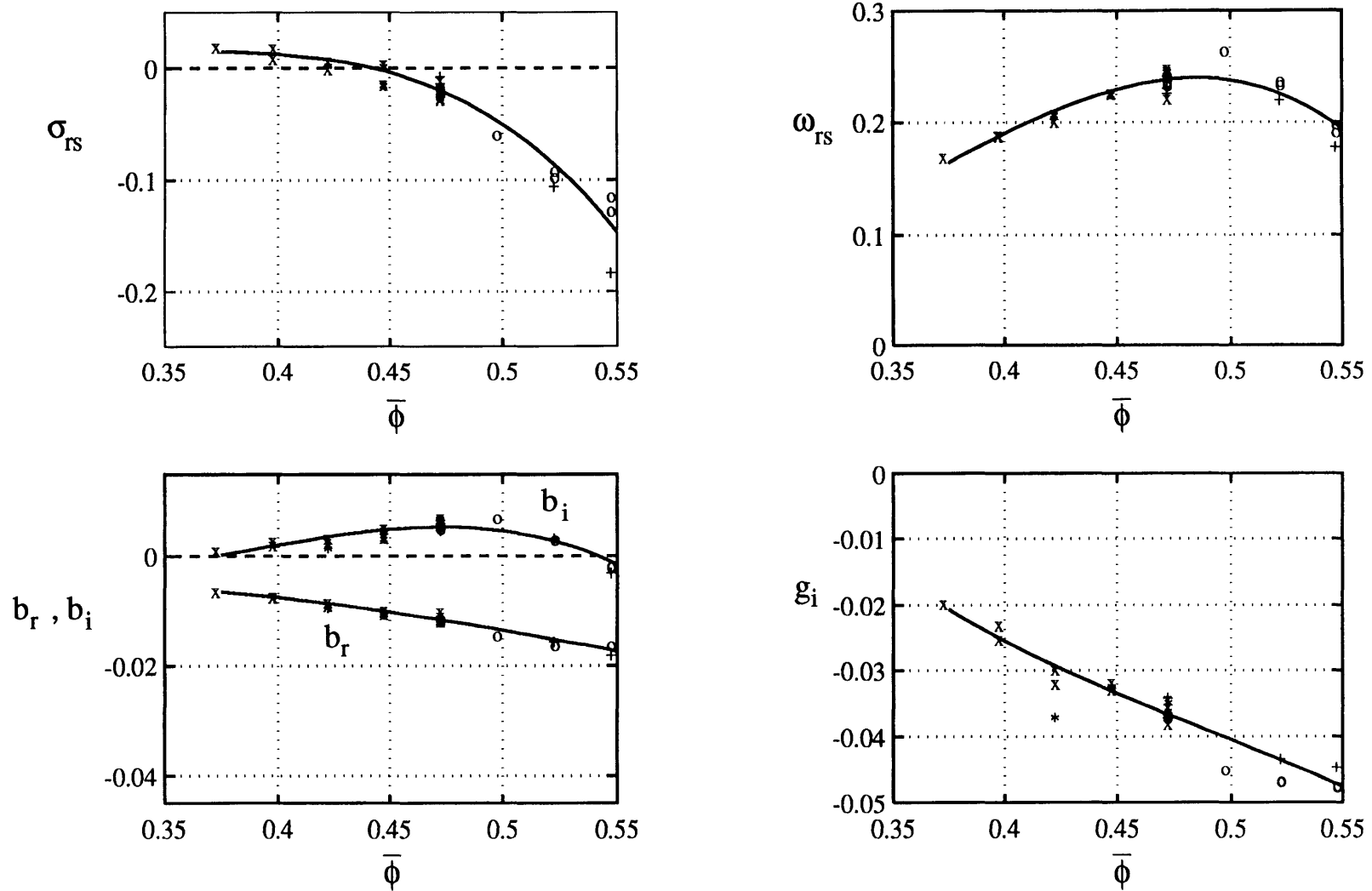


Figure 5.9 - Parameter estimates plotted as functions of flow coefficient - first mode
 Legend: o - spectral estimates, + - RIV-AML estimates
 x - NF/RIV-AML estimates, * - TR/RIV-AML estimates

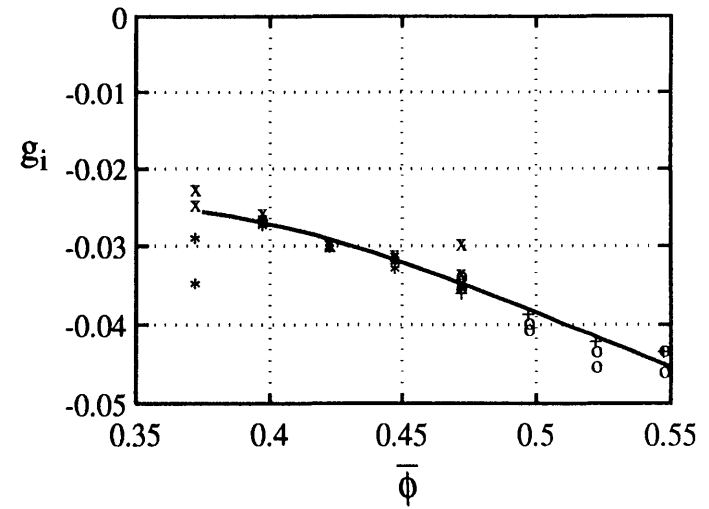
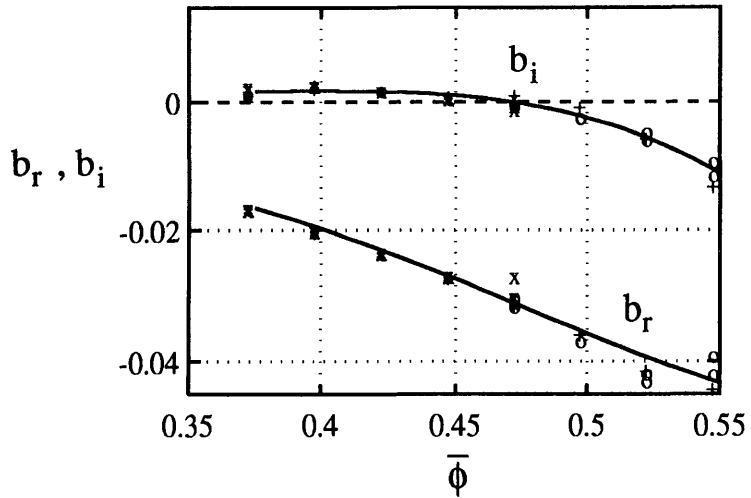
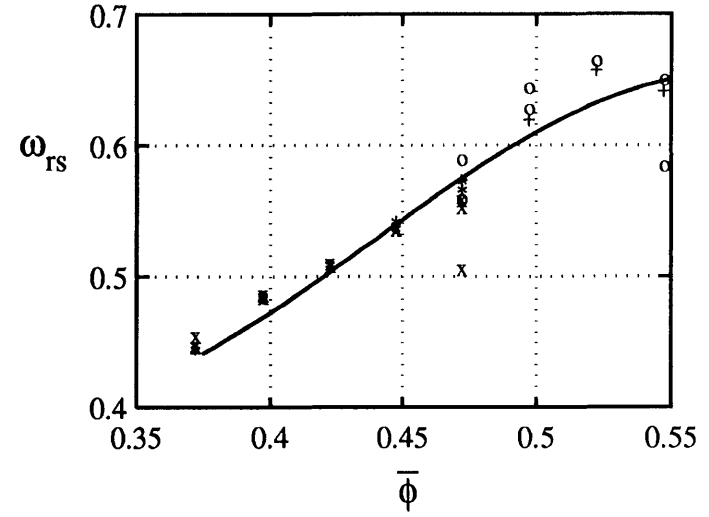
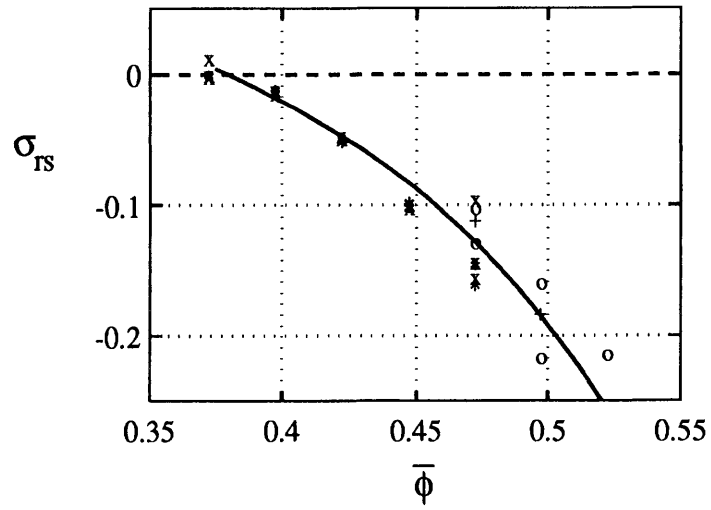


Figure 5.10 - Parameter estimates plotted as functions of flow coefficient - second mode
 Legend: o - spectral estimates, + - RIV-AML estimates
 x - NF/RIV-AML estimates, * - TR/RIV-AML estimates

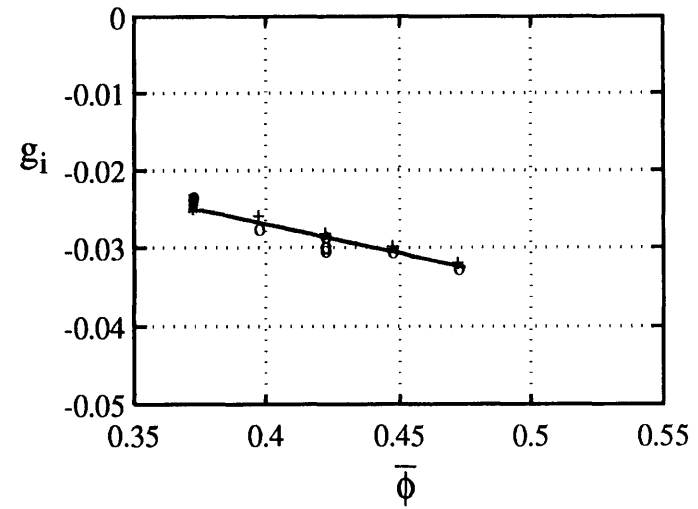
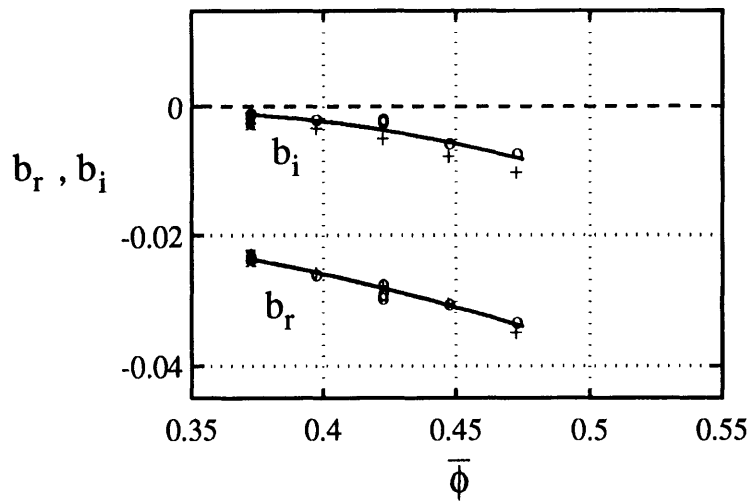
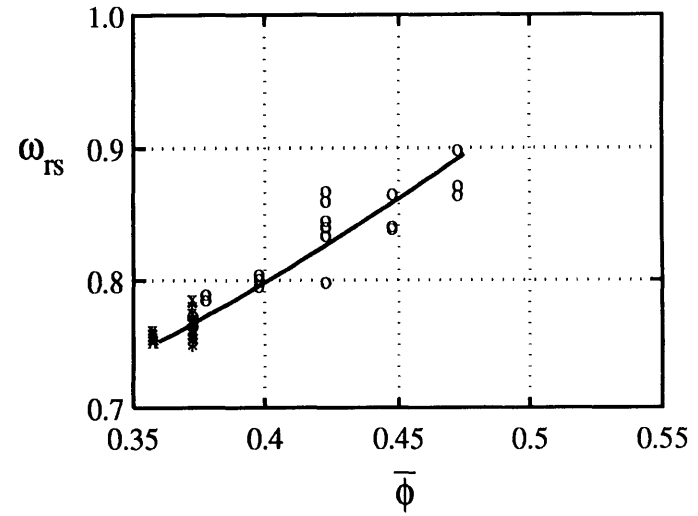
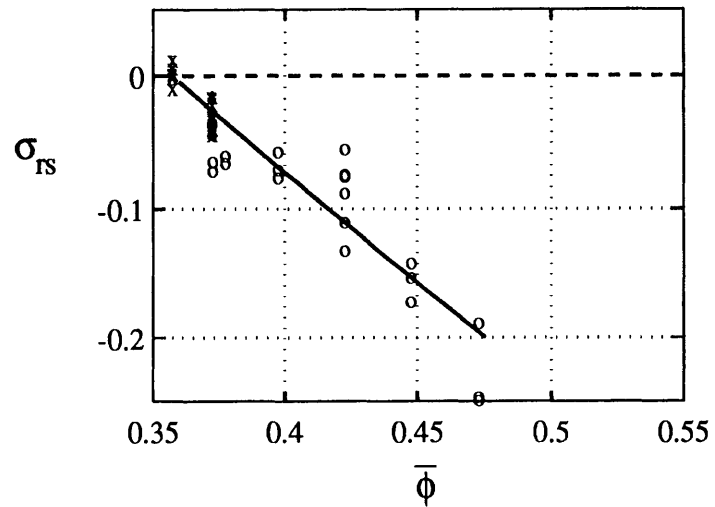


Figure 5.11 - Parameter estimates plotted as functions of flow coefficient - third mode
 Legend: o - spectral estimates, + - RIV-AML estimates
 x - NF/RIV-AML estimates, * - TR/RIV-AML estimates

Pole-Zero Migration for First Mode - Upstream Hot Wires

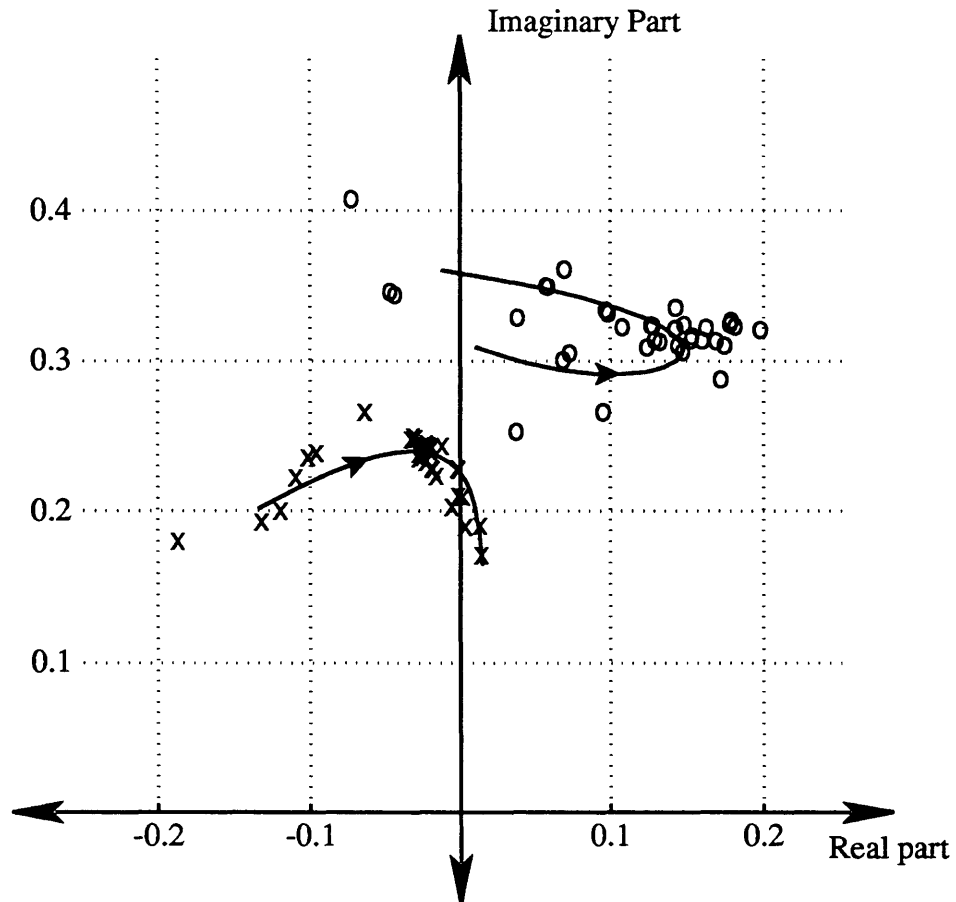


Figure 5.12 - First mode pole (x) and zero (o) migration with flow coefficient. Arrows show direction of decreasing flow coefficient. Transfer function for first mode ($G_1(s)$), hot wires upstream of IGVs.

Pole-Zero Migration for Second Mode - Upstream Hot Wires

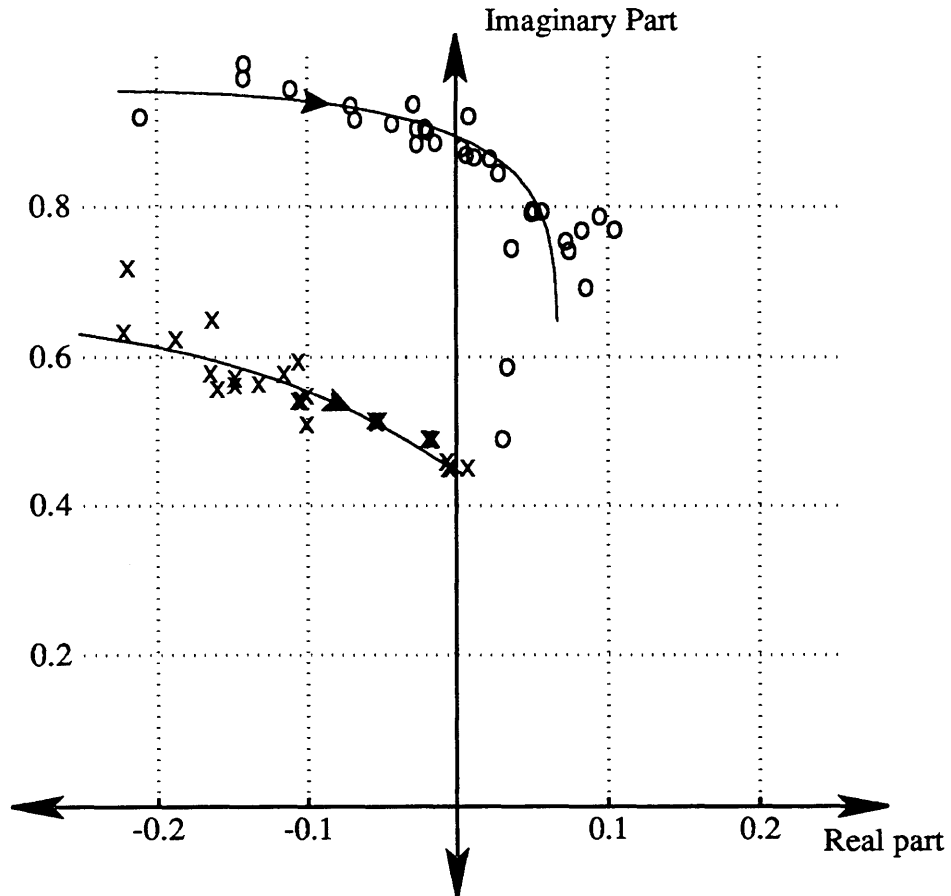


Figure 5.13- Second mode pole (x) and zero (o) migration with flow coefficient. Arrows show direction of decreasing flow coefficient. Transfer function for second mode ($G_2(s)$), hot wires upstream of IGVs.

Pole-Zero Migration for Third Mode - Upstream Hot Wires

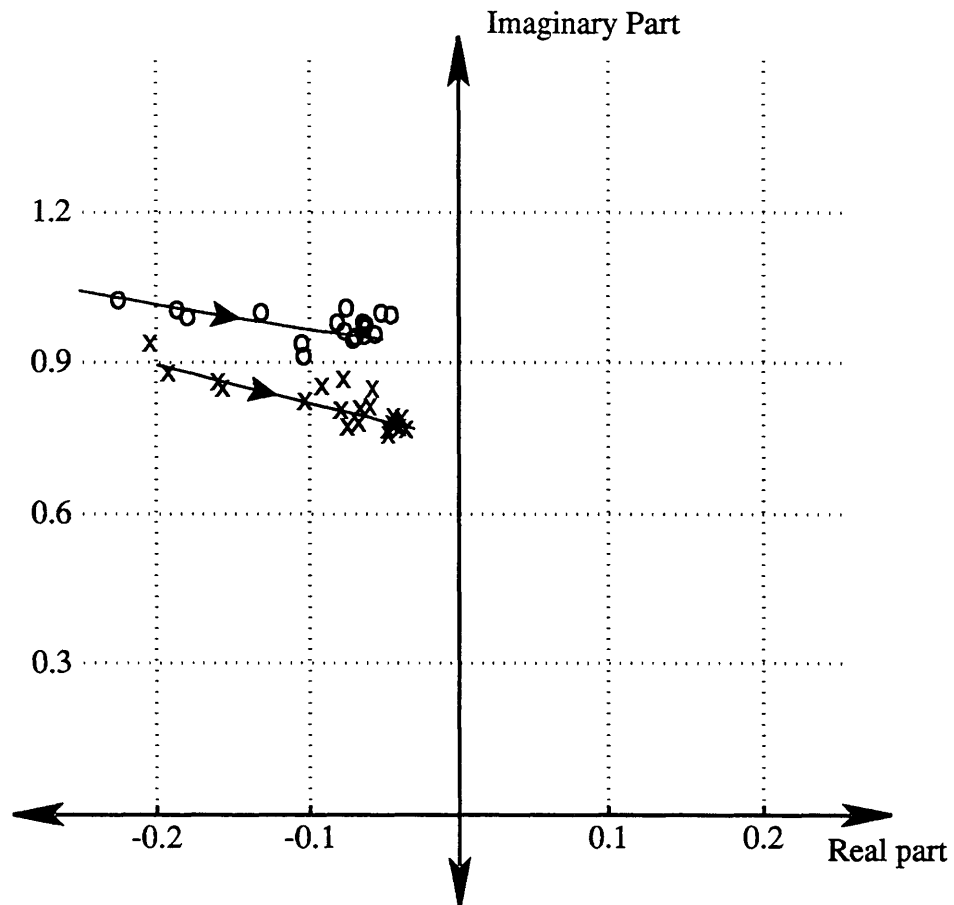


Figure 5.14 - Third mode pole (x) and zero (o) migration with flow coefficient. Arrows show direction of decreasing flow coefficient. Transfer function for third mode ($G_3(s)$), hot wires upstream of IGVs.

The first thing to note about the results is that all of the different parameter estimation methods provide comparable estimates. All the curves are smooth functions of flow coefficient, indicating that closed-loop identification does not bias the results. The good agreement between various methods gives us confidence that the estimates do in fact reflect the input-output behavior of the plant.

The characteristics of the compressor response can now be described in detail. We are primarily interested in the stability of the system, characterized by σ_{rsn} , the rotating stall frequency, characterized by ω_{rsn} , and the response of the system to IGV control, characterized by the magnitude and zero of $G_n(s)$.

Stability characteristics - σ_{rsn}

According to the model in Chapter 3, σ_{rs} should be a function of the overall fluid inertia μ (Equation 3.4), the slope of the compressor characteristic $\frac{\partial\psi}{\partial\phi}$, and the mode number n :

$$\sigma_{rs(n,\bar{\phi})} = \frac{\partial\psi}{\partial\phi} / \left(-\frac{2}{n} + \mu \right). \quad (5.55)$$

This equation says that all of the modes are neutrally stable at $\frac{\partial\psi}{\partial\phi} = 0$, i.e. the peak of the compressor characteristic. It also says that the *rate* at which σ_{rs} changes with $\bar{\phi}$ depends on 3 things:

- 1) The rate at which the compressor slope changes with flow coefficient,
- 2) The amount of inertia in the system (more inertia means stability is less sensitive to slope and mode number),
- 3) The mode number (higher mode numbers are more sensitive to slope and inertia).

Although simply computing σ_{rs} using (5.55) yields poor prediction, some of the *trends* predicted by this equation are born out qualitatively in the data. Discrepancies suggest modifications to the model, some of which are discussed in Appendix A.

The σ_{rsn} curve fits for $n = 1, 2,$ and 3 are shown on the same plot in Figure 5.15, to clarify the trends. To check the trend with $\frac{\partial\psi}{\partial\phi}$ discussed above, we use an estimate of $\frac{\partial\psi}{\partial\phi}$, shown in Figure 5.16 ($\psi(\bar{\phi})$ is also plotted in Figure 5.16 - a more

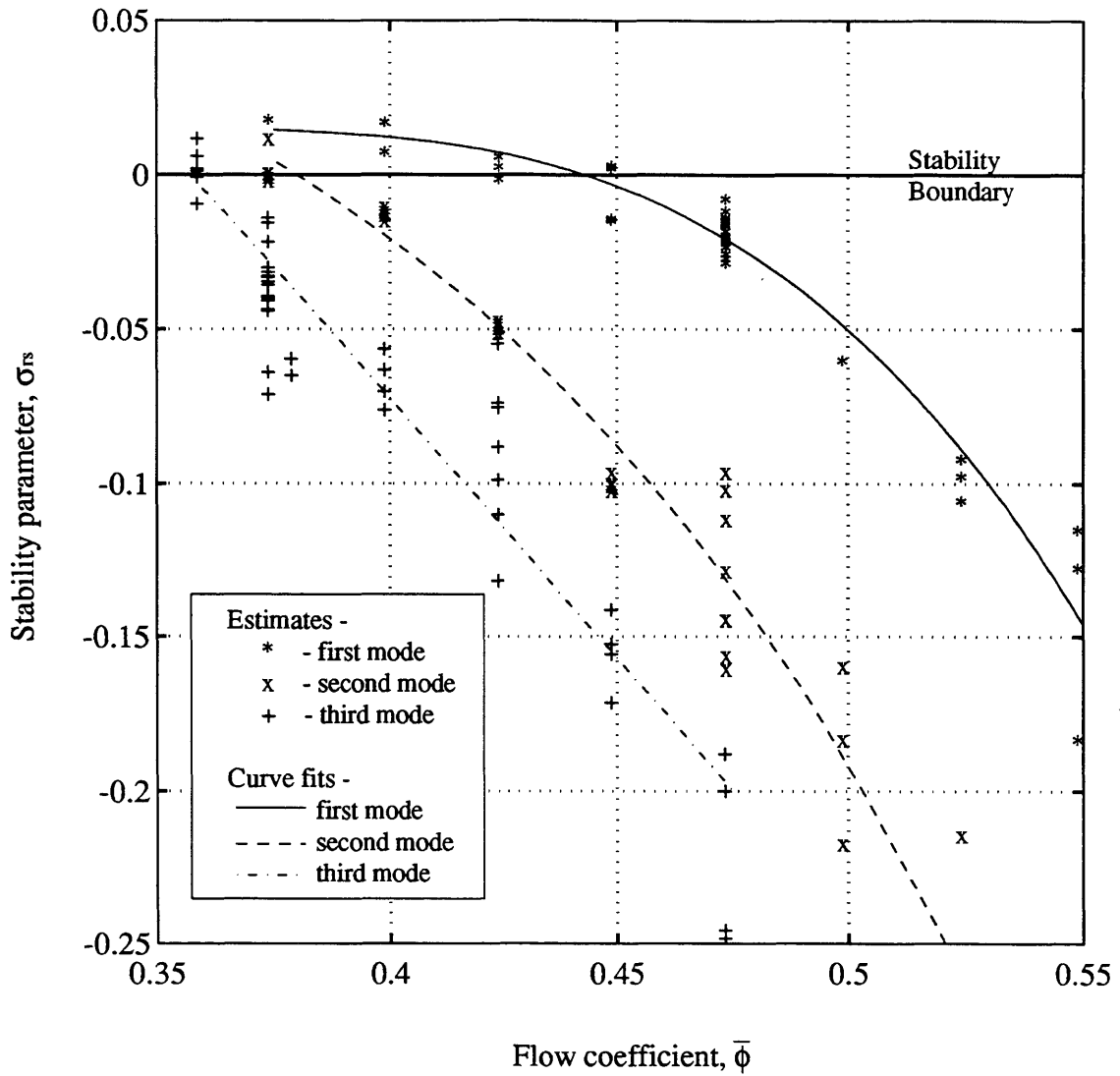


Figure 5.15 - Comparison of stability variation with flow coefficient for the first three modes. Hot wires are upstream of the IGVs.

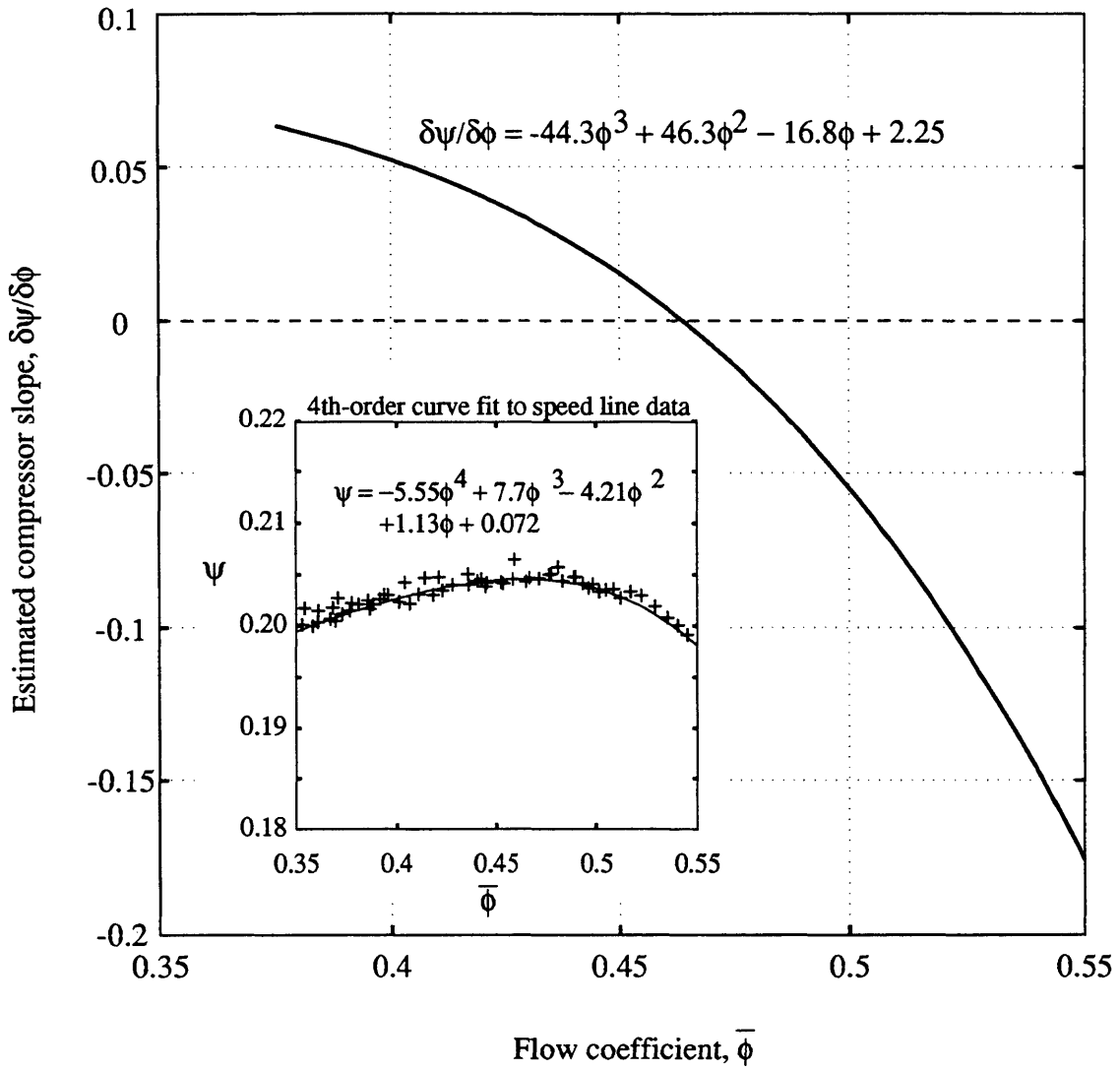


Figure 5.16 - Estimated slope of the compressor characteristic, based on a 4th-order curve fit to the speed line (see Figure 6.1 for more complete speed line information).

complete plot of $\psi(\bar{\phi})$ appears in Figure 6.1). The curves for σ_{rs_n} and $\frac{\partial\psi}{\partial\phi}$ are qualitatively similar - they all tend from negative to positive as flow coefficient is reduced (throttle closure). The curvature of the plots is also similar. However, the σ_{rs_n} curves go through zero at lower values of $\bar{\phi}$ than the $\frac{\partial\psi}{\partial\phi}$ curve. We interpret this as a downward shift of the σ_{rs_n} curves from their predicted positions - that is, at a given $\bar{\phi}$, each mode is more stable than one would predict based on (5.55). As mode number increases, the downward (stable) shift also increases; higher modes are consistently more stable than lower modes.

Higher stability of higher modes is a fortuitous circumstance, because it means that by stabilizing only the first few modes, the flow coefficient at which the system stalls can be reduced. The results of Chapter 6 verify this claim. The higher stability of higher modes is attributed to the effect of unsteadiness on the losses [37,38] (see Appendix A). Taking into account unsteadiness results in changing the "effective $\frac{\partial\psi}{\partial\phi}$ " seen by each individual mode. This effective slope argument will also appear in our discussion of the IGV response.

Although the higher modes are more stable in Figure 5.15, they proceed from stable to unstable more quickly as $\bar{\phi}$ is reduced. This trend agrees with the appearance of $\frac{2}{n}$ in the denominator of (5.55) - as mode number increases, sensitivity to compressor slope also increases. The effect of this trend is to reduce the difference in stability between modes as flow coefficient is reduced. By $\bar{\phi} = 0.375$, the difference in stability is quite small.

We have described two competing trends. The first trend, probably due to the effect of unsteadiness on losses, is that higher modes tend to be more stable than lower modes. This is a desirable trend, because we would like to actuate as few modes as possible to stabilize the system. The second trend, which agrees with linearized fluid mechanics predictions, is that the higher modes are more sensitive to compressor slope than lower modes. Thus, as compressor slope becomes more

positive, the higher modes tend towards instability faster than the lower modes. This is an undesirable trend, because it tends to nullify the advantages of the first trend and make higher modes less stable than lower modes.

Higher modes tax both the spatial and temporal bandwidth of the control scheme. A given control mechanization will have a mode number above which it cannot operate. Thus the balance between the two competing trends described above could define the limit to control for a given combination of compressor, sensors, and actuators.

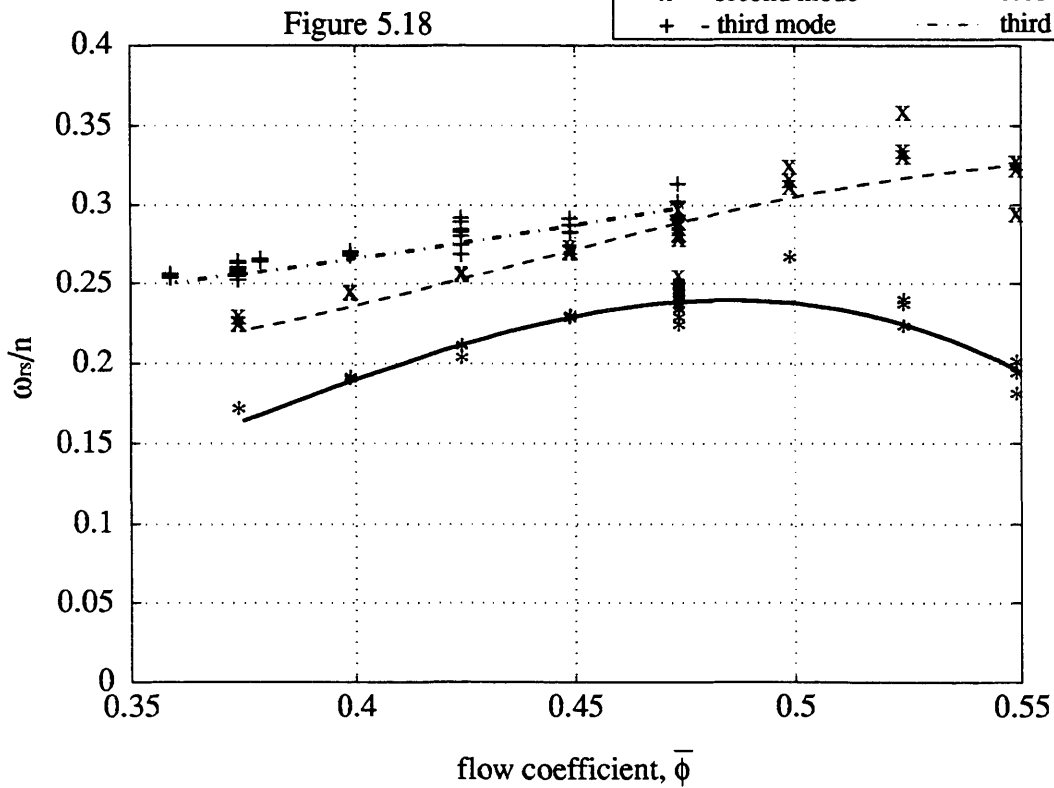
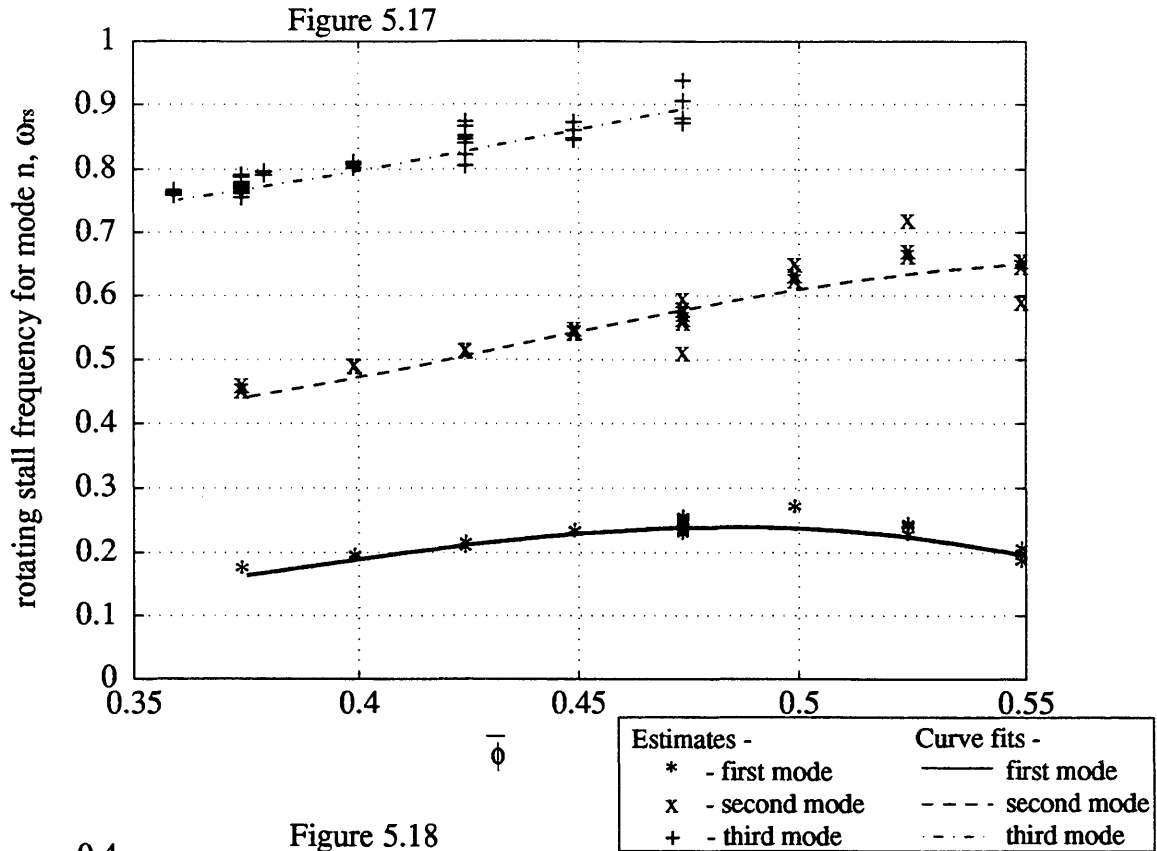
Rotating Stall Frequency - ω_{rs_n}

According to the model in Chapter 3, ω_{rs} should be a function of the fluid inertias λ and μ (Equation 3.1 and 3.4) and the mode number n :

$$\omega_{rs}(n) = n \cdot \lambda / \left(\frac{2}{n} + \mu \right). \quad (5.56)$$

As with the stability parameter σ_{rs} , direct prediction using this equation does not yield good estimates. For instance this equation admits no variation in the rotating stall frequency with flow coefficient. Figure 5.17, which plots ω_{rs_n} for the first three modes, shows a fairly strong dependence on $\bar{\phi}$, indicating that the model needs modification.

The primary trend with mode number n is due to the fact that higher modes have more 'lobes', so that passage of a full cycle past a stationary point is n times as fast for the n th mode. Thus if all modes travel at the same 'group velocity' Ω , the apparent rotating stall frequency of the n th mode (ω_{rs_n}) is $n\Omega$. To check the deviation from this trend, ω_{rs_n}/n is plotted in Figure 5.18. This plot allows us to check the weaker trend with n which appears in the denominator of Equation (5.56): according to this term, lower modes should travel at a slightly slower group velocities than higher modes. This weak trend with mode number does show up in the data.



Figures 5.17 and 5.18- Comparison of rotating stall frequency variation with flow coefficient for the first three modes. 5.17 shows ω_{rs} , and fig 5.18 shows ω_{rs}/n .

IGV response

Two characteristics of the IGV response are of primary concern. First, we are interested in the overall effectiveness or 'control power' that is available for stabilization; this can be characterized by the steady-state gain of the transfer function $G_n(s)$. Second, behavior of the zero of $G_n(s)$ is important; this depends on the relative magnitudes of b_r , b_i , and g_i . The accuracy of predictions is again poor; clearly more research is needed in this area. Here we will present and comment on the experimental results, comparing them to predicted trends only when such trends are obvious. It is hoped that this data will aid in future refinement of predictive capability.

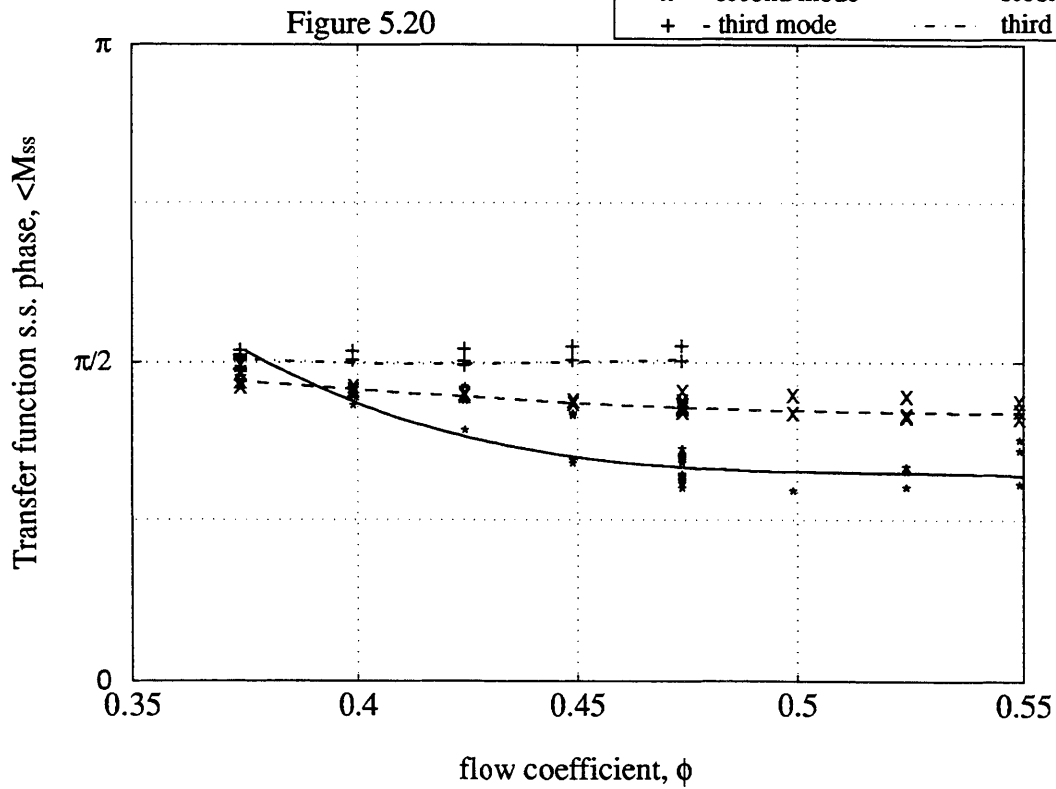
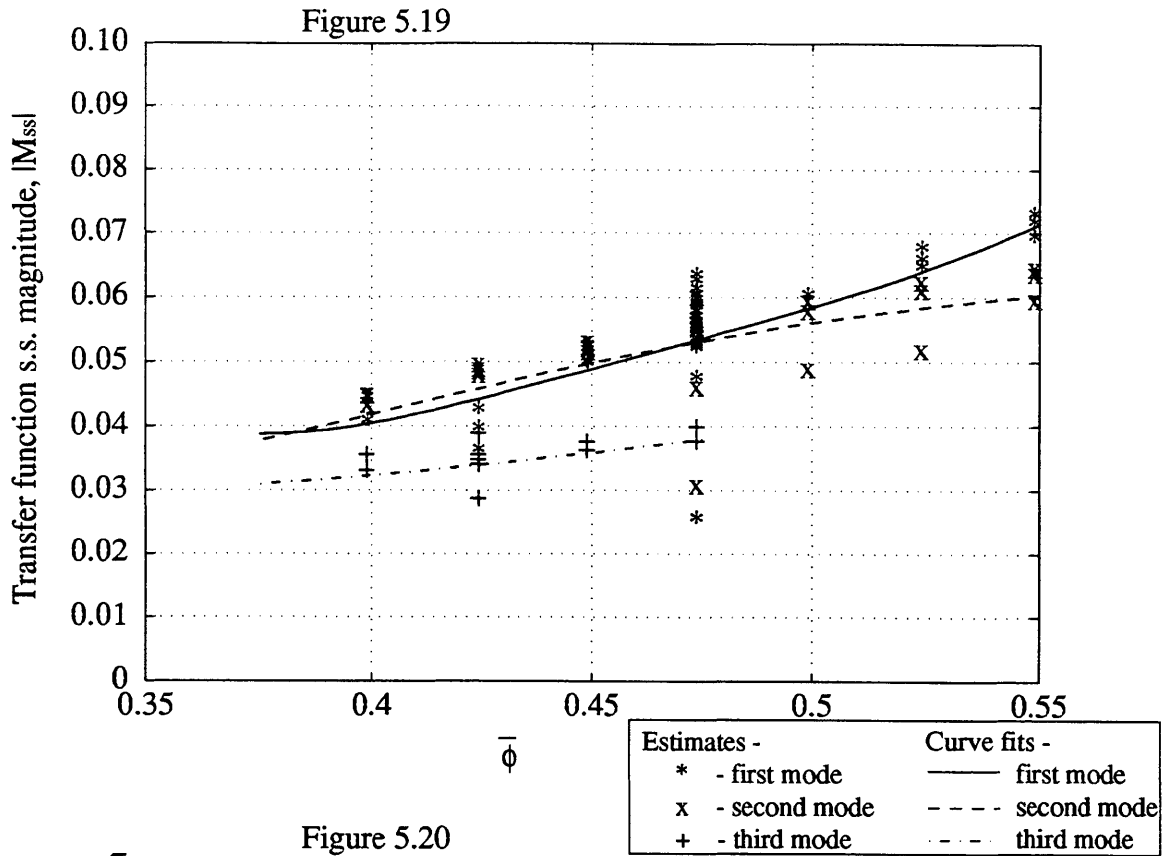
The steady-state magnitude of $G_n(s)$ is computed by letting $s \rightarrow 0$ in (3.48):

$$M_{ssn} = \left. \frac{b_r + jb_i}{\sigma_{rs} + j\omega_{rs}} \right|_n. \quad (5.57)$$

Figure 5.19 plots the magnitude of M_{ssn} for the first three modes as functions of $\bar{\phi}$. It can be seen from this plot that control effectiveness is steadily declining as the flow coefficient is reduced. Control power is similar for the first and second modes, but reduced by about 25% for the third mode.

Figure 5.20 shows the phase of M_{ssn} for the first three modes as a function of $\bar{\phi}$. These curves indicate the phase shift (at steady state) between the input wave on the IGVs and the output wave of axial velocity. A strong variation of $\angle M_{ssn}$ with mode number is observed - each mode is shifted by a different amount. The net effect is that a wave shape (of arbitrary modal content) introduced at the IGVs will not produce the same wave shape in axial velocity. One must take this behavior into account when designing control laws.

To characterize the actuator effectiveness during transients, the zero of the transfer function $G_n(s)$ must also be studied. Figures 5.12 through 5.14 show how the zeros change with flow coefficient. The zeros of all three transfer functions go from



Figures 5.19 and 5.20- Magnitude and phase of the steady-state gain, M_{ss} , for the first three modes.

minimum phase (negative real part) to non-minimum phase (positive real part) as flow coefficient is reduced. Since the closed-loop poles of the controlled system will approach the open-loop zeros as the feedback gain is increased, non-minimum phase (NMP) zeros are undesirable - they tend to make the system either go unstable or remain unstable under feedback. Thus the problem of stabilization becomes more difficult as flow coefficient is reduced, not only because the system is going unstable (as characterized by the poles), but also because the actuator effectiveness is becoming NMP (as characterized by the zeros).

The real part of the zero of $G_n(s)$ determines whether or not the system is NMP. Chapter 3 results ((3.43), (3.44), and (3.48)) can be manipulated to yield the following prediction:

$$\sigma_p = \frac{\frac{\partial \psi}{\partial \phi}}{\left[\frac{1}{n} + \mu_c + \frac{\mu_{IGV}}{2} \right]} \quad (5.58)$$

Where we have introduced the notation σ_p to indicate the similarity to σ_{rs} . Both σ 's represent the real part of a complex number, and both indicate that $G_n(s)$ has undesirable properties when they are positive ($\sigma_{rs} > 0 \Rightarrow$ unstable, $\sigma_p > 0 \Rightarrow$ non-minimum phase). Since the denominator of (5.58) is always positive, the sign of σ_p is tied to exactly the same condition as the sign of σ_{rs} - namely, the slope of the characteristic, $\frac{\partial \psi}{\partial \phi}$.

If we plot σ_p of the data for $n = 1, 2,$ and 3 (Figure 5.21), we see that indeed the curves are very similar to the curves in Figure 5.15 for σ_{rs} . The curves tend from minimum phase to non-minimum phase as $\bar{\phi}$ is reduced, and higher modes tend to be more negative than lower modes. Also, the curvature and slope of the σ_p curves show the same trends with mode number as the curves for σ_{rs} .

Major differences do exist between the σ_p curves and the σ_{rs} curves. Nevertheless, it seems clear that the slope $\frac{\partial \psi}{\partial \phi}$ affects the sign of both σ_p and σ_{rs} ,

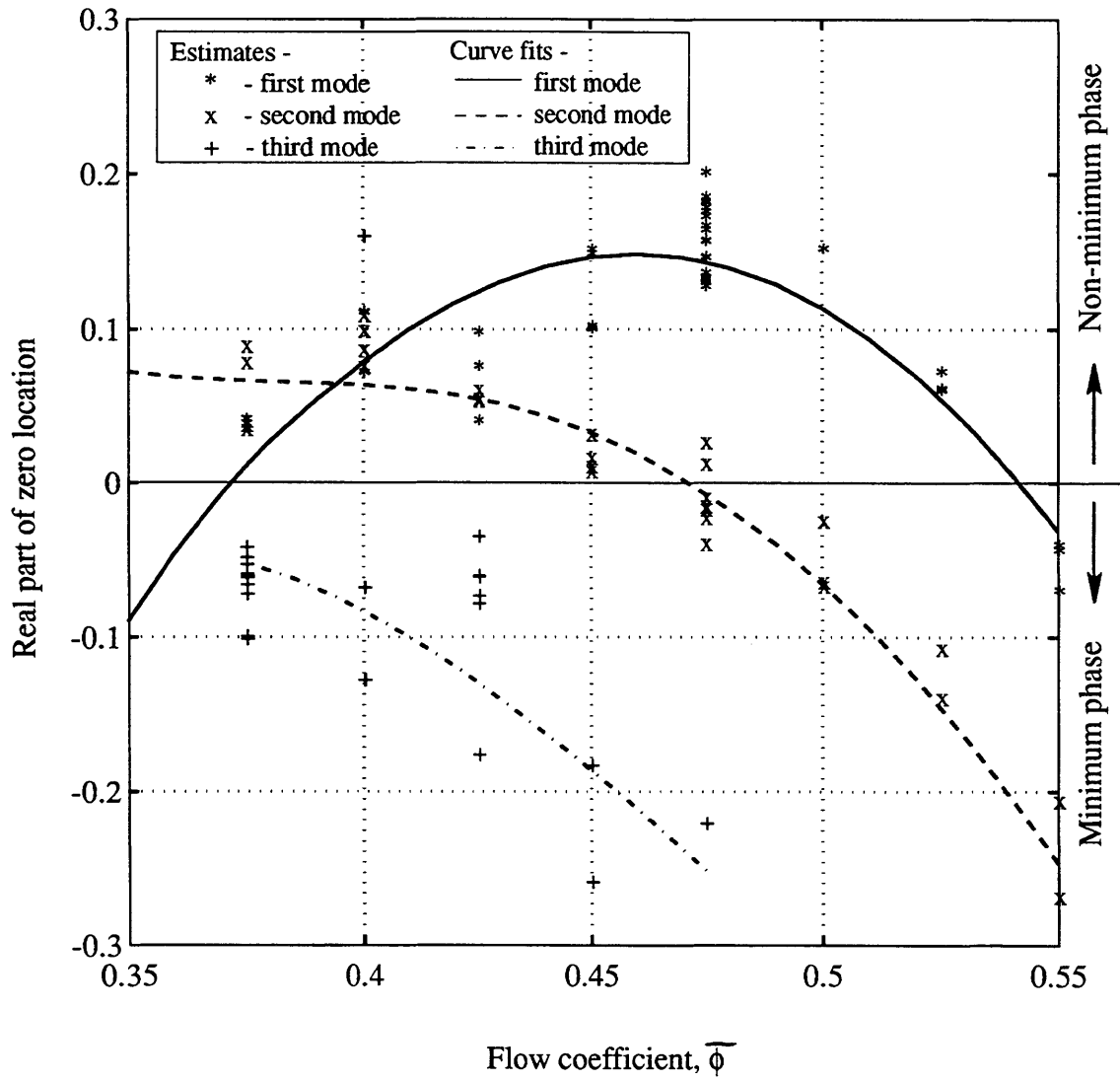


Figure 5.21 - Variation of the real part of the zero with flow coefficient, for the first three modes.

which means that the transfer function $G_n(s)$ tends to become more NMP as it become less stable. The effect of a NMP zero on our ability to stabilize the system depends strongly on the frequency of the zero, i.e. its imaginary part. If the zero frequency is sufficiently high, it will not alter the stabilization problem substantially. Unfortunately, Figures 5.12-5.14 show that the zero frequencies are relatively close to the pole frequencies. Therefore, they must be taken into account in any feedback analysis. Section 6.2.2 further discusses the effect of NMP zeros.

5.3.3 Configuration Studies

This section describes briefly the measured effects of three separate changes to the configuration. The technique is to change the configuration in a single way, and then do identification experiments like those described in the previous sections. Transfer functions or parameters are then compared to those for the configuration discussed in Section 5.3.2.

Spacer Ring

A spacer ring can be placed between the IGVs and the rotor, increasing the gap between these two blade rows. The experimentally determined effect of this extra gap on $G_n(s)$ can be seen in Figures 5.22 and 5.23, where the parameter estimates for the first and second modes are plotted as functions of $\bar{\phi}$. Curve fits are shown, as well as the curve-fits for the no-spacer ring results presented in Section 5.3.2. Comparing the results with the spacer ring in and out shows several effects. The stability of the system at a given $\bar{\phi}$ is reduced by increased gap, while the rotating stall frequency is slightly decreased. The parameters b_r and b_i are not affected very strongly, but g_i is reduced. This indicates that the steady-state response behavior is not strongly affected, but the transient behavior is attenuated 10 to 20 percent. The trends with flow coefficient are similar with or without the spacer ring.

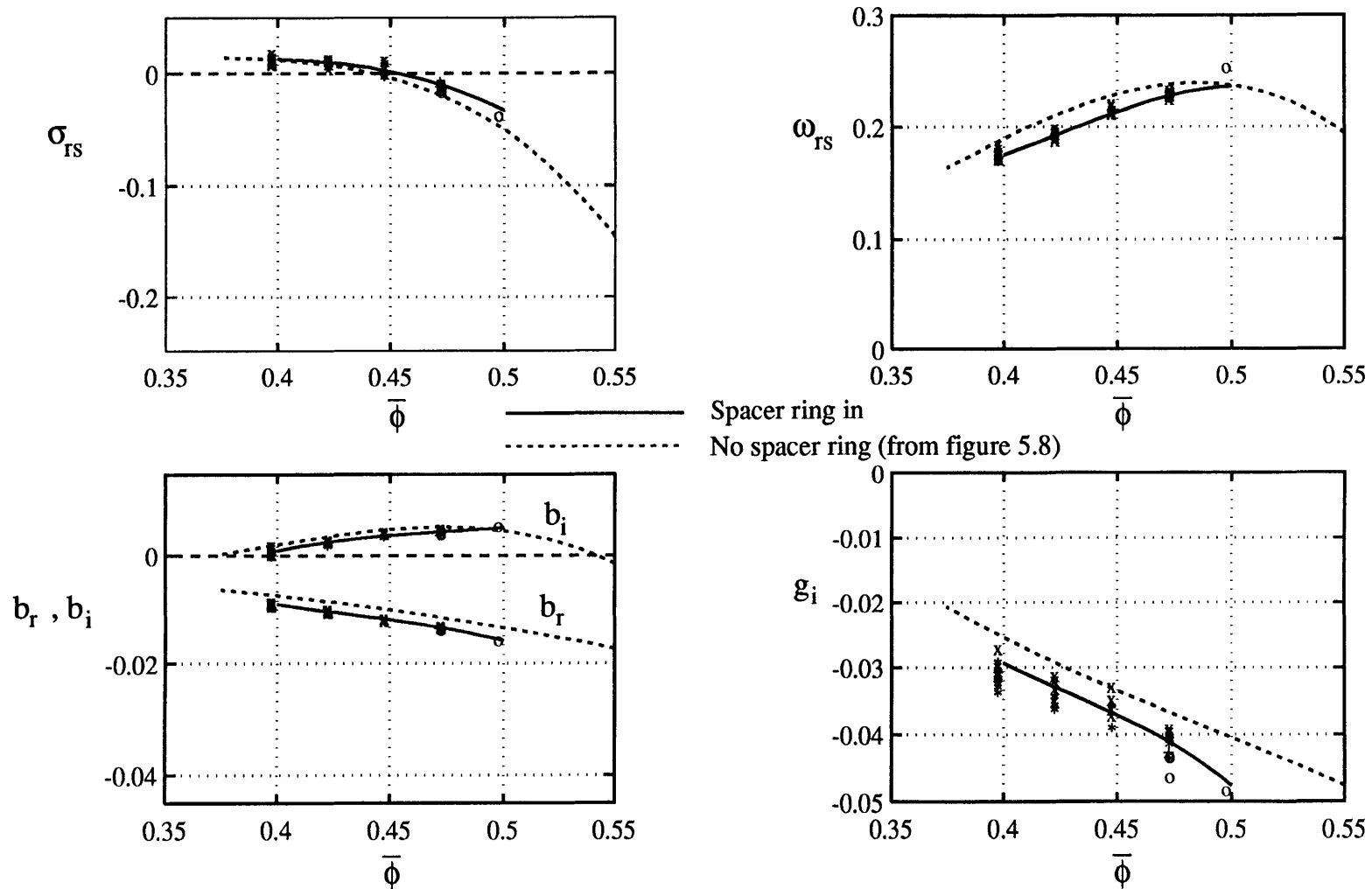


Figure 5.22 - Parameter estimates plotted as functions of flow coefficient - first mode, spacer ring in (compare to no spacer ring data, (Figure 5.9))

Legend: o - spectral estimates, + - RIV-AML estimates

x - NF/RIV-AML estimates, * - TR/RIV-AML estimates

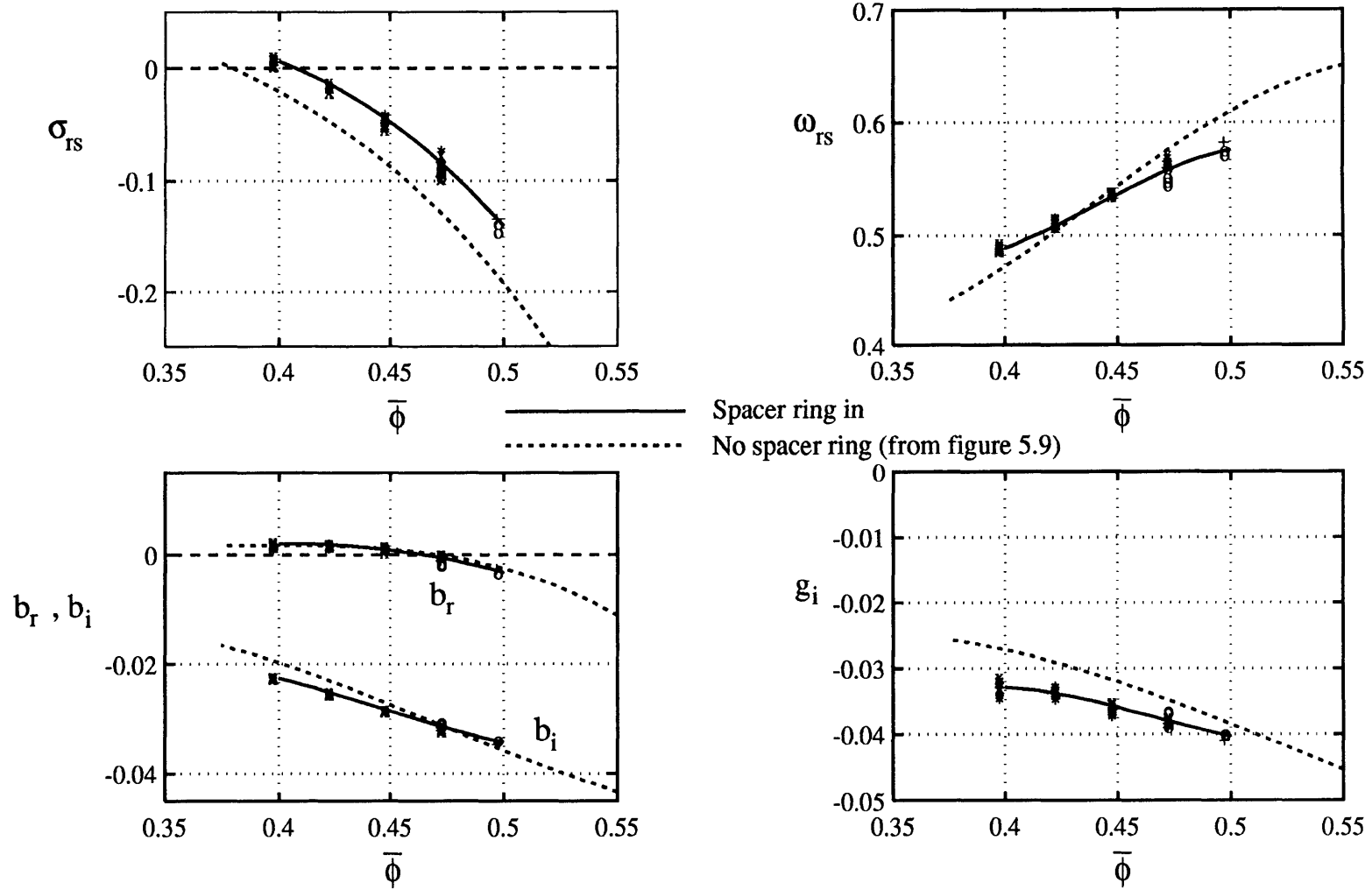


Figure 5.23 - Parameter estimates plotted as functions of flow coefficient - second mode, spacer ring in (compare to no spacer ring data, (Figure 5.10))

Legend: o - spectral estimates, + - RIV-AML estimates

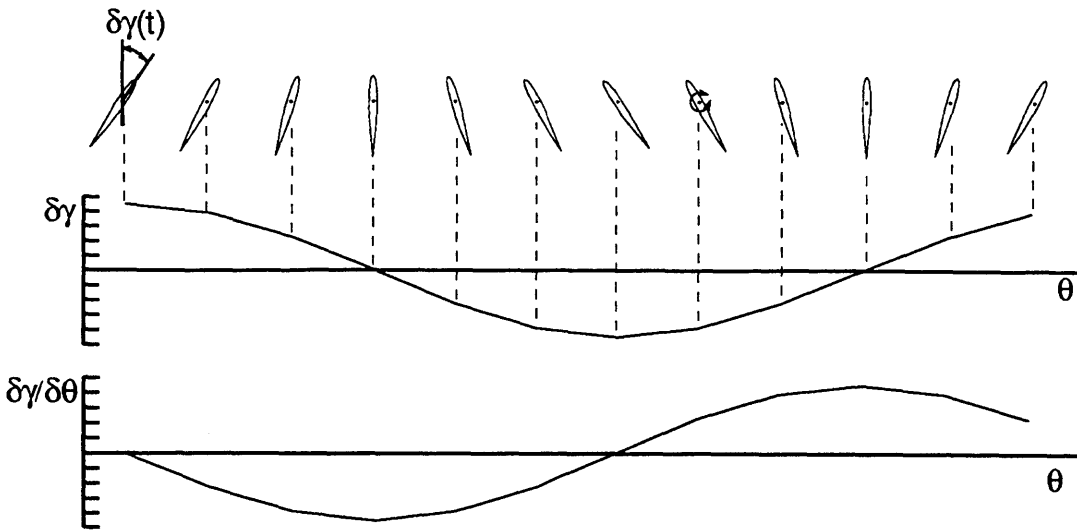
x - NF/RIV-AML estimates, * - TR/RIV-AML estimates

Intermediate IGVs

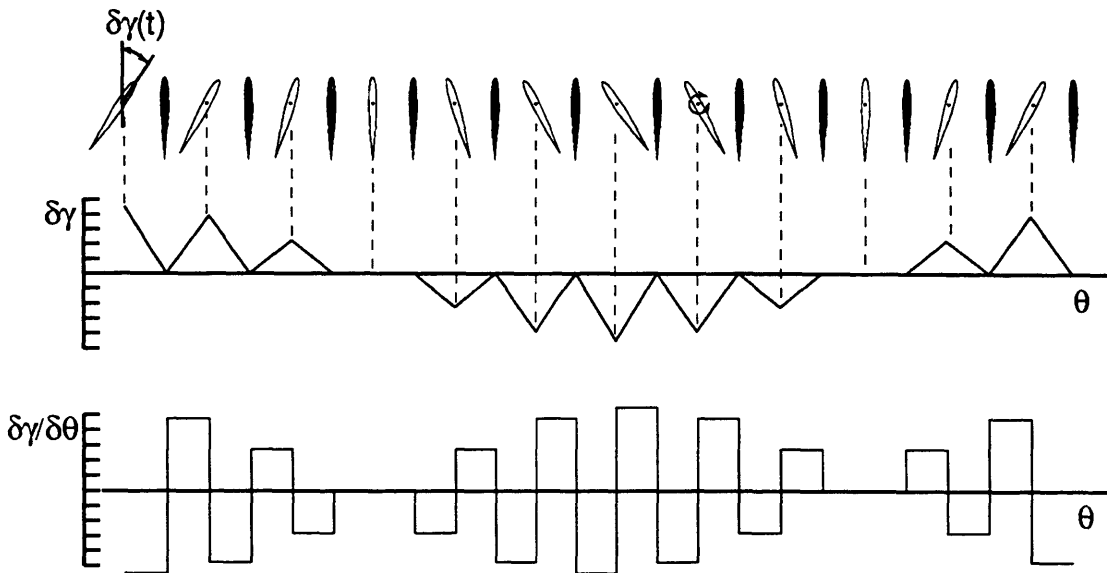
In Chapter 3, the coefficient g_i is derived by looking at the unsteady affect of non-axisymmetric IGV turning. The idea is that, when the IGVs are not turned by the same angle, adjacent passages have different area ratios (see Section 3.2.4 and Figure 3.2). The effect was seen to be proportional to $\frac{\partial(\delta\gamma)}{\partial\theta}$, which indicates the degree of difference between area ratios in adjacent passages. Thus an n^{th} mode turning in the IGVs $\delta\gamma(\theta)=\cos(n\theta)$ has an effect on the n^{th} mode of $\delta\phi$ proportional to $-n \cdot \sin(n\theta)$. But, if an intermediate *stationary blade* is placed between each pair of moving blades, the effect is completely removed. Instead of the n^{th} mode in $\delta\gamma$ affecting the n^{th} mode in $\delta\phi$, it affects the 12^{th} and higher modes. Figure 5.24 illustrates how intermediate IGVs make $\frac{\partial(\delta\gamma)}{\partial\theta}$ effectively zero for a given mode number n . In this case, then, $g_i=0$ according to the model.

If g_i can in fact be made zero, the transfer function $G_n(s)$ will be changed dramatically. Because g_i is the coefficient of s in the numerator of $G_n(s)$ (Equation 3.48), $g_i=0$ implies that there is no zero in the transfer function. Thus the magnitude response $|G_n(j\omega)|$ should 'roll off' at high frequencies, becoming very small rather than reaching a constant magnitude. The phase response should also show the effect of removing the zero: $\angle G_n(j\omega)$ should change by at most π over the entire frequency range of the test, rather than the 2π phase change shown in, for example, Figure 5.1.

To test these hypotheses, spectral estimates of $G_n(s)$ for $n=1$ and 2 were made at $\bar{\phi}=.475$ and $\bar{\phi}=.50$, with stationary intermediate IGVs. The estimates are plotted in Figures 5.25 through 5.28, along with estimates of the transfer functions without intermediate IGVs (based on the results of Section 5.3.2). It is clear from these plots that the transfer function shapes are not affected in the way anticipated. The zero of $G_n(s)$ in all cases is not significantly altered by the introduction of intermediate IGVs. The only noticeable effects are a slight attenuation of the magnitude plot, and a slight reduction in the rotating stall frequency (ω_{rs}).



a) no intermediate IGVs; $\delta\gamma = \cos(\theta) \Rightarrow \delta\gamma/\delta\theta = -\sin(\theta)$



b) intermediate IGVs; first mode in $\delta\gamma \neq$ first mode in $\delta\gamma/\delta\theta$

Figure 5.24 - Effect of intermediate IGVs on $\delta\gamma/\delta\theta$

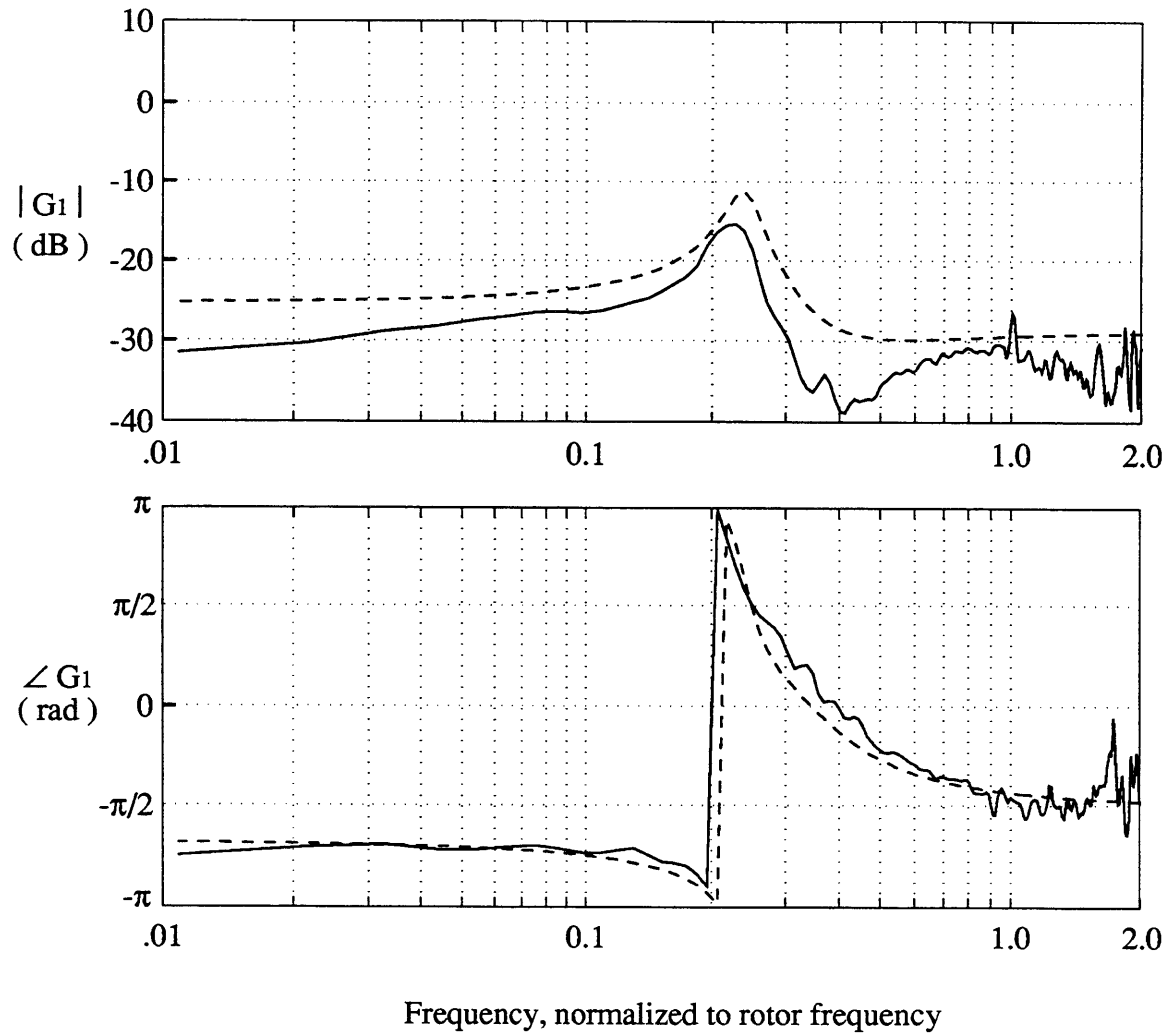


Figure 5.25 Effect of intermediate stationary IGVs on the first mode transfer function at $\bar{\phi}=0.475$. Dotted line shows transfer function without intermediate IGVs, solid line shows transfer function with intermediate IGVs. Hot wires are upstream of the IGVs.

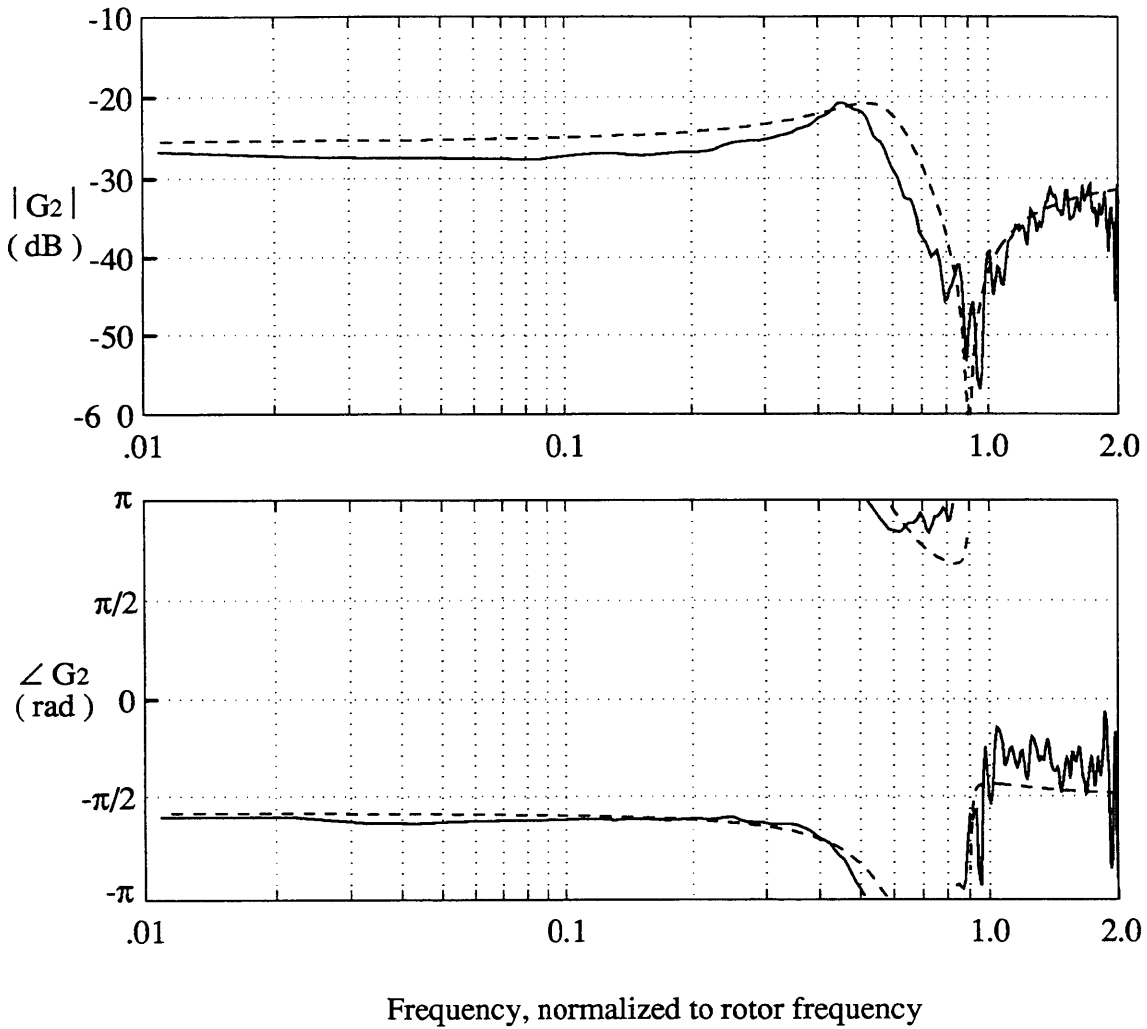


Figure 5.26 - Effect of intermediate stationary IGVs on the second mode transfer function at $\bar{\phi}=0.475$. Dotted line shows transfer function without intermediate IGVs, solid line shows transfer function with intermediate IGVs. Hot wires are upstream of the IGVs.

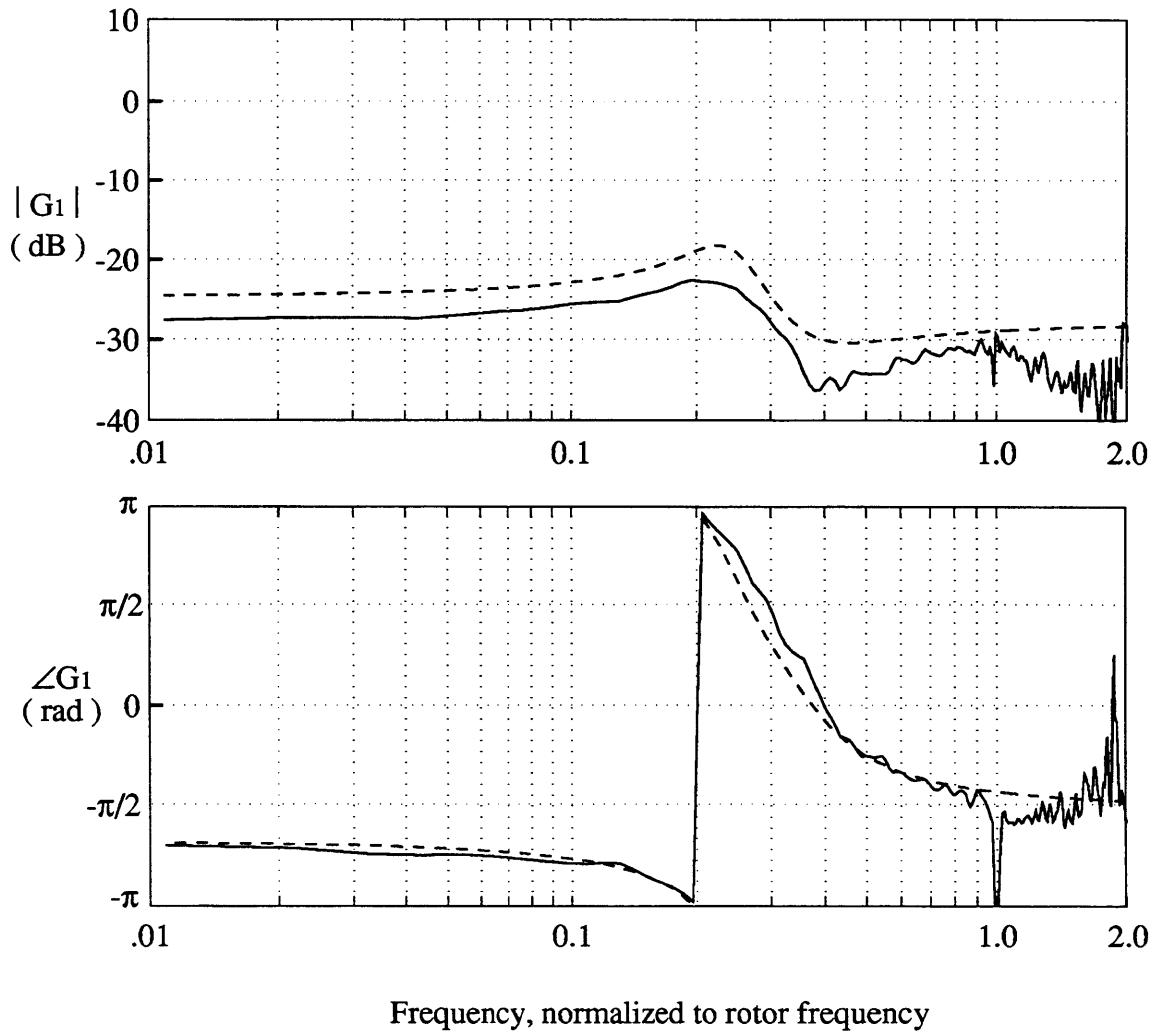


Figure 5.27- Effect of intermediate stationary IGVs on the first mode transfer function at $\bar{\phi}=0.500$. Dotted line shows transfer function without intermediate IGVs, solid line shows transfer function with intermediate IGVs. Hot wires are upstream of the IGVs.

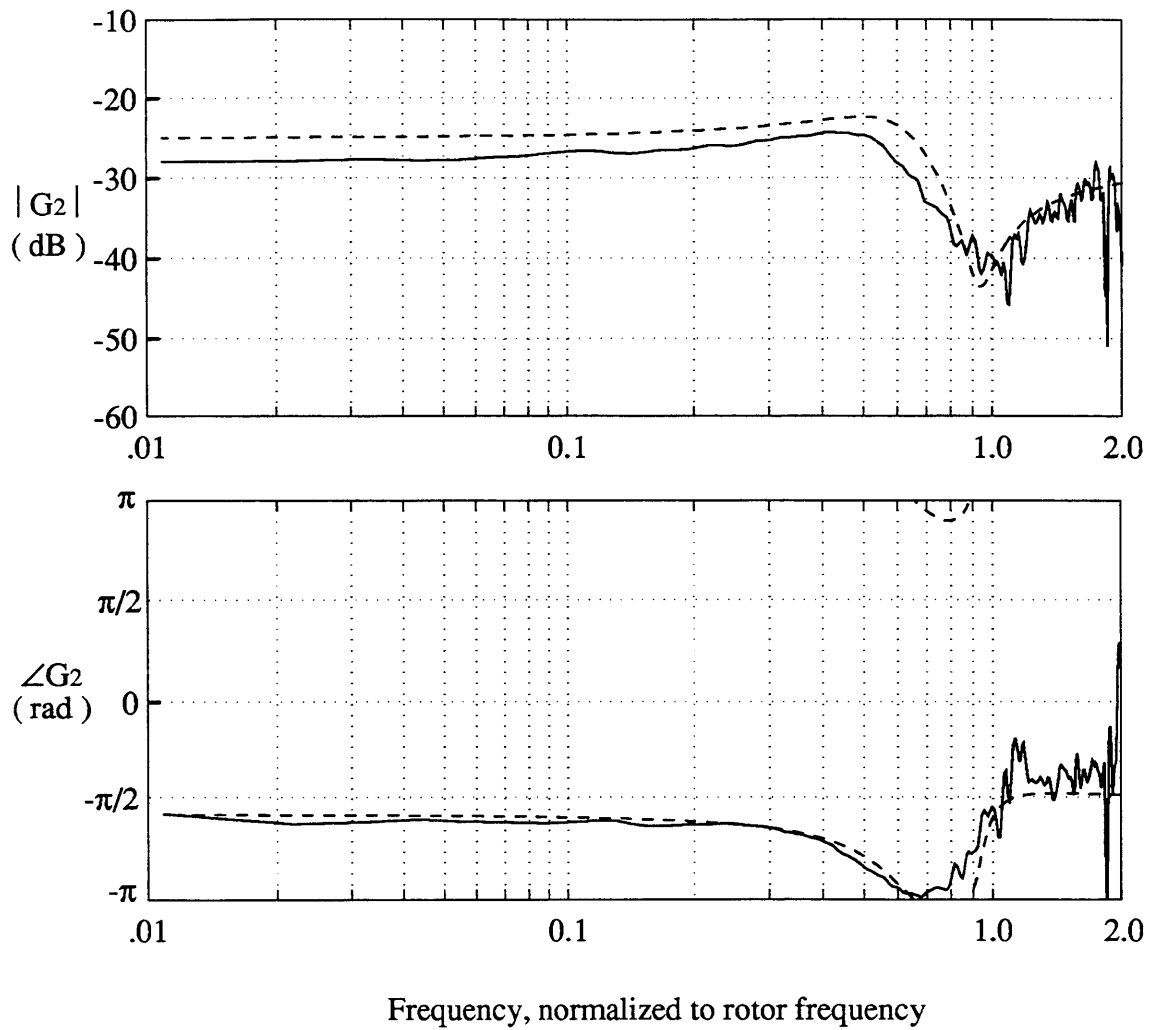


Figure 5.28 - Effect of intermediate stationary IGVs on the second mode transfer function at $\bar{\phi}=0.500$. Dotted line shows transfer function without intermediate IGVs, solid line shows transfer function with intermediate IGVs. Hot wires are upstream of the IGVs.

These experimental results show that there is a feature of the higher-mode dynamics which is completely unexplained by the current theory. The feature can be described as follows: The modes of the flow coefficient, $\tilde{\phi}_n$, respond not only to the modes of the IGV deflections $\tilde{\gamma}_n$, but also to their *rate of change*, $\frac{\partial}{\partial \tau}(\tilde{\gamma}_n)$, thus introducing a zero into $G_n(s)$. The effect is strong enough that the zero frequency is only about twice the pole frequency. Thus the ability to stabilize the system pole is significantly affected by the zero. Furthermore, the introduction of intermediate IGVs does not significantly alter the zero position.

Hot wires Downstream of the IGVs

All of the data presented so far has been taken with an array of hot wires mounted 0.5 compressor radii upstream of the IGVs. There are also provisions for mounting the hot wire array downstream of the IGVs. This location should have two main effects, according to the theory presented in Chapter 3:

- 1) From of the form of the flowfield upstream of the compressor:

$$\tilde{\phi}_n = \int_0^{2\pi} \delta\phi_1(\theta, \tau) \cdot e^{(n\eta_{HW})} \cdot e^{in\theta}, \quad (5.59)$$

we see that $\tilde{\phi}_n$ will be largest at $\eta_{HW} = 0$ (i.e. the compressor face), and die away exponentially upstream. Thus moving the hot wires to the rotor face should increase the magnitude of the transfer function $G_n(s)$. The effect will be more dramatic for larger values of n .

- 2) Since we are moving the hot wires from in front of to behind the IGVs, we predict an effect due to the unsteady pressure rise across the IGVs. The predicted effect is in Equation (3.12) where station 2 is behind the IGVs (see Figure 3.1):

$$\tilde{\phi}_{2n} = e^{(-n\eta_{HW})} \cdot \tilde{\phi}_n + in\bar{\phi} \cdot \mu_{IGV} \tilde{\gamma}_n \quad (5.60)$$

This can be rewritten as an effect on the transfer function we will be measuring:

$$\frac{\tilde{\phi}_2(s)}{\tilde{\gamma}(s)} = e^{(-n\eta_{HW})} \cdot \frac{\tilde{\phi}(s)}{\tilde{\gamma}(s)} + in\bar{\phi} \cdot \mu_{IGV} \quad (5.61)$$

The added term $in\bar{\phi} \cdot \mu_{IGV}$ will change the zero location of the transfer function $G_n(s)$. The effect will again be more dramatic for larger modes.

Thus the model presented in Chapter 3 predicts that the transfer function magnitude will be larger and the zero will shift.

To test these hypotheses, spectral estimates of $G_n(s)$ for $n=1$ and 2 were made at $\bar{\phi}=.475$, with the hot wires mounted downstream of the IGVs. The estimates are plotted in Figures 5.29 and 5.30, along with estimates of the transfer functions upstream of the IGVs (based on the results in Figures 5.22 and 5.23). These plots do show an increase in transfer function amplitude and a shift of the zero for both $G_1(s)$ and $G_2(s)$. The first mode zero moves from about 40% to about 100% rotor frequency, and the second mode zero moves from about 90% rotor frequency to about 150% of rotor frequency. In addition, closer study of the transfer functions reveals that the dynamics cannot be attributed to a single pole-zero combination: an additional pole and zero are necessary to account for the dynamics shown.

Figure 5.31 shows the results of fitting the data in Figure 5.29 with a two-pole, two-zero transfer function. The resulting estimate of the transfer function is

$$G_1(s) = (-0.0517+0.0158j) \cdot \frac{[s - (0.4+1.1j)][s - (-0.125+0.04j)]}{[s - (-0.017+0.223j)][s - (-0.85+0.6j)]} \quad (5.62)$$

The excellent fit in Figure 5.31 confirms that two poles and two zeros are necessary to properly account for the dynamics measured at the downstream hot wire location. Since the single-pole single-zero model presented thus far works well at the upstream measurement location, we conclude that dynamics across the IGVs, or effects not measurable upstream of the IGVs are responsible for the extra pole and zero.

We verify that Figure 5.31 is an accurate measure of $G_1(s)$ in two ways. First, we compare the estimate of $G_1(s)$ obtained using spectral techniques with that obtained via the sinusoidal excitation technique. Figure 5.6 shows this comparison - both estimates have the same shape. Second, we compare the eigenvalue measured upstream with that measured downstream. Since the homogeneous dynamics of the

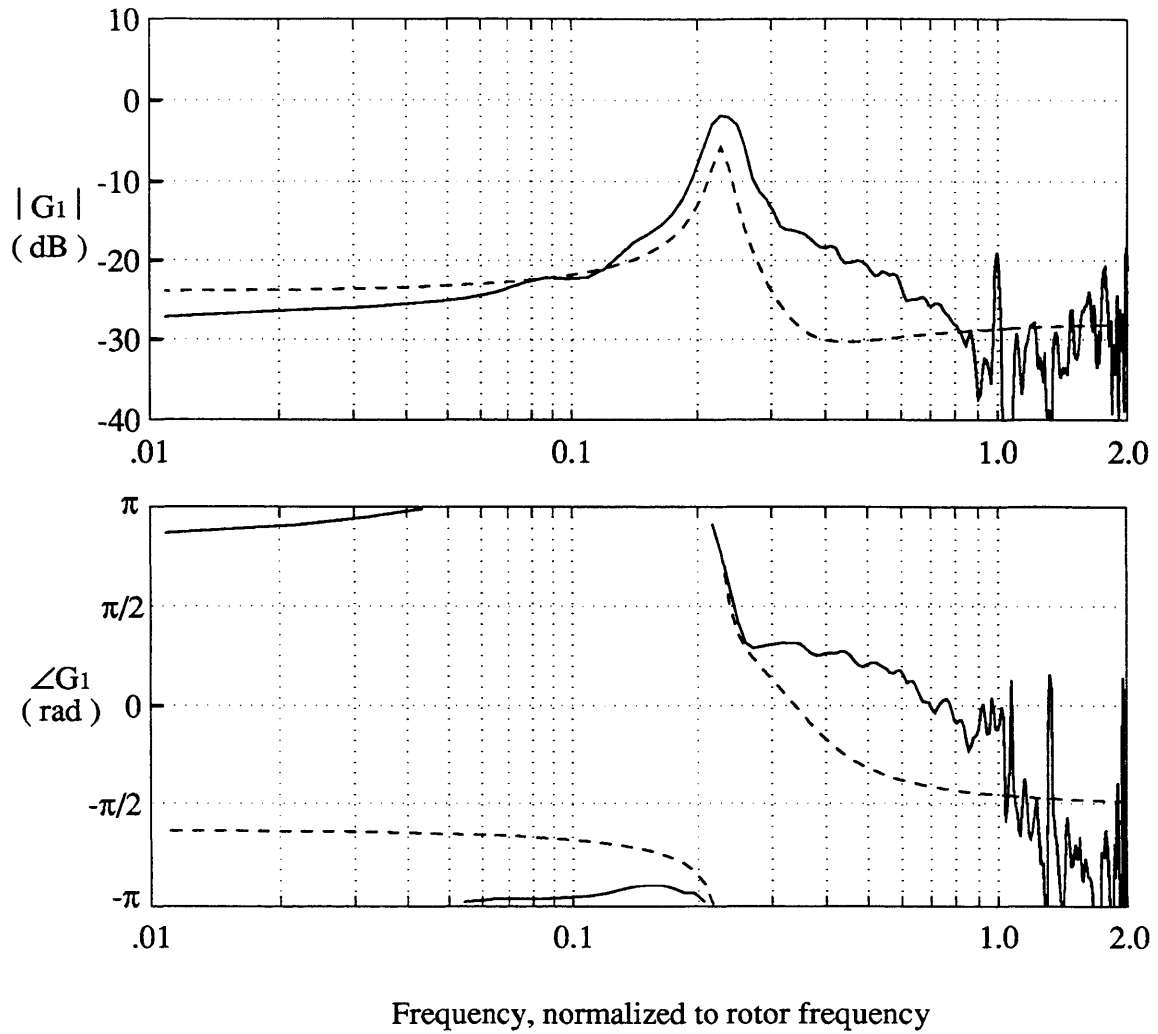


Figure 5.29 -Effect of moving the hot wires downstream of the IGVs on the first mode transfer function at $\bar{\phi}=0.475$. Dotted line shows transfer function upstream of the IGVs, solid line shows transfer function downstream of the IGVs. In both cases, the spacer ring is in.

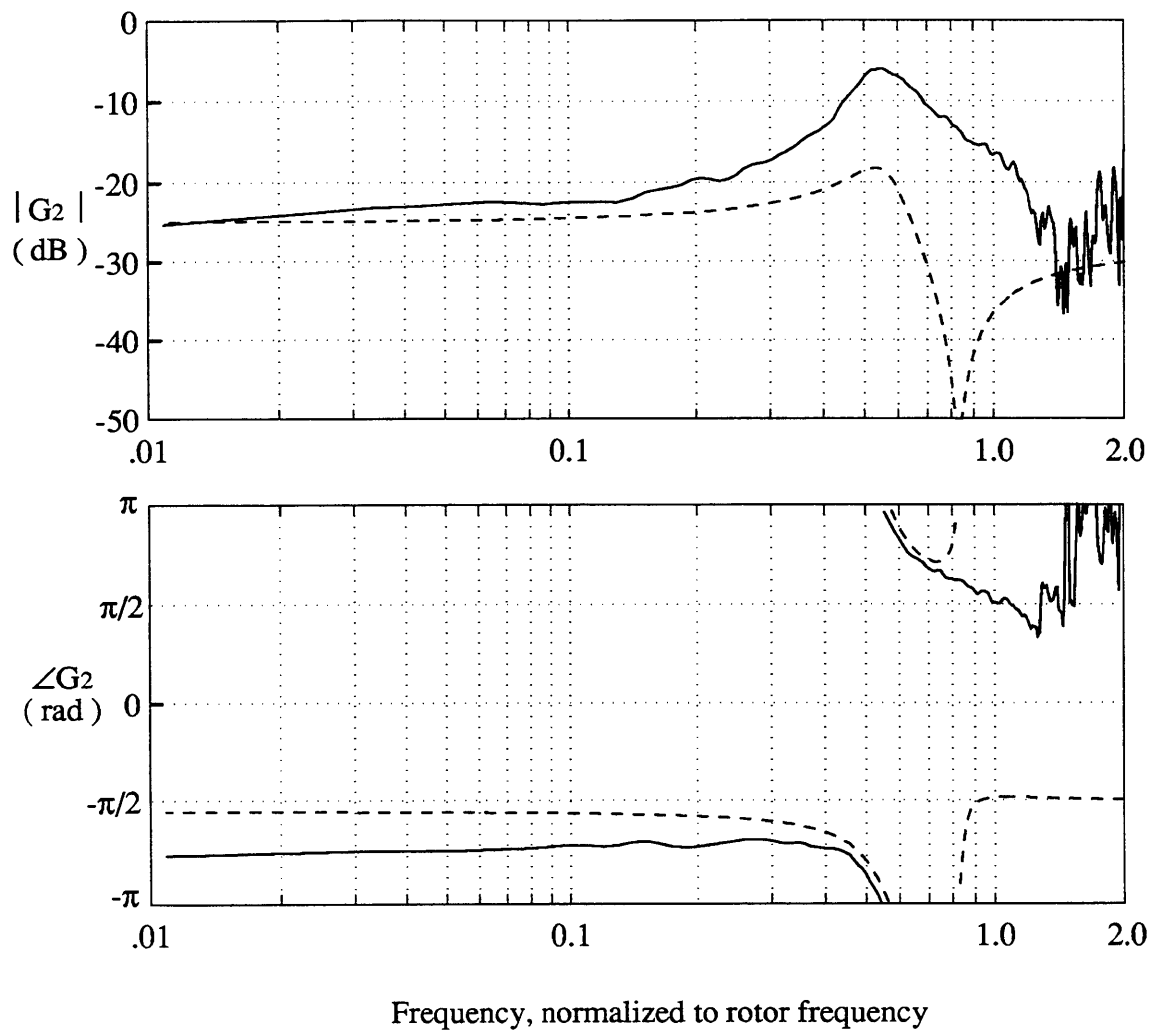


Figure 5.30 -Effect of moving the hot wires downstream of the IGVs on the second mode transfer function at $\bar{\phi}=0.475$. Dotted line shows transfer function upstream of the IGVs, solid line shows transfer function downstream of the IGVs. In both cases, the spacer ring is in.

$\frac{\tilde{\phi}_1(s)}{\tilde{\gamma}_1(s)}$, First Mode, $\bar{\phi} = 0.475$, Downstream Hot Wires

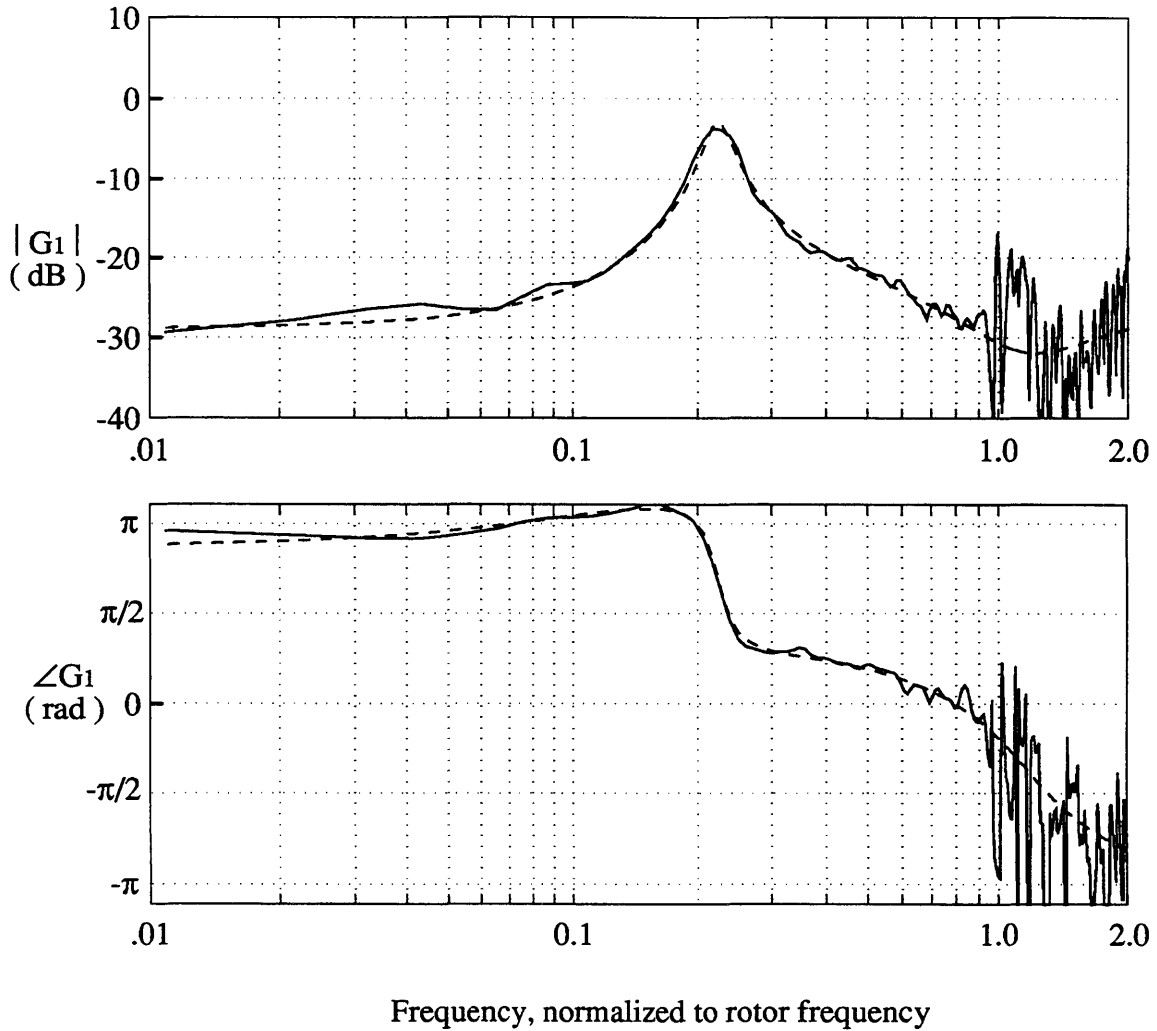


Figure 5.31 - Transfer function fit to spectral estimate of $G_1(s)$ downstream of the IGVs. Two poles and two zeros are used to achieve the fit shown:

$$G_{1\text{fit}}(s) = (-0.0517+0.0158j) \frac{[s - (0.4+1.1j)] [s - (-0.125+0.04j)]}{[s - (-0.017+0.223j)] [s - (-0.85+0.6j)]}$$

system cannot change when the sensors are moved, one of the downstream poles must match the upstream pole. Thus we have the following comparison:

$$\sigma_{rs} + j \cdot \omega_{rs} = -0.022 + 0.234j \quad (\text{upstream measurements})$$

$$\sigma_{rs} + j \cdot \omega_{rs} = -0.017 + 0.223j \quad (\text{downstream measurement})$$

These two measurements of the eigenvalue are the same, within the experimental error shown in Figure 5.9.

Our main conclusion based on the downstream transfer function data is that the dynamic effect of the IGVs on the compressor flow is poorly understood. There are significant dynamics between the axial velocity upstream and downstream of the IGVs, and these dynamics are captured only in part by the model presented in Chapter 3.

Table 5.1a - First Mode Parameter Identification Results
(no spacer ring, upstream hot wires) [th11]

$\bar{\phi}$	σ_{rs}	ω_{rs}	b_r	b_i	g_i	data set/ method
0.375	0.0182	0.168	-0.0065	0.00083	-0.0199	080790a/NF
0.400	0.0173	0.188	-0.0074	0.00258	-0.0232	080790a/NF
0.400	0.0074	0.187	-0.0076	0.00184	-0.0254	080790b/NF
0.425	0.0059	0.207	-0.0091	0.00229	-0.0299	080790a/NF
0.425	0.0026	0.207	-0.0092	0.00151	-0.0369	080790a/TR
0.425	-0.0015	0.200	-0.0085	0.00316	-0.0321	080790b/NF
0.450	-0.0148	0.226	-0.0100	0.00498	-0.0329	080790a/NF
0.450	-0.0143	0.225	-0.0100	0.00483	-0.0325	080790a/TR
0.450	0.0029	0.225	-0.0106	0.00321	-0.0320	080790b/NF
0.450	0.0021	0.226	-0.0106	0.00329	-0.0323	080790b/TR
0.475	-0.0286	0.245	-0.0116	0.00653	-0.0357	080790a/NF
0.475	-0.0258	0.246	-0.0116	0.00655	-0.0360	080790a/TR
0.475	-0.0271	0.247	-0.0119	0.00626	-0.0381	080790b/NF
0.475	-0.0256	0.246	-0.0118	0.00616	-0.0370	080790b/TR
0.475	-0.0217	0.240	-0.0110	0.00695	-0.0345	073090a/NF
0.475	-0.0162	0.237	-0.0111	0.00643	-0.0347	073090a/TR
0.475	-0.0184	0.242	-0.0115	0.00637	-0.0369	073090b/NF
0.475	-0.0147	0.240	-0.0116	0.00581	-0.0370	073090b/TR
0.475	-0.0203	0.241	-0.0119	0.00544	-0.0372	073090c/GA
0.475	-0.0199	0.241	-0.0119	0.00545	-0.0372	073090c/GC
0.475	-0.0079	0.241	-0.0116	0.00583	-0.0372	073090c/IV
0.475	-0.0168	0.241	-0.0113	0.00653	-0.0367	073090d/IV
0.475	-0.0118	0.221	-0.0102	0.00626	-0.0356	072490a/NF
0.475	-0.0235	0.236	-0.0119	0.00480	-0.0369	072490b/GA
0.475	-0.0223	0.236	-0.0118	0.00486	-0.0369	072490b/GC
0.475	-0.0184	0.230	-0.0114	0.00502	-0.0342	072490b/IV
0.475	-0.0234	0.232	-0.0116	0.00494	-0.0372	052490a/GA
0.475	-0.0213	0.233	-0.0116	0.00508	-0.0373	052490a/GC
0.475	-0.0138	0.225	-0.0113	0.00468	-0.0367	052490a/IV
0.500	-0.0601	0.263	-0.0145	0.00683	-0.0450	072490a/GC
0.525	-0.0976	0.233	-0.0163	0.00284	-0.0467	072490a/GA
0.525	-0.0919	0.236	-0.0163	0.00291	-0.0468	072490a/GC
0.525	-0.1055	0.220	-0.0156	0.00319	-0.0434	072490a/IV
0.550	-0.1277	0.190	-0.0163	-0.00204	-0.0475	072490a/GA
0.550	-0.1152	0.198	-0.0163	-0.00189	-0.0477	072490a/GC
0.550	-0.1833	0.178	-0.0181	-0.00308	-0.0446	072490a/IV

Table 5.1b - Second Mode Parameter Identification Results
(no spacer ring, upstream hot wires) [th21]

$\bar{\phi}$	σ_{rs}	ω_{rs}	b_r	b_i	g_i	data set/ method
0.375	-0.0010	0.446	-0.0168	0.0017	-0.0228	080790a/NF
0.375	0.0000	0.445	-0.0168	0.0010	-0.0288	080790a/TR
0.375	-0.0022	0.454	-0.0170	0.0022	-0.0247	080790b/NF
0.375	0.0003	0.445	-0.0168	0.0011	-0.0346	080790b/TR
0.375	0.0116	0.446	-0.0168	0.0009	-0.0228	080790c/NF
0.400	-0.0124	0.484	-0.0203	0.0025	-0.0259	080790a/NF
0.400	-0.0110	0.484	-0.0202	0.0028	-0.0265	080790a/TR
0.400	-0.0152	0.486	-0.0204	0.0023	-0.0267	080790b/NF
0.400	-0.0134	0.485	-0.0204	0.0020	-0.0273	080790b/TR
0.425	-0.0478	0.510	-0.0236	0.0016	-0.0299	080790a/NF
0.425	-0.0487	0.510	-0.0236	0.0015	-0.0300	080790a/TR
0.425	-0.0498	0.508	-0.0235	0.0016	-0.0298	080790b/NF
0.425	-0.0515	0.510	-0.0236	0.0017	-0.0299	080790b/TR
0.450	-0.1001	0.536	-0.0272	0.0004	-0.0316	080790a/NF
0.450	-0.0966	0.543	-0.0275	0.0010	-0.0327	080790a/TR
0.450	-0.1026	0.537	-0.0272	0.0002	-0.0312	080790b/NF
0.450	-0.1010	0.538	-0.0273	0.0003	-0.0316	080790b/TR
0.475	-0.1567	0.553	-0.0305	-0.0013	-0.0336	080790a/NF
0.475	-0.1610	0.574	-0.0316	-0.0005	-0.0352	080790a/TR
0.475	-0.1448	0.558	-0.0306	-0.0008	-0.0348	080790b/NF
0.475	-0.1450	0.567	-0.0311	-0.0003	-0.0352	080790b/TR
0.475	-0.0967	0.505	-0.0273	0.0003	-0.0298	072490a/NF
0.475	-0.1024	0.589	-0.0317	-0.0006	-0.0352	072490b/GC
0.475	-0.1289	0.560	-0.0305	-0.0007	-0.0338	072490b/GA
0.475	-0.1123	0.573	-0.0310	0.0009	-0.0360	072490b/TV
0.500	-0.1600	0.645	-0.0370	-0.0026	-0.0406	072490a/GC
0.500	-0.2173	0.628	-0.0370	-0.0026	-0.0398	072490a/GA
0.500	-0.1840	0.619	-0.0361	-0.0009	-0.0387	072490a/TV
0.525	-0.2147	0.713	-0.0432	-0.0048	-0.0453	072490a/GC
0.525	-0.2921	0.665	-0.0419	-0.0060	-0.0434	072490a/GA
0.525	-0.2937	0.658	-0.0416	-0.0058	-0.0421	072490a/TV
0.550	-0.2947	0.650	-0.0421	-0.0095	-0.0460	072490a/GC
0.550	-0.3475	0.584	-0.0394	-0.0116	-0.0433	072490a/GA
0.550	-0.4214	0.642	-0.0444	-0.0133	-0.0435	072490a/TV

Table 5.1c - Third Mode Parameter Identification Results
(spacer ring IN, upstream hot wires) [th32]

$\bar{\phi}$	σ_{rs}	ω_{rs}	b_r	b_i	g_i	data set/ method
0.375	-0.0395	0.769	-0.0233	-0.00150	-0.0246	051091a/NF
0.375	-0.0410	0.772	-0.0234	-0.00131	-0.0246	051091a/TR
0.375	-0.0442	0.759	-0.0229	-0.00249	-0.0246	051091b/NF
0.375	-0.0437	0.750	-0.0226	-0.00250	-0.0250	051091b/TR
0.375	-0.0401	0.785	-0.0237	-0.00172	-0.0237	051091c/NF
0.375	-0.0349	0.782	-0.0237	-0.00151	-0.0244	051091c/TR
0.375	-0.0318	0.759	-0.0230	-0.00161	-0.0243	051091d/NF
0.375	-0.0359	0.764	-0.0231	-0.00142	-0.0239	051091d/TR
0.375	-0.0640	0.772	-0.0234	-0.00100	-0.0237	013191a/GC
0.375	-0.0713	0.765	-0.0232	-0.00114	-0.0234	013191a/GA
0.400	-0.0565	0.805	-0.0260	-0.00189	-0.0276	051091a/GC
0.400	-0.0633	0.801	-0.0258	-0.00331	-0.0259	051091a/IV
0.425	-0.0739	0.860	-0.0295	-0.00186	-0.0304	051091a/GC
0.425	-0.0755	0.799	-0.0274	-0.00211	-0.0287	051091b/GC
0.425	-0.0549	0.841	-0.0288	-0.00181	-0.0299	051091c/GC
0.425	-0.0880	0.846	-0.0291	-0.00234	-0.0299	051091c/GA
0.425	-0.0989	0.816	-0.0278	-0.00497	-0.0282	051091c/IV
0.450	-0.1526	0.841	-0.0305	-0.00559	-0.0305	051091a/GC
0.450	-0.1558	0.854	-0.0305	-0.00774	-0.0298	051091a/IV
0.475	-0.1882	0.872	-0.0332	-0.00722	-0.0327	051091a/GC
0.475	-0.2001	0.932	-0.0349	-0.01022	-0.0320	051091a/IV

Table 5.2a - First Mode Parameter Identification Results
(spacer ring IN, upstream hot wires) [th12]

$\bar{\phi}$	σ_{rs}	ω_{rs}	b_r	b_i	g_i	data set/ method
0.400	0.0080	0.171	-0.0088	0.0012	-0.0301	010991a/NF
0.400	0.0091	0.171	-0.0087	0.0013	-0.0327	010991a/TR
0.400	0.0090	0.171	-0.0088	0.0018	-0.0310	010991b/NF
0.400	0.0103	0.171	-0.0088	0.0014	-0.0336	010991b/TR
0.400	0.0129	0.174	-0.0089	0.0011	-0.0273	010991c/NF
0.400	0.0136	0.176	-0.0091	0.0009	-0.0301	010991c/TR
0.400	0.0108	0.176	-0.0091	0.0019	-0.0296	010991d/NF
0.400	0.0107	0.177	-0.0092	0.0008	-0.0322	010991d/TR
0.400	0.0122	0.178	-0.0093	0.0001	-0.0306	122090a/NF
0.400	0.0127	0.178	-0.0093	0.0007	-0.0317	122090a/TR
0.400	0.0174	0.183	-0.0096	0.0008	-0.0313	122090b/NF
0.400	0.0171	0.183	-0.0096	0.0008	-0.0290	122090b/TR
0.425	0.0127	0.190	-0.0103	0.0023	-0.0313	010991a/NF
0.425	0.0127	0.191	-0.0105	0.0014	-0.0341	010991a/TR
0.425	0.0111	0.194	-0.0105	0.0029	-0.0321	010991b/NF
0.425	0.0111	0.194	-0.0106	0.0025	-0.0354	010991b/TR
0.425	0.0087	0.198	-0.0107	0.0021	-0.0333	010991c/NF
0.425	0.0096	0.198	-0.0108	0.0029	-0.0360	010991c/TR
0.425	0.0039	0.188	-0.0101	0.0028	-0.0352	122090a/NF
0.450	-0.0003	0.220	-0.0123	0.0044	-0.0373	010991a/NF
0.450	-0.0020	0.218	-0.0121	0.0048	-0.0388	010991a/TR
0.450	0.0109	0.212	-0.0119	0.0035	-0.0349	010991b/NF
0.450	0.0111	0.212	-0.0120	0.0033	-0.0355	010991b/TR
0.450	0.0061	0.212	-0.0118	0.0038	-0.0330	010991c/NF
0.450	0.0031	0.218	-0.0123	0.0030	-0.0363	122090a/NF
0.475	-0.0097	0.227	-0.0133	0.0045	-0.0397	010991a/NF
0.475	-0.0084	0.229	-0.0135	0.0048	-0.0435	010991a/TR
0.475	-0.0127	0.233	-0.0137	0.0044	-0.0403	010991b/NF
0.475	-0.0095	0.232	-0.0139	0.0045	-0.0406	010991b/TR
0.475	-0.0151	0.224	-0.0132	0.0045	-0.0398	010991c/NF
0.475	-0.0131	0.226	-0.0133	0.0041	-0.0413	010991c/TR
0.475	-0.0108	0.228	-0.0135	0.0045	-0.0392	010991d/NF
0.475	-0.0091	0.228	-0.0136	0.0043	-0.0403	010991d/TR
0.475	-0.0120	0.229	-0.0138	0.0039	-0.0435	122090a/GC
0.475	-0.0158	0.228	-0.0138	0.0037	-0.0434	122090a/GA
0.475	-0.0076	0.226	-0.0136	0.0031	-0.0434	122090a/IV
0.475	-0.0141	0.233	-0.0140	0.0047	-0.0464	121890b/GC
0.475	-0.0175	0.230	-0.0136	0.0045	-0.0435	121890b/GA
0.475	-0.0117	0.227	-0.0135	0.0043	-0.0427	121890b/IV
0.500	-0.0378	0.253	-0.0159	0.0051	-0.0484	122090a/GC
0.500	-0.0384	0.253	-0.0160	0.0051	-0.0485	122090a/GA

Table 5.2b - Second Mode Parameter Identification Results
(spacer ring IN, upstream hot wires) [th22]

$\bar{\phi}$	σ_{rs}	ω_{rs}	b_r	b_i	g_i	data set/ method
0.400	0.0016	0.486	-0.0225	0.00142	-0.0322	010991a/NF
0.400	0.0022	0.486	-0.0225	0.00102	-0.0341	010991a/TR
0.400	0.0078	0.487	-0.0225	0.00224	-0.0314	010991b/NF
0.400	0.0074	0.487	-0.0225	0.00202	-0.0316	010991b/TR
0.400	0.0099	0.489	-0.0225	0.00216	-0.0330	010991c/NF
0.400	0.0095	0.489	-0.0226	0.00178	-0.0341	010991c/TR
0.400	0.0073	0.492	-0.0227	0.00175	-0.0321	010991d/NF
0.400	0.0083	0.491	-0.0227	0.00162	-0.0345	010991d/TR
0.400	0.0027	0.490	-0.0226	0.00194	-0.0334	122090a/NF
0.425	-0.0219	0.507	-0.0253	0.00175	-0.0330	010991a/NF
0.425	-0.0186	0.508	-0.0253	0.00190	-0.0342	010991a/TR
0.425	-0.0176	0.513	-0.0255	0.00195	-0.0338	010991b/NF
0.425	-0.0153	0.510	-0.0255	0.00155	-0.0346	010991b/TR
0.425	-0.0136	0.511	-0.0255	0.00156	-0.0335	010991c/NF
0.425	-0.0147	0.510	-0.0254	0.00122	-0.0325	010991c/TR
0.425	-0.0158	0.515	-0.0256	0.00185	-0.0339	010991d/NF
0.425	-0.0162	0.517	-0.0257	0.00224	-0.0347	010991d/TR
0.425	-0.0224	0.510	-0.0254	0.00140	-0.0334	122090a/NF
0.450	-0.0552	0.536	-0.0286	0.00075	-0.0356	010991a/NF
0.450	-0.0491	0.535	-0.0285	0.00080	-0.0365	010991a/TR
0.450	-0.0446	0.537	-0.0286	0.00143	-0.0356	010991b/NF
0.450	-0.0401	0.538	-0.0286	0.00161	-0.0370	010991b/TR
0.450	-0.0452	0.535	-0.0285	0.00113	-0.0363	010991c/NF
0.450	-0.0408	0.534	-0.0284	0.00116	-0.0373	010991c/TR
0.450	-0.0499	0.538	-0.0287	0.00080	-0.0353	010991d/NF
0.450	-0.0454	0.538	-0.0287	0.00092	-0.0362	010991d/TR
0.450	-0.0522	0.538	-0.0287	0.00031	-0.0359	122090a/NF
0.475	-0.0986	0.570	-0.0323	-0.00014	-0.0377	010991a/NF
0.475	-0.0929	0.567	-0.0321	-0.00023	-0.0379	010991a/TR
0.475	-0.0922	0.561	-0.0318	-0.00046	-0.0379	010991b/NF
0.475	-0.0946	0.561	-0.0318	-0.00046	-0.0380	010991b/TR
0.475	-0.0784	0.564	-0.0318	-0.00007	-0.0382	010991c/NF
0.475	-0.0725	0.560	-0.0316	-0.00010	-0.0388	010991c/TR
0.475	-0.0893	0.567	-0.0321	-0.00047	-0.0376	010991d/NF
0.475	-0.0825	0.563	-0.0318	-0.00044	-0.0388	010991d/TR
0.475	-0.0898	0.547	-0.0309	-0.00210	-0.0368	122090a/GC
0.475	-0.0934	0.544	-0.0307	-0.00216	-0.0366	122090a/GA
0.475	-0.0958	0.565	-0.0320	-0.00057	-0.0384	122090a/IV
0.475	-0.0887	0.558	-0.0315	-0.00167	-0.0390	121890b/GC
0.475	-0.0975	0.550	-0.0312	-0.00177	-0.0385	121890b/GA
0.475	-0.0838	0.560	-0.0316	-0.00109	-0.0390	121890b/IV
0.500	-0.1389	0.574	-0.0342	-0.00345	-0.0403	122090a/GC
0.500	-0.1466	0.570	-0.0340	-0.00354	-0.0400	122090a/GA
0.500	-0.1338	0.582	-0.0346	-0.00261	-0.0410	122090a/IV

Table 5.2c - Third Mode Parameter Identification Results
(spacer ring IN, DOWNSTREAM hot wires) [th33]

$\bar{\phi}$	σ_{rs}	ω_{rs}	b_r	b_i	g_i	data set/ method
0.360	0.0010	0.758	-0.0428	0.00364	-0.0020	050991a/NF
0.360	0.0019	0.759	-0.0424	0.00681	-0.0179	050991b/NF
0.360	0.0117	0.753	-0.0417	0.00902	0.0008	050991c/NF
0.360	0.0058	0.755	-0.0418	0.00888	0.0012	050991d/NF
0.360	-0.0009	0.761	-0.0429	-0.00375	-0.0110	050991e/NF
0.360	-0.0097	0.755	-0.0420	0.00809	-0.0117	050991f/NF
0.375	-0.0334	0.767	-0.0433	0.00834	-0.0013	050991a/NF
0.375	-0.0329	0.768	-0.0431	0.00976	0.0024	050991a/TR
0.375	-0.0218	0.763	-0.0435	0.00538	-0.0107	050991b/NF
0.375	-0.0141	0.765	-0.0431	0.00892	-0.0091	050991b/TR
0.375	-0.0304	0.756	-0.0424	0.00968	0.0128	050991c/NF
0.375	-0.0142	0.756	-0.0426	0.00844	-0.0141	050991c/TR
0.375	-0.0158	0.774	-0.0434	0.00977	0.0019	050991d/NF
0.380	-0.0599	0.790	-0.0422	0.01759	0.0159	022291a/GC
0.380	-0.0651	0.785	-0.0426	0.01594	0.0182	022291a/GA
0.400	-0.0702	0.801	-0.0473	0.00099	0.0020	050991a/GC
0.400	-0.0762	0.796	-0.0470	-0.00071	0.0045	050991a/GA
0.425	-0.1103	0.868	-0.0518	0.00896	0.0090	050991a/GC
0.425	-0.1321	0.834	-0.0508	0.00072	0.0205	050991a/GA
0.450	-0.1414	0.866	-0.0393	0.03693	0.0132	050991a/GC
0.450	-0.1715	0.839	-0.0444	0.02828	0.0280	050991a/GA
0.475	-0.2459	0.899	-0.0522	0.02653	0.0208	050991a/GC
0.475	-0.2486	0.865	-0.0515	0.02348	0.0314	050991a/GA

CHAPTER 6
Active Stabilization
of a
Single-Stage Low-Speed Research Compressor

In this chapter we demonstrate the stabilization of rotating stall and subsequent reduction of the stall flow coefficient. Furthermore, we present evidence that the compressor higher-mode dynamics behave as anticipated by the linearized model presented in Chapters 3, 4 and 5. We use the model to motivate the control system configuration, feedback gain determination, and the experimental approach. Thus the model provides a proven framework for design of rotating stall control systems.

The model motivates the control system configuration in several ways. Most important in this respect is the conception that the fundamental states of the system are the spatial Fourier coefficients (SFCs). The control system takes the distributed measurements and actuators, and transforms them into SFCs. It then operates on these as the inputs and outputs of the system. Because only the first few modes (3 at most) are considered, the controller sees only disturbances which have significant circumferential extent in the annulus. A very localized disturbance will go virtually unnoticed by the control system. Similarly, actuation waves extend around the entire annulus, rather than being localized to narrow circumferential bands.

Each SFC is the complex magnitude of an eigenmode of the compressor higher-mode dynamics, and as such it is seen by the model as an independent entity. Its evolution and response to actuation are completely unaffected by other SFCs. Thus, the input-output dynamics are decoupled, and we can consider the stabilization of each mode separately (Figure 4.2). For instance, the velocity perturbation wave

with a circumferential mode number 2, $\tilde{\phi}_2$, is controlled by the actuation wave with the same mode number, $\tilde{\gamma}_2$. Other modes ($\tilde{\phi}_1$ and $\tilde{\phi}_3$), although derived from the *same* measurements, are separate dynamic systems that can be stabilized separately (using $\tilde{\gamma}_1$ and $\tilde{\gamma}_3$ respectively). In this way, the eigenmode structure of the system is preserved under active control.

By using our linearized understanding of the compressor higher-mode dynamics, we simplify the control system design problem - we need design only 3 SISO control laws to stabilize the system. Such design is aided by further details about the model. For instance, the modes go from stable to unstable sequentially as the flow coefficient is reduced (see Chapter 5): At $\bar{\phi} \cong 0.45$ the first mode goes unstable, at $\bar{\phi} \cong 0.38$ the second mode goes unstable, and at $\bar{\phi} \cong 0.36$ the third mode goes unstable. Therefore, stabilization of the first mode alone should yield some reduction in the stall flow coefficient, and extra reduction should be gained for each additional mode stabilized.

This behavior suggests a straightforward experimental approach to control law design. Because the first mode goes gradually from stable to unstable, while the other modes remain stable, a single proportional feedback gain on this mode can be used to achieve stabilization. The value of gain required can be determined experimentally, since only a single gain is needed, and since operation at a *nearly unstable* flow coefficient is possible (see the following paragraph). A gain determined in this way, as it happens, is sufficient to allow stabilization down to $\bar{\phi} = 0.38$, where the second mode goes unstable. Now the second mode feedback gain can be determined. This is still only a single parameter search, since the first mode is stabilized and the third mode is still naturally stable. The third mode can be stabilized with a similar single-parameter search.

The experimental procedure for gain determination is also motivated by the modeling. We know that, since $\tilde{\phi}_n$ and $\tilde{\gamma}_n$ are both complex, the feedback gain

between them may also be complex:

$$\tilde{u}_{c_n} = Z_n \cdot \tilde{y}_n, \quad Z_n \text{ complex} \quad (6.1)$$

(here we have used the measurement (\tilde{y}_n) of $\tilde{\phi}_n$ and the command (\tilde{u}_{c_n}) to $\tilde{\gamma}_n$, to remain consistent with the modeling in previous chapters). We also know from Sections 3.3.1 and 5.3.2 that spatial phase shift exists between the actuation and its effect on flow perturbations:

$$\dot{\tilde{\phi}}_n \Leftarrow (b_r + j \cdot b_i) \cdot \tilde{\gamma}_n.$$

Thus we expect the stabilizing value of Z_n to have non-zero phase, denoted $\angle Z_n$. Presumably the best value of $\angle Z_n$ will also damp the resonance peak of the underdamped system when $\tilde{\phi}_n$ is *nearly* unstable. Using this understanding, the gain determination proceeds as follows:

1. Pick a reasonable magnitude value for Z_n , denoted $|Z_n|$.
Stabilization is relatively insensitive to $|Z_n|$ because the system goes slowly from stable to unstable. Refinement of $|Z_n|$ can be conducted once $\angle Z_n$ is determined.
2. Set the flow coefficient near the value at which $\tilde{\phi}_n$ is unstable.
3. Measure the open loop resonance peak of the system, using a power spectrum of $\tilde{\phi}_n$.
4. Measure the closed loop resonance peak, for various values of $\angle Z_n$.
5. Choose the value of $\angle Z_n$ which best damps the system.

The only step which requires the use of measured response data is step 1. Although any 'reasonable magnitude' for Z_n is theoretically sufficient to provide extra damping and change the closed-loop resonance peak, in practice we need a value of $|Z_n|$ which is large enough to produce a measurable change, yet not so large that the actuators are saturated. The latter consideration restricts the maximum value of $|Z_n|$ to about 25. The former consideration requires that we compute a minimum value for $|Z_n|$, which will depend on the control power of the actuators.

A minimum value for $|Z_n|$ can be roughly estimated by writing the

closed-loop eigenvalue of the system, assuming no actuators or other lags. To do this, we let $\tilde{\gamma}_n = Z_n \cdot \tilde{\phi}_n$ in Equation (3.39) and find the eigenvalue of the resulting homogeneous system. The close loop eigenvalue estimated in this way is:

$$\lambda_{c.l.} = \frac{[(\sigma_{rs} + i\omega_{rs}) + (b_r + ib_i)Z_n]}{[1 - ig_i Z_n]}$$

For the magnitude values that we will finally use, the denominator in this expression is roughly one, because g_i is small (see Tables 5.1 and 5.2). We can further simplify by choosing the phase of Z_n so that it modifies only the real part of $\lambda_{c.l.}$. This phase roughly maximizes the effectiveness of the feedback in attenuating the spectral peak. An expression for the Z_n which has this phase is:

$$Z_n = - \frac{(b_r - ib_i)}{|b_r + ib_i|} \cdot |Z_n|$$

The expression for $\lambda_{c.l.}$ can now be simplified to the following:

$$\lambda_{c.l.} \cong (\sigma_{rs} - |b_r + ib_i| \cdot |Z_n|) + i\omega_{rs}$$

Here it is clear that the control power terms determine the necessary magnitude for Z_n . One can estimate reasonable magnitudes for $|Z_n|$ based on this formula, using either predicted or measured values for the parameters. For instance, in the experiment described in Section 6.1.1, $\sigma_{rs} \cong -0.022$, $b_r \cong -0.012$ and $b_i \cong 0.0053$. Using the above formula, the magnitude of Z_n required to double σ_{rs} (thus creating a large change in the spectral resonance peak) is $|Z_n| = 1.7$. The value chosen for this experiment was $|Z_n| = 6.4$. This value is a factor of about 4 away from both the estimated minimum (1.7) and the estimated maximum (25) allowable values for $|Z_n|$.

Once a reasonable value for $|Z_n|$ is determined, the phase determination procedure described above is workable as a quick method to demonstrate stabilization. It is experimentally time-consuming, however, and there is no guarantee that the performance will be optimum at flow coefficients other than that at which the 'best' value of Z_n is first determined. Thus a new search - somewhat more narrow, perhaps - must be conducted to improve damping as flow coefficient is further reduced. Here, a

quantitative model of the dynamics becomes useful. By identifying the system dynamics as in Chapter 5, we can do the control system design theoretically rather than experimentally, and performance limitations can be better understood.

The ultimate goal for control system design would be to develop a quantitative model based on a geometric compressor description and a limited set of experiments. The model could then be used to design an *a priori* control system. More work remains to be done to provide the predictive capability necessary for such an approach.

Since the approach to control system design is primarily experimental we will present these results first, in Section 6.1. Section 6.2 then discusses some theoretical aspects of the control system design, based on the identification results in Chapter 5.

6.1 Experimental Results

Here we present experimental evidence to support the claims of the previous discussion. Most importantly, stabilization of compressor higher-mode dynamics is demonstrated for the first time. This stabilization allows operation significantly below the flow coefficient at which rotating stall normally occurs. Furthermore, we will show that, for the axial research compressor tested,

- A) Both the homogeneous and the forced dynamics of the SFCs behave as though they are decoupled. Thus $e^{in\theta}$, $n = 1, 2, 3, \dots$ can be treated as the mode shapes of the distributed dynamics.
- B) Mode numbers 1, 2, and 3 go from stable to unstable at separate flow coefficients, sequentially as flow coefficient is reduced.
- C) Decoupled proportional feedback of the modes is sufficient to stabilize them, if appropriate spatial phase shift between measurement and actuation is provided.

The experimental apparatus and procedure are described in Chapter 2. Section 2.5 is of particular interest, as it describes the basic experimental procedure for taking data.

In Section 6.1.1, we will show the experimental results of the gain

determination procedure described in the previous section. In the remaining sections, we will show what happens to various measures of the system behavior as the number of modes under control is increased from none ('no control') to first mode only (' Z_1 control'), to first plus second mode (' Z_1+Z_2 control'), to all three modes (' $Z_1+Z_2+Z_3$ control').

6.1.1 Feedback Phase Sensitivity of First Mode Stability

A primary goal of this research is to experimentally establish a connection between the damping of small amplitude waves and the onset of rotating stall. We can do this using the procedure described in the previous section for determining the best feedback gain Z_n .

Figure 6.1 shows the results of the procedure, conducted on the first mode, at a flow coefficient $\bar{\phi} \cong 0.475$. The magnitude of Z_1 was set at $|Z_1| = 6.4$, and the phase was varied between 0 and 360 degrees. At each value of $\angle Z_1$, closed-loop data was taken for the first mode without changing the flow coefficient. The spectral peak in each case was either amplified or attenuated. The ratio of the closed-loop to the open-loop resonance peak, as a function of $\angle Z_1$, is shown in Figure 6.1.

The stall point during closed-loop operation was also recorded for each value of $\angle Z_1$, and is shown in Figure 6.2. Note the strong resemblance between Figures 6.1 and 6.2. Clearly, the amount of improvement in compressor operating range is directly related to the level of extra damping provided by the feedback system. For values of phase which damp the waves, stall onset is delayed to lower flow coefficients. Also, for values of phase which make waves larger, stall onset is moved to *higher* flow coefficients - these values of phase *destabilize* the small amplitude waves, causing them to go unstable at higher than normal flow coefficients.

This set of experiments demonstrates that the stability of small amplitude sinusoidal waves determines the flow coefficient at which the system goes into

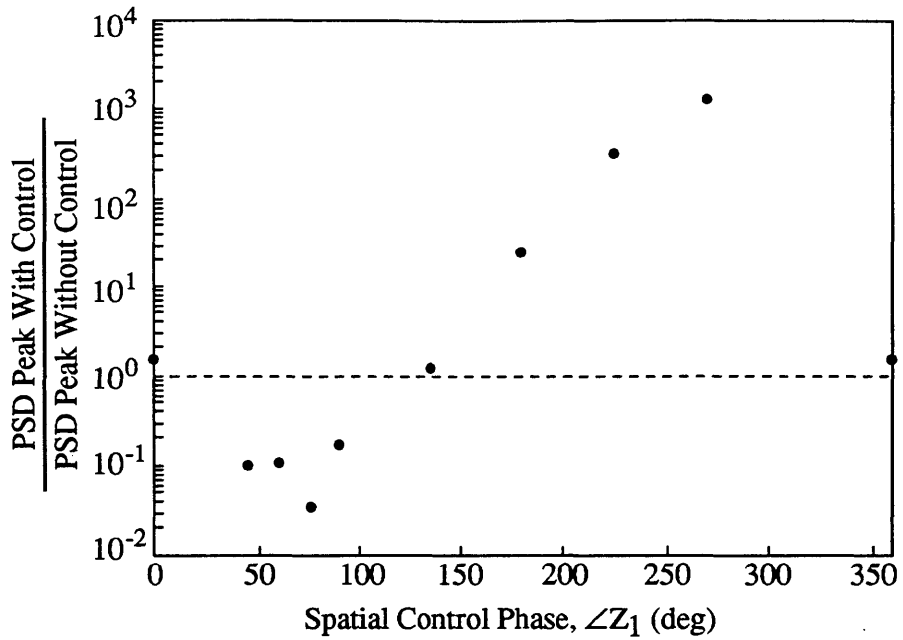


Figure 6.1- Effect of feedback phase on the magnitude of the spectral peak. Experiments were conducted at a single flow coefficient (0.475) with $|Z_1| = 6.4$.

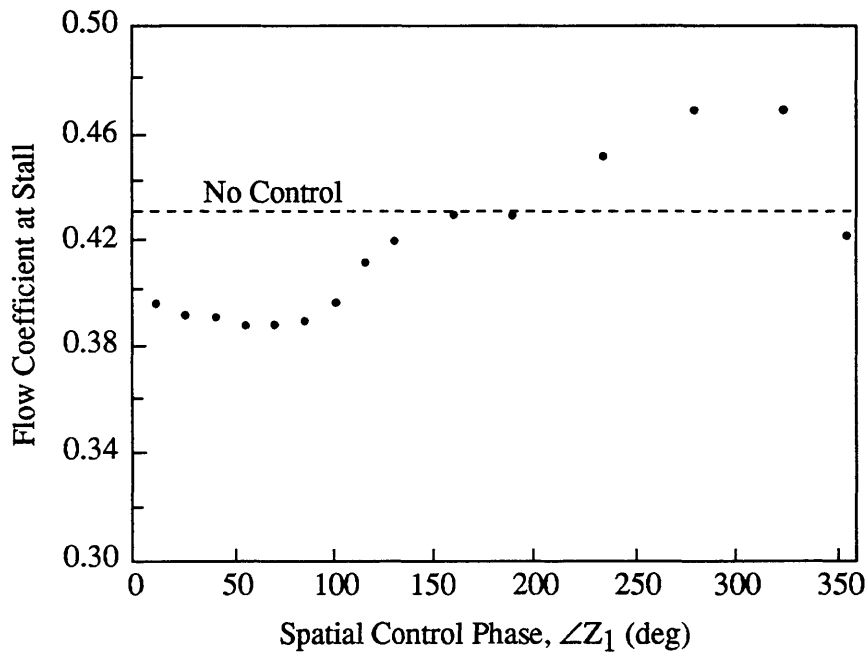


Figure 6.2- Effect of feedback phase on the stall flow coefficient.

rotating stall. In this section, we showed the effect of first mode stability on the stall point. The following sections show that the stability of higher modes is also important in determining the stall point.

6.1.2 Speed Lines

The total-to-static pressure rise drops sharply when rotating stall is encountered. Thus the pressure/flow characteristic, or speed line, is a steady-state measurement which indicates the flow coefficients for which the system is stable. It also shows the pressure rise performance of the compressor in the new, stabilized regime.

Figure 6.3 shows the speed line for various levels of stabilization - no control, Z1 control, Z1+Z2 control, and Z1+Z2+Z3 control. As the number of modes stabilized increases, the minimum flow coefficient at which the system can operate is reduced. Z1 control results in approximately 11% reduction in stall flow coefficient, Z1+Z2 control gives about 18% reduction, and Z1+Z2+Z3 control gives about 23% reduction.

The data points on the speed line in Figure 6.3 were taken at 10 second intervals, so the compressor was operating for at least 10 seconds at each flow coefficient shown. Operation for longer periods of time at the lowest values of $\bar{\phi}$ on this plot is usually not possible. In other words, these points are very near instability, so the uncontrolled modes are strongly resonant; eventually the system 'trips' into a nonlinear rotating stall condition. However, if the flow coefficient is increased by 2 or 3% above the minima shown in Figure 6.3, then 5 to 10 minute periods of operation have been recorded, and there is every reason to believe that the system could operate indefinitely. This description of the stall behavior applies whether or not the feedback loop is closed; even in the no control case, the flow coefficient must be increased slightly to avoid eventually tripping into rotating stall. We conclude,

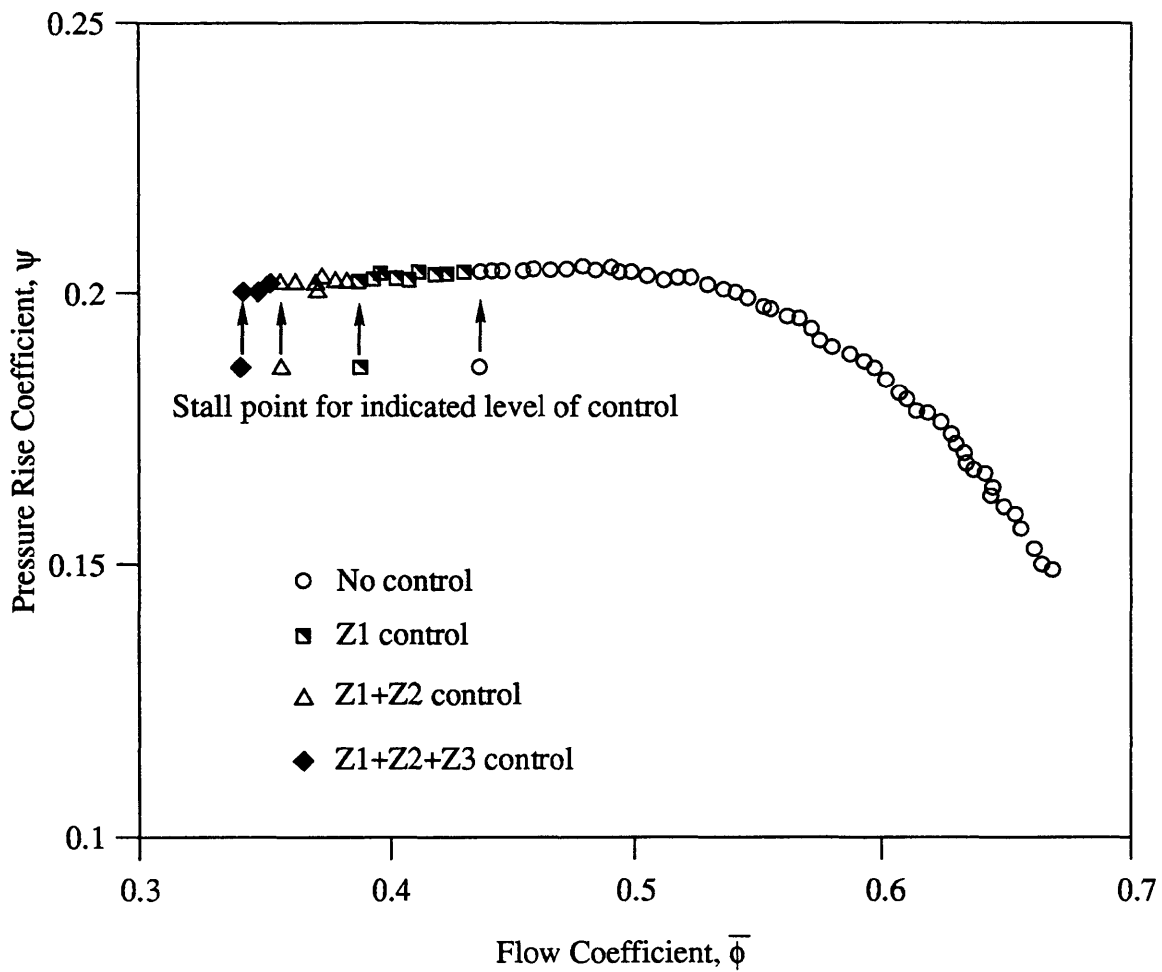


Figure 6.3 - Speed lines for various levels of active control

therefore, that the percentage reduction in flow coefficient for 'indefinite operation' is probably very similar to the values given above for '10 seconds of operation'.

The speed lines can be interpreted as follows: adding an extra mode to the control scheme, without changing anything else, reduces the stall flow coefficient. Therefore, the extra mode must have been responsible for stall. Results in the following sections clearly demonstrate that this is in fact the case.

6.1.3 Stall Events

We can judge the cause of stall in more detail by looking at the time-resolved stall event. A circumferential array of hot wires records the axial velocity distribution around the annulus at the inception of rotating stall, at a sample rate of 500 Hz (11.1 samples per rotor rev). The velocity traces can be studied directly, or they can be transformed into spatial Fourier coefficients (see discussion in Section 4.1.2), which can also be plotted as time functions.

Since the SFCs are complex numbers, their magnitude and phase are plotted separately as functions of time. Phase is usually confined between $-\pi$ and π , because phases outside this range are indistinguishable from those inside this range. But when a wave is traveling around the annulus, its phase as a function of time is continuously increasing, which causes a plot confined between $-\pi$ and π to repeatedly 'jump' as in Figure 6.4. These jumps cause confusion in noisy situations. To remedy this confusion, the phase is 'unwrapped' so that it is no longer constrained to lie between $-\pi$ and π ; an example of unwrapped phase is also shown in Figure 6.4. Such unwrapping must be done carefully to avoid misleading results - every time the phase passes from π to $-\pi$ or from $-\pi$ to π sufficiently quickly, one must judge whether the wave actually travelled forward or backward across the π / $-\pi$ boundary. If done properly, unwrapping does not presuppose rotation in any specific direction: in highly damped cases, the phase executes a random walk and shows no preferred direction of rotation.

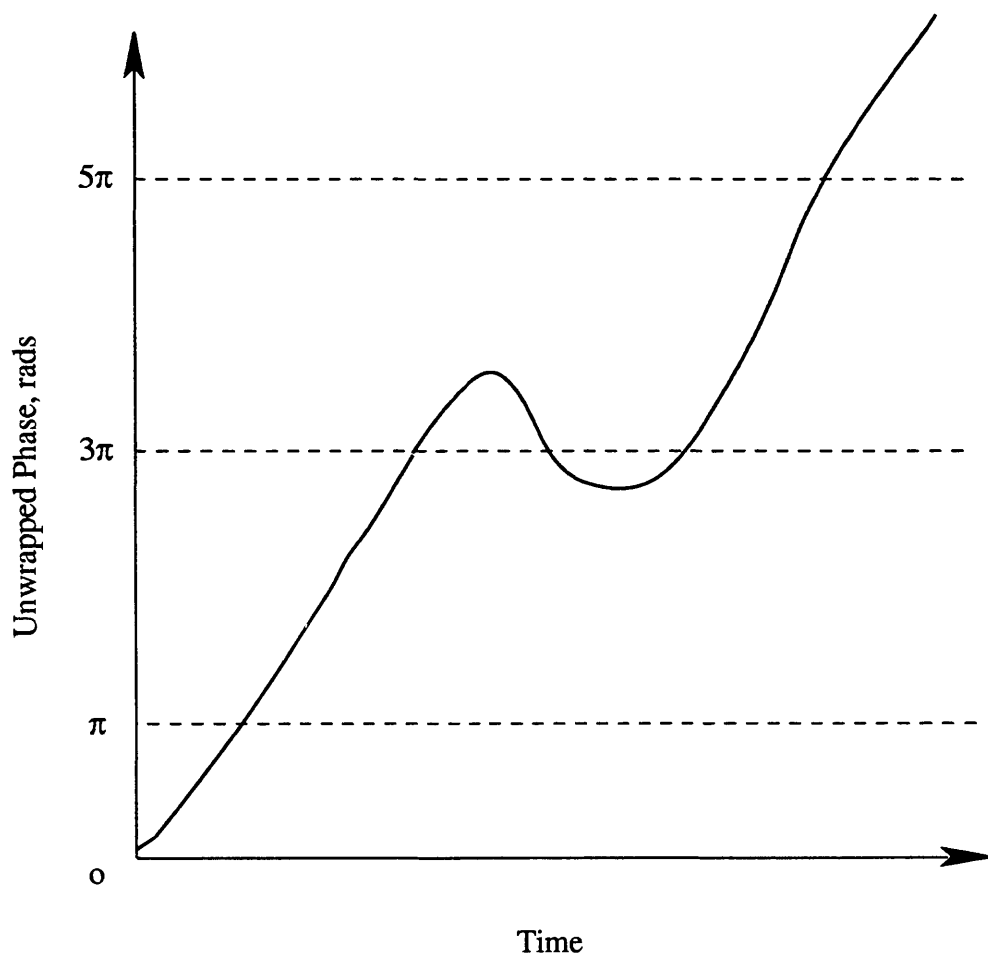
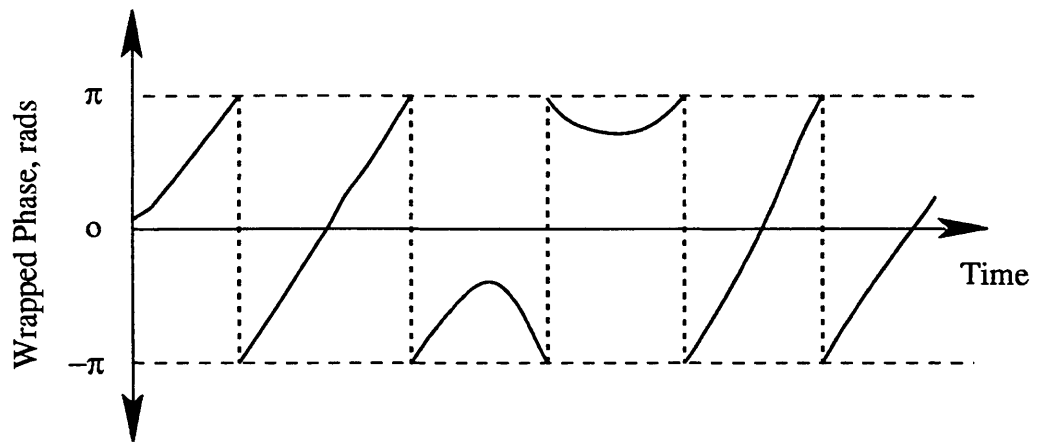


Figure 6.4 - Examples of wrapped and unwrapped phase plots

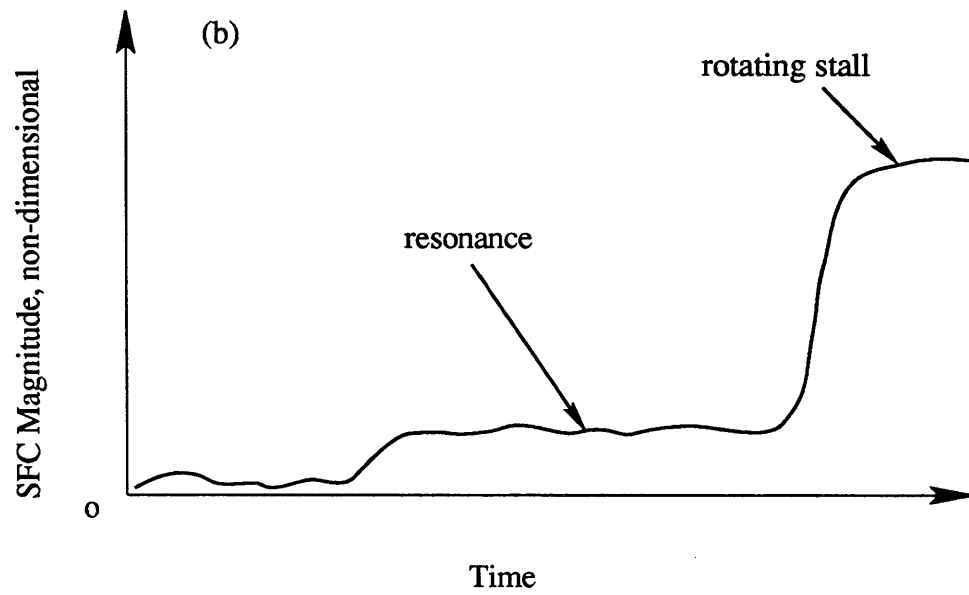
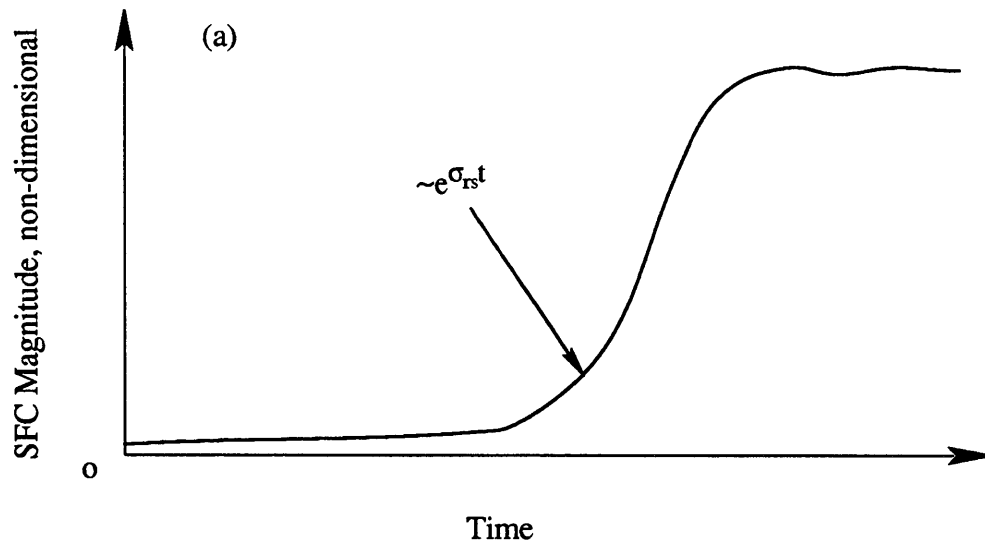


Figure 6.5 - Examples of (a) exponential growth into stall and (b) resonance leading into stall

The magnitude of the n^{th} SFC indicates the size of the n^{th} wave of velocity perturbation. If the mode is unstable, this magnitude should increase exponentially, as $e^{\sigma_{rs}\tau}$, where σ_{rs} is the stability parameter for the n^{th} mode. Since the flow coefficient is being reduced very slowly in the experiments described here, σ_{rs} for the unstable mode should go through zero and become slightly positive immediately prior to stall. Alternatively, the system could resonate very strongly while σ_{rs} is still negative (stable), eventually tripping (via some non-linear coupling) the compressor into a rotating stall condition. These two possibilities are illustrated in Figure 6.5.

Another possibility is that the system stalls in a way which is not 'modal' at all - in this case, no traveling waves or resonance of the modes would be sensed prior to stall. Furthermore, the transient into stall would not be initiated by a single mode, but instead would involve several modes. Stall must eventually show up in the SFCs, because they are derived from signals which directly measure the effects of fully-developed rotating stall. But if stall inception is not dominated by modal behavior, the transient signals will 'smear' across several SFCs, and no single mode will be clear.

Figure 6.6 shows the hot wire traces as the system goes into stall with no control. A traveling wave is extremely clear prior to stall - the dotted line in Figure 6.6 indicates how a trough in the waves travels from one hot wire to the next, suggesting a wave pattern rotating around the annulus [17]. Apparently the system is resonating strongly prior to stall, and then the traveling wave grows smoothly into stall. Figure 6.7 shows the SFCs computed from these hot wire traces. Here we see definitely the dominance of the first mode. The phase plot indicates that the first mode is rotating at a steady speed for at least 40 rotor revolutions before stall. It grows to a magnitude of 0.1 (30% of its final size) before there is any significant contribution of the second or third modes to the wave (measured at the upstream hot wire position). Clearly, the first mode is the unstable mode which is driving the

system into rotating stall.

Figure 6.8 and 6.9 show the stall event for Z_1 control. Again a traveling wave is clear in the raw hot wire data, but the frequency of the resonance is higher - closer inspection of the hot wire traces reveals that there are two lobes of axial velocity deficit traveling around the compressor immediately prior to stall. The SFCs make this behavior clearer - the magnitude of the second mode is now dominating the signals, and the phase indicates that the wave is rotating at a steady speed for 25 rotor revolutions before stall. The second mode is undoubtedly resonating in this case, while the first mode is relatively well damped. The stall event is initiated by the growth of the second mode. In fact, the fully developed stall cell is a two lobed stall! Thus we have powerful evidence that the 1st mode (now under active control) is still stable when the system goes into rotating stall. It is the second, as yet uncontrolled, mode which is causing rotating stall.

The data in Figures 6.8 and 6.9 are taken at a lower flow coefficient than the no control data (Figures 6.6 and 6.7), so the dynamics of the compressor have changed. The first mode open-loop stability has changed somewhat (see Section 5.3.2), but the value of Z_1 chosen is still capable of stabilizing it. The second mode, however, has gone from stable to unstable with the flow coefficient reduction. Therefore, we must add Z_2 to the control law if we want to operate at lower flow coefficients.

Figures 6.10 and 6.11 show stall with Z_1+Z_2 control. Because we are looking for the third or higher modes, this data was taken with 13 hot wires downstream of the IGVs. At this axial location, the modes (especially those with large n) are no longer attenuated. But the signals are noisier due to the proximity to the rotor, and modes above the spatial Nyquist mode may alias down into the estimates of the first four modes, corrupting them. Consequently, discerning the cause of stall by studying these figures is more difficult. Nevertheless, the hot wire traces show a clear

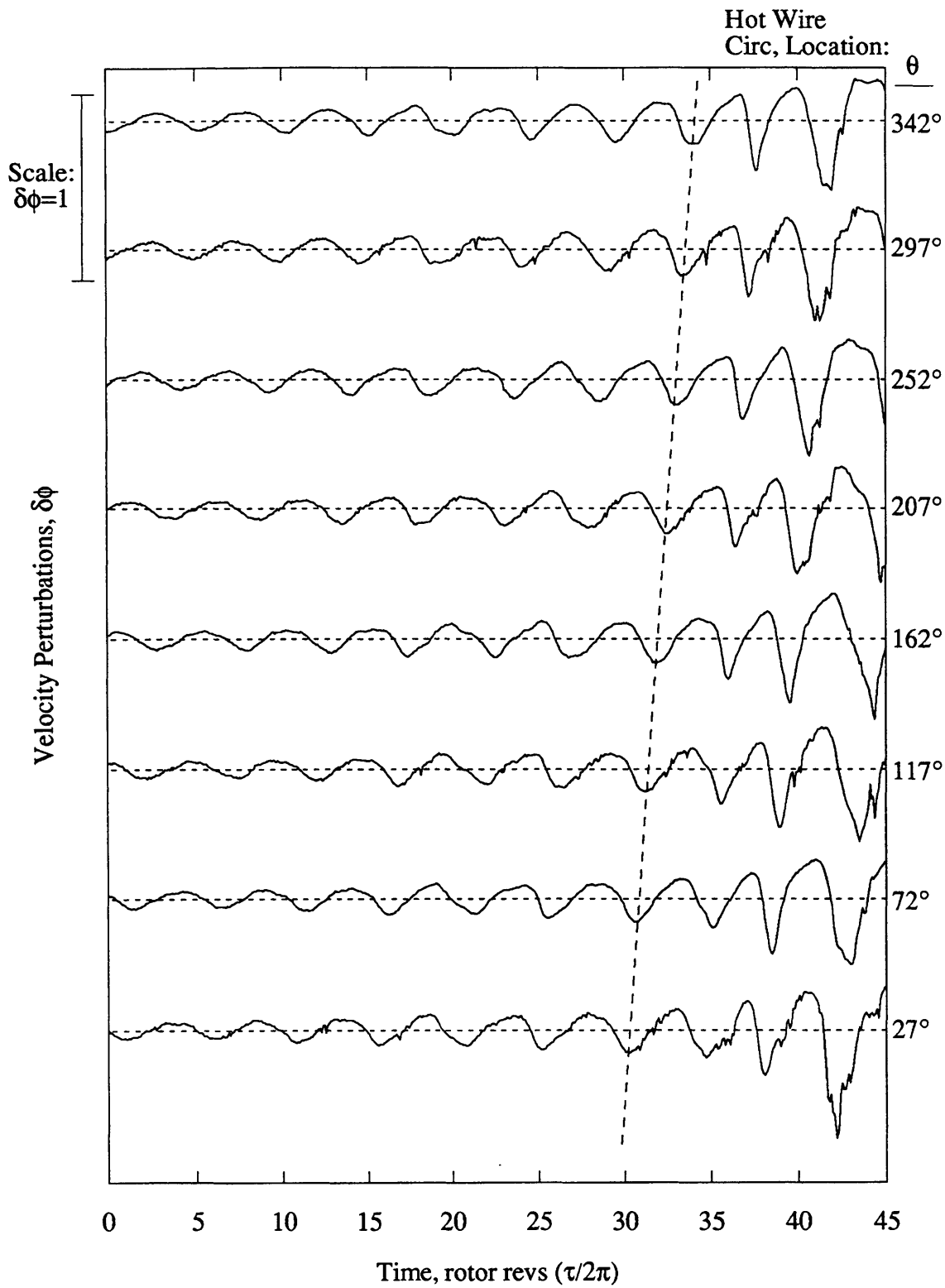


Figure 6.6 - Hot wire traces for a stall event with no control.
 $\bar{\phi} = 0.44$, hot wires upstream of IGVs

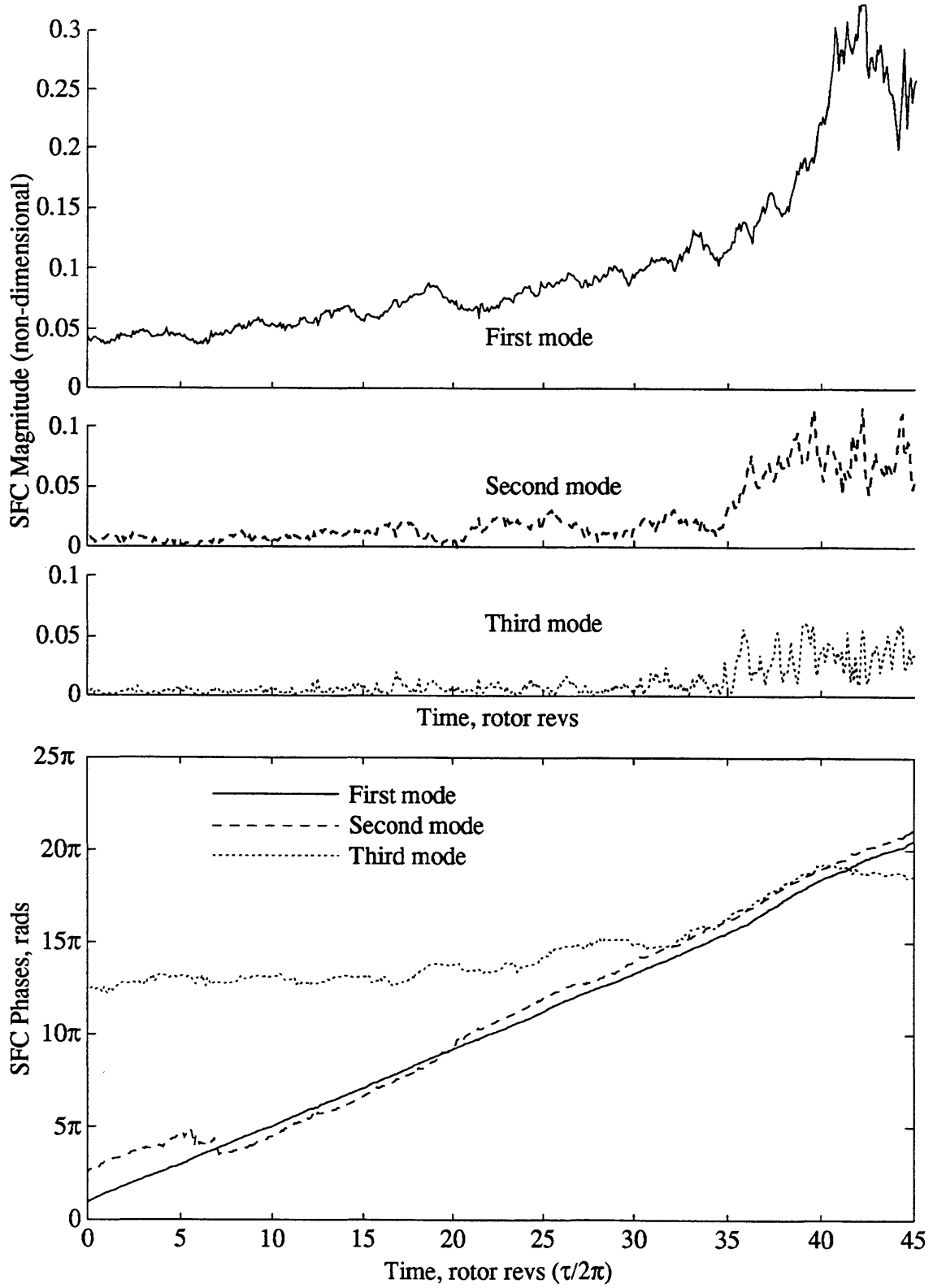


Figure 6.7 - Magnitude and phase of first three Fourier coefficients during the stall event with no control, computed from the hot wire data in Figure 6.6.

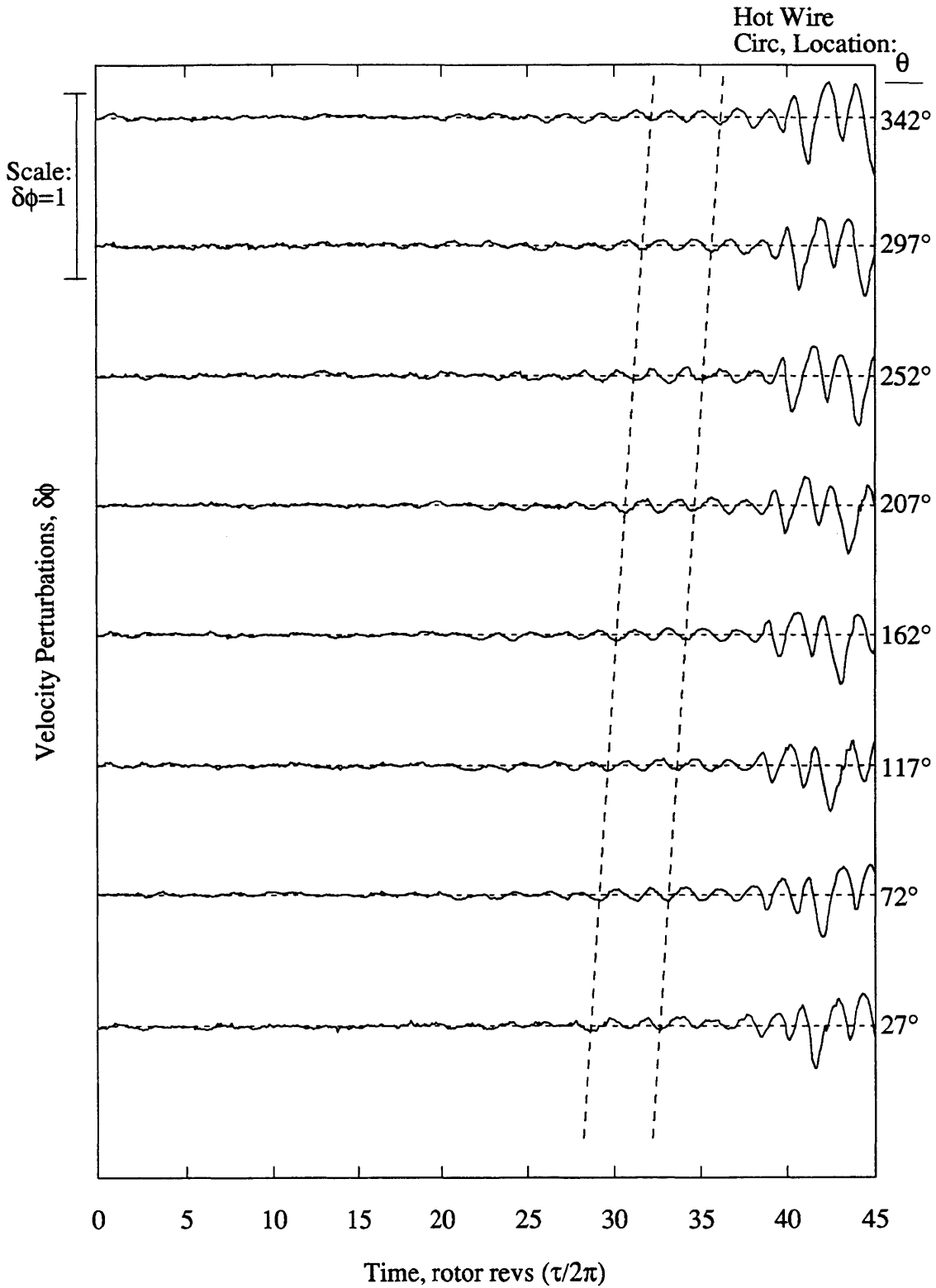


Figure 6.8 - Hot wire traces for a stall event with Z1 control.
 $\bar{\phi} = 0.39$, Hot wires upstream of IGVs
 $|Z1| = 10$, $\angle Z1 = 60^\circ$

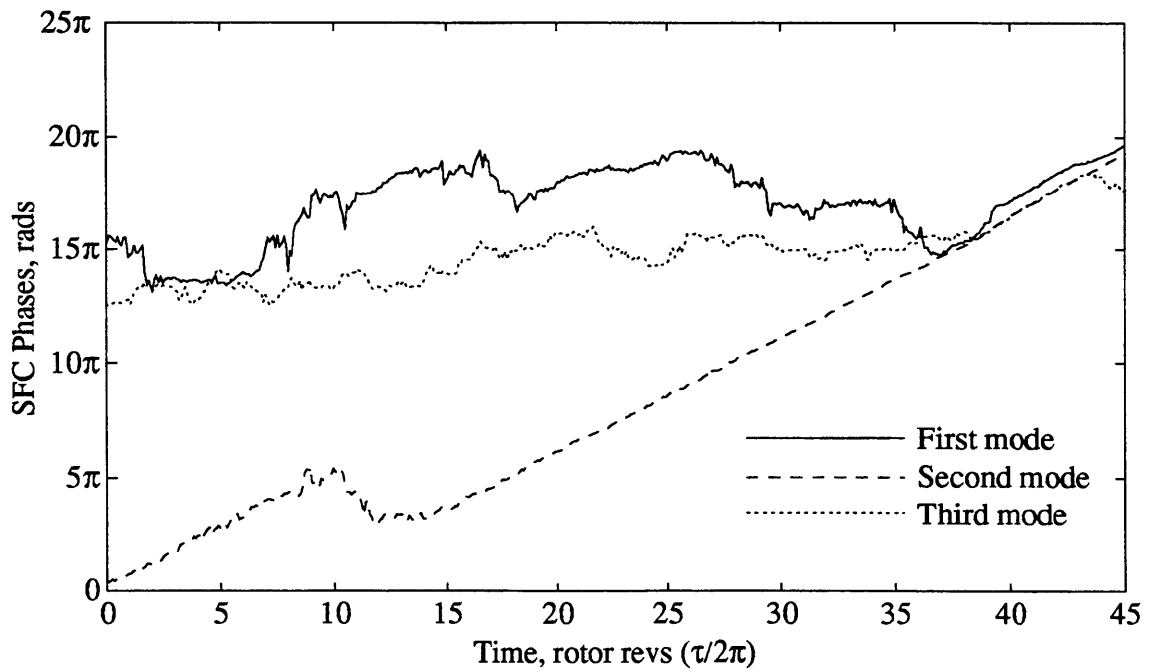
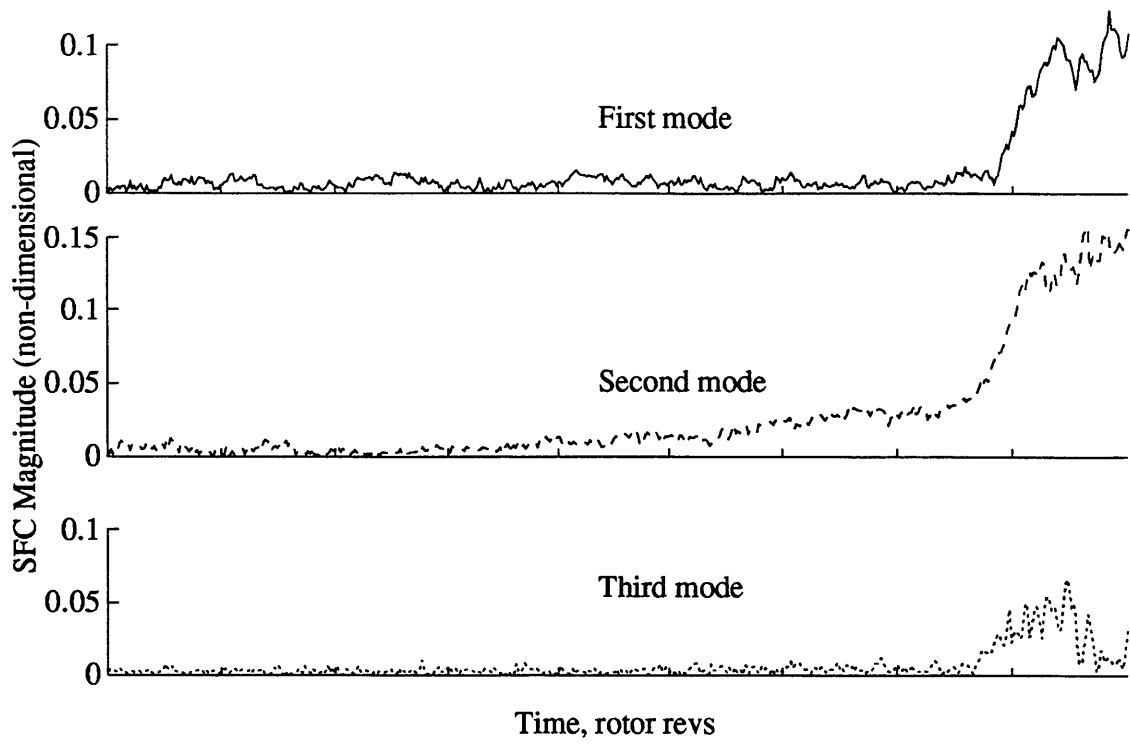


Figure 6.9 - Magnitude and phase of first three Fourier coefficients during a stall event with Z1 control, computed from the hot wire data in Figure 6.8 .

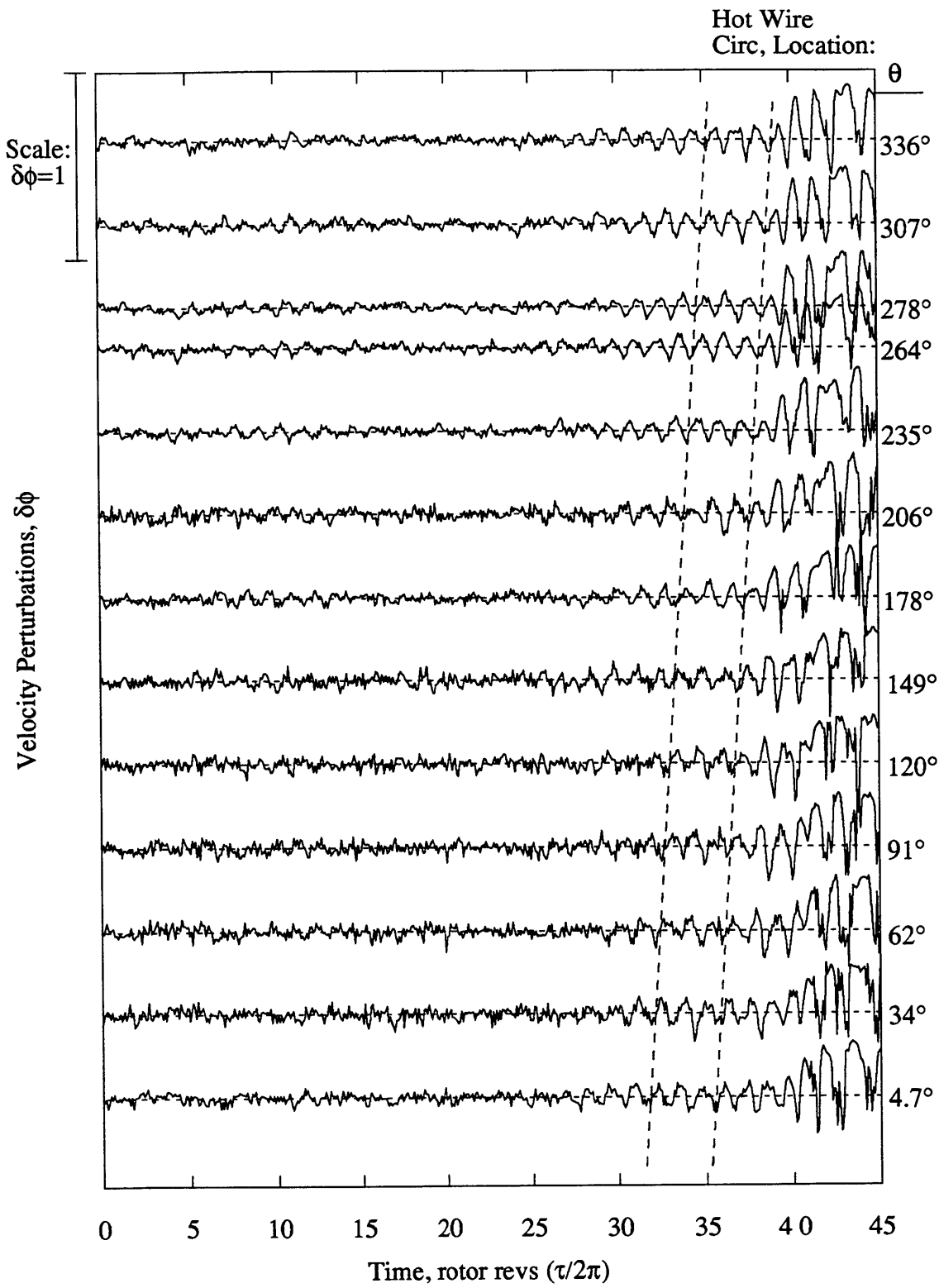


Figure 6.10 - Hot wire traces for a stall event with Z1+Z2 control
 $\bar{\phi} = 0.36$, Hot wires downstream of IGVs
 $|Z1|=10, \angle Z1=30^\circ; |Z2|=6, \angle Z2=80^\circ$

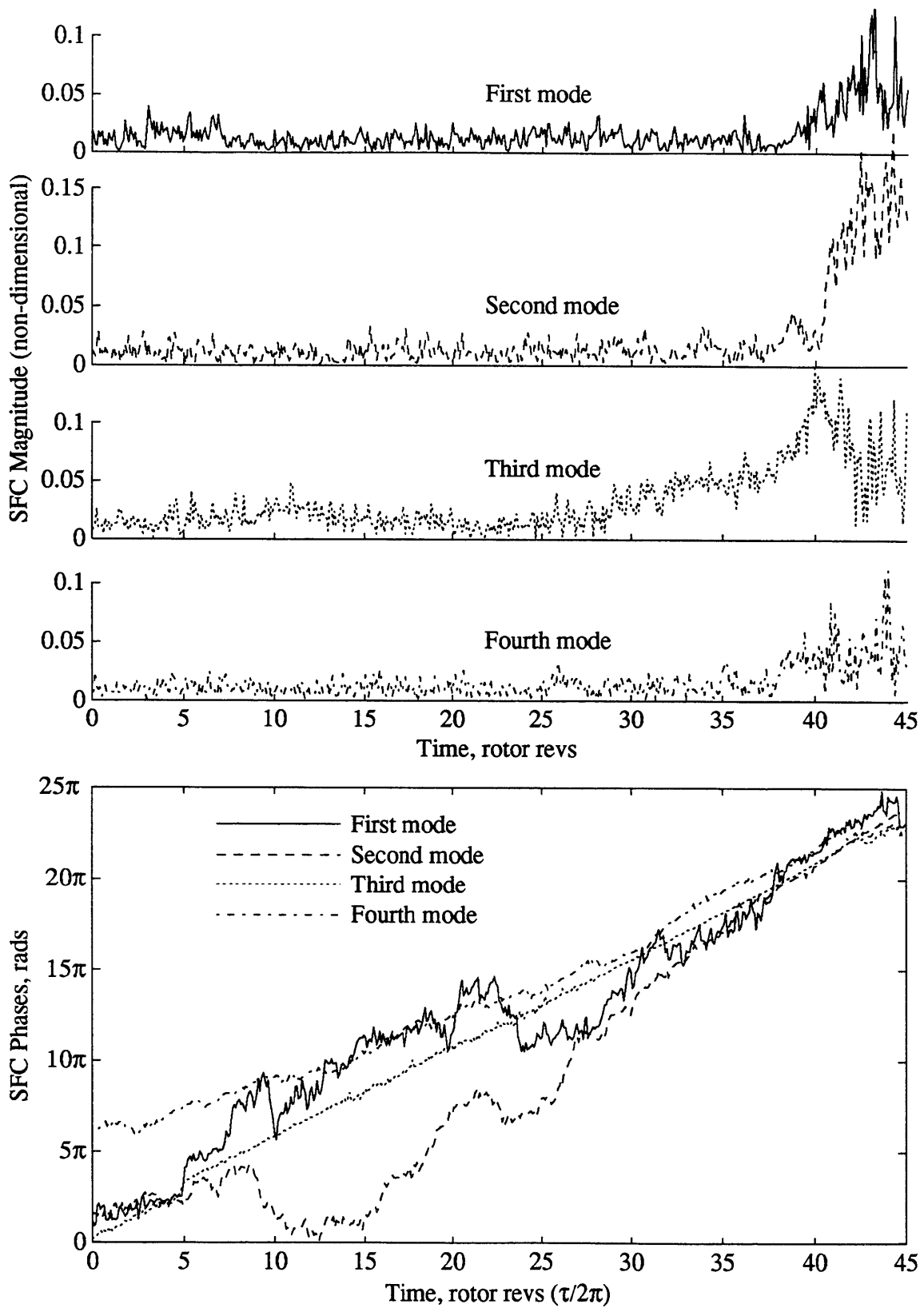


Figure 6.11 - Magnitude and phase of first four Fourier coefficients during a stall event with Z1+Z2 control, computed from the hot wire data in Figure 6.10.

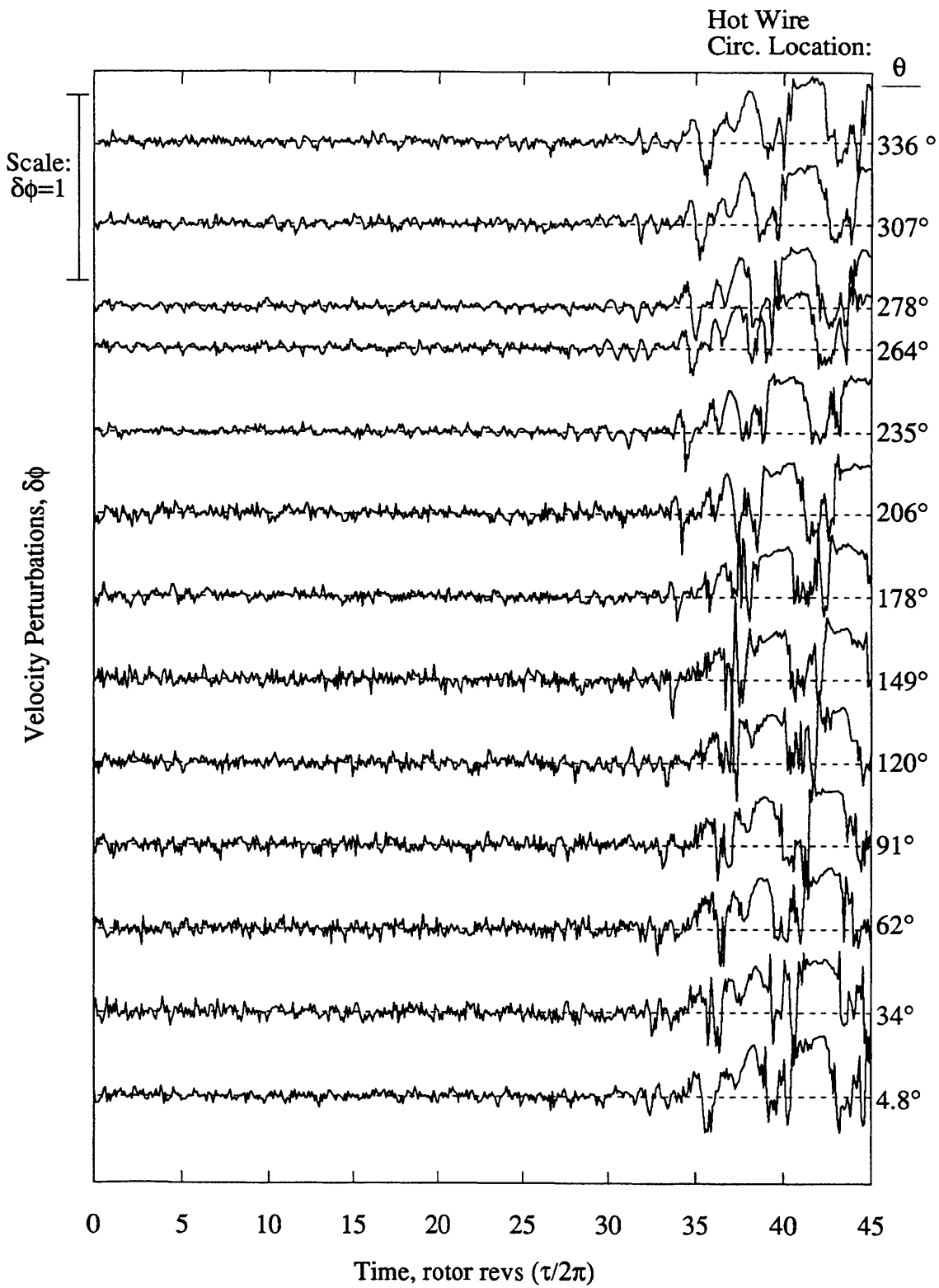


Figure 6.12 - Hot wire traces for a stall event with Z1+Z2+Z3 control
 $\bar{\phi} = 0.36$, Hot wires downstream of IGVs
 $|Z1|=10, \angle Z1=30^\circ; |Z2|=6, \angle Z2=80^\circ; |Z3|=3.5, \angle Z2=100^\circ$

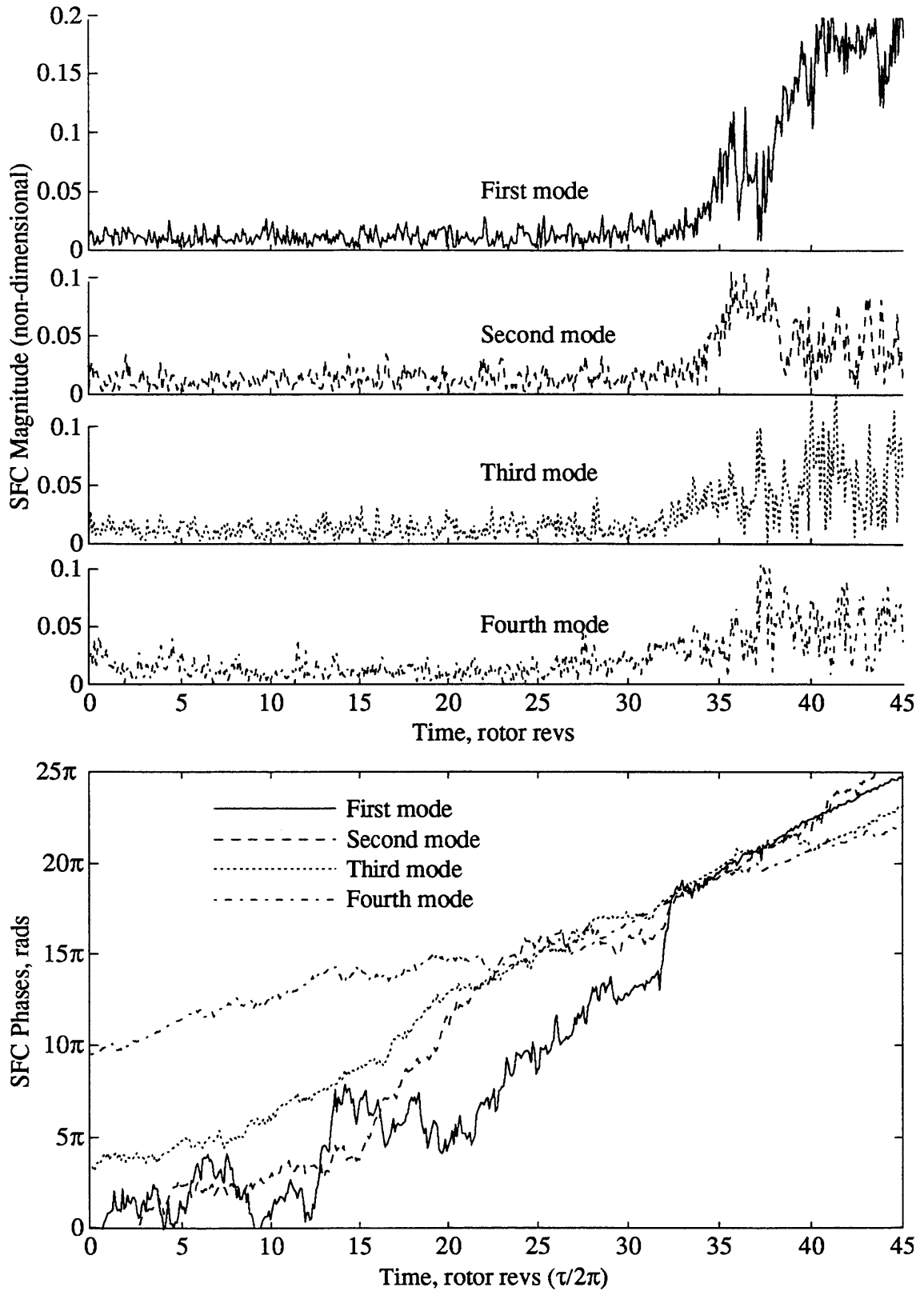


Figure 6.13 - Magnitude and phase of first four Fourier coefficients during a stall event with Z1+Z2+Z3 control, computed from the hot wire data in Figure 6.12.

resonance prior to stall at an even higher frequency than that seen in Figure 6.8. The plots of the SFCs also clearly show a resonance in the third mode immediately prior to stall. However, the first and second modes become large within 5-10 rotor revolutions of the appearance of a strong third mode. Fully developed stall is primarily second mode.

This data for Z_1+Z_2 control suggests that as the flow coefficient is reduced, stall behavior becomes more complicated. The third mode resonates, but does not go unstable independently. Instead, interaction between modes occurs at stall inception. The clear resonance of the third mode, as well as the PSD results of the next section do confirm, however, that the third mode is underdamped immediately before stall, so $Z_1+Z_2+Z_3$ control is justified.

Figures 6.12 and 6.13 show stall with $Z_1+Z_2+Z_3$ control. Data is again taken behind the IGVs. Here it is difficult to see resonance of the fourth mode in either the hot wire traces or the SFCs. Also note strong spikes in the hot wire traces at stall inception. The phase plots in both Figure 6.11 and 6.13 indicate, however, that the fourth mode is traveling prior to stall. Such traveling indicates that the fourth mode is either resonating, or being driven at its natural frequency. Results of the next section confirm that the fourth mode does play a part in the compressor dynamics at stall inception during $Z_1+Z_2+Z_3$ control.

6.1.4 Power Spectra

Spectral analysis of the SFCs offers another way to look at the behavior of the system, to help determine the causes of stall. The procedure is to plot the power spectral density (PSD) of each SFC during a period prior to stall. The stall event itself is not a part of the analysis, so the spectra show resonant behavior which exists in the small amplitude (linear) behavior of the system rather than the nonlinear limit cycle behavior. Analyzing the SFCs in this way helps verify our claim that, even

before stall inception, the SFCs behave like a set of decoupled linear oscillators.

Because the SFCs are *complex* functions of time, the PSDs are not symmetric with respect to zero frequency, as is usually the case. This is true because, for a complex signal, the sign of the frequency has a very specific meaning. In the context of rotating stall, the sign of the frequency indicates the *direction of rotation of the wave*. To see this, consider a first-mode SFC whose PSD is a delta function at some frequency ω_d *alone*; that is, there is no peak at $-\omega_d$. The time-domain signal for this PSD is

$$\tilde{\phi}_1(\tau) = e^{j\omega_d\tau}, \quad (6.2)$$

i.e. a complex signal. Converting this back to the spatial domain, we have

$$\begin{aligned} \delta\phi(\theta, \tau) &= \text{Re}\{ \tilde{\phi}_1^*(\tau) \cdot e^{i\theta} \} \\ &= \cos(\theta - \omega_d\tau), \end{aligned} \quad (6.3)$$

i.e. a rotating wave, *whose direction of rotation depends on the sign of ω_d* . A PSD which is symmetrical indicates a standing wave with oscillating amplitude:

$$\begin{aligned} \tilde{\phi}_1(\tau) &= e^{j\omega_d\tau} + e^{-j\omega_d\tau} \\ \Rightarrow \delta\phi(\theta, \tau) &= \text{Re}\{ 2 \cdot \cos(\omega_d\tau) \cdot e^{i\theta} \} \\ &= 2 \cdot \cos(\omega_d\tau)\cos(\theta). \end{aligned} \quad (6.4)$$

Here we see that ω_d is the rate at which the standing wave *magnitude* changes with time, rather than the rotation rate of the wave.

With this explanation we see that when we plot a PSD, we must plot both the negative and positive frequencies, preferably flipping the negative frequency plot to overlay with the positive frequency plot. Then, only the peaks which do not exist at both negative and positive frequencies indicate waves which rotate.

Figures 6.14 through 6.17 present the PSDs for no control, Z1 control, Z1+Z2 control, and Z1+Z2+Z3 control. Each set of PSDs is taken immediately prior to the stall event, which is a different flow coefficient in each case.

The behavior of the modes is clear in these figures. The controlled modes in

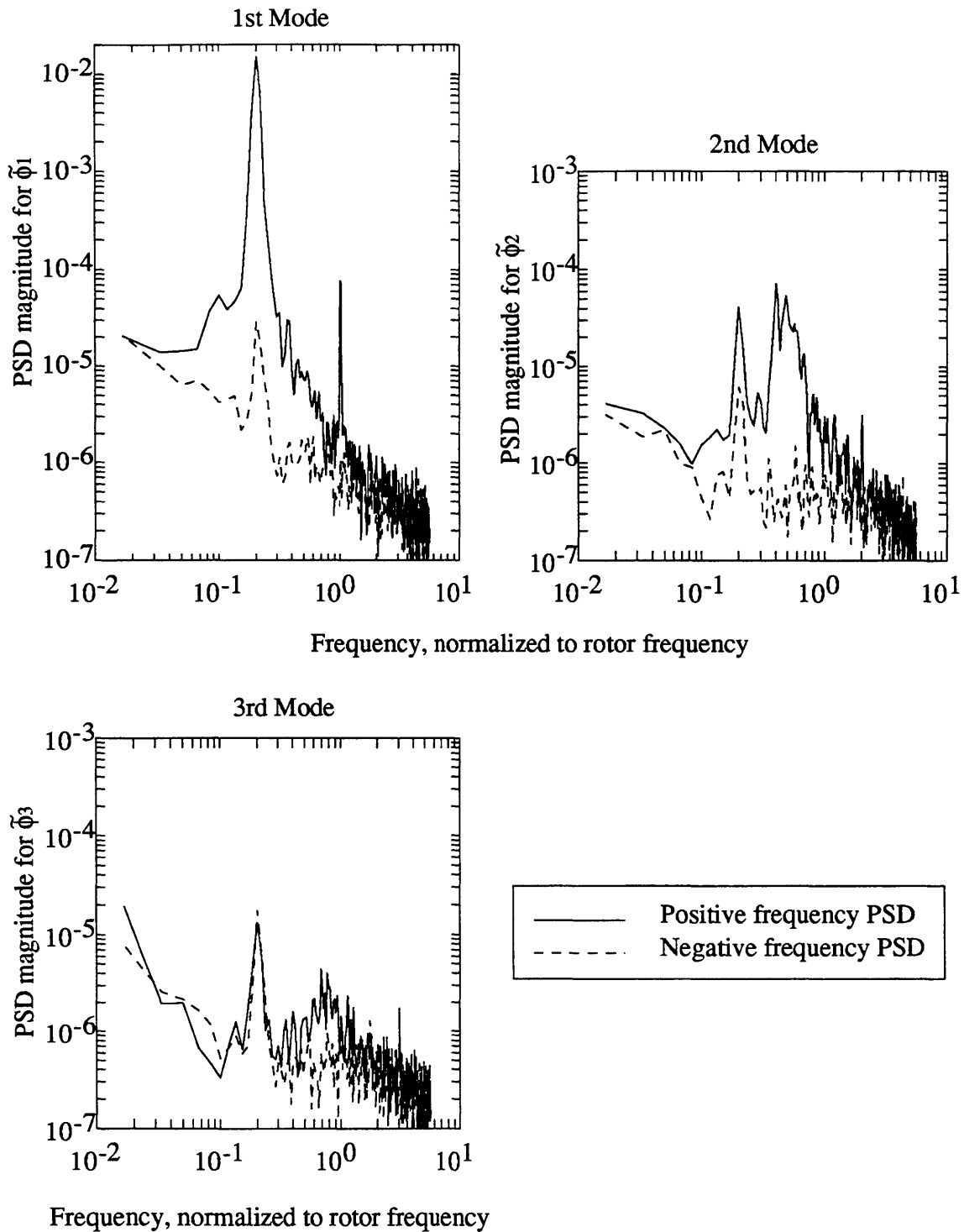


Figure 6.14 - PSDs of the first three SFCs, using data immediately prior to stall, with no control (i.e. open loop). $\phi = 0.44$, Hot wires upstream of IGVs.

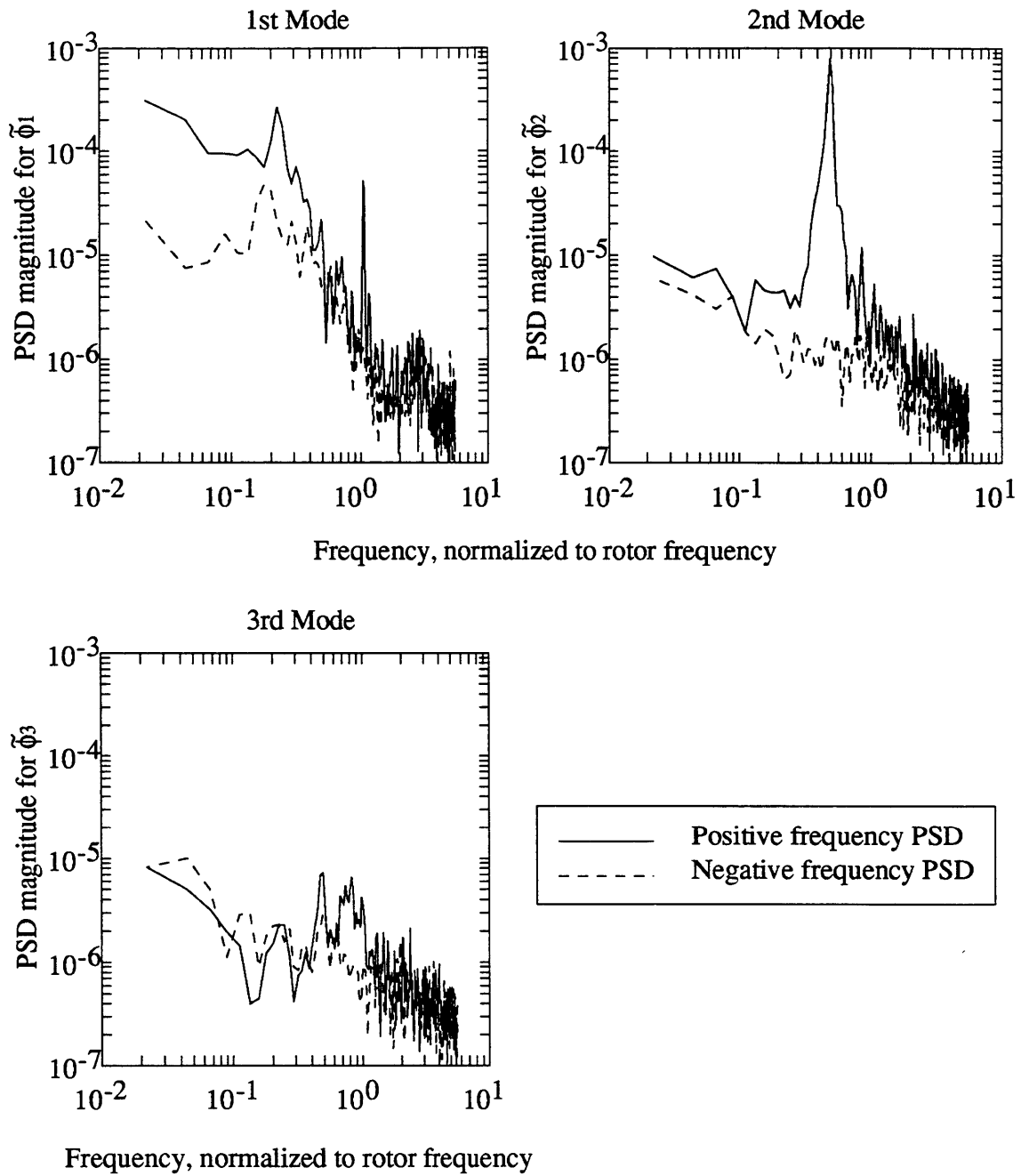


Figure 6.15 - PSDs of the first three SFCs, using data immediately prior to stall, during Z1 control. $\bar{\phi} = 0.39$, Hot wires upstream of IGVs $|Z1|=10, \angle Z1=60^\circ$

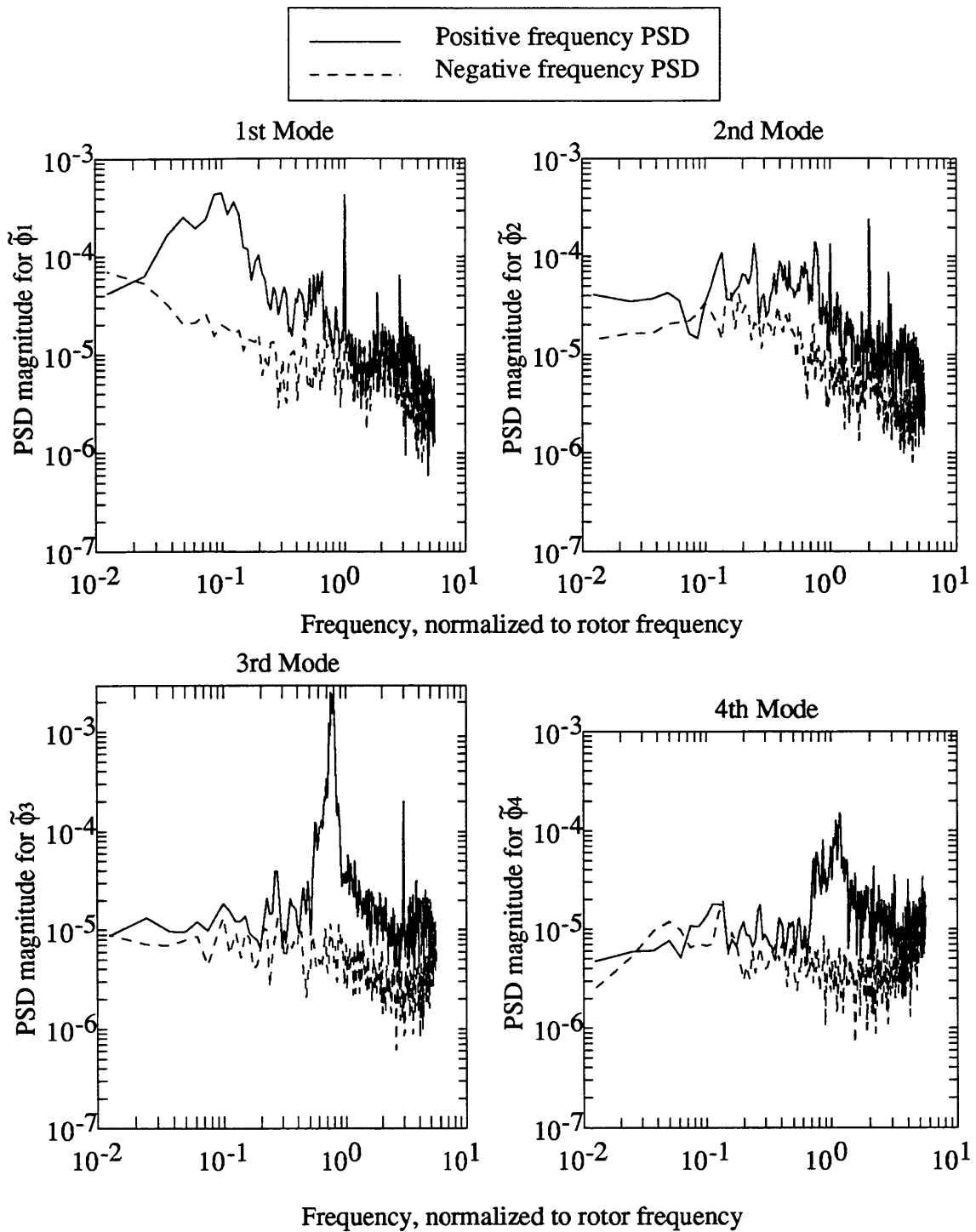


Figure 6.16 - PSDs of the first four SFCs, using data immediately prior to stall, during Z1+Z2 control. $\bar{\phi} = 0.36$, Hot wires downstream of IGVs $|Z1|=10, \angle Z1=30^\circ; |Z2|=6, \angle Z2=80^\circ$

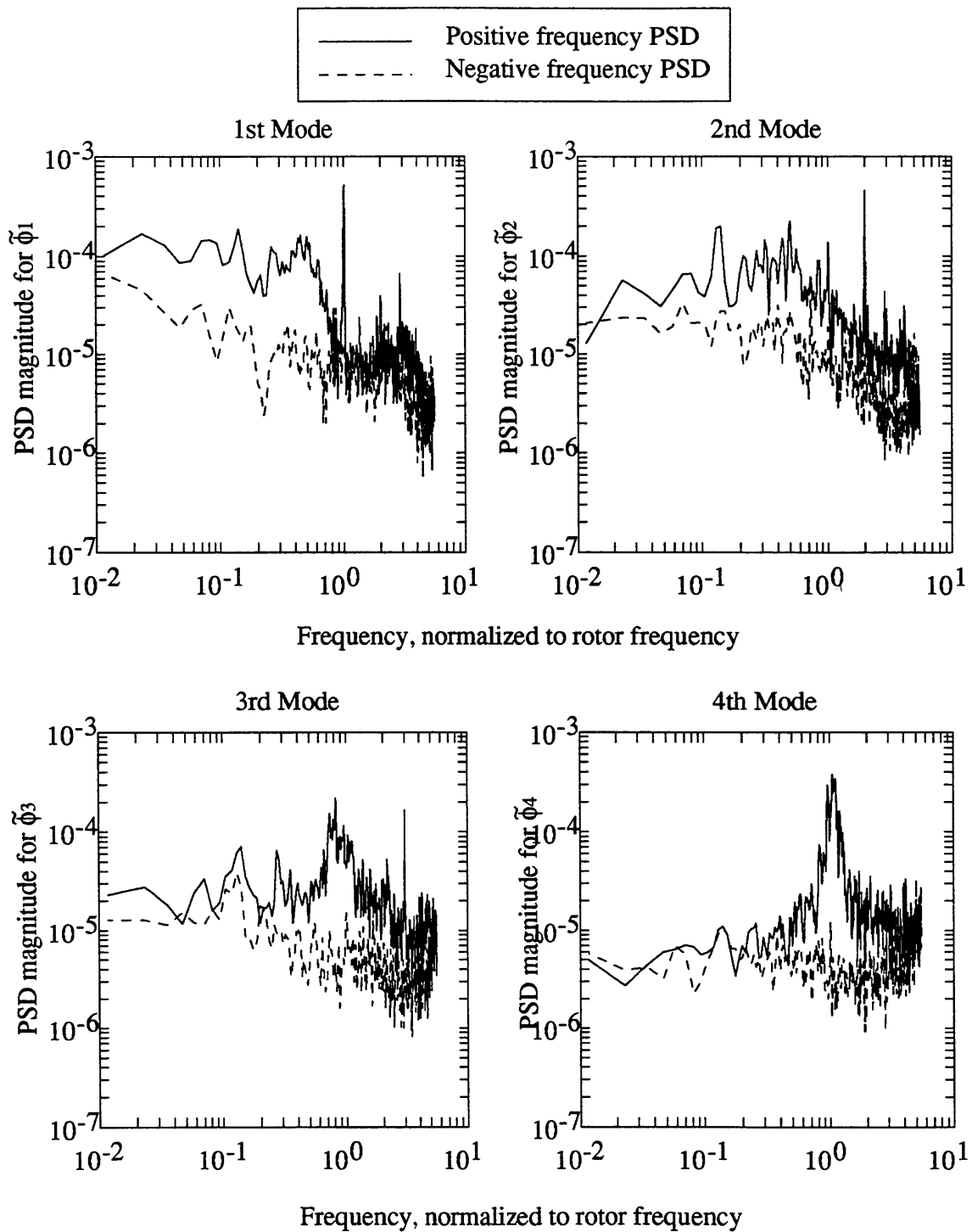


Figure 6.17 - PSDs of the first four SFCs, using data immediately prior to stall, during Z1+Z2+Z3 control.

$\bar{\phi} = 0.36$, Hot wires downstream of IGVs
 $|Z1|=10, \angle Z1=30^\circ; |Z2|=6, \angle Z2=80^\circ; |Z3|=3.5, \angle Z3=100^\circ$

each case are seen to be adequately damped, exhibiting low, wide peaks at their natural frequencies. The lowest uncontrolled mode *in every case* shows a strong, narrow peak, indicating resonance of that mode. These resonating modes do tend to *rotate* at their natural frequency, so that negative frequencies show no peaks. This data further validates the claim that under control of a certain number of modes, stability will persist until the next higher mode goes unstable. Even in the Z1+Z2 and Z1+Z2+Z3 control cases, for which the results of the previous section were unclear, the pattern is obvious. Most notable is the strong presence of the *fourth* mode when the first three modes are being stabilized (Figure 6.17). Whatever other effects are present in the Z1+Z2 and Z1+Z2+Z3 case, resonance of the lowest uncontrolled mode is definitely a factor in the inception of rotating stall.

These PSDs also demonstrate the decoupled nature of the modes. In every case, although a strong peak (indicating a rotating wave) exists for one spatial mode (the lowest uncontrolled mode), such a strong rotating wave peak does not show up in the PSD of any other mode. This is extraordinary because all of the PSDs in a given figure are derived from the *same set of hot wire traces*. Thus it seems that the resonances are due entirely to a single spatial eigenmode rotating around the annulus.

One can detect discrepancies from the decoupled behavior described above. For instance, in the no control case (Figure 6.14), there are small peaks at ~ 0.20 (which is the first mode rotation frequency) in the PSDs of the 2nd and 3rd modes. Notice, however, that these peaks appear in *both* the negative and the positive frequency plots, indicating *standing waves* in the 2nd and 3rd mode. These peaks could be due to slight miscalibration of the hot wires, or due to nonlinear coupling of higher modes into the traveling wave. In any case, these peaks are small compared to the first mode peak, and resonance of the first mode is clearly the primary effect.

Figures 6.16 and 6.17 also show some slight cross-over of spectral peaks, this time between the 3rd and 4th modes. Again, this could indicate measurement

difficulties, or some coupling between the modes. Such intermode coupling may become important at very low flow coefficients, and the nonlinear stall event itself may be dominated by such coupling. But, for the flow coefficients studied by these PSDs, treating the modes as independent entities is clearly a good approximation, and stabilizing the modes separately yields results which are largely consistent with our assumptions.

6.1.5 Discussion

Most of the hypotheses advanced at the beginning of this section have been experimentally verified. We will briefly summarize here.

- A) Both the homogeneous and the forced dynamics of the SFCs behave as though they are decoupled. Thus $e^{in\theta}$, $n = 1, 2, 3, \dots$ can be treated as the mode shapes of the distributed dynamics.

The PSDs provide the most direct evidence of the decoupled nature of the SFCs. A resonance occurs in only one mode at a time, showing up in only one of the 3 or 4 PSDs shown in each of Figures 6.14 through 6.17. There seems to be little 'cross-feed' of resonance peaks between the modes, even when some modes are under feedback control. Apparently, forcing the system does not couple the modes (in the limited sense) either. In fact, by keeping the magnitudes of the controlled modes small, feedback may actually reduce coupling between modes, because waves with smaller amplitudes should behave more linearly.

Also supporting point A is the fact that designing control laws in a mode-by-mode fashion successfully stabilizes the system. From a pragmatic viewpoint, treating the system modally is very useful.

- B) Mode numbers 1, 2, and 3 go from stable to unstable at separate flow coefficients, sequentially as flow coefficient is reduced.

The stall inception data, as well as the PSDs, indicate that stabilizing m modes is sufficient to stabilize the compressor down to the flow coefficient at which mode $m+1$ becomes either unstable or very lightly damped. This has been shown to

be the case for $m = 0, 1,$ and $2.$

At larger values of $m,$ several effects obscure the ability to draw conclusions. Modes higher than the third are difficult to measure with a limited number of hot wires. Since these modes are highly attenuated upstream of the compressor, the hot wires must be moved behind the IGVs. But, at this position, the signal to noise ratio is lower [22], and modes above the Nyquist frequency are also potentially large. These modes alias into the measurements and corrupt them. Finally, control of three modes with 12 IGVs is a coarse approximation, and cross-coupling to modes above the Nyquist frequency may be significant.

Because of these difficulties, the stall inception data does not show unequivocally that the fourth mode is responsible for stall when three modes are under control. The PSD data does show, however, that the fourth mode becomes lightly damped.

- C) Decoupled proportional feedback of the modes is sufficient to stabilize the compressor, if appropriate spatial phase shift between measurement and actuation is provided.

The speed line data in Figure 6.3, and the hot wire traces presented in Sections 6.1.3 and 6.1.4 show that the approach to stabilization was successful. Thus the assumptions and approximations made in modeling the compressor and configuring the control system are justified from the point of view of stabilization. Section 6.2 discusses the importance of properly phase shifting (in space) the actuation wave with respect to the measured velocity perturbation wave.

6.2 Gain Determination Using Linear Control Theory

In the Section 6.1, experiments showed the qualitative accuracy and practical applicability of our view of the compressor as a linear, decoupled, modal dynamic system. Our qualitative understanding of the trends obeyed by the compressor dynamics led to a workable experimental procedure for determining stabilizing

feedback gains. In this section we briefly explore quantitative determination of feedback gains, using the compressor dynamics identified in Chapter 5. In Section 6.2.1, we show for an experimental example that linear control theory predicts the closed-loop behavior of the system accurately. In Section 6.2.2, we discuss feedback gain determination via the root locus method.

6.2.1 Prediction of Closed-Loop Performance

Active control of axial compressor higher-mode dynamics has not been studied in detail before the work presented here. One important issue is whether linear control theory sufficiently accounts for the main features of the process. The results of Chapter 5 indicate that the open-loop dynamics behave 'linearly' - that is, their input-output properties are accurately described by linear differential and difference equations. Section 6.1 then demonstrates that linear control concepts can be successfully applied to stabilize the compressor. To complete this picture, we will show that (for a limited set of experiments) the experimentally determined closed-loop compressor performance is similar to that predicted by linear control theory.

Closed-loop performance is measured as the transfer function between the external command and the measured output during closed-loop operation. Figure 6.18 serves to define the signals for the first mode: external commands, \tilde{r}_1 , enter the closed loop system and modify the feedback command, $Z_1 \cdot \tilde{y}_1$. This summed signal goes through the servo dynamics, $S(s)$, the compressor dynamics, $G_1(s)$, and the sensors and delays, $Q(s)$. Thus, the measured output is a filtered and delayed version of the first SFC, $\tilde{\phi}_1$. The theoretical closed-loop transfer function is

$$\frac{\tilde{y}_1(s)}{\tilde{r}_1(s)} = \frac{Q \cdot G_1 \cdot S}{1 - Q \cdot G_1 \cdot S \cdot Z_1} \quad (6.5)$$

where $Q(s)$, $S(s)$, and Z_1 are the known dynamics of the feedback system (presented

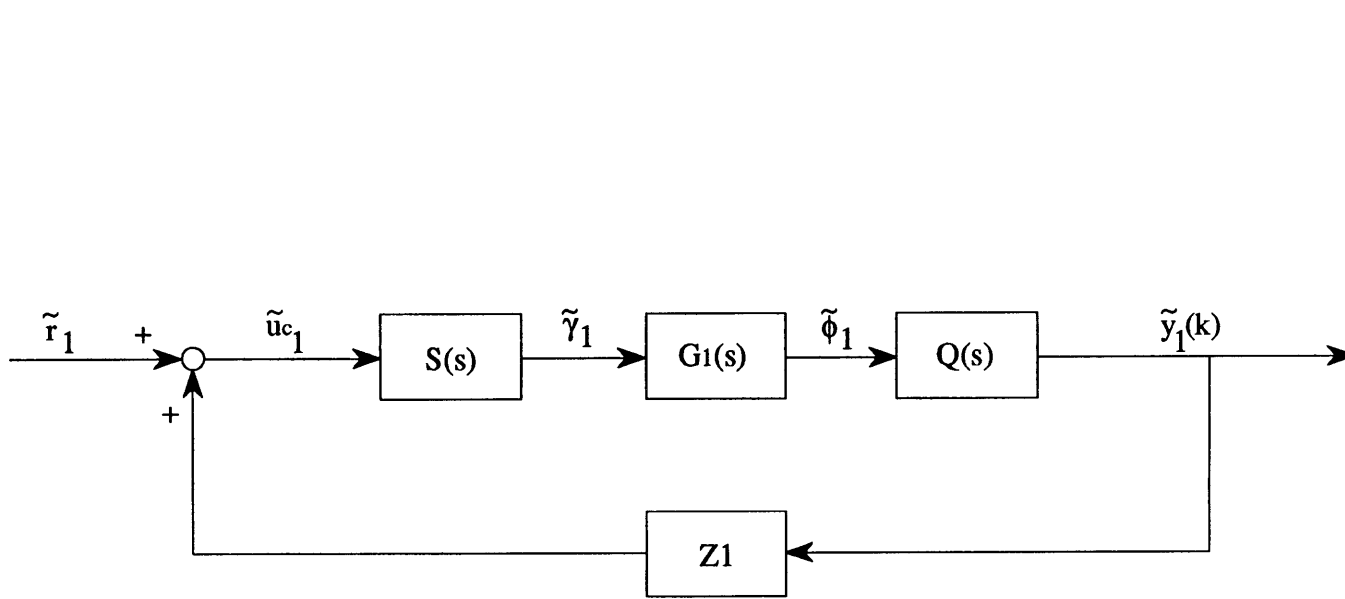


Figure 6.18 - Closed loop system notation

in Section 4.2), and $G_1(s)$ is the open-loop transfer function of the first SFC (the estimate of $G1(s)$ that we will use here is presented in Section 5.3.3, Equation 5.62).

Equation 6.5 provides a theoretical prediction of the closed-loop transfer function, based on open-loop data. The closed-loop transfer function can also be measured experimentally. We use the spectral estimation technique described in Section 5.1.2, where the input in this case is \tilde{r}_1 and the output is \tilde{y}_1 .

We will compare predicted and actual closed-loop transfer functions for the first mode only, at a single flow coefficient, $\bar{\phi} = 0.475$. At this operating point, the compressor is open-loop stable, but the first mode is lightly damped. Thirteen hot wires, mounted behind the IGVs, were used for data acquisition and feedback. Closed-loop data was taken for six values of Z_1 . The magnitude of Z_1 was held constant at $|Z_1| = 8.2$ (6.5 deg per m/s), and the phase of Z_1 was varied over a wide range:

$$\angle Z_1 = -45^\circ, 0^\circ, 45^\circ, 90^\circ, 135^\circ, \text{ and } 180^\circ.$$

for each value of Z_1 , the closed loop transfer function was both predicted and measured. The results are shown in Figure 6.19.

In Figure 6.19 a and b ($\angle Z_1 = -45^\circ$ and 0°), the predicted transfer functions are slightly unstable (this statement is based on the numerical values which generated Figures 6.19 a and b). The actual transfer functions, on the other hand, are stable, because no rotating stall was encountered during the test. Thus, at this extreme of our study of various phases, our predictions of stability are not accurate. But the frequencies of the poles are in the right range, and the general frequency behavior is similar. In Figures 6.19 c, d, and e ($\angle Z_1 = 45^\circ, 90^\circ$, and 135°), the predictions are quite accurate. All of the pole locations are well predicted, both in frequency and damping ratio. This confirms that the experimental behavior conforms to linear control theory. Figure 6.19 f ($\angle Z_1 = 180^\circ$) again shows a slightly unstable predicted system, while the actual system is slightly stable - nevertheless, the frequency of the

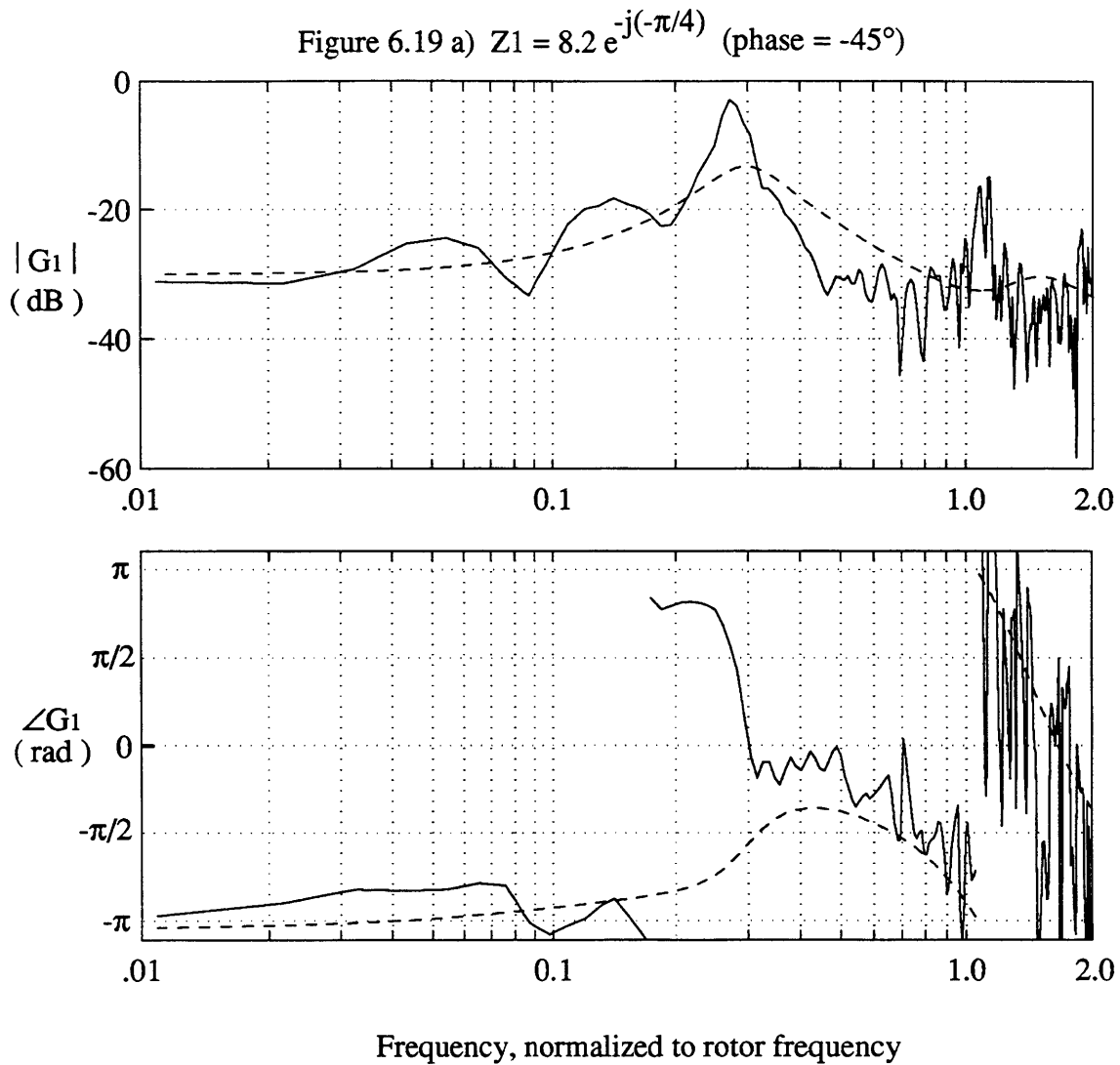
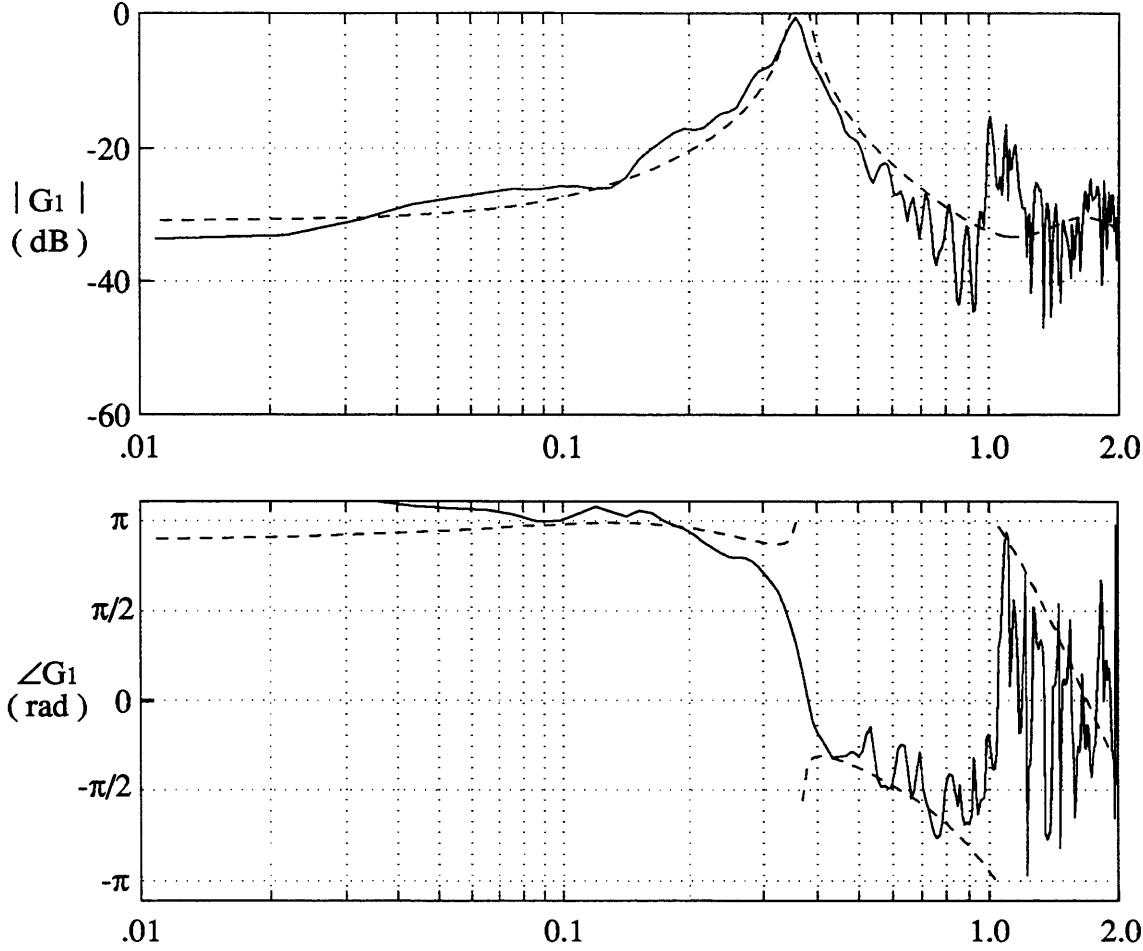


Figure 6.19- Comparison of predicted (dashed lines) and actual (solid lines) closed-loop transfer functions for the first mode. Feedback gain is shown at top of figure. Data taken with 13 hot wires downstream of the IGVs, at $\bar{\phi} = 0.475$.

Figure 6.19 b) $Z1 = 8.2$ (phase = 0°)



Frequency, normalized to rotor frequency

Figure 6.19 - (Continued)

Figure 6.19 c) $Z_1 = 8.2 e^{-j(\pi/4)}$ (phase = 45°)

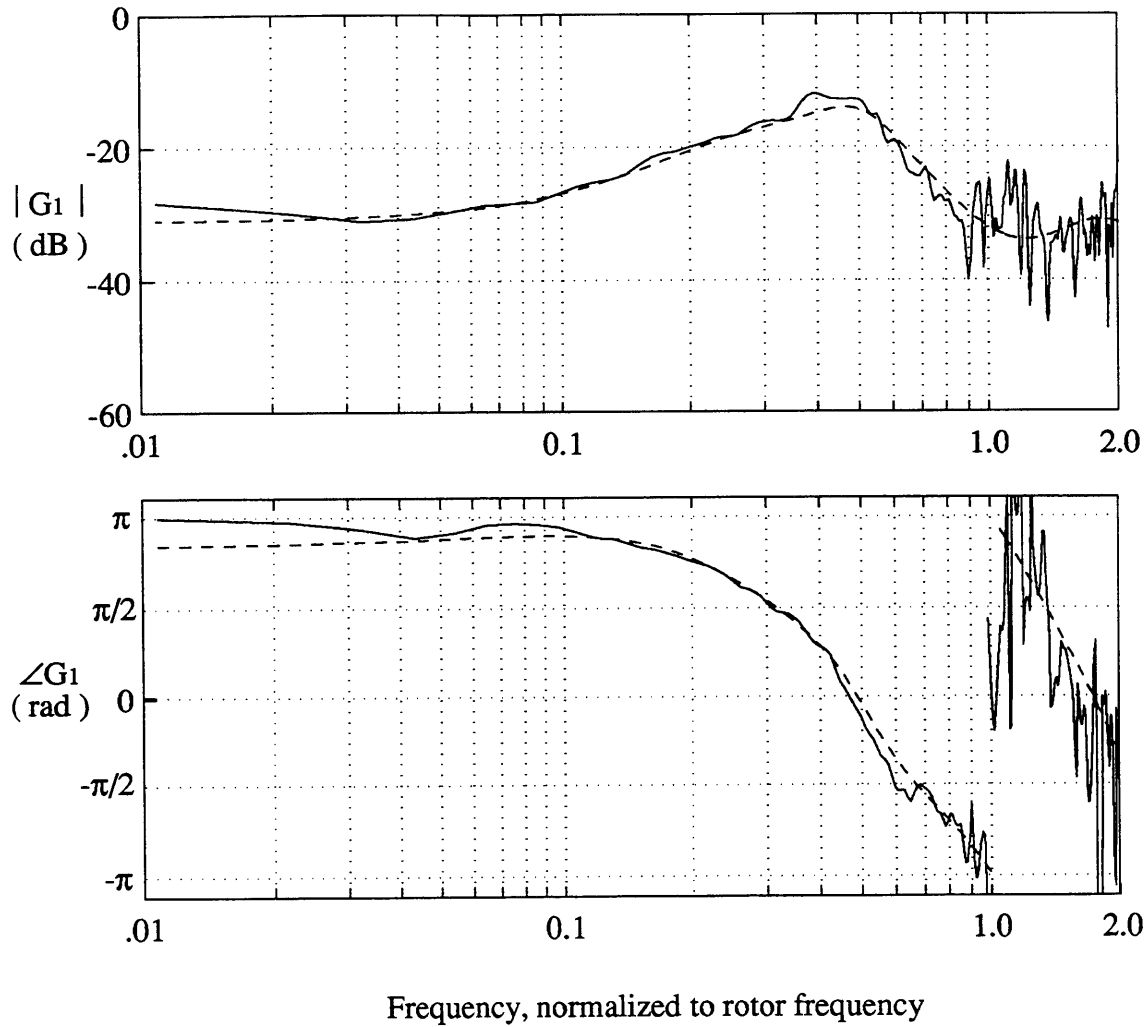


Figure 6.19 - (Continued)

Figure 6.19 d) $Z_1 = 8.2 e^{-j(\pi/2)}$ (phase = 90°)

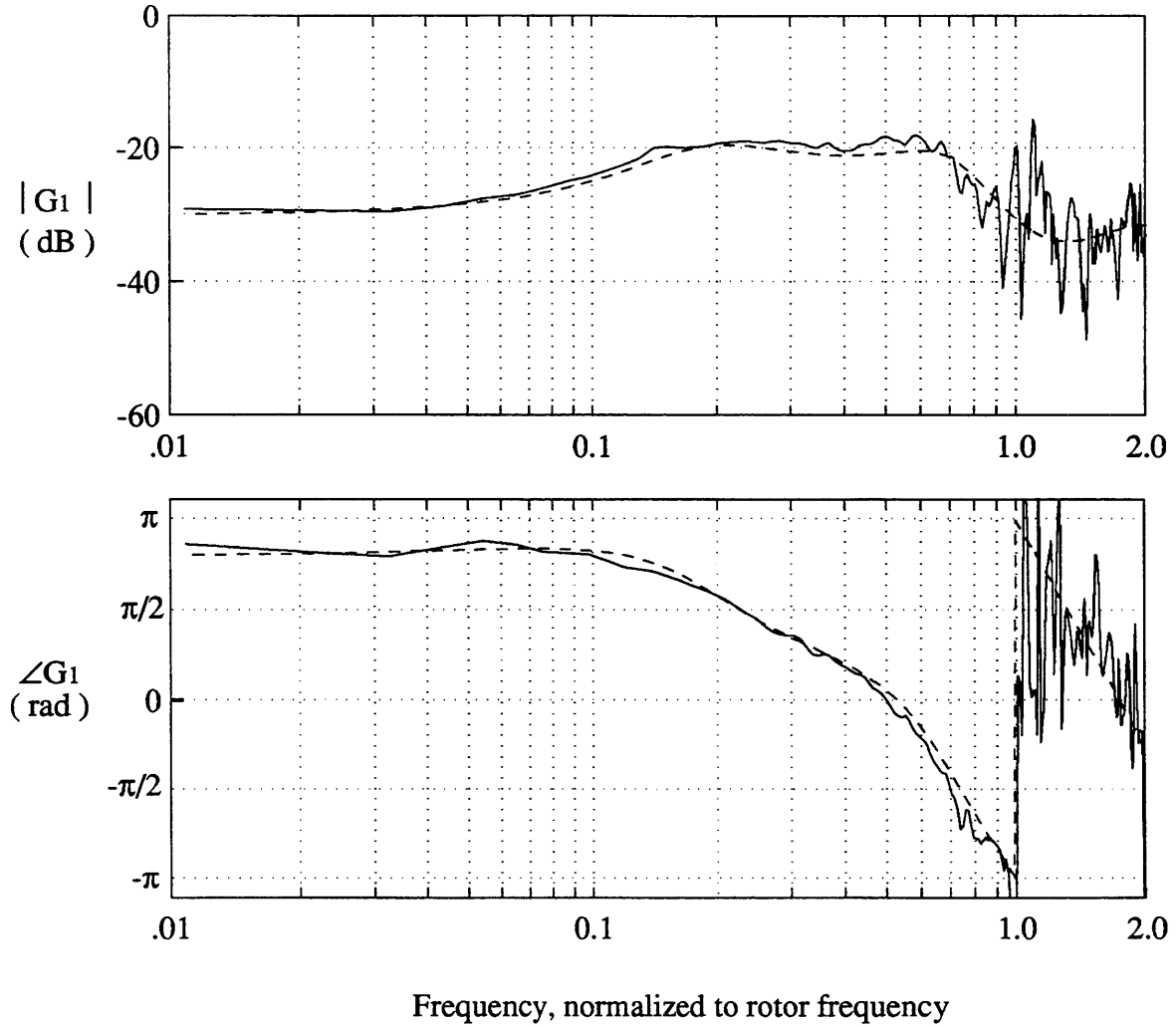


Figure 6.19 - (Continued)

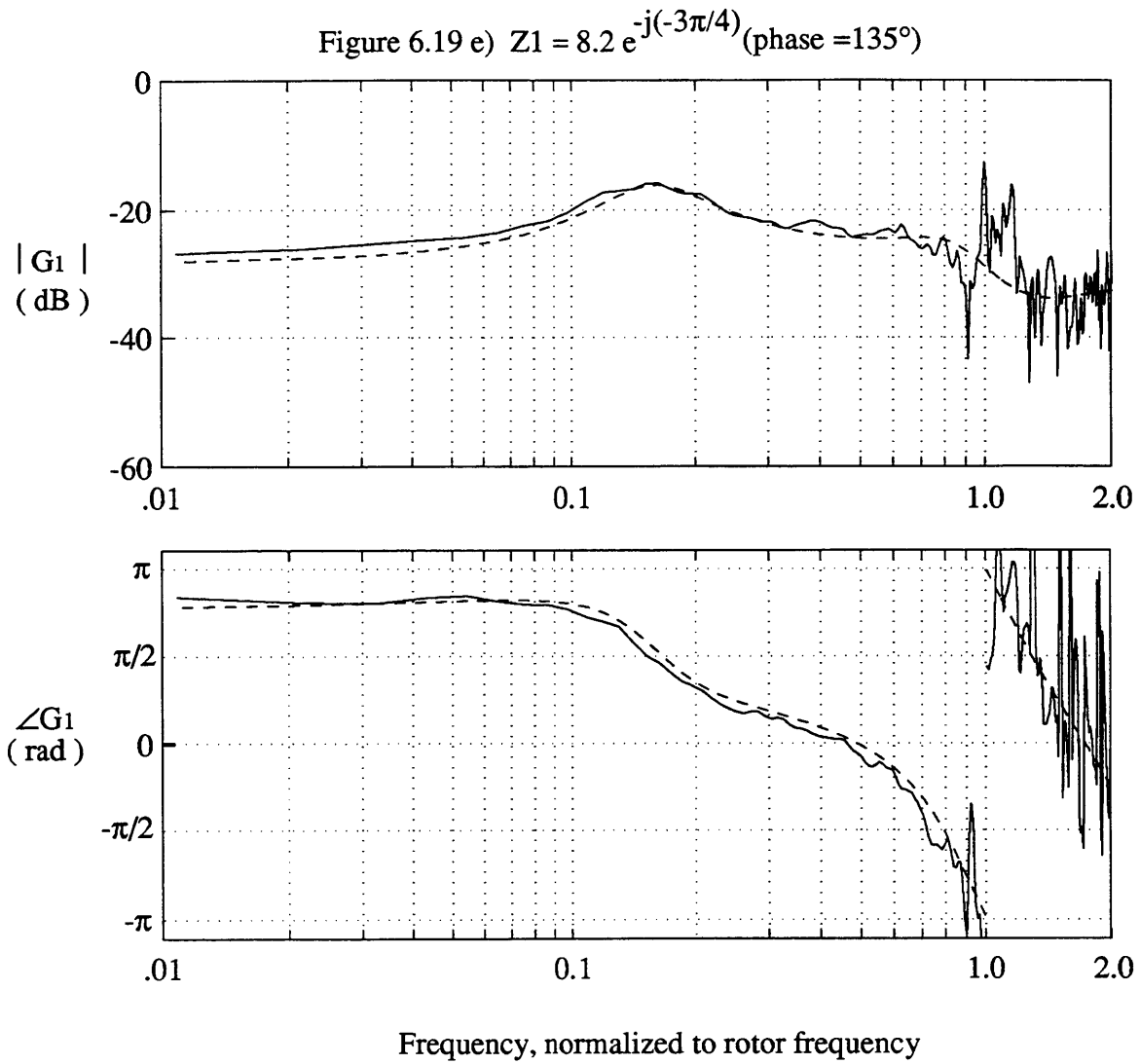


Figure 6.19 - (Continued)

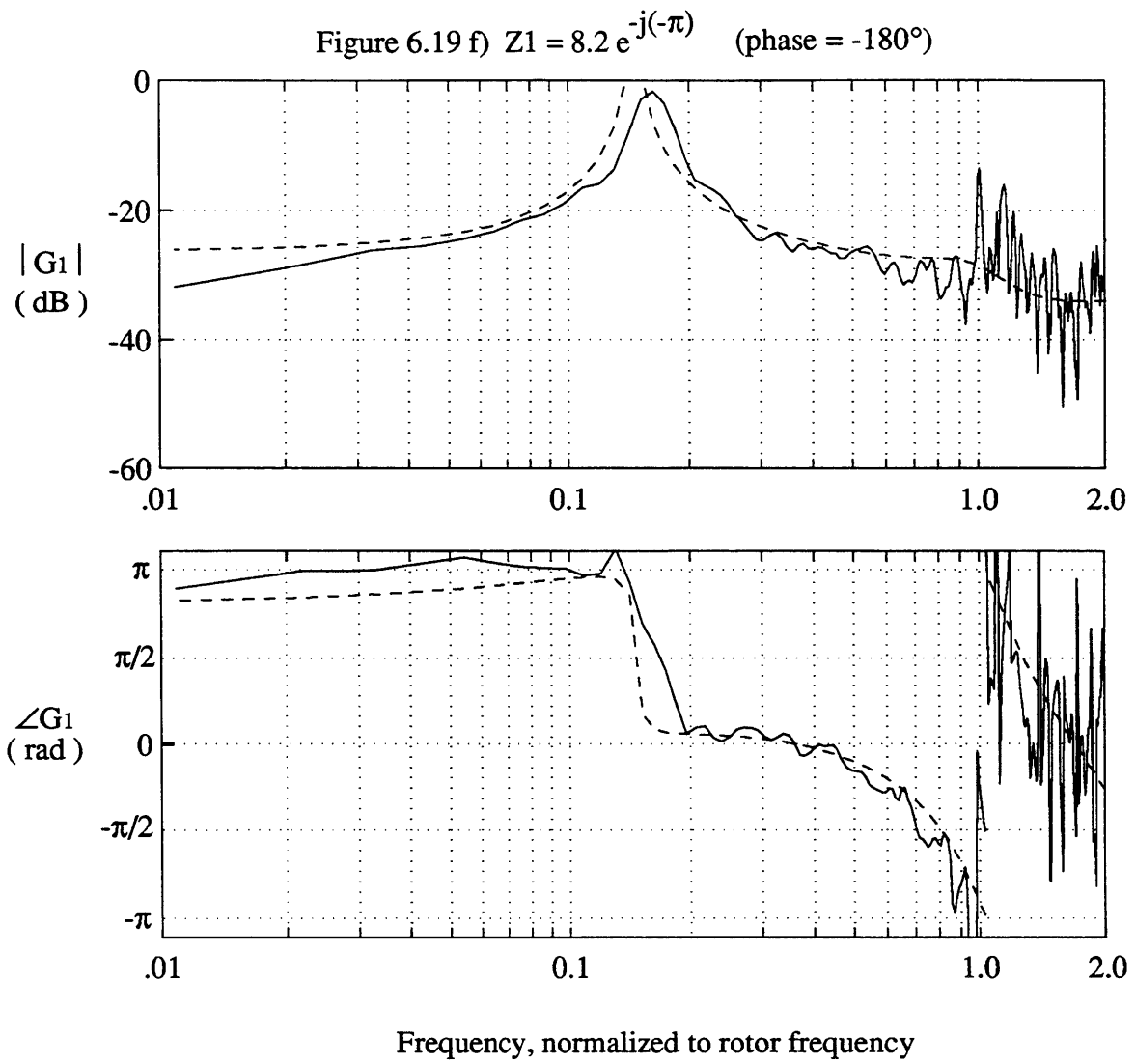


Figure 6.19- (Continued)

poles and the general transfer function shape are well predicted.

We can draw several conclusions from these results. The most important is that applying linear control theory to the compressor yields accurate quantitative results. Thus linear control law design based on the concept of modal dynamics is justified. We can also conclude that our modeling of the feedback system is reasonably accurate. Finally, we have shown that the best value of phase for the feedback gain Z_1 is definitely not zero - a value between 45° and 135° is necessary to achieve good damping.

Nonzero phase of Z_n means that the commanded actuation wave is spatially out-of-phase with the measured velocity perturbation wave. This commanded spatial phase shift can serve two purposes. First, it compensates for the steady-state spatial phase shift which exists between IGV deflections and the axial velocity changes they induce. This phase shift was identified in Chapter 5 to be significant. Second, the commanded spatial phase shift provides a way to *lead* the perturbation wave, thus compensating for *time* lags in the feedback system and compressor dynamics. For instance, the first mode wave travels about 7 degrees during the 2 msec time delay in the computer, so we should base our feedback command on the measured wave, shifted 7 degrees circumferentially. Other time lags (such as actuator dynamics and fluid mechanical delays) can also be partially compensated using 'spatial lead'.

The model described in Chapter 4 accounts for all of these effects automatically. Furthermore, applying linear control theory to this model provides an accurate quantitative approach to stabilization, as we have demonstrated. One can also apply slightly more sophisticated control laws (such as PID-type lead-lag controllers) to the rotating stall problem, and experiments show that the damping of the modes at a given flow coefficient can be improved. Such improvement does not increase the flow range of the compressor, however, because higher modes become underdamped or unstable before simple proportional feedback becomes inadequate. Apparently,

stabilization of this compressor is limited not by controller performance, but by the number of modes which are sensed and actuated.

6.2.2 Gain Determination Using Root Loci

The previous section, although limited in scope, suggests that linear control theory is a viable tool for studying feedback stabilization. We thus expect theoretical studies using the modeling and identification results of Chapters 3 through 5 to yield insights which are physically meaningful. This section presents one such study, which uses root loci to explore the implications of the system input-output dynamics.

Root loci allow the limitations of proportional control to be illustrated, and demonstrate the behavior of the closed-loop system for different values of feedback gains. No attempt is made here to design 'optimal' controllers, or to exhaust the possibilities for control system design. Rather, we use the root locus method to point out some fundamental characteristics of the system that may be of interest for future work in active control of axial compressors. We first briefly review the method.

The eigenvalues of the closed loop system, which determine its stability, are the 'poles' of Equation (6.5) or, equivalently, the roots of the characteristic equation:

$$1 - Q(s) \cdot G_n(s) \cdot S(s) \cdot Z_n = 0 \quad (6.6)$$

A plot of the solutions to (6.6) for various values of feedback gain Z_n is called a root locus. Root loci are useful in designing feedback gains because they show the limitations imposed by the system dynamics, and the sensitivity of the eigenvalues to changes in the gain. The 'best' value or values of the feedback gain can be read directly from the root locus, by choosing the gain which results in the most highly damped set of eigenvalues.

Root loci are plotted for the first three modes in Figures 6.20, 6.21, and 6.22. The system dynamics used to compute these root loci are based on the identification results from Chapter 5 and the system modeling in Chapter 4. We plot the root locus

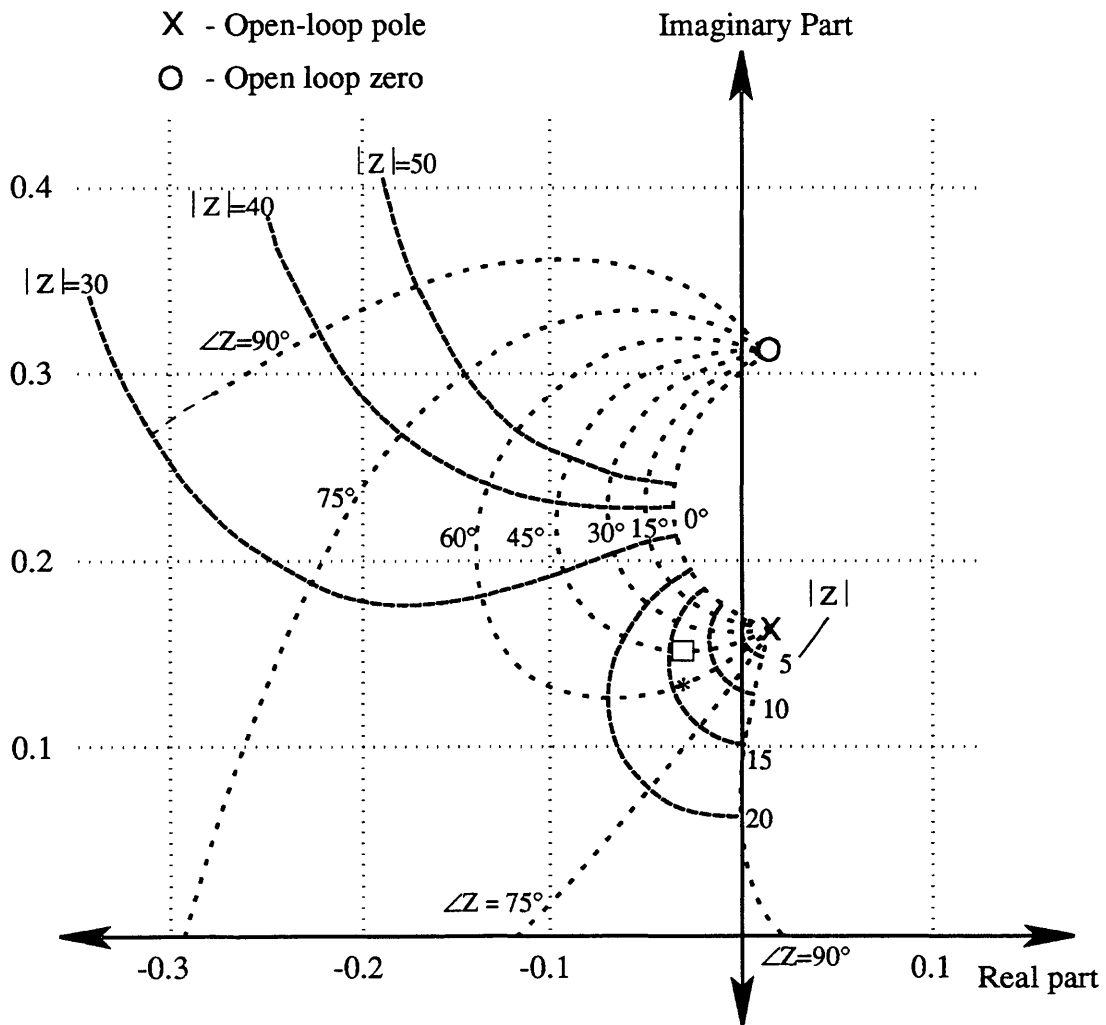


Figure 6.20 - Root locus of dominant roots for the first mode, $\bar{\phi}=0.375$.
 Square indicates experimentally determined gain. Star
 indicates gain with the same magnitude which yields the
 best damping.

- lines of constant feedback amplitude
- lines of constant feedback phase

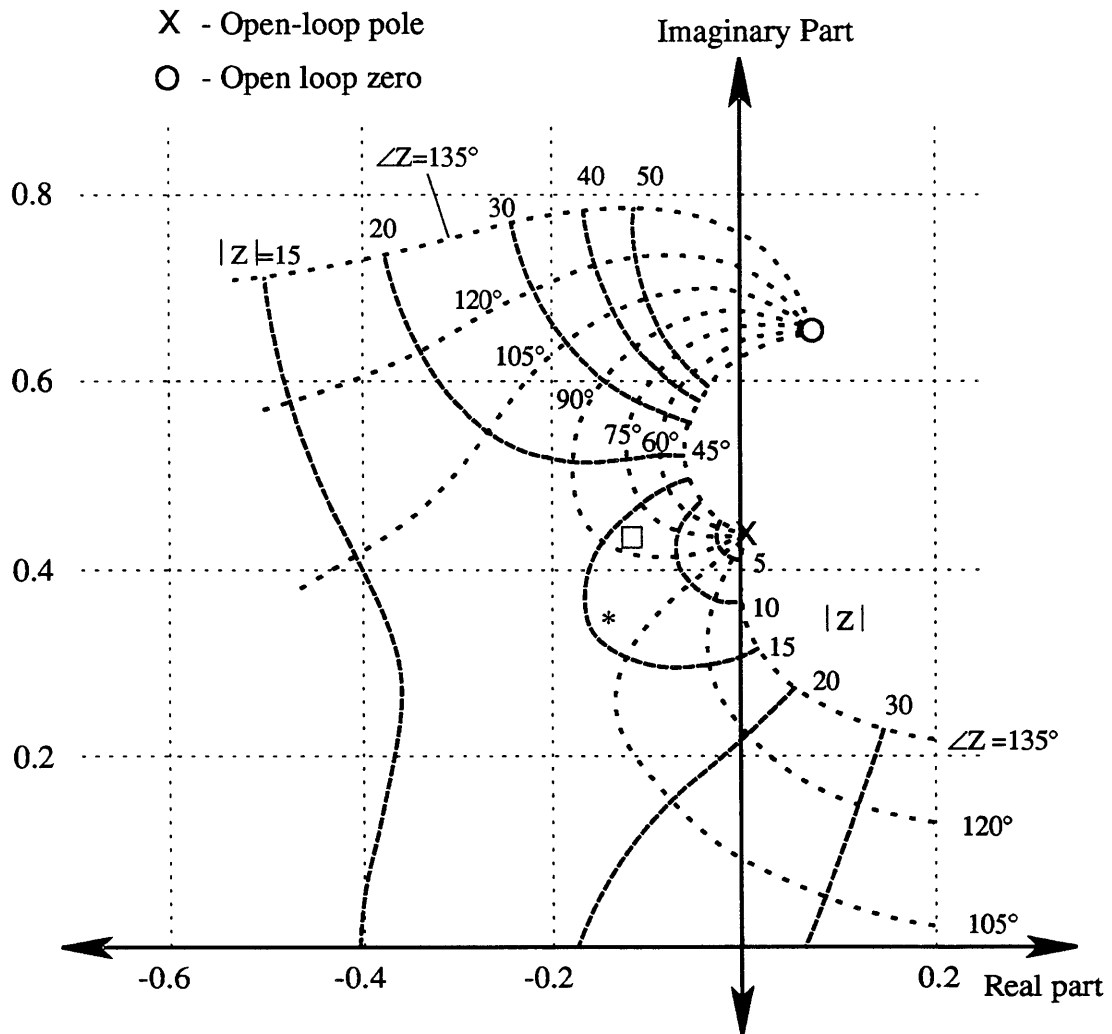


Figure 6.21 - Root locus of dominant roots for the second mode, $\bar{\phi}=0.375$. Square indicates experimentally determined gain. Star indicates gain with the same feedback amplitude which yields the best damping.

----- lines of constant feedback amplitude
 lines of constant feedback phase

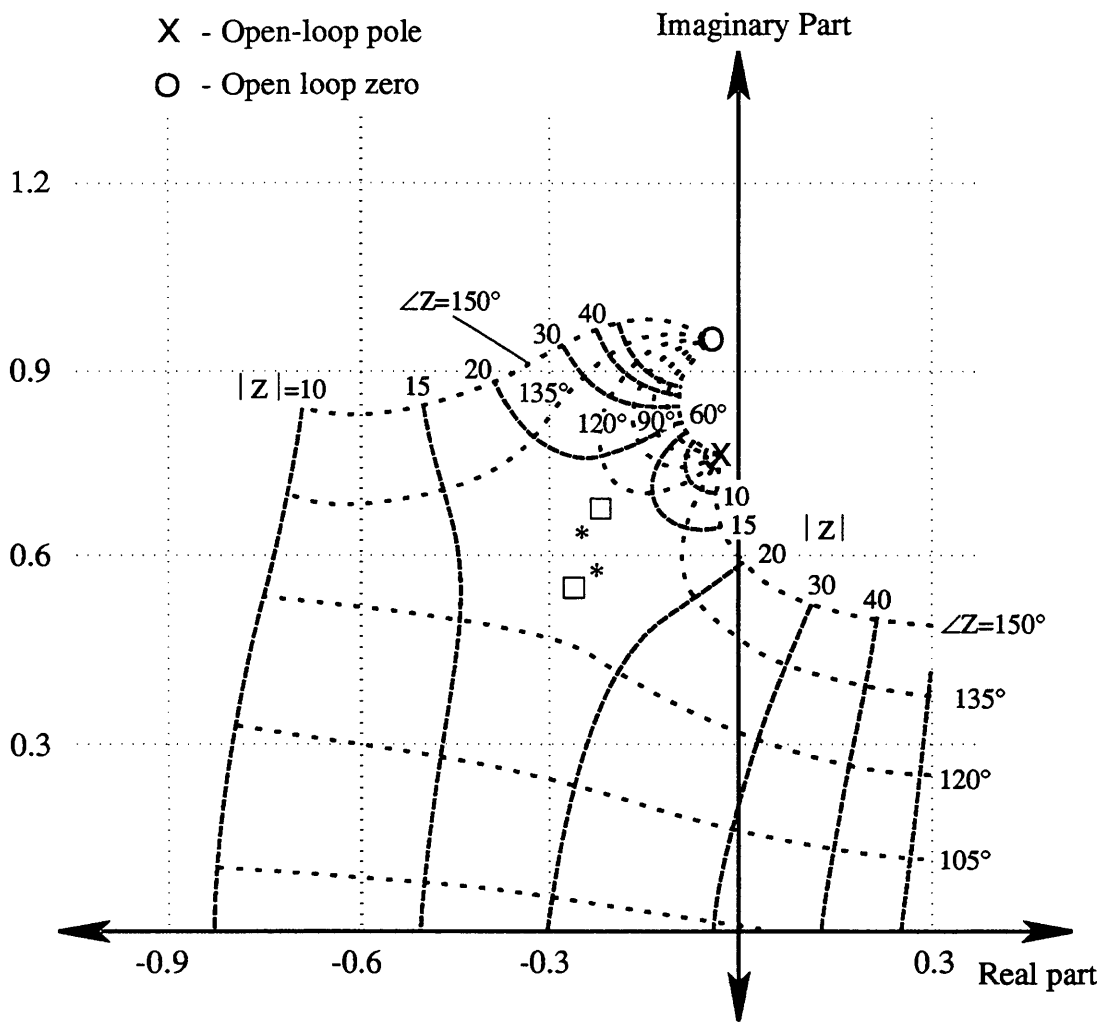


Figure 6.22 - Root locus of dominant roots for the third mode, $\bar{\phi}=0.375$. Squares indicates experimentally determined gain (note that two poles become dominant at gain chosen). Stars indicate gain with the same feedback amplitude which yields the best damping.

----- lines of constant feedback amplitude
 lines of constant feedback phase

for $\bar{\phi} = 0.375$, which is the lowest value of $\bar{\phi}$ for which the dynamics of all the modes are available. Different values of $\bar{\phi}$ yield different root loci, but we are interested in the least stable case - gains that work well at this value of $\bar{\phi}$ yield the largest improvement in operating range of the compressor.

Only the dominant roots are plotted in Figures 6.20 - 6.22. There are actually 11 roots to Equation 6.6, most of which are very fast because they represent ZOH, delay, and filter dynamics. Only the servo poles can sometimes interact with the root locus in such a way that they become dominant. This situation can be seen most clearly in Figure 6.22, where one of the servo poles couples with the rotating stall pole.

The pole locations for the experimental feedback gains are also shown in the root locus figures. These gains were found to give the largest increase in operating range for the compressor. In every case, the phase $\angle Z_n$ of the experimental gain is within 15° of the phase that achieves maximum damping. The magnitudes of the experimental gains, $|Z_n|$, are large enough to stabilize the system, but somewhat lower than what one would choose based on the root loci. One reason for this discrepancy is that the servo poles, not shown on these figures, can become underdamped at high values of gain. Another reason is that there are practical problems associated with very high feedback gains. For instance, a gain of 25 causes a full scale (.25 rad) command to the IGVs for a measured wave magnitude of .01 (0.73 m/s, or 5 A/D counts). Thus gains above 15-20 are very susceptible to noise, and in practice do not work well.

The desire for better stabilization and noise rejection suggests the need for more sophisticated control laws. Experience to date suggests that such control laws can indeed improve the stability and robustness of the modes under control. But since our primary objective here is to increase the compressor operating range, such improvement must be accompanied by the stabilization of additional modes. For

instance, if one stabilizes modes 1 and 2 with sophisticated control laws, no improvement in operating range will result unless the 3rd mode is also stabilized. Thus the problem of increasing compressor operating range is limited (for this particular compressor) not by the ability to design stabilizing controllers, but by the ability to sense and actuate higher modes.

Figures 6.20 - 6.22 show that, even at $\bar{\phi} = 0.375$, stabilization of the first three modes with proportional feedback is possible with realistic feedback gains. Note that for all three modes, significant values of phase ($\angle Z_n$) must be used to stabilize the system. Sensitivity to the value of phase is relatively low, however: choice of phase can vary ± 15 degrees about the optimum value without significantly affecting stability. Larger variations yield closed-loop poles which are still stable, although underdamped. Thus an experimental approach to determining the phase has a strong chance of success, if reasonable values of feedback magnitude ($|Z_n|$) are used.

It is also clear from these plots that the zero of $G_n(s)$ (discussed in Chapter 5) has a strong effect on the level of stability which can be attained. Since the closed-loop poles approach the zeros as gain is increased, and since the zeros are either underdamped or non-minimum phase (depending on n), the zeros have a destabilizing effect on the closed-loop poles. For the flow coefficients studied, this effect is not severe enough to jeopardize our ability to stabilize this particular compressor. This is because none of the modes are highly unstable, even at the lowest flow coefficient yet achieved. Highly unstable modes (which may very well exist in many axial compressors) would suffer more severely from the destabilizing effect of non-minimum phase zeros.

The zeros of the feedback system can be changed by changing the sensors or the actuators. One example of moving the sensors was discussed in Section 5.3.3. This study showed that moving the sensors downstream of the IGVs increased the frequency of the zeros. This is a favorable effect, but the non-minimum phase

characteristic was not eliminated. The modeling in Chapter 3 indicates that the actuators, rather than the sensors, are primarily responsible for the zero behavior. Thus we tentatively conclude that IGV deflection has some unfavorable characteristics for actuation of compressor higher-mode dynamics. Other approaches to actuation, such as blowing and suction, may avoid non-minimum phase problems [38], and might therefore be preferred, because we expect most compressors to be more highly unstable than the one studied here.

CHAPTER 7

Summary, Conclusions, and Recommendations

7.1 Summary

Small perturbation traveling waves have been modeled, identified, and actively stabilized in a single-stage axial compressor. Stabilization of small perturbation waves was experimentally demonstrated, and shown to eliminate the occurrence of rotating stall in a heretofore unreachable region of the compressor map. By eliminating rotating stall in this region, the stable operating range of the compressor was increased by 23%. Linearized fluid mechanics and linear control theory were sufficient tools for the design and implementation of the feedback system.

In Chapter 3, the fluid mechanical model of small perturbation waves was cast into time ordinary differential equation form. This is a new development which makes possible the direct application of linear control theory concepts to a distributed fluid mechanical system. Several forms of the model were developed, each of which may be useful for future work on active control of rotating stall. The symmetry properties of the compressor annulus result in dynamic equations whose special properties are elucidated in this thesis.

The experimental apparatus described in Chapter 2 is the first of its kind. It provides a unique opportunity to investigate the distributed dynamics of a compressor. Identification of what we term 'compressor higher-mode dynamics' was presented in Chapter 5. When the dynamics being identified are unstable or underdamped, identification must be conducted closed-loop. Synthesis of an instrumental-variable technique which is applicable to closed-loop, possibly unstable

systems was carried out in Chapter 5. This is a new combination of several methods from the literature, and contains an extension for analyzing unstable systems. This extension is believed to be new.

Chapter 6 presents experimental results which verify the view that instability of small perturbation waves leads to rotating stall. By actively stabilizing these waves in a mode-by-mode fashion, the flow rate at which stall occurs and the detailed behavior at stall inception are altered. The behavior under active control is consistent (over the flow range studied) with the linearized fluid mechanics model developed by Moore and Greitzer in [23].

7.2 Conclusions

The experimental results in Chapters 5 and 6 serve to increase the current knowledge of compressor higher-mode dynamics. Before this work, such dynamics were studied theoretically, and experimentally at or near stall inception. Here we have examined the dynamics over the entire range where they are significant - from well-damped, through neutral stability, into a new region in which they are unstable. Thus many previously untested theoretical ideas are experimentally verified by this work. Some of the conclusions are listed here:

- 1) Circumferential sinusoidal waves of axial velocity perturbation behave like eigenmodes of the compressor dynamics. Sinusoids with mode numbers 1, 2, and 3 all appear to be eigenmodes. The magnitude and phase (rotation) of the eigenmodes can be represented by the spatial Fourier coefficients (SFCs) of axial velocity perturbation measured at an axial station near the face of the compressor.
- 2) The eigenvalues of the compressor dynamics are such that the sinusoidal waves ('modes') tend to rotate at a fraction of rotor rotation rate, and grow or decay exponentially. The growth or decay rates (damping characteristics) depend on the annulus averaged flow rate and the mode number. Eigenvalues go from stable to unstable as flow coefficient is reduced. When any of the first three eigenvalues becomes unstable or severely underdamped, rotating stall is initiated in the compressor.
- 3) The sinusoidal axial velocity perturbation waves can be forced with a circumferential array of high-response inlet guide vanes (IGVs). Such forcing can be used to increase their damping or stabilize them, using linear feedback of velocity perturbation measurements.

- 4) Properly feeding back the first mode reduces the stall-onset flow rate by 11%. Properly feeding back both the first and second modes reduces the stall-onset flow rate by 18%. Properly feeding back the first three modes reduces the stall-onset flow rate by 23%. In each case, rotating stall is initiated by instability or resonance of the lowest uncontrolled mode.
- 5) The array of active IGVs can be used to identify the compressor dynamics. Some of the conclusions based on this identification have already been stated. Others are:
 - i) Over the flow range studied, the first mode is less stable than the second mode, which is in turn less stable than the third mode. This separation between eigenvalues becomes progressively smaller as flow coefficient is reduced.
 - ii) The waves represented by the SFCs rotate at between 15% and 35% of the rotor speed, depending on flow rate and mode number. The second mode travels slightly faster than the first, and the third mode travels slightly faster than the second.
 - iii) The input-output dynamics from the n^{th} SFC of IGV deflection to the n^{th} SFC of velocity perturbation ($n = 1, 2, \text{ and } 3$) can be identified. These dynamics are consistently and accurately characterized by decoupled linear differential and difference equations over the flow range studied. Identified dynamics can be used to design successful feedback control laws.

More detailed comments on the compressor higher-mode dynamics appear in Section 5.3. This section also compares theoretical and experimental trends, and discusses their implications in the context of control. Section 6.1.4 discusses experimental results during active control.

7.3 Recommendations for Future Work

The conclusions stated here apply to a specific low-speed single-stage research compressor. It is of interest to determine the applicability of our results to other compressors. A low-speed three-stage compressor has been fitted with sensing and actuation hardware which is almost identical to the hardware described here. Results to date [40] agree with the conclusions stated here (except for specific numerical results, such as stall cell speed and flow range improvement). Research by Day [2,17]

and others suggests, however, that instability of sinusoidal perturbation waves may not be the only mechanism for stall inception. This research further contends that in some compressors, rotating stall can be initiated independent of the stability of the SFCs. The mechanism for stall inception in such compressors is not well understood, and research is ongoing. If such research is fruitful, then the question can be asked: under what conditions do such alternate stall-inception mechanisms dominate, and under what conditions is it sufficient to stabilize small-perturbation waves?

The ultimate goal of the research presented here is operating range extension in a gas turbine engine. Many extensions to the existing work are necessary to reach this goal. We will mention only a few here, to indicate the scope of the problem.

- 1) Modeling - Further assessment and possible improvement of the predictive capability of the model presented here is necessary to allow future design of rotating stall controllers. Extensions to the model in Chapter 2, which are discussed in Appendix A, greatly improve the match between theoretical prediction and experimental results *for the homogeneous dynamics*. Actuator models are less well developed, especially for actuator configurations which could be applied in high-speed compressors.
- 2) Although many extensions to the basic model exist, few of them have been added to the control-theoretic form of the model. Continued collaboration between fluid mechanics and controls specialists will help keep control-theoretic models 'up-to-date' with their fluid-mechanics counterparts.
- 3) Theoretical and experimental work on high-speed compressor stall is ongoing [41]. The applicability of the results presented here to high-speed compressors is still an open research question.
- 4) Actuators which have sufficient bandwidth and control power to control rotating stall in high-speed compressors must be designed and tested.
- 5) Sensor configurations for high-speed compressors and gas turbines must be studied and tested.

References

1. Greitzer, E. M., "Surge and Rotating Stall in Axial Flow Compressors; Part I: Theoretical Compression System Model," J. of Eng. for Power, vol. 98, 1976, pp. 190-198.
2. Day, I. J., "Active Suppression of Stall and Surge in Axial Compressors," Proceedings, ASME International Gas Turbine Conference, Orlando, June 1991.
3. Lavrich, P. L., "Time Resolved Measurements of Rotating Stall in Axial Flow Compressors," Ph.D. Thesis, Massachusetts Institute of Technology, 1988.
4. Takata, H., and Nagano, S., "Nonlinear Analysis of Rotating Stall," J. of Eng. for Power, Vol. 94, No. 4, 1972.
5. Pandolfi, M. and Colasurdo, G., "Numerical Investigations on the Generation and Development of Rotating Stalls," ASME paper 78-WA/GT-5, 1978.
6. Stenning, A. H. "Rotating Stall and Surge," Trans. of the ASME, Vol. 102, March 1980, pp. 14-20.
7. Smith, G. D. J., "Casing Treatment in Axial Compressors," Ph.D. Thesis, Engineering Department, University of Cambridge, April 1980.
8. Greitzer, E. M., "Review - Axial Compressor Stall Phenomena," ASME J. of Fluids Eng., vol. 102, June 1980, pp. 134-151
9. Ludwig, G. R., and Nenni, J. P., "Tests of an Improved Rotating Stall Control System on a J-85 Turbojet Engine," ASME Paper 80-GT-17, 1980.
10. Moore, F. K., "A Theory of Rotating Stall of Multistage Compressors, Parts I-III," ASME J. of Eng. for Power, Vol. 106, 1984, pp 313-336.
11. Greitzer, E. M. and Moore., F. K., "A Theory of Post-Stall Transients in Axial Compressors: Part II - Applications," ASME J. of Eng. for Gas Turbines and Power, Vol. 108, 1986, pp. 231-239.
12. Ffowcs-Williams, J. E., and Huang, X. Y., "Active Stabilization of Compressor Surge," J. of Fluid Mechanics, Vol. 204, 1989, pp. 245-269.
13. McDougall, N. M., "Stall Inception in Axial Compressors," Ph.D. Thesis, Cambridge University, 1988.
14. Longley, J. P., "Inlet Distortion and Compressor Stability", Ph.D. Thesis, Trinity College, Cambridge University, 1988.
15. Garnier, V. H., Epstein, A. H., and Greitzer, E. M., "Rotating Waves as a Stall Inception Indication in Axial Compressors," J. of Turbomachinery, Vol. 113, April 1991.

16. Epstein, A. H., Ffowcs-Williams, J. E., and Greitzer, E. M., "Active Suppression of Aerodynamic Instabilities in Turbomachines," AIAA Paper 86-1994. Also J. of Propulsion, Vol. 5., No. 2, pp 204-211.
17. Day, I. J., "Modal Perturbations and Stall Inception," Proceedings, ASME International Gas Turbine Conference, Orlando, June 1991.
18. Chue, R., Greitzer, E. M., and Tan. C. S., "An Analysis of General Post-Stall Transients in Axial Compression Systems", unpublished MIT GTL Report, April 1984.
19. Johnson, M. C., "The Effect of Hub Treatment on Compressor Endwall Flow-fields," M.S. Thesis, MIT Dept. of Aeronautics and Astronautics, January 1985.
20. Silkowski, P. D., "Aerodynamic Design of Moveable Inlet Guide Vanes for Active Control of Rotating Stall," M.S. Thesis, MIT Dept. of Aeronautics and Astronautics, February, 1990.
21. Goldstein, R. J., editor, "Thermal Anemometers," Chapter IV, Fluid Mechanics Measurements, Hemisphere Publishing Corporation, New York, 1983.
22. Garnier, V. H., "Experimental Investigation of Rotating Waves as a Rotating Stall Inception Indication in Compressors," M.S. Thesis, MIT Dept. of Aeronautics and Astronautics, May 1988.
23. Moore, F. K., and Greitzer, E. M., "A Theory of Post-Stall Transients in Axial Compressors: Part I - Development of the Equations," ASME J. of Eng. for Gas Turbines and Power, Vol. 108, 1986, pp. 68-76.
24. Hynes, T. P. and Greitzer, E. M., "A Method for Assessing Effects of Inlet Flow Distortion on Compressor Stability," ASME J. of Turbomachinery, vol. 109, pp. 371-379.
25. Longley, J. P., unpublished notes.
26. Nagano, S., Machida, Y., and Takata, H., "Dynamic Performance of Stalled Blade Rows," Japan Soc. of Mech. Eng. Paper #JSME 11, Presented at Tokyo Joint Int. Gas Turbine Conf., Tokyo, Japan, Oct. 1971.
27. Truxal, Control Engineers Handbook, McGraw-Hill, 1958, pp. 4-26.
28. Franklin, G. F., and Powell, J. D., Digital Control of Dynamic Systems, Addison-Wesley, 1980.
29. Åström, K. J., and Wittenmark, B., Computer Controlled Systems - Theory and Design, Prentice-Hall, New Jersey, 1984.
30. Ljung, L., System Identification - Theory for the User, Prentice-Hall, New Jersey, 1987.
31. Ljung, L., System Identification Toolbox for use with MATLAB, The MathWorks, Inc., 1988.

32. Lamaire, R. O., Valavani, L., Athans, M. and Stein, G., "Robust Frequency and Time Domain Identification Methods with Guaranteed Error Bounds," to appear in Automatica, 1991.
33. Young, P., Recursive Estimation and Time-Series Analysis, Springer-Verlag, 1984.
34. Wang, H, and Cao, D., "Two Instrumental Variable Methods for Closed Loop System Identification," Identification and System Parameter Estimation 1988, selected papers from the Eighth IFAC/IFORS Symposium, Beijing, China, August 1988, pp.543-547.
35. Söderström, T., Stoica, P., and Trulsson, E., "Instrumental Variable Methods for Closed Loop Systems," Automatic Control - World Congress, 1987 selected papers from the 10th Triennial World Congress of IFAC, Munich, July 1987, pp. 363-368.
36. Oppenheim, A. V., and Schaffer, R. W., Discrete-Time Signal Processing, Prentice-Hall, 1989.
37. Mazzawy, R. S., "Multiple Segment Parallel Compressor Model for Circumferential Flow Distortion," ASME J. of Eng. for Power, vol. 99, April 1977, pp. 228-246.
38. Strang, E. J., "Influence of Unsteady Losses and Deviations on Compression System Stability with Inlet Distortion", M.S. Thesis, MIT Dept. of Aeronautics and Astronautics, May 1990.
39. Gysling, D. L., Personal communication.
40. Haynes, J., Personal communication.
41. Bonnaure, L. P., "Modeling High Speed Multistage Compressor Stability," M.S. Thesis, MIT Dept. of Aeronautics and Astronautics, September 1991.
42. Chue, R., Hynes, T. P., Greitzer, E. M., Tan, C.S., and Longley, J. P., "Calculation of Inlet Distortion Induced Compressor Flow Field Instability," Int. J. of Heat and Fluid Flow, Vol. 10, No. 3, September 1986, pp. 211-233.
43. Stenning, A. H., "Inlet Distortion Effects in Axial Compressors," J. of Fluids Eng., March 1980, Vol. 102, pp. 7-13.
44. Cargill, A. M., and Freeman, C., "High Speed Compressor Surge with Application to Active Control," J. of Turbomachinery, Paper No. 90-GT-354, April 1991.
45. Lavrich, Personal Communication.
46. Paduano, J., Epstien, A. H., Valavani, L., Longley, J. P., Greitzer, E. M., and Guennette, G. R., "Active Control of Rotating Stall in A Low Speed Axial Compressor," ASME Paper 91-GT-88, Proceedings, ASME International Gas Turbine Conference, Orlando, June 1991. To be published in Transactions of the ASME.

Appendix A

Modifications to the Compression System Model

The model of axial compressor higher-mode dynamics described in Chapter 3 is presented in numerous documents, with various modifications. These modifications will be briefly described here, to indicate the type of information that can be incorporated into the model. More detailed descriptions can be found in the cited references.

A.1 Upstream and Downstream Flow Fields

Sections 3.2.3 and 3.2.6 present the upstream and downstream flow field equations. These equations were found to be adequate to describe experimental results in a 3-stage low-speed high hub-to-tip ratio compressor by Lavrich [3]. In his experiment, the downstream duct was a straight continuation of the annulus at the last row of stators. In compressors which do not have a straight duct downstream, Moore [10] suggests a modification to Equation (3.20):

$$\frac{\partial(\delta p_{s3})}{\partial \eta} = -(m-1) \frac{\partial(\delta \phi_2)}{\partial \tau} \quad (\text{A.1})$$

where $m=2$ for a straight channel downstream of the compressor, and $m=1$ for a sudden expansion. See [10] for more details on this approximation.

A.2 Unsteady Losses and Deviations

Chue, Greitzer, and Tan [18] suggest that losses in the compressor do not occur in a quasi-steady manner, and that subsequently the compressor pressure rise is

not simply $\delta\psi(\delta\phi)$ in the case where $\delta\phi$ is unsteady. As an approximation, they suggest adding extra dynamics for the losses across the rotor and stator as follows:

$$\psi(\tau, \theta) = \psi_{id}(\phi) - L_R(\tau, \theta) - L_S(\tau, \theta) \quad (\text{A.2})$$

$$\tau_L \cdot \frac{\partial L_S}{\partial \tau} = L_{ss} - L_S \quad (\text{A.3})$$

$$\tau_L \cdot \left[\frac{\partial L_R}{\partial \tau} + \frac{\partial L_R}{\partial \theta} \right] = L_{ss} - L_R \quad (\text{A.4})$$

where ψ_{id} is the 'ideal' pressure rise characteristic based on actual flow angles and zero losses [42], and L_{ss} is half the steady state loss [18], so that in steady state we recover the measured characteristic from Equations (A.2 - A.4):

$$\psi(\phi) = \psi_{id}(\phi) - 2 \cdot L_{ss} \quad (\text{A.5})$$

Equations (A.2 - A.4) increase the complexity of the model, but may be necessary to predict certain effects.

Deviation angles within the compressor may also be affected by unsteadiness. Unsteady deviations can be modeled in a fashion similar to that shown above, further increasing both the fidelity and the complexity of the model.

Modeling unsteady losses and deviations is discussed in detail by Strang [38].

A.3 Modifications to the Inertia Parameter, λ

Various modifications to the calculation of λ (introduced in Section 3.1.2.4) have been suggested. Moore [10] initially suggested that gaps may be important to the inertia in the machine; he suggests multiplying λ by 2 to account for this extra inertia. Chue et al [12] use a model of unsteady losses similar to (A.2 - A.4) to suggest an 'effective λ ' which depends on τ_L . A similar derivation can be done for unsteady deviations. Longley presents a critical comparison of these methods in [14].

A.4 Swirl Sensitivity

Yet another modification can be made if the sensitivity of the compression system to inlet swirl is included. This sensitivity can be written functionally as follows, where $\delta\alpha_1$ is the perturbation flow angle at a particular station i:

$$\delta(\mathcal{P}_{s_3} - \mathcal{P}_{t_2}) \Big|_{\text{quasi-steady}} = \frac{\partial \psi}{\partial \phi} \cdot \delta\phi_2 + \frac{\partial \psi}{\partial \gamma} \cdot \delta\gamma + \frac{\partial \psi}{\partial \alpha_1} \cdot \delta\alpha_1$$

(A.6)

This equation modifies Equation (3.13).

The downstream flow field must also be modified, because we are no longer assuming that the exit swirl is constant around the annulus. Longley [25] introduces the following modification to Equation (3.20):

$$\frac{\partial(\delta\mathcal{P}_{s_3})}{\partial \eta} = -\frac{\partial(\delta\phi_2)}{\partial \tau} - (\Phi \cdot \sec(\alpha_3))^2 \cdot \frac{\partial(\delta\alpha_3)}{\partial \theta} \quad (\text{A.7})$$

where:

$$\delta\alpha_3 = \frac{\partial\alpha_3}{\partial\phi_1} \cdot \delta\phi_1 + \frac{\partial\alpha_3}{\partial\alpha_1} \cdot \delta\alpha_1 \quad (\text{A.8})$$

and $\delta\alpha_1$ can be derived using the small angle approximation and the equation for circumferential velocity (refer to Section 3.1.2.3):

$$\delta\alpha_1 \equiv \frac{\delta v}{\bar{\phi}} = \frac{1}{\bar{\phi}} \cdot \frac{\partial(\delta\Phi_1)}{\partial \theta} \quad (\text{A.9})$$

the additional terms in (A.6) and (A.7) can change the 'effective λ ' for the system substantially, and can be added without adding complexity to the differential equations (i.e. no new dynamics are introduced).

A.5 Other Work

Two areas of current research require significant modification of the modeling techniques described in this thesis. These areas are inlet distortion, and compressibility.

Several documents [14, 24, 38, 42, 43] describe the effects of inlet distortion on the phenomenology and modeling of rotating stall. The impact of inlet distortion on the active stabilization problem is an area of current research.

Less work has been done to model high-speed compressors, in which compressibility must be modeled. Bonnaure [41] and Cargill and Freeman [44] are two references which discuss compressibility effects.

Appendix B

Theoretical Representation of Waves in Axial Compressors

This appendix discusses some of the theoretical properties of 2-D wave dynamics in axial compressors. These properties are derived from the results of Chapter 3.

Consider a general sinusoidal perturbation axial velocity wave:

$$\delta\phi_n = A_n \cos(n\theta) + B_n \sin(n\theta) \quad (\text{B.1})$$

This wave repeats itself every 2π , and has a phase angle and magnitude which depend on A and B as follows:

$$\delta\phi_n = M \cdot \cos(n\theta + \beta) \quad (\text{B.2})$$

where:

$$M = \sqrt{A_n^2 + B_n^2}$$

$$\beta = \text{atan}\left(-\frac{B_n}{A_n}\right)$$

The mode number n determines the number of cycles or 'lobes' which appear in the wave in one circumference of the compressor annulus. Because the annulus is a closed circle, superposition of waves with integer mode numbers is sufficient to represent any general wave within the compressor. Such superposition gives a Fourier series for the periodic signal $\delta\phi$, where the period is 2π (i.e. one circumference of the compressor):

$$\delta\phi = \sum_{n>0} \delta\phi_n = \sum_{n>0} A_n \cos(n\theta) + \sum_{n>0} B_n \sin(n\theta) \quad (\text{B.3})$$

One can discuss a single component of this summation without loss of generality,

because the dynamics of the waves are linear and decoupled.

To fully represent the time variable, 2-D wave which exists in the compressor annulus, we must express A_n and B_n as functions of time, τ , and axial position, η . We will leave the time dependence of A_n and B_n as a variable, but we can, according to the results of Chapter 3, write the axial dependence as follows:

$$A_n(\tau, \eta) = a_n(\tau) \cdot e^{-n|\eta|}, \quad (\text{B.4})$$

$$B_n(\tau, \eta) = b_n(\tau) \cdot e^{-n|\eta|}. \quad (\text{B.5})$$

These equations indicate that perturbations are largest at the compressor face ($\eta=0$), and decay exponentially upstream and downstream. Keeping this axial dependence in mind, we can simplify notation by introducing a measurement station somewhere upstream of the compressor, at η_{HW} ($\eta_{\text{HW}} < 0$), and representing the wave as follows:

$$\begin{aligned} \delta\phi_n(\theta, \eta_{\text{HW}}, \tau) &= a_n(\tau) \cdot e^{(n\eta_{\text{HW}})} \cdot \cos(n\theta) + b_n(\tau) \cdot e^{(n\eta_{\text{HW}})} \cdot \sin(n\theta) \quad (\text{B.6}) \\ &\equiv x_{r_n}(\tau) \cdot \cos(n\theta) + x_{i_n}(\tau) \cdot \sin(n\theta) \end{aligned}$$

Where $x_{r_n}(\tau)$ and $x_{i_n}(\tau)$ are defined to satisfy the identity. Equations (B.5) and (B.6) are important, because they give a formulae for computing the *entire* n^{th} mode perturbation flowfield, for all values of η and θ , based on x_{r_n} and x_{i_n} alone. Superposition over all $n>0$ then gives the general solution to the system of equations (3.22 - 3.27).

Based on this discussion, we see that $x_{r_n}(\tau)$ and $x_{i_n}(\tau)$ completely specify the state of the system at time τ . x_{r_n} and x_{i_n} are real variables, and can be measured directly, using the DFT of evenly spaced hot wires placed at the measurement station η_{HW} (provided the number of transducers satisfies the spatial Nyquist criterion - see Section 4.1.2). Hence x_{r_n} and x_{i_n} are natural choices for the state variables of the system. If we represent the IGV deflections in a similar fashion:

$$\delta\gamma(\theta, \tau) = u_{r_n}(\tau) \cdot \cos(n\theta) + u_{i_n}(\tau) \cdot \sin(n\theta) \quad (\text{B.7})$$

then we can write a state-space matrix differential equation for the wave dynamics, based on the results of Sections 3.2.7, 3.3.1, and 3.3.2. The equation for a single mode number n is given in Equation (3.53). Here we write the equation for the first three modes, including an output equation for a typical 8-hot wire arrangement of sensors:

$$\begin{aligned}
 \begin{bmatrix} \dot{x}_{r1} \\ \dot{x}_{i1} \\ \dot{x}_{r2} \\ \dot{x}_{i2} \\ \dot{x}_{r3} \\ \dot{x}_{i3} \end{bmatrix} &= \begin{bmatrix} \begin{bmatrix} \sigma_{rs} & \omega_{rs} \\ -\omega_{rs} & \sigma_{rs} \end{bmatrix}_1 & & & \\ & \begin{bmatrix} \sigma_{rs} & \omega_{rs} \\ -\omega_{rs} & \sigma_{rs} \end{bmatrix}_2 & & \\ & & \begin{bmatrix} \sigma_{rs} & \omega_{rs} \\ -\omega_{rs} & \sigma_{rs} \end{bmatrix}_3 & \\ & & & \end{bmatrix} \cdot \begin{bmatrix} x_{r1} \\ x_{i1} \\ x_{r2} \\ x_{i2} \\ x_{r3} \\ x_{i3} \end{bmatrix} \quad (\text{B.8}) \\
 &+ \begin{bmatrix} \begin{bmatrix} b_r & b_i \\ -b_i & b_r \end{bmatrix}_1 \begin{bmatrix} u_r \\ u_i \end{bmatrix}_1 \\ \begin{bmatrix} b_r & b_i \\ -b_i & b_r \end{bmatrix}_2 \begin{bmatrix} u_r \\ u_i \end{bmatrix}_2 \\ \begin{bmatrix} b_r & b_i \\ -b_i & b_r \end{bmatrix}_3 \begin{bmatrix} u_r \\ u_i \end{bmatrix}_3 \end{bmatrix} + \begin{bmatrix} \begin{bmatrix} 0 & g_i \\ -g_i & 0 \end{bmatrix}_1 \begin{bmatrix} \dot{u}_r \\ \dot{u}_i \end{bmatrix}_1 \\ \begin{bmatrix} 0 & g_i \\ -g_i & 0 \end{bmatrix}_2 \begin{bmatrix} \dot{u}_r \\ \dot{u}_i \end{bmatrix}_2 \\ \begin{bmatrix} 0 & g_i \\ -g_i & 0 \end{bmatrix}_3 \begin{bmatrix} \dot{u}_r \\ \dot{u}_i \end{bmatrix}_3 \end{bmatrix} \\
 \begin{bmatrix} \delta\phi(0) \\ \delta\phi(\pi/4) \\ \delta\phi(\pi/2) \\ \delta\phi(3\pi/4) \\ \delta\phi(\pi) \\ \delta\phi(5\pi/4) \\ \delta\phi(3\pi/2) \\ \delta\phi(7\pi/4) \end{bmatrix} &= \begin{bmatrix} 1.0 & 0.0 & 1.0 & 0.0 & 1.0 & 0.0 \\ 0.7071 & 0.7071 & 0.0 & 1.0 & -0.7071 & 0.7071 \\ 0.0 & 1.0 & -1.0 & 0.0 & 0.0 & -1.0 \\ -0.7071 & 0.7071 & 0.0 & -1.0 & 0.7071 & 0.7071 \\ 1.0 & 0.0 & 1.0 & 0.0 & -1.0 & 0.0 \\ -0.7071 & -0.7071 & 0.0 & 1.0 & 0.7071 & -0.7071 \\ 0.0 & -1.0 & -1.0 & 0.0 & 0.0 & 1.0 \\ 0.7071 & -0.7071 & 0.0 & -1.0 & -0.7071 & -0.7071 \end{bmatrix} \cdot \begin{bmatrix} x_{r1} \\ x_{i1} \\ x_{r2} \\ x_{i2} \\ x_{r3} \\ x_{i3} \end{bmatrix} \\
 &= [\cos(\theta) \sin(\theta) \cos(2\theta) \sin(2\theta) \cos(3\theta) \sin(3\theta)] \cdot x
 \end{aligned}$$

Some notes about these equation:

- 1) The block-diagonal form of the system allows it to be considered mode-by mode.

- 2) The matrix in the output equation is the inverse DFT of the state variables. This matrix performs the superposition of sinusoids, giving the wave shape which the 8 hot wires measure (compare this equation to Equation (B.3)).
- 3) Equation (B.8) contains the implicit assumption that the spatial Nyquist criterion is satisfied - that is, there are no waves in $\delta\phi$ or $\delta\gamma$ with mode number greater than 3.

Equations (B.8) can be recast using *complex* spatial Fourier coefficients (SFCs). This greatly simplifies the mathematics and notation for compressor higher-mode dynamics, so SFCs are used for most of the discussions in this thesis. In Section 3.1.2.6, we defined the SFCs in such a way that the following relationships hold:

$$\tilde{\phi}_n \equiv x_{rn} + i \cdot x_{in}, \quad (\text{B.9})$$

$$\tilde{\gamma}_n \equiv u_{rn} + i \cdot u_{in}. \quad (\text{B.10})$$

Use of complex notation should be considered as a shorthand method for keeping track of the symmetry properties of the compressor. At any point, one can switch from complex (SFC) to real-valued expressions by expanding the equations into their real and imaginary parts (Section 3.3.2 and Equation (3.52) give examples of such expansion). In this appendix, we avoid complex notation, in order to better emphasize the physical (i.e. real-valued) significance of the structure of the dynamics. Although many of the features of the dynamics are more succinctly derivable using complex notation, confusion sometimes results from the presence of imaginary numbers. The reader is encouraged to convert the explanations given here to the complex plane whenever such conversion might be enlightening.

Let us first look at the homogeneous dynamics of the n^{th} mode wave. We can break out one diagonal block from Equation (B.8) and write (for $\delta\gamma=0$):

$$\begin{bmatrix} \dot{x}_r \\ \dot{x}_i \end{bmatrix}_n = \begin{bmatrix} \sigma_{rs} & -\omega_{rs} \\ \omega_{rs} & \sigma_{rs} \end{bmatrix}_n \cdot \begin{bmatrix} x_r \\ x_i \end{bmatrix}_n \quad (\text{B.11})$$

The skew-symmetric structure of the system is derived in Section 3.3.2. One can verify (by looking at the eigenvectors, or by solving (B.11) with an initial condition) that this structure causes the homogeneous solutions for x_{r_n} and x_{i_n} to oscillate 90 degrees out of phase with one another. For instance, one solution to (B.11) is

$$x_{r_n} = e^{\sigma_{rs} \cdot \tau} \cdot \cos(\omega_{rs} \cdot t) \quad (\text{B.12})$$

$$x_{i_n} = e^{\sigma_{rs} \cdot \tau} \cdot \sin(\omega_{rs} \cdot t) \quad (\text{B.13})$$

The out-of-phase oscillation of x_{r_n} and x_{i_n} causes the spatial wave $\delta\phi$ (which we can reconstruct using (B.6)) to rotate around the compressor annulus, with phase speed $\omega_{rs} \cdot \tau$ and magnitude $e^{\sigma_{rs} \cdot \tau}$:

$$\begin{aligned} \delta\phi &= e^{\sigma_{rs} \cdot \tau} \cdot \left[\cos(\omega_{rs} \cdot t) \cdot \cos(n\theta) + \sin(\omega_{rs} \cdot t) \cdot \sin(n\theta) \right] \quad (\text{B.1}) \\ &= e^{\sigma_{rs} \cdot \tau} \cdot \cos(n\theta - \omega_{rs} \cdot t) \end{aligned}$$

We have shown that the homogeneous behavior of the system consists of rotating waves. But the real compressor is not a deterministic system in which we can specify an initial condition. Rather, it is a stochastic system which is continually forced by random processes. One way to try to capture this behavior is to add a forcing term to the homogeneous dynamics:

$$\begin{bmatrix} \dot{x}_r \\ \dot{x}_i \end{bmatrix}_n = \begin{bmatrix} \sigma_{rs} & -\omega_{rs} \\ \omega_{rs} & \sigma_{rs} \end{bmatrix}_n \cdot \begin{bmatrix} x_r \\ x_i \end{bmatrix}_n + \begin{bmatrix} v_r \\ v_i \end{bmatrix}_n \quad (\text{B.15})$$

where v_{r_n} and v_{i_n} are random noise processes of unknown character. The question is: in this more realistic situation, will a rotating wave develop?

To answer this question, we rely on digital simulation of Equation (B.15). We simulate time histories of x_{r_n} and x_{i_n} , reconstruct the wave as in (B.14), and then see if it tends to rotate. Plotting the entire wave $\delta\phi$ at each instant of time, however, is tedious and unnecessary for our purposes. One can easily visualize the development

of the wave by plotting its magnitude and phase as functions of time:

$$\delta\phi = M(\tau) \cdot \cos(n\theta + \beta(\tau)) \quad (\text{B.16})$$

If we plot $\beta(\tau)$ and it behaves like $\omega_{rs} \cdot t$, we can conclude that a rotating wave exists, with amplitude $M(\tau)$.

To run a simulation, one must decide what type of excitation noise to apply. In a real experiment, the compressor is experiencing axial velocity perturbations due to various sources, such as turbulence and separation within the compressor, variation in the tip clearance due to vibration, unsteady interaction between the rotors and the stators, and inlet flow variations. Little is known about the modal characterization of these phenomena. We will see, however, that underdamped rotating stall dynamics exhibit clearly visible behavior even when the noise driving the system is of a very general character. To see this, we run the simulations with independent white noise sequences for v_{rn} and v_{in} . This characterization is modal, but assumes that both the magnitude and phase of the excitation wave are varying randomly with time.

Figure B.1 shows the simulation results. Four different time histories are shown, representing various levels of stability of the system. In all four plots, the rotating stall frequency is the same, $\omega_{rs} = 0.25$. The excitation noise sequences v_r and v_i are also identical in all four simulations. Only the stability parameter, σ_{rs} , varies - the system becomes progressively less stable in each subsequent plot: $\sigma_{rs} = -0.625, -0.125, -0.025, \text{ and } -0.05$.

Examination of Figure (B.1) supports the following conclusions: As σ_{rs} becomes smaller, the system tends to resonate more strongly in response to the excitation. $M(\tau)$ becomes progressively larger (in an rms sense), and the frequency ω_{rs} becomes progressively more prominent in $\beta(\tau)$. For σ_{rs} values below 0.025, the wave travels very distinctly for periods of 10 rotor revolutions or more. Thus the linear dynamics in (B.15) are sufficient to account for the traveling wave phenomena seen in the experiments presented in Chapter 6.

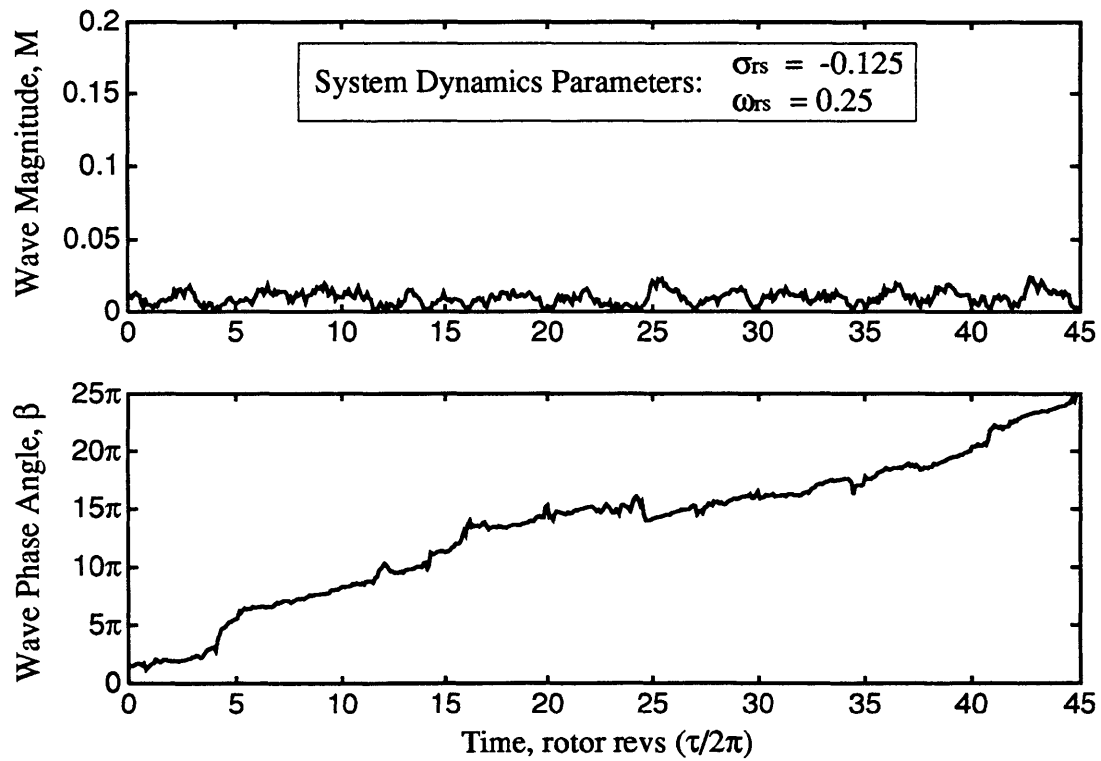
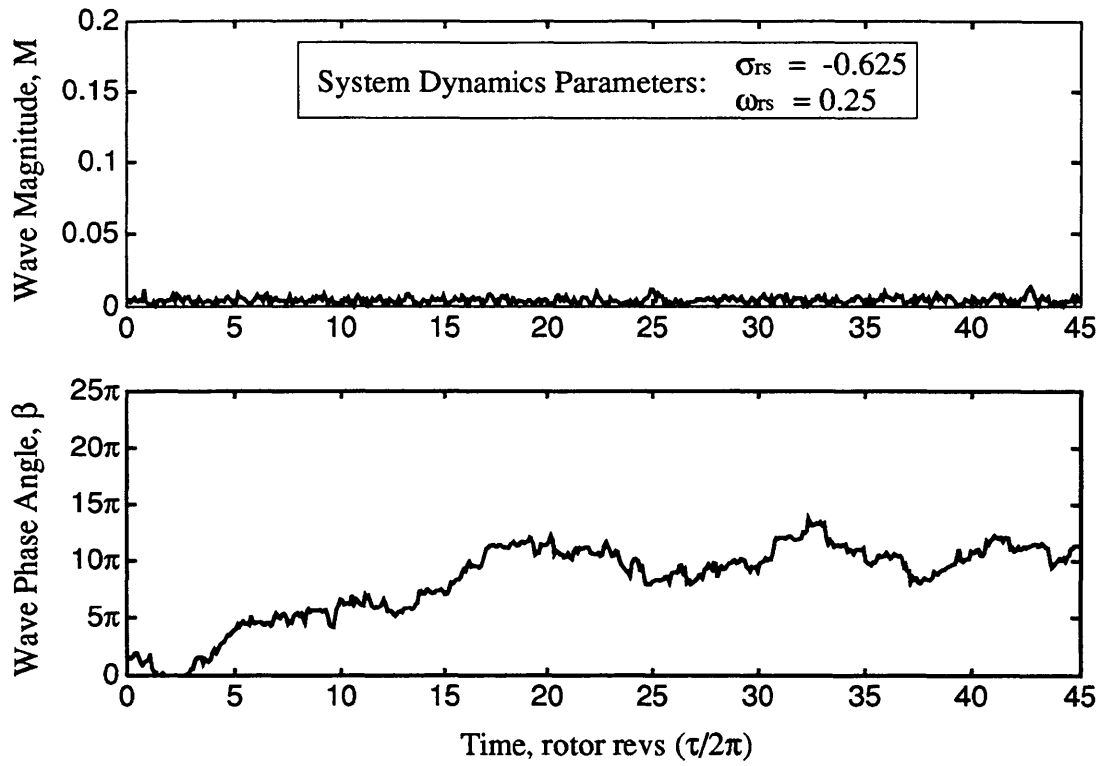


Figure B.1 - Simulation results for a skew-symmetric dynamic system, forced with random signals.

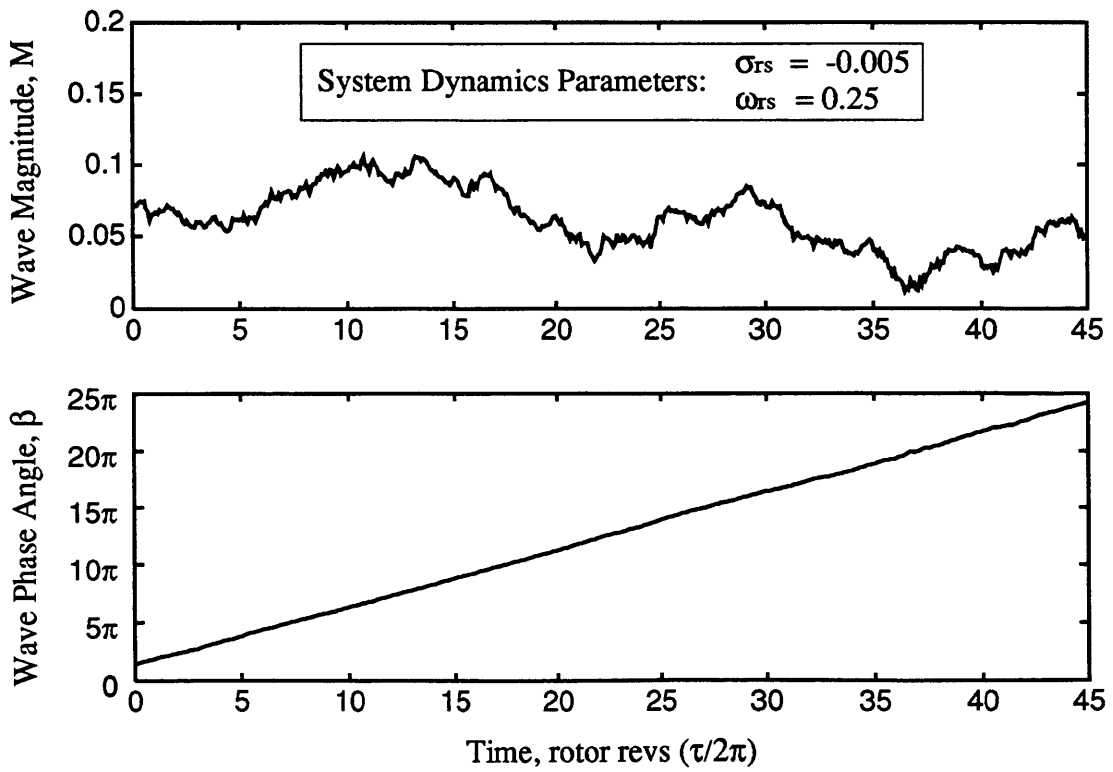
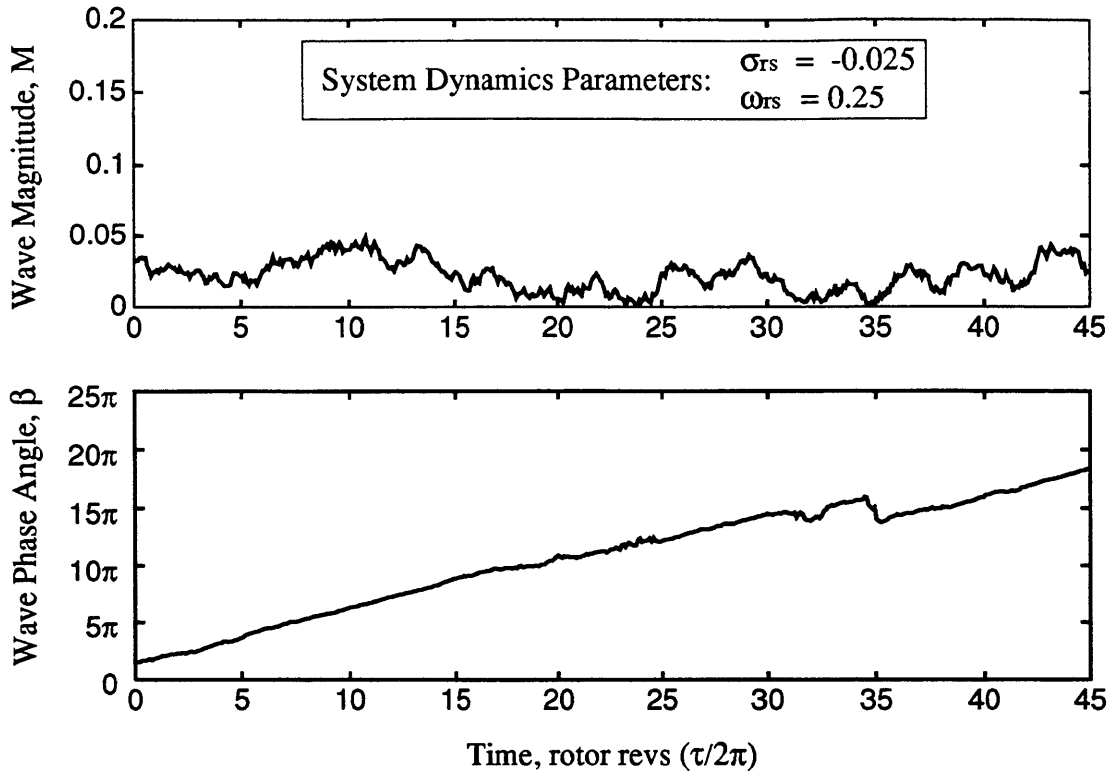


Figure B.1 (Continued) - Simulation results for a skew-symmetric dynamic system, forced with random inputs.

Appendix C

Stall Inception Data for Various Compressor Builds

The body of this thesis presents results for the particular compressor geometry given in Table 2.1. This geometry can be varied in the following ways:

- 1) IGV mean stagger angle can be changed.
- 2) Rotor and stator stagger angles can be changed.
- 3) Rotor blades can be changed from low twist (10°) to high twist (30°).

'IGV mean stagger' refers to the steady-state, axisymmetric turning of the blades, defined as positive if pre-swirl is introduced in the direction of rotor rotation. The terms 'stagger' and 'twist' are defined in Table 2.1. If any combination of the geometric parameters listed above is changed, then we have a different 'compressor build'. Each compressor build has its own performance and stall behavior. It is the purpose of this appendix to study the effect of compressor build on stall inception behavior for the single-stage research compressor.

Since we are studying compressor dynamics which lead to rotating stall, we are primarily interested in the transients associated with these dynamics. These transients are most visible at *stall inception* - that is, during the transition from axisymmetric operation to the fully developed rotating stall condition. Thus we will present several views of stall inception for each compressor build studied. We will begin by discussing different types of fully-developed stall versus different types of stall inception behavior.

C.1 Fully-Developed Stall and Stall Inception Behavior

In [8], Greitzer describes two types of fully-developed rotating stall. These two types are broad categories into which most observed stall cells fit. They are distinguished mainly by the *radial extent* of the stall cells: 'Full-span stall' refers to stall cells which extend from hub to tip, while 'part-span stall' refers to stall cells which are confined to a specific radial region, such as the rotor tip. The stall inception data we will present in Section C.3 also falls into these two broad categories. Full-span stall inception consists of growing perturbations which are essentially constant across the annulus, while part-span stall inception involves radially localized perturbations.

Full-span stall inception, since it involves the entire radial extent of the compressor, can potentially be modelled using the 2-D methods described in Chapter 3. If the other assumptions in Chapter 3 are valid, we expect full-span stall inception to involve the resonance or instability of the compressor higher-mode dynamics. Instability is predicted to occur where the compressor characteristic slope ($-\frac{\partial \psi}{\partial \phi}$) becomes positive. As the stall flow coefficient is approached, strong resonance waves should be visible prior to stall - these waves are called 'pre-stall' or 'precursor' waves by Garnier [15], and were originally measured by McDougall [13]. These waves should, according to the theory, grow smoothly into fully developed, full-span stall. Furthermore, stabilization of the higher-mode compressor dynamics should damp these waves, and subsequently delay the onset of rotating stall to lower flow coefficients.

Part-span stall inception, on the other hand, is strongly 3-dimensional in character, and thus violates a primary assumption in the compressor modeling of Chapter 3. Part-span stall inception also tends to be very localized both circumferentially and axially [8,17], which makes it difficult to model using

semi-actuator disk methods. This does not mean that higher-mode compressor dynamics (i.e. 2-D wave phenomena) do not exist in compressors which exhibit part-span stall inception; rather it means that such dynamics may not be resonant or unstable at stall inception (this concept was first introduced by Day [17]). Thus the analysis methods presented in Chapters 5 and 6 might indicate that the system is stable, even though stall inception is imminent.

In some cases, part-span stall inception develops into part-span stall. If flow coefficient is further reduced, this part-span stall cell usually transitions into full-span stall. In some of the compressor builds we will present, transition to full-span stall occurs with little or no reduction in flow coefficient. In these builds, part-span stall is not a stable operating condition of the compressor, but instead an intermediate stage in the development of rotating stall. Yet another case exists, in which *only the inception phase* admits part-span behavior; as soon as the stall cell begins to grow, it immediately transitions to full-span stall.

From the previous discussion we see that it is important to distinguish between *inception* behavior and the *fully-developed* rotating stall condition. Active control schemes attempt to stabilize the perturbations which lead to rotating stall, so that fully-developed stall never occurs. Thus the characteristics of the inception phase determine the type of actuation, sensing, and control which should be applied.

C.2 Description of the Experiments

Six rotor-stator geometries are presented in Figures C.1 through C.40. For each rotor-stator geometry, data for three settings of IGV mean stagger angle are tested, for a total of 18 compressor builds. A table of compressor builds appears in Table C.1. Each compressor build has its own total-to-static pressure rise characteristic, $\psi(\phi)$, and its own stall inception behavior.

Total-to-static characteristics, $\psi(\bar{\phi})$, are presented in groups of three, grouped

according to rotor-stator geometry. See Table C.1 for the figure numbers associated with each compressor build. Plots of $\psi(\phi)$ for various values of $\delta\gamma$ (IGV stagger) give a way to estimate $\frac{\partial\psi}{\partial\gamma}$.

For each compressor build, hot wires are used to record the axial velocity transients leading to rotating stall. 8 hot wires are placed upstream of the IGVs, and 8 more are placed downstream of the rotor. The upstream hot wires are placed at midspan, because this is the configuration desired for implementation of a 2-D active control scheme. The downstream hot wires, on the other hand, are positioned at alternating radial locations - half are placed at 15% of rotor span (near the hub), and the other half are placed at 85% of rotor span (near the casing). Hot wires alternate between 15% and 85% span as their circumferential angle θ increases. This hub/tip alternation of the downstream hot wires allows disturbances which are not radially constant (i.e. part-span disturbances) to be detected as they travel around the annulus.

Stall inception is recorded during extremely slow throttle transients (less than 0.1% change in flow coefficient per second) as described in Section 2.5. Sample rates, hot wire calibration, hot wire axial and circumferential positions, and other experimental details are presented in Chapter 2.

C.3 Measurements of Part-Span and Full-Span Stall Inception

Figure C.5 shows the hot wire traces behind the rotor for a part-span stall. The velocity traces near the casing (every other trace) show a severe velocity deficit which travels around the annulus - i.e. a stall cell. Notice that the stall cell has relatively small circumferential extent - about 90 degrees of the compressor annulus. More importantly, however, is the difference between these traces and the velocity traces at the hub. Hub traces show *peaks* instead of troughs when the stall cell passes. This behavior indicates that the stall cell is radially nonuniform. One explanation of the data is that the stall cell causes blockage of flow at the tip. The flow is

subsequently redirected to the hub, causing a velocity peak at the hub at roughly the same position as the stall cell.

Figure C.7 shows the hot wire traces behind the rotor for a part-span stall *inception*. In this case, the stall cell in its fully-developed stage is full-span - thus the hub and tip velocity traces look very similar by the end of the data window. However, during the transition from axisymmetric operation to full-span stall, there is distinct radially nonuniform behavior which closely resembles the part-span stall behavior seen in Figure C.5. Thus we label this 'part-span stall inception'.

The hub/tip velocity traces behind the rotor are by far the easiest way to detect part-span stall inception. However, it is important to see the effects of part-span stall inception on the measurements which we intend to use for active control. These measurements are all taken at mid-span, consistent with our 2-dimensional approach to active control. They are placed upstream of the IGVs to improve signal-to-noise ratio, under the assumption that stall inception is dominated by first, second, or possibly third mode perturbation waves, which are measurable upstream.

Since the assumptions we used to rationalize sensor placement are not valid when stall inception is part-span, we expect the measurements to be somewhat ambiguous. Figures C.7 and C.8 indicate what happens. In Figure C.7, the upstream velocity traces show what looks like a smooth, 2-D transition into rotating stall. The plot of the first spatial Fourier coefficient (SFC) in Figure C.8 is more ambiguous: although the stall cell seems to grow smoothly into rotating stall, no precursor waves exist - the measured first mode does not tend to travel before stall begins, and its magnitude is small (compare Figure C.8 to Figure 6.5). Apparently, the first mode is not resonating at all prior to stall - the higher-mode (2-D wave) dynamics seem to be stable.

Another indication that stall inception is part-span is the change in rotation speed of the first SFC during transition to fully-developed stall. This change in

rotation speed causes a noticeable change in slope of the phase curve in Figure C.8. The transition from part-span to full-span stall often causes such a kink in the SFC phase plot.

Finally, the lack of resonance of the first mode can be verified using the PSD method (introduced in Section 6.1.3). The PSD in Figure C.8 shows almost no resonance in the first mode prior to stall (compare Figure C.8 to Figure 6.12). Again, 2-D interpretation of the data seems to indicate that the higher-mode dynamics are stable.

Figures C.37 and C.38 show an example of full-span stall inception. The hub/tip hot wire traces show slight differences between the hub and the tip, but no indication of part span stall. In concurrence with this essentially 2-D behavior, both the upstream hot wire traces (Figure C.37) and the first SFC plot (Figure C.38) indicate a period of strong resonance prior to stall which is at least 100 revolutions long. Thus it seems that the higher mode dynamics are indeed resonating. Phase of the first mode travels at a single speed, starting well before stall and continuing without break until stall is fully developed. The underdamped nature of the first mode is also verified by the PSD plot in Figure C.38. Finally, the results of Chapter 6 show that damping the first mode delays stall onset for this compressor build.

C.4 Discussion

Using arguments similar to those presented in Section C.3, one can readily interpret Figures C.1 through C.40. We will make a few overall comments here about the results. Rotor-stator geometries are described in Table C.1 for reference.

Rotor-stator geometries #1, #2, and #3 all exhibit very clear part-span stall, or part-span stall inception followed by full-span stall. Thus these geometries are not particularly suited for the 2-D control scheme used in this thesis. The prevalence of part span stall might be explained by two factors: First, single-stage compressors are

more prone to part-span stall than are multi-stage compressors [39,45]. Second, the rotor blades used in these experiments were originally designed to operate with significant inlet swirl from the IGVs - in the range of 30 degrees. However, the movable IGVs (which replaced the original IGVs - see Chapter 2) are uncambered, so staggers above 10 degrees on the IGVs would cause separation. Thus for the mean IGV staggers used (-10° , 0° , and 10°) the rotor is often operating off-design, making it difficult to achieve even loading across the span of the blades at stall inception.

Since both the number of stages in the experiment, and the spanwise loading of the rotor are not typical of multi-stage compressors which are designed to have balanced spanwise loading, the prevalence of part-span stall in this compressor is not an indication of the general prevalence of part-span stall in all compressors. We present this data to show the variations in behavior that are possible, rather than to determine the types of stall that are most common.

Of all the builds tested, only those with rotor-stator geometry #6 exhibit clear full-span stall inception. This geometry, with 0° mean IGV stagger, is used for all of the experiments described in the body of this thesis.

Table C.1 - Compressor Builds Tested

<u>Rotor-Stator Geometry #1:</u>	<u>Build #</u>	<u>IGV mean stagger</u>	<u>Figure numbers</u>
Rotor Stagger 45°	1	-10	C.2
Rotor Twist 10°	2	0	C.3, C.4
Stator Stagger 22.5°	3	10	C.5
Speed lines: Figure C.1			
<u>Rotor-Stator Geometry #2:</u>	<u>Build #</u>	<u>IGV mean stagger</u>	<u>Figure numbers</u>
Rotor Stagger 35°	4	-10	C.7, C.8
Rotor Twist 10°	5	0	C.9, C.10
Stator Stagger 22.5°	6	10	C.11, C.12
Speed lines: Figure C.6			
<u>Rotor-Stator Geometry #3:</u>	<u>Build #</u>	<u>IGV mean stagger</u>	<u>Figure numbers</u>
Rotor Stagger 35°	7	-10	C.14, C.15
Rotor Twist 10°	8	0	C.16, C.17
Stator Stagger 12.5°	9	10	C.18, C.19
Speed lines: Figure C.13			
<u>Rotor-Stator Geometry #4:</u>	<u>Build #</u>	<u>IGV mean stagger</u>	<u>Figure numbers</u>
Rotor Stagger 25°	10	-10	C.21, C.22
Rotor Twist 10°	11	0	C.23, C.24
Stator Stagger 12.5°	12	10	C.25, C.26
Speed lines: Figure C.20			
<u>Rotor-Stator Geometry #5:</u>	<u>Build #</u>	<u>IGV mean stagger</u>	<u>Figure numbers</u>
Rotor Stagger 45°	13	-10	C.28, C.29
Rotor Twist 30°	14	0	C.30, C.31
Stator Stagger 22.5°	15	10	C.32, C.33
Speed lines: Figure C.27			
<u>Rotor-Stator Geometry #6:</u>	<u>Build #</u>	<u>IGV mean stagger</u>	<u>Figure numbers</u>
Rotor Stagger 35°	16	-10	C.35, C.36
Rotor Twist 30°	17	0	C.37, C.38
Stator Stagger 22.5°	18	10	C.39, C.40
Speed lines: Figure C.34			

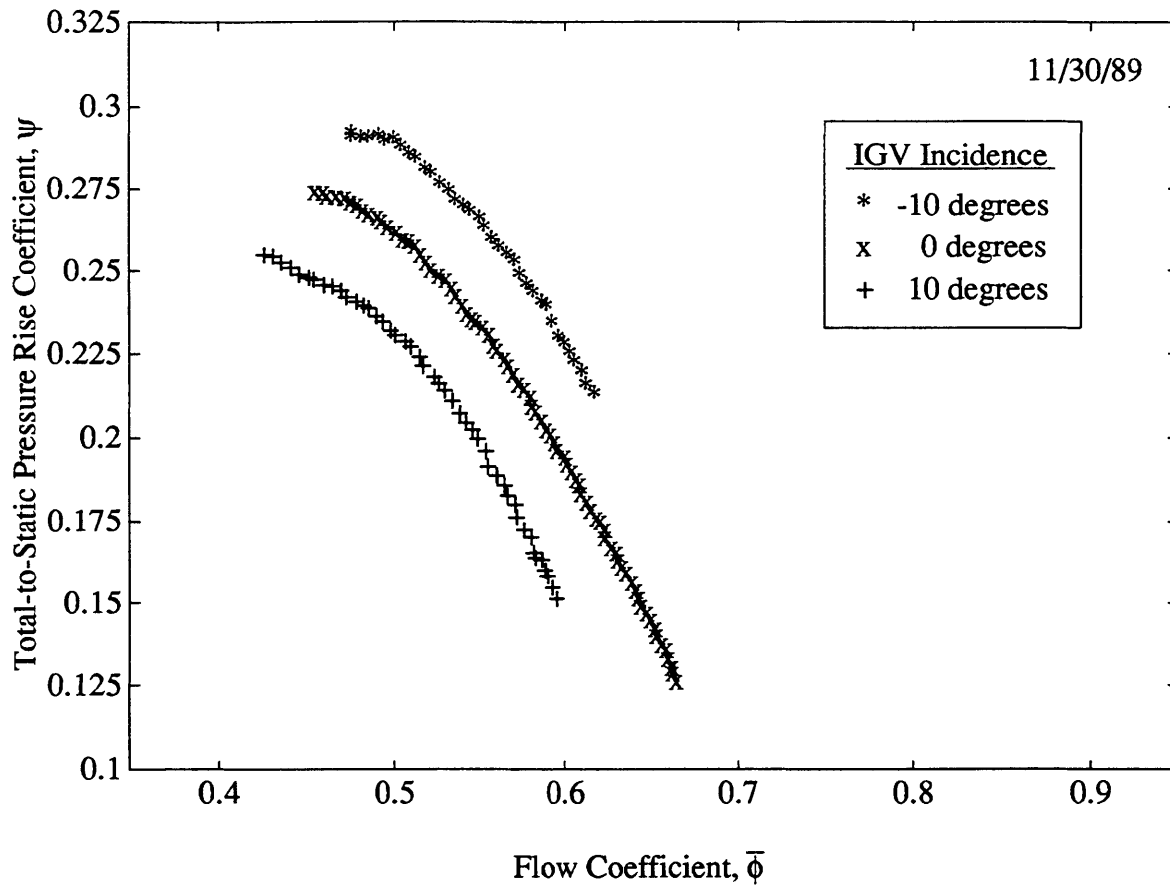


Figure C.1 - 2700 RPM Speed Lines for Rotor-Stator Geometry #1

Notes:

- 1) Geometry is given in Table 2.1 except:
 - Rotor Stagger: 45°
 - Rotor Twist: 10°
 - Stator Stagger: 22.5°
- 2) Hot wire data for IGV @ -10° indicate **part-span stall inception**.
- 3) Hot wire data for IGVs @ 0°, 10° show that part-span stall is a stable operating condition for these builds.
- 4) Upstream hot wire traces are not available for this build.

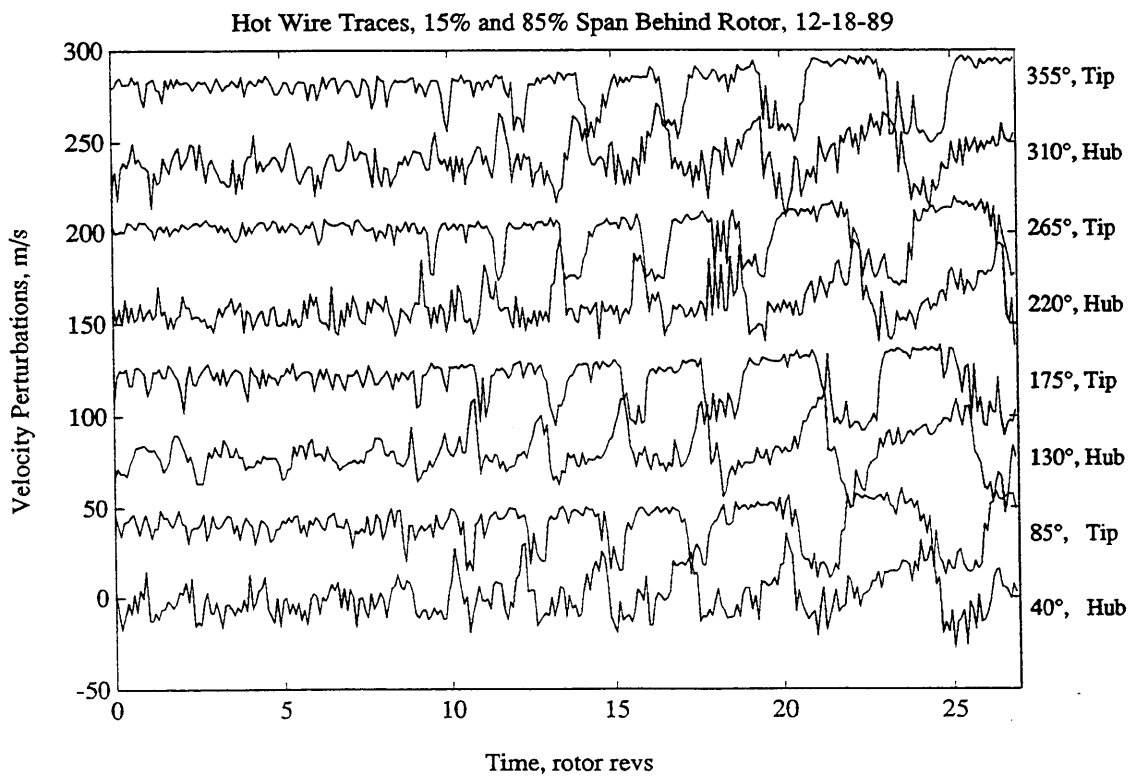


Figure C.2 - Hot wire traces at stall inception for Build #1A (IGVs @ -10 deg)

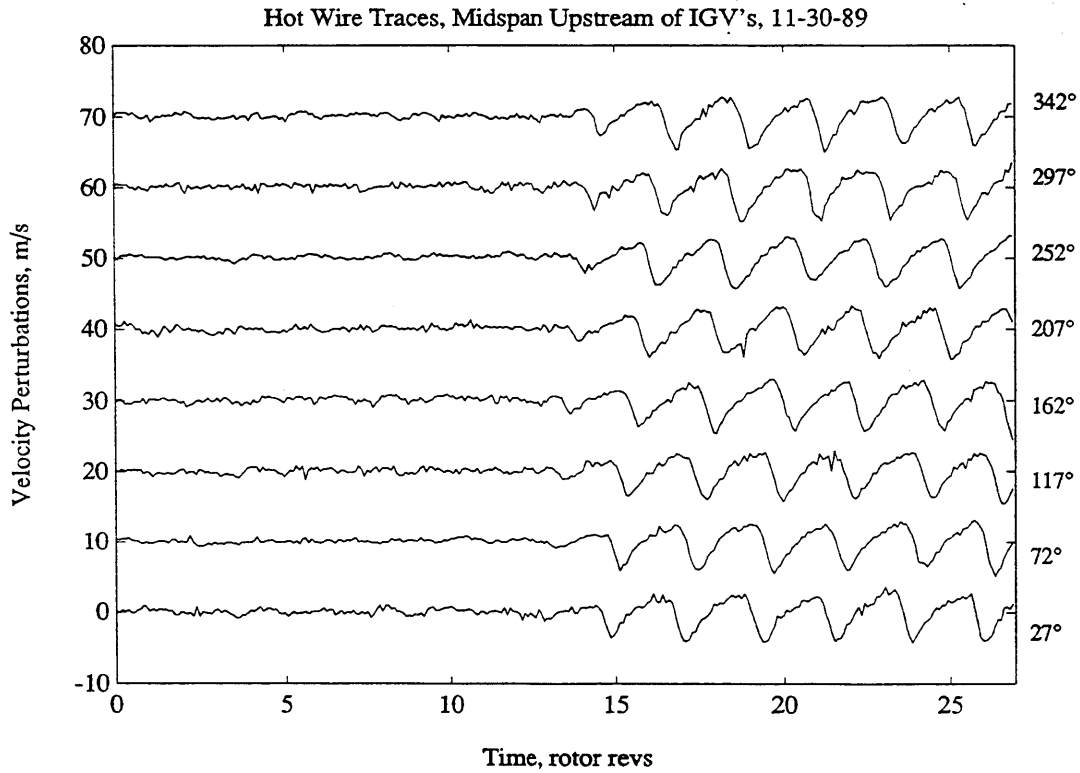
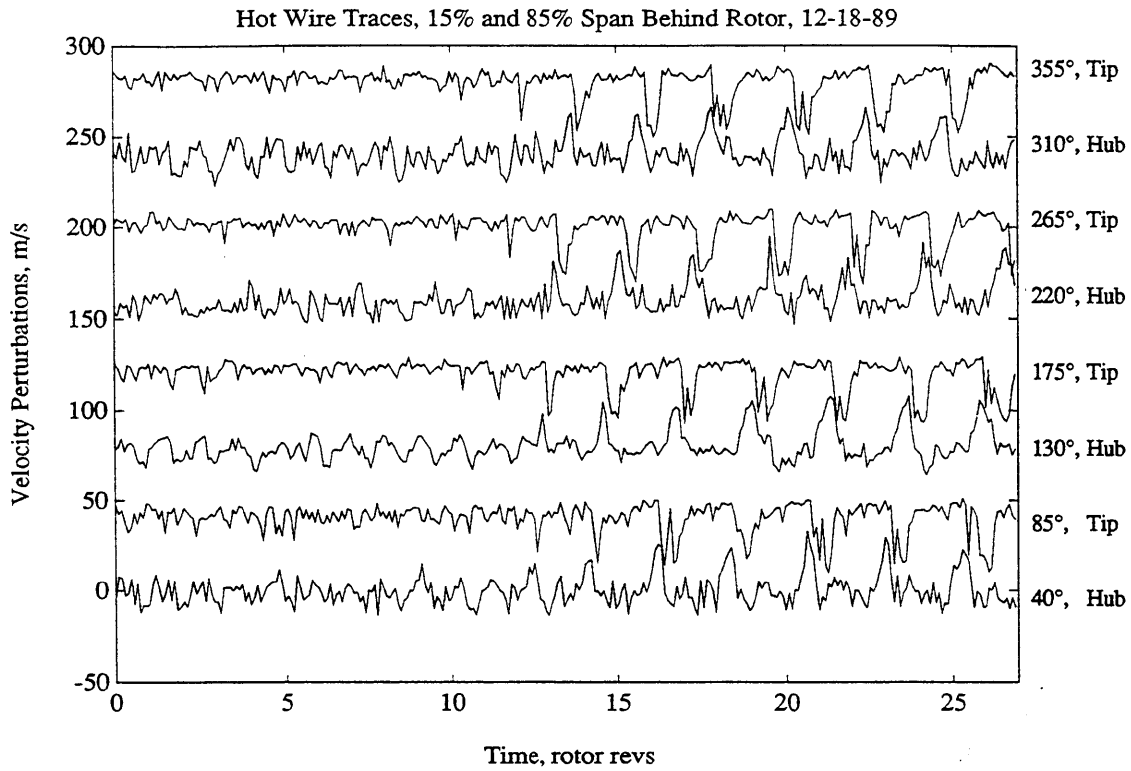


Figure C.3 - Hot wire traces at stall inception for Build #1B (IGVs @ 0 deg)

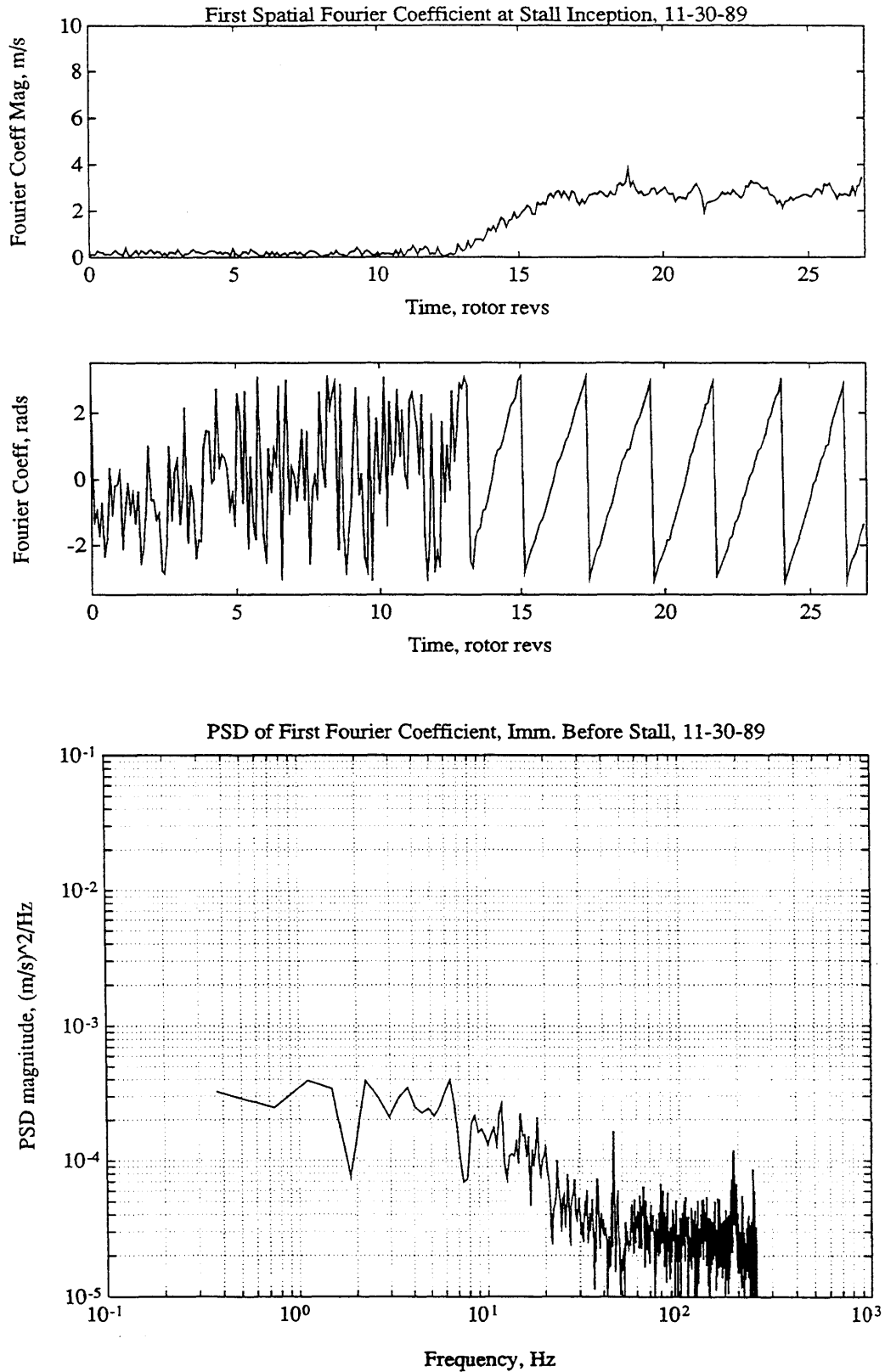


Figure C.4 - Analysis of first spatial Fourier coefficient. Derived from hot wire data from Build #1B (see Figure C.3, second plot).

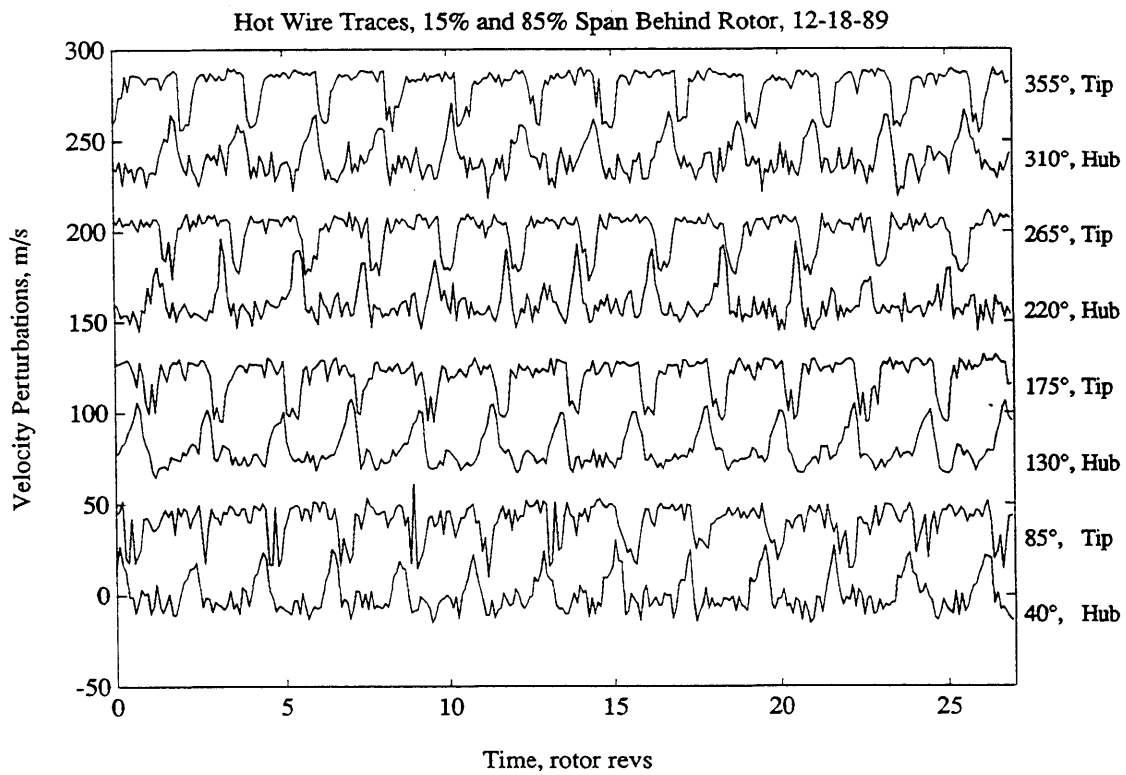


Figure C.5 - Hot wire traces at stall inception for Build #1C (IGVs @ 10 deg)

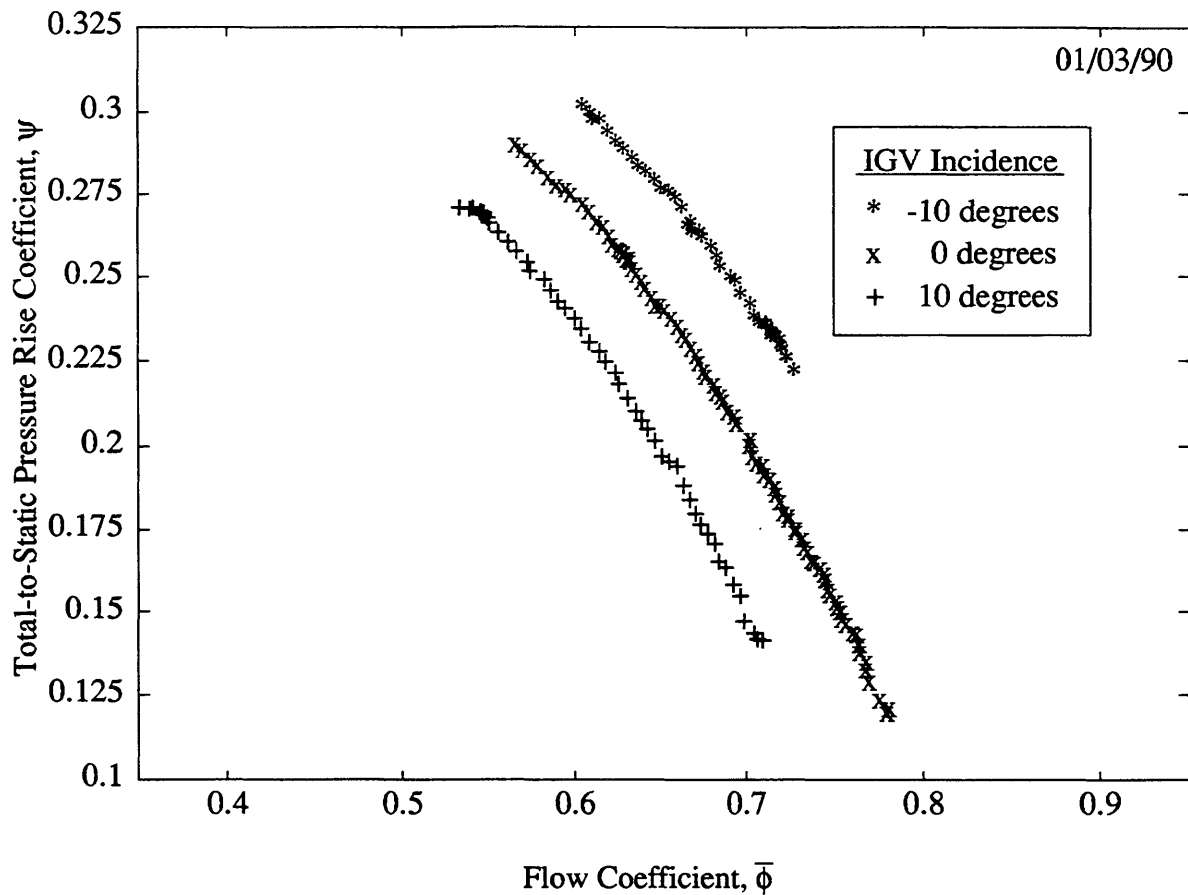


Figure C.6 - 2700 RPM Speed Lines for Rotor-Stator Geometry #2

Notes:

- 1) Geometry is given in Table 2.1 except:
 - Rotor Stagger: 35°
 - Rotor Twist: 10°
 - Stator Stagger: 22.5°
- 2) Hot wire data for IGV incidences -10° , 0° exhibit **part-span stall inception**.
- 3) Hot wire data for IGVs @ 10° shows that part-span stall is a stable operating condition for this build.

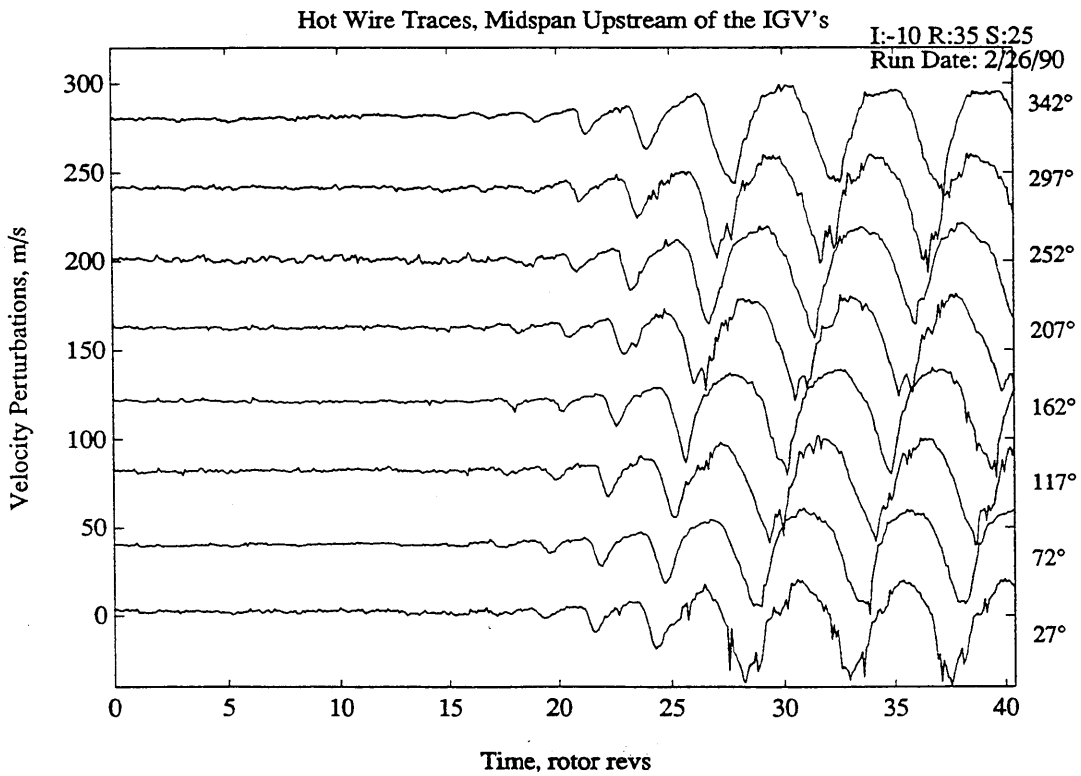
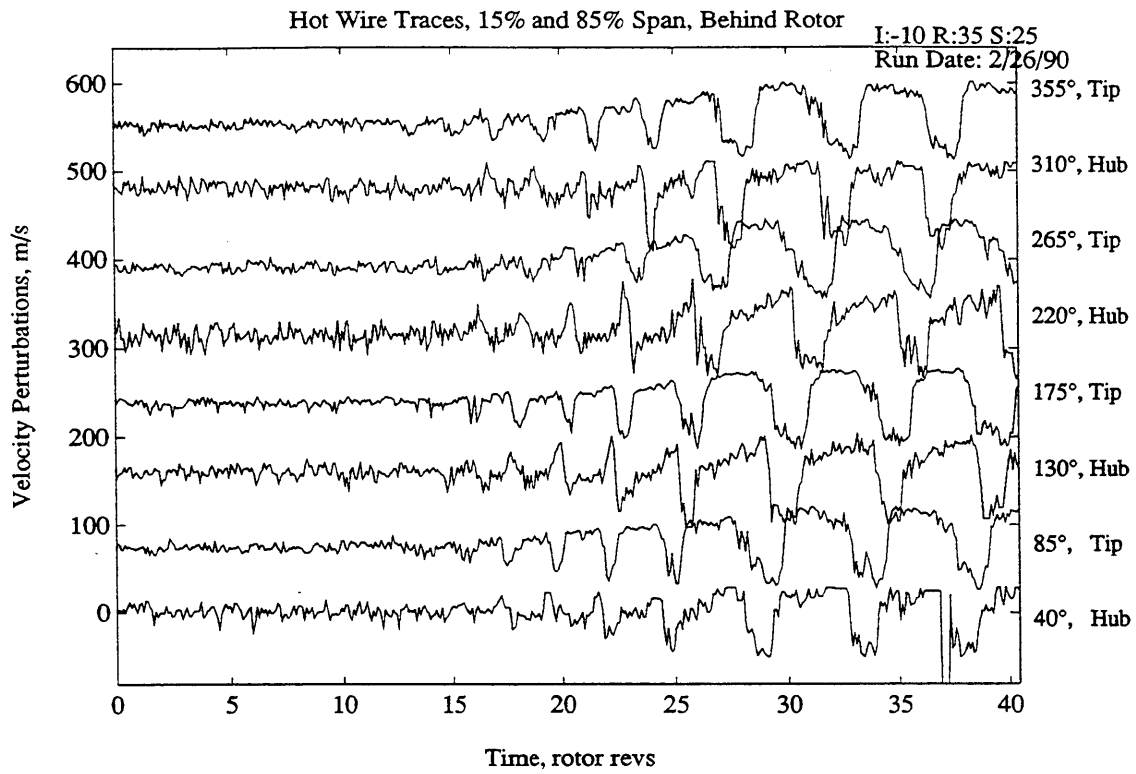


Figure C.7 - Hot wire traces at stall inception for Build #2A (IGVs @ -10 deg)

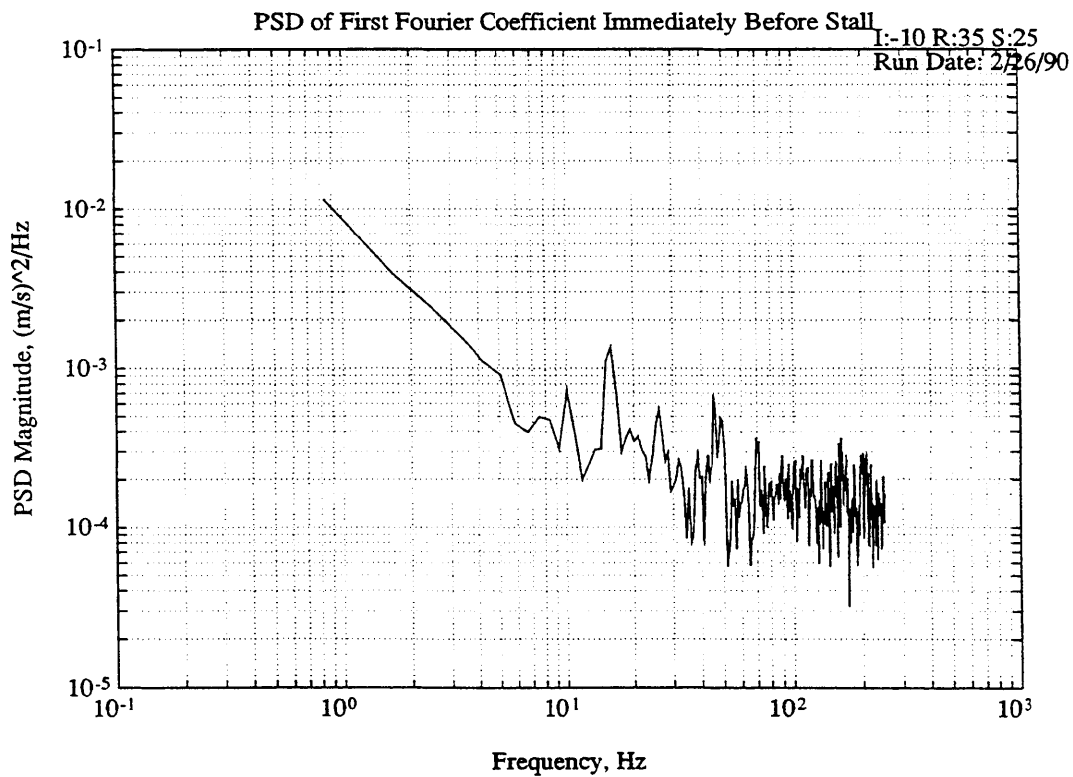
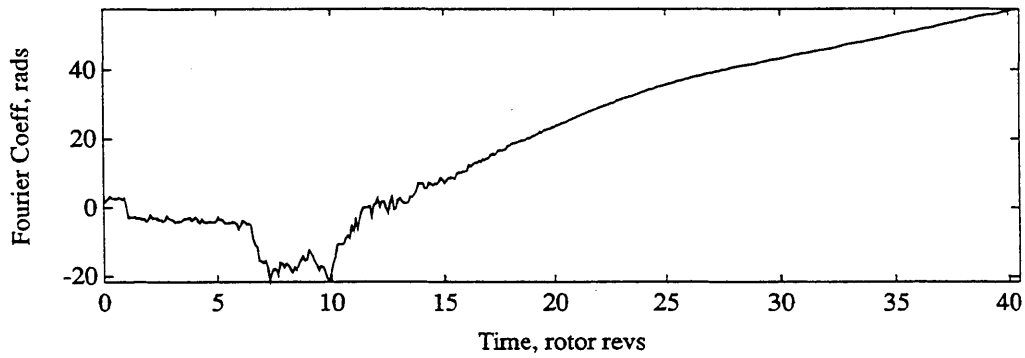
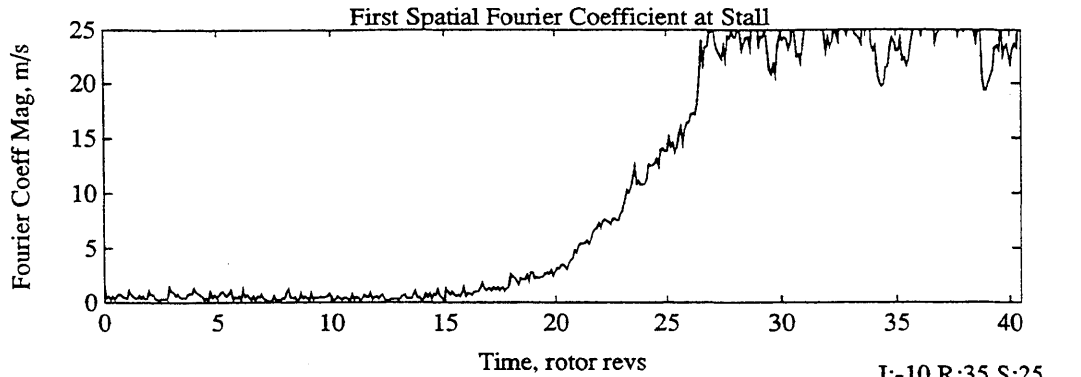


Figure C.8 - Analysis of first spatial Fourier coefficient. Derived from hot wire data from Build #2A (see Figure C.7, second plot).

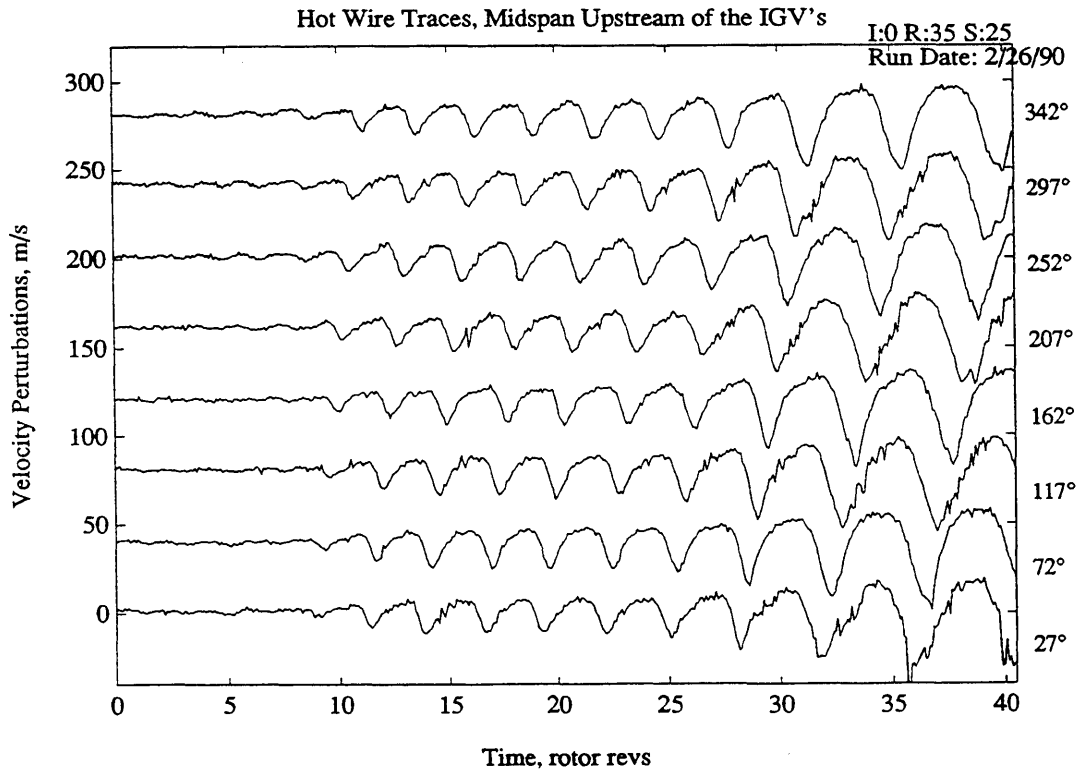
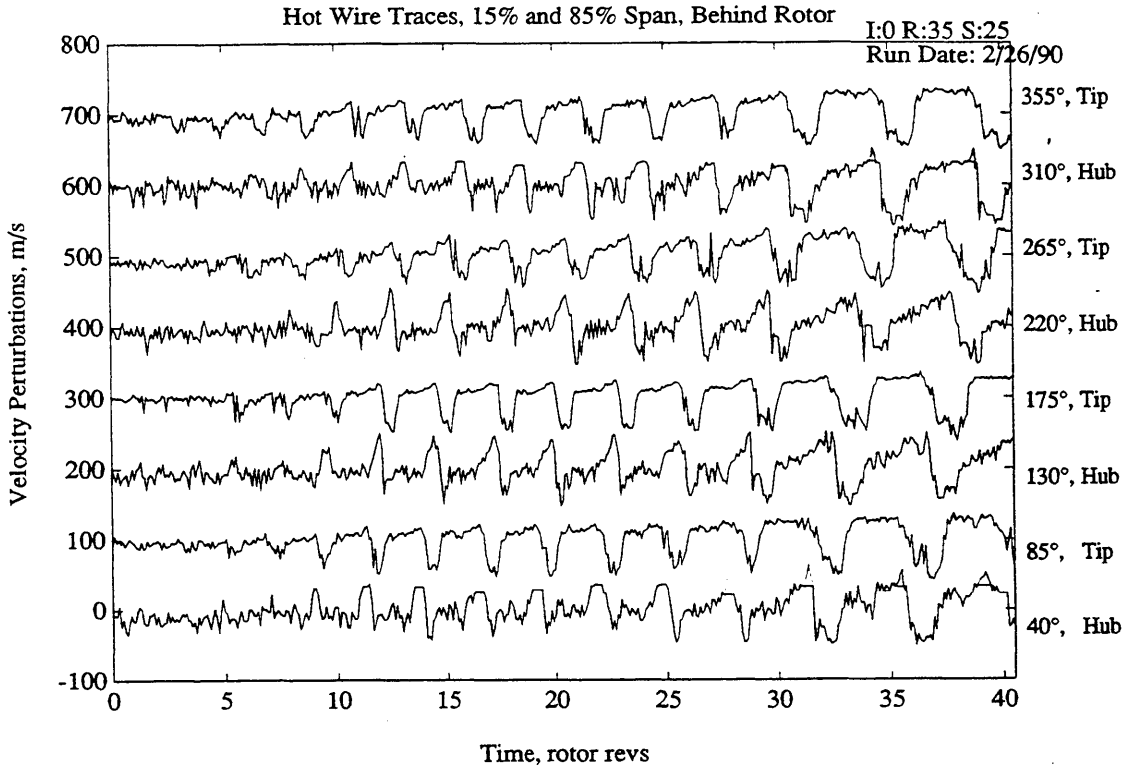


Figure C.9 - Hot wire traces at stall inception for Build #2B (IGVs @ 0 deg)

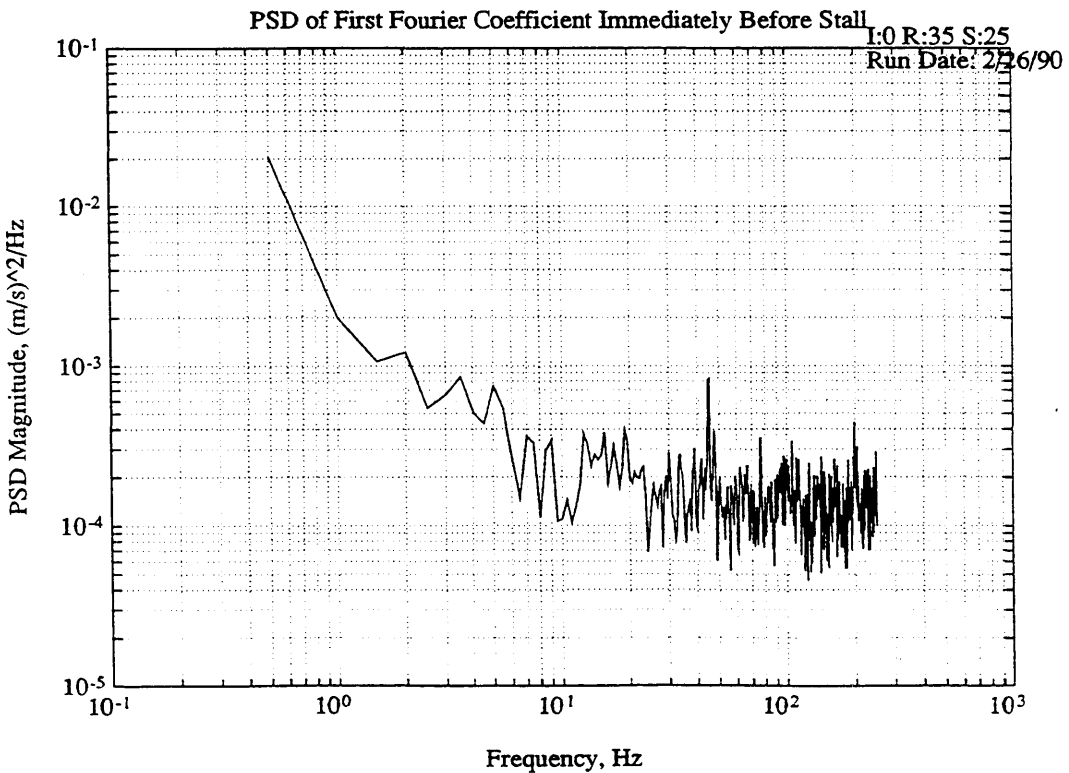
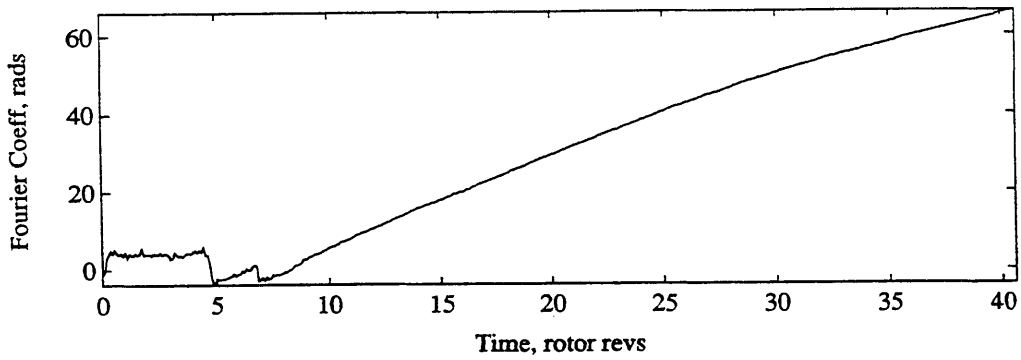
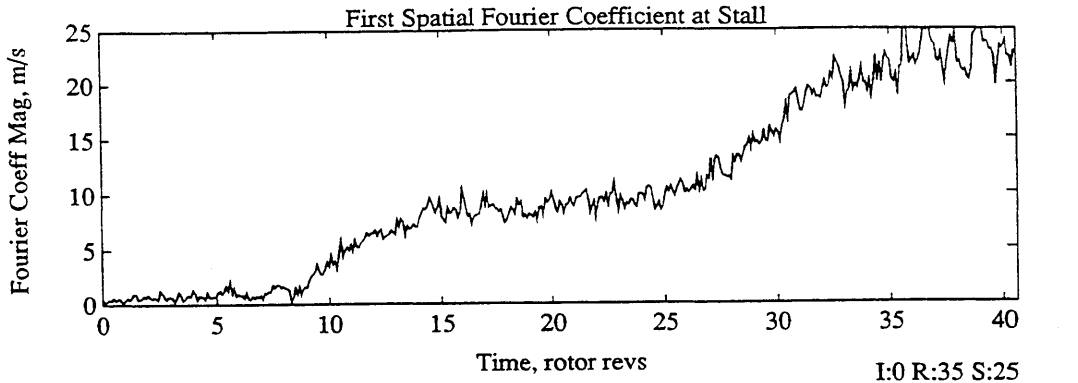


Figure C.10 - Analysis of first spatial Fourier coefficient. Derived from hot wire data from Build #2B (see Figure C.9, second plot).

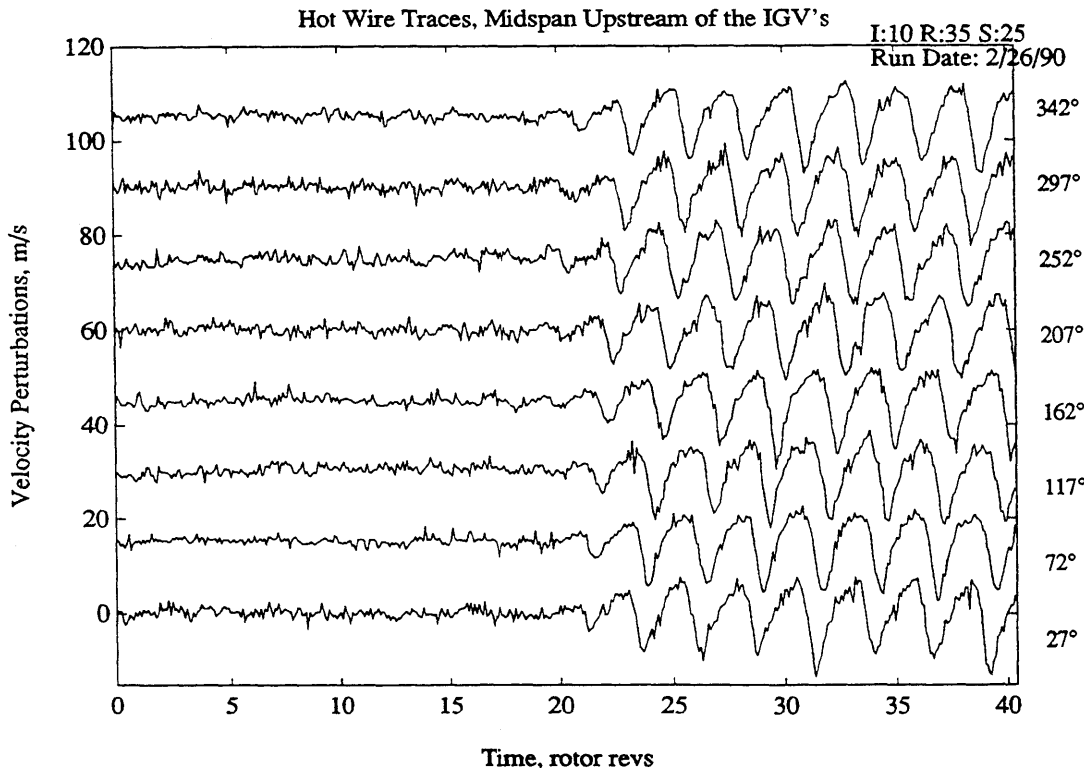
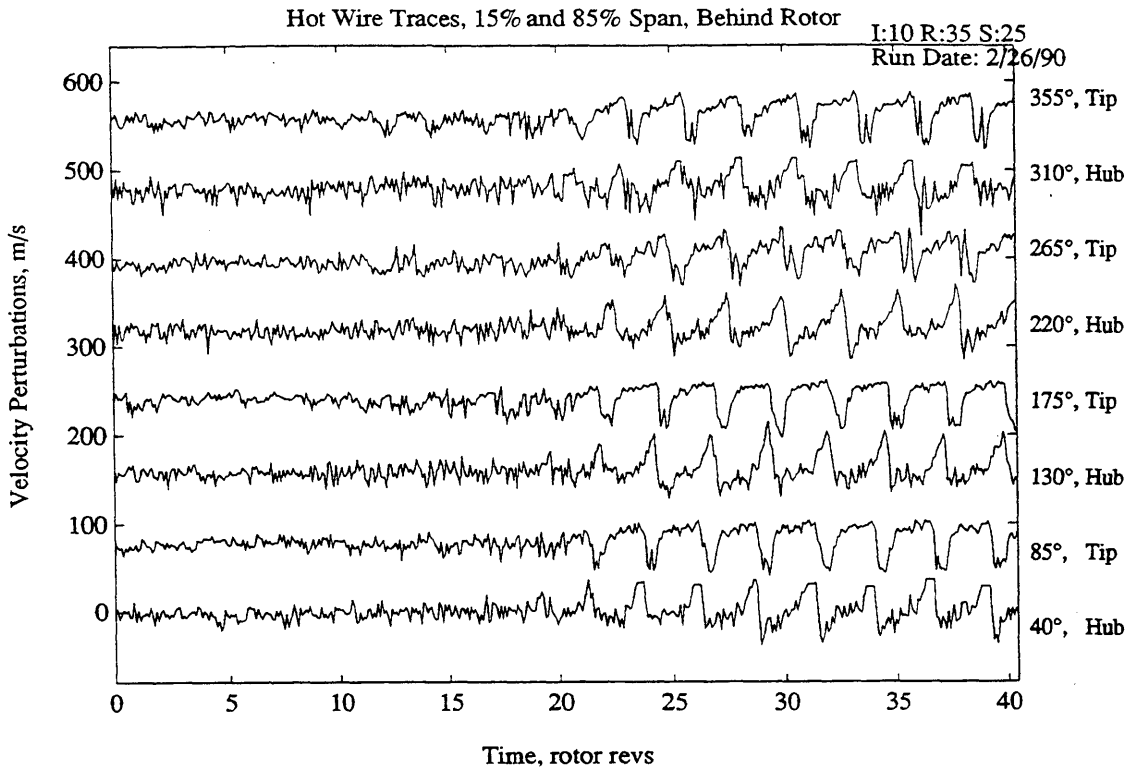


Figure C.11 - Hot wire traces at stall inception for Build #2C (IGVs @ 10 deg)

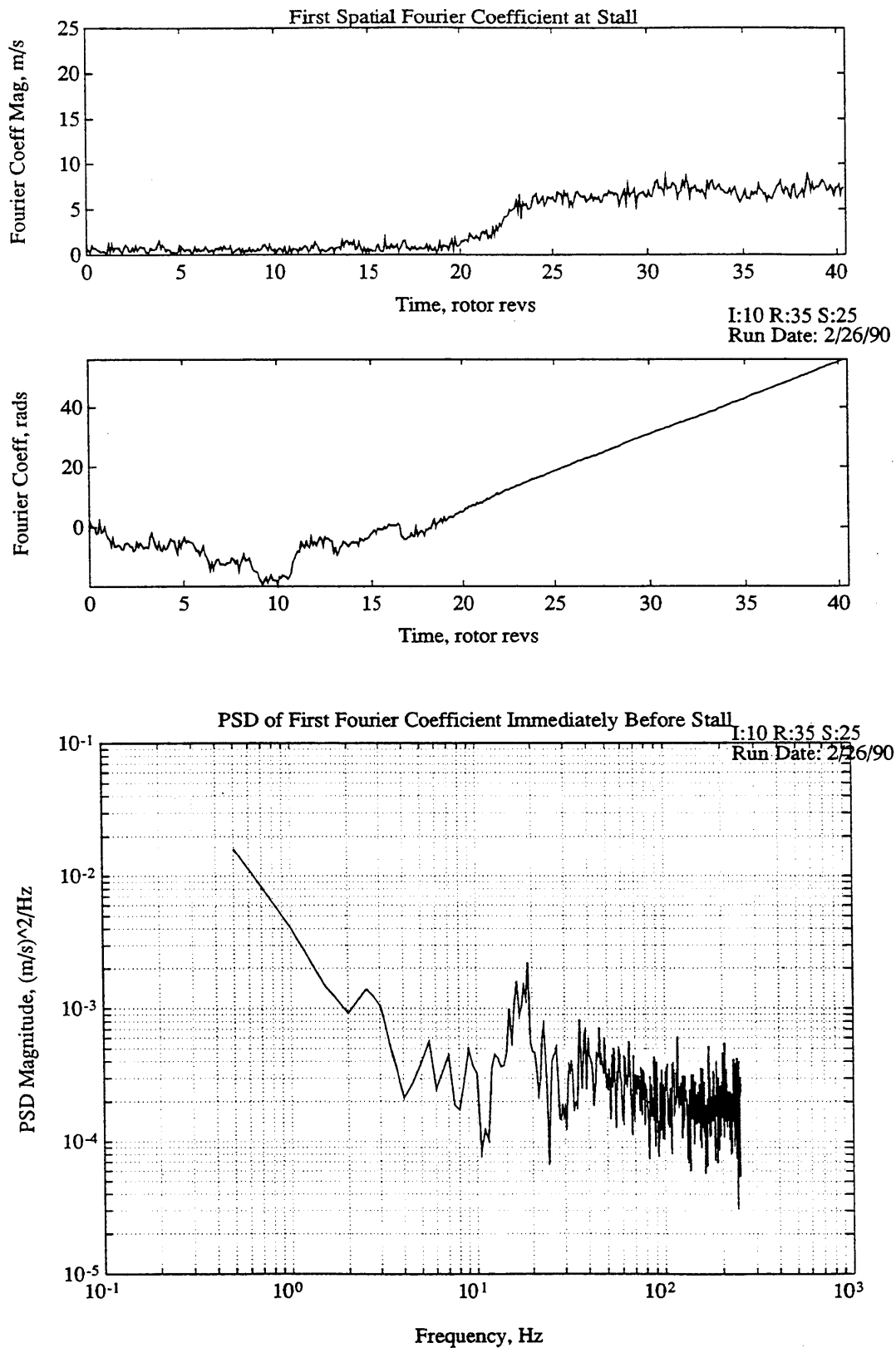


Figure C.12 - Analysis of first spatial Fourier coefficient. Derived from hot wire data from Build #2C (see Figure C.11, second plot).

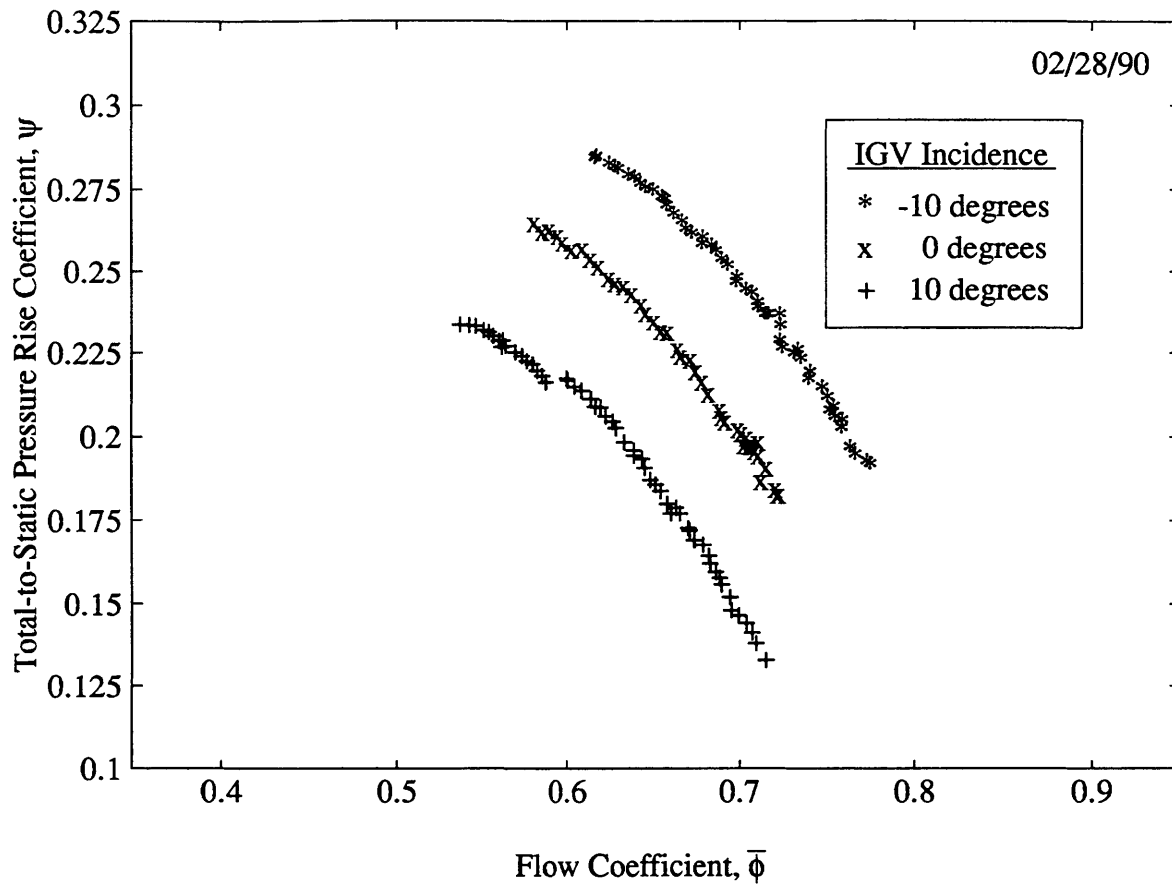


Figure C.13 - 2700 RPM Speed Lines for Rotor-Stator Geometry #3

Notes:

- 1) Geometry is given in Table 2.1 except:
 - Rotor Stagger: 35°
 - Rotor Twist: 10°
 - Stator Stagger: 12.5°
- 2) Hot wire data for IGV incidences $-10^\circ, 0^\circ$ exhibit **part-span stall inception**.
- 3) Hot wire data for IGVs @ 10° shows stable part-span stall.

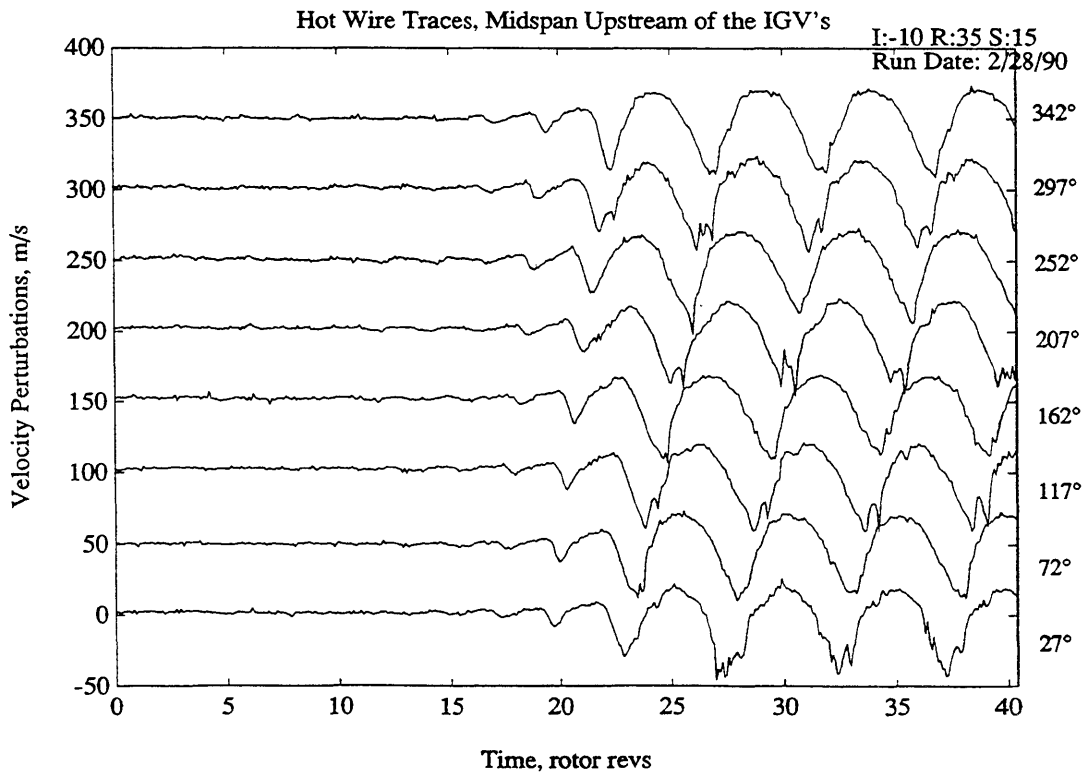
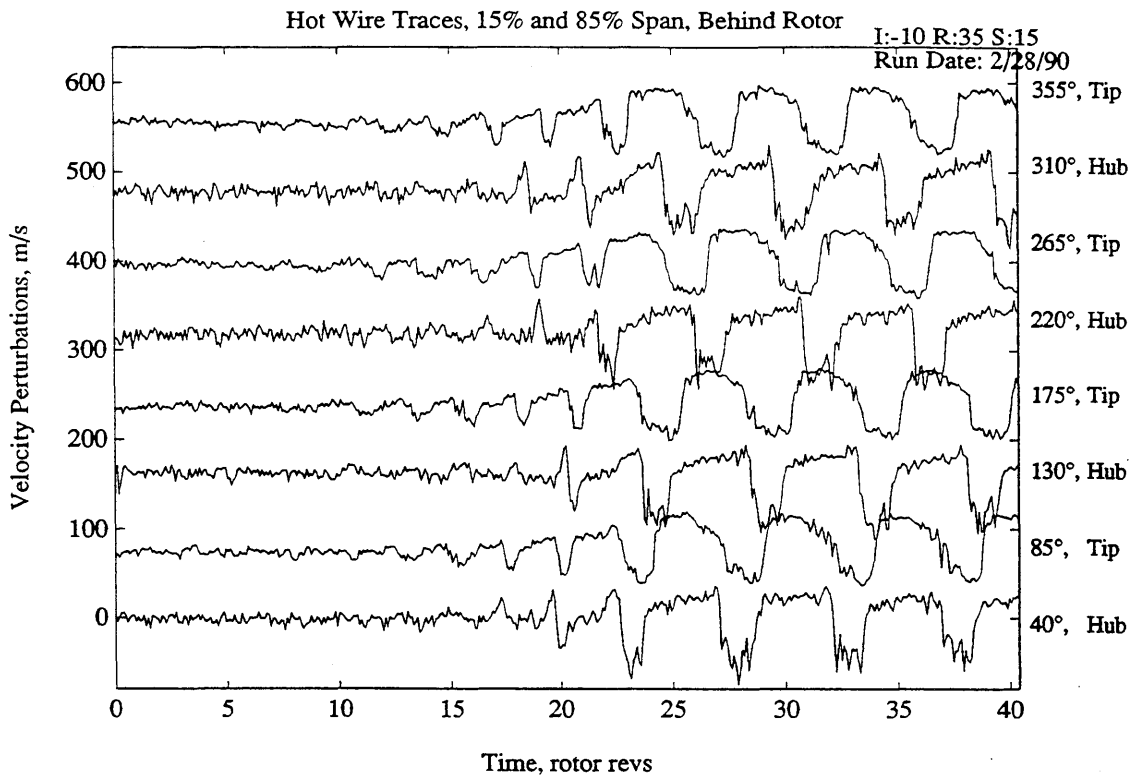


Figure C.14 - Hot wire traces at stall inception for Build #3A (IGVs @ -10 deg)

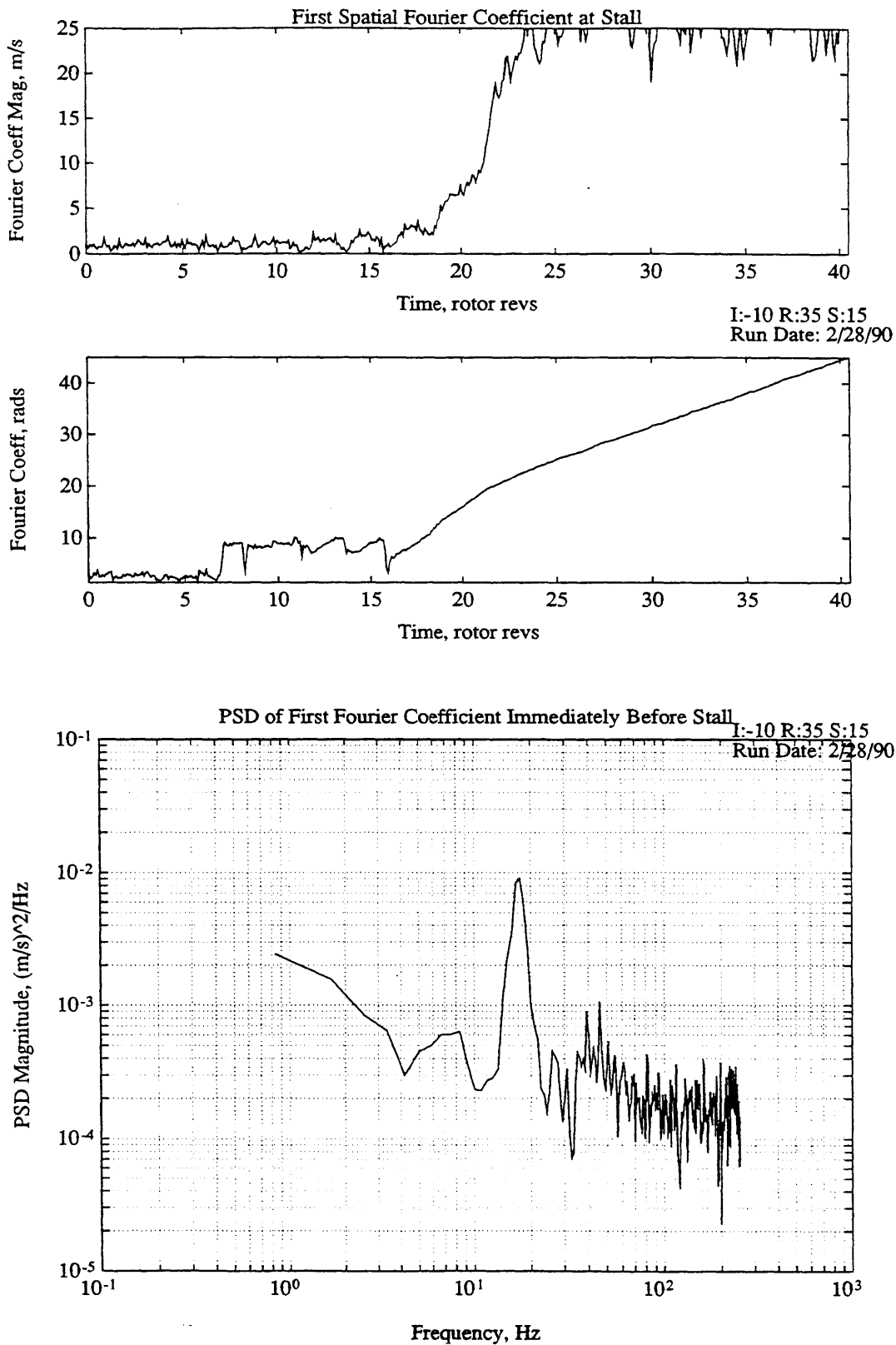


Figure C.15 - Analysis of first spatial Fourier coefficient. Derived from hot wire data from Build #3A (see Figure C.14, second plot).

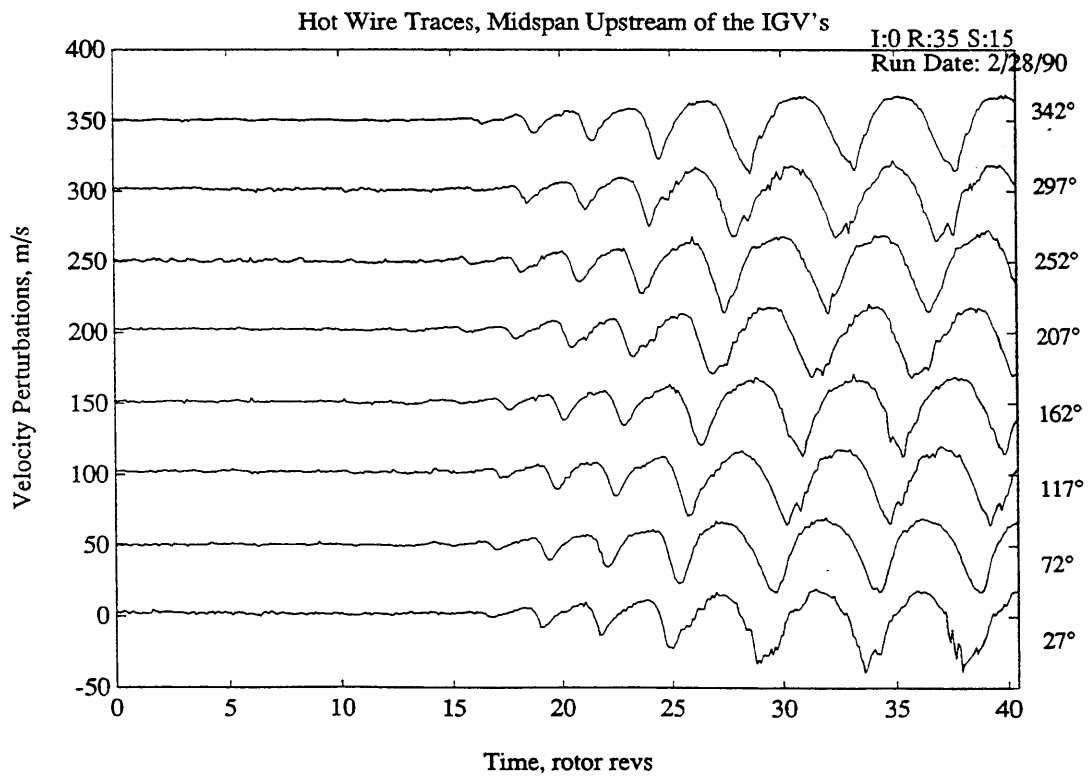
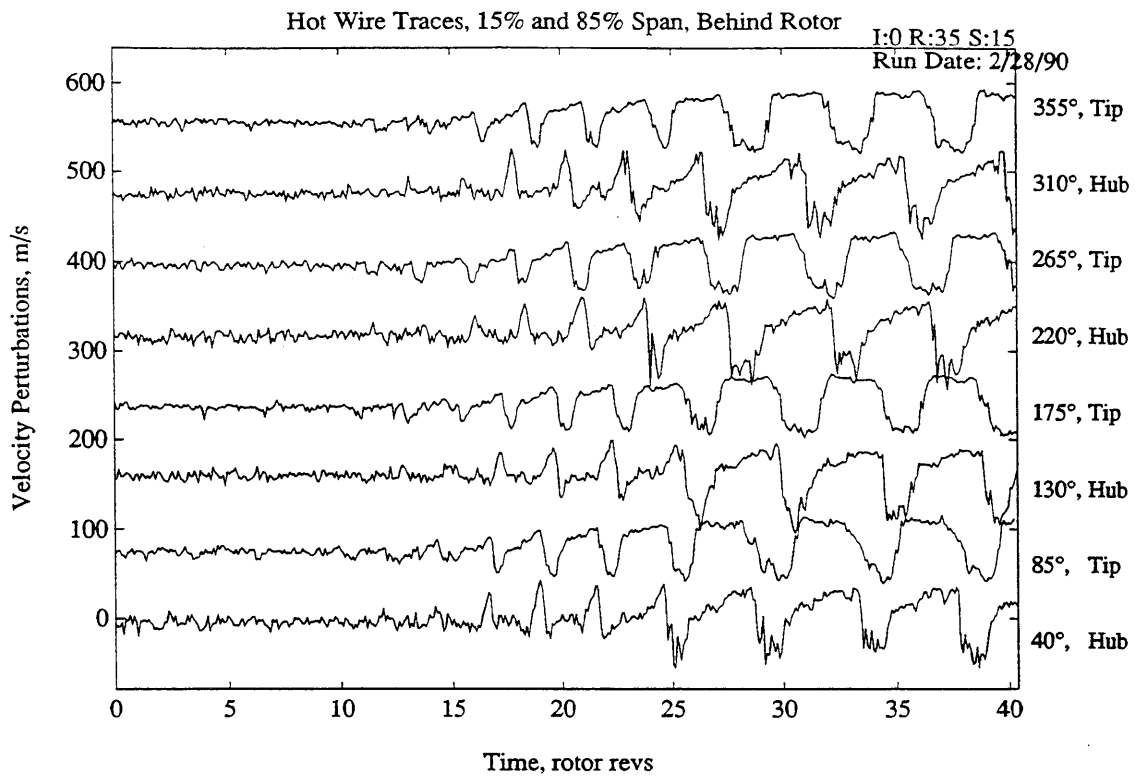


Figure C.16 - Hot wire traces at stall inception for Build #3B (IGVs @ 0 deg)

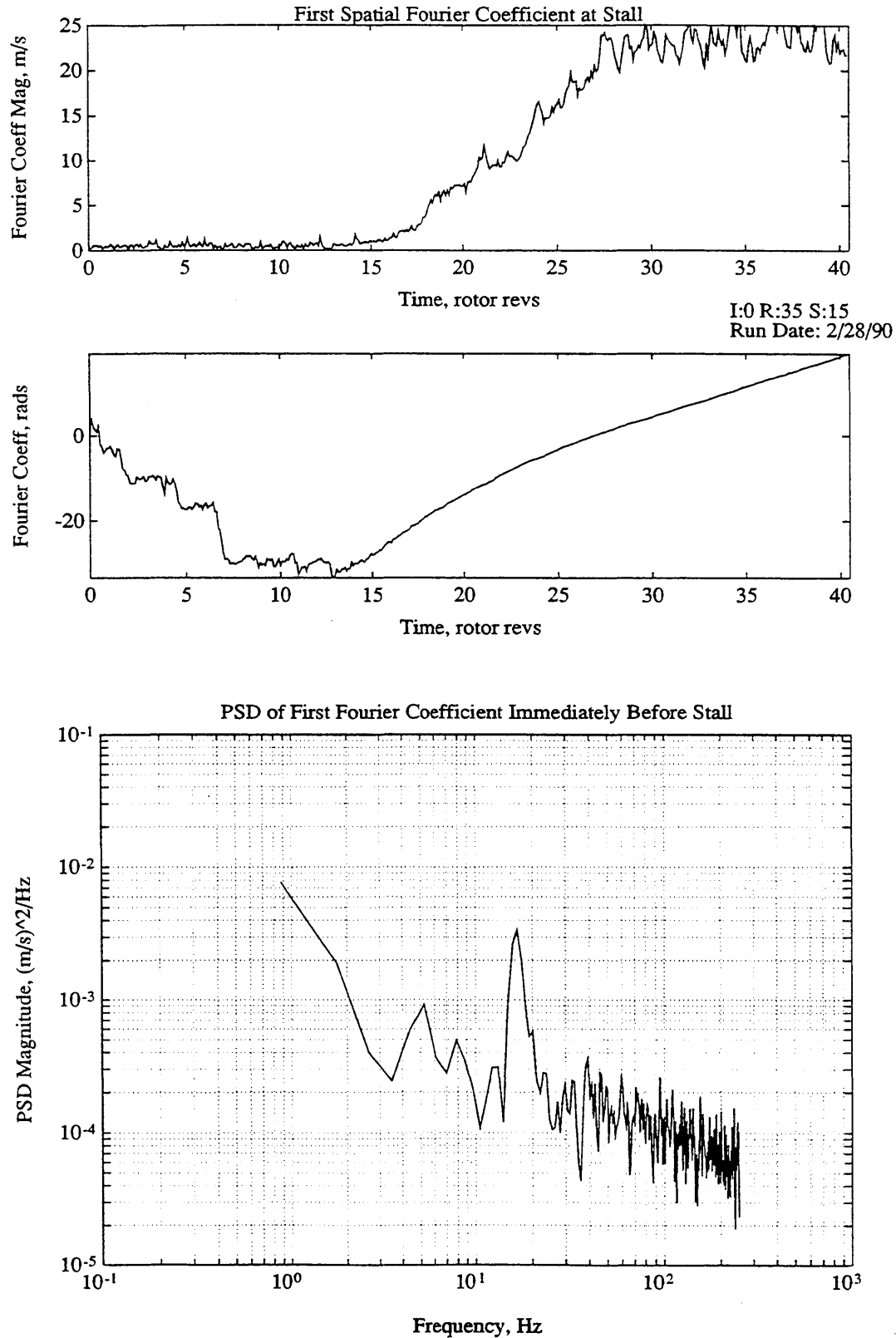


Figure C.17 - Analysis of first spatial Fourier coefficient. Derived from hot wire data from Build #3B (see Figure C.16, second plot).

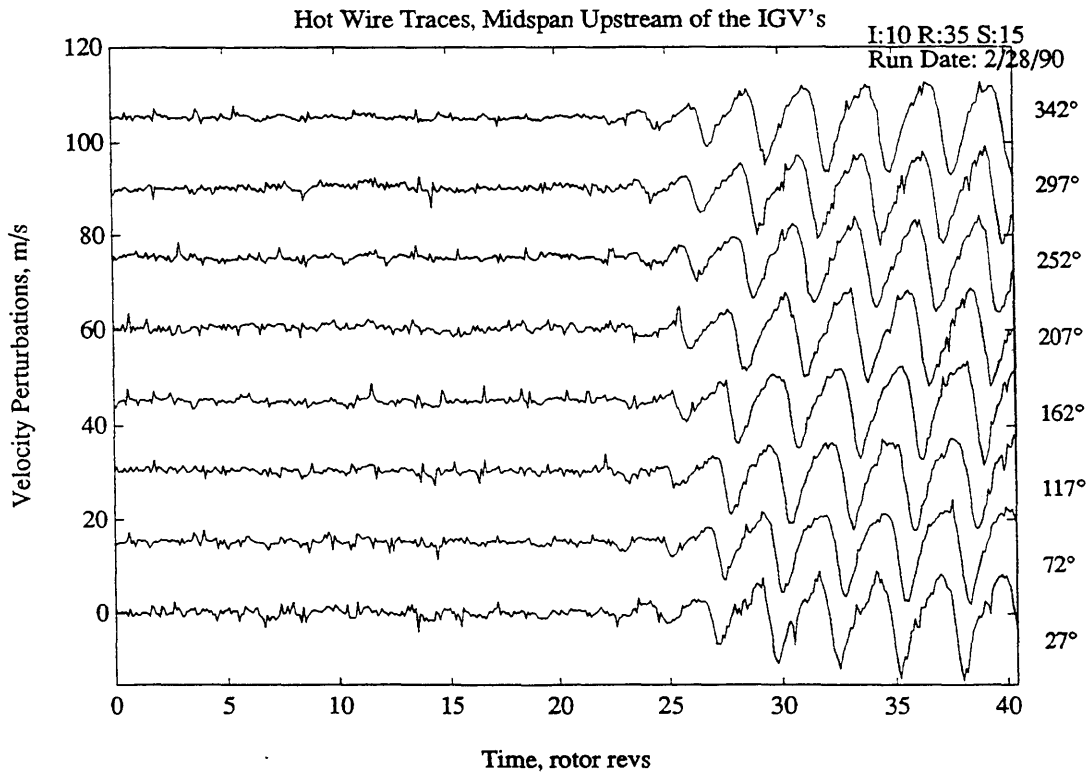
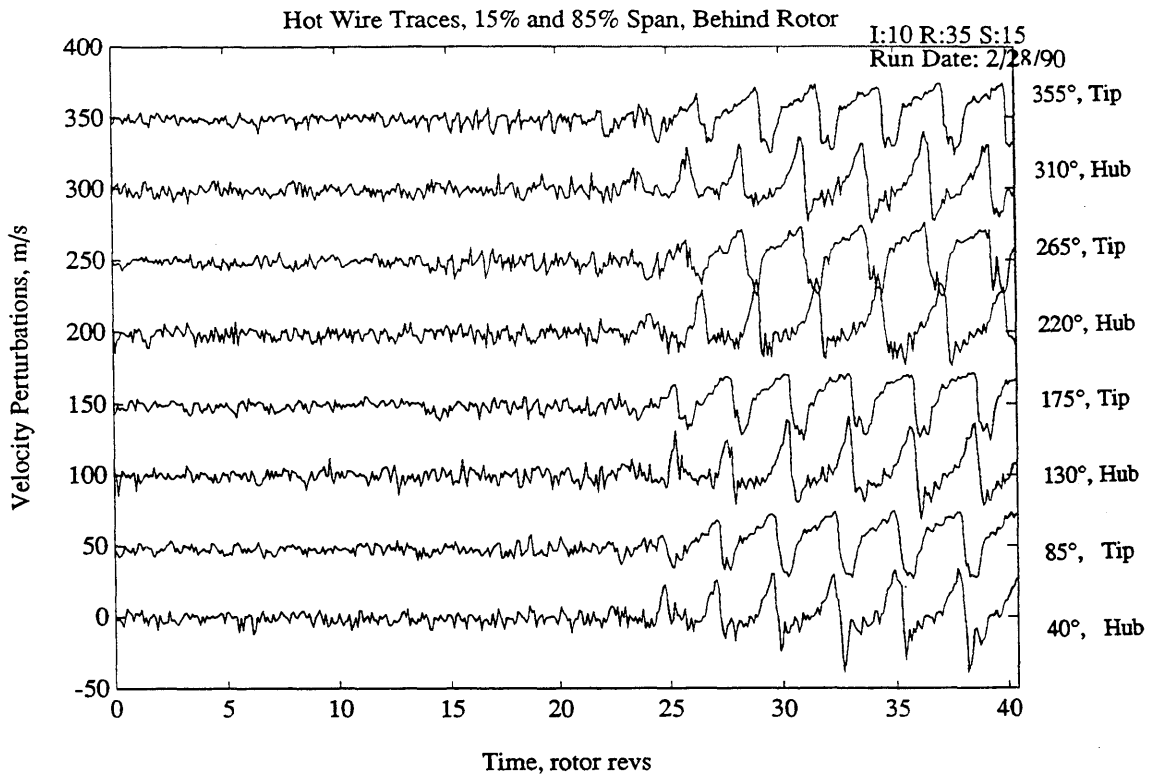


Figure C.18 - Hot wire traces at stall inception for Build #3C (IGVs @ 10 deg)

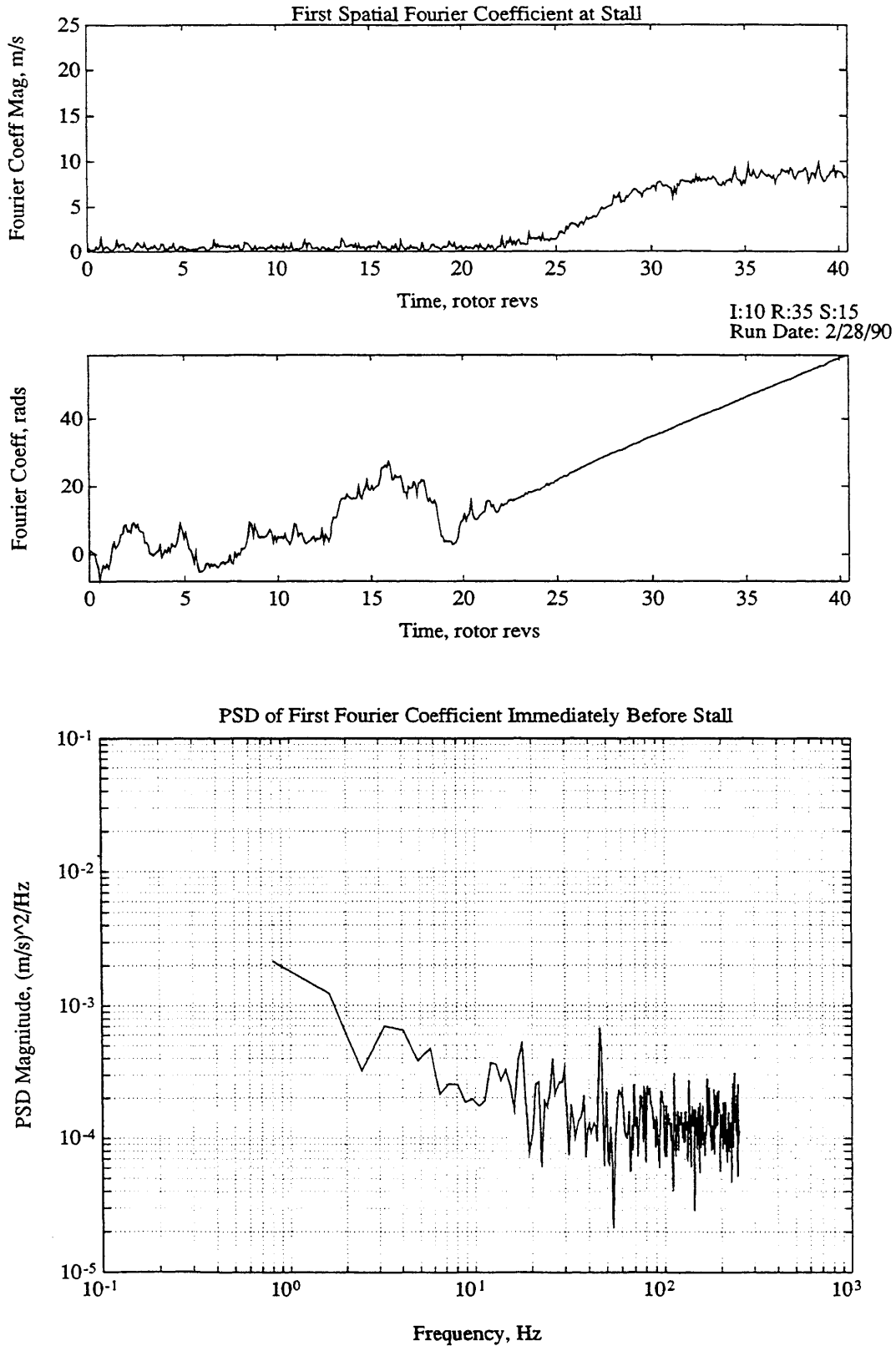


Figure C.19 - Analysis of first spatial Fourier coefficient. Derived from hot wire data from Build #3C (see Figure C.18, second plot).

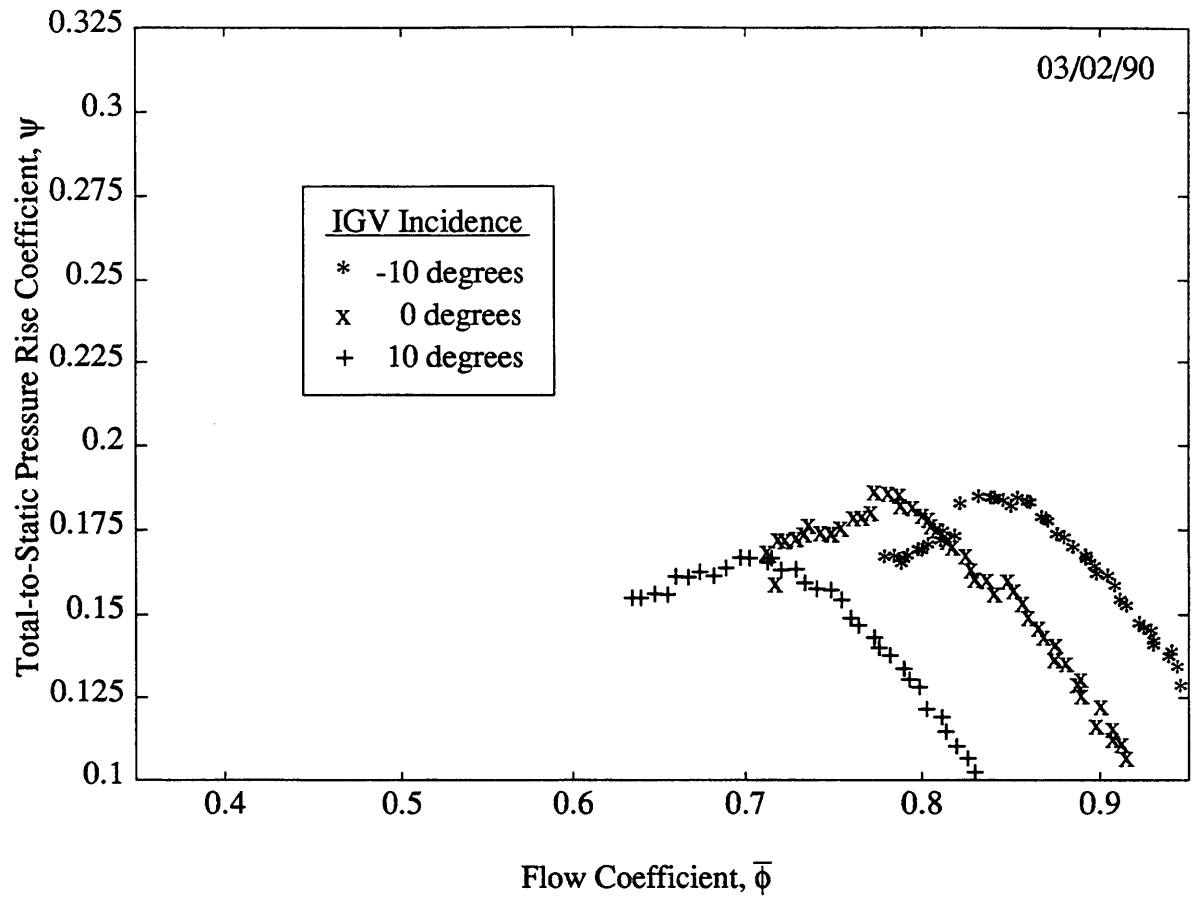


Figure C.20 - 2700 RPM Speed Lines for Rotor-Stator Geometry #4

Notes:

1) Geometry is given in Table 2.1 except:

Rotor Stagger: 25°

Rotor Twist: 10°

Stator Stagger: 12.5°

2) The speed lines and the hot wire data suggest that there is no clear stall point for these builds - exhibits 'soft' or 'recoverable' stall.

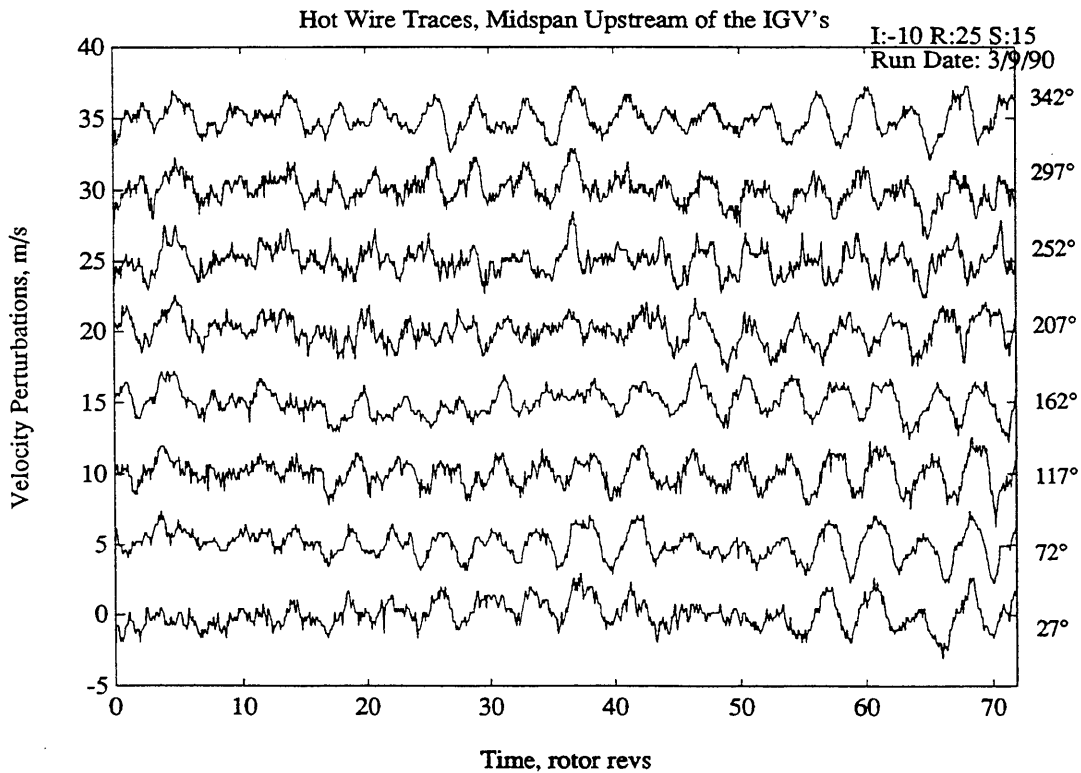
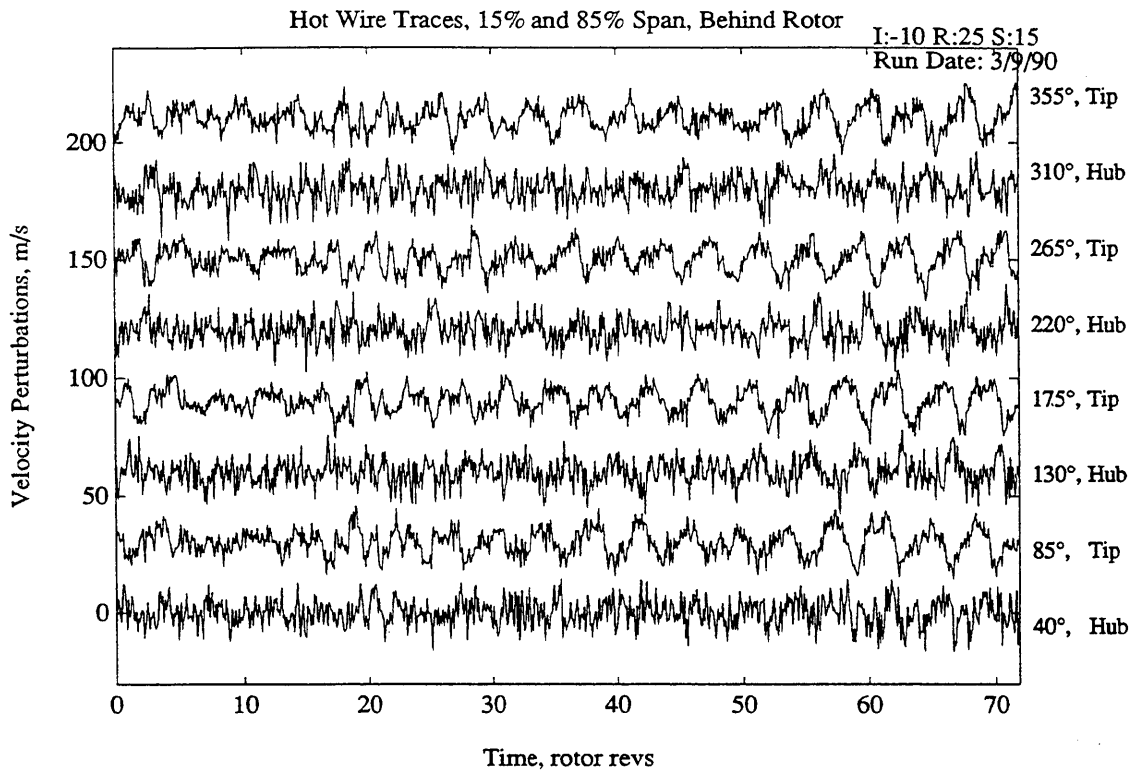


Figure C.21 - Hot wire traces at stall inception for Build #4A (IGVs @ -10 deg)

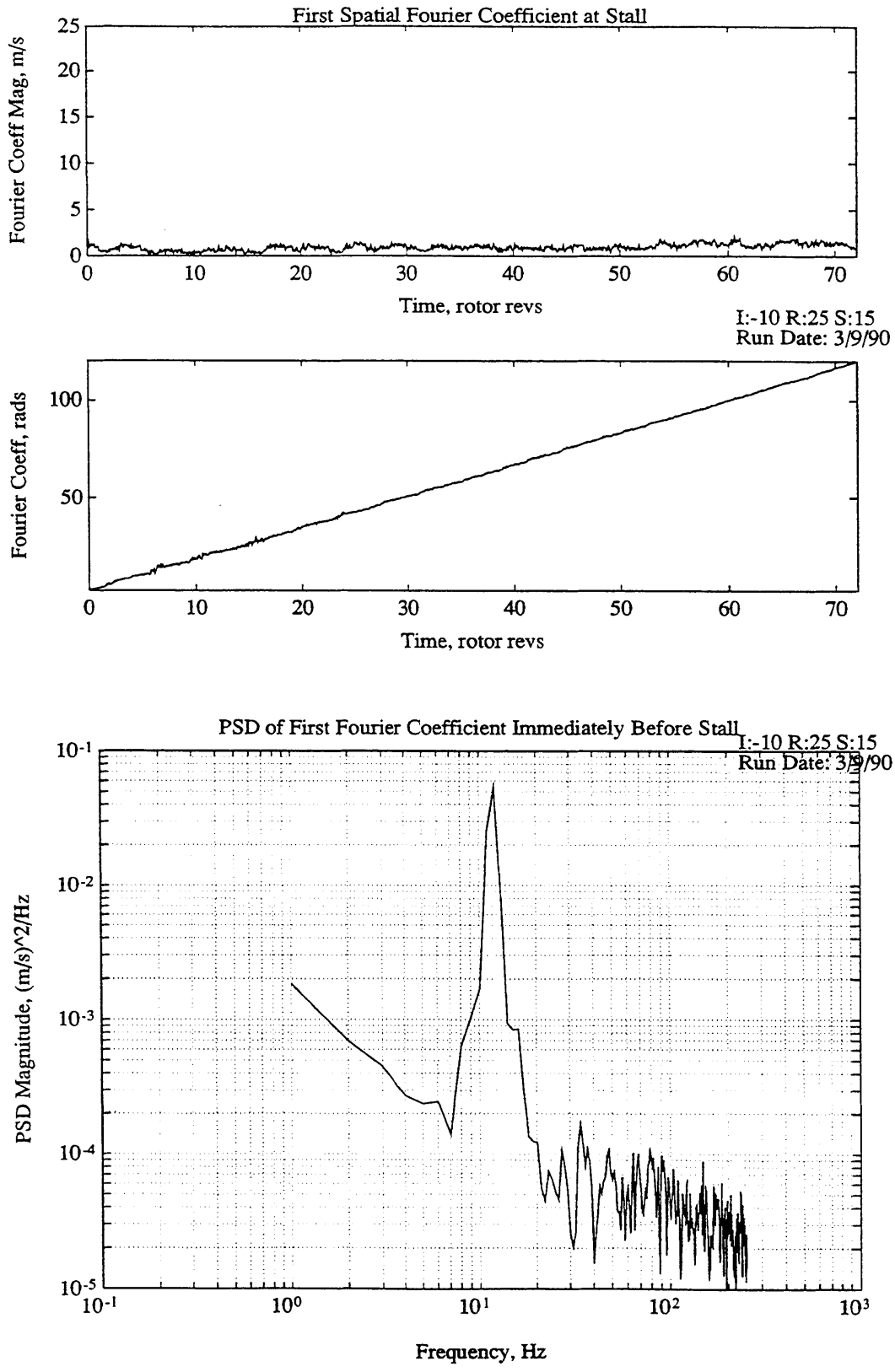


Figure C.22 - Analysis of first spatial Fourier coefficient. Derived from hot wire data from Build #4A (see Figure C.21, second plot).

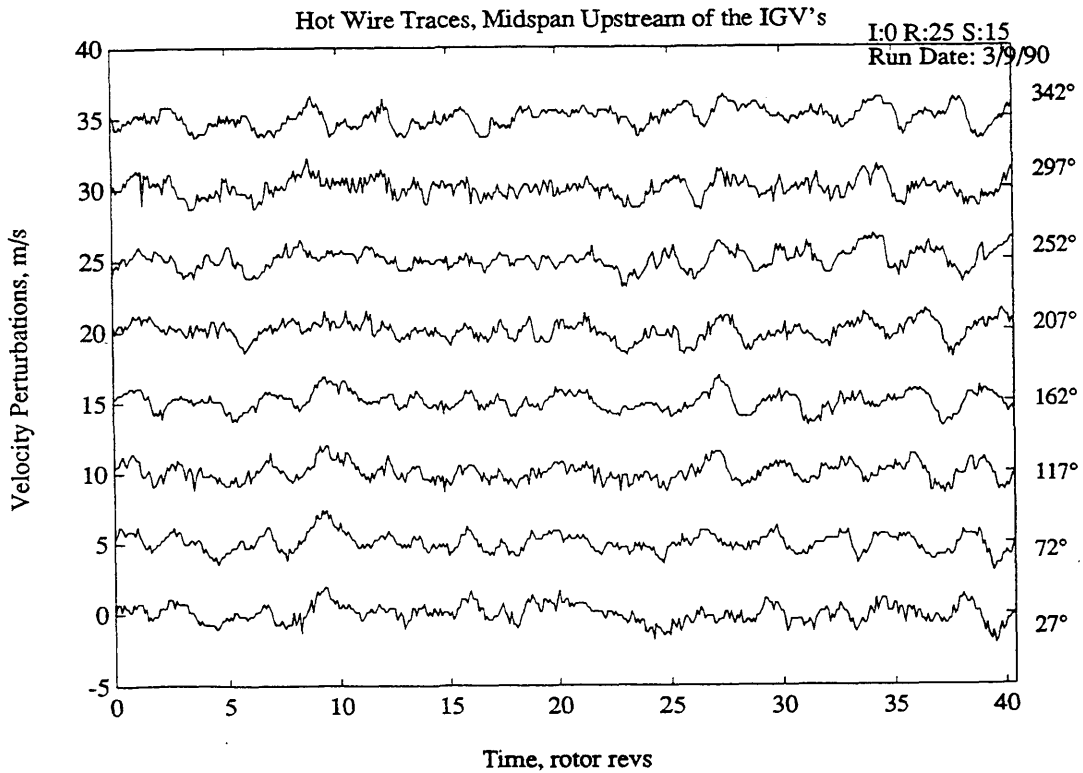
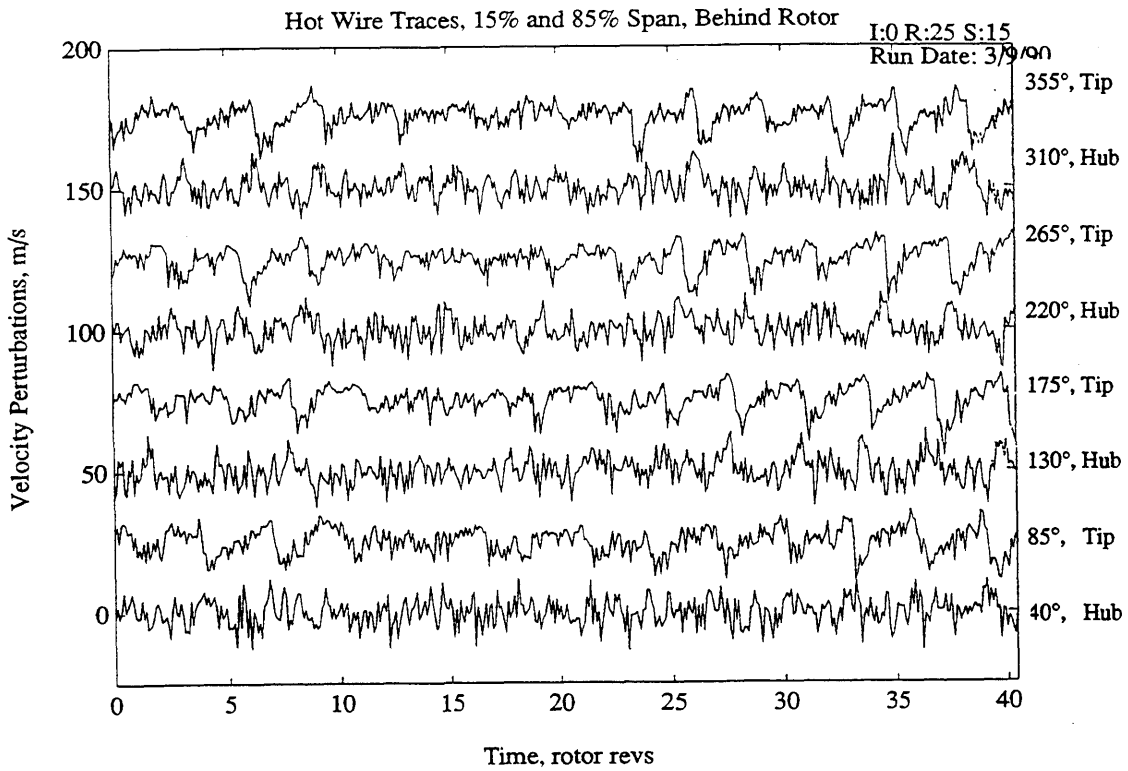


Figure C.23 - Hot wire traces at stall inception for Build #4B (IGVs @ 0 deg)

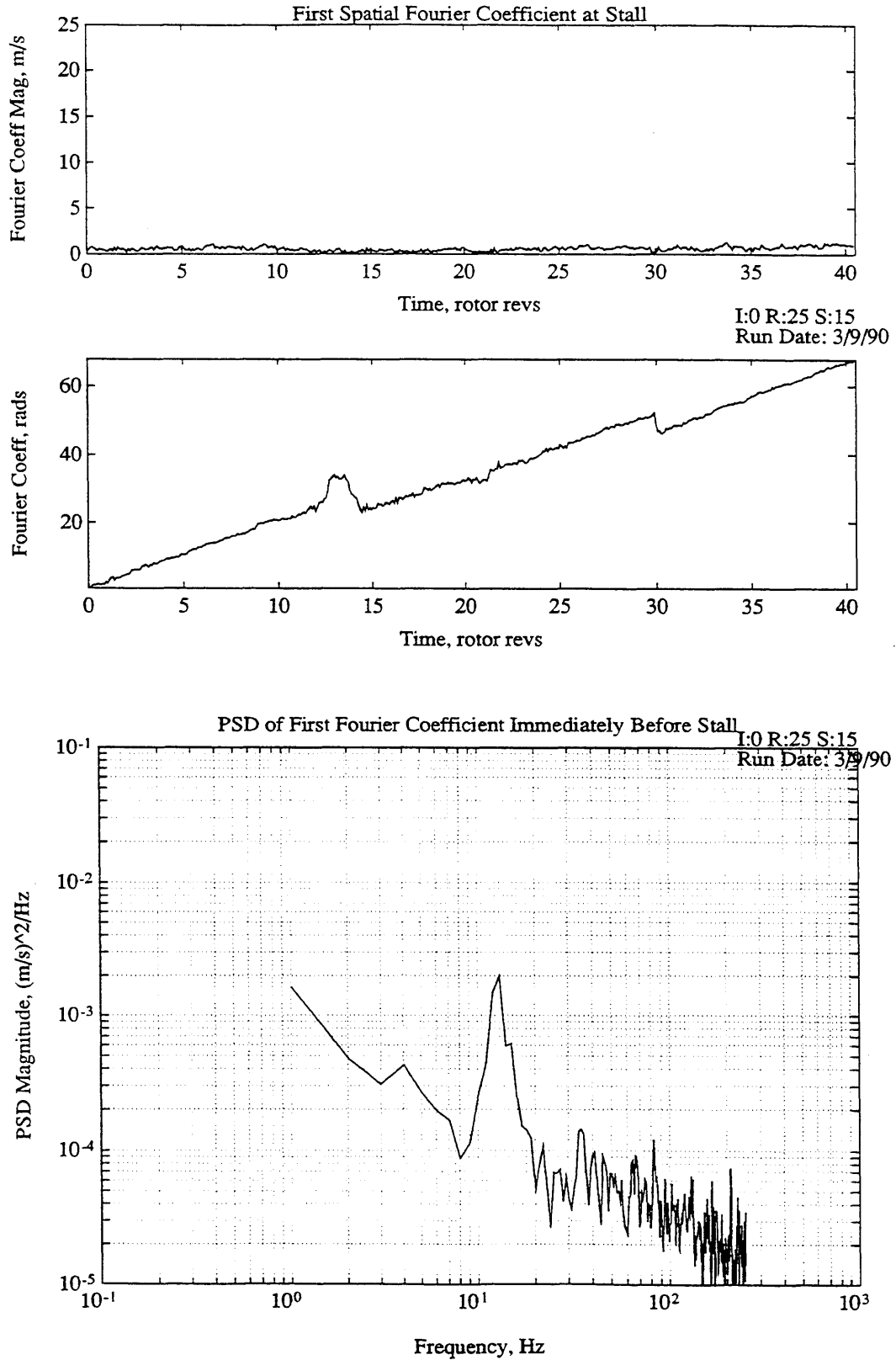


Figure C.24 - Analysis of first spatial Fourier coefficient. Derived from hot wire data from Build #4B (see Figure C.23, second plot).

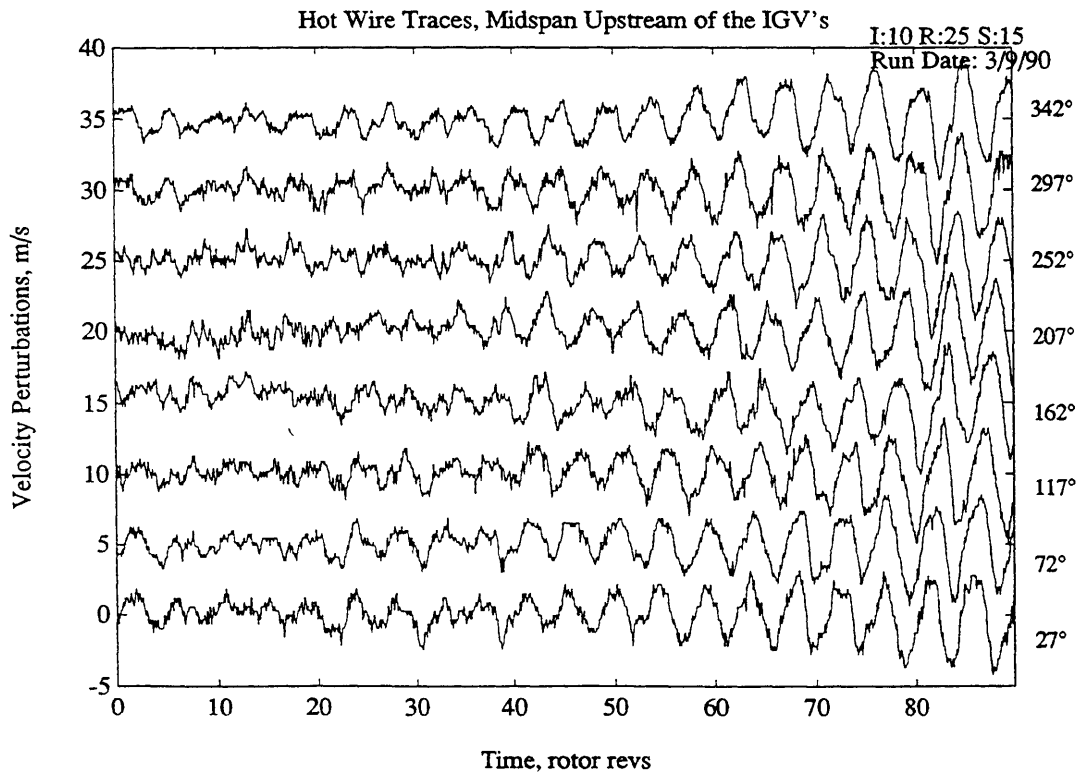
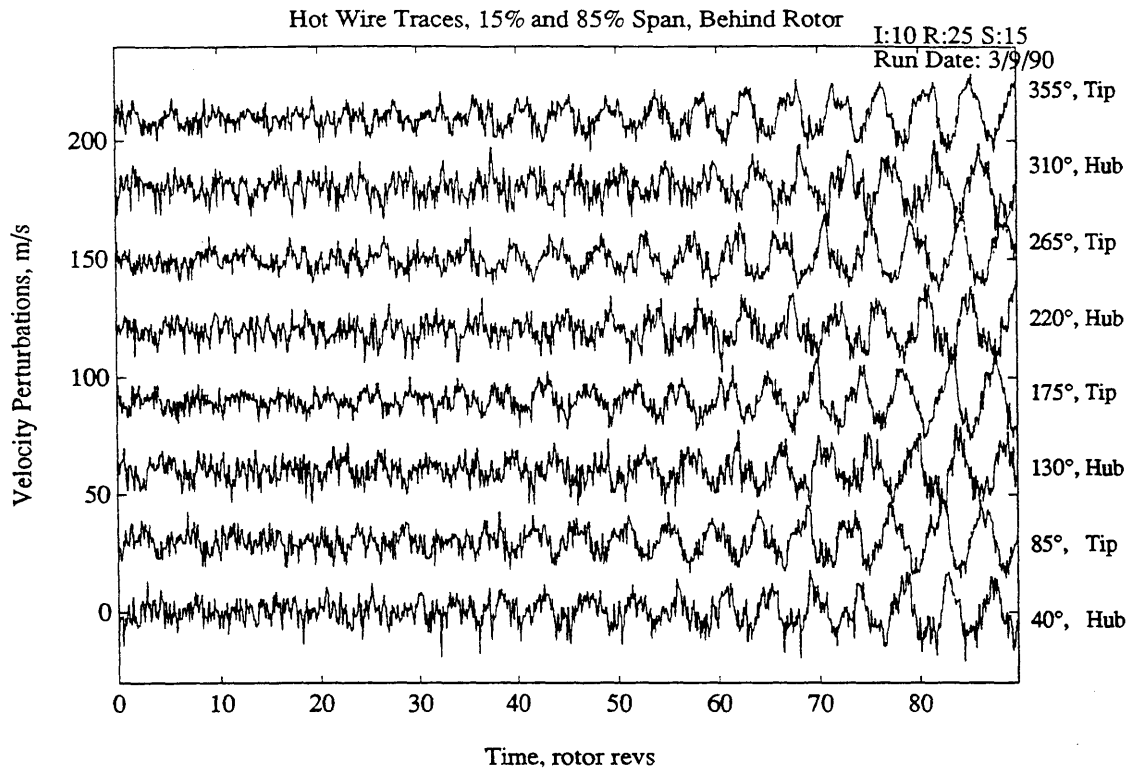


Figure C.25 - Hot wire traces at stall inception for Build #4C (IGVs @ 10 deg)

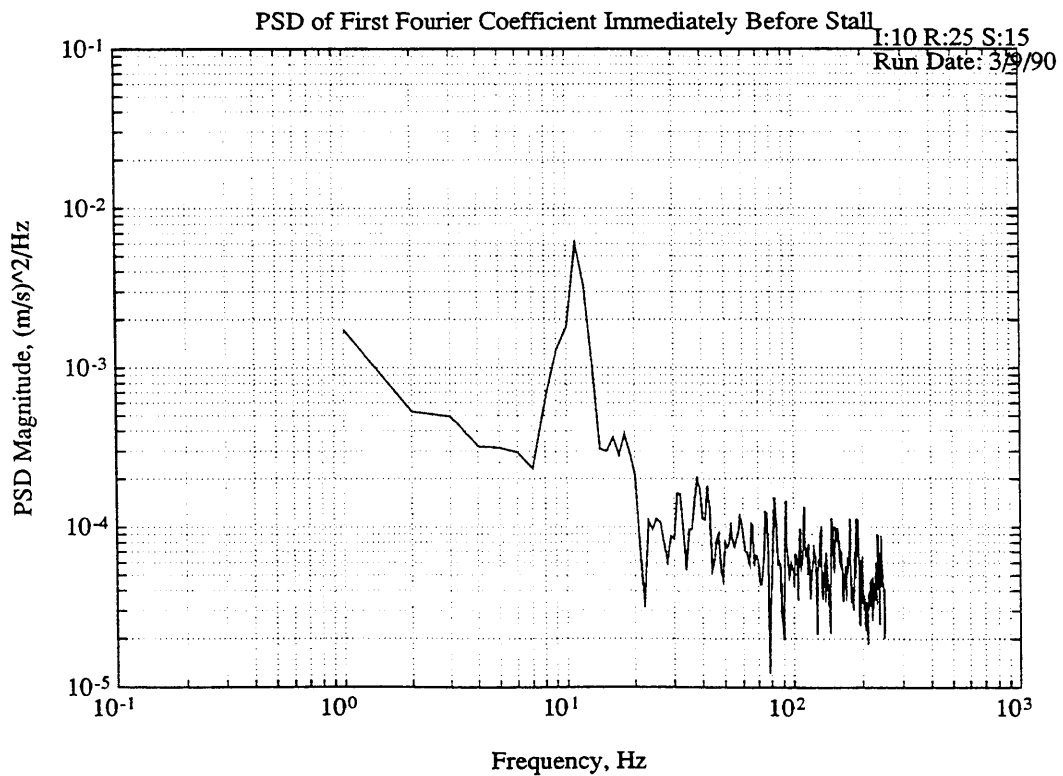
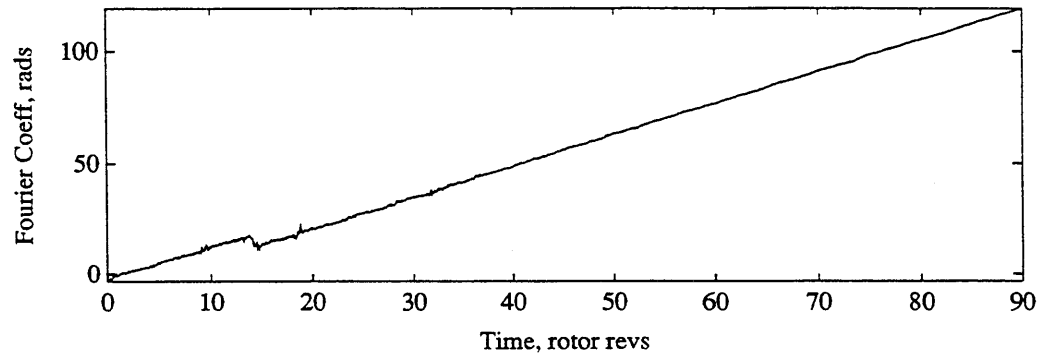
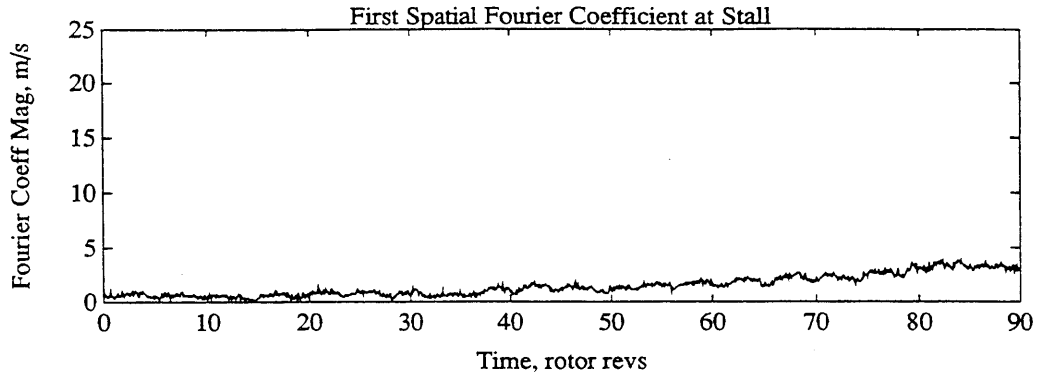


Figure C.26 - Analysis of first spatial Fourier coefficient. Derived from hot wire data from Build #4C (see Figure C.25, second plot).

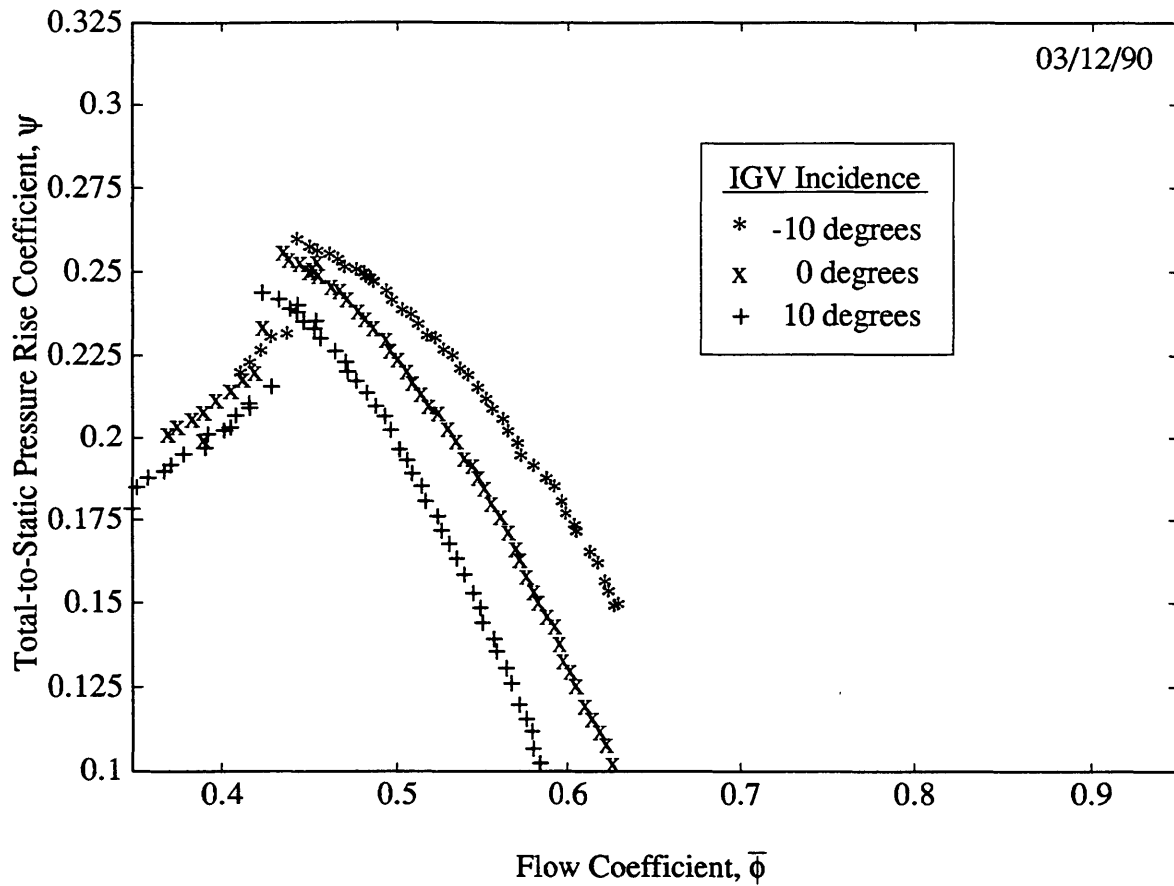


Figure C.27 - 2700 RPM Speed Lines for Rotor-Stator Geometry #5

Notes:

- 1) Geometry is given in Table 2.1 except:
 Rotor Stagger: 45°
 Rotor Twist: 30°
 Stator Stagger: 22.5°
- 2) Secondary curves are operation in **part-span stall**.
- 3) Hot wire traces for all IGV incidences show that part-span stall is a stable operating condition for these builds.

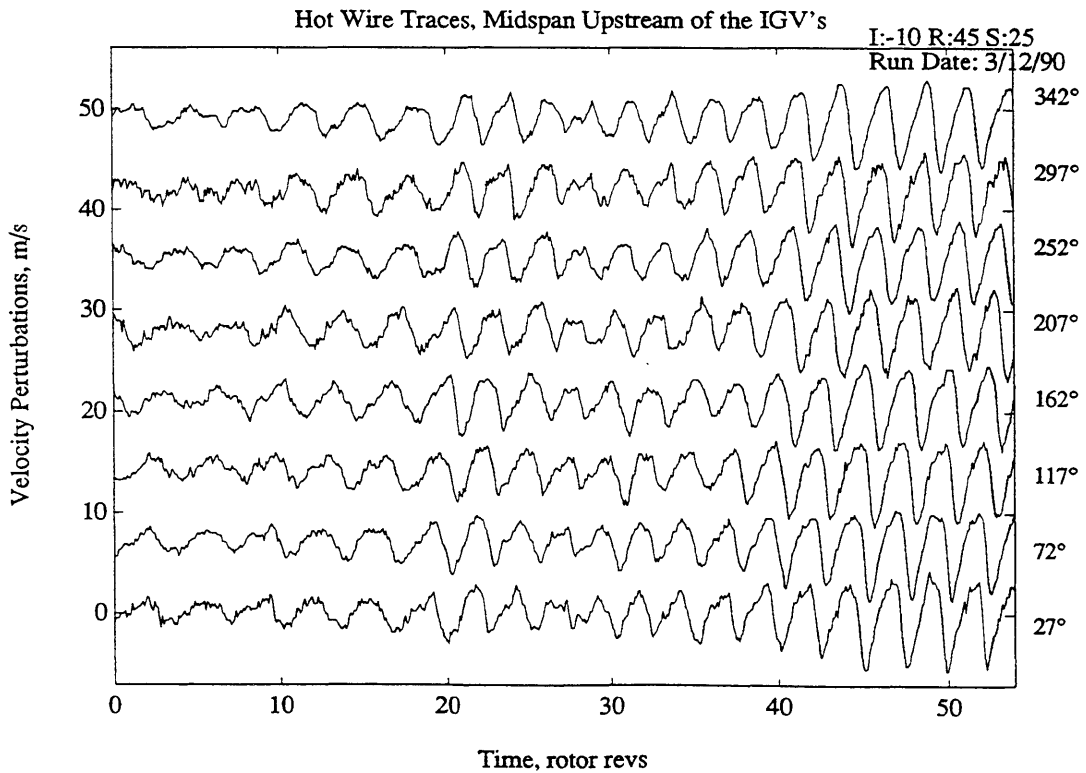
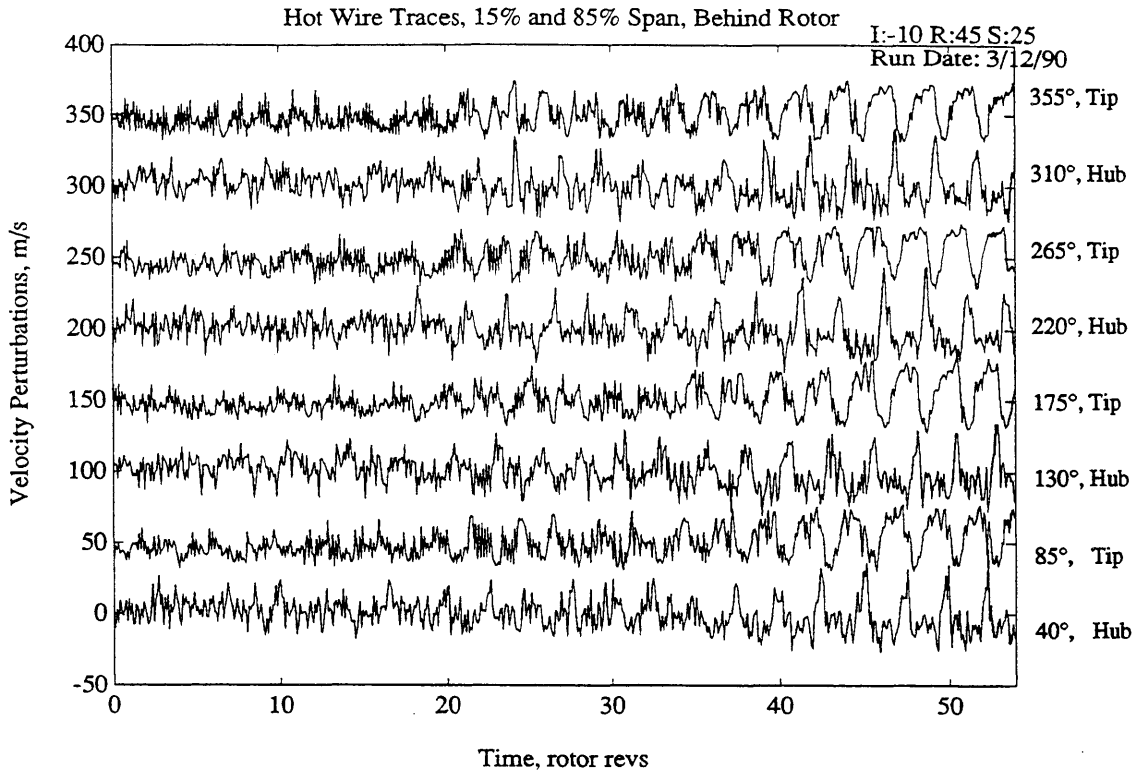


Figure C.28 - Hot wire traces at stall inception for Build #5A (IGVs @ -10 deg)

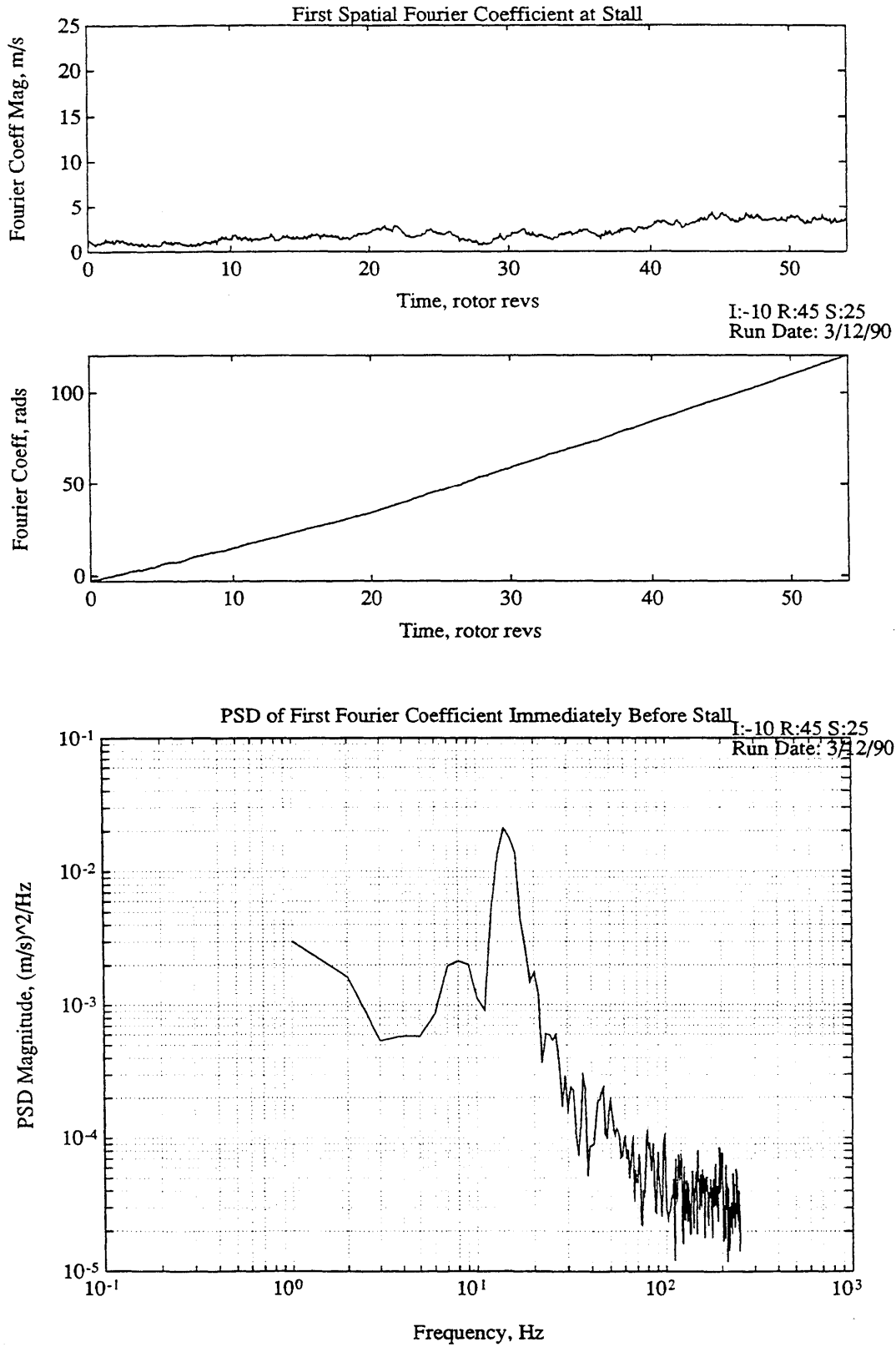


Figure C.29 - Analysis of first spatial Fourier coefficient. Derived from hot wire data from Build #5A (see Figure C.28, second plot).

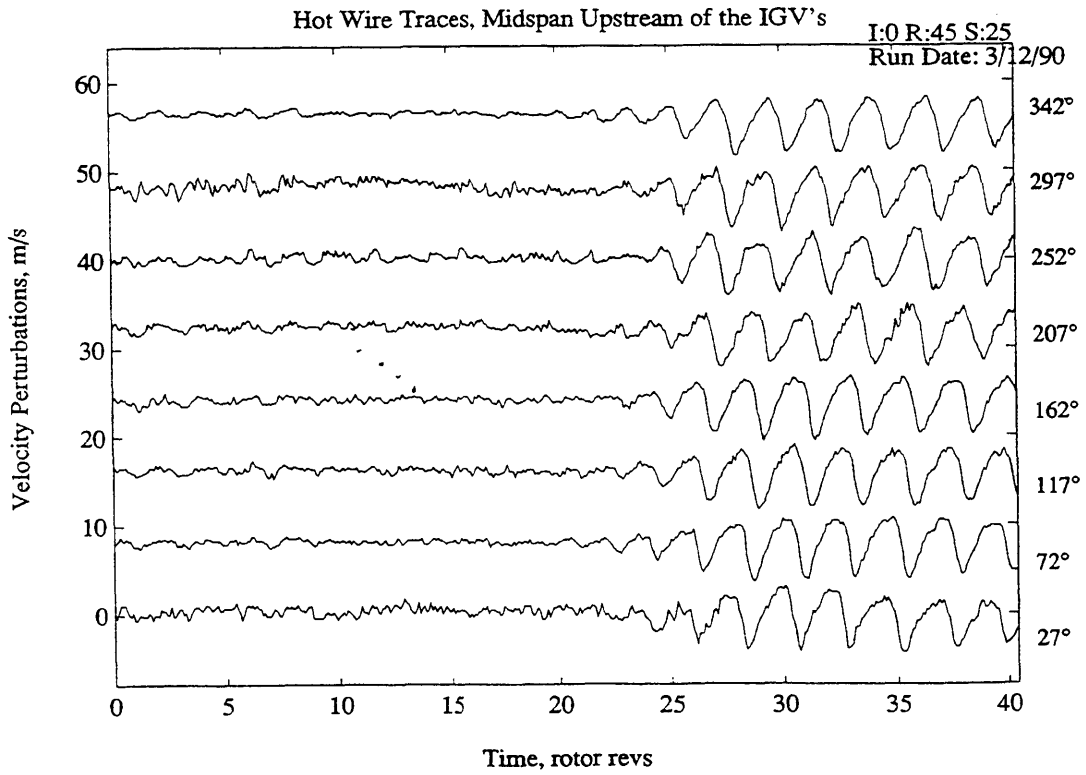
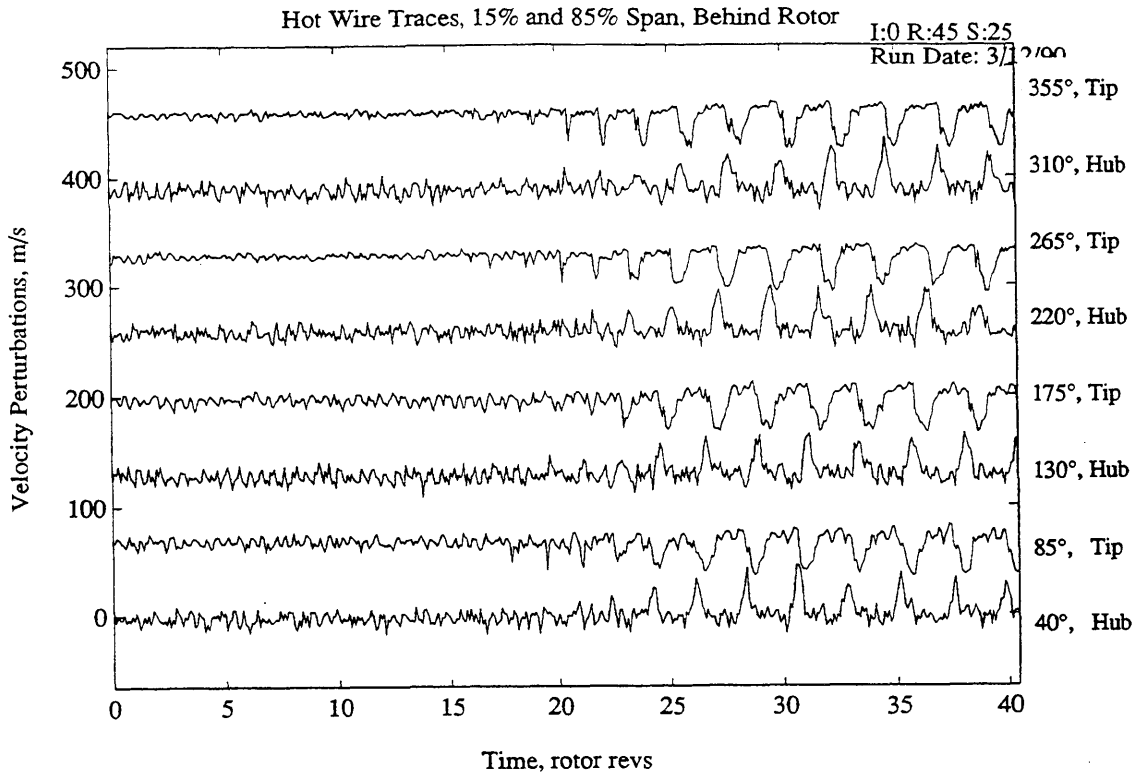


Figure C.30 - Hot wire traces at stall inception for Build #5B (IGVs @ 0 deg)

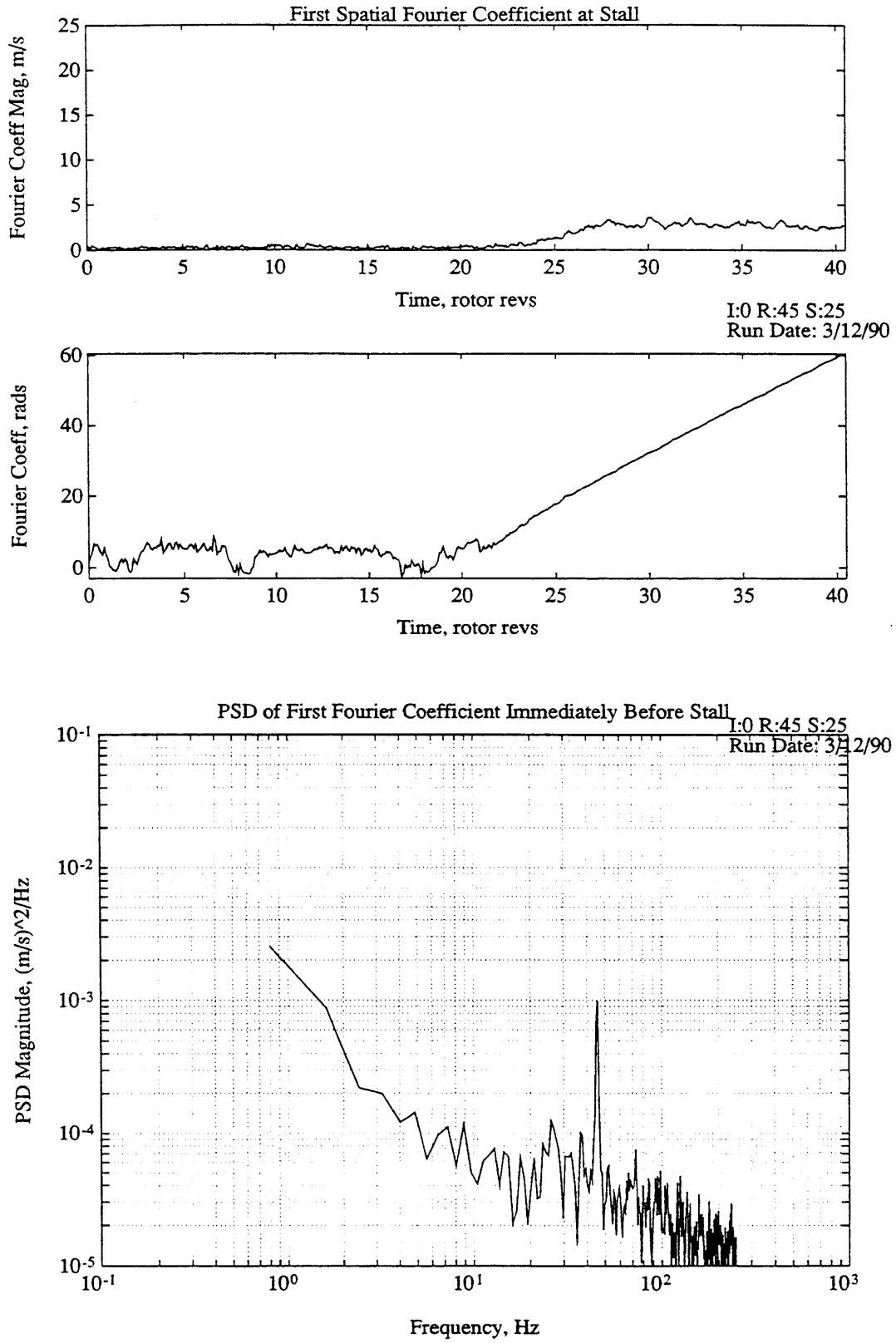


Figure C.31 - Analysis of first spatial Fourier coefficient. Derived from hot wire data from Build #5B (see Figure C.30, second plot).

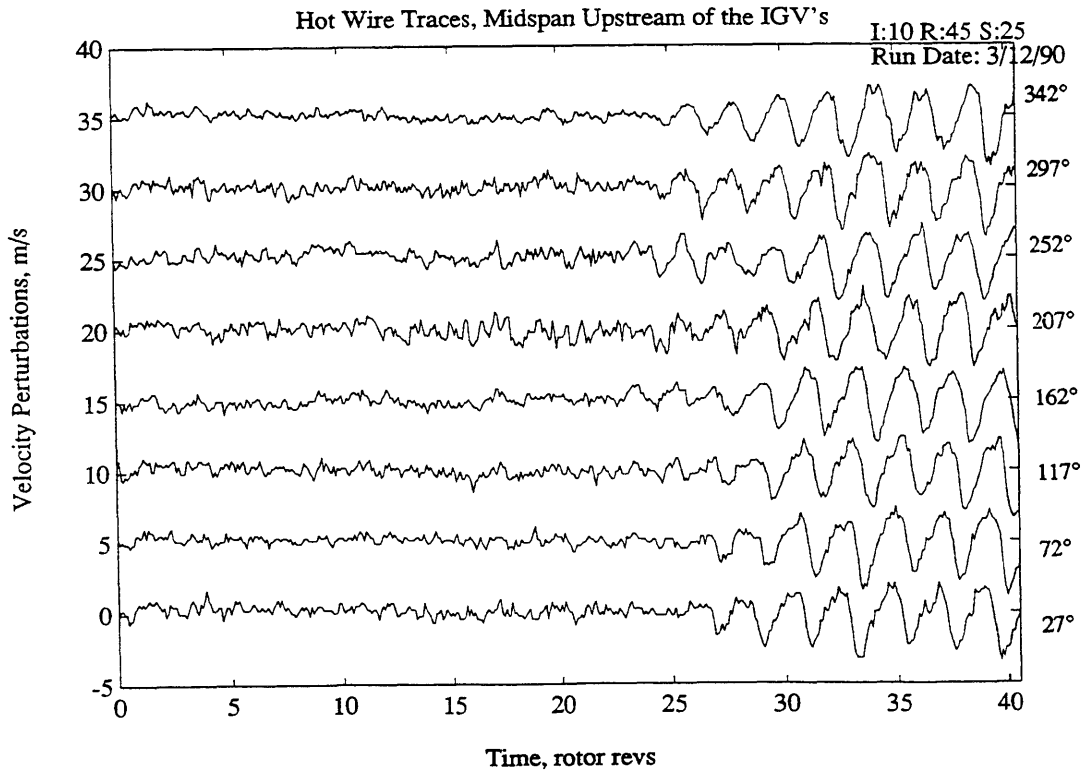
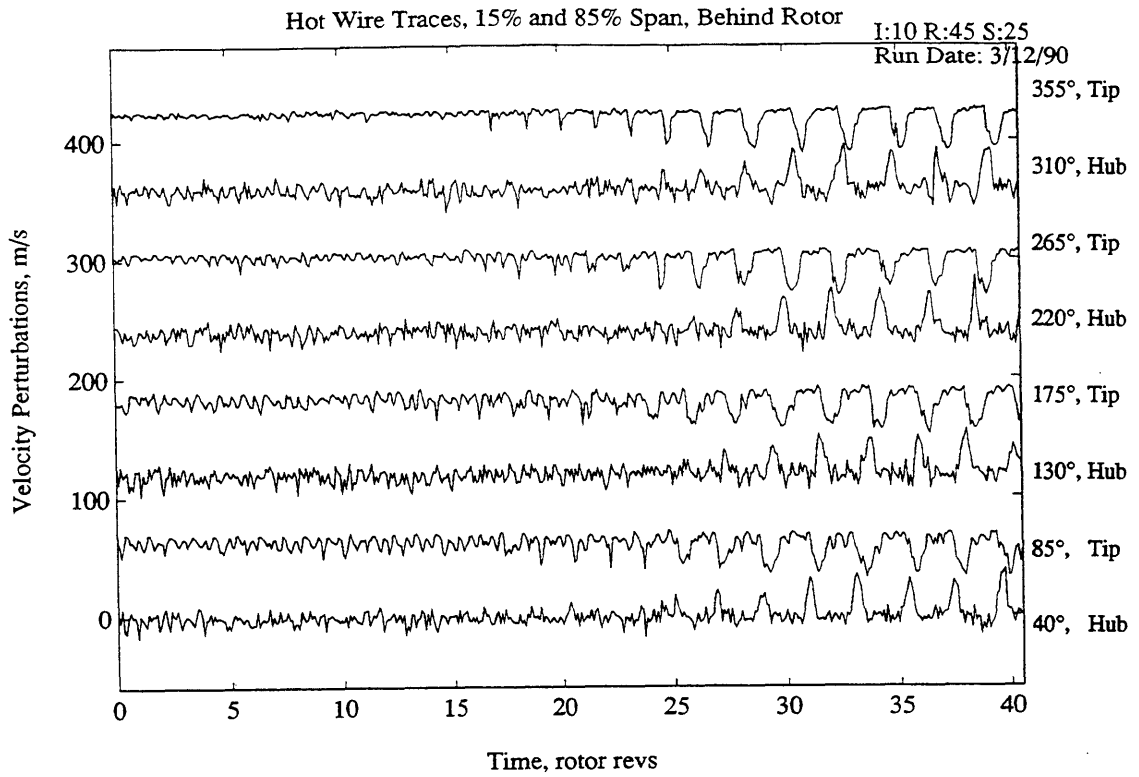


Figure C.32 - Hot wire traces at stall inception for Build #5C (IGVs @ 10 deg)

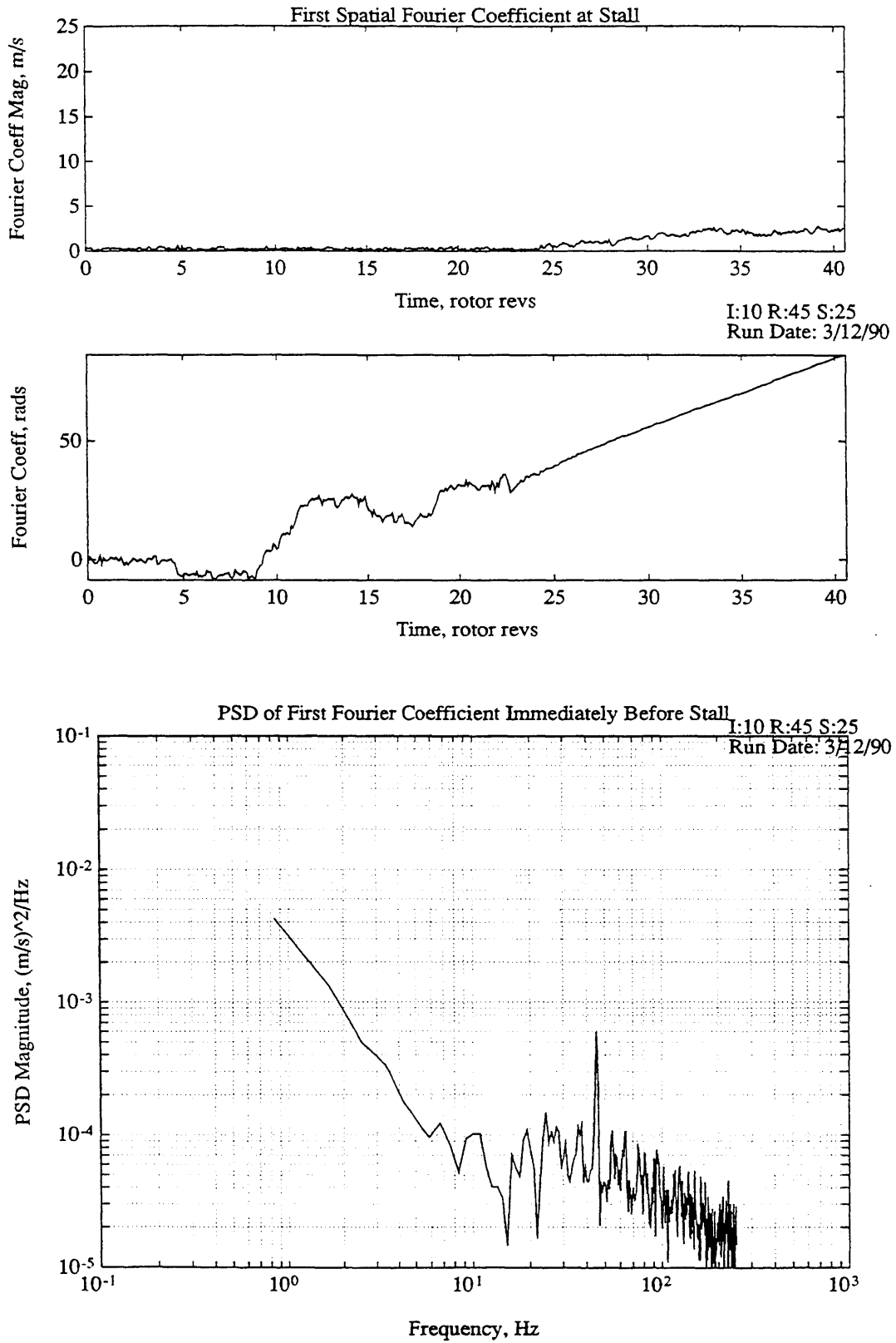


Figure C.33 - Analysis of first spatial Fourier coefficient. Derived from hot wire data from Build #5C (see Figure C.32, second plot).

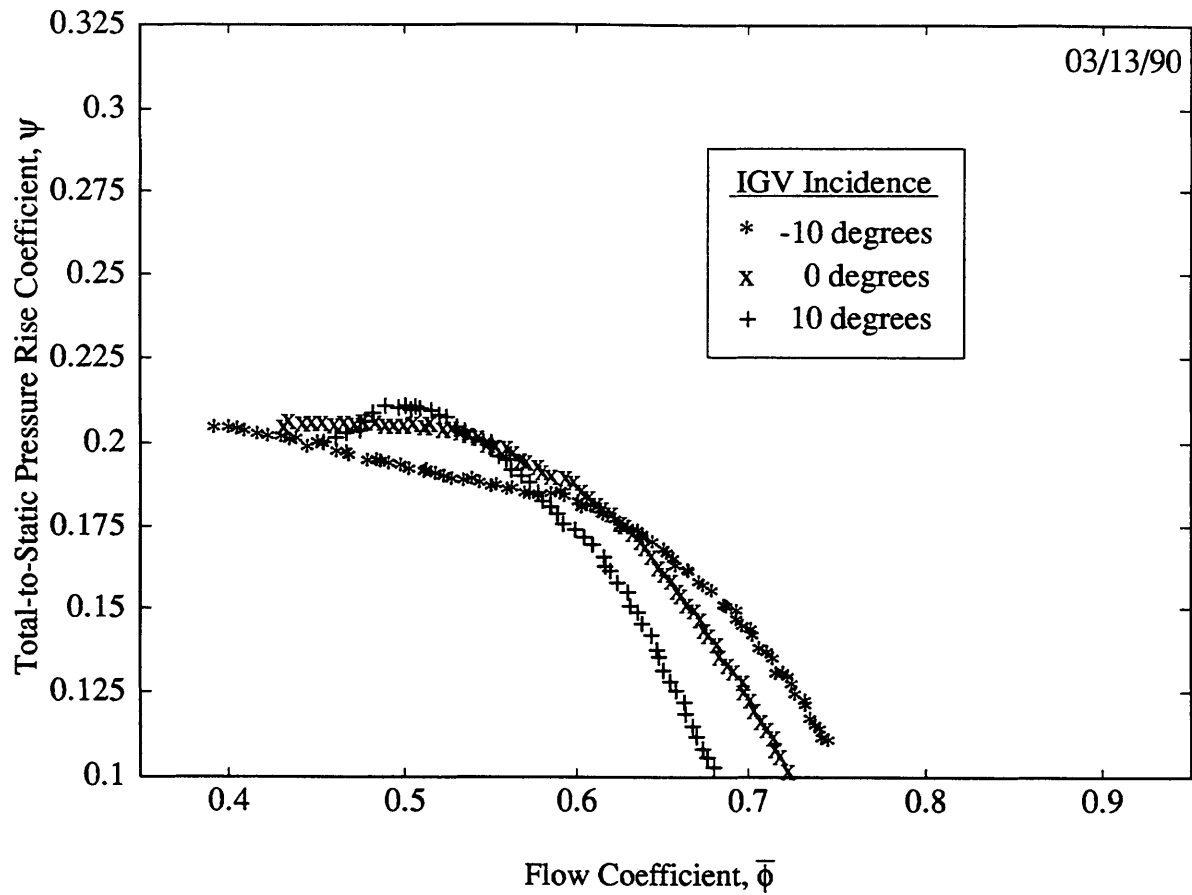


Figure C.34 - 2700 RPM Speed Lines for Rotor-Stator Geometry #6

Notes:

- 1) Geometry is given in Table 2.1.
- 2) Hot wire traces for IGVs @ 0° indicate **full-span stall inception**.
- 3) This build, with IGVs @ 0° , is used for all the experiments presented in the body of this thesis.

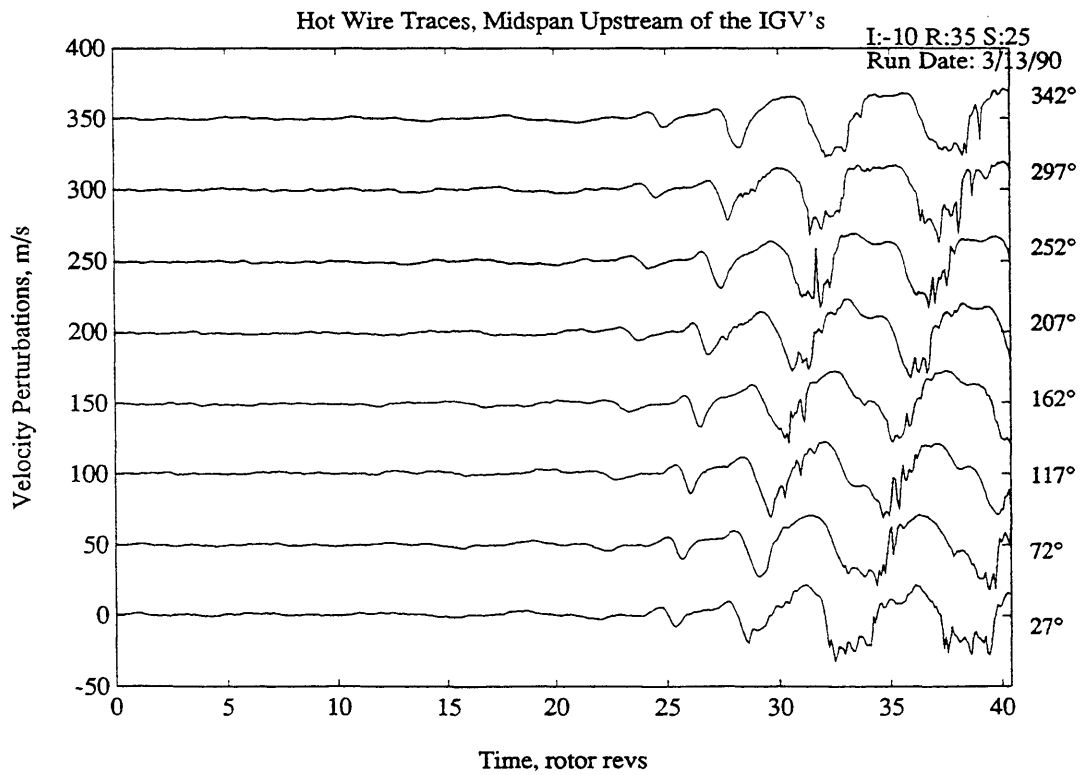
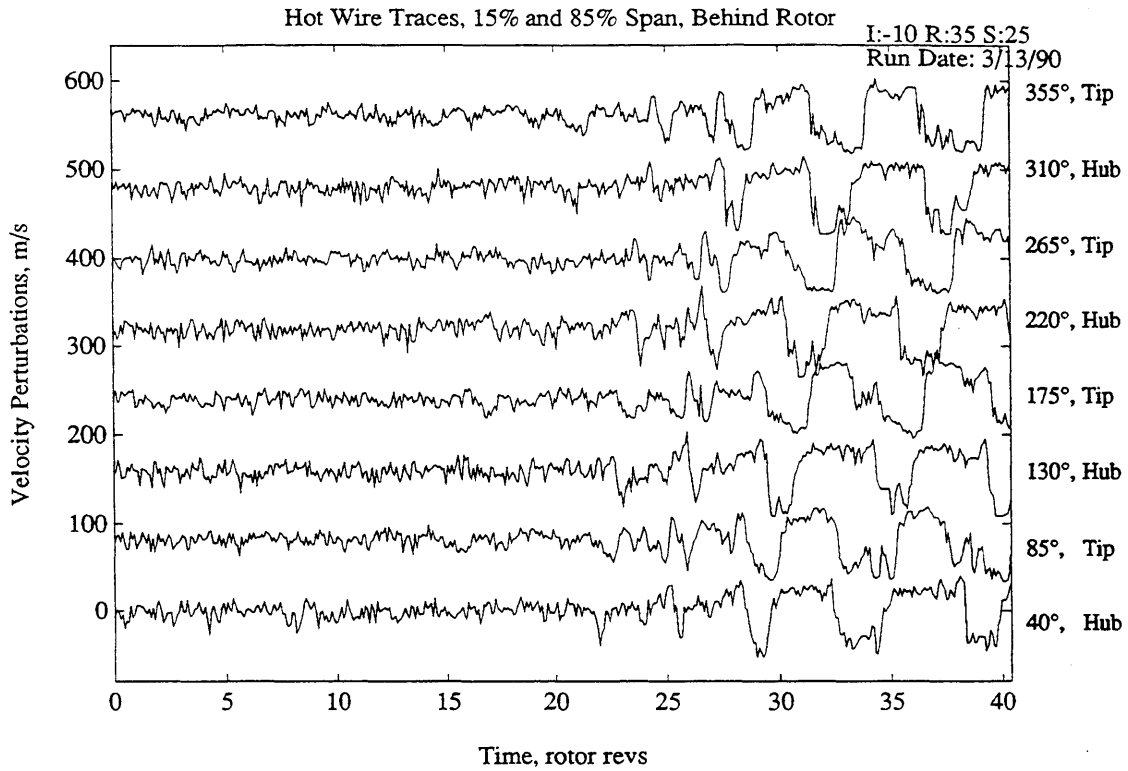


Figure C.35 - Hot wire traces at stall inception for Build #6A (IGVs @ -10 deg)

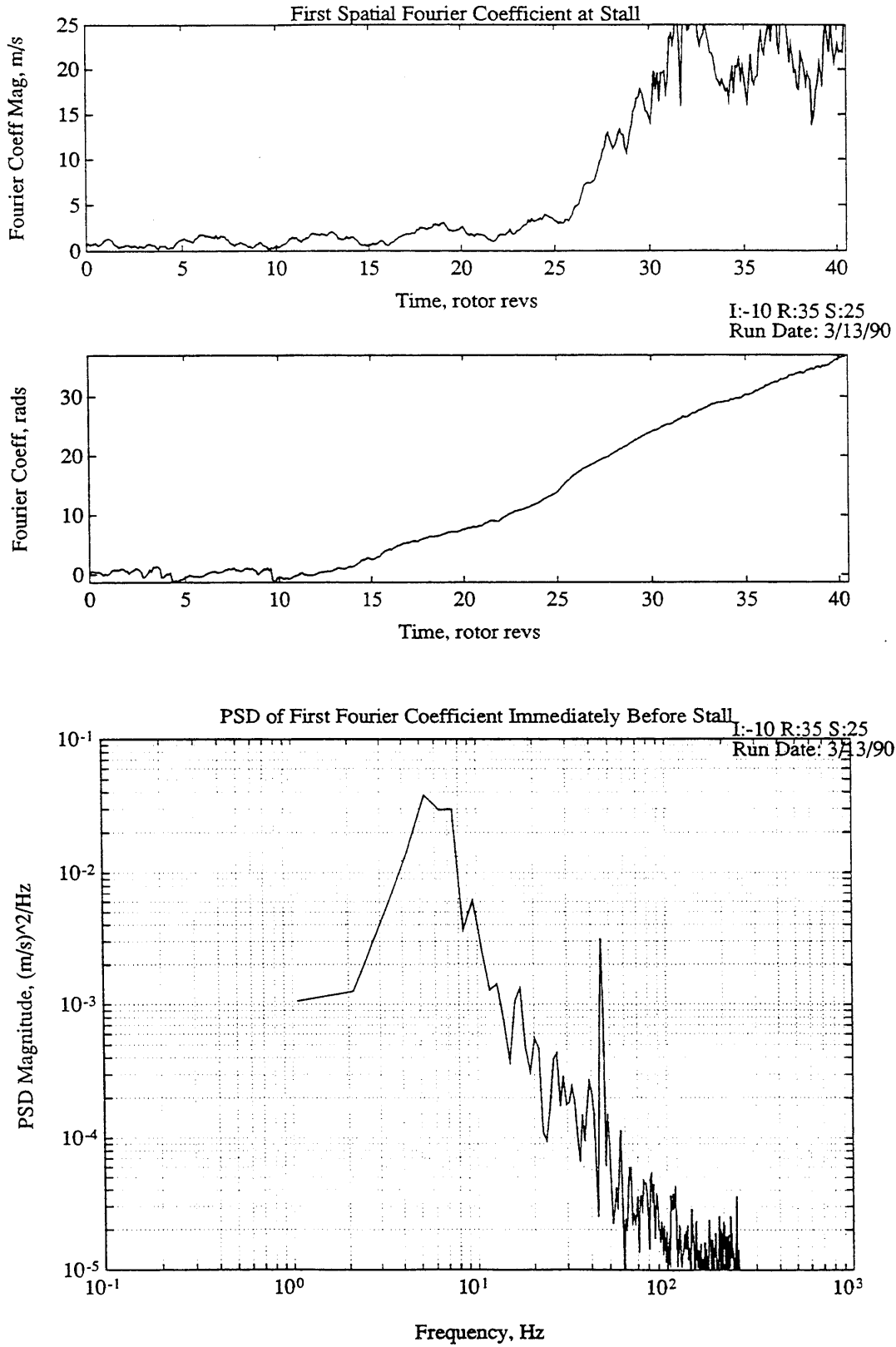


Figure C.36 - Analysis of first spatial Fourier coefficient. Derived from hot wire data from Build #6A (see Figure C.35, second plot).

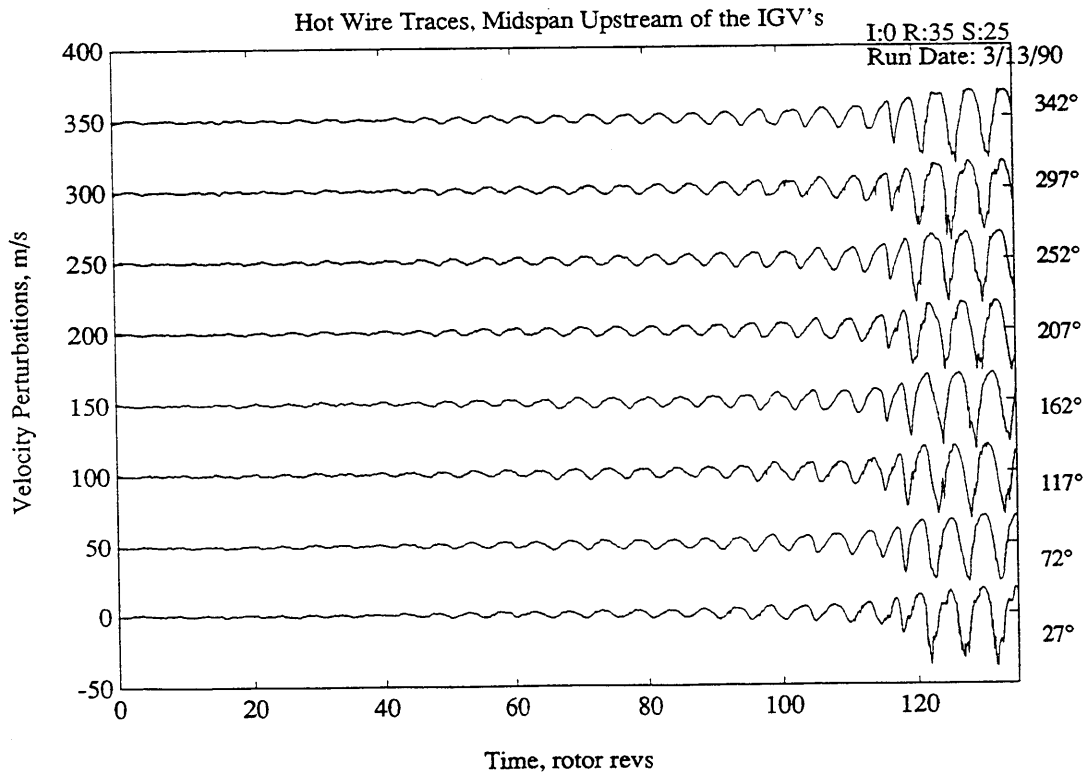
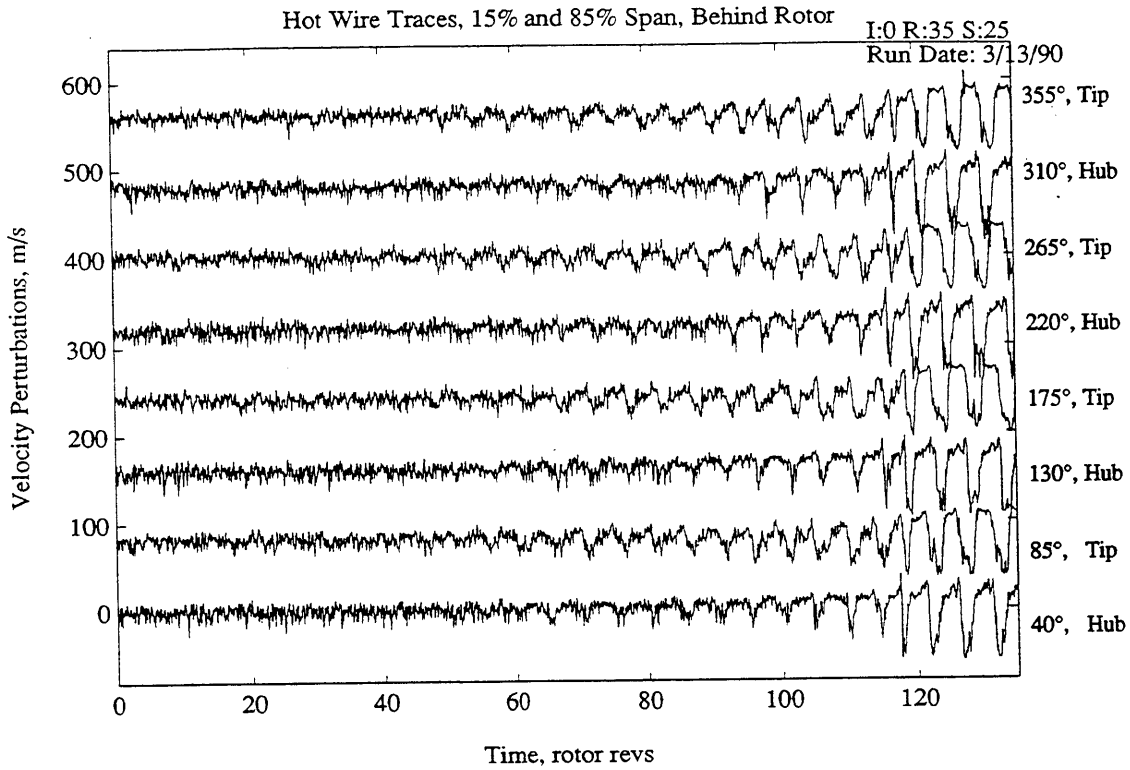


Figure C.37 - Hot wire traces at stall inception for Build #6B (IGVs @ 0 deg)
NOTE: This is the build throughout the body of the thesis.

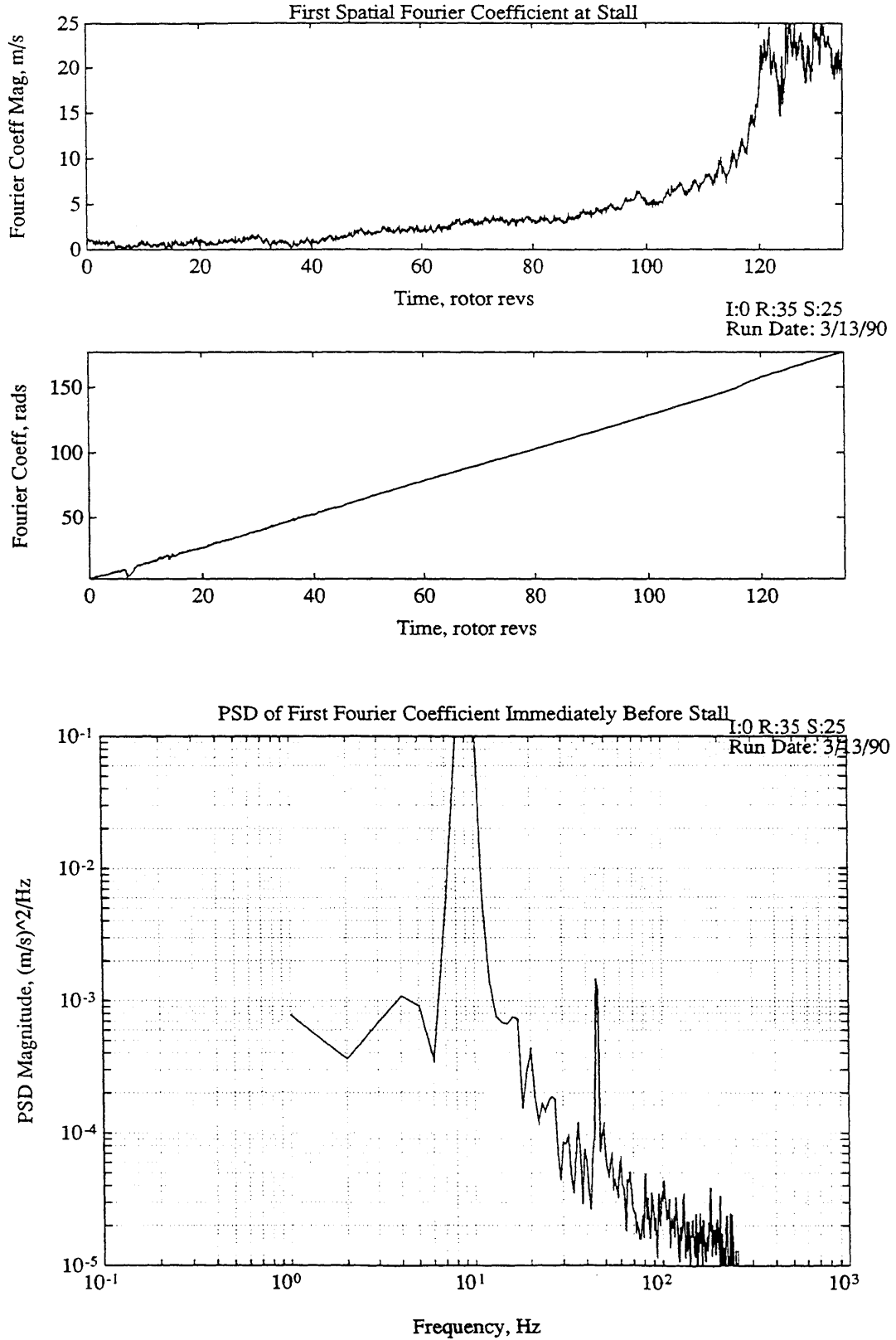


Figure C.38 - Analysis of first spatial Fourier coefficient. Derived from hot wire data from Build #6B (see Figure C.37, second plot).

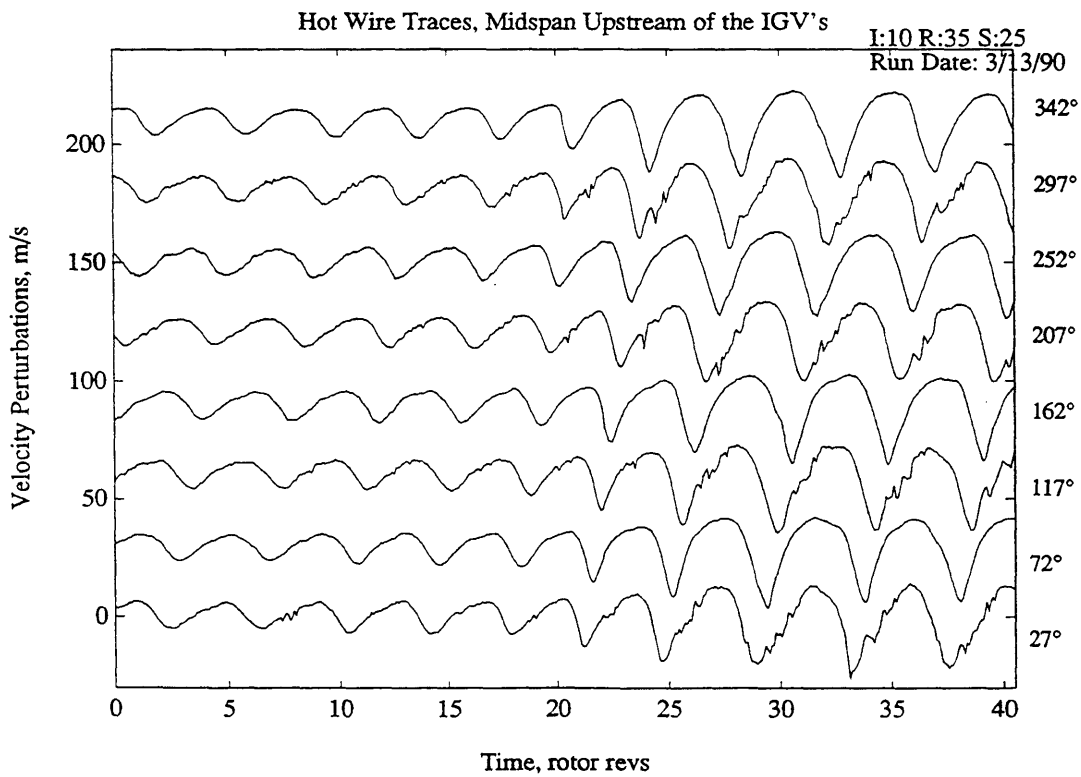
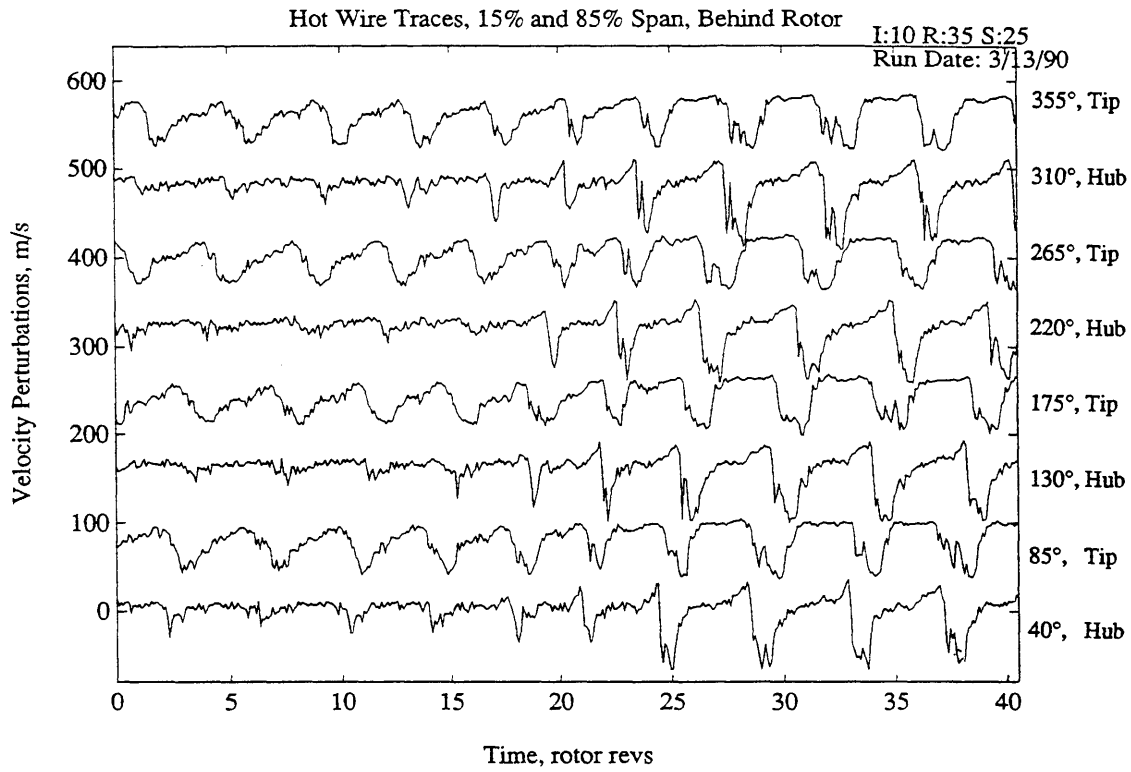


Figure C.39 - Hot wire traces at stall inception for Build #6C (IGVs @ 10 deg)

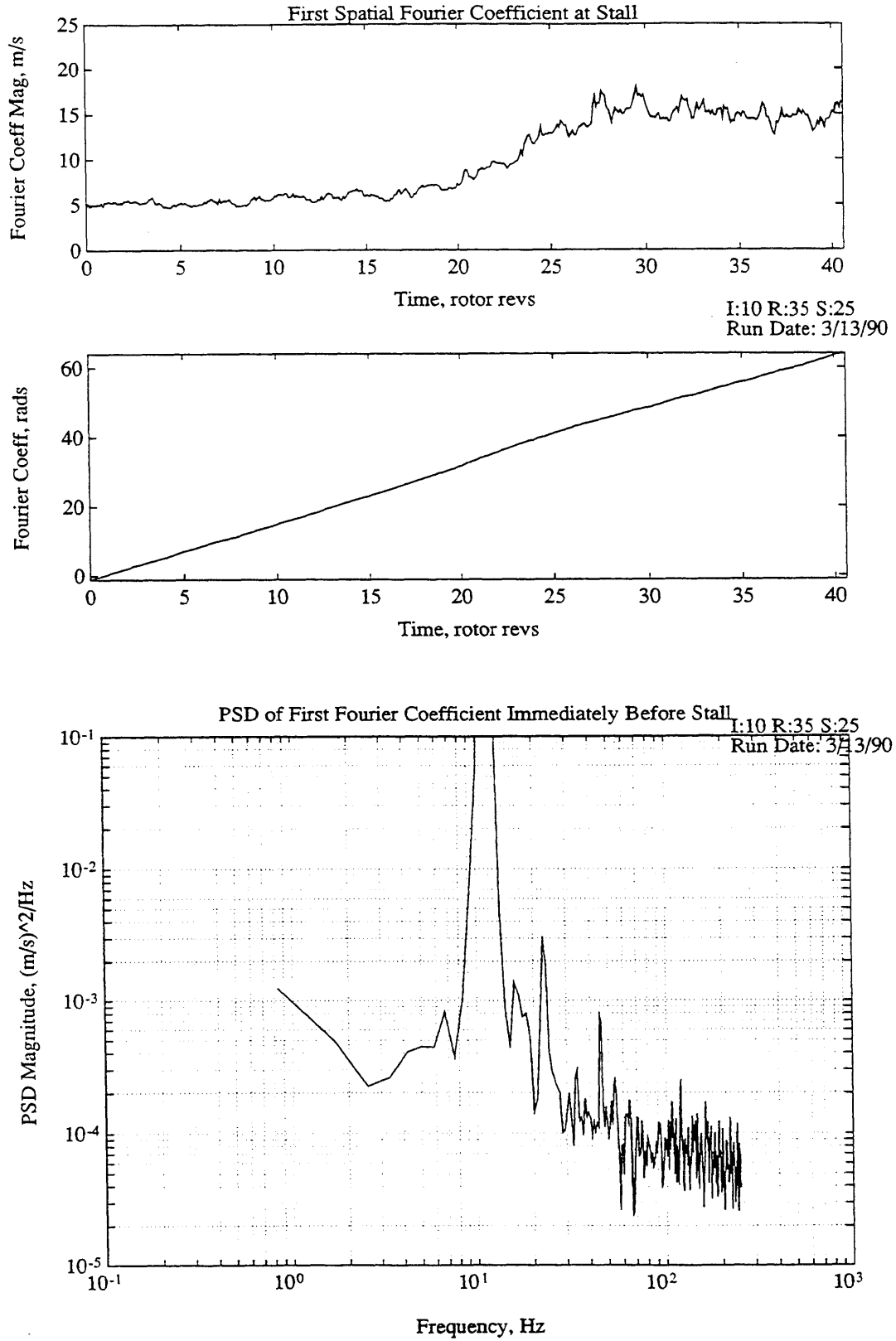


Figure C.40 - Analysis of first spatial Fourier coefficient. Derived from hot wire data from Build #6C (see Figure C.39, second plot).

Appendix D

Frequency Response Data

This appendix presents transfer function shapes for the compressor higher-mode dynamics. These transfer functions, their parameterization, and the procedures used to estimate them, are discussed in Chapter 5. We will use nomenclature and concepts from Chapter 5 to facilitate the current discussion.

In Chapter 5, the parameter set Θ :

$$\Theta(n, \bar{\phi}) = [\sigma_{rs} \ \omega_{rs} \ b_r \ b_i \ g_i]_n^T, \quad (D.1)$$

is used to characterize the input-output behavior of the compressor higher-mode dynamics. Figures 5.9, 5.10, and 5.11 show the variation of Θ with flow coefficient, $\bar{\phi}$, based on various identification experiments. The parameter set Θ can be converted to a frequency response using Equation (3.48), repeated here for convenience:

$$G_n(s) = \frac{i \cdot g_i \cdot s + (b_r + i \cdot b_i)}{s - (\sigma_{rs} + i \cdot \omega_{rs})} \quad (D.2)$$

Thus for every parameter set Θ there is a corresponding transfer function shape. We call the transfer function shape obtained in this way the 'parametric estimate' of $G_n(s)$. The parametric estimate gives another way to view the experimental results, and to see how the system behavior changes with flow coefficient and mode number.

At flow coefficients where the plant is stable, we can also get a *spectral* estimate of the transfer function $G_n(s)$. Section 5.1.2 discusses the spectral estimation method, and several examples of spectral estimates are given throughout Chapter 5. Spectral estimates are useful because they are *non-parametric* estimates of the transfer characteristics of the plant. As such, they make no assumptions about the structure of

the system behavior - they are simply frequency-domain presentation of experimental input-output data.

Figures D.1 through D.21 plot the parametric estimates of $G_n(s)$ for $n=1, 2,$ and $3,$ over the range of flow coefficients $\bar{\phi} = 0.375$ to $\bar{\phi} = 0.550.$ Where such data is available, a non-parametric spectral estimate of $G_n(s)$ is plotted along with the parametric estimate, for comparison.

Comparing the experimental spectral results and the parametric estimates serves two purposes. First, it shows that there are no significant input-output dynamics which are not accounted for by the model. Second, it allows one to visually judge how well the model fits the data. This is important because of the way the parametric estimates are derived, which is as follows: all of the estimates of Θ for a given mode number n are curve-fit using second order polynomials in $\bar{\phi}.$ The curve-fits are shown in Figures 5.9, 5.10, and 5.11. The curve-fit polynomials are then evaluated at the flow coefficient of a given plot, and the resulting Θ is used to compute $G_n(s).$ Thus each parametric estimate represents a *cumulative* estimates, rather than a curve-fit to the spectral estimate in the figure. Thus these figures (when they include spectral estimates) allow the consistency of the estimates, as well as the variance of the specific experimental results shown, to be qualitatively judged.

A few additional comments are necessary to interpret these results:

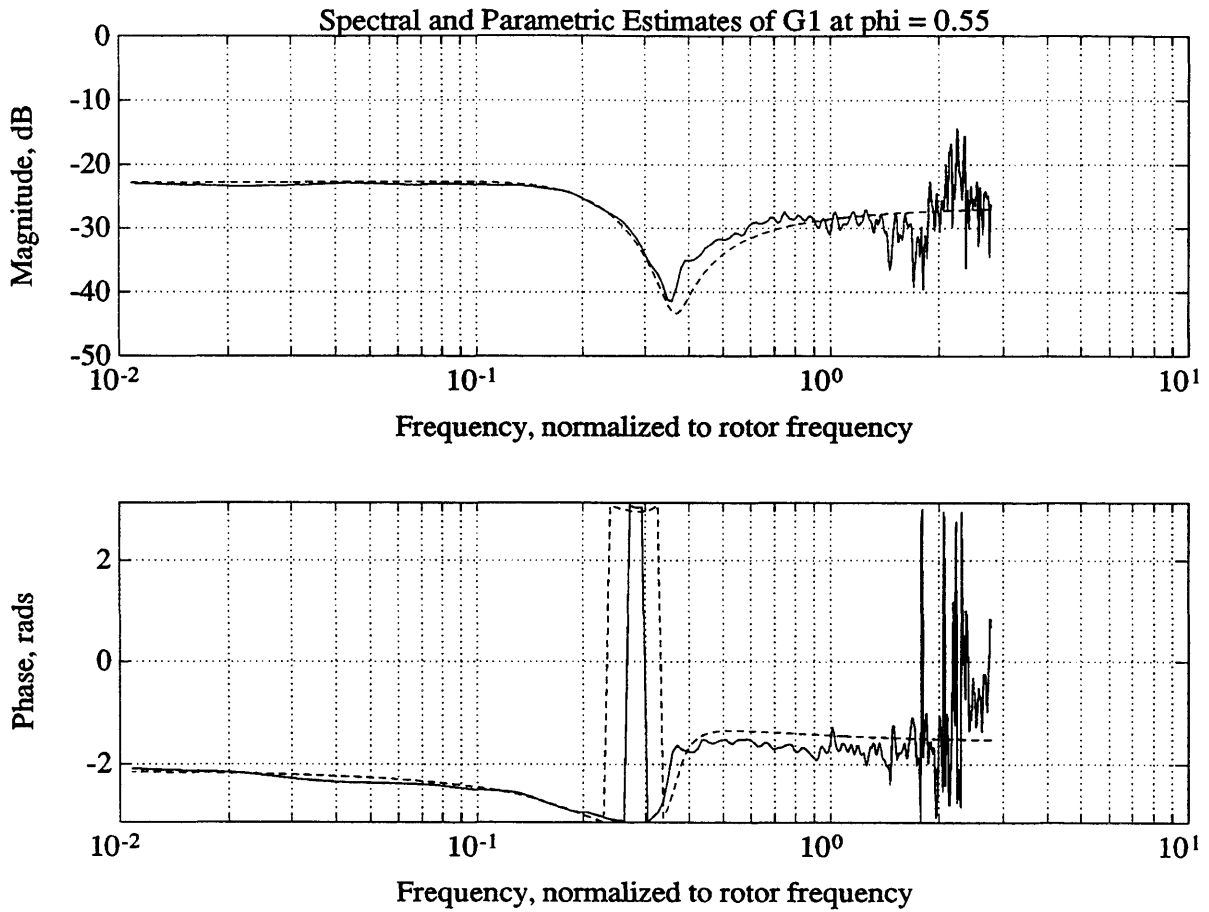
- 1) The variance of the spectral estimates becomes large for frequencies above the rotor frequency (10^0 on the plots) because the excitation is small at these frequencies. The IGVs are being driven by a command which is band-limited, to avoid overheating the motors. Furthermore, the servos are themselves bandlimited to a frequency of about 80 Hz (1.75 times rotor frequency), so very little blade motion above this frequency actually occurs.

The pseudo-random binary signal (PRBS) which commands the servos is

bandlimited by specifying the minimum switch interval in the binary trace (see Equation (5.9) and Figure 5.5 for explanation and an example of a PRBS). Bandlimiting the PRBS in this way causes excitation at certain frequencies to be nearly zero. Figure D.22 shows the PSD of a typical PRBS bandlimited to 50 Hz. This is the bandlimit chosen for most of the experiments presented here. The near-zero amplitude of excitation at 100 Hz causes the variance of the spectral estimates to be very large at this frequency (2.22 in non-dimensional frequency). Thus we judge that 'bumps' in spectral estimates at or near 2.22 are due to this artifact, and do not represent extra dynamics.

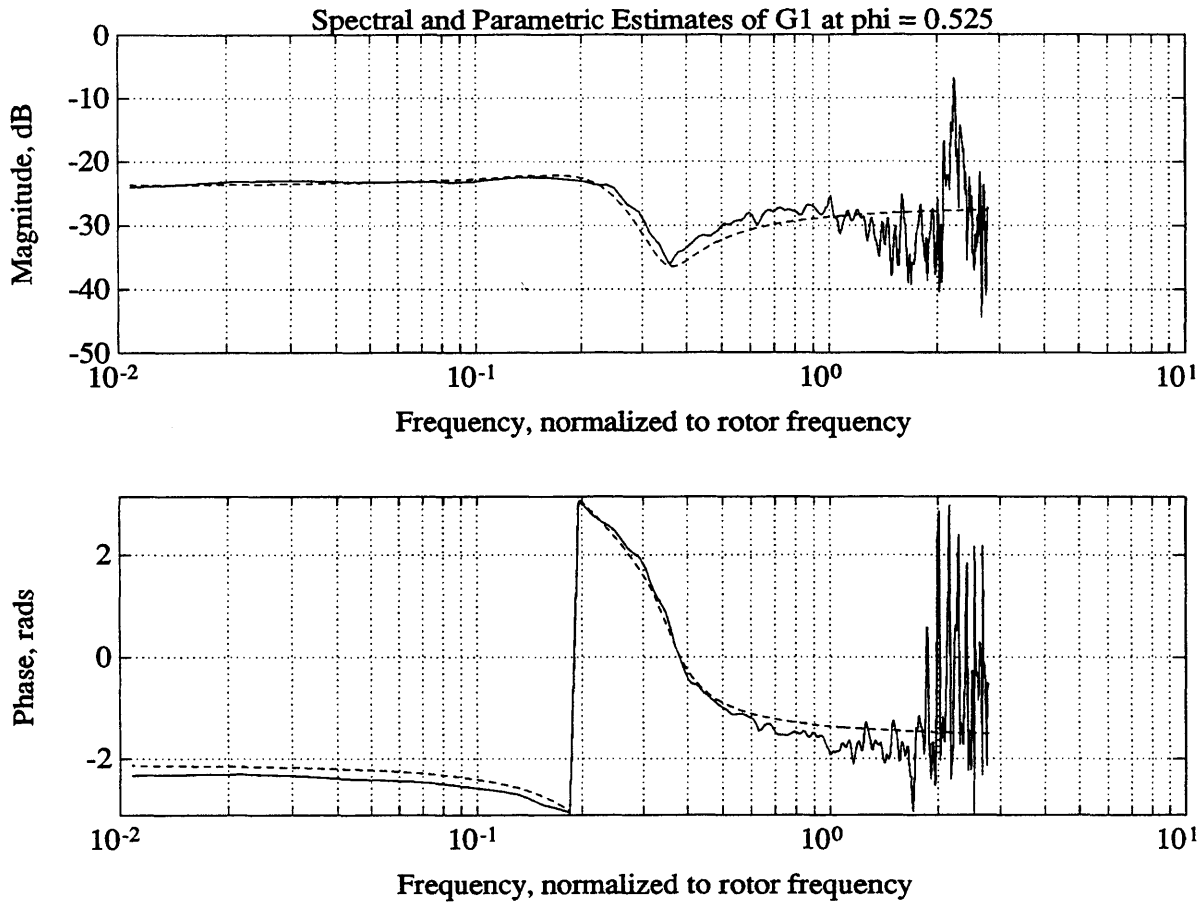
2) Jumps in phase from $-\pi$ to π do not indicate discontinuity in the transfer function. Such jumps result because the phase is confined to lie between $-\pi$ and π , instead of being allowed to vary continuously outside these limits. This artifact sometimes causes the variance at high frequencies to appear much larger than it actually is.

3) Spectral estimates are shown at all flow coefficients where the necessary data is available. The data necessary to compute spectral estimates is open-loop data, based on the discussion of Section 5.2.2. Thus data is unavailable wherever the desired mode is unstable or underdamped. When the system is operating open-loop, underdamped modes tend to resonate strongly enough to 'trip' the nonlinear phenomena which lead to rotating stall, so exciting underdamped modes is impractical. One can, however, stabilize the modes which are not being tested, and excite the mode being tested in an open-loop fashion, if it is sufficiently well damped. This was the procedure used to get the results for the third mode.



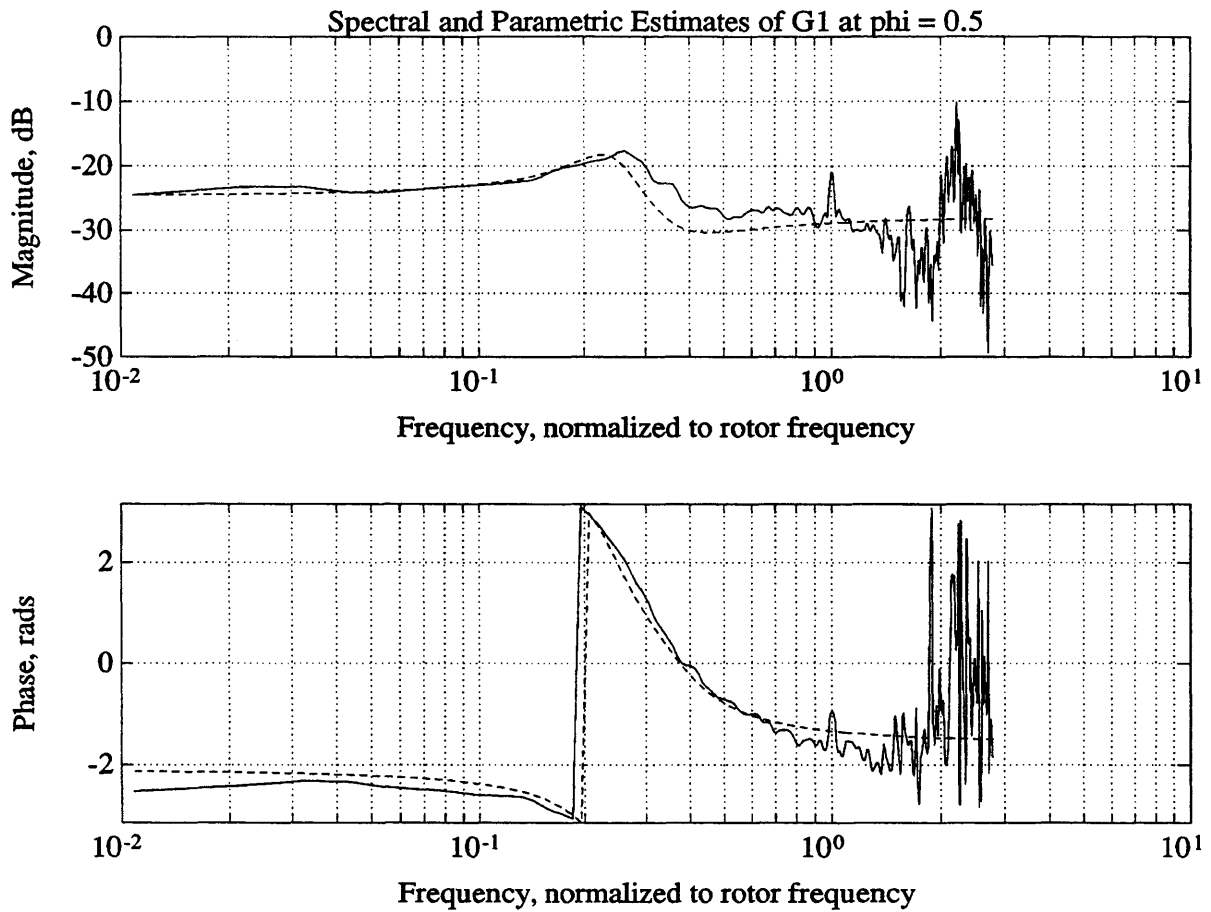
Parameter Set 'Theta' Used to Compute Estimate (dotted curve):
 [-0.146 0.1943 -1.7299e-02 -1.5108e-03 -4.7601e-02]

Figure D.1 - Comparison of a spectral estimate and a parametric estimate of the transfer function G1. Spectral estimate (solid line) was computed from data taken on 07/24/90 using PRBS input signals. Parametric estimate uses the estimate of 'Theta' shown. This estimate comes from the curve fits in Figure 5.9.



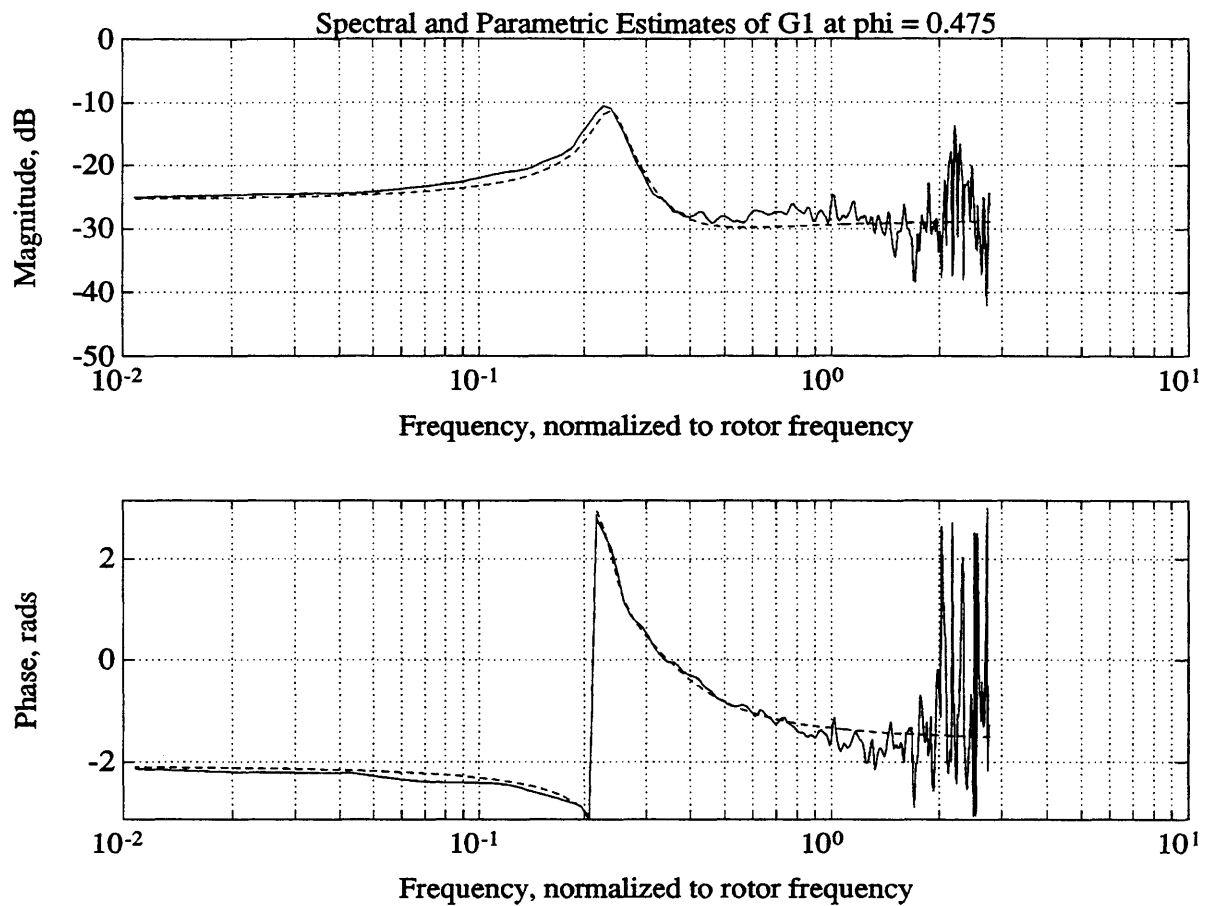
Parameter Set 'Theta' Used to Compute Estimate (dotted curve):
 [-9.0715e-02 0.2235 -1.5312e-02 2.4285e-03 -4.3900e-02]

Figure D.2 - Comparison of a spectral estimate and a parametric estimate of the transfer function G1. Spectral estimate (solid line) was computed from data taken on 07/24/90 using PRBS input signals. Parametric estimate uses the estimate of 'Theta' shown. This estimate comes from the curve fits in Figure 5.9.



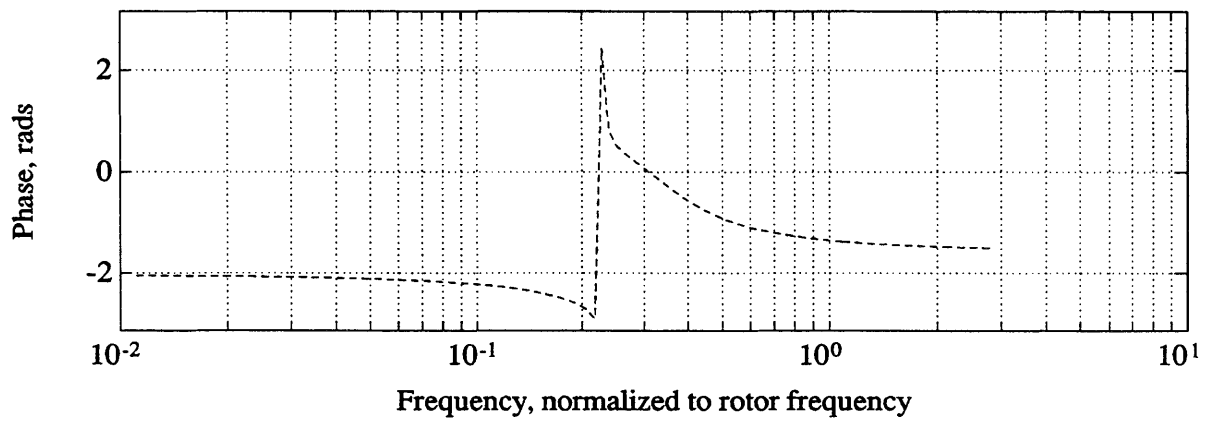
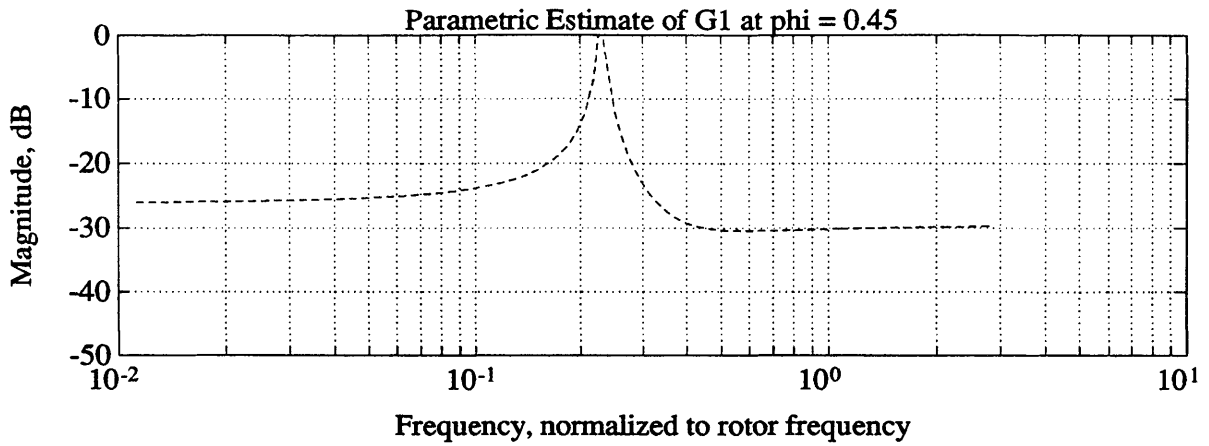
Parameter Set 'Theta' Used to Compute Estimate (dotted curve):
 [-5.0172e-02 0.2375 -1.3439e-02 4.5846e-03 -4.0407e-02]

Figure D.3 - Comparison of a spectral estimate and a parametric estimate of the transfer function G1. Spectral estimate (solid line) was computed from data taken on 07/24/90 using PRBS input signals. Parametric estimate uses the estimate of 'Theta' shown. This estimate comes from the curve fits in Figure 5.9.



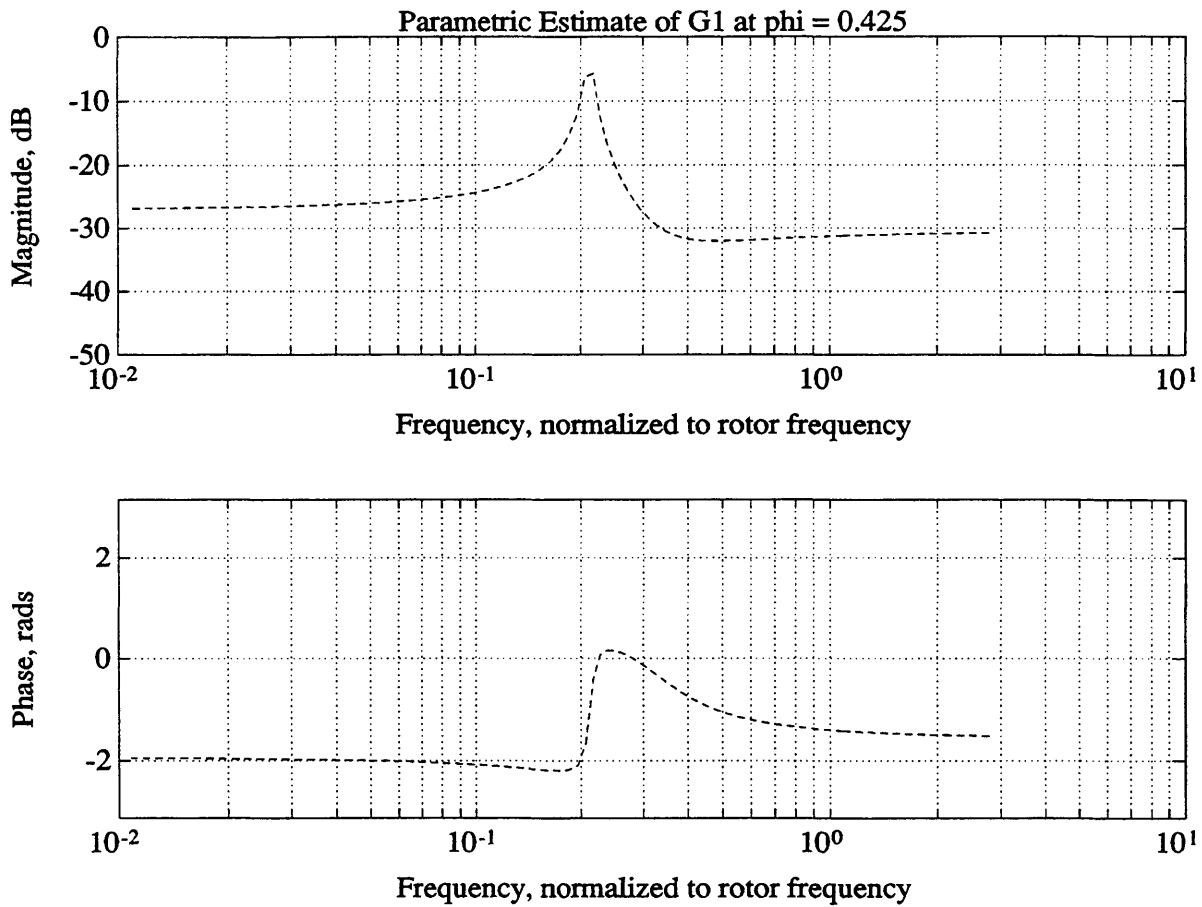
Parameter Set 'Theta' Used to Compute Estimate (dotted curve):
 $[-2.1968e-02 \ 0.2386 \ -1.1696e-02 \ 5.2888e-03 \ -3.6969e-02]$

Figure D.4 - Comparison of a spectral estimate and a parametric estimate of the transfer function G1. Spectral estimate (solid line) was computed from data taken on 07/24/90 using PRBS input signals. Parametric estimate uses the estimate of 'Theta' shown. This estimate comes from the curve fits in Figure 5.9.



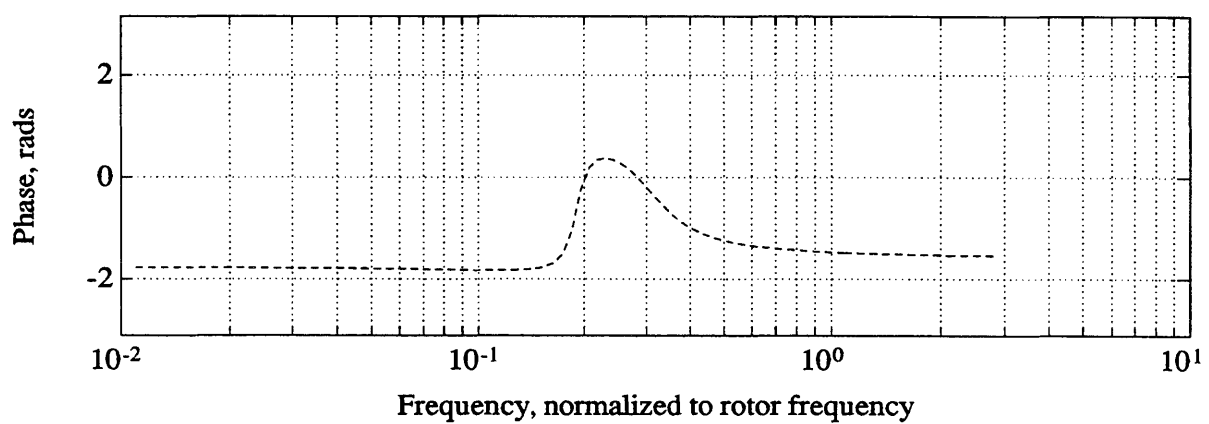
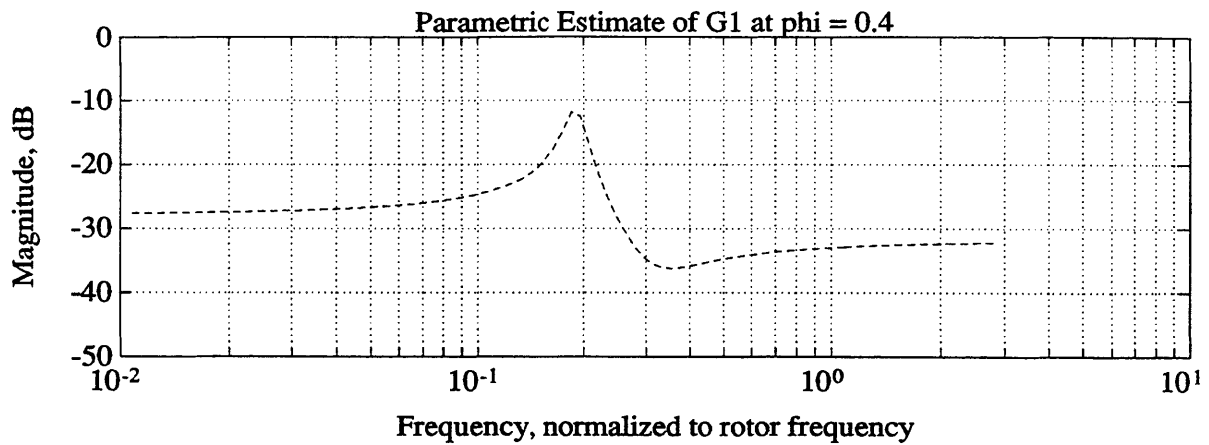
Parameter Set 'Theta' Used to Compute Estimate (dotted curve):
 [-3.7455e-03 0.2294 -1.0104e-02 4.8725e-03 -3.3432e-02]

Figure D.5 - Parametric estimate of the transfer function G1 (a Spectral estimate is not available at this flow coefficient because system cannot be excited open-loop). Parametric estimate uses the estimate of 'Theta' shown above. This estimate comes from the curve fits in Figure 5.9.



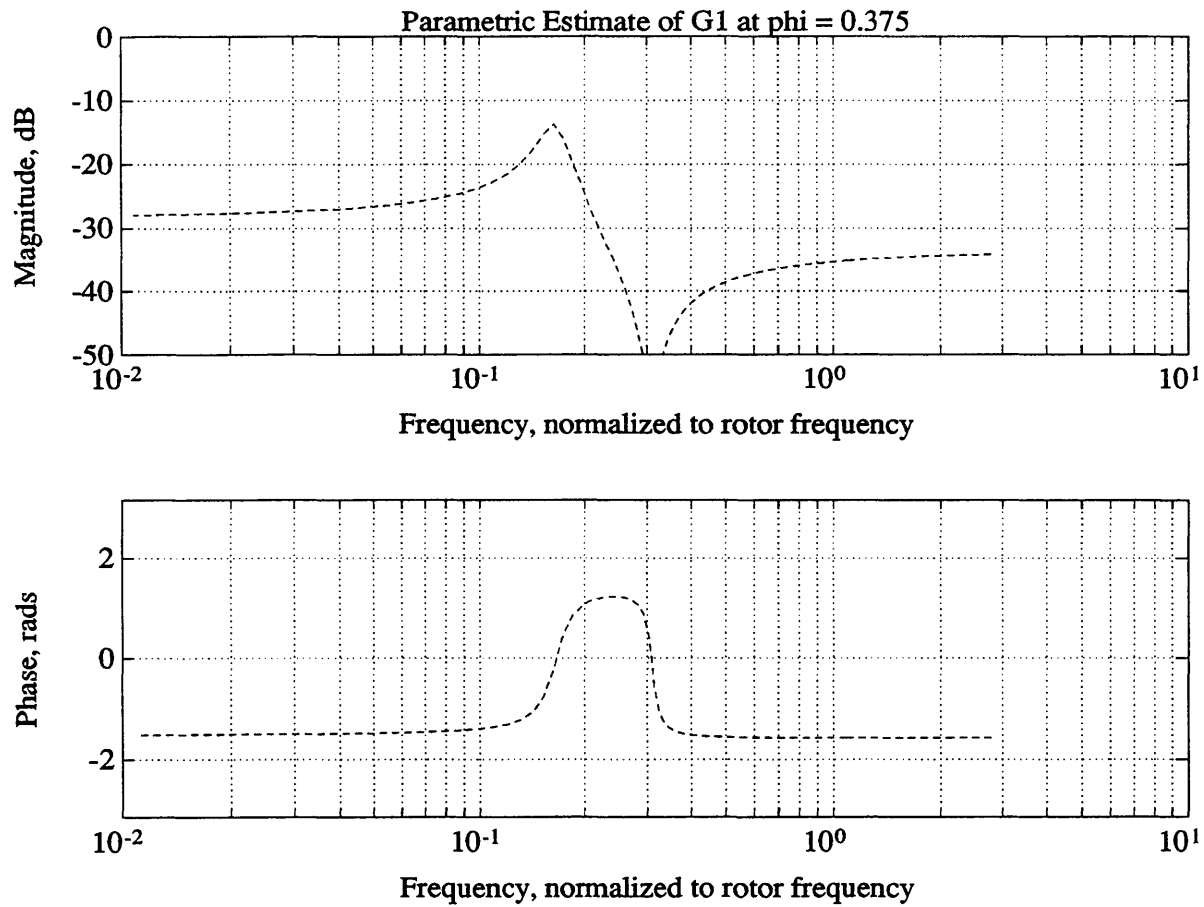
Parameter Set 'Theta' Used to Compute Estimate (dotted curve):
 [6.8511e-03 0.2123 -8.6784e-03 3.6670e-03 -2.9643e-02]

Figure D.6 - Parametric estimate of the transfer function G1 (a Spectral estimate is not available at this flow coefficient because system cannot be excited open-loop). Parametric estimate uses the estimate of 'Theta' shown above. This estimate comes from the curve fits in Figure 5.9.



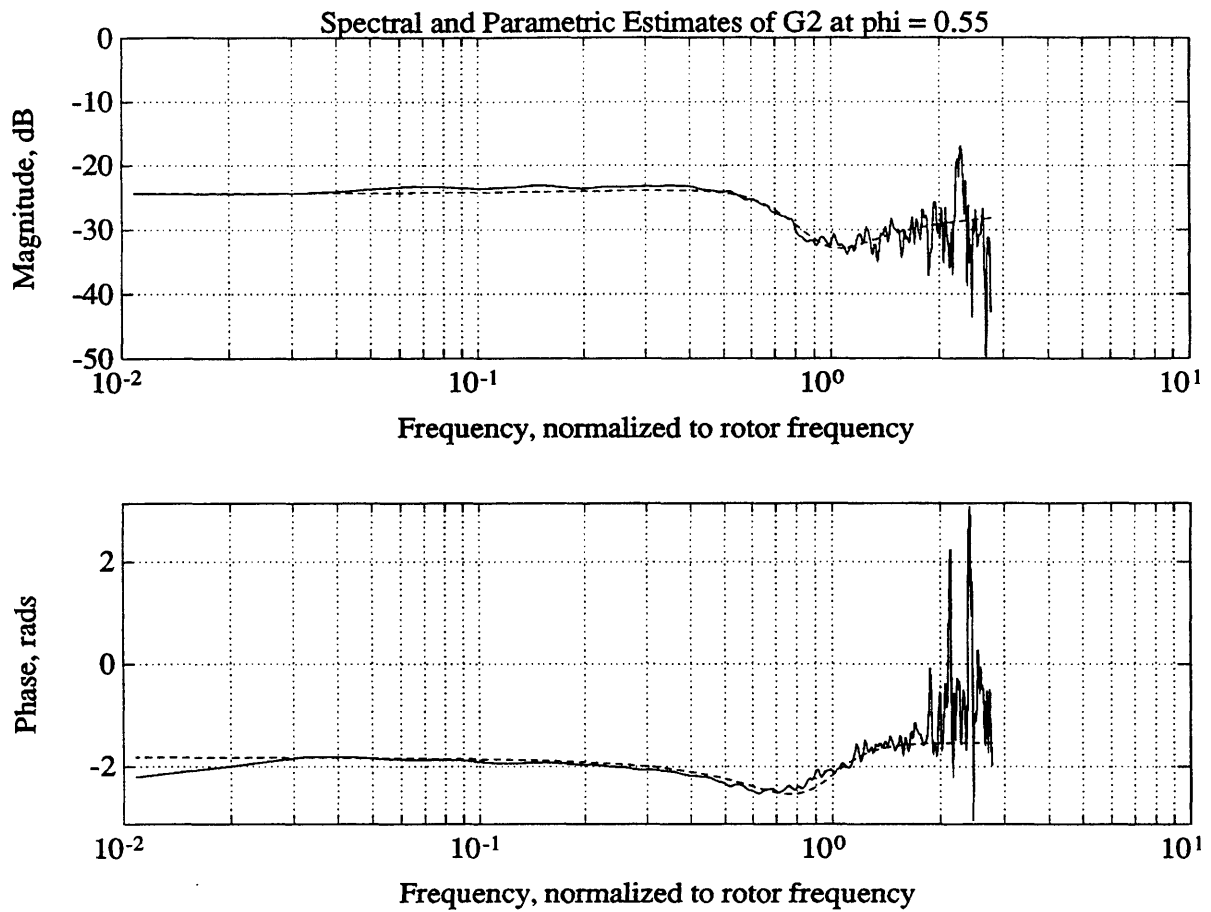
Parameter Set 'Theta' Used to Compute Estimate (dotted curve):
 [1.2179e-02 0.1898 -7.4386e-03 2.0037e-03 -2.5449e-02]

Figure D.7 - Parametric estimate of the transfer function G1 (a Spectral estimate is not available at this flow coefficient because system cannot be excited open-loop). Parametric estimate uses the estimate of 'Theta' shown above. This estimate comes from the curve fits in Figure 5.9.



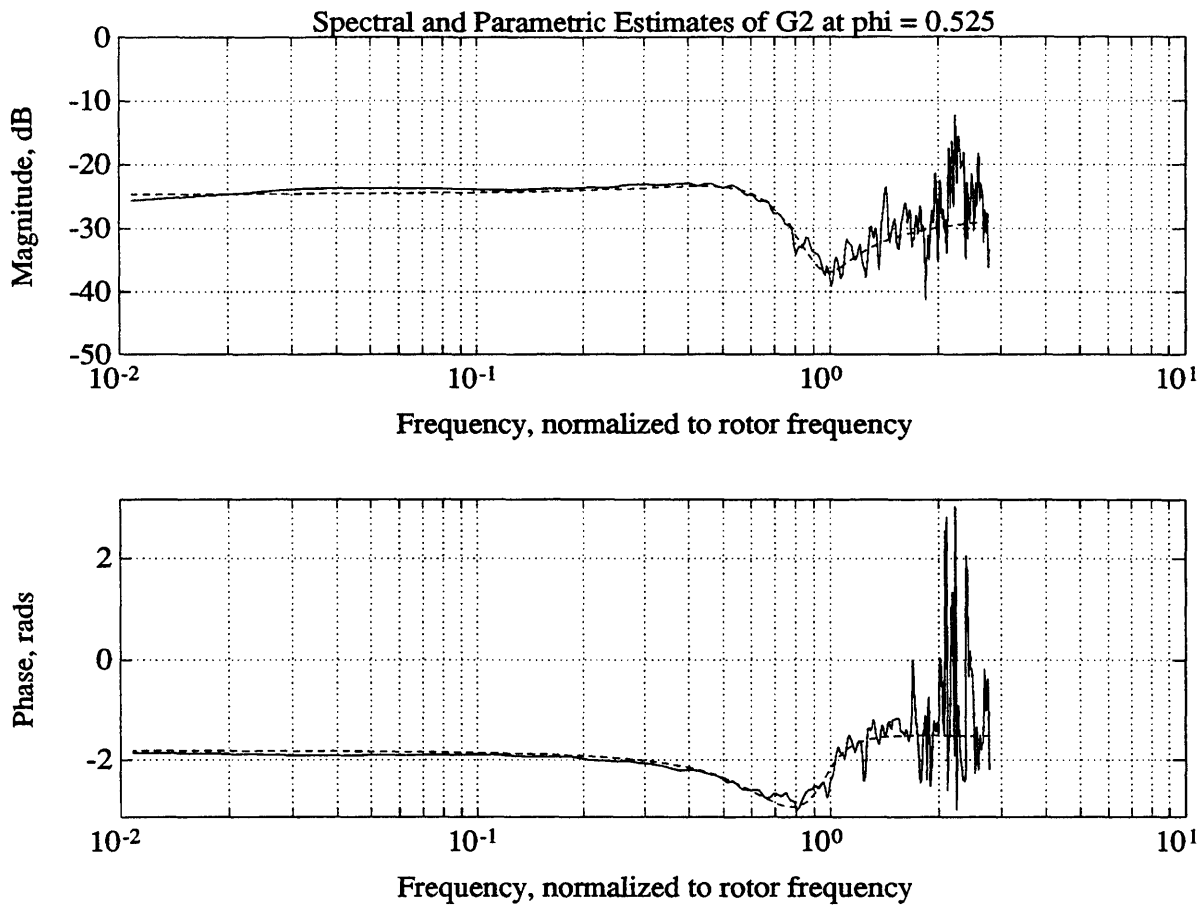
Parameter Set 'Theta' Used to Compute Estimate (dotted curve):
 [1.4596e-02 0.1644 -6.4022e-03 2.1386e-04 -2.0695e-02]

Figure D.8 - Parametric estimate of the transfer function G1 (a Spectral estimate is not available at this flow coefficient because system cannot be excited open-loop). Parametric estimate uses the estimate of 'Theta' shown above. This estimate comes from the curve fits in Figure 5.9.



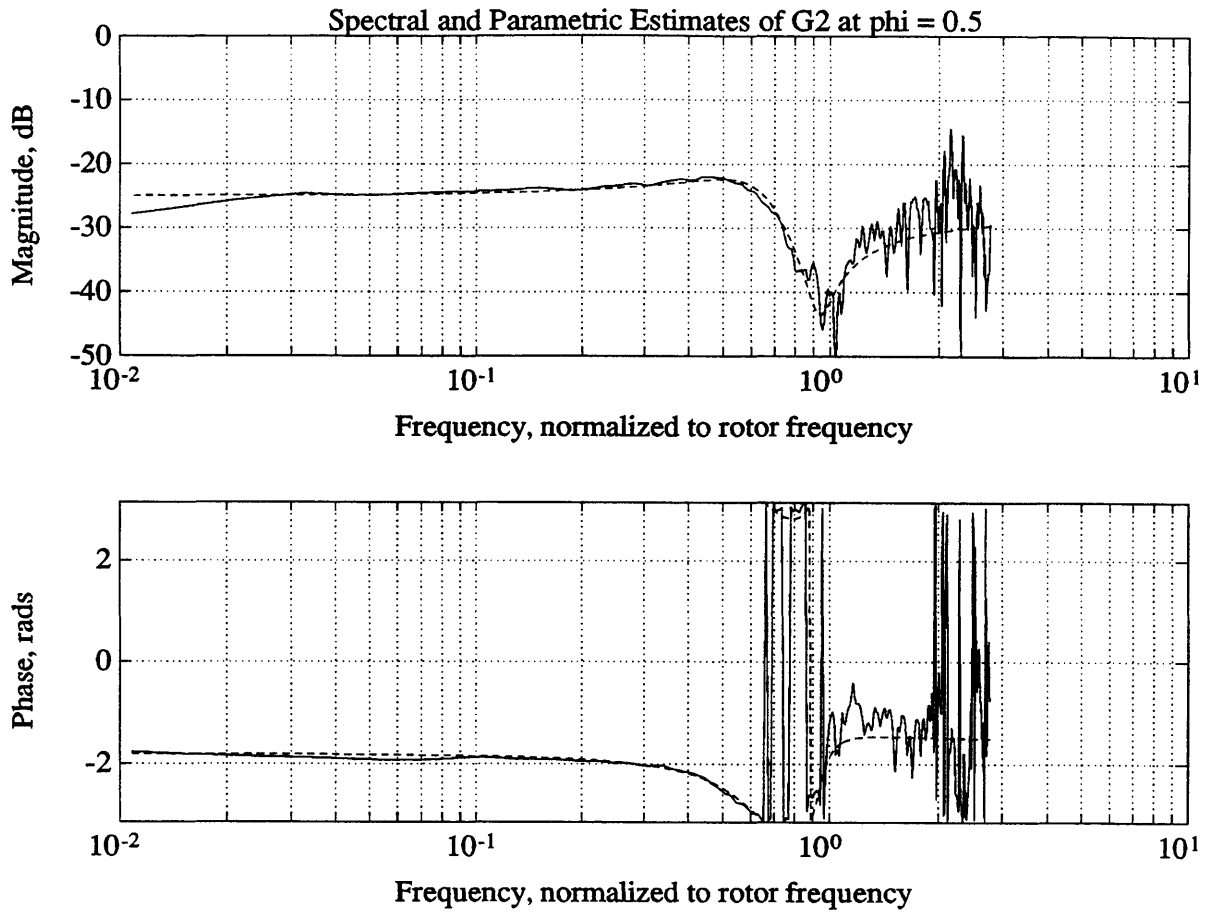
Parameter Set 'Theta' Used to Compute Estimate (dotted curve):
 [-0.3541 0.6508 -4.3323e-02 -1.1195e-02 -4.5340e-02]

Figure D.9 - Comparison of a spectral estimate and a parametric estimate of the transfer function G2. Spectral estimate (solid line) was computed from data taken on 07/24/90 using PRBS input signals. Parametric estimate uses the estimate of 'Theta' shown. This estimate comes from the curve fits in Figure 5.10.



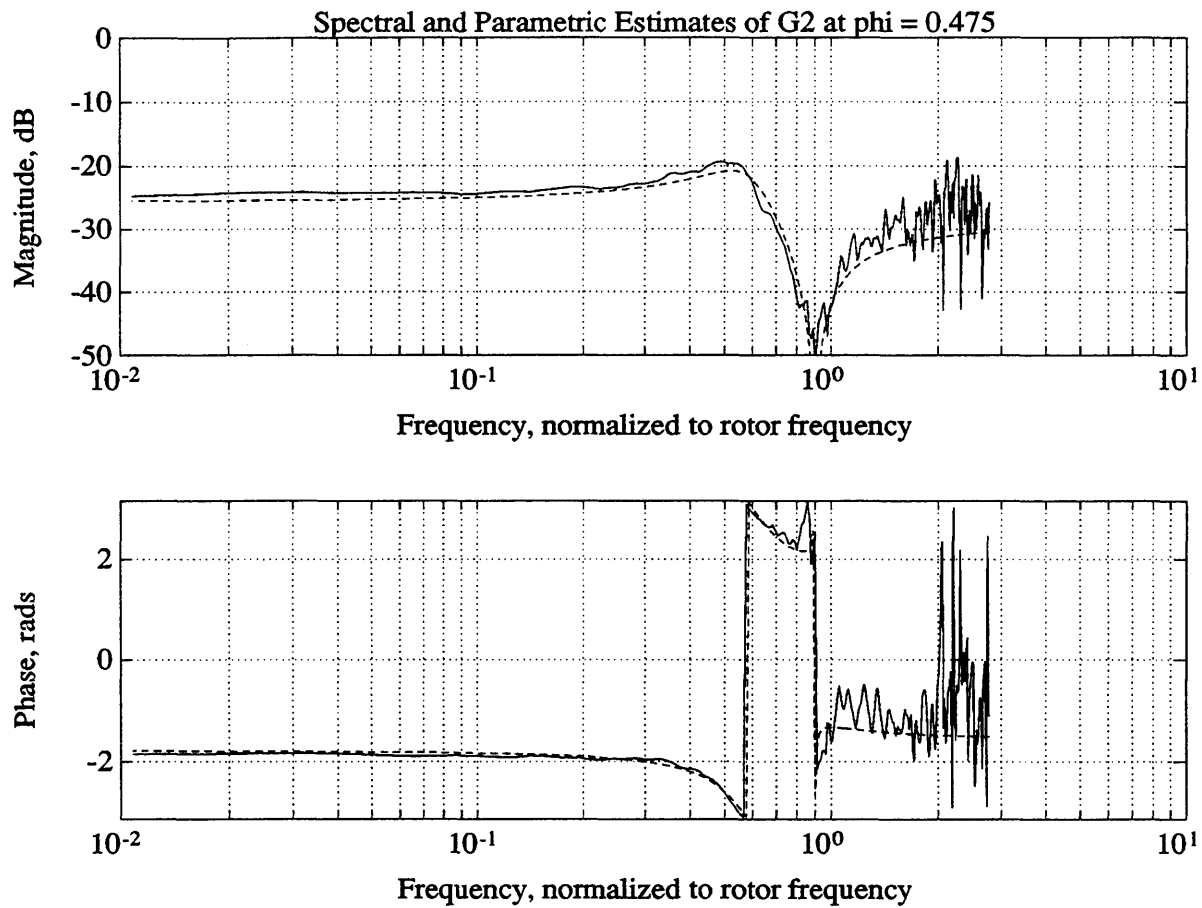
Parameter Set 'Theta' Used to Compute Estimate (dotted curve):
 [-0.2645 0.6349 -3.9740e-02 -6.0778e-03 -4.1880e-02]

Figure D.10 - Comparison of a spectral estimate and a parametric estimate of the transfer function G2. Spectral estimate (solid line) was computed from data taken on 07/24/90 using PRBS input signals. Parametric estimate uses the estimate of 'Theta' shown. This estimate comes from the curve fits in Figure 5.10.



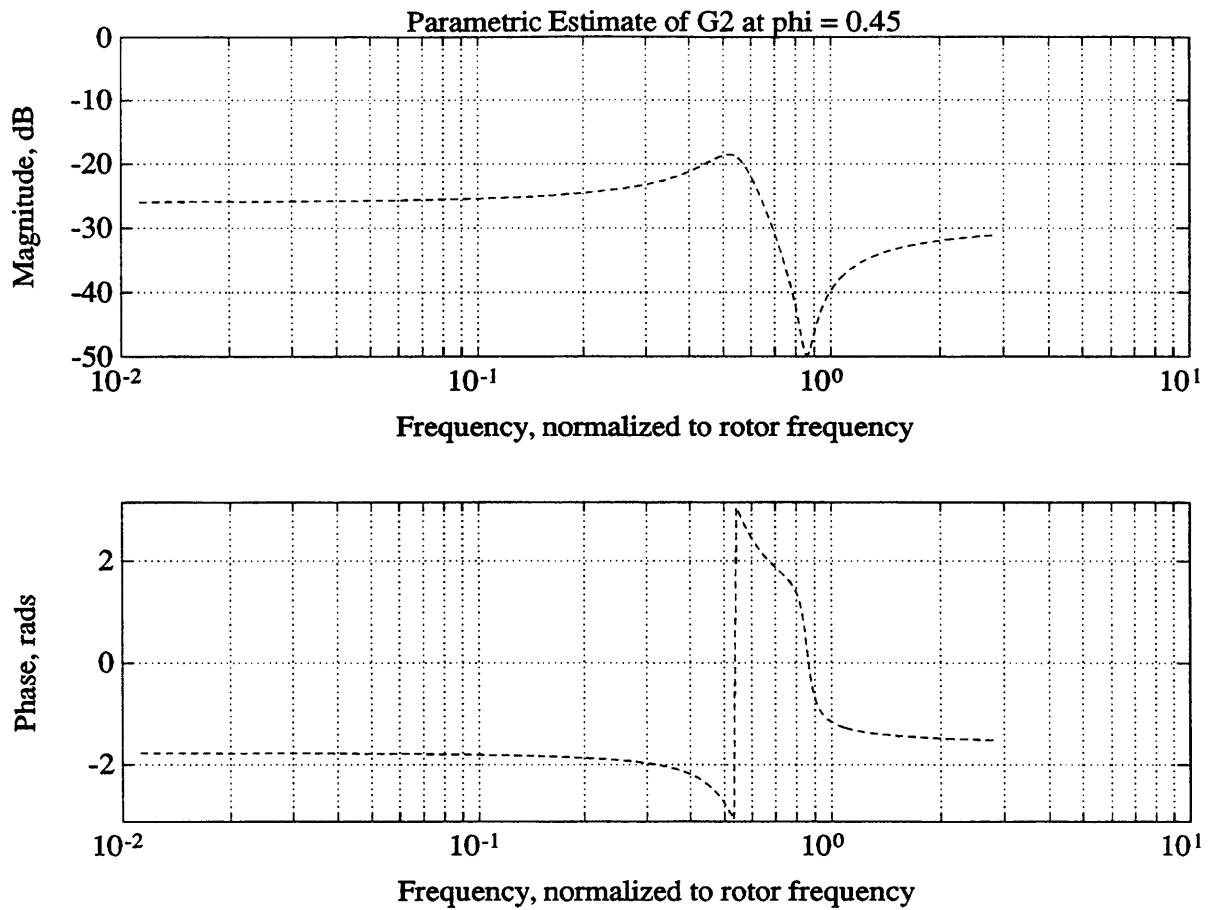
Parameter Set 'Theta' Used to Compute Estimate (dotted curve):
 [-0.1919 0.6101 -3.5769e-02 -2.5194e-03 -3.8426e-02]

Figure D.11 - Comparison of a spectral estimate and a parametric estimate of the transfer function G2. Spectral estimate (solid line) was computed from data taken on 07/24/90 using PRBS input signals. Parametric estimate uses the estimate of 'Theta' shown. This estimate comes from the curve fits in Figure 5.10.



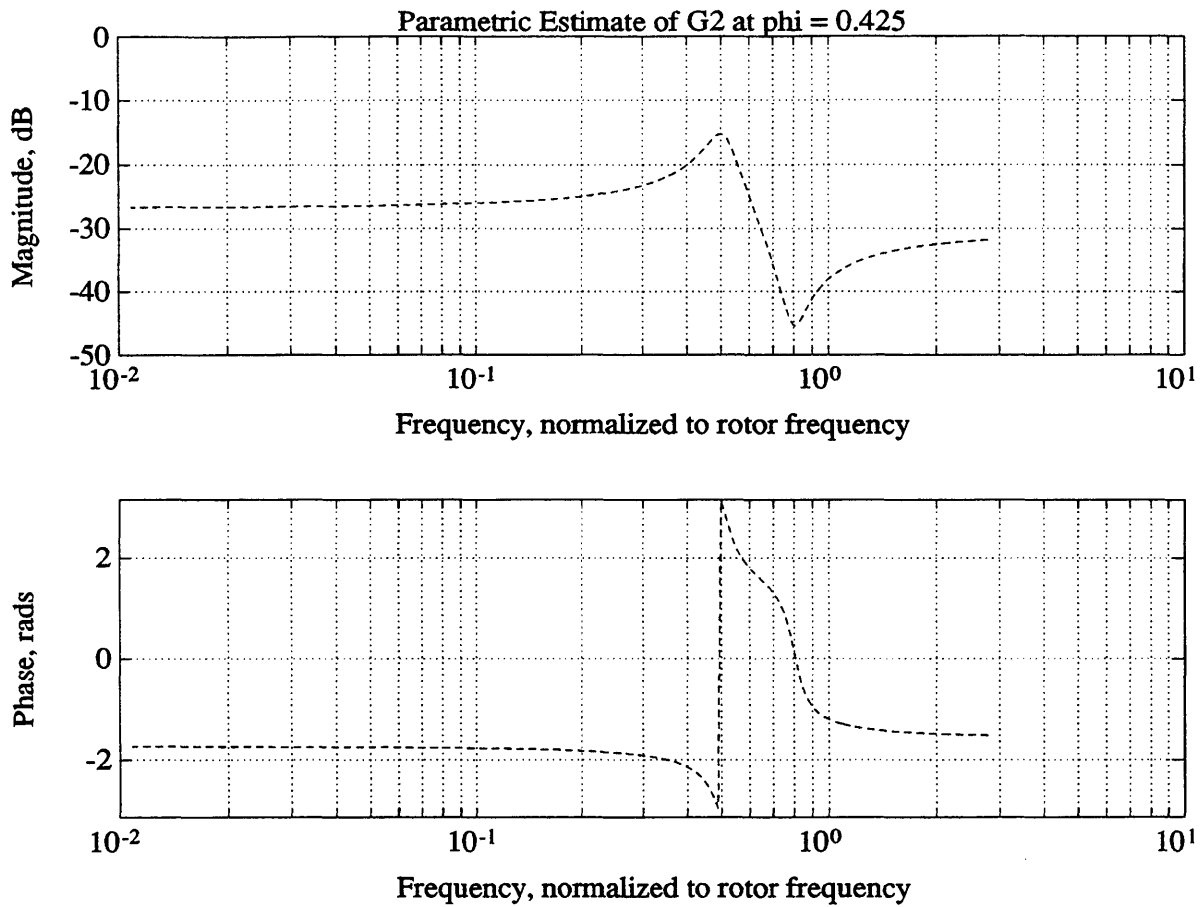
Parameter Set 'Theta' Used to Compute Estimate (dotted curve):
 [-0.1337 0.5788 -3.1597e-02 -2.3927e-04 -3.5102e-02]

Figure D.12 - Comparison of a spectral estimate and a parametric estimate of the transfer function G2. Spectral estimate (solid line) was computed from data taken on 07/24/90 using PRBS input signals. Parametric estimate uses the estimate of 'Theta' shown. This estimate comes from the curve fits in Figure 5.10.



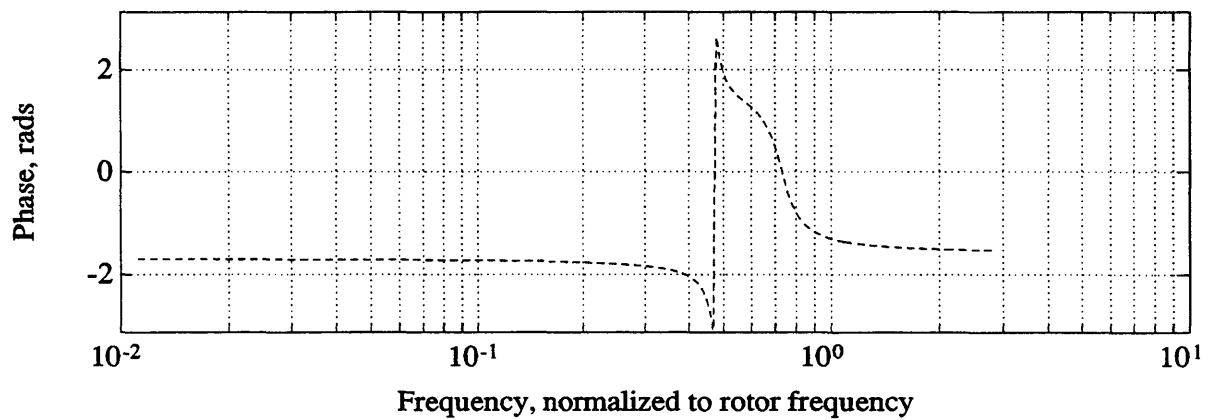
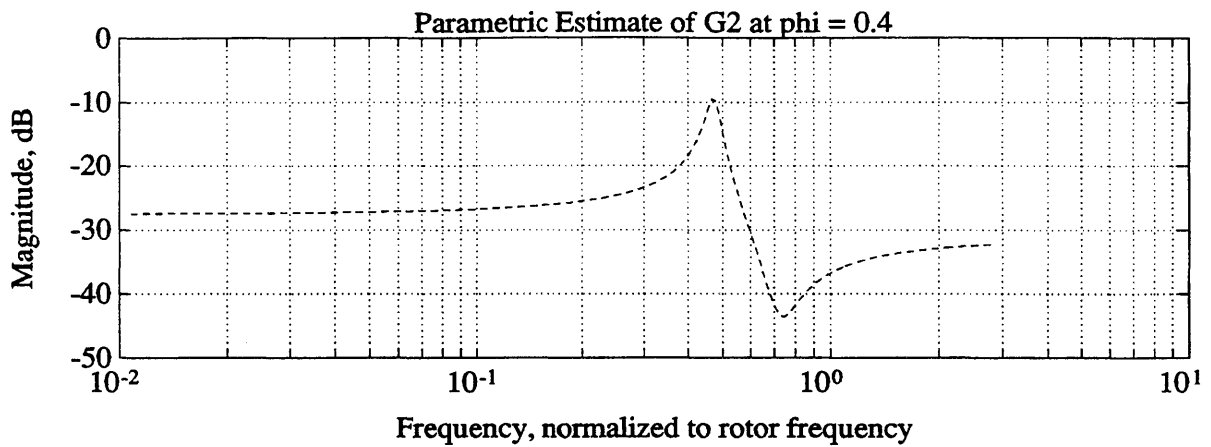
Parameter Set 'Theta' Used to Compute Estimate (dotted curve):
 [-8.7480e-02 0.5437 -2.7407e-02 1.0428e-03 -3.2035e-02]

Figure D.13 - Parametric estimate of the transfer function G2 (a Spectral estimate is not available at this flow coefficient because system cannot be excited open-loop). Parametric estimate uses the estimate of 'Theta' shown above. This estimate comes from the curve fits in Figure 5.10.



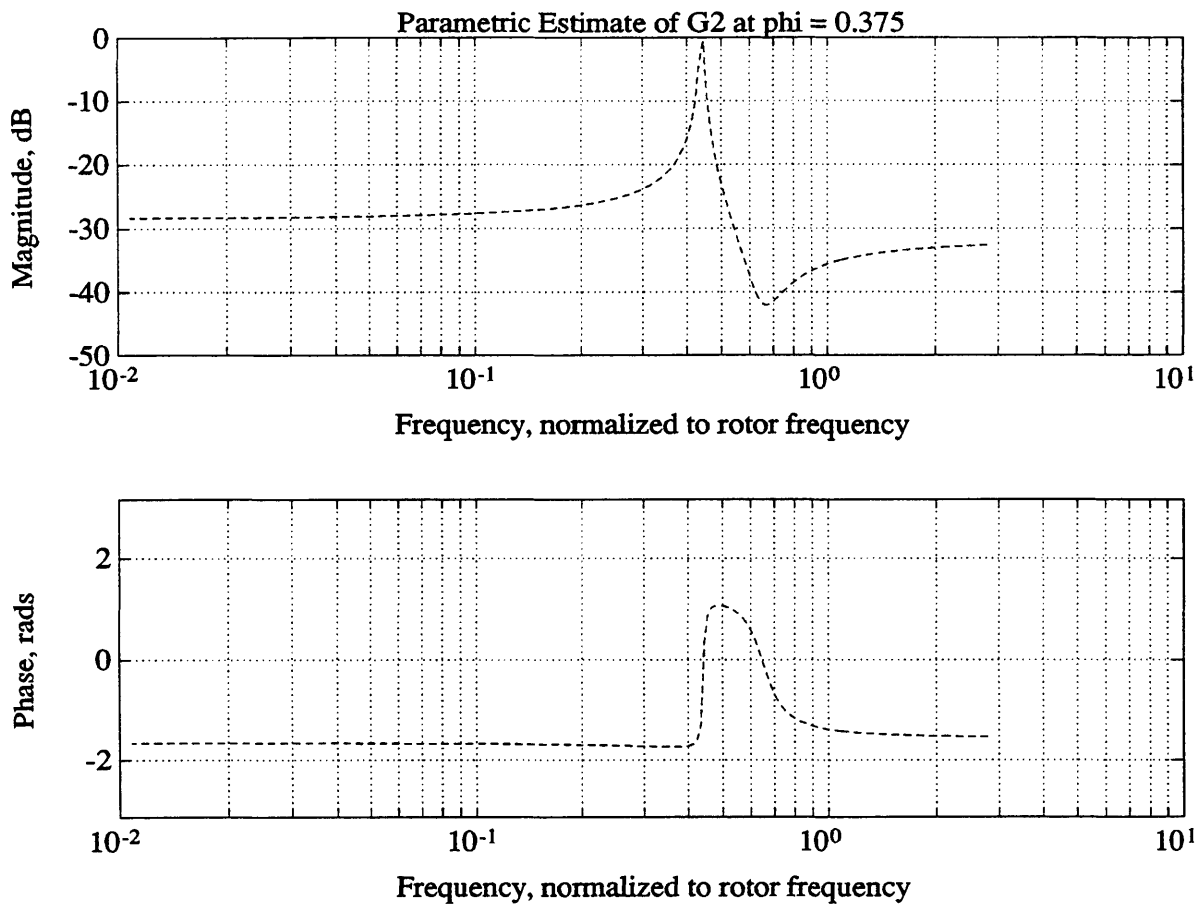
Parameter Set 'Theta' Used to Compute Estimate (dotted curve):
 [-5.0688e-02 0.5073 -2.3385e-02 1.6070e-03 -2.9351e-02]

Figure D.14 - Parametric estimate of the transfer function G2 (a Spectral estimate is not available at this flow coefficient because system cannot be excited open-loop). Parametric estimate uses the estimate of 'Theta' shown above. This estimate comes from the curve fits in Figure 5.10.



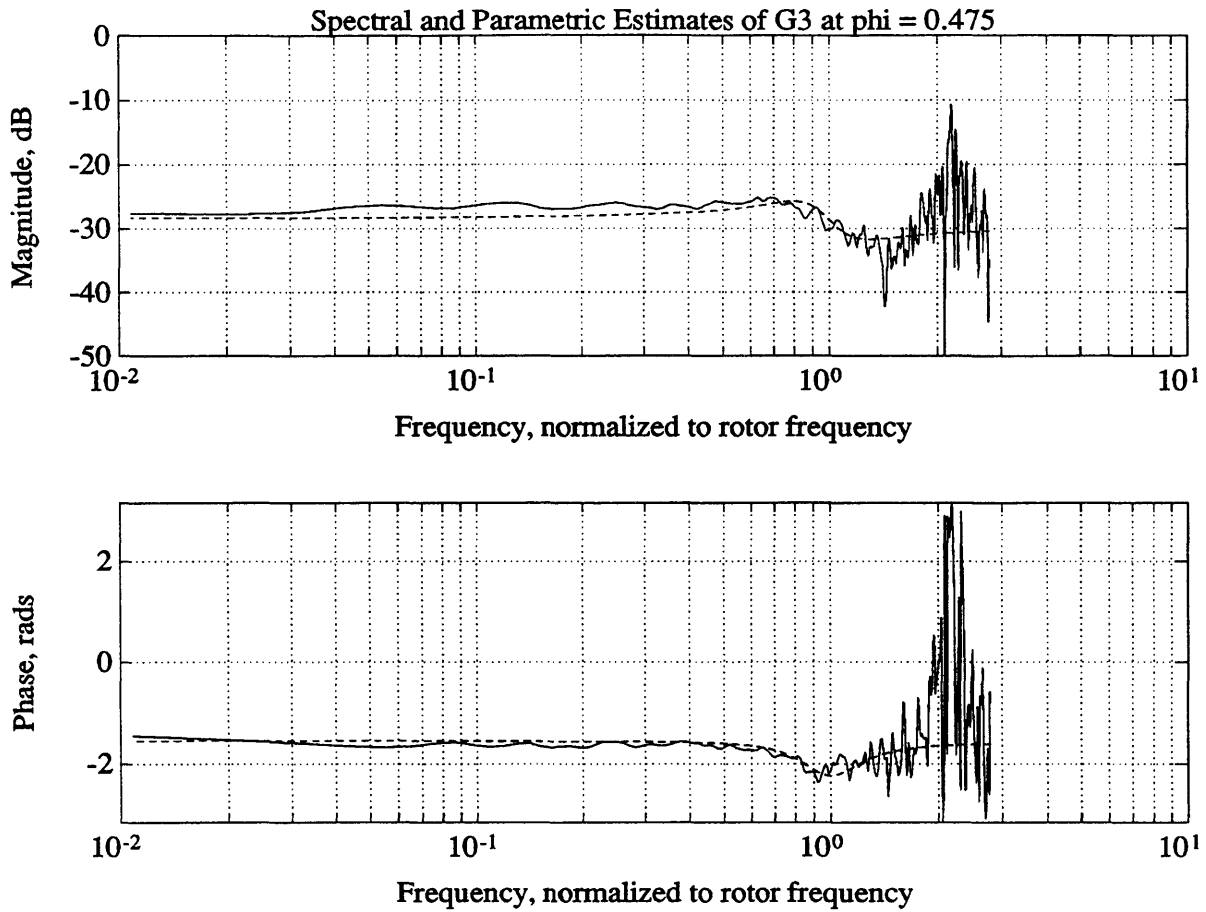
Parameter Set 'Theta' Used to Compute Estimate (dotted curve):
 [-2.0834e-02 0.4724 -1.9715e-02 1.7339e-03 -2.7174e-02]

Figure D.15 - Parametric estimate of the transfer function G2 (a Spectral estimate is not available at this flow coefficient because system cannot be excited open-loop). Parametric estimate uses the estimate of 'Theta' shown above. This estimate comes from the curve fits in Figure 5.10.



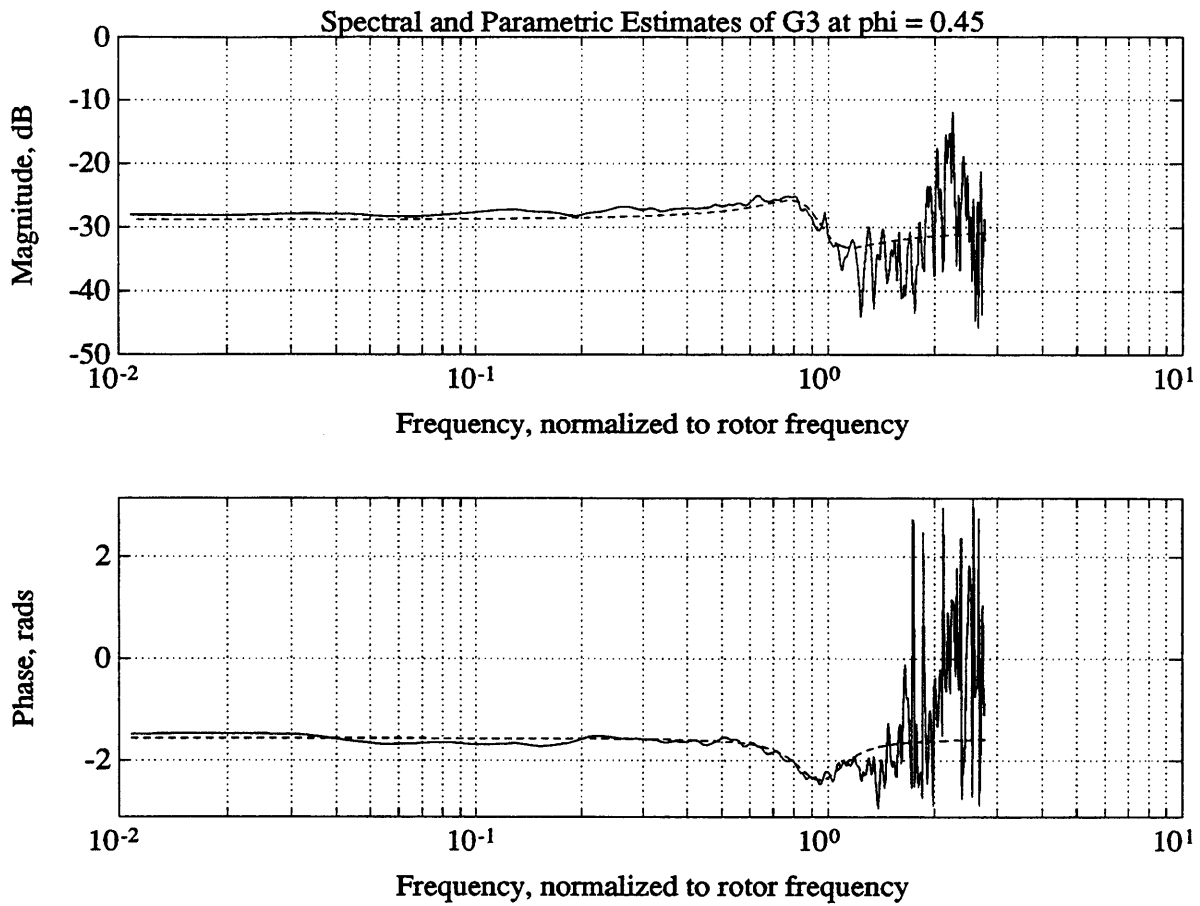
Parameter Set 'Theta' Used to Compute Estimate (dotted curve):
 [4.5851e-03 0.4414 -1.6584e-02 1.7036e-03 -2.5630e-02]

Figure D.16 - Parametric estimate of the transfer function G2 (a Spectral estimate is not available at this flow coefficient because system cannot be excited open-loop). Parametric estimate uses the estimate of 'Theta' shown above. This estimate comes from the curve fits in Figure 5.10.



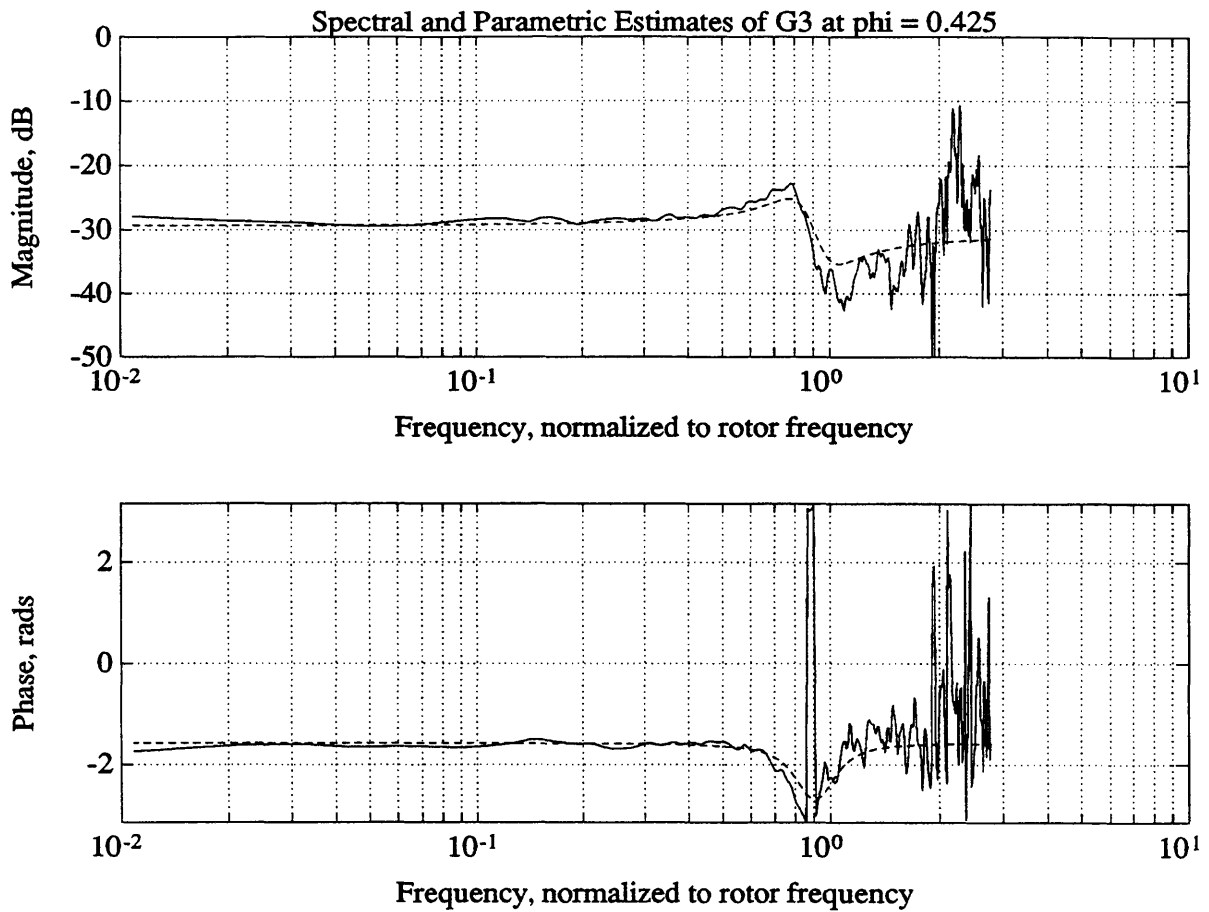
Parameter Set 'Theta' Used to Compute Estimate (dotted curve):
 [-0.1991 0.8949 -3.3955e-02 -8.1687e-03 -3.2542e-02]

Figure D.17 - Comparison of a spectral estimate and a parametric estimate of the transfer function G3. Spectral estimate (solid line) was computed from data taken on 05/10/91 using PRBS input signals. Parametric estimate uses the estimate of 'Theta' shown. This estimate comes from the curve fits in Figure 5.11.



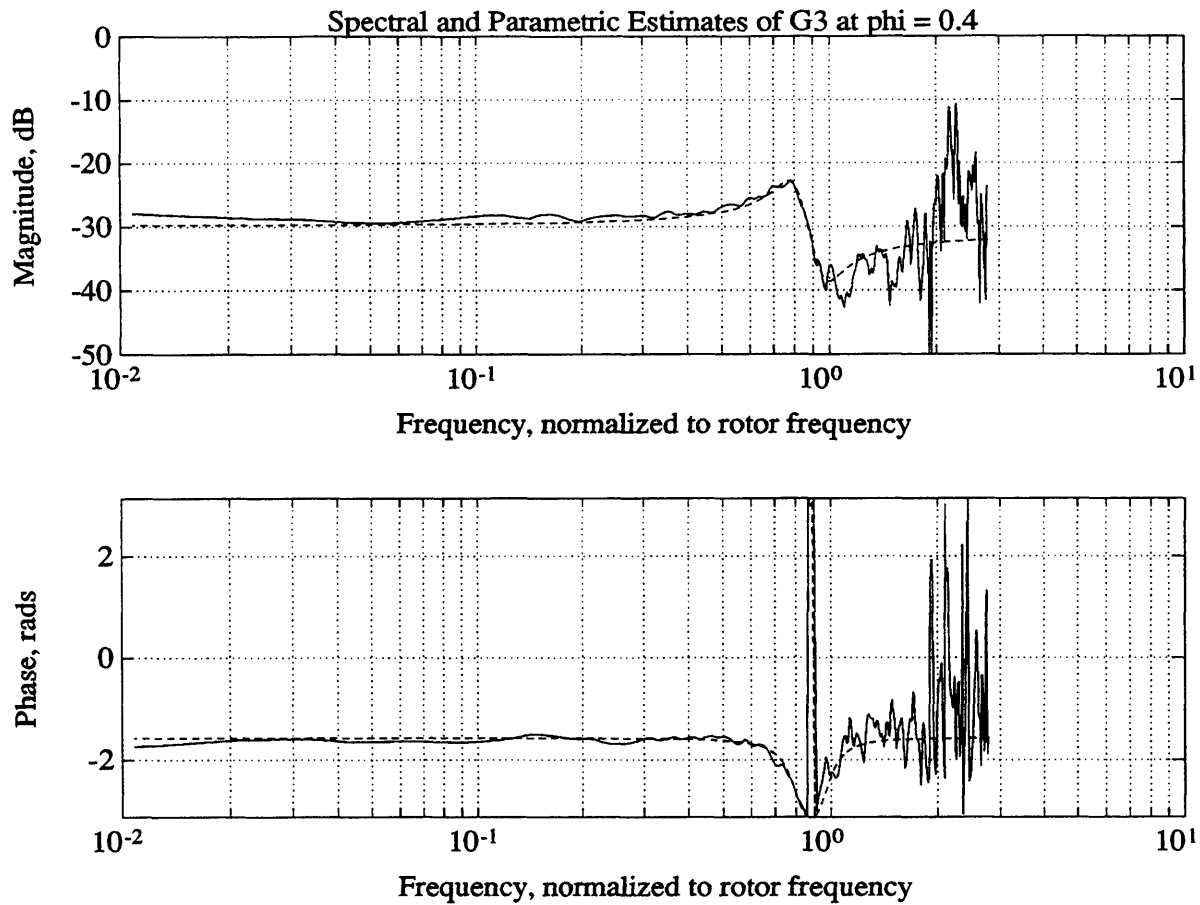
Parameter Set 'Theta' Used to Compute Estimate (dotted curve):
 [-0.1568 0.8619 -3.0972e-02 -5.7113e-03 -3.0724e-02]

Figure D.18 - Comparison of a spectral estimate and a parametric estimate of the transfer function G3. Spectral estimate (solid line) was computed from data taken on 05/10/91 using PRBS input signals. Parametric estimate uses the estimate of 'Theta' shown. This estimate comes from the curve fits in Figure 5.11.



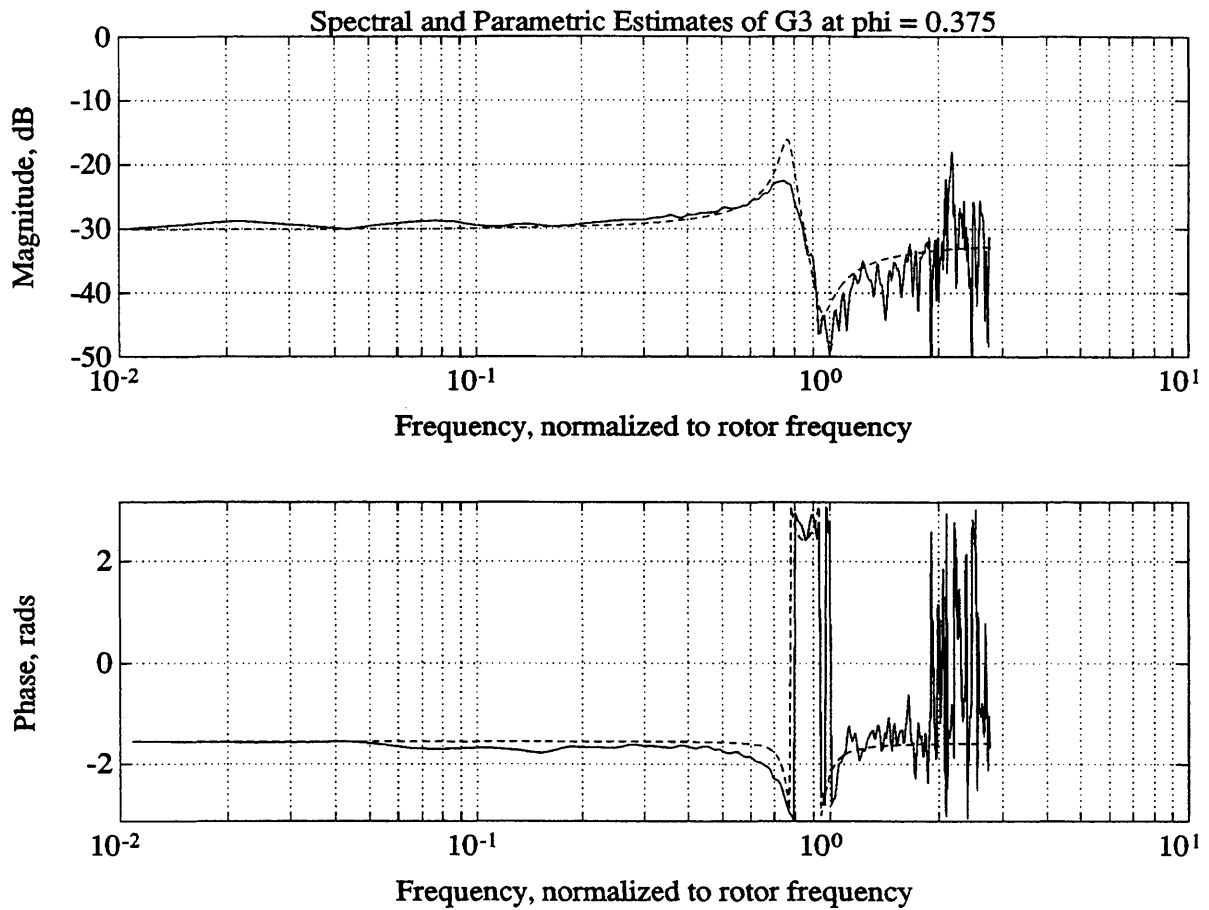
Parameter Set 'Theta' Used to Compute Estimate (dotted curve):
 [-0.1145 0.8294 -2.8268e-02 -3.7262e-03 -2.8870e-02]

Figure D.19 - Comparison of a spectral estimate and a parametric estimate of the transfer function G3. Spectral estimate (solid line) was computed from data taken on 05/10/91 using PRBS input signals. Parametric estimate uses the estimate of 'Theta' shown. This estimate comes from the curve fits in Figure 5.11.



Parameter Set 'Theta' Used to Compute Estimate (dotted curve):
 $[-7.2252e-02 \quad 0.7982 \quad -2.5868e-02 \quad -2.2459e-03 \quad -2.7001e-02]$

Figure D.20 - Comparison of a spectral estimate and a parametric estimate of the transfer function G3. Spectral estimate (solid line) was computed from data taken on 05/10/91 using PRBS input signals. Parametric estimate uses the estimate of 'Theta' shown. This estimate comes from the curve fits in Figure 5.11.



Parameter Set 'Theta' Used to Compute Estimate (dotted curve):
 [-2.9955e-02 0.7689 -2.3800e-02 -1.3029e-03 -2.5140e-02]

Figure D.21 - Comparison of a spectral estimate and a parametric estimate of the transfer function G3. Spectral estimate (solid line) was computed from data taken on 01/31/91 using PRBS input signals. Parametric estimate uses the estimate of 'Theta' shown. This estimate comes from the curve fits in Figure 5.11.

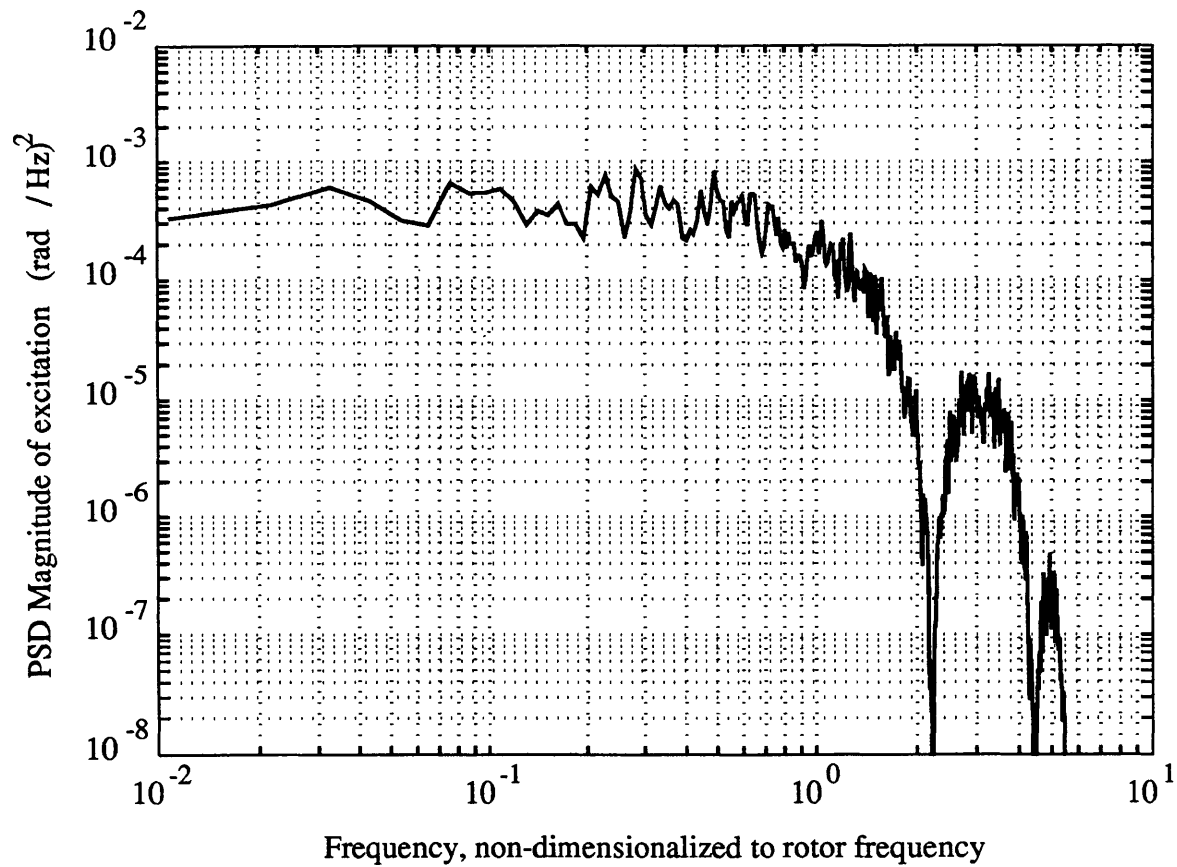


Figure D.22 - PSD of a typical PRBS used to drive the IGVs during a spectral estimation experiment.